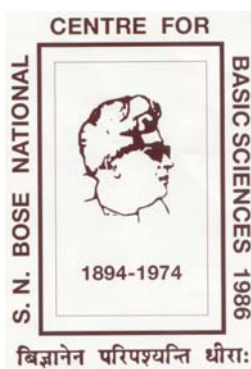


# **STUDY OF LOW FREQUENCY CONDUCTION FLUCTUATIONS IN PEROVSKITE MANGANITES**

A THESIS  
SUBMITTED FOR THE DEGREE OF  
*Doctor Of Philosophy*  
IN THE FACULTY OF SCIENCE

by  
**Sudeshna Samanta**



Department of Material Science  
S. N. Bose National Centre for Basic Sciences  
Salt Lake, Kolkata 700 098, India.  
July 2009

*for my  
Grandmother and Mother*

*..... origin of inspirations*

# **Declaration**

The work reported in this thesis titled “*Study of Low Frequency Conduction Fluctuations in Perovskite Manganites*” is original and was carried out by me during my tenure as a Ph.D student at the Department of Material Science, S. N. Bose National Centre for Basic Sciences, Kolkata, India under the supervision of Prof. A. K. Raychaudhuri. This thesis has not formed the basis for the award of any degree, diploma, associateship, membership or similar title of any university or institution.

**(Sudeshna Samanta)**

Date:

Department of Material Science  
S. N. Bose National Centre for Basic Sciences  
Salt Lake, Kolkata, India.

# Acknowledgement

I wish to express my deep sense of gratitude to my supervisor Prof. A. K. Raychaudhuri for his guidance and constant inspirations throughout the course of my research work. The mentoring that I received from him has helped me on both professional and personal fronts. He introduced me to a wonderful world of experimental physics with his constant encouragement, enthusiasm, ideas, freedom and occasional “bangings”. He always asked for the “toy experiments”, “fun experiments” with the instruments around our lab and to explore physics that way. It is a great pleasure to have a guide like him and I want to convey my sincere thanks to him. Without him, it would be quite impossible for me to prepare this dissertation.

I would like to thank Prof. Abhijit Mookerjee, Head Of Department, Department of Material Science, Prof. Alak K. Majumder for their support and help during my PhD period. I want to convey my sincere thanks to Dr. Tanusri Saha Dasgupta and Dr. Priya Mahadevan for their helpful suggestions.

A good part of this thesis work has been done in Indian Institute of Science, Bangalore. I am thankful to Dr. Arindam Ghosh, IISC, Bangalore for allowing me to use low-temperature (Helium facility) noise set-up at their lab. I want thank his students Amrita, Chandni for their help during my work in their lab and being good friends during the IISC days. I specially thank Aveek da, Achut da, Priya di and Sai from IISC for helpful discussions.

My lab is a wonderful place to work and the people like Venkat, Tapati, Subrata, Rajesh, Manoranjan, and Soma are the best labmates. We always fought for pin to tweezers, sample boxes to cables, but I am really grateful to them for every aspect. I shared my memorable moments with them. Venkat is my only in-house “collaborator”; we always shared the CCR for R-T measurements and talked nonsense in the lab in spare times. During working at in the lab, he entertained us by his enthusiastic songs. Tapati was always most dependable and responsible one. Subrata doesn’t know how to say “NO” and I learnt interfacing programming from him. Rajesh is one of my beloved juniors. I would like to thank Ritwik, Anindya di for their constant help, support and suggestions. Barnali di, Kaustuv da, Kuntal da, Sarathi da were there with their helpful attitudes. Rajib, Monotosh, Shahnewaz are my recent labmates and I enjoyed a nice time with them. I always miss our labmates, our parties, canteen, the moments, and gossips we shared together in the lab.

I found friends like Bipul, Subarna di and Soumen da, Debabrata during my research period.

Didu is my soul mate and she is the source of my strength. She is the strongest inspiration behind every work I do. My dissertation is a tribute to my mother. I shall always miss her presence at every step in rest of my life. My Baba, Kaku, Kakima, pisimoni, pisimosai, and my parent-in-laws remained always the most caring persons in my family. Without their support and compassion it would never been possible complete my thesis. I love and adore them for their constant support and being patient for the work I did. Bhai, Bhaiya, Tinku, Pomu are by great brothers and my only sister Bonu made my life cheerful.

And finally, I thank Bhaskar being most caring, supportive and understating. He always stood beside me at ups and downs I faced during my PhD days. He is my best friend and I am lucky that I found him. Without his encouragement it would never been possible to write this dissertation.

# Abstract

The dissertation describes the results from experimental studies of low frequency resistance fluctuations of two strongly correlated transition metal oxides (hole doped lanthanum calcium manganites) and one magnetic (nickel) nanowire system. Two manganites under study are with optimum and very low doping concentration of calcium respectively. We study the first manganite system in a form of oriented film and other is in a form of single crystal. The third sample is single crystalline nickel nanowire.

Resistance fluctuations phenomena in oriented manganite films of  $\text{La}_{0.67}\text{Ca}_{0.33}\text{MnO}_3$  have been experimentally investigated. The films exhibit low frequency Random Telegraphic Noise (RTN) over  $1/f$  noise near magnetic transition temperature  $T_c$ . The films exhibited low noise magnitude due to strain relaxation. The noise spectroscopy with external magnetic field revealed the coupling of magnetization fluctuations with resistance fluctuations through magnetoresistance.

We investigate nature of ferromagnetic insulating state (FMI) of low doped manganite single crystals with composition  $\text{La}_{0.80}\text{Ca}_{0.20}\text{MnO}_3$ . The electrical transport property in FMI state is governed by Efros-Shklovskii variable range hopping (ES-VRH) conduction which opens up a soft Coulomb gap of energy  $\Delta_{CG} \approx 152$  meV. With the application of sufficiently high bias the system shows non-linear conduction (NLC) effect. We establish that the FMI state turns to be a Coulomb glass due to the presence of long range Coulomb interactions among the charge carriers. The charge fluctuation dynamics and freezing of these charge fluctuators in FMI state are studied by low frequency noise spectroscopy. We experimentally demonstrate that the fluctuators were activated by energy barrier  $E_a \approx 163$  meV which is of the same order with  $\Delta_{CG}$ . The above two independent results (conduction in FMI state and noise spectroscopy) establish the presence of glassy dynamics in FMI state.

A “hot electron” model is introduced, which quantitatively explains the bias and temperature dependence of NLC effect in FMI state. The “white” noise spectroscopy in presence of varying dc input bias are studied. For sufficiently high dc bias, the system falls out of equilibrium and becomes non-ergodic. The Fluctuation Dissipation Theorem (FDT) breaks down. The validity of the model and results of noise spectroscopy are discussed.

The resistance fluctuations in single crystalline magnetic nickel nanowires of diameter 35 nm are investigated. Experimental studies indicate the presence of coupling between magnetic noise and resistance noise. The origin of magnetic noise is attributed to domain wall resistance. We show that the low field magnetoresistance (MR) which due to finite resistance of the domain walls can couple to low frequency domain wall dynamics and can show noise that is correlated to the MR.

# Publications

1. Sudeshna Samanta, A. K. Raychaudhuri and Joy Mitra, *Very low frequency resistance fluctuations in thin films of  $La_{0.67}Ca_{0.33}MnO_3$  with quenched disorder*, Phys. Rev. B **78**, 014427 (2008).
2. Sudeshna Samanta, M. Venkata Kamalar and A. K. Raychaudhuri, *Investigation of Very Low-Frequency Noise in Ferromagnetic Nickel Nano wires*, Journal of Nanoscience and Nanotechnology **9**, 5243 (2009).
3. Sudeshna Samanta, M. Venkata Kamalar and A. K. Raychaudhuri, *Resistance fluctuations and 1/f noise in single crystalline Ni nanowires*, arXiv:0906.4227v1 [cond-mat.mes-hall] 23 Jun 2009 (Submitted to Appl. Phys. Lett.).

# Contents

|          |   |           |
|----------|---|-----------|
| <b>1</b> | <b>Introduction.....</b>  | <b>1</b>  |
| 1.1      | Motivation .....  | 1         |
| 1.2      | Introduction to Perovskite .....  | 5         |
| 1.2.1    | Introduction.....   | 5         |
| 1.2.2    | Manganite parameters .....  | 6         |
| 1.2.3    | The main classes of ordering .....  | 10        |
| 1.2.4    | Doping dependent magnetization.....   | 16        |
| 1.2.5    | Cationic disorder .....   | 17        |
| 1.2.6    | Magnetic and electronic phase diagram.....                                    | 17        |
| 1.2.7    | Colossal magnetoresistance (CMR .....   | 20        |
| 1.2.8    | Ferromagnetic metallic state of manganites.....                               | 21        |
| 1.2.9    | Ferromagnetic insulating state of manganites.....                             | 24        |
| 1.2.10   | Phase coexistence of manganites .....   | 26        |
| 1.3      | Introduction to noise.....  | 28        |
| 1.3.1    | Basics of random signal theory and<br>probability density function .....      | 28        |
| 1.3.2    | Types of noise and shape of the spectra.....                                  | 34        |
| 1.4      | Use of noise spectroscopy to probe manganites: A brief review .....           | 39        |
| 1.4.1    | Introduction.....   | 39        |
| 1.4.2    | Overview on published results .....   | 40        |
| 1.5      | The layout of the thesis.....   | 50        |
|          | Bibliography .....  | 53        |
| <b>2</b> | <b>Sample growth and characterization techniques .....</b>                    | <b>57</b> |
| 2.1      | Introduction .....  | 57        |
| 2.2      | Growth of films of $\text{La}_{0.67}\text{Ca}_{0.33}\text{MnO}_3$ .....       | 58        |
| 2.2.1    | Growth of films of $\text{La}_{0.67}\text{Ca}_{0.33}\text{MnO}_3$ .....       | 58        |
| 2.2.2    | Preparation of precursor solution.....  | 59        |
| 2.2.3    | Preparation of films.....   | 60        |
| 2.3      | Growth of single crystals by floating zone techniques.....                    | 63        |
| 2.3.1    | Instrumental overview.....  | 63        |
| 2.3.2    | Growth of $\text{La}_{0.80}\text{Ca}_{0.20}\text{MnO}_3$ single crystals..... | 65        |
| 2.4      | Experimental tools used for characterization .....                            | 66        |
| 2.4.1    | X-ray diffraction (XRD) .....   | 66        |
| 2.4.2    | Scanning Electron Microscopy (SEM) .....                                      | 67        |
| 2.4.3    | Atomic Force Microscopy (AFM) .....   | 67        |
| 2.4.4    | Temperature dependence resistivity measurement .....                          | 68        |
| 2.4.5    | Temperature dependent electroresistance measurement.....                      | 69        |

|          |   |            |
|----------|---|------------|
| 2.4.6    | Temperature dependent low field magnetoresistance measurement .....                                 | 70         |
| 2.4.7    | Magnetic measurements.....  | 71         |
|          | Bibliography .....  | 73         |
| <b>3</b> | <b>Noise measurement techniques.....</b>  | <b>74</b>  |
| 3.1      | Introduction to low frequency noise measurement .....   | 74         |
| 3.2      | The framework of noise experiments .....  | 75         |
| 3.2.1    | The general noise (ac) detection scheme .....   | 75         |
| 3.2.2    | Impedance-mismatch problem and solution .....   | 76         |
| 3.2.3    | The four-probe ac noise detection system.....   | 78         |
| 3.2.4    | The five-probe ac noise detection system.....   | 80         |
| 3.2.5    | The five-probe ac noise detection system<br>in presence of dc bias .....                            | 83         |
| 3.3      | Data acquisition .....  | 85         |
| 3.3.1    | The aliasing effect and its removal .....   | 87         |
| 3.3.2    | Decimation: downsampling and digital filtering .....  | 89         |
| 3.3.3    | Scheme to construct digital filter .....  | 91         |
| 3.3.4    | Scheme for multistage decimation.....   | 93         |
| 3.3.5    | Detrend, a linear trend removal process.....  | 94         |
| 3.4      | Data analysis: estimation of power spectral density.....  | 95         |
| 3.4.1    | Welch's method for averaged periodogram.....  | 95         |
| 3.4.2    | Recovery of uncorrupted time domain signal:<br>Weiner filtering .....                               | 97         |
| 3.4.3    | Test of Gaussianity of noise and<br>quantifying non-Gaussian noise.....                             | 99         |
| 3.5      | Low temperature noise measurement setup .....   | 104        |
| 3.5.1    | Design of a cryostat.....   | 104        |
| 3.5.2    | The experimental setup .....  | 105        |
| 3.5.3    | Calibration of the setup.....   | 107        |
| 3.5.4    | Controlling noise.....  | 108        |
|          | Bibliography .....  | 112        |
| <b>4</b> | <b>Study of very low frequency resistance fluctuations<br/>in perovskite manganite films .....</b>  | <b>114</b> |
| 4.1      | Introduction .....  | 114        |
| 4.1.1    | Microscopic phase separation .....  | 116        |
| 4.2      | Structural disorder and phase separation.....   | 122        |
| 4.3      | Film preparation and characterization .....   | 129        |
| 4.3.1    | X-ray diffraction .....   | 130        |
| 4.3.2    | Atomic Force microscopy .....   | 131        |
| 4.3.3    | Electrical transport measurements .....   | 131        |
| 4.3.4    | Magnetic measurements.....  | 133        |
| 4.4      | Resistance fluctuations in $\text{La}_{0.67}\text{Ca}_{0.33}\text{MnO}_3/\text{SrTiO}_3$ films..... | 135        |

|          |   |            |
|----------|---|------------|
| 4.4.1    | Noise measurements .....  | 135        |
| 4.4.2    | Noise in a strain relaxed films at room temperature .....   | 137        |
| 4.4.3    | Temperature dependent low frequency noise<br>in strain relaxed films.....   | 139        |
| 4.4.4    | Temperature dependent time-series of voltage fluctuations<br>and analysis of noise spectral power density .....                                       | 142        |
| 4.4.5    | Comparison of noise in strain relaxed films with<br>films of low and negligible strain .....  | 146        |
| 4.4.6    | Discussion on the results obtained for strain relaxed films .....   | 148        |
| 4.5      | Dependence of resistance fluctuation on magnetic field in<br>$\text{La}_{0.67}\text{Ca}_{0.33}\text{MnO}_3/\text{SrTiO}_3$ strain relaxed films ..... | 149        |
| 4.6      | Investigation of correlation between temporal<br>and special fluctuations .....   | 152        |
| 4.7      | Conclusions .....   | 154        |
|          | Bibliography .....  | 155        |
| <b>5</b> | <b>Probing ferromagnetic insulating state of manganites<br/>by resistance fluctuations .....</b>  | <b>159</b> |
| 5.1      | Introduction .....  | 159        |
| 5.1.1    | Theoretical models regarding insulating temperature<br>dependence of resistivity.....   | 166        |
| 5.1.2    | Electrical conduction process in ferromagnetic insulating phase .....   | 168        |
| 5.1.3    | Glassiness in electronic systems .....  | 172        |
| 5.1.4    | Review of published reports on $1/f$ noise in Coulomb glass.....  | 176        |
| 5.2      | Experimental methodology .....  | 181        |
| 5.3      | Non-linear conduction and colossal electroresistance.....   | 181        |
| 5.4      | Temperature dependent noise spectroscopy without dc bias .....  | 187        |
| 5.4.1    | Magnitude of excess noise .....   | 187        |
| 5.4.2    | Analysis of resistance fluctuation time series .....  | 190        |
| 5.4.3    | Analysis of second moment .....   | 193        |
| 5.4.4    | Power spectral density of resistance fluctuation .....  | 195        |
| 5.5      | Investigation of hot electron effect using non-linear resistance and<br>“white” noise spectroscopy .....  | 199        |
| 5.5.1    | Hot electron effects and two separate temperature scale<br>for electron and photon baths.....   | 200        |
| 5.5.2    | Hot electron temperature estimated from<br>the non-linear resistivity data.....   | 202        |
| 5.5.3    | The broad band white noise and its comparison to the electron<br>temperature.....   | 206        |
| 5.6      | Conclusions .....   | 212        |
|          | Bibliography .....  | 213        |
| <b>6</b> | <b>Study of low frequency resistance fluctuations in magnetic nanowires .....</b>   | <b>217</b> |
| 6.1      | Introduction .....  | 217        |

|          |   |            |
|----------|---|------------|
| 6.1.1    | Domain and domain wall resistance in ferromagnetic systems .....                                    | 218        |
| 6.2      | Diameter dependent in nanowires at room temperature.....  | 222        |
| 6.3      | Origin of excess noise in nanowires.....  | 224        |
| 6.4      | Noise spectroscopy in nanowires ( $d \approx 35$ nm)<br>in presence of external magnetic field..... | 226        |
| 6.4.1    | Magnitude of the noise as a function of<br>magnetic field and temperature.....                      | 227        |
| 6.4.2    | Power spectral density of noise as a function of<br>applied magnetic field and temperature .....    | 230        |
| 6.4.3    | Magnetic fluctuation at 80 K .....  | 233        |
| 6.5      | Conclusions .....   | 235        |
|          | Bibliography .....  | 236        |
| <b>7</b> | <b>Concluding remarks and scope for future work</b>   | <b>237</b> |
| 7.1      | Conclusions .....   | 237        |
| 7.2      | Scope for further investigations .....  | 239        |

# List of figures

|      |   |    |
|------|---|----|
| 1.1  | The schematic diagram showing different coupling mechanisms for “strongly correlated systems”.....  | 3  |
| 1.2  | (a) Dark-field images for $\text{La}_{5/8-y}\text{Pr}_y\text{Ca}_{3/8}\text{MnO}_3$ near MIT,(b) Topography information from $\text{L}_{1-x}\text{A}_x\text{MnO}_3$ surface with the 3D conductance map. ....   | 4  |
| 1.3  | A sketch of ideal perovskite <u>Pnma</u> structure.....   | 7  |
| 1.4  | (a) The <u>Pnma</u> unit cell of $\text{La}_{1-x}\text{Ca}_x\text{MnO}_3$ , giving an impression of the distortions from the cubic unit cell. (b) Orthorhombic (thick lines) and cubic (thin lines) unit cells for $\text{La}_{1-x}\text{Ca}_x\text{MnO}_3$ and the relative orientations of the crystallographic axes. ..... | 8  |
| 1.5  | Structure of <i>d</i> - orbitals in manganites and show the single-electron wavefunctions for the <i>d</i> -shell in Mn .....   | 8  |
| 1.6  | Illustration of orbital overlaps between Mn $t_{2g}$ and Mn $e_g$ orbitals with a <i>p</i> orbital of a neighbouring O ion.....   | 9  |
| 1.7  | Charge ordering for a half-doped system: a “checker board type” ordering .....  | 10 |
| 1.8  | (a) The JT distorted perovskite structure (the rotation is not indicated).<br>(b) The ab plane highlighting the alternation of the short and long Mn-O distances in <i>a</i> and <i>b</i> directions. (c) The shape of $\text{MnO}_6$ octahedra in $\text{Mn}^{4+}$ and $\text{Mn}^{3+}$ ions .....                           | 11 |
| 1.9  | A schematic diagram of the double exchange mechanism showing the simultaneous transfer of electrons between adjacent ions and the orientation of the Mn spins .....   | 13 |
| 1.10 | Schematic diagram for double exchange mechanism.....  | 13 |
| 1.11 | Schematic diagram showing the arrangement of spins and orbitals in superexchange in an (a) antiferromagnetic, (b) antiferromagnetic and (c) ferromagnetic arrangement of the core manganese spins respectively .....  | 15 |
| 1.12 | Predicted intensity of magnetization $M_s$ as a function of $x$ in $\text{La}_{1-x}\text{Ca}_x\text{MnO}_3$ system .....  | 17 |
| 1.13 | Phase diagram of $\text{La}_{1-x}\text{Ca}_x\text{MnO}_3$ in doping versus temperature plot .....   | 18 |
| 1.14 | The insulator-metal transition in $\text{La}_{0.7}\text{Ca}_{0.3}\text{MnO}_3$ at $T = T_c \cong 270$ K.....  | 20 |

|   |    |
|---|----|
| 1.15 (a) Temperature $T$ dependent resistivity $\rho$ in the absence of a magnetic field, and in the presence of a magnetic field for (a) $\text{La}_{0.82}\text{Ca}_{0.18}\text{MnO}_3$ and (b) $\text{La}_{0.7}\text{Ca}_{0.3}\text{MnO}_3$ .....   | 21 |
| 1.16 (a) Magnetization, (b) resistivity and (c) magnetoresistance of $\text{La}_{0.75}\text{Ca}_{0.25}\text{MnO}_3$ , as a function of temperature for various magnetic fields .....  | 22 |
| 1.17 (a) The magnetic field $H$ dependent resistivity $\rho(H, T)$ for $\text{La}_{0.70}\text{Ca}_{0.30}\text{MnO}_3$ . (b) The resistivity vs $T^2$ and deviation from $T^2$ behaviour in $\text{La}_{0.70}\text{Ca}_{0.30}\text{MnO}_3$ thin film sample .....  | 23 |
| 1.18 (a) Magnetization versus temperature and (b) Magnetization versus magnetic field isotherms in the vicinity of $T_c$ for $\text{La}_{0.67}\text{Ca}_{0.33}\text{MnO}_3$ .....   | 24 |
| 1.19 Phase diagram of the $\text{La}_{1-x}\text{Ca}_x\text{MnO}_3$ system .....   | 25 |
| 1.20 Temperature dependent resistivity of $\text{La}_{1-x}\text{Ca}_x\text{MnO}_3$ showing the onset of FMI state in these samples .....  | 26 |
| 1.21 (a) Generic phase diagram of two competing phases in the absence of quenched disorder, (b) With increase in disorder, (c) In the limit of substantial disorder.....  | 27 |
| 1.22 (a) Scanning tunneling spectroscopy images of the local electronic structure of $\text{La}_{1-x}\text{Ca}_x\text{MnO}_3$ , obtained just below $T_c$ in magnetic fields .....  | 27 |
| 1.23 Schematic diagram of thermal motion of electrons in a conductor .....  | 34 |
| 1.24 Left image: Voltage fluctuation across a conductor due to thermal fluctuation of the carriers inside, Right image: Spectral density of thermal fluctuation $S_{th} = 4k_B T R$ .....   | 35 |
| 1.25 $1/f$ noise in ten metal films .....   | 38 |
| 1.26 Temperature dependent $1/f$ noise magnitude normalized by volume and resistivity .....   | 41 |
| 1.27 Comparison of the normalized noise power spectral density of epitaxial thin films of $\text{La}_{0.67}\text{Ca}_{0.33}\text{MnO}_3$ and $\text{Pr}_{0.67}\text{Sr}_{0.33}\text{MnO}_3$ with that of epitaxial thin films of $\text{YBa}_2\text{Cu}_3\text{O}_7$ as a function of temperature ..... | 42 |
| 1.28 Temperature dependent normalized resistance fluctuation $a_R$ with different applied magnetic fields for strain free film (Left image) and for a strained film (Right image) .....   | 43 |
| 1.29 Magnetic-field dependence of noise level for low fields, with $H$ parallel (a) and perpendicular (b) to the grain boundary at $T = 10$ K. In (c) and (d) the noise levels are plotted vs the dc resistance .....   | 44 |

|  |    |
|--|----|
| 1.30 (a) The spectral power as a function of frequency at few representative temperatures ( $0.94 < T / T_{co} < 1.04$ ). (b) The contribution of the $1/f$ component $\langle (\Delta R)^2 / R^2 \rangle_1$ and that of the Lorentzian $\langle (\Delta R)^2 / R^2 \rangle_2$ as function of the dc bias $J_{dc}$ at $T = 226$ K.....   | 45 |
| 1.31 (a) Resistivity and $1/f$ noise intensity at $f = 1$ Hz as a function of temperature in $\text{La}_{0.82}\text{Ca}_{0.18}\text{MnO}_3$ single crystals .....  | 46 |
| 1.32 Left image: $\Delta R / R$ vs time at different temperatures showing random telegraphic noise (RTN). Right image: (a) Schematic representation of an asymmetric double -well model; (b) The measured average lifetimes ( $\tau_{up}$ ) and ( $\tau_{down}$ ) are plotted versus the reciprocal temperatures; (c) $\tau_{up}$ and $\tau_{down}$ versus magnetic field .....  | 48 |
| 1.33 (a) Frequency dependence of noise spectral power at temperature $T = 86$ K.<br>(b) Temperature dependence of the normalized noise at 20 Hz (c) Magnetic field dependence of the normalized noise power spectral density at room temperature and at 20 Hz, (d) Frequency dependence of the normalized noise power spectral density at 12 Tesla and 300 K for the same filmStructure of $d$ - orbitals in manganites and show the single-electron ..... | 49 |
| <br>2.1 Flow-sheet describing the steps for chemical solution deposition technique.....  | 58 |
| 2.2 The molecular structures of the three compounds used for precursor solution preparation.....   | 59 |
| 2.3 The schematic diagram of precursor solution preparation from three oxide components .....  | 60 |
| 2.4 The schematic diagram of the cleaning steps followed to clean $\text{SrTiO}_3$ substrates .....  | 61 |
| 2.5 The schematic diagram of epitaxial film growth technique from precursor solution .....   | 62 |
| 2.6 Typical weight versus temperature graph for a solution-to-oxide conversion and schematic illustration of phase evolution.....  | 63 |
| 2.7 (a) Schematic of the floating zone melting apparatus used for the growth of single crystals of $\text{La}_{0.80}\text{Ca}_{0.20}\text{MnO}_3$ and (b) Schematic of crystallization chamber .....   | 64 |
| 2.8 The pseudobinary $\text{La}_2\text{O}_3$ - $\text{Mn}_2\text{O}_3$ phase diagram in air.....   | 65 |
| 2.9 Schematic diagram of basic AFM operation .....   | 67 |
| 2.10 (a) Optical microscope image gold contact pads made by gold evaporation on film surface, (b) Optical microscope image of Ag-In contact pads made on single crystal surface .....  | 68 |
| 2.11 The temperature dependent resistivity measurement setup   |    |

|   |     |
|---|-----|
| using low temperature cryostat.....   | 70  |
| 2.12 (a) The schematic diagram of VSM with basic components, (b) The detection coils and sample position with principle of operation is shown, (c) The commercial setup from Lakeshore (7400 series) used for magnetization measurements .....                                  | 72  |
| <br>  |     |
| 3.1 Schematic diagram of the basic scheme to obtain power spectra from the time series .....  | 76  |
| 3.2 The NF as a function of frequency of (a) SR554 transformer preamplifier and (b)SR560 low noise FFT preamplifier .....   | 77  |
| 3.3 (a) A plot of gain versus frequency of a SR554 transformer preamplifier and (b) A plot of low noise preamplifier's input noise voltage versus frequency .....   | 77  |
| 3.4 Schematic diagram of four-probe noise measurement technique.....  | 78  |
| 3.5 The raw time series data of voltage fluctuation recorded at 300 K<br>(a) across a good quality $1\Omega$ carbon film resistor and<br>(b) from the background. (c) The corresponding power spectral density along with the background noise estimated from time-series ..... | 79  |
| 3.6 A schematic diagram of five-probe ac noise measurement setup .....  | 80  |
| 3.7 (a) The raw time series data of voltage fluctuation measured across a $10\Omega$ carbon resistor in five-probe ac noise detection method at 300 K.<br>(b) The corresponding spectral power density and the background noise .....   | 83  |
| 3.8 The schematic diagram for noise measurement setup with ac bias in presence of dc bias .....   | 84  |
| 3.9 Comparison of noise data taken with ac bias with and without superimposed dc bias as well as with and without $L$ and $C$ for a $10\Omega$ carbon film resistor.....  | 85  |
| 3.10 Waveforms illustrating the digitization process. (a) The time-domain analog voltage signal (b) S/H stage, (c) Process showing conversion of the voltage to the nearest integer number .....  | 86  |
| 3.11 A schematic diagram for realizing aliasing phenomena and its contribution to the noise power spectral density.....   | 87  |
| 3.12 An example of aliasing. (a) The original sinusoidal continuous signal at frequency 4 Hz (b) The digitized signal suffered from aliasing effect.....  | 88  |
| 3.13 Frequency response of (a) an ideal low-pass filter (b) of an impulse (c) of an actual low-pass filter .....  | 90  |
| 3.14 The Hanning, Hamming, and Kaiser window functions .....  | 91  |
| 3.15 The parameter dependence of the frequency responses of for low-pass filters.<br>(1) roll-off sharpness, shown in (a) and (b), (2) passband ripple, shown in (c) and (d), and (3) stopband attenuation, shown in (e) and ( f ) .....  | 92  |
| 3.16 (a) A schematic diagram showing the multistage decimation process.<br>(b) The response functions of the three stage digital filters used .....   | 93  |
| 3.17 (a) Voltage fluctuations showing linear trend due to drift and<br>(b) same voltage fluctuations after trend removal .....  | 94  |
| 3.18 The flow chart of the algorithm used to execute the “Weiner filter” to eliminate the background noise from the “in-phase” signal.....  | 98  |
| 3.19 The flowchart showing the detailed procedure for estimation of PDF from sample time series data .....  | 100 |
| 3.20 (a) The raw time series of voltage fluctuations recorded for a $50 \mu\text{m}$  |     |

|  |     |
|--|-----|
| wire nickel wire at few representative temperatures. (b) The Probability Density function (PDF) of voltage fluctuations of respective time series.....   | 101 |
| 3.21 The flow chart showing the procedure for obtaining second spectrum from the time series data of voltage fluctuations.....   | 102 |
| 3.22 The plot of normalized second spectrum as a function of frequency at few representative temperatures for a 50 $\mu$ m nickel wire .....   | 103 |
| 3.23 A schematic design of the cryostat used for resistivity and noise measurement setup.....  | 104 |
| 3.24 (a) Schematic diagram of noise measurement setup, (b) The actual noise measurement setup at our laboratory.....   | 106 |
| 3.25 The representative noise data for a 1 $\Omega$ carbon resistor .....  | 107 |
| 3.26 The grounding effect: (a) Series ground connection,<br>(b) Parallel ground connection .....   | 108 |
| 3.27 The schematic diagram of a ground loop affecting the noise measurements.....  | 110 |
| 3.28 (a) Shielded twisted pair cable and (b) unshielded twisted pair cables.....   | 110 |
| 3.29 (a) Schematic diagram of a coaxial cable and<br>(b) the actual coaxial cables available commercially .....  | 111 |
|  |     |
| 4.1 Electronic structure of (a) Mn <sup>3+</sup> in octahedral coordination, before and after Jahn-Teller distortion; (b) Mn <sup>4+</sup> in octahedral coordination;<br>(c) energy band diagram in ferromagnetic manganites La <sub>0.67</sub> Ca <sub>0.33</sub> MnO <sub>3</sub> ) .....               | 114 |
| 4.2 Schematic phase diagram of La <sub>1-x</sub> Ca <sub>x</sub> MnO <sub>3</sub> .....  | 117 |
| 4.3 (a)Temperature variation of resistance and normalised noise power for La <sub>0.67</sub> Ca <sub>0.33</sub> MnO <sub>3</sub> . (b) Time traces exhibiting discrete fluctuators at different temperatures .....   | 118 |
| 4.4 The time series of voltage fluctuation ( $\Delta V(t)$ ) at four representative temperatures in the range $0.94 \leq T / T_{CO} \leq 1.04$ .....   | 119 |
| 4.5 MFM images of La <sub>0.65</sub> Ca <sub>0.35</sub> MnO <sub>3</sub> film on SrTiO <sub>3</sub> taken at decreasing temperatures of (A) 250 K, (B) 233 K, and (C) 207 K .....  | 120 |
| 4.6 Temperature dependence of local magnetization calculated from MFM images and the magnetization measured by SQUID on La <sub>0.8</sub> Ba <sub>0.2</sub> MnO <sub>3</sub> thin film on STO.....   | 121 |
| 4.7 (I). La <sub>0.67</sub> Sr <sub>0.3</sub> MnO <sub>3</sub> thin film (a) STM topography and (b) corresponding conductance map (with PtIr tip); (II) La <sub>0.67</sub> Sr <sub>0.3</sub> MnO <sub>3</sub> thin film (a) STM topography and (b) corresponding conductance map (with magnetic tip) ..... | 121 |
| 4.8 Experimentally observed dependence of $T_c$ on biaxial strain in epitaxial strained La <sub>0.67</sub> Ca <sub>0.33</sub> MnO <sub>3</sub> films on STO .....  | 123 |
| 4.9 Schematic diagram for the mechanism of tensile or compressive strain arises in the film due to lattice mismatch between film and substrate .....   | 125 |
| 4.10 Schematic diagram showing the microstructure of an epitaxial film that is (a) coherently strained, (b) partially relaxed and (c) fully relaxed .....  | 126 |
| 4.11 STM images across the platelet and step for ~ (a) LCMO/STO(200),<br>(b) LCMO/ STO(50), and (c) LCMO/NGO(50) films (d) The temperature dependence of the resistivity of LCMO/STO(200),<br>LCMO/STO(50), and LCMO/NGO(50) .....   | 127 |
| 4.12 La <sub>0.67</sub> Ca <sub>0.33</sub> MnO <sub>3</sub> thin film (a) Resistivity versus temperature for films deposited on NGO and STO; (b) AFM topography images for LAO (left image) and for NGO (right image) films; (c) MFM images  |     |

|   |     |
|---|-----|
| of the LAO film at 80 K .....   | 128 |
| 4.13 Field-cooling M-T (left) and R-T (right, lines) curves measured from the films grown on STO (001) substrates with thicknesses of 15, 30, 45, 60, and 150 nm, respectively.....   | 129 |
| 4.14 A typical XRD line scan data for 500 nm thick film grown on STO (002) substrate.....   | 130 |
| 4.15 (a) AFM image of LCMO33 film surface grown on oriented single crystal STO .....  | 131 |
| 4.16 The temperature dependent resistivity data for a LCMO33 film grown on STO with thickness ~500 nm .....   | 132 |
| 4.17 Temperature dependent magnetization (M-T) for field-cooling (FC) and zero-field-cooling (ZFC) conditions.....  | 133 |
| 4.18 (a) Magnetic fields dependent magnetization (M-H) curve at few representative temperatures around $T_c$ . (b) The hysteresis loop expanded around origin showing the coercive field appears at $H_c \approx 0.01$ Tesla..... | 134 |
| 4.19 Plot showing the $V^2$ dependence of the measured noise for LCMO33/STO (500 nm) film at 300 K.....   | 137 |
| 4.20 The raw voltage time-series measured across the film sample (upper panel) and from background (lower panel) at 300 K .....   | 138 |
| 4.21 (a) The plot showing the power spectra $S_v(f)$ along with the background estimated from the two time series represented.<br>(b) The power spectral density $S_v(f)/V^2$ for three different ac bias voltages at 300 K ..... | 138 |
| 4.22 The plot showing the power spectral density $S_v(f)/V^2$ as a function of frequency for few representative temperatures below $T_c$ .....  | 139 |
| 4.23 The plot showing the power spectral density $f.S_v(f)/V^2$ as a function of frequency for the same temperatures mentioned in Fig. 4.22 .....   | 140 |
| 4.24 The spectral power $S_v(f)/V^2$ measured at few representative temperatures as a function of f covering the transition temperature $T_c$ .....   | 140 |
| 4.25 The spectral power $f.S_v(f)/V^2$ measured at few representative temperatures as a function of f covering the transition temperature $T_c$ .....   | 141 |
| 4.26 The scaled spectral power $S_v(f)/V^2$ measured at few representative frequencies as a function of T along the sample resistivity $\rho(T)$ .....  | 141 |
| 4.27 The voltage time series data at few representative temperatures showing RTN in time series .....   | 142 |
| 4.28 The plot of temperature dependent weightage of $1/f$ noise $A(T)$ .....  | 143 |
| 4.29 The temperature dependence of $B(T)$ and Lorentzian corner frequency $f_c(T)$ .....  | 144 |
| 4.30 The variation of relative resistive fluctuation $\langle(\Delta R)^2 / R^2 \rangle$ with temperature along with Lorentzian corner frequency $f_c$ .....  | 145 |
| 4.31 Plot of $f_c$ and activation energy $E_a$ with temperature .....   | 145 |
| 4.32 Temperature variation of $\beta$ for LCMO33/STO (50 nm), LCMO33/NGO (50 nm), and LCMO33/STO (500 nm) film .....  | 147 |

|      |   |     |
|------|---|-----|
| 4.33 | The variation of relative resistive fluctuation $\langle (\Delta R)^2 / R^2 \rangle$ with temperature measured in two different samples i.e., for Sample-2 (upper panel) and Sample-1 (lower panel) .....   | 147 |
| 4.34 | $\beta$ as function of magnetic field $H$ at few representative temperatures .....  | 149 |
| 4.35 | MR as a function of magnetic field for few representative temperatures .....  | 150 |
| 4.36 | $\left\langle \frac{(\Delta R)^2}{R^2} \right\rangle$ as a function of $dR/dH$ at temperatures $T < T_c$ .....  | 151 |
| 4.37 | STM topography of LCMO33 films. (A) LCMO/NGO, (B) LCMO/STO(50) and (C) LCMO/STO(200) .....  | 151 |
| 4.38 | The temperature dependence of $\langle (\Delta g)^2 \rangle^{0.5} / g$ calculated from line scans across local conductance mapping of LCMO33/STO (50 nm), LCMO33/STO (200 nm), LCMO33/NGO (50 nm) films.....  | 153 |
|      |   |     |
| 5.1  | Phase diagram of $\text{La}_{1-x}\text{Ca}_x\text{MnO}_3$ near the FMI-FMM transition.....  | 160 |
| 5.2  | Schematic drawings of the orbital polaron around $\text{Mn}^{4+}$ -ion .....  | 161 |
| 5.3  | (a) Temperature dependence of the resistivity for (a) LCMO20.<br>(b) The intensity of neutron diffuse scattering at the peak positions of charge ordering modulation wave vectors ( $\bullet$ ) and away from them<br>(o) for LCMO20. (c) The observed neutron diffraction patterns of LCMO20 at various temperatures in the [H,K,0] reciprocal plane obtained by the WAND diffractometer ..... | 162 |
| 5.4  | (a) Field cooled and zero field cooled magnetization ( $M_{FC}, M_{ZFC}$ ) of $\text{La}_{0.8}\text{Ca}_{0.2}\text{MnO}_3$ single crystal, (b) Temperature dependence of ac susceptibility of $\text{La}_{0.8}\text{Ca}_{0.2}\text{MnO}_3$ single crystal measured at different frequencies.....  | 163 |
| 5.5  | Critical doping levels $x_{c1}$ and $x_{c2}$ . $x_{c1}$ separates the lightest region.<br>The darkest shaded region, with $x > x_{c1}$ , has some occupied $b$ states that percolate through the $10^3$ box .....   | 165 |
| 5.6  | The temperature dependence of resistivity $\rho$ of LCMO20.....   | 169 |
| 5.7  | The experimental $\ln(\rho)$ vs. $1000/T$ data and compared with different theoretical models like: (a) Arrhenius model, (b) Mott variable range hopping model, (c) ES-VRH model in the FMI state of LCMO20,<br>(d) Polaronic hopping model (with $n = 1$ ) .....   | 170 |
| 5.8  | Temperature dependence of ES-VRH hopping length $l_h$ , correlation length $\xi$ and unit cell parameter $a_0$ in FMI phase of LCMO20.....  | 171 |
| 5.9  | The schematic diagram for ES-VRH mechanism .....  | 173 |
| 5.10 | (a) The temperature dependence of specific heat $c_\mu$ and linear variation of it.<br>(b) Molar specific heat $C_p$ versus temperature $T$ for LCMO20 .....  | 174 |
| 5.11 | Glassy behaviour in disordered Coulomb systems.....   | 176 |
| 5.12 | (a) Noise amplitude ( $S^{1/2}$ ) spectra of an 81% Si:B sample at several different temperatures. (b) Noise amplitude ( $S^{1/2}$ ) at 1Hz and 10 Hz as a function of temperature at same bias current.....  | 177 |
| 5.13 | (a) $\rho(T)$ and $1/f$ noise intensity at $f = 1$ Hz as a function of temperature.<br>(b) Current dependence of the noise intensity at $f = 1$ Hz .....  | 180 |

|      |  |     |
|------|--|-----|
| 5.14 | Temperature dependence of resistivity $\rho$ in the absence of a magnetic field, and in the presence of the magnetic field 14 Tesla .....  | 182 |
| 5.15 | (a) Temperature dependence of resistivity $\rho$ for four representative current bias ranging from $1\mu\text{A}$ - $1000\mu\text{A}$ . (b) Temperature dependence of electroresistance at three current densities $j_{high}$ ( $1000\mu\text{A}$ , $100\mu\text{A}$ , and $10\mu\text{A}$ ) ..... | 183 |
| 5.16 | (a) Current density versus electric field ( $j - E$ ) characteristics at few representative temperatures covering two transition temperatures $T_{FMI}$ and $T_C$ . (b) The same $j - E$ characteristics in log-log scale .....  | 184 |
| 5.17 | Representative log-log plots showing two regimes of power law variation of representative $\rho$ as a function of current density $j$ for different temperatures .....   | 185 |
| 5.18 | (a) The temperature dependence of threshold current density $j_{th}$ showing a distinct feature below $T_{FMI}$ .....  | 186 |
| 5.19 | <b>5.19:</b> The noise power spectrum as a function of frequency at $80\text{ K}$ below $T_{FMI}$ along with its background noise .....  | 188 |
| 5.20 | The relative resistance fluctuations $\langle(\Delta R)^2\rangle/R^2$ as a function of $T$ .....   | 188 |
| 5.21 | (a) The variation of $S_V(f)/V^2$ as a function of temperature at eight representative frequencies. (b) The plot of $\ln(f/f_0)$ versus $1/T$ for the above three frequencies.....   | 189 |
| 5.22 | (a) PDF at $4.2\text{ K}$ for the metallic sample PS41, and insulating samples K242 and K139. The growth of non-Gaussian tail for insulating sample K240 with decreasing $T$ . (b) Normalized second spectrum $S^{(2)}(f)$ at $4.2\text{ K}$ .....   | 191 |
| 5.23 | The calculated Probability Density Functions (PDF) as a function of voltage fluctuations $((\Delta V)^2)$ for few representative temperatures (a) below and (b) above $T_{FMI}$ .....  | 192 |
| 5.24 | Plot of normalised second spectra $S_N^{(2)}(f)$ as a function of frequency at frequency representative temperatures (a) $T < T_{FMI}$ , and (b) $T > T_{FMI}$ .....   | 194 |
| 5.25 | Plot of normalised second spectra $S_N^{(2)}(f)$ as a function of temperature below $T_{FMI}$ at frequency $f \approx 60\text{ mHz}$ .....   | 195 |
| 5.26 | The noise power spectra as a function of frequency at few representative temperatures in LCMO20 single crystal have been plotted in (I) and (II) $T_{FMI}$ respectively. Corresponding $f.S_V(f)/V^2$ as a function of frequency in two temperature regions (I.(b)) and (II.(b)) .....             | 196 |
| 5.27 | The temperature dependence of the total fluctuation $\langle(\Delta R)^2\rangle/R^2$ and the contribution of $1/f$ component [ $\langle(\Delta R)^2\rangle/R^2$ ] <sub>1</sub> and that of the Lorentzian [ $\langle(\Delta R)^2\rangle/R^2$ ] <sub>2</sub> .....                                  | 197 |
| 5.28 | The variation of fitting parameters (a) $A(T)$ , (b) $B(T)$ , (c) $B(T)/A(T)$ , (d) $f_c$ and (e) $\alpha$ as a function of temperature encompassing   |     |

|  |     |
|--|-----|
| three different temperature regimes: $T < T_{FMI}$ , $T_{FMI} < T < T_c$ , and<br>$T \geq T_c$ .....   | 198 |
| 5.29 The schematic diagram of hot-electron model where $T_e$ and $T_{ph}$ are<br>the electron and lattice/phonon temperatures respectively.....  | 200 |
| 5.30 Experimentally observed variation of resistivity $\rho$ as a function of<br>power $P$ at fixed phonon temperature $T_{ph}$ and electron temperature<br>$T_e$ . The fixed phonon temperatures are (a) $T_{ph} = 80$ K, (b) $T_{ph} = 90$ K,<br>(c) $T_{ph} = 100$ K, and (d) $T_{ph} = 110$ K..... | 203 |
| 5.31 The ratio of $(T_e / T_{ph} - 1)$ as a function of power $P$ for fixed phonon<br>temperatures $T_{ph}$ , i.e., (a) 80 K, (b) 90 K, (c) 100 K, and (d) 110 K.....  | 204 |
| 5.32 The plot of $T_e / T_{ph}$ as a function of $(P / P_c)$ . Each curve is for a<br>fixed phonon temperature mentioned in the graph and all temperatures<br>are considered below $T_{FMI}$ .....   | 205 |
| 5.33 The plot showing the comparison between the threshold power ( $P_{th}$ )<br>for NLC and $P_c$ .....   | 205 |
| 5.34 Typical WBN voltage fluctuation time series data at 80 K for few<br>representative dc current biases.....   | 206 |
| 5.35 The raw time series of voltage fluctuations taken at three different<br>dc current biases for a fixed resistor .....  | 208 |
| 5.36 The frequency dependence of $\zeta$ for a standard resistor for three<br>representative dc bias currents and shows the power independent<br>character of $\zeta$ for the standard resistor.....   | 208 |
| 5.37 The plot of spectral decomposition of $\zeta$ at $T_{ph} = 80$ K at few<br>representative dc current biases mentioned in the graph.....   | 209 |
| 5.38 Plot of normalized white noise as a function of frequency<br>at few representative temperatures below $T_{FMI}$ .....   | 210 |
| 5.39 The variation of $\zeta$ as a function of $(P / P_c)$ for all $T_{ph}$ below $T_{FMI}$ .....  | 211 |
| <br>6.1 The magnetization ( $M$ ) versus ( $H$ ) loops studied on Ni nanowires of diameter $D_p = 40$<br>nm. The applied magnetic field is along parallel ( $\parallel$ ) and perpendicular ( $\perp$ ) direction to<br>the wire axes .....  | 219 |
| 6.2 (a) X-ray diffraction data and (b) TEM image and (c)selected area diffraction<br>pattern of 35 nm Ni nanowires .....   | 220 |
| 6.3 (a) Schematic diagram for electrical measurements on arrays of nanowires. (b) The<br>schematic of the equivalent circuit described in (a) .....  | 221 |
| 6.4 The $V^2$ dependence of spectral power $S_V(f)$ at 1 Hz for (a) 35 nm and (b) 50 $\mu\text{m}$ wire<br>.....   | 222 |
| 6.5 Frequency dependence of (a) $S_V(f)$ (b) $f.S_V(f)/V^2$ of the voltage noise arising from<br>the resistance fluctuations in current biased Ni nanowires of diameters ranging from 15<br>nm to 200 nm.....  | 223 |
| 6.6 Diameter dependence of frequency exponent (a) $\alpha$ and (b) normalised relative<br>resistance fluctuation $\langle (\Delta R)^2 \rangle / R^2$ at 300 K .....   | 224 |

|      |   |     |
|------|---|-----|
| 6.7  | Schematic representation of the energy barrier for the magnetization in double well potential model .....   | 225 |
| 6.8  | The variation of $\langle (\Delta R)^2 \rangle / R^2$ as a function of magnetic field at few representative temperatures for nanowires of diameter 35 nm.....                                 | 227 |
| 6.9  | The variation of magnetization ( $M$ ) as a function of magnetic field ( $B$ ) at 300 K for 35 nm nickel wires .....  | 228 |
| 6.10 | The variation of normalized resistance fluctuations $\langle (\Delta R)^2 \rangle / R^2$ as a function of temperature in presence and absence of magnetic field in 35 nm nickel nanowires.... | 228 |
| 6.11 | (a) The variation of magnetic noise component [ $\langle (\Delta R)^2 \rangle / R^2$ ] <sub>m</sub> at few representative magnetic field $\leq 0.04$ Tesla .....                              | 229 |
| 6.12 | Plot showing $\ln[\langle (\Delta R)^2 \rangle / R^2]$ as a function of $1/T$ for $B = 0$ and $B = 0.12$ Tesla ...  | 230 |
| 6.13 | The variation $S_V(f)/V^2$ few representative magnetic fields at temperatures (a) 80 K, (b) 110 K, (c) 160 K, (d) 210 K, (e) 250 K and (f) 300 K.....   | 231 |
| 6.14 | The magnetic filed dependence of frequency exponent $\alpha$ at few representative temperatures .....   | 232 |
| 6.15 | [ $S_V(f)/V^2$ ] <sub>m</sub> as a function of temperature at few representative frequencies.....   | 232 |
| 6.16 | The variation of $\ln(f/f_0)$ as function of $1/T$ to estimate the activation energy in presence of magnetic field.....   | 233 |
| 6.17 | The variation of (a) $\langle (\Delta R)^2 \rangle / R^2$ , (b) $R$ and (c) MR as a function of magnetic field $B$ at 80 K .....  | 234 |

# List of tables

|     |   |     |
|-----|---|-----|
| 1.1 | Approximate values for the energy scales of interaction mechanisms<br>in manganites.....  | 16  |
| 1.2 | A comparative study: the characteristics of Random Telegraphic noise<br>and typical $1/f$ noise .....   | 37  |
| 2.1 | Table of lattice parameters of different substrates .....   | 61  |
| 4.1 | A survey of published literature on variation of $T_p$ with LCMO33 film<br>thickness $t$ grown on oriented single crystals of $\text{SrTiO}_3$ substrates .....   | 116 |
| 4.2 | Lattice parameters of different substrates and amount of in-plane ( $\varepsilon_{xx}$ )<br>and out-of plain ( $\varepsilon_{zz}$ ) strain components for LCMO33 films grown on<br>them STO and LAO substrates..... | 125 |
| 4.3 | Electrical characterizations of sample used.....  | 133 |
| 5.1 | The list showing some of the important physical parameters in LCMO20<br>and NPMO30 single crystal samples.....  | 164 |
| 5.2 | The list of parameters estimated from temperature dependent<br>resistivity data of LCMO20.....  | 170 |

# Chapter 1

## Introduction

### 1.1 Motivation

The random back and forth motion of the charge carriers in any conductor is a source of fluctuation (“*noise*”) in current i.e., by the fluctuations of the directions of the charge carriers velocities. In the same systems many other physical quantities also fluctuate: the temperature, the number of scattering centres and their orientation in the crystal, the distribution of charge carriers in energy, and so on. However, these fluctuations, due to their symmetry, are not measured (revealed) in the current or voltage fluctuations unless a mean current, generated by an external current source, is passed through the conductor. The magnitude of the mean current, which is sufficient to reveal the “hidden” fluctuations and generate a measurable “excess” noise is often so small that the conductor in all other respects can be considered as equilibrium one. In resistors, the excess noise becomes prominent at low frequencies. The occurrence of these fluctuations is one of the most fundamental and universal phenomenon in a diverse class of systems. The conduction fluctuation mechanism is very important and challenging problems in the field of condensed matter. Several efforts have been given to formulate a unified model to explain the phenomena in all classes of the systems but failed even after decades. The dependence of these fluctuations is directly correlated with time or, equivalent the frequency dependence of spectral density in any physical system. On the other hand, the response of the same system to external perturbations is governed by the kinetic processes which are directly related to the fluctuation dynamics. Hence, study of fluctuation phenomenon is a sensitive and successful approach to condensed matter for investigation of fundamental kinetics or dynamics as well as from an applied perspective. This sensitivity of these processes is the basis of fluctuation spectroscopy. For measurements in physics using electronics, noise is thought to be a nuisance. This motivated researchers of physics in early days [1, 2, 3, 4], so that one can reduce the noise in measurements. These efforts lead to a great importance to study of electrical noise from the technological point of view.

The fluctuations in conduction process affect the important physical quantity of electronic transport i.e., resistance  $R$ . The fluctuations in resistance (called “electrical noise”) arise from very fundamental reasons namely, various relaxation processes of the charge carriers, defects, group of defects etc. Resistance noise is quantified by the dynamical fluctuations  $\delta R(t) = R(t) - \langle R \rangle$  of the resistance about its time averaged mean value  $\langle R \rangle$ . On the other hand, noise may come from the fluctuations of macroscopic entities, and it can thus act as a probe of what is happening physically in the system at the microscopic scale. It can also arise from mechanisms which are not microscopic as we see later in this thesis. The behaviour of current flow accompanied with resistance fluctuations is not well understood [5] in many materials. In such systems with a variety of morphologies (e.g., amorphous, single crystalline, polycrystalline, porous, granular materials etc.), there are several possible reasons for the resistance to fluctuate: simple scattering events at fluctuating cross-section defects, generation-recombination events, passage of charge carriers through nearly same conductivity regimes, and fluctuating percolating paths between grains. More complicated collective mechanism, where interaction takes place due to long-range forces, like strain, electrostatic, or magnetic forces etc, may also determine the fluctuating resistance noise phenomena. Due to diversity of the physical systems producing noise, it is believed now that each system must be individually investigated [5], rather than searching for a universal

general mechanism. The most successful approach towards understanding the kinetics and dynamics related to conduction fluctuations and the noise spectra have been investigated in very specific systems [6]. Attempts have been made to distinguish and classify the variety of systems in order to shed some light on the mechanism responsible for fluctuation and still some of the questions remain unanswered. For these reasons study of noise is still under intensive research though being a well developed field.

In this thesis we describe, in detail, extensive investigation of noise spectroscopy from the perspectives stated above. We have chosen well known hole doped transition metal oxides (manganites) having the general chemical formula  $L_{1-x}A_xMnO_3$ , where L is a rare earth transition metal Lanthanum (La) and A is a divalent species Calcium (Ca) at doping levels  $x \leq 0.33$ . The manganites, a member of perovskite family of oxides are complex oxides and have long been subjects of study, because they exhibit a wide range of exotic and not very well understood structural, magnetic and electronic behaviour [7]. By simply varying their doping concentration the resistivity and mobility of the charge carriers can be tuned by several orders of magnitude. In particular, these materials display a Curie transition from metallic magnetically ordered low-temperature phase to a paramagnetic disordered high-temperature phase and below Curie temperature the conduction electrons are highly spin polarized. Metallic conductivity is also associated with magnetism at lower temperatures in these systems. In the high temperature state spins are disordered and scatter electrons, while in the low-temperature phase the spins are ordered and do not scatter electrons. The spin scattering increases the resistivity, but it localizes only a negligible part of the carriers leading to a complicated charge transport properties in manganites. The existence of nonmagnetic disorder in the samples is confirmed with the fact that charge transport properties are very dependent on the oxygen content. Moreover, measurements of magnetization indicate the occurrence of small magnetic domains in them. Almost in all cases these properties cannot be explained within a context of the usual one-electron band theory indicating the importance of strong electron-electron and electron-lattice correlations. With an understanding of the complexity of the problem came the realization of the uniqueness of manganites as a test field for condensed matter physics theories and experiments.

Manganites are electron systems where strong couplings between the electronic (charge carrier, orbital), magnetic (charge carrier spin, localized core spin), and lattice (phonon) are at play simultaneously, and where classical simplifications that neglect some interactions to study others in details simply do not work. The tunability of the properties can be achieved by changing ionic sizes, chemical compositions, external perturbations like magnetic and electric field, pressure, etc. These systems appeared as a prototypical example of “*strongly correlated electronic systems*” as a result of delicate energy balance among the coupling mechanisms shown schematically in Fig. 1.1. As a result, the electron conduction process is greatly affected and materials have different conductivity regimes. Again, in the transition state there is a distribution of metastable magnetic domains or distribution of regions with different conductance, the flipping between those metastable states implies the likelihood of conduction fluctuations additional to the thermal fluctuations. Hence, the investigation of fluctuations will be interesting which are not only coming from the structural sources but also from electronic and magnetic sources. The fluctuation study has the same importance as the dependence of resistance on the magnetic field and temperature. We found that study of electrical noise in manganites is an evidence of correlation between noise type and magnitude of the resistivity as a function of temperature. The influence of magnetic field, external electric field on the shape of the noise spectra as well noise magnitude has not been clearly demonstrated experimentally. We experimentally try to elucidate the origin of noise in the manganites, since it would be possible to further characterize the crossover from localized to itinerant charge carriers. From the theoretical point of view, conduction fluctuations in the

transition region reveal new features of the charge transport, supplementing the results from conventional resistance measurements of the manganite systems. We will introduce results where noise measurements provided key information in a broad range of investigations in such complex oxide systems.

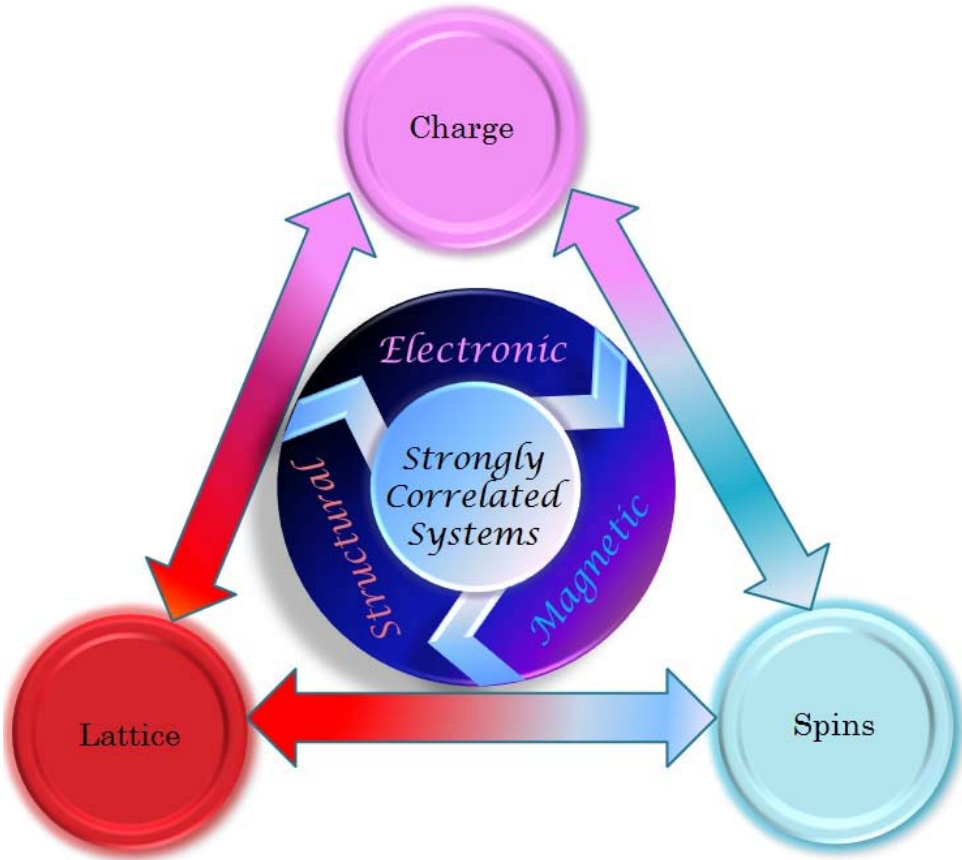


**Figure 1.1:** The schematic diagram showing different coupling mechanisms responsible for “strongly correlated systems”.

Significant contributions to these complex oxide fields have been made by numerous workers. What started as a quest to understand why these systems contribute different kind of temperature dependent transport properties due to the interaction at the atomic and electronic levels? With the development of advance experimental techniques a number of issues have opened up to be looked into. One of these issues is metal insulator transition (MIT) for the complex systems. In this dissertation we shall discuss why MIT is important as well as interesting in  $L_{1-x}A_xMnO_3$  systems and how we explored the phenomena of MIT by low-frequency noise spectroscopy. In perovskite materials, the MITs are associated with distinct magnetic phases [7]. There are possibilities of existence of different phases simultaneously around MIT in macroscopically small regions. These phenomenon leads to the competition among free energies associated with them and regions near MIT appeared to be spatially inhomogeneous. The theoretical studies regarding MIT have been investigated earlier [8, 9] in these materials whereas, several advanced experimental studies have been done using Scanning Tunnel Microscopy (STM) [10, 11], Scanning Tunnel Spectroscopy (STS) [12, 13], Small Angle Neutron Scattering (SANS) [14] to reveal the nature of MIT and related phenomena. The authors were able to visualise the regions with mixture of electronically, magnetically, structurally distinct phases of manganites at atomic scale around MIT.

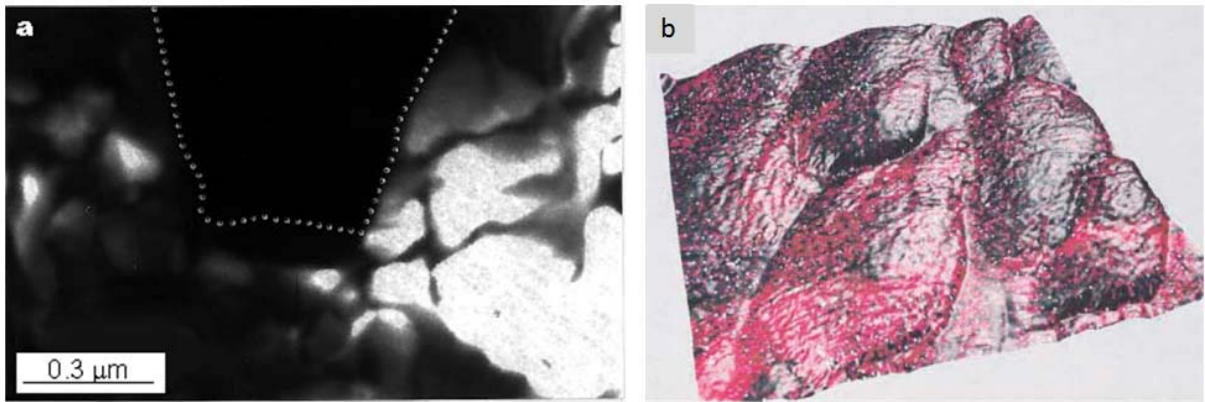


**Fig. 1.2:** (a) Dark-field images for  $\text{La}_{5.8-y}\text{Pr}_y\text{Ca}_{3.8}\text{MnO}_3$  showing simultaneous presence of insulating and metallic regions near MIT [11], (b) Topography information from  $\text{L}_{1-x}\text{A}_x\text{MnO}_3$  surface with the 3D conductance map where red areas are highly conducting and black regions are insulating [12].

The typical examples of microscopic picture of the mixture of different conductivity regions are shown in Fig. 1.2. The submicron metallic and insulating regions are dynamic in nature and they are directly correlated to charge inhomogeneity and conductivity fluctuations. Moreover, fluctuations could come from different sources like defect dynamics, carrier density or even the density of states near Fermi level. Any of these fluctuations is likely to have an impact on the conductivity of the system. There are other external effects like pressure, magnetic field, electric field, film thickness, oxygen stoichiometry, x-rays can tune this dynamics significantly. According to the most theoretical models, magnetic and transport properties of these compounds are determined by magnetic interactions and electron exchange between Mn ions. Significant effects of electron-lattice interactions observed manganites point to the important role of the lattice in transport and other properties of these materials. In spite of many aspects of charge transport dynamics and electron-lattice interactions are still unclear. Our aim is to investigate the nature of complex dynamics in different conductivity regimes including MIT using noise spectroscopy.

Another important issue we have studied in our thesis is: depending on doping concentration how the system  $\text{L}_{1-x}\text{A}_x\text{MnO}_3$  can give rise to a number of distinctly different transport dynamics which relate to conduction fluctuations. We worked on two doping concentrations of manganites,  $x = 0.33$  and  $x = 0.20$  where at high temperatures we find paramagnetic insulating states in both. But at low temperatures they are markedly different from electronically as well as magnetically from each other. Both the systems undergo a Curie transition (magnetic) at  $T_C$  and appeared to be metallic and ferromagnetic below  $T_C$ . But the low doped one ( $x = 0.20$ ) fails to retain its metallic behaviour throughout the low temperature regime and becomes highly insulating being in the ferromagnetic phase and gives rise to another MIT. The other sample has only one MIT  $\sim T_C$ . We can expect distinct signature of fluctuation processes in different phases of them. We found discrete two-level fluctuation processes (generally called Random Telegraphic Noise, i.e., RTN) near MIT in  $x = 0.33$  systems. We also found that these fluctuations can dominate at very low frequency domains and carry clear evidence of simultaneous presence of different electronic and magnetic phases near MIT. Again, the low doped one in the insulating side shows a very slow and correlated dynamics which can be interpreted as an onset of glassy electronic system via long range Coulomb interaction. The physics of glassy systems is one of the most interesting and least understood problems in condensed matter physics. In the field of disordered systems investigating several topics including the Coulomb glasses and the low temperature properties of these are very important to discuss. The glassy dynamics of these low doped

manganites have been explored theoretically but experimentally it is not revealed completely. By noise spectroscopy we focused to the charge fluctuations phenomena in glassy phase and as per our knowledge which is not done till date.

Our thesis is an attempt to understand the nature of correlated dynamics and some fundamental physical phenomena in manganites. The motivation of our present work is to try and characterize the behaviour of these fluctuations near the MIT point over time scales ranging from 1-1000 sec. Spectral analysis and distributions give important information about nature of dynamics occurring in various states of perovskite manganites.

In the next section we shall introduce about the perovskite system under study and then we shall discuss the basic theories regarding noise spectroscopy. Hence, understanding the physics of the fundamental processes going on in manganites can be probed by simple resistance fluctuations phenomena and this is the main interest of this dissertation.

## 1.2 Introduction to Perovskite Manganites

### 1.2.1 Introduction:

The aim of this section is to give a general introduction to structural, magnetic, and electronic properties of doped lanthanum manganites, and thereby form the basis for the discussion on the experimental results obtained for the  $\text{La}_{1-x}\text{A}_x\text{MnO}_3$  compounds at doping level  $x \leq 0.33$  under investigation. The samples belong to the broad family of manganese oxide,  $RE_{1-x}A_x\text{MnO}_3$ , where  $A$  is the rare-earth cation ( $\text{La}^{3+}$ ,  $\text{Pr}^{3+}$ ,  $\text{Y}^{3+}$ ,  $\text{Nd}^{3+}$ ...) and  $A$  is an -alkali or alkaline earth cation ( $\text{Ca}^{2+}$ ,  $\text{Sr}^{2+}$ ,  $\text{Ba}^{2+}$ ,  $\text{Na}^+$ ,  $\text{K}^+$ ....). These are known as mixed-valence manganites, because Mn may consist in several valence states. They are also called doped manganites, referring to the fact that the substitution of the rare-earth cation ( $RE$ ) with an alkali- or alkaline earth cation ( $A$ ) serves as hole doping. Most manganites form perovskite crystals (crystal structure resembles with mineral perovskite), including the layered perovskites (the Ruddlesden-Popper phases).

These materials display Curie transition ( $T_C$ ) below which the conduction electrons are highly spin polarized. There exists delicate energy balance among electronic, magnetic, and lattice which makes ground state inhomogeneous, leading to a multitude of ordered phases and thus a very rich phase diagram. There are varieties of ordered ground states for manganites, ranging from ferromagnetic metallic state to charge and orbital ordered insulating states can also have antiferromagnetic spin order. The most fascinating properties of the manganites are the influence of a magnetic transition on the electronic conduction. Already in 1950, Jonker and Van Santen [15] discovered that the resistance below the magnetic ordering,  $T_C$  exhibits a positive thermal coefficient, indicating metallic-like behaviour and a negative gradient above  $T_C$ . This brings maximum in the resistivity near  $T_C$ . This behaviour were only explored in 1993, when a reduction of the resistance was observed in thin films under application of an external magnetic field by Chahara et al. [16] and Von Helmolt et al. [17]. This reduction was only 50% of the zero field resistance. A year later it proved to be possible to reduce the resistivity by several orders of magnitude [18] and could not be compared with any other kind of magnetoresistance. To distinguish this effect from the Giant Magnetoresistance (GMR) observed in multilayers [19, 20] it was called “Colossal Magnetoresistance” (CMR). Where GMR is restricted below  $T_C$ , CMR is a bulk property which originates from magnetic ordering and is usually confined to the vicinity of  $T_C$ . This effect opened up a new era of practical and potential applications for magnetic sensors, read-write heads in the magnetic storage devices having larger efficiency and capacity.

The coupling between electrons and lattice vibrations (phonons) are unusually strong in these materials and brings about that a small change in chemical composition, like the ratio between trivalent and divalent ions at the *A* site or the average ionic radius of the ions on the *A* site, leading to a wide range of striking physical phenomena. And most crucially, a similar effect can occur due to external effects, such as temperature, hydrostatic pressure and external magnetic field. These materials therefore provide an unprecedented opportunity to study the physics of strongly coupled system and to elucidate the interplay between local structure and global properties. The following subsections will be on a brief overview of the physics of manganite system in general, where we discuss crystallographic structure, energy scales which have dominant effect on electrical conduction and magnetic transitions and the phase diagrams. Following this, we give a brief review of the ferromagnetic metallic (FMM) and ferromagnetic insulating (FMI) states in manganites. Extensive reviews are available in the published literatures [7-9, 21-26].

## 1.2.2 Manganite Parameters

This section will discuss the definite ionic composition, and crystallographic structures of transition metal oxides. In this section we give a brief phenomenological introduction to the exotic features of these materials.

### 1.2.2.1 Ionic composition

Lanthanum manganites,  $\text{La}_{1-x}A_x\text{MnO}_3$ , can be regarded as a binary system consisting of a solid solution between the end-members  $\text{LaMnO}_3$  and  $AM\text{nO}_3$ , corresponding to  $x = 0$  and  $x = 1$ , respectively. In general, the oxygen atom has a great avidity for two electrons and studies of the crystal chemistry of lanthanum manganites Jonker and van Santen (1950) have shown that oxygen occurs exclusively as  $\text{O}^{2-}$ , regardless of the nature of the atom *A* and the value of *x*. Thus, the formal valence states of the  $x = 0$  is end-member  $\text{La}^{3+}_{1-x}\text{Mn}^{3+}\text{O}^{2-}_3$ . If, however, a number of  $\text{La}^{3+}$  ions are substituted by a divalent ion, such as  $\text{Ca}^{2+}$ , a corresponding number of Mn ions become tetravalent. Hence, the resulting compound have mixed manganese valence and can be written  $\text{La}^{3+}_{1-x}A^{2+}_x(\text{Mn}^{3+}_{1-x}\text{Mn}^{4+}_x)\text{O}^{2-}_3$ . Thus, substitutions and the co-existence of manganese in two valence states provide extensive possibilities to tailor the chemical compositions, and thereby the properties of the materials. The substitution affects mainly two things:

- The interatomic distances and angles causing distortions that influence not only the crystallographic structure but also the physical properties.
- The number outer shell electrons present in the Mn ions-some of the effects of this on magnetic and electronic properties will be discussed in the next subsections.

### 1.2.2.2 Crystallographic structure

The parent compound  $\text{LaMnO}_3$  crystallize in the various derivatives of the so-called perovskite structure of empirical formula  $REM\text{nO}_3$  as shown in Fig. 1.3. The ideal perovskite structure is cubic, and can be regarded as three dimensional networks of  $\text{MnO}_6$  octahedra, with smaller Mn ions in the middle of the octahedra. In the cubic perovskite the *RE* site is twelve-fold surrounded by oxygen ions. But the ionic radius of the *RE* ion is smaller than the volume, enclosed by the oxygen ions. The volume can be reduced by rotating the octahedra with respect to each other. Many perovskite adopt this structure at high temperatures, but are distorted at lower temperatures.

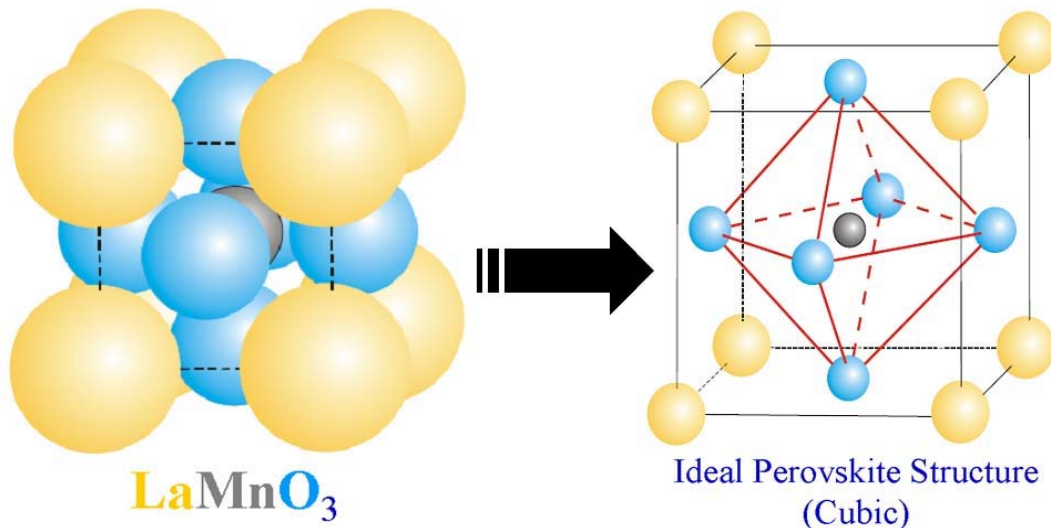


**Figure 1.3:** Left image is a sketch of the ideal perovskite *Pnma* structure. The detailed illustration of the structure emphasizing the octahedral environment of the Mn cations where the oxygens are situated at the corners of the octahedras is shown in the right image [27].

The first report on the crystal structure of the manganites dates back to 1943 by Náray-Szabá [28]. In 1968 it was first reported that  $\text{REMnO}_3$  has the *Pnma* space group [29], but this report did not include  $\text{LaMnO}_3$ . Just  $\text{LaMnO}_3$  has nearly cubic (pseudocubic) lattice parameters, which makes a structure solution and refinement very hard. Elemans *et al.* were the first to report the *Pnma* space group for pure  $\text{LaMnO}_3$  [30]. In order for the ions to be in contact with each other in the ideal cubic structure,  $(r_{RE} + r_O)$  must be equal to  $\sqrt{2}(r_{Mn} + r_O)$ , where  $r_{RE}$ ,  $r_{Mn}$  and  $r_O$  are the ionic radii of  $RE$ , Mn and oxygen ions. From this relation Goldschmidt has defined a tolerance factor,  $t' = (r_{RE} + r_O)/[\sqrt{2}(r_{Mn} + r_O)]$ . This criterion is fulfilled if the radius of the  $RE$ -site cation equals that of oxygen (0.140 nm) and the radius of the  $A$ -site cation is equal to  $(\sqrt{2} - 1)r_O = 0.058$  nm. If  $t'$  differs slightly from unity the atoms are displaced from their ideal positions to minimize the free energy and a distorted perovskite structure is formed. The perovskite structures are stable within the range  $0.89 < t' < 1.2$  in oxides. Larger deviations from unity will lead to a different structure, e.g. ilmenite for  $t' < 1$  and calcite for  $t' > 1$  [15].

The oxygen stoichiometry of these  $\text{REMnO}_3$  compounds is very sensitive to the synthesis conditions. Most of the perovskite manganites are of cubic structure with  $t'=1$ , is distorted by cation concentration, cation size mismatch and Jahn-Teller (JT) effect, and there is a variety of cubic, tetragonal, rhombohedral, hexagonal, orthorhombic and monoclinic structures with rhombohedral and monoclinic angles close to the ideal values  $\alpha_r = 60^\circ$  and  $\alpha_m = 90^\circ$ ,  $\beta_m = 90^\circ$  respectively.  $\text{LaMnO}_3$  has an orthorhombic, perovskite structure (at ambient conditions), which apart from the buckling of the network of  $\text{MnO}_6$  octahedra arising from the misfit in ionic sizes ( $t' = 0.95$ ), incorporates a severe distortion of the  $\text{MnO}_6$  octahedra due to JT effect of  $\text{Mn}^{3+}$  [21]. The insulating nature and the anisotropic magnetic nature of  $\text{LaMnO}_3$  arises out of its structural distortions, in particular the JT distortion and orbital ordering. Thus the structure and the distortions around the  $\text{Mn}^{3+}$  play a crucial role in determining the electronic transport and magnetic properties of these oxides. The true unit cell of  $\text{La}_{1-x}\text{Ca}_x\text{MnO}_3$  is orthorhombic *Pnma* with  $a \approx c \approx \sqrt{2}a_p$ , and  $b \approx 2a_p$ , where  $a_p$  is the lattice parameter of the pseudo-cubic unit cell and remains orthorhombic for all levels of

Ca doping. The true unit cell is shown in Fig. 1.4(a) and the relationship between cubic and orthorhombic unit cells is given in Fig. 1.4(b).

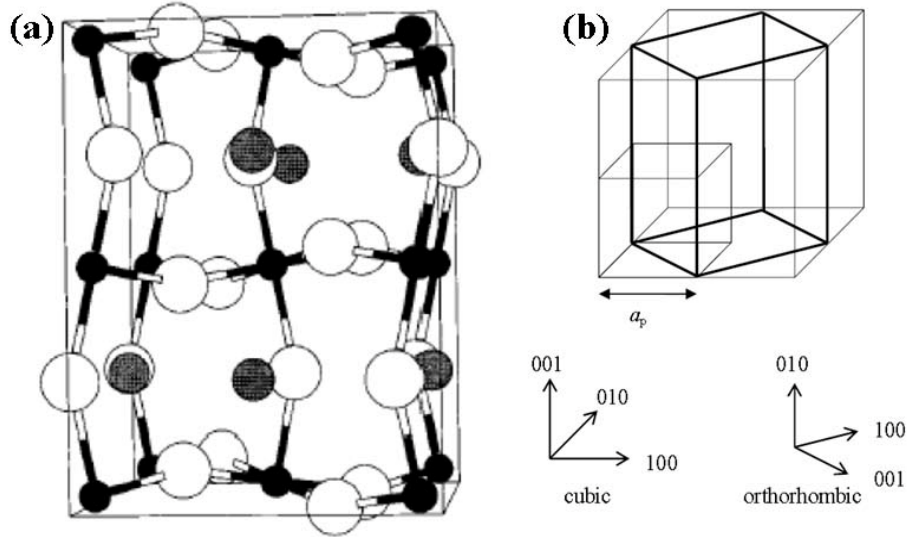


**Figure 1.4:** (a) The *Pnma* unit cell of  $\text{La}_{1-x}\text{Ca}_x\text{MnO}_3$ , giving an impression of the distortions from the cubic unit cell. The ions are represented by black (manganese), grey (La or Ca) and white (oxygen) spheres respectively. The region shown comprises four cubic perovskite building blocks. [31] (b) Orthorhombic (thick lines) and cubic (thin lines) unit cells for  $\text{La}_{1-x}\text{Ca}_x\text{MnO}_3$  and the relative orientations of the crystallographic axes [32].

### 1.2.2.3 Orbital structure

The end-members,  $x = 0$  and  $x = 1$ , containing Mn in only one valence state are usually antiferromagnetic insulators, but intermediate compositions, which have mixed Mn valence, may be ferromagnetic and have good conducting properties.

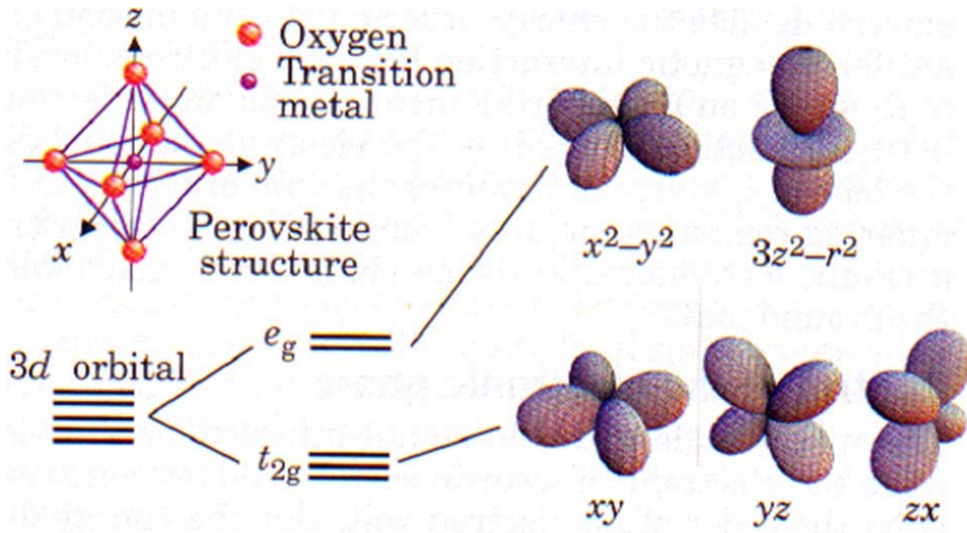


**Figure 1.5:** Structure of  $d$ -orbitals in manganites and show the single-electron wavefunctions for the  $d$ -shell in Mn. The  $e_g$  orbitals are higher in energy in the manganites (top orbitals) whereas the bottom three orbitals represent single particle  $t_{2g}$  states. The  $t_{2g}$  states are oriented with electron cloud lobes directed in between the oxygen bonds. The images are taken from [34].

The  $\text{Mn}^{2+}$ ,  $\text{Mn}^{3+}$ , and  $\text{Mn}^{4+}$  valence state of Mn found in manganites have 5, 4, and 3 electrons in  $3d$  levels. For manganese we shall focus only on the electronically active orbitals i.e., manganese  $d$  orbitals. Many properties of these materials, from colour to magnetism, are strongly determined by energetics of the complex ion formation by the  $d$ -orbitals of transition metal compounds [34].

In free space, the manganese  $d$ -levels are 5-fold degenerate. Due to the presence of nearby atoms there is a crystal field which lift this degeneracy wholly or partially through hybridization or by Coulombic interactions. Fig. 1.5 shows 5-fold degenerate  $d$ -orbitals. The orbital structures have been constructed from single-particle spherical harmonic wavefunctions and Hydrogen atom solutions.

In manganese the crystal field splitting is cubic as Mn atom is enclosed by octahedra of oxygen atoms. This geometry splits the 5-fold degenerate states into two sets: 3-fold set of  $t_{2g}$  orbitals (lower energy) and 2-fold degenerate set of  $e_g$  orbitals (higher energy). The ground state electronic configuration of trivalent ( $\text{Mn}^{3+}$ ) and quadrivalent ( $\text{Mn}^{4+}$ ) Mn is  $3d^4$  and  $3d^3$ , respectively. The  $\text{Mn}^{3+}$  ion has four electrons in its outermost  $3d$  energy level, out of possible ten. Among the five  $d$  orbitals, each of which can accommodate one spin-up and one spin-down electron. Hund's atomic rule dictates that the four electrons in manganese ion should point in the same direction to minimize the electrostatic repulsions. As spin-up and spin-down states are separated in energy, four electrons occupy the spin state with the lowest energy. Electrostatic interactions between these four electrons and the neighbouring six oxygen ions cause this single spin state to split by the octahedral crystal field into triplet with three electrons and doublet with one electron.

### ***The triple degenerate electron states:***

The  $t_{2g}$  orbitals are with energy 1eV [21] and are lower than two higher lying  $e_g$  states. These three degenerate states ( $d_{xy}$ ,  $d_{yz}$  and  $d_{zx}$ ) are energetically favourable for the electrons to occupy before either of  $e_g$  orbitals. Hence, these three  $t_{2g}$  orbitals are filled at first and are largely localized. These spins couple strongly ferromagnetically to each other and hybridize weakly with O  $2p$  states-strengthening the tendency to remain immobile.

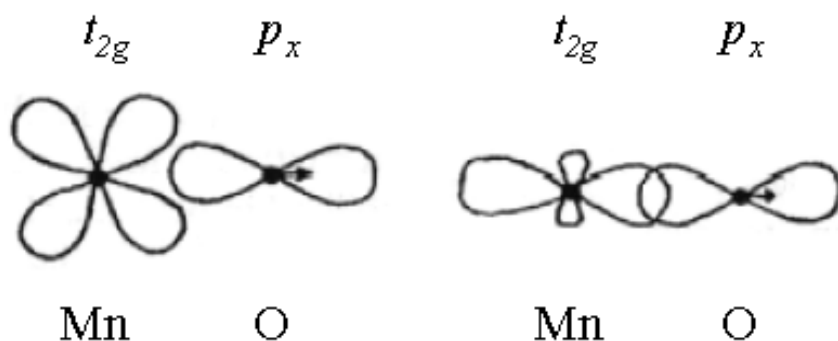


**Figure 1.6:** Illustration of orbital overlaps between Mn  $t_{2g}$  and Mn  $e_g$  orbitals with a  $p$  orbital of a neighbouring O ion.

The  $t_{2g}$  orbitals have their lobes oriented between the oxygen neighbours as shown in Figure 1.6. Again, there exists strong electrostatic repulsion between the electron orbitals and the negatively charged O bonds. Thus these electrons take more energy to be activated. This set

of spin is treated as “core spin” of magnitude  $S = 3/2$ . The on-site Hund’s coupling tends to align the  $e_g$  spin to the  $t_{2g}$  core spin. The exchange energy due to Hund’s rule coupling is  $\sim 2\text{-}3$  eV for the manganites. Regardless of doping, each Mn site will normally produce the spin  $3/2$  magnetic moment below magnetic transition temperature.

### **The double degenerate electron states:**

The rest 2-fold degenerate states ( $d_{x^2-y^2}, d_{3z^2-r^2}$ ) are  $e_g$  orbitals point directly to O atoms (compare Fig. 1.3 and Fig. 1.5). Hence, they hybridize with the oxygen  $2p$  orbitals giving strong itinerant characteristics [35]. Due to the presence of this hybridization, the energy bands are dispersive and electrons would traditionally form the conduction band in ferromagnetic states. We mentioned earlier that each Mn atom has either three or four  $d$ -electrons. This implies that there is a degree of freedom for the  $e_g$  orbitals. These states contain either none or one valence electron available for filling.

After considering the degeneracy, the electronic configuration of  $\text{Mn}^{3+}$  is  $t_{2g}^{3\uparrow} e_g^{\uparrow}$ , while  $\text{Mn}^{4+}$  having configuration  $t_{2g}^{3\uparrow}$ . However all the  $3d$  electrons are subject to strong electron correlation effect.

## **1.2.3 The Main Classes of Ordering**

The interesting property of manganites is its complex phase diagram with doping concentration. There is critical energy balance among different interactions which govern the nature of the phase diagram as well as complex structures of these systems. In this section we shall discuss four relevant ordering mechanisms, charge, lattice, magnetic and orbital.

### **1.2.3.1 Charge ordering**

By substituting alkaline earth atoms for rare-earths, the doping effectively changes the Mn lattice from  $d^4$  to  $d^3$ . As a result, there is a mixture of Mn species.

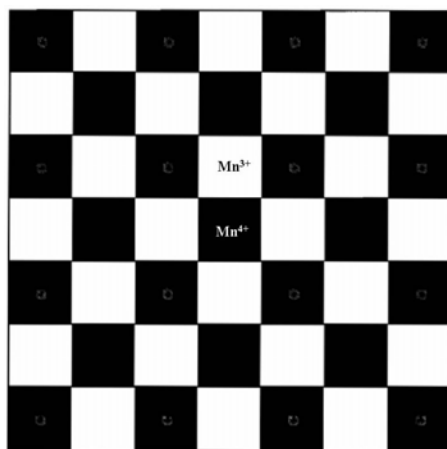


**Figure 1.7:** Charge ordering for a half-doped system: a “checker board type” ordering is shown [37]. Each black square represents  $\text{Mn}^{4+}$  charged ions, and white  $\text{Mn}^{3+}$ .

A typical example of these doped manganites is the class of manganites formed by the doping of the parent compound  $\text{LaMnO}_3$ . The doping is achieved by replacing a fraction of La with

divalent alkaline earth cations  $A$  to have mixed valence  $\text{La}_{1-x}\text{A}_x\text{MnO}_3$ . These doped manganites have simultaneous presence of manganese in different valence states and  $x$  fraction of  $\text{Mn}^{3+}$  changes to  $\text{Mn}^{4+}$  creating  $(1-x)$  itinerant  $e_g$  electrons. It has been investigated that, below some ordering temperature, the  $\text{Mn}^{4+}$  ions will order mostly due to Coulomb repulsion. Goodenough [36] presented a “checker board type” cartoon diagram of this ordering as shown in Fig. 1.7.

This cartoon is the simplest one where equal number of sites that differ in charge by one unit. The author found that when Coulomb interaction between “extra” charged valance electrons dominate, the system forms a pattern that maximizes the distance between that charges in all directions. The author has described an energy point where kinetic energy of the itinerant electrons decreases to the energy scale of the Coulomb repulsion which localizes the charge carriers. Below this point Coulomb energy dominates the energy decrease due to conduction mechanism and the electrons are affiliated with the respective Mn sites. As a result, the states become insulating with the relative energy balance of kinetic and coulomb terms.

### 1.2.3.2 Jahn-Teller effect

In 1948, H. J. Jahn and E. Teller introduced theory [37] which described the electron trapping in solids considering symmetry considerations. This effect is now well known as Jahn-Teller (JT) effect which does not imply a lifting of degeneracy but an asymmetry corresponding to an instability of the lattice.

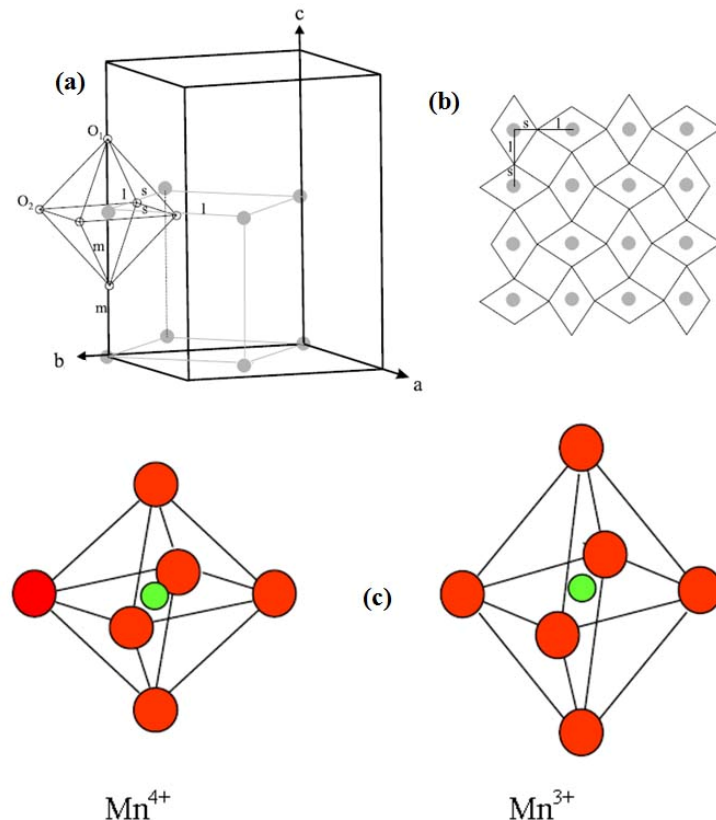


**Figure 1.8:** (a) The JT distorted perovskite structure (the rotation is not indicated). The cubic and orthorhombic unit cells are indicated by thin and thick contours respectively. (b) The  $ab$  plane highlighting the alternation of the short and long  $\text{Mn}-\text{O}$  distances in  $a$  and  $b$  directions. (c) The shape of  $\text{MnO}_6$  octahedra in  $\text{Mn}^{4+}$  and  $\text{Mn}^{3+}$  ions [32].

In the manganites, this instability leads to a distortion of the local oxygen lattice around the immediate vicinity of the Mn, which effectively lifts the degeneracy of the two  $e_g$   $d$ -states. Crystal field splitting, as noted earlier, is responsible for lifting the degeneracy of the 5-fold degenerate  $d$ -states, but leaves two  $e_g$  states set with equal energies. The  $e_g$  splitting takes place due to the oxygen distortion and this distortion can act as an anomaly that traps the electron, removing its itinerancy. The Jahn-Teller distortion is only energetically favourable if either of the  $t_{2g}$  or  $e_g$  sets is partially occupied. This only occurs for  $\text{Mn}^{3+}$  with its single  $e_g$  electron.  $\text{Mn}^{4+}$  gains nothing from distortion of the oxygen octahedron. In a Jahn-Teller distortion the Mn-O bond length is increased in the  $c$  direction and increased slightly in the  $a-b$  plane as shown in Fig. 1.8(a) and Fig. 1.8(b). When an  $e_g$  electron moves between adjacent Mn ions the Jahn-Teller induced lattice distortion moves with it. This coupling between the lattice distortion and the  $e_g$  electron is known as a polaron. At room temperature, the polarons are free to move throughout the crystal and the paramagnetic state is essentially a polaronic liquid [38].

### 1.2.3.3 Magnetic ordering

The magnetic properties are largely dominated by the transfer of electrons between Mn and O orbitals. Actually, there is an exchange interaction between the Mn ions spins. These interactions are relatively large between the two Mn spins separated by an O atom and are controlled by the overlap between the Mn  $d$ -orbitals and the O  $p$ -orbitals. Depending on the types of the orbitals involved, the interaction is antiferromagnetic (AFM), or ferromagnetic (FM). For an example:  $\text{Mn}^{4+}$ -O- $\text{Mn}^{4+}$  interaction is AFM type whereas,  $\text{Mn}^{3+}$ -O- $\text{Mn}^{3+}$  interaction may be AFM or FM type.  $\text{LaMnO}_3$  has all the Mn ions at 3+ states, both FM and AFM type interactions coexist.

Zener [39] and Anderson [40] have shown that Mn-O-Mn bonding arrangement determines the magnetic coupling in perovskite manganites. They inferred that if neighbouring Mn ions point their empty orbitals towards  $\text{O}^{2-}$  then Mn-Mn separation is small and coupling between Mn ions is AFM. But if one of the neighbouring Mn ion points its occupied orbital towards O then the two Mn ions will be ferromagnetically coupled. Generally there are two different types of interactions possible for magnetic coupling in these manganites namely, double exchange and superexchange.

#### ***Double exchange:***

Due to parallel coupling to the Mn core spin moments, electrons moving with conserved spin are origin of a ferromagnetic exchange interaction.

Zener [39] introduced the concept of the ferromagnetic double exchange for manganites, assuming two simultaneous electron transfers: one electron from  $\text{Mn}^{3+}$  to a neighbouring O  $2p$  orbital, and a second electron transfer from this  $2p$  orbital to an adjacent  $\text{Mn}^{4+}$  ion. The final and initial states after going through this process are degenerate. Hence, these two states coexist and the two Mn core moments couple ferromagnetically. The schematic diagram of the double exchange (DE) mechanism is shown in Fig. 1.9. According to Zener double exchange is a magnetic interaction mediated by itinerant spin polarized  $d$ -electrons which couple according to Hund's rule to localized magnetic moments [9]. These itinerant electrons are energetically favourable to gain kinetic energy. The DE neglects the role of oxygen. The author also postulated the electrical conduction mechanism by double exchange in manganites.

Zener calculated the electrical conductivity  $\sigma$  was given by equation 1.1 as

$$\sigma = \left( \frac{xe^2}{a_p h} \right) \left( \frac{T}{T_c} \right) \quad (1.1)$$

where  $x$  is the level of calcium doping,  $a_p$  is the pseudo-cubic lattice parameter,  $h$  is the Planck's constant,  $e$  is the electronic charge,  $T_c$  is the Curie temperature. DE is a very simple model to explain the basic ferromagnetism in the system. Beyond that it fails to explain - neither the metal-insulator transition at  $T_c$  nor the Colossal Magnetoresistance (CMR) effects (discussed later).

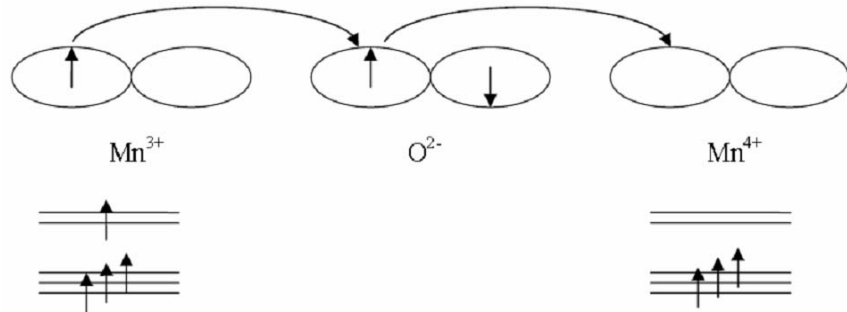


**Figure 1.9:** A schematic diagram of the double exchange mechanism showing the simultaneous transfer of electrons between adjacent ions and the orientation of the Mn spins.

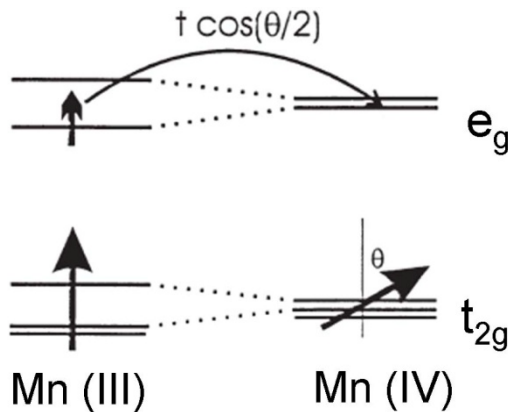


**Figure 1.10:** Schematic diagram for double exchange mechanism. Adapted from reference Mathur et al. [24].

The theory was further enriched by Anderson and Hasewaga [41] to calculate the exact hopping amplitude of electrons. The double exchange Hamiltonian can be written in block form as

$$\begin{bmatrix} -J_H S_1 \cdot s & t_0 I \\ -t_0 I & -J_H S_2 \cdot s \end{bmatrix}, \quad (1.2)$$

where  $J_H$  is the on-site Hund rule coupling. The diagonal elements corresponds to energy states of one electron and a Mn<sup>4+</sup> core at site 1 and 2 respectively. The off-diagonal elements

correspond to transfer between the two sites, where  $t_0$  is transfer integral and  $I$  is the  $(2 \times 2)$  unit matrix. The detailed diagonalization calculations are not shown here. For  $J_H \gg t_0$ , there are two low-energy solutions are possible, which gives

$$E = -\frac{J_H S}{2} \pm t_0 \cos\left(\frac{\theta}{2}\right), \quad (1.3)$$

where  $\theta$  is the angle between two  $Mn^{4+}$  core spins. The ground state energy is lowest when these neighbouring core spins are parallel ( $\theta = 0$ ). Thus double exchange mechanism favours the ferromagnetism and the transfer integral can be written in a simplified form as

$$t = t_0 \cos\left(\frac{\theta}{2}\right). \quad (1.4)$$

Figure 1.10 shows the double exchange mechanism schematically. The double exchange mechanism is based on two assumptions: the electron transfer takes place with spin memory and the transfer integral  $t_0$  depends on the angle between two adjacent core spins. An electron travelling from a  $Mn^{4+}$  core with one spin direction to other  $Mn^{4+}$  core with different spin direction causes the direct violation of first Hund's rule and the energy is required to align the core spins on the Mn sites where the electron arrives. Since the electron transfer depends on the angle between neighbouring magnetic moments, double exchange mechanism explains why the mixed valence manganites show a close relationship between magnetism and electrical transport. As it was earlier mentioned that amount of  $Mn^{4+}$  present in a mixed valence manganites ( $La_{1-x}A_xMnO_3$ ) depends on  $x$ . The basic DE model is in qualitative agreement with the experimental data. However, it cannot successfully explain the resistivity of the insulating state, the magnitude of the CMR effect or the observed transition temperatures.

#### **Superexchange:**

This is a very common interaction in most of the oxides mainly in insulating magnetic oxides where the magnetic interaction between adjacent ions is mediated by that inter medium non-magnetic ion with a closed shell. The intermediate ion is  $O^{2-}$  in superexchange.

If two orbitals on adjacent ions point towards each other, with one orbital fully occupied and the other orbital having a vacancy, then the electron will spend part of its time in the empty orbital on the other ion. For the case of the manganites, the orbitals involved are the vacant Mn  $e_g$  orbital and the occupied O  $2p$  orbital, and so it is the O  $2p$  electron that is ‘shared’ between the two ions. This *virtual transfer* of the electron is what characterises superexchange. This mechanism leads to either FM or an AFM alignment of the spins, depending on the occupancy of Mn orbitals as depicted in Fig. 1.11. There is strong Hund coupling between the core Mn  $t_{2g}$  spins and any  $e_g$  electron(s). There are two cases to consider, namely when the Mn  $e_g$  orbital has one permanent electron ( $Mn^{3+}$ ) and occasionally the virtual electron, or only the virtual electron ( $Mn^{4+}$ ). For  $Mn^{4+}$ , the  $t_{2g}$  and permanent  $e_g$  electron will be spin-aligned (Hund’s rules), so the spin of the transferred electron has to have the opposite sign, as required by the Pauli Exclusion Principle.

Conversely, for  $\text{Mn}^{4+}$ , the electrons in the Mn  $t_{2g}$  orbitals align with the virtual electron from the oxygen ion.

By applying these two rules and noting that the two electrons from the O  $2p$  orbital have opposite spins, we find that two adjacent empty Mn orbitals or two half-full orbitals will lead to antiferromagnetic order, whereas an empty Mn orbital pointing towards a half-full one will lead to a ferromagnetic alignment of the core Mn spins. However, unlike double exchange, superexchange always results in an insulating state.

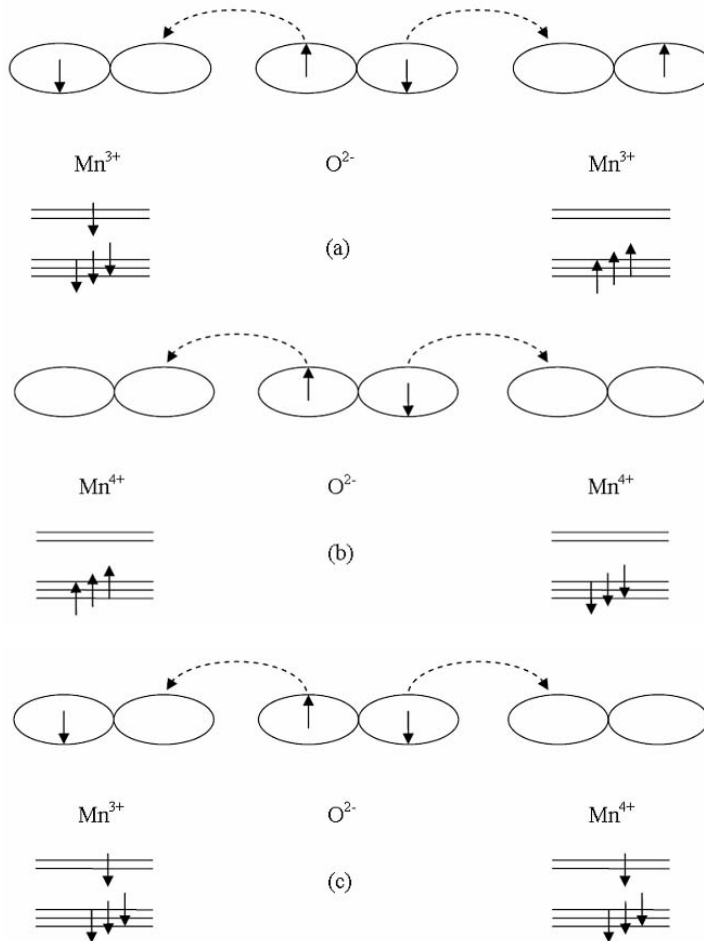


**Figure 1.11:** Schematic diagram showing the arrangement of spins and orbitals in superexchange. The orbitals involved are the Mn  $e_g$  and O  $2p$ , and the dashed arrows represent the virtual transfer of the electron between these orbitals. This means that the electron is located on the oxygen ion for the majority of the time, but can be found in the manganese orbital indicated by the arrow. The three panels result in an (a) antiferromagnetic, (b) antiferromagnetic and (c) ferromagnetic arrangement of the core manganese spins respectively.

#### 1.2.3.4 Orbital ordering

The orbital ordering refers to the ordering of the valence electron wavefunctions between sites that occupy a similar state. Due to a number of different interactions, a certain type of pattern can occur among sites that share the same orbital characteristics. This type of ordering is common to many  $d$ -electron systems to understand the magnetism in them. This is an important phenomenon which is believed to be responsible for the richness of the phase diagram of the manganites. Some of the exciting and also poorly understood functions in

these systems are thought to be the direct consequence of orbital ordering, including ferromagnetic insulating (FMI) states, stripes, or the asymmetry in the phase diagrams [41].

The orbital ordering means the ordering of the  $e_g$   $d$ -states of manganese. In the Mn lattice of  $\text{CaMnO}_3$  with  $x = 1$ , every site has an unoccupied  $e_g$  orbital, and so any amount of distortion of the oxygen sub-lattice will not display an effect on the  $d$ -orbitals in a cubic crystal field. As these orbitals are largely unoccupied, the JT effect merely refers to the structural distortion of the oxygen lattice. The magnetism has been experimentally demonstrated by taking into the orbital ordering mechanism. In this situation, JT effect is much stronger and is a direct effect, the orbital structure is largely dominated by the distortion of the oxygen octahedra due to Coulomb effects between the oxygen valence and manganese  $d$ -shell electrons. When the JT effect is weak or absent, the superexchange mechanism will completely determine the orbital ordering. In this case the distortion of oxygen atoms is not present yet having a strong self-ordering of the  $e_g$  Mn orbitals can be found. The orbital degree of freedom controls the sign and magnitude of the spin exchange interaction. Parallel orbitals are AFM ordered while orthogonal ones are FM. This usually is accompanied by a JT-distortion of the oxygen octahedra, but in certain cases can occur with very little lattice distortion.

We have discussed different effects in manganite systems. The energy scales involved for different mechanisms discussed so far are listed in Table 1.1 below.

| Hund's coupling [23, 42] | Crystal field splitting [23, 43] | Jahn-Teller distortion [44, 45] | Coulomb interaction [21] | Transfer hopping amplitude [46, 49] | AFM exchange energy [50] | $n$ [23, 42] |
|--------------------------|----------------------------------|---------------------------------|--------------------------|-------------------------------------|--------------------------|--------------|
| $E_H$ (ev)               | $E_{CF}$ (ev)                    | $E_{JT}$ (ev)                   | $U$ (ev)                 | $t$ (ev)                            | $E_{AFM}$ (ev)           | $E_{JT}/t$   |
| 0.8-2                    | 1-1.5                            | 0.2-0.3                         | 2-5                      | 0.2-0.5                             | 0.02-0.05                | 1-1.5        |

**Table 1.1:** Approximate values for the energy scales of interaction mechanisms in manganites.

## 1.2.4 Doping Dependent Magnetization

The electron transfer depends on the angle between neighbouring magnetic moments. As it was earlier mentioned that amount of  $\text{Mn}^{4+}$  present in a mixed valence manganites ( $\text{La}_{1-x}\text{A}_x\text{MnO}_3$ ) depends on  $x$ . Figure 1.12 shows the ferromagnetic moment of  $\text{La}_{1-x}\text{Ca}_x\text{MnO}_3$  as a function of  $x$  (or equivalently the  $\text{Mn}^{4+}$  content).

For  $x = 0$  the material is antiferromagnetic, but as  $x$  is increased and double exchange becomes dominant, the ferromagnetic moment increases.

For  $x = 0.33$ , maximum value of moment is observed around where the ferromagnetic moment approaches the theoretical spin-only value for a ferromagnetic mixture of  $\text{Mn}^{3+}$  and  $\text{Mn}^{4+}$  (calculated as  $(1-x)\mu_B + 3x\mu_B$ , where  $\mu_B$  is the Bohr magneton). Upon a further increase of  $x$  the ferromagnetic moment starts to decrease. This is due to the direct overlap between  $t_{2g}$  orbitals, which leads to antiparallel exchange coupling because only the spin-down states are empty [36].

For  $0.33 < x < 0.5$ , there exists a competition between the ferromagnetic  $\text{Mn}^{3+}$ - $\text{Mn}^{4+}$  double exchange coupling and the antiferromagnetic  $\text{Mn}^{4+}$ - $\text{Mn}^{4+}$  coupling.

For  $x = 0.5$ , antiferromagnetism becomes dominant due to superexchange, charge and orbital ordering becomes important for conduction process.

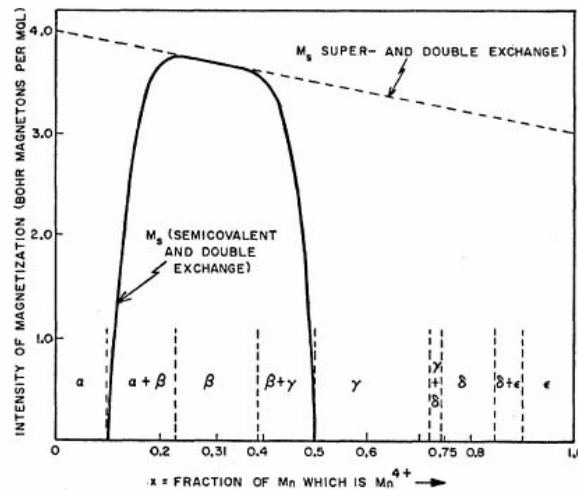


**Figure 1.12:** Predicted intensity of magnetization  $M_S$  as a function of  $x$  in  $La_{1-x}Ca_xMnO_3$  system [36].

### 1.2.5 Cationic Disorder

Other than doping concentration another important parameter is cationic radius  $\langle r_A \rangle$  which determines the physical properties of manganites. There is no doped manganite without disorder, as long as two or more different ions reside on the La lattice site at random. For instance,  $La^{3+}$ , and  $Ca^{2+}$  in  $La_{0.7}Ca_{0.3}MnO_3$  have different ionic radius and charge. This disorder will be induced by the radius variation on the La site has been quantified by the variance  $\langle \delta^2 \rangle = \langle r_A^2 \rangle - \langle r_A \rangle^2$  [51].

The amount of the substitution of divalent cations controls the valence of Mn ions while the average radius of the cations (both divalent and trivalent), is given by

$$\langle r_A \rangle = (1-x)r_{La}^{3+} + xr_A^{2+}. \quad (1.5)$$

The radius variation introduces the distortion in lattice. We have mentioned earlier that transfer integral  $t$  of an  $e_g$  electron between two neighbouring Mn sites is mediated by the O  $2p$ -orbitals and hence the hybridization between Mn  $3d$ -orbitals and O  $2p$ -orbitals is sensitive to lattice distortion and tilting of  $MnO_6$  octahedra. The distortion increases with the decrease of  $\langle r_A \rangle$  which causes the narrowing of  $e_g$  band. This will destabilize the DE FM state and directly affecting the ferromagnetic and metallic transition temperature.

The parameter  $\langle \delta^2 \rangle$  allows explaining discrepancies of  $T_C$  (Curie temperature),  $T_N$  (AFM transition temperature),  $T_{CO}$  (Charge ordering temperature) that are exhibited by two compounds with same doping level and  $\langle r_A \rangle$  but different cations. Whatever the value of  $\langle r_A \rangle$  and manganese valency are, the increased  $\langle \delta^2 \rangle$  depresses the magnetic interaction in FM and AFM and destroy CO into weak ferromagnetism when the value becomes very high.

### 1.2.6 Magnetic and Electronic Phase diagrams

In previous sections the essential contributions to the electronic energy in manganites have been outlined. Summarized these are (i) the kinetic energy of  $e_g$  electrons, (ii) the Hund on-

site magnetic coupling between  $e_g$  and  $t_{2g}$  electron spins, (iii) the coupling between  $e_g$  electrons and distortion of  $\text{MnO}_6$  octahedra (JT Effect), (iv) the crystal field splitting in the octahedral coordination, (v) the Heisenberg magnetic coupling between nearest neighbour localized electron spins, and (vi) the Coulomb interaction between  $e_g$  electrons. Dominance of one or combination of these contributions results in a multitude of different ground states. With respect to the chemical composition, the ground state of  $\text{La}_{1-x}\text{A}_x\text{MnO}_3$  depends on (i) the number of doped charge carriers  $x$ , (ii) the average ionic radii on La and Mn lattice sites and (ii) the scatter of ionic radii on La site measured by a disorder parameter  $\delta$ . In this section we discuss about the ground states (in general) observed for manganites include ferromagnetic metals (frequent), antiferromagnetic insulators (very frequent), ferromagnetic insulators (rare), antiferromagnetic metals (rare), glassy insulators, and more complex canted magnetic structures and even mixed-phase states as described in Fig. 1.13.

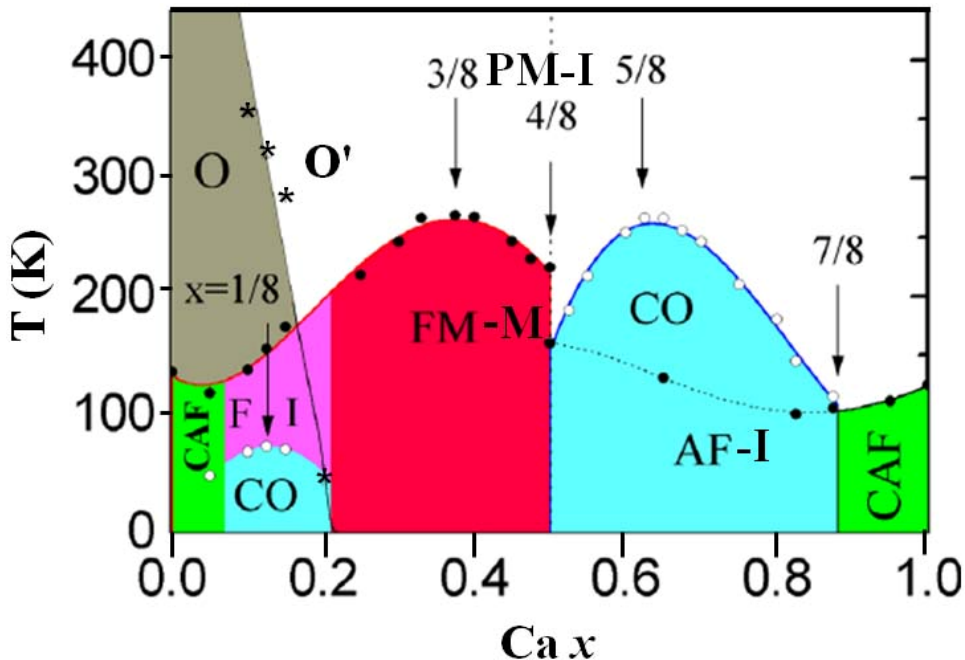


**Figure 1.13:** Phase diagram of  $\text{La}_{1-x}\text{Ca}_x\text{MnO}_3$ . PM-I: Paramagnetic Insulator, FM-M: Ferromagnetic Metal, FM-I: Ferromagnetic Insulator, AF-I: Antiferromagnetic Insulator, CAF: Canted AF and CO: Charge/Orbital Ordering. Filled and open circles indicate Neel ( $T_N$ ) and Curie ( $T_C$ ) temperatures. Stars indicate the orbitally ordered Orthorhombic (O) to orbitally disordered pseudo-Orthorhombic ( $O^*$ ) phase structural transition (Too \*) temperature. The lines joining the data points are guide to the eye [53, 54].

In this dissertation  $\text{La}_{1-x}\text{Ca}_x\text{MnO}_3$  is the main compound of our interest and here we try to give a brief phenomenological introduction to its intricate phase diagram rich with resistive, magnetic and structural phases. This system is very susceptible to lattice and other interactions. The Ca doped  $\text{LaMnO}_3$  is the prototype of the intermediate bandwidth mixed valence perovskite manganite because the ionic size of Ca ( $\sim 1.16\text{\AA}$ ) is almost identical to the ionic size of La ( $\sim 1.18\text{\AA}$ ) and thus a true solid solution forms in the entire range of Ca concentration [52]. Furthermore, the structure, unlike other perovskite manganites, remains orthorhombic below  $\sim 700\text{K}$  in the entire doping concentration. So,  $\text{La}_{1-x}\text{Ca}_x\text{MnO}_3$  is a good candidate material for basic understanding and hence its phase diagram has been described in detail which will also help to understand the experimental data prepared for this dissertation.

Figure 1.13 illustrates the complex phase diagram of  $\text{La}_{1-x}\text{Ca}_x\text{MnO}_3$ . The competing phases in  $\text{La}_{1-x}\text{Ca}_x\text{MnO}_3$  have similar free energies and can coexist in equilibrium with each other.

The parent  $\text{LaMnO}_3$  and  $\text{CaMnO}_3$  are antiferromagnetic insulator at low temperatures with  $A$  and  $G$  type of magnetic ordering respectively. ( $A$  type ordering refers to in-plane FM ordering with interplaner AFM order.  $G$  type ordering refers to inplane and interplane AFM ordering).

- **$0 < x < 0.1$ , Antiferromagnetic insulator:** For low doing, the substitution creates the non-JT  $\text{Mn}^{4+}$  ions that breaks the cooperative nature of the JT and suppresses the  $T_{OO^*}$  very rapidly. This slowly destroys the AFM order and the system exhibits a FM-AFM mixed phase or a canting of spins within the AFM ordered lattice (as suggested by de Gennes).
- **$0.1 < x < 0.2$ , Ferromagnetic insulator-charge ordered insulators:** Ferromagnetism sets in and exhibits an insulating nature of the system.
- **$0.2 < x < 0.5$ , Ferromagnetic metal:** Regime is ferromagnetic metallic ground state and CMR effect is found. The regime becomes paramagnetic insulating for  $T > T_c$  (Ferromagnetic ordering temperature). The metal-insulator transition temperature ( $T_{MIT}$ ) in this regime is very close to ferromagnetic-paramagnetic transition temperature ( $T_c$ ). Increased hole doing leads to decrease in collective JT distortion present in the system. This is manifested by the structural transition between two types of orthorhombic forms, O (with C-type orbital ordering) and  $O^*$  (without long-range orbital ordering).
- **$0.5 < x < 0.88$ , Charge ordered insulator:** At close to  $x = 0.5$ , where the ratio of  $\text{Mn}^{3+}$  and  $\text{Mn}^{4+}$  ions is 1:1 a CO and AFM insulating phase starts to evolve. This phase is real space alternate arrangement of  $\text{Mn}^{3+}$  and  $\text{Mn}^{4+}$  ions. This is followed by an AFM ordering at low temperatures.
- **$x > 0.88$ , Antiferromagnetic insulator:** Canted AFM (mixture of FM and AFM phases) phase starts growing.

Some comments are relevant about Fig. 1.13:

- (i) The phase diagram shows the idea of double-exchange, the large Hund coupling lead to phase diagram mirror symmetry between  $x < 0.5$  and  $x > 0.5$ , are not suitable to describe these materials. In general, the  $x > 0.5$  regime in the phase diagram is dominated by low temperature AFM phase whereas  $x < 0.5$  regime is dominated by low temperature FM phase. The phase diagram has clear electron-hole asymmetry.
- (ii) The AF/CO/OO phase has a very complicated arrangement of spin, charge, and orbital order. The results at  $x = 0.0$  and  $x = 0.5$  are widely accepted and later confirmed using resonant X-ray experiments.

The magnetic phase boundary also separates a low temperature “metallic” phase from a high temperature “insulating” phase. We have used terms “metallic” or “insulating” by considering the temperature dependent resistivity as  $\partial\rho/\partial T > 0$  or  $\partial\rho/\partial T < 0$  respectively. A typical example of this is shown in Fig. 1.14 for “optimal” doping level  $x = 0.33$  with composition  $\text{La}_{0.67}\text{Ca}_{0.33}\text{MnO}_3$  [55]. Considering the phase diagram represented in Fig. 1.13 we can expect a paramagnetic (PM)-ferromagnetic (FM) transition at  $T_c$ . This transition is also accompanied by a sudden reduction in the resistivity  $\rho$  showing an insulator-metal

transition (peak in the temperature dependence of resistivity) at a temperature  $T = T_p$ . The sample undergoes a paramagnetic insulator (PI)-ferromagnetic metal (FMM) at a temperature  $T = T_c \sim T_p$ . Such a drop is well known in other ferromagnetic metallic systems and is caused by the transition from a state with spin disorder to one without. Disorder causes charge carriers with different spin orientations to scatter from each other, which increase the electrical resistivity.

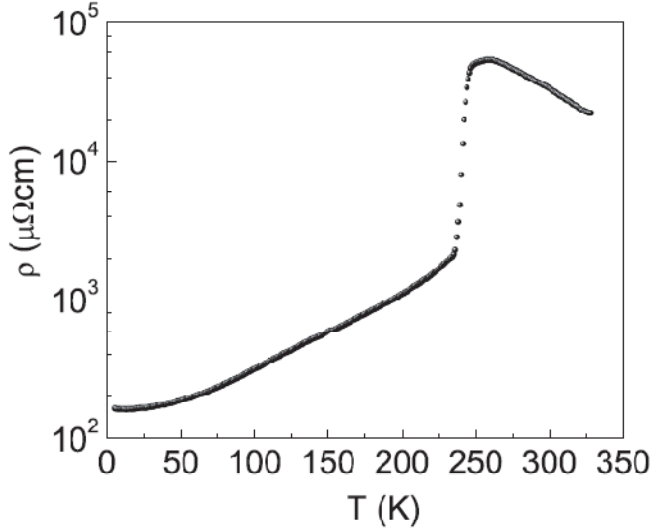


**Figure 1.14:** The insulator–metal transition in  $\text{La}_{0.7}\text{Ca}_{0.3}\text{MnO}_3$  at  $T = T_c \approx 270$  K. The sample is insulating above  $T_c$  and metallic below  $T_c$  (adapted from Jain et al. [55]).

### 1.2.7 Colossal Magnetoresistance (CMR): an intrinsic electrical property

The manganites became much interesting due to observation of large magnetoresistance (MR) effect in these compounds. MR is the change in resistance of a material in response to a magnetic field. It is a result of the ability of magnetic fields to change the scattering of the conduction electrons. This is commonly defined as  $\Delta\rho/\rho = (\rho_H - \rho_0)/\rho_0$  where  $\rho_0$  is the resistivity without a magnetic field, and  $\rho_H$  is the resistivity in presence of magnetic field. In normal ferromagnetic materials the magnetoresistance effect is just a few percent. But in perovskite manganites, the values can be as high as  $\sim 100\%$  in magnetic fields of few teslas. Hence this is commonly known as “colossal” magnetoresistance (CMR) materials.

The basis of the theoretical understanding of the CMR is usually referred to the DE mechanism where the itinerant charge carriers (holes) provide the mechanism for ferromagnetic interaction between  $\text{Mn}^{3+}$  and  $\text{Mn}^{4+}$  ions. The ferromagnetic Curie temperature is related to the strength of the transfer integral  $t$  between  $\text{Mn}^{3+}$  and  $\text{Mn}^{4+}$  ions which itself controls the electronic (hole) conductivity. It follows that in this system one should expect a strong interplay between magnetic, transport and structural properties. But most experimental data in recent works show that the DE alone would not be able to explain. Hence the effect of electron-lattice coupling comes into play by supplementing the DE mechanism [56]. The strong electron-lattice coupling appears in explaining the high-temperature paramagnetic state, since only the spin disorder scattering does not provide with enough localized charge carriers to explain insulator behaviour. The link between the tolerance factor, ionic disorder, and the energy bandwidth tune the electronic and magnetic properties of the perovskites. The

electron-phonon coupling coupling may localize carriers, because presence of an electron in a given Mn orbital causes a local lattice distortion which produces a potential minimum: this minimum tends to trap the electron in that orbital. If the coupling is strong enough, these tendencies lead to the formation of a polaron. This polaron formation competes with the delocalizing tendency of electron hybridization. In the manganites, the nature of the DE, electron-lattice coupling, type of ionic composition, carrier concentrations may change over a wide range which change spin correlations. As a result we can see the dramatic effect of magnetic field with temperature [53]. We have picked up two typical examples of MR done on good quality single crystals of  $\text{La}_{1-x}\text{Ca}_x\text{MnO}_3$  are shown in Fig. 1.15. Both the samples undergo PI-FMM transition at  $T_C$ . But at low temperature first one is ferromagnetic insulator (FMI) and second one is FMM. The changes in MR characteristic are markedly different in these two cases. Again, both cases we can observe a collapse of MR belonging to different phases (FMI or FMM) depending on  $x$ . We are not going into the details of these systems. But we want to mention that the conduction processes in these two samples are very different from each other at low temperatures, which are prominent from MR data also.

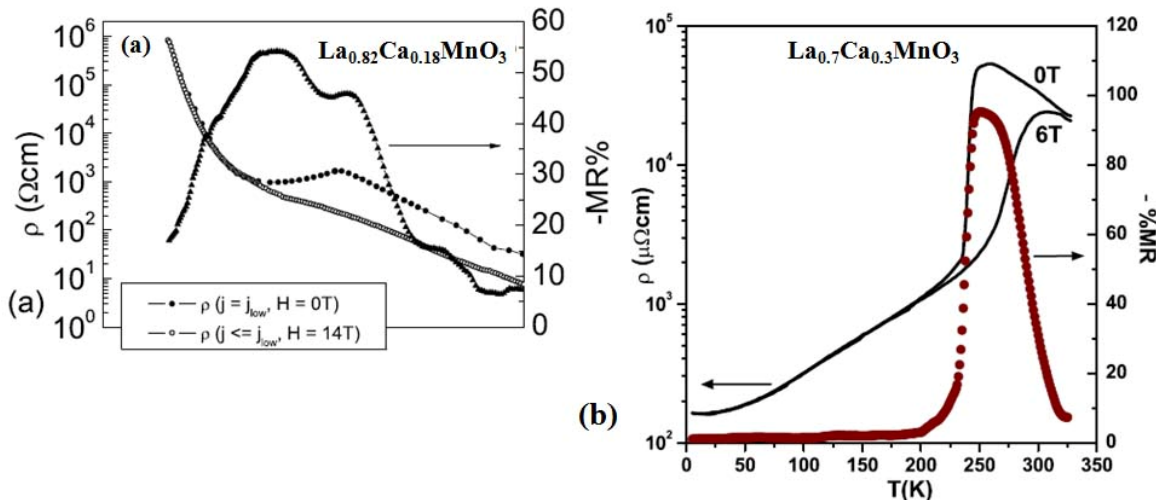


**Figure 1.15:** (a) Temperature  $T$  dependent resistivity  $\rho$  in the absence of a magnetic field, and in the presence of a magnetic field for (a)  $\text{La}_{0.82}\text{Ca}_{0.18}\text{MnO}_3$  with  $H = 14$  Tesla [57] and (b)  $\text{La}_{0.7}\text{Ca}_{0.3}\text{MnO}_3$  with  $H = 6$  Tesla [58]. The respective right ordinates denote the magnetoresistance %MR.

Thus interesting and complicated electrical and magnetic properties makes the physics of manganites most challenging and interesting. The rich phase diagram consists of various phases like AFM, CO, FMM, FMI, PMI and others containing information about electronic and magnetic characteristics of the system. It should be noted that the FMM and the FMI are the most significant phases for the study. In this dissertation will mainly focus on the dynamics related to these states. In the following sections we shall discuss about the two phases of our interest in  $\text{La}_{1-x}\text{Ca}_x\text{MnO}_3$  in brief.

### 1.2.8 Ferromagnetic Metallic (FMM) state of manganites

The ferromagnetic and metallic phases are generally present the phase diagrams as we discussed earlier. It is generally happens at doping levels ( $0.22 < x < 0.5$ ) where phase is ferromagnetic as well as metallic.

$\text{La}_{1-x}\text{Ca}_x\text{MnO}_3$  was the material first studied in the full range of densities  $0 < x < 1$  by Schiffer *et al.* [59]. These authors measured the temperature dependent magnetization,

resistivity, and MR in  $\text{La}_{0.75}\text{Ca}_{0.25}\text{MnO}_3$  which are shown in Fig. 1.16(a), Fig. 1.16(b) and Fig. 1.16(c) respectively. The temperature dependence of resistivity of this material shows MIT from a low-temperature metallic phase to a high-temperature insulating phase characterized by the peak at  $T_p$ . Accompanying the MIT, a magnetic transition from a high-temperature PM phase to a low-temperature FM phase characterized by the Curie temperature  $T_c$  at which spontaneous magnetization appears.

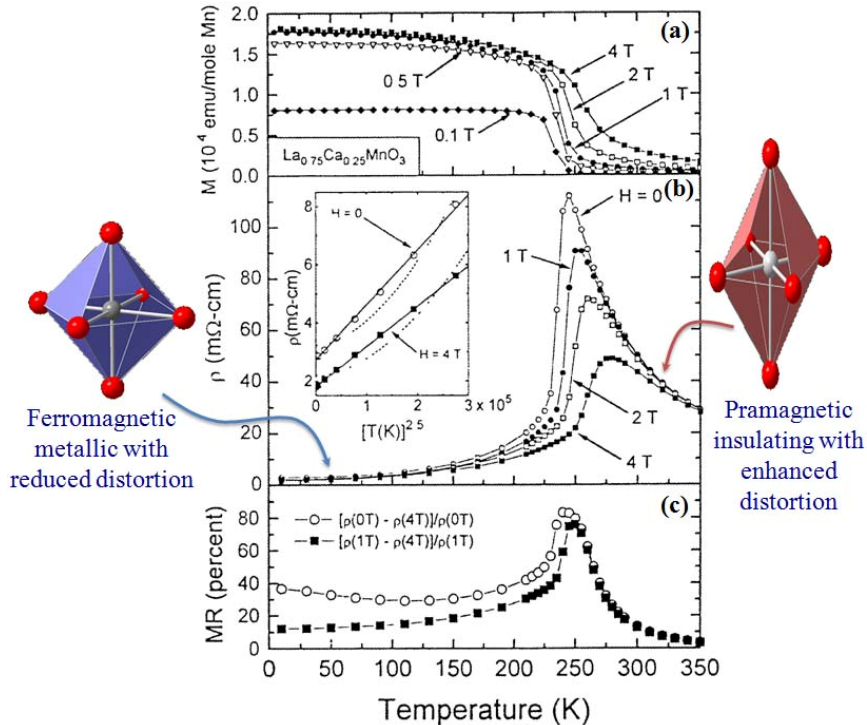


**Figure 1.16:** (a) Magnetization, (b) resistivity and (c) magnetoresistance of  $\text{La}_{0.75}\text{Ca}_{0.25}\text{MnO}_3$ , as a function of temperature for various magnetic fields (from reference [59]).

For all values of  $x$  the various low-temperature phases seen in  $\text{La}_{1-x}\text{Ca}_x\text{MnO}_3$  eventually give way on warming to a PMI state. In the PMI state the extra electron on the  $\text{Mn}^{3+}$  ions are arranged at random throughout the lattice. The  $\text{Mn}^{3+}$  ions can lower their energy by JT distortion (shown in Fig. 1.16(b)). This leads to a coupling between JT distortion and  $e_g$  electrons. The paramagnetic state of  $\text{La}_{1-x}\text{Ca}_x\text{MnO}_3$  is effectively a polaronic liquid that is insulating. The method of conduction in the high-temperature paramagnetic phase is not well understood. The insulating state of  $\text{La}_{1-x}\text{Ca}_x\text{MnO}_3$  has well defined activation energy  $E_a$  in the range 0.1-0.24 eV [60]. There are three possible mechanisms are a thermally activated model [61], a nearest neighbour hopping model [62] and a variable range hopping (VRH) model [63]. We have already shown the temperature dependent resistivity with and without magnetic field as shown in Fig. 1.15(b) which has a distinct PMI and FMM states. The intrinsic low temperature transport properties in manganites are far from trivial. The intrinsic MR vanishes of these compounds at low temperatures, and correlates well with magnetization. Hundley *et al.* [64] investigated these correlations by relating resistivity and magnetization with an empirical expression as

$$\rho(H, T) = \rho_m \exp\left[-\frac{M(H, T)}{M_0}\right], \quad (1.6)$$

over a wide temperature range all the way up to  $T_C$ . A typical example of this formalism is shown in Fig. 1.17(a). This model considers DE mechanism as an important effect. But in contrast to exponential dependence Tokura *et al.* [65] found to decrease of  $\rho(H, T)$  as a square of magnetic field.

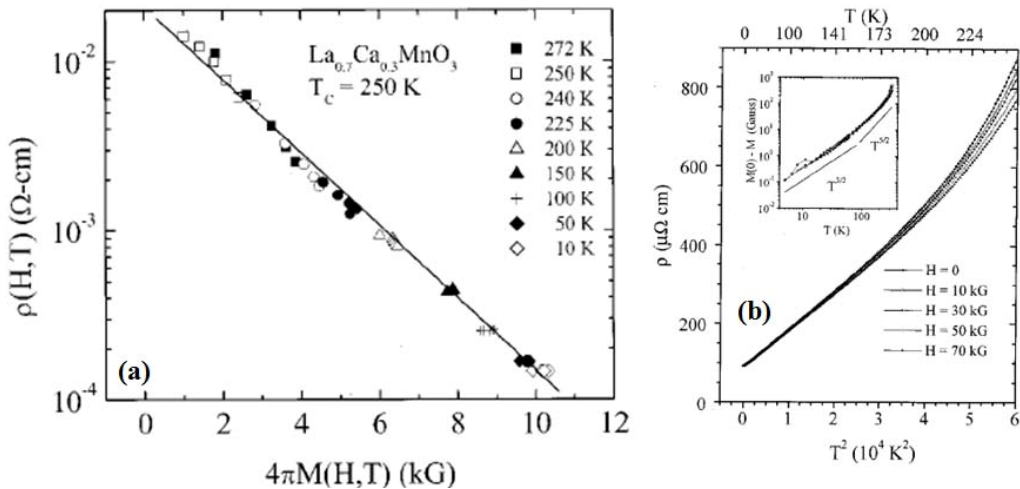


**Figure 1.17:** (a) The magnetic field  $H$  dependent resistivity  $\rho(H, T)$  for  $\text{La}_{0.70}\text{Ca}_{0.30}\text{MnO}_3$  [65]. (b) The resistivity vs  $T^2$  and deviation from  $T^2$  behaviour in  $\text{La}_{0.70}\text{Ca}_{0.30}\text{MnO}_3$  thin film sample [66]. Inset shows the difference in magnetization and its zero temperature extrapolation vs temperature.

It has long been thought that the MIT and FM-PM transition are qualitatively correlated via the DE interaction mechanism, i.e., the hopping of  $e_g$  electrons from the  $e_g$  orbital of  $\text{Mn}^{3+}$  to the neighbouring empty  $e_g$  orbital of  $\text{Mn}^{4+}$  ions through  $2p$  orbital of  $\text{O}^{2-}$  ions in-between [39]. The hopping of the  $e_g$  electrons is enhanced in the FM state in which the core spins ( $t_{2g}$  electron spin of  $\text{Mn}^{3+}$  and  $\text{Mn}^{4+}$ ) are parallel. In turn, the hopping  $e_g$  electrons promote FM order because they energetically prefer to polarize the spins in their vicinity. The hopping  $e_g$  electron does not pay strong Hund coupling energy if both  $e_g$  and  $t_{2g}$  electron spins are parallel. The electron-spin scattering is minimized in this process and the kinetic energy of  $e_g$  is optimized. The applied magnetic field can suppress the spin disorder around  $T_C$  and shift both  $T_P$  and  $T_C$  to higher temperatures. However as seen from Fig. 1.17(b), the resistivity for the sample  $\text{La}_{1-x}\text{Ca}_x\text{MnO}_3$  with  $x = 0.30$ , obeys the relation  $\rho(T) = \rho(0) + AT^2$  ( $T < 200\text{K}$ ) studied by Jaime *et al.* [66]. For  $T > 50\text{ K}$ ,  $T^2$  dependence of resistivity but there exists a fair contribution from  $T^5$  term indicating electron-phonon coupling to resistivity phenomena. The  $T^2$  dependence vanishes below 20 K and the coefficient of  $T^2$  term is 60 times larger than the expected electron-electron coupling and hence ruled out proposed electron-electron coupling contribution to conduction mechanism and single magnon scattering theory came up.

Figure 1.18 shows the low-field (5 Oe) variation of magnetization ( $M$ ) with temperature ( $T$ ) for  $\text{La}_{0.67}\text{Ca}_{0.33}\text{MnO}_3$  [67]. The PM-FM transition occurs at  $T_C \sim 260\text{ K}$ . But

these data can not give an idea about the order of transition (1st order/2nd order) in these two cases. Though the DE mechanism is the predominant source of ferromagnetism in manganites is based on electron transfer between Mn core spins but is not sufficient to extract all information related to ferromagnetism in manganites like some PM-FM transitions accompanied with structural changes, long-rang and the short-range nature of ferromagnetic ordering etc. We can not have idea that  $\text{La}_{0.67}\text{Ca}_{0.33}\text{MnO}_3$  shows a first order transition near  $T_C$ . These results were explained by examination of critical behaviour of manganites. The critical behaviour has been studied in several manganite systems listed in [68]. Most FM compounds exhibit a 2nd order transition near  $T_C$ . A first order transition changes to second order when disorder is introduced by proper substitution of divalent ions and hence introducing a strong contribution from lattice (JT distortion of  $\text{MnO}_6$  octahedra and orbital ordering). Most of the reports suggest an activated polaronic transport due to strong JT distortion for  $\text{La}_{0.67}\text{Ca}_{0.33}\text{MnO}_3$  system. Theoretical calculations [69] also predict that a strong polaronic effect can be responsible to explain the basic physics of manganite in the FM phase.

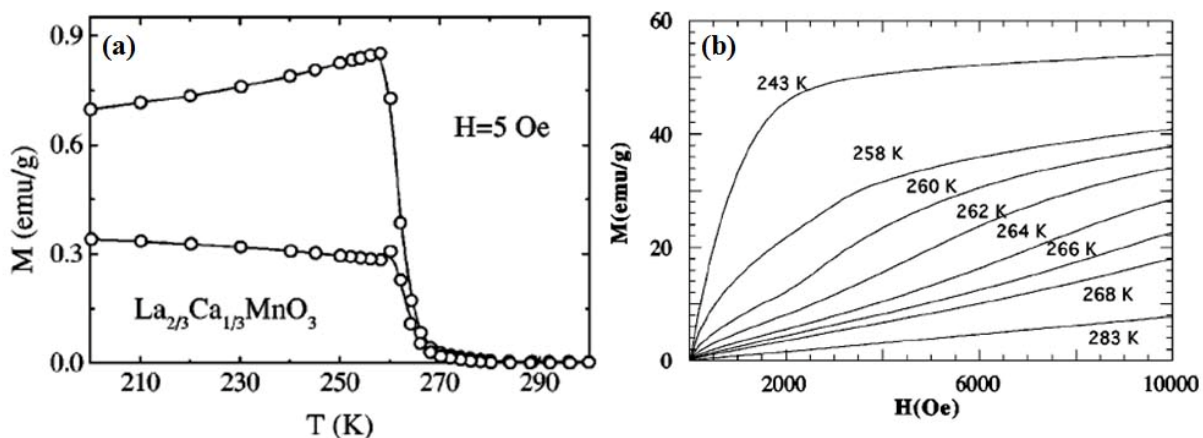


**Figure 1.18:** (a) Magnetization versus temperature under an applied magnetic field of 5 Oe and (b) Magnetization versus magnetic field isotherms in the vicinity of  $T_C$  for  $\text{La}_{0.67}\text{Ca}_{0.33}\text{MnO}_3$  [67].

### 1.2.9 Ferromagnetic Insulating (FMI) state of manganites

We have discussed FMM state so far, the basic mechanism that couples to the spin and charge in these materials can be explained by DE interaction. Another fascinating state of our interest is ferromagnetic insulating (FMI) region for low doping concentration. The unexpected coexistence of ferromagnetism and insulating behaviour seems to contradict the conventional double- and super exchange models. In this section we shall try to give a brief literature survey on FMI phase of manganites. As we are interested only on low doped  $\text{La}_{1-x}\text{Ca}_x\text{MnO}_3$  systems for this dissertation, we shall discuss it in Chapter 5 in details.

Fig. 1.19 shows the explored phase diagram at low doping concentration of Ca ions [70]. For critical doping concentration  $x = x_c \approx 0.225$  the doping-induced FMM to FMI transition is observed in  $\text{La}_{1-x}\text{Ca}_x\text{MnO}_3$ . The origin of the coexistence of ferromagnetism with insulating behaviour is not clear, but might stem from a delicate balance of charge localisation by orbital ordering (OO), due to the JT effect, and ferromagnetic interactions between  $\text{Mn}^{3+}$ - $\text{Mn}^{4+}$ . The exact concentration dependence of this transition or the interaction of this orbital order transition with the magnetic ordering is not known. Moreover, the temperature- or doping-induced MIT is also not clear till date.

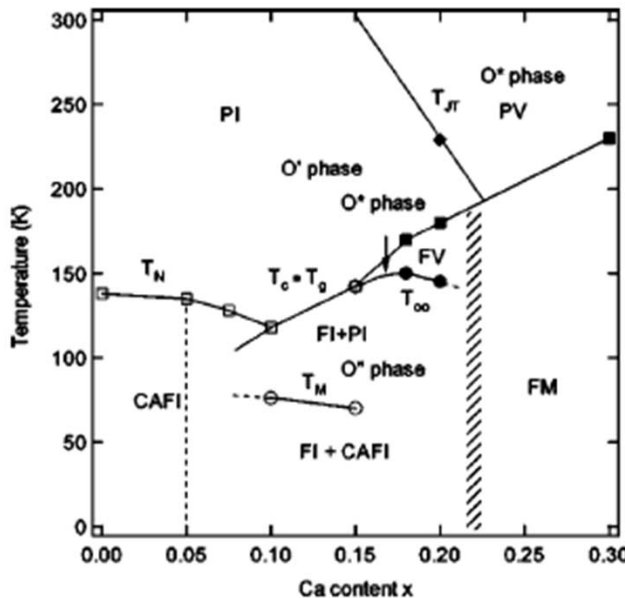


**Figure 1.19:** Phase diagram of the  $\text{La}_{1-x}\text{Ca}_x\text{MnO}_3$  system. The open rectangle and circle are from low-fields (20 Oe) magnetization; the filled rectangle and circle are from resistivity data; the filled diamond is from a specific-heat measurement. The magnetically ordered two-phase region extends between the two vertical dashed lines [70].

By detailed theoretical calculations by Millis *et al.* [71] had shown that there is an electron-lattice coupling along with JT polaron effects can explain some important effects of these systems. Van Aken *et al.* [54] proposed that the suppression of coherent JT distortions arising from  $d$ -type OO needed for stabilization of FMI states. They also found evidence for coexistence between an  $OO$  and orbital disordered state. Papavassiliou *et al.* [72] also supported the conjecture of  $OO$  phenomena for the appearance of FMI phase. By  $^{55}\text{Mn}$  NMR study Savosta *et al.* [73] have shown the coexistence of FMM and FMI clusters and proposed that FMI state of manganites can be viewed as cluster glass. They mentioned that their results contradict the previous idea regarding charge and  $OO$  phenomena. Markovich *et al.* [74] carried out several experiments like electrical resistance, MR, ac susceptibility, and electron magnetic resonance studies in FMI state of low doped perovskite. They found coexistence of ferromagnetic cluster glass with paramagnetic phase, i.e., insulating magnetic phase born in FMM cluster glass. Again, by magnetization studies under consideration Hong *et al.* [75] proposed that short-range charge/orbital ordering may be the issue for stabilization of FMI state.

Ramakrishnan *et al.* [45] has proposed theory of the existence of virtual-DE mechanism which arises when a JT polaron and a hole are nearest neighbour. Recently, Shenoy *et al.* [76] had shown that an insulating state augmented by cationic disorder can arise under this virtual double-exchange mechanism. It was been further shown that the long range Coulomb interactions that are inevitably present due to doping can lead to nanoscale electronic inhomogeneities even in FMM phase. They also proposed that due to long range Coulomb interaction the FMI state appears to “Coulomb glass”. Jain *et al.* [57] also explored the low-doped manganite system  $\text{La}_{0.82}\text{Ca}_{0.18}\text{MnO}_3$  in details which also exhibit FMI state at low temperatures.

The temperature dependent resistivity in the FMI state is shown in Fig 1.20 which can readily differentiate the behaviour different from FMM state. The sudden drop in the resistivity near  $T_c$  indicates the onset of ferromagnetic “metallic” state, and then it starts to increase. The resistivity upturn identifies the growth of ferromagnetic “insulating” state. The

transport property of FMI state is unique because Coulomb interactions between the carriers directly change the conduction mechanism qualitatively. This is activated below the ferromagnetic insulating transition temperature ( $T_{FMI}$ ). The low temperature resistivity ( $\rho$ ) in FMI state shows a Efros-Shklovskii variable range hopping (ES-VRH) [78] with temperature dependence  $\rho = \rho_0 \exp(T_0 / T)^{1/2}$  where  $\rho_0 = \rho_0 T^{1/2}$ .  $T_0$  represents an energy scale expressed in Kelvin. A soft Coulomb gap opens up near Fermi energy level due to localized charge carriers.

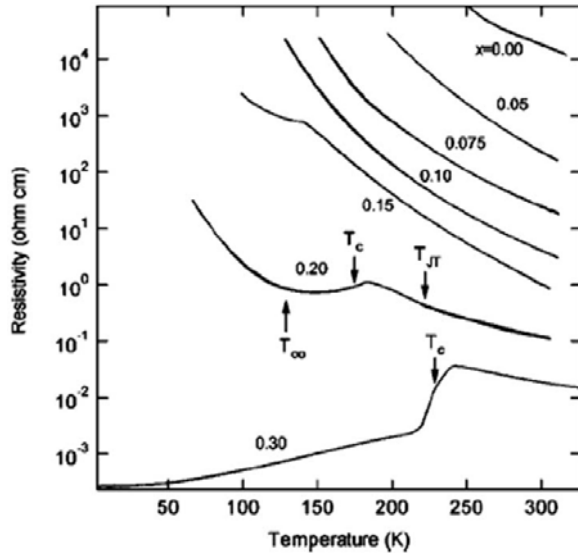


**Figure 1.20:** Temperature dependent resistivity of (a)  $La_{1-x}Ca_xMnO_3$  [77] showing the onset of FMI state in these samples.

Here we have just introduced the basic features regarding the dynamics for FMI state which is still ill understood. There exist theoretical difficulties to explain the ferromagnetic state which is as well as insulating. We shall discuss this state in specific context of our thesis again and try to open up new underlying physics of FMI states of manganites.

Till now we have discussed the basic characteristics of manganites. Their diverse dynamics make any phase diagram complex and interesting. We have also studied the basic characteristics of FMM and FMI phases. Though we have discussed the phases individually so far, but there exists regions where two phases exist together, we call it “phase coexistence” region over surprisingly small lengthscales. In the following section we shall discuss about the phase coexistence in manganites in brief.

### 1.2.10 Phase coexistence in manganites

The term “phase” in this context refers to spin, charge, and orbital patterns formed in the inhomogeneous states. Although the basic phases like paramagnetic insulator, ferromagnetic metal, charge order insulator seen generally in the phase diagram, initially appear to be quite distinct, it is nevertheless possible to have multiple phases coexisting over a microscopically small regions. The free energies of the phases involved are quite similar and the system may be intrinsically inhomogeneous due to the competition between the various phases to be the stable thermodynamic phase. As a result, the “bubbles”, “clusters”, or stripes found in the inhomogeneous states. This phase coexistence becomes important in context of manganites because of their stability in different conditions.

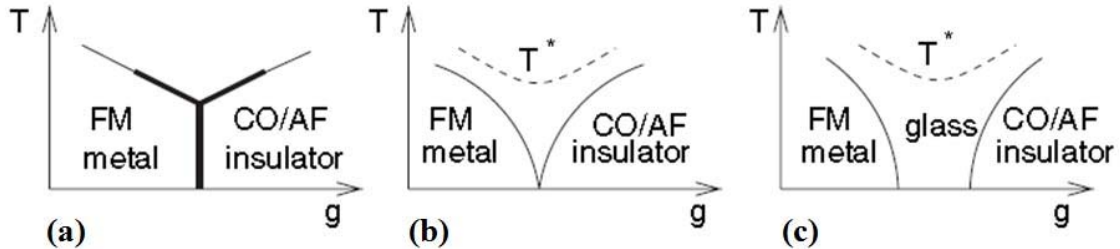


**Figure 1.21:** (a) Generic phase diagram of two competing phases in the absence of quenched disorder (or when this disorder is very weak). Thick (thin) lines denote first (second)-order transitions. (b) With increase in disorder, the temperature range of first-order transitions separating the ordered states is decreased, (c) In the limit of substantial disorder, a window opens between the ordered phases. The state in between has glassy characteristics and it is composed of coexisting clusters of both phases.

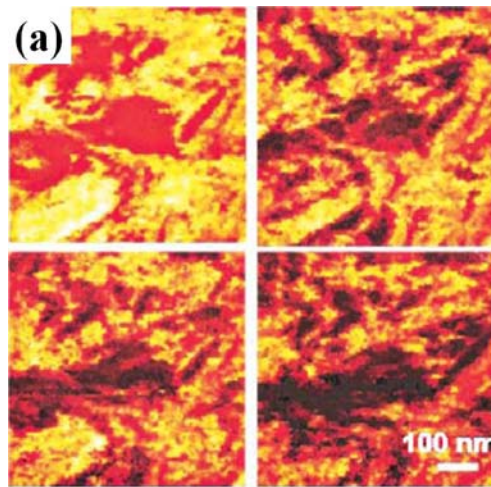


**Figure 1.22:** (a) Scanning tunneling spectroscopy images of the local electronic structure of  $\text{La}_{1-x}\text{Ca}_x\text{MnO}_3$ , obtained just below  $T_c$  in magnetic fields of 0, 0.3, 1, 3, 5, and 9 Tesla (from left to right and top to bottom). The data was taken on a thin film sample with  $x \sim 0.3$  (adapted from [10]).

Figure 1.21 shows the schematic diagram of different competing phases. Theoretical studies have predicted that the metal and insulator phases of manganites are separated by first-order transitions leading to bicritical or tricritical behaviour ([8], [9], [79]) (see Fig. 1.21(a)). When the disorder is sufficiently strong, a “window” with disorder characteristics opens in between the two phases as shown in figure 1.21(b) and 1.21(c). A glassy phase exists between FM metal and AF insulator. Related to previous studies have unveiled the existence of a new temperature  $T^*$  where clusters starts forming well above Curie temperature. The size of the coexisting islands can be regulated by disorder and by the proximity to the original first-order transition. The phase coexistence occurs in a wide region of phase diagram and not just close to the phase boundaries as thought earlier. There were several attempts and models to investigate the phase coexistence of manganites based on electronic phase separation on a nanometer length scales and disordered-induced inhomogeneity. However, the presence of two distinct length scales for phase separation was in disagreement with the majority of the rapidly accumulating experimental evidence. Mathur and Littlewood [80] used Landau theory to explain the coexistence and predicted the phase separation on a mesoscopic length scale. Then Ahn *et al.* [81] proposed that strain can tune the phase separation and found the phase coexistence over a micron scale. There are several

experimental evidences to prove the phase coexistence but the results were modified by effects due to defects, grain boundaries or dislocations. Such defects can alter the delicate energy balance between the competing phases.

The visual evidence of phase coexistence was done by Uehara *et al.* [11] by electron microscopy study. Fäth *et al.* [10] investigated samples of  $\text{La}_{0.7}\text{Ca}_{0.3}\text{MnO}_3$  near the Curie temperature  $T_C$  by STM study and picked up real space pictures at a microscopic level, mainly the surface and shown in Fig. 1.22(a). They found spatial variations of the local electronic properties on a submicrometer scale forming “cloudlike” regions of conducting, insulating, and intermediate phases. At high temperatures, they observed a growth of the insulating domains. In this temperature regime, metallic and insulating domains coexist (“electronic phase separation”) in a chemically homogeneous sample. This is an intrinsic behaviour of the sample. Electron microscopy and STM results suggest that phase coexistence occurs over hundreds of nanometers lengthscales.

In the last section we have discussed about the fundamental properties of the perovskite system which we are going to investigate in this thesis. In the next section we shall discuss about our measurement tool, i.e., the fundaments about noise spectroscopy.

## 1.3 Introduction to Noise

In this dissertation the resistance fluctuation (noise) has been used extensively as a unique and fundament measurement tool to investigate the fundamental aspects of manganites. The underlying physics of perovskite manganites are fascinating and complex from doping concentration, resistivity, magnetoresistance, phase-separation point of view. The charge transport, magneto-transport, and the correlated dynamics in these systems have been studied by the noise spectroscopy.

In the following context we shall introduce the basic principles of regarding noise phenomena and mathematical expressions to quantify noise. In general, noise is a random and spontaneous fluctuation of any physical quantity about its mean value. In physics, as everywhere else, together with the strongly expected and deterministic processes we have to deal with uncertain and random processes. The theory which treats the laws and relation of random processes is called the probability theory. Random signal theory is one of the important parts of probability theory which can describe the nature of fluctuation processes satisfactorily. This section is mostly compiled from reference [82].

### 1.3.1 Basics of Random Signal Theory and Probability Density Function

Probability can be thought of as a numerical measure of the likelihood that a particular event will occur. Let  $P\{\dots\}$  be the probability of an event indicated in the curly brackets. The distribution functions can be written for a random process  $x(t)$  as:

$$\begin{aligned} W_1(x_1, t_1) &= P\{x(t_1) \leq x_1\}, \\ W_2(x_1, t_1, x_2, t_2) &= P\{x(t_1) \leq x_1; x(t_2) \leq x_2\}, \\ W_n(x_1, t_1; \dots; x_n, t_n) &= P\{x(t_1) \leq x_1; \dots; x(t_n) \leq x_n\}, \end{aligned} \tag{1.7}$$

where  $x_i$  is value of random quantity at instant  $t_i$ .

For instance,  $W_n(x_1, t_1; \dots; x_n, t_n)$  is the probability that random quantity  $x$  at instant  $t_1$  is less than a value  $x_1$ , and at instant  $t_n$  is less than  $x_n$ .

If  $W_n(x_1, t_1; \dots; x_n, t_n)$  is a differentiable function of the variables  $x_1, \dots, x_n$ ; one can write the corresponding probability density functions:

$$\begin{aligned} w_1(x_1, t_1) &= \frac{\partial W_1(x_1, t_1)}{\partial x_1}, \\ w_2(x_2, t_2) &= \frac{\partial W_2(x_1, t_1; x_2, t_2)}{\partial x_1 \partial x_2}, \\ w_n(x_1, t_1; \dots; x_n, t_n) &= \frac{\partial W_n(x_1, t_1; \dots; x_n, t_n)}{\partial x_1 \partial x_2 \dots \partial x_n}. \end{aligned} \quad (1.8)$$

The functions  $w_n$  are called  $n$ -dimensional probability density functions of the random quantity  $x(t)$ . The calculated probability of a variable  $x$  at instant  $t$  falls in the interval  $a < x \leq b$  can be expressed by using one-dimensional probability density function  $w_1(x, t)$  as

$$P\{a < x(t) \leq b\} = \int_a^b w_1(x, t) dx. \quad (1.9)$$

If all the distributions  $w_n(x_1, t_1; \dots; x_n, t_n)$  remain constant under any identical shift of all time points  $t_1, \dots, t_n$ , the random processes are called stationary. In this case  $w_1(x, t)$  does not depend on time  $t_1$ , whereas  $w_n(x_1, t_1; \dots; x_n, t_n)$  depends only on  $(t_1 - t_2)$ , that is may be written as  $w_n(x_1, x_2, t_1, t_2)$ , and so on.

The mean value of the random variable  $x(t)$  or its “expectation” value is equals to

$$\langle x(t) \rangle = \int_0^1 x(t) dW_1(x, t) = \int_{-\infty}^{+\infty} x(t) w_1(x, t) dx. \quad (1.10)$$

The mean value of  $x^r(t)$  is called the  $r$ -th order moment. The mean value of random quantity  $\delta(x(t))^r$ , where  $\delta(x, t) = x(t) - \langle x(t) \rangle$  is the deviation of the random quantity  $x(t)$  from its mean value  $\langle x(t) \rangle$  ( $r$ -th order central moment).

The mean value of any fluctuation squared is second order central moment, called variance. This can be written as

$$\langle (\delta x(t))^2 \rangle = \int_{-\infty}^{+\infty} (\delta x(t))^2 w_1(x, t) dx. \quad (1.11)$$

A distribution is not uniquely specified by its moments, but is uniquely specified by its characteristic function. Generally, a random quantity has a characteristic function defined as the mean value of the function  $e^{ivx}$ , where  $x$  is the random variable and  $v$  is a real

parameter. As we mentioned earlier that  $W_1(x, t)$  is differentiable, then the characteristic function is the Fourier transform of the probability density function (equation 1.8):

$$\varphi_x(v) \equiv \langle e^{ivx} \rangle = \int_{-\infty}^{+\infty} dx e^{ivx} w_1(x, t). \quad (1.12)$$

If the random variable is the sum of  $N$  independent random variables, i.e.,

$$X = \sum_{i=1}^N x_i, \quad (1.13)$$

Then the characteristic function of  $X$  is simply product of the characteristic functions of the variables  $x_i$ :

$$\varphi_x(v) = \varphi_{x_1}(v) \cdot \varphi_{x_2}(v) \cdots \varphi_{x_n}(v). \quad (1.14)$$

In the random signal theory the most important distribution is the normal (Gaussian) distribution. The one-dimensional probability density function is

$$w_1(x) = \frac{1}{\sqrt{2\pi\sigma^2}} e^{-\frac{(x-\mu)^2}{2\sigma^2}}, \quad (1.15)$$

where  $\delta x = x(t) - \langle x(t) \rangle$  is the fluctuation and  $\sigma^2$  is the variance. According to the central limit theorem, the data of small and unrelated random effects tends to be normally distributed, so often random signals with unknown distributions in a good approximation are assumed to be Gaussian.

The statistical characteristics of a random process are non-random quantities, which measures by a corresponding averaging of the random quantities. There are two possible ways of averaging:

**(a)** Averaging over time, i.e., over a sufficiently long record of the random process. In this case the distribution function  $W_1(x_1)$  of a stationary process is equal to that part of the total time  $t_m$  of measurement of this process during which random quantity  $x < x_1$ . The mean value of the random quantity is then:

$$\overline{x(t)} = \lim_{t_m \rightarrow \infty} \frac{1}{t_m} \int_{-t_m/2}^{t_m/2} dt \cdot x(t). \quad (1.16)$$

**(b)** Averaging over an ensemble average of large number  $N$  of identical systems. The mean value is in this case is:

$$\langle x_i(t) \rangle = \lim_{N \rightarrow \infty} \frac{1}{N} \sum_{i=1}^N x_i(t). \quad (1.17)$$

Here  $x_i(t)$  is the value of random quantity at instant  $t$  in the  $i$ -th system of the ensemble. It is not obvious that the above two averaging will give identical mean values. The random process is called “ergodic” when these two mean values are identical. It may happen that in some physical processes these two averaging may break down and we get “Non-ergodicity”.

### 1.3.1.1 Correlation function

The correlation function is the most fundamental characteristic of any random process. It is a non-random characteristic of the kinetic of the random fluctuations  $\delta(x, t) = x(t) - \langle x(t) \rangle$  and shows how those fluctuations evolve in time on average.

Let there is an ensemble of a large number  $N$  of systems with identical conditions where  $\delta x_i(t_1)$  and  $\delta x_i(t_2)$  are the fluctuations in the  $i$ -th system of the ensemble at instant  $t_1$  and  $t_2$  respectively. The correlation can be defined by the following equation:

$$k_x(t_1, t_2) = \langle \delta x(t_1) \delta x(t_2) \rangle = \lim_{N \rightarrow \infty} \frac{1}{N} \sum_{i=1}^N \delta x_i(t_1) \delta x_i(t_2). \quad (1.18)$$

In a *stationary* system the correlation function remains invariable if both instances  $t_1$  and  $t_2$  are shifted identically. Then  $k_x$  depends only on  $(t_1 - t_2)$ .

The correlation can be expressed by averaging over a sufficiently long record of random process  $x(t)$  in one system.

$$k_x(t_1, t_2) \equiv \overline{\delta x(t_1) \delta x(t_2)} = \lim_{t_m \rightarrow \infty} \frac{1}{t_m} \int_{-t_m/2}^{t_m/2} dt \cdot x(t_1 + t) x(t_2 + t). \quad (1.19)$$

The above two correlation functions are identical when the system is ergodic. In stationary systems  $k_x$  depend on  $\tau = t_1 - t_2$ . Function  $k_x(\tau)$  is called autocorrelation function. At  $\tau = 0$ , the autocorrelation function is simply variance, i.e.,  $k_x(0) = \langle (\delta x)^2 \rangle$ . As  $|\tau| \rightarrow \infty$  the autocorrelation function of the fluctuation in stationary system is zero. The time in which  $k_x(\tau)$  decays to zero is called “relaxation time”. In real systems a number of kinetic processes with different relaxation times exist.

### 1.3.1.2 Spectral density and Weiner-Khintchine theorem

Weiner-Khintchine theorem establishes a relation between the spectral density and correlation function and was discovered by Weiner (1930) and Khintchine (1934). The fluctuation  $\delta x(t)$  recorded over a sufficiently long time  $t_m$  from  $t = -t_m/2$  to  $t = t_m/2$ . The spectral power density is a quantity which describes the characteristics of a random signal. It gives information about the distribution of that random signal in frequency domain as:

$$S_x(f) = 2 \lim_{t_m \rightarrow \infty} \frac{1}{t_m} \left| \int_{-t_m/2}^{t_m/2} dt \cdot e^{i2\pi f t} dx(t) \right|^2. \quad (1.20)$$

Considering a random process  $x(t)$  which is continuous and infinite. This is a continuous and infinite signal and can not be evaluated in frequency domain unless it is made periodic. We can define a periodic function  $x_T(t)$  with time period  $T$  and is  $x(t)$  within  $-T/2$  and  $T/2$ . Thus we can define Fourier series of  $x_T(t)$  by the Fourier coefficient  $C_n$  as

$$C_n = \frac{1}{T} \int_{-T/2}^{T/2} dt \cdot x_T(t) e^{-i\frac{2\pi n t}{T}}. \quad (1.21)$$

The periodic function can then be defined in terms of the Fourier basis function as

$$x_T(t) = \sum_{n=-\infty}^{\infty} C_n e^{i\frac{2\pi n t}{T}} \quad (1.22)$$

This above equation (equation 1.22) must satisfy Perseval's theorem which states that

$$\frac{1}{T} \int_{-T/2}^{T/2} |x(t)|^2 dt = \sum_{n=-\infty}^{\infty} |C_n|^2 \quad (1.23)$$

The equation 1.23 is the time average of the squared sample function giving the “mean squared value”. This represents the integral power of the signal. Since power depends on the sample function of an ensemble chosen is a random variable. Thus the time dependence of power can be written explicitly as

$$P(t) = \frac{1}{T} \int_{-T/2}^{T/2} |x(t, t')|^2 dt' = \sum_{n=-\infty}^{\infty} |C_n|^2. \quad (1.24)$$

Thus, the power in the  $n$ -th frequency is also a random variable. Now we have to correlate the above result with correlation function. It can be shown easily that if a signal has a periodic component, then its autocorrelation function is also periodic over the same interval, i.e.  $k_{xT}(T) = k_x(0)$ . Hence one can write the autocorrelation function in terms of Fourier series as

$$k_{xT}(\tau) = \sum_{k=-\infty}^{\infty} b_k e^{i\frac{2\pi k \tau}{T}}, \quad (1.25)$$

where

$$b_n = \frac{1}{T} \int_{-T/2}^{T/2} d\tau k_{xT}(\tau) e^{-i\frac{2\pi n \tau}{T}}. \quad (1.26)$$

Considering the Fourier coefficient of two of our periodic sample functions as defined in equation 1.21. Performing the complex multiplication of two coefficients we get

$$C_m C_n^* = \frac{1}{T^2} \int_{-T/2}^{T/2} \int_{-T/2}^{T/2} dt_1 dt_2 x_T(t_1) x_T(t_2) e^{-i \frac{2\pi(m t_1 - m t_2)}{T}} \quad (1.27)$$

Defining  $\tau = (t_2 - t_1)$  and using the autocorrelation function (equation 1.19) we can write:

$$\lim_{T \rightarrow \infty} |C_n|^2 = \lim_{T \rightarrow \infty} \frac{1}{T} \int_{-T/2}^{T/2} d\tau k_x(\tau) e^{-i \frac{2\pi n \tau}{T}} = b_n. \quad (1.28)$$

Thus the autocorrelation function and the power spectrum are a transform pair and

$$k_x(\tau) = \sum_{n=-\infty}^{\infty} |C_n|^2 e^{i \frac{2\pi n \tau}{T}}. \quad (1.29)$$

If we assume that power spectrum made up of a set of discrete expected power terms (i.e.,  $|C_n|^2$ ), then the definition of power density can be defined as

$$\int_{-\infty}^{\infty} S_x(f) = \frac{1}{T} \sum_{n=-\infty}^{\infty} \langle |C_n|^2 \rangle \text{rect}(f - n/T) \quad (1.30)$$

where  $\text{rect}$  is the standard unit function defined as 1 between  $(n/T - 1/2)$  and  $(n/T + 1/2)$  and 0 (zero) everywhere else.  $f$  is a continuous frequency variable. We can create a continuos power spectral density for all frequency  $f$ . If we integrate the power sepctral density over all frequency we get

$$\int_{-\infty}^{\infty} S_x(f) = \sum_{n=-\infty}^{\infty} \langle |C_n|^2 \rangle \frac{1}{T} \int_{-\infty}^{+\infty} \text{rect}(f - n/T) df = \sum_{n=-\infty}^{\infty} \langle |C_n|^2 \rangle = \langle P(t) \rangle. \quad (1.31)$$

Thus, the Weiner-Khintchinen theorem is

$$S_x(T) = \int_{-\infty}^{\infty} d\tau \cdot k_x(\tau) e^{-i 2\pi f \tau}, \quad (1.32)$$

which establishes that the spectral density is the Fourier transform of the autocorrelation function.

In the light of above discussion we can quantify resistance fluctuations and corresponding spectral power density of fluctuation. The fluctuation of resistance in a current

carrying conductor about its time averaged value  $\langle R \rangle$  is  $\delta R(t) = R(t) - \langle R \rangle$ . Then noise can be described in the frequency domain by spectral density of resistance fluctuation as:

$$S_R(f) = 2 \int_{-\infty}^{+\infty} \kappa_R(\tau) e^{-i2\pi f\tau} d\tau = 4 \int_{-\infty}^{+\infty} \kappa_R(\tau) \cos(2\pi f\tau) d\tau, \quad (1.33)$$

where,  $\kappa_R(\tau)$  is the auto-correlation function of resistance (applying Weiner-Khintchine theorem) and can be defined as:

$$\kappa_R(\tau) = \lim_{T \rightarrow \infty} \frac{1}{T} \int_0^T R(t) R(t + \tau) dt. \quad (1.34)$$

When a constant current bias  $I$  is applied to the system then resistance fluctuation is equivalent to voltage fluctuation  $\delta V(t) = V(t) - \langle V \rangle$  about the time averaged mean voltage drop  $\langle V \rangle$  across the system. Then the power spectral density of voltage fluctuation is  $S_V(f) = I S_R(f)$ . The dimensionality of voltage power spectral density is  $V^2/\text{Hz}$ . Depending on the physical origins of fluctuations underlying in the system, the characteristics of power spectrum vary. In the next subsection we shall discuss about different types noise and their shape of the power spectra.

### 1.3.2 Types of noise and shape of the spectra

#### 1.3.2.1 Nyquist Noise

The voltage fluctuations caused by the thermal motion (noise termed as “thermal noise”) of the charge carriers in any conductor. A schematic sketch of thermal agitation of electrons in conductor is shown in Fig. 1.23.

**Random electron motion due to heat**

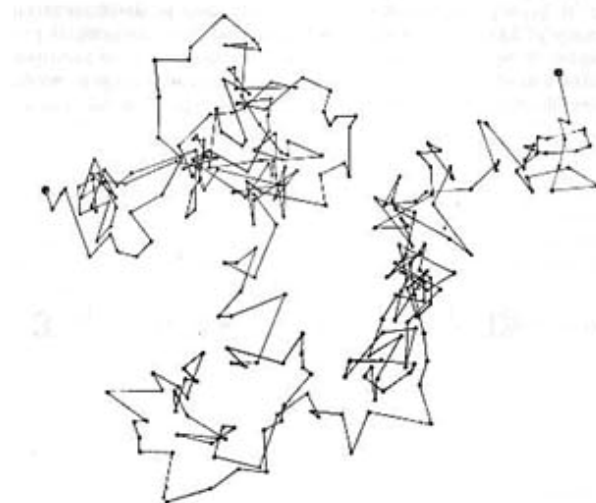


**Figure 1.23:** Schematic diagram of thermal motion of electrons in a conductor.

Due to randomness of the thermal motion, the current carried by the flow of those charge carriers moving in a given direction is, in general is not counterbalanced by the current of those moving in the opposite direction. So the net current flowing in the system is nonzero even absence of any external current sources. The mean value of this random fluctuation current is zero. This noise is universal and present in all types of conductor irrespective of the type of conduction (electronic, ionic) or type of material (metal or semiconductor).

The random motion of charge carries generate an equilibrium current noise, i.e., by the fluctuation of charge carrier velocities. So Nyquist noise is an equilibrium fluctuation process. In the same equilibrium system other physical quantities like temperature, distribution of charge carriers in energy, scattering centres (like defects or dislocations) and their orientations in the crystal fluctuate. However, these fluctuations, due to symmetry, are not measured in the current or voltage noise unless a mean current, generated by an external current source, is passed through the conductor. The mean current should be sufficient to reveal the fluctuations and generate non-equilibrium (or near equilibrium) “excess” noise. So the sensitivity is the keyword of fluctuation spectroscopy. The power spectral density of thermal noise at an equilibrium temperature  $T$  is given by ([1], [2]):

$$S_{th} = 4k_B T R . \quad (1.35)$$

Thus, power spectral density of Johnson noise is “white” (no frequency dependence) over the frequency range. A  $50\Omega$  resistor has about  $1 \text{ nV}/\sqrt{\text{Hz}}$  of thermal noise. Thermal noise stops completely at absolute zero temperature. The left side image of Figure 1.24 shows the voltage fluctuation across a conductor due to thermal agitation and right hand image is the spectral density due to that thermal fluctuation.

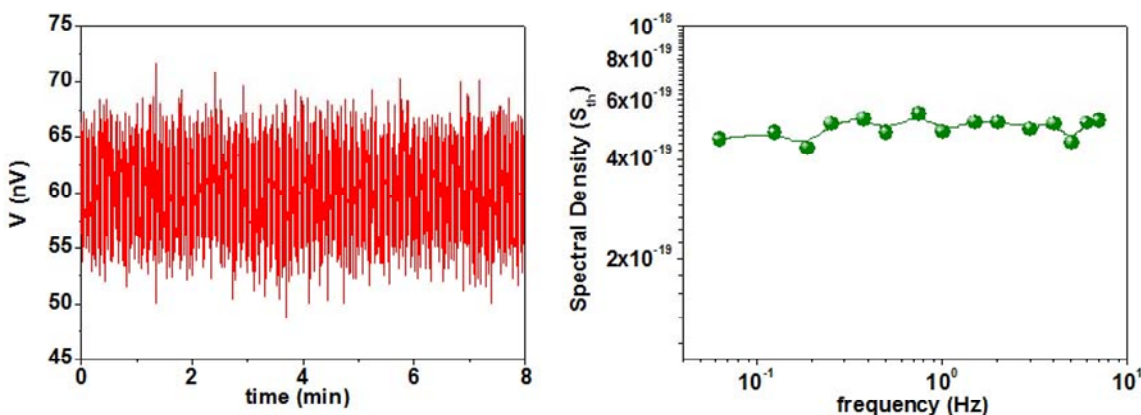


**Figure 1.24:** Left image: Voltage fluctuation across a conductor due to thermal fluctuation of the carriers inside, Right image: Spectral density of thermal fluctuation  $S_{th} = 4k_B T R$ .

### 1.3.2.2 Shot noise

The name shot noise is short of Schottky noise and sometimes it is referred as quantum noise. Shot noise arises across a junction due to arrival of individual electron at random times. This gives rise to broadband white noise and increases with increase of average current flow. It is independent of temperature. The spectral density of the shot noise is given by

$$S_e = 2e|I|. \quad (1.36)$$

For  $I=1\times 10^{-3}$  Amp,  $S_e \sim 2\text{pA}/\sqrt{\text{Hz}}$  is observed. The shot noise is expected in devices like tunnel junctions, vacuum tubes where electron arrives randomly and independently and their distribution can be described by Poissonian distribution only. In sufficiently small metallic film of length  $L$  where  $l < L < l_{e-ph}$ ,  $S_e = 2/3e|I|$  and  $l$  is the elastic mean free path and  $l_{e-ph}$  is electron-phonon scattering length. If  $l_{ee} < L < l_{e-ph}$ , then  $S_e = 0.89e|I|$  [83]. The prediction was proved experimentally by Steinbach *et al.* [84].

### 1.3.2.3 Flicker noise

Flicker noise is found in all active devices including homogenous semiconductors, junction devices, metal films, liquid metals, electrolytic solutions, and even superconducting Josephson junctions. In addition it has been observed in mechanical, biological, geological, and even musical systems, in active devices and some of the passive devices like carbon resistors. Flicker noise was first observed in vacuum tubes [85] and gets its name from the anomalous “flicker” observed in the plate current. Flicker noise is known as “ $1/f$  noise” as its spectral power varies as  $1/f^\alpha$  where  $\alpha$  is very close to unity ( $\alpha = 1.0 \pm 0.2$ ). This is “excess” noise and is made visible by passing a current through the resistor. There are some systems that show often large departure from this behaviour showing a very large  $\alpha$  and some systems show “Random Telegraphic Noise” (RTN) (discussed later) that shows a Lorentzian power spectrum which has  $1/f^2$  frequency dependence.

A simple model to get  $1/f$  spectra was first proposed by F. K. Du Pfe [86]. Consider a simple double well potential where two accessible energy states are separated by energy  $E_a$ . The system fluctuates between two states with a characteristic time  $\tau$  (relaxation time) which depends on  $E_a$ . According to random signal theory discussed earlier, one can define an autocorrelation function  $C(\tau) \propto \exp(-t/\tau)$  of the fluctuation. Hence the spectral density of the fluctuation is of Lorentzian form:

$$S(f) \propto \frac{2\tau}{1 + (2\pi f \tau)^2}. \quad (1.37)$$

For  $f\tau \ll 1$  the power spectrum is white and for  $f\tau \gg 1$ ,  $S_v(f) \propto 1/f^2$ . The time series of this fluctuation gives RTN. If  $D(\tau)$  is a distribution of relaxation times for fluctuation processes the spectral power will be a superposition of Lorentzians given by

$$S(f) = \int d\tau D(\tau) \frac{2\tau}{1 + (2\pi f \tau)^2}. \quad (1.38)$$

If we choose  $D(\tau) \propto 1/\tau$  and  $\tau_1 \leq \tau \leq \tau_2$ , spectral density  $S_v(f) \propto 1/f^\alpha$  ( $\alpha \sim 1$ ) within the frequency range  $2\pi/\tau_2 \leq f \leq 2\pi/\tau_1$ . At a glance the characteristics discussed above is given in Table. 1.2.

|           | Schematic energy diagram | Schematic time series | Relaxation time   | Spectral power $S(f)$  | Characteristic of spectrum |
|-----------|--------------------------|-----------------------|---|--|----------------------------|
| RTN       |                          |                       | Single relaxation time $\tau$                                     | $S_V(f) \propto 1/f^2$<br>Lorentzian spectrum  |                            |
| 1/f Noise |                          |                       | Distribution of relation times $\tau$<br>$D(\tau) \propto 1/\tau$ | $S_V(f) \propto 1/f^\alpha$<br>( $\alpha \sim 1$ )<br>Superposition of Lorentzian spectrum |                            |

**Table 1.2:** A comparative study: the characteristics of Random Telegraphic noise and typical  $1/f$  noise.

In metal, two-level system can be realized as a defect fluctuation between two double well potential levels separated by energy  $E_a$ . So the relaxation time scale  $\tau = \tau_0 \exp(-E_a/k_B T)$  assuming the defect obey thermally activated kinetics. Similarly distribution of relaxation times can be related to distribution of activation energy as  $D(E) = \tau D(\tau)/k_B T$ . Which implies that, at a certain temperature, the criterion for the spectral density to have  $1/f$  form for the frequency range  $f_2 \leq f \leq f_1$  becomes  $D(E) = \text{constant}$ , for the range of activation energy  $k\beta T \ln(\tau_1/\tau_0) \leq E \leq k\beta T \ln(\tau_2/\tau_0)$ .

There are three relevant models which appeared in literature to explain the origin of  $1/f$  noise: the McWhorter number fluctuation model [87], Hooge mobility fluctuation model [88-90] and Dutta-Horn model [91]. There are experimental evidences to support these theories.

- *The McWhorter Model (Number Fluctuations):* The McWhorter number fluctuation ( $\Delta n$ ) theory [87] states that  $1/f$  noise is generated by fluctuations in the number of carriers due to charge trapping in surface states. The theory explained origin of  $1/f$  noise in semiconductor-oxide interface. This process will be activated with the quantity  $E_a$  in this case being the depth of the trap. The fluctuation of the carrier density will cause the resistance to fluctuate giving rise to noise. If the traps are distributed throughout the width of the oxide and if the rate limiting step for the trapping and detrapping is the tunneling of carriers from bulk to the traps, then the distribution  $D(\tau)$  will depend upon the distribution  $D(l)$  of the distances of the trap from the interface. For a tunnelling process  $\tau = \exp(l/l_0)$  and hence :

$$D(\tau) \propto \left| \frac{\partial l}{\partial \tau} \right| D(l) \propto l_0 D(l) \tau . \quad (1.39)$$

Thus a uniform distribution of the depth of the traps ( $D(l) \sim \text{constant}$ ) will give  $D(\tau) \propto 1/\tau$  and hence  $1/f$  power spectrum of the resistance fluctuations. Being a fluctuation in ( $\Delta n$ ) it is better for semiconductors or for systems close to the Metal-insulator transition.

- *The Hooge Model (Mobility Fluctuations):* In his paper “ $1/f$  noise is no surface effect”; F. N. Hooge [88] proposed that  $1/f$  noise is essentially a bulk phenomenon. Working with metal films [88], he championed an empirical relation for  $1/f$  noise in terms of resistance fluctuations, where the spectral density of the resistance is:

$$S_R(f) = \frac{\alpha_H}{N} \frac{R^{2+\beta}}{f^\alpha}, \quad (1.40)$$

where  $N$  is the total number of free carriers in the bulk,  $\alpha$  and  $\beta$  are constants ( $\beta \approx 0$ ).  $\alpha_H$  is known as “Hooge's constant” an empirical parameter with value about  $2 \times 10^{-3}$ . According to this equation, the spectral density is independent of temperature and material parameters and is a power law at all frequencies. This equation fit his data for metal films very well (see his plots in Figure 1.25).

These results [88], proved that the fluctuations in the conductivity are due to fluctuations in mobility and not in the number of charge carriers. Hooge summarized experimental support for his mobility fluctuation ( $\Delta\mu$ ) theory in [90] and some theoretical support (a development of a phonon scattering theory) was provided by Jindal and van der Ziel [92].

This simple model fails to explain some of the experimental results, e.g. in case of manganin, contact noise measurement yield close to the Hooge value for  $\alpha_H$ , whereas bulk measurements [93] yield  $\alpha_H < 10^{-4}$ . In case of such metals like Cu, Ag and Au, the noise in bulk samples at room temperature is indeed in one order of magnitude agreement with above equation. The noise is temperature dependent an in ways that are characteristics of each metal and therefore can not be described by a universal function  $\alpha_H(T)$ .

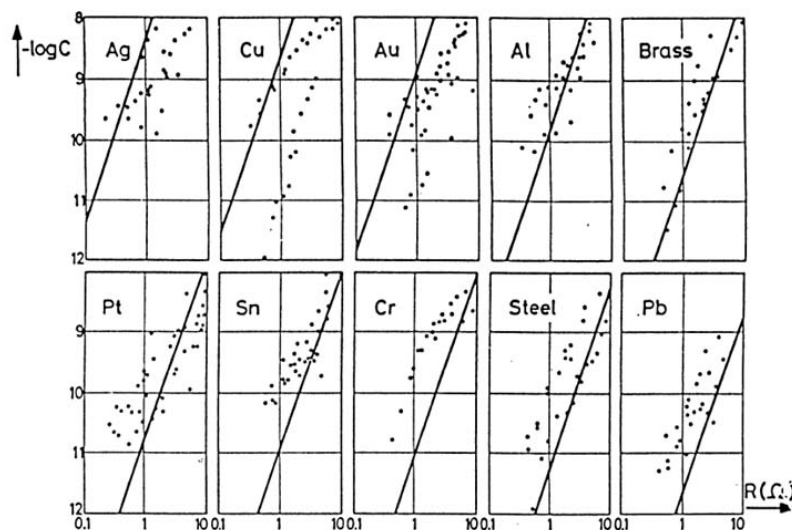


**Figure 1.25:**  $1/f$  noise in ten metal films [88]. The solid line correspond to a value of  $\alpha_H = 2 \times 10^{-3}$  for Hooge's empirical parameter.

- *The Dutta-Horn Model:* To explain the temperature dependence of experimental data for frequency exponent  $\alpha$  ( $\alpha_H(T)$  in Hooge model) in metal films, Dutta-Horn [91] left the concept  $D(E) \sim$  constant criteria and proposed  $D(E)$  to be slowly varying within the activation energy range. The model based on thermally activated kinetics, i.e.,  $\tau = \tau_0 \exp(-E_a/k_B T)$ . Then the expression for spectral density can be written as:

$$S(f) \propto \int \frac{\tau_0 \exp(E_a/k_B T)}{1 + (2\pi\tau_0)^2 \exp(2E_a/k_B T)} D(E) dE. \quad (1.41)$$

Integrating the above equation and expanding  $D(E)$  in Taylor's series the expression for spectral density can be written as:

$$S(f) \propto \frac{k_B T}{2\pi f} D(E'), \quad (1.42)$$

where  $E' = -k_B \ln(2\pi f \tau_0)$ . So the frequency exponent  $\alpha = -\partial \ln S(f)/\ln f$ . Dutta-Horn model derived the temperature dependent form of  $\alpha$  as;

$$\alpha = 1 - \frac{1}{\ln(2\pi f \tau_0)} \left[ \frac{\partial \ln S(f, T)}{\partial \ln T} - 1 \right]. \quad (1.43)$$

Dutta-Horn model of  $1/f$  noise is a good explanation of the spectral shape over a wide frequency band. The experimental observations show the coupling mechanism of defect motion is the manifestation of resistance fluctuation. But none of the above models can describe this coupling mechanism. However, this model implies that there are scale  $1/\tau_1$  and  $1/\tau_2$  of the frequency defined by the two extremities of  $D(\tau)$ .

In the linear conduction regime, the normalized spectral densities for voltage, current and resistance fluctuations have the same value and are independent on  $V$ ,  $I$  and  $R$ :

$$\frac{S_V(f)}{V^2} = \frac{S_I(f)}{I^2} = \frac{S_R(f)}{R^2}. \quad (1.44)$$

The above relation is experimentally proved and cannot be interpreted properly. But the relation allows a statement that voltage and current fluctuation spectral densities are determined by the resistance fluctuations spectral density.

## 1.4 Use of noise spectroscopy to probe manganites: A brief review

### 1.4.1 Introduction

For the basic physics of manganites, the investigation of low frequency fluctuation has the same importance as the dependence of resistance on the external parameters like temperature, magnetic field, current injection. The magnitude of the low frequency noise carries

information about the quality of the samples, films and crystals. From the theoretical point of view resistance fluctuations in the transition regime reveal new features of the charge transport, magnetotrasport. There are some other generic issues concerning noise in these perovskite manganites,

(a) The most likely source of noise in these materials is associated with motion of oxygen. In most of the perovskite oxides, oxygen is a particularly mobile species and has much smaller activation energy of migration (often  $< 1$  eV). This is much less than that of the cations. Also the perovskites are defect stabilized and contain oxygen vacancies that facilitate oxygen migration. Interestingly oxides like the rare earth manganites (CMR oxides) are used as oxygen conductors. In fact it has been established in the general context of metallic perovskite oxides like  $\text{LaNiO}_3$  that oxygen motion does cause noise in resistance as well as drift in resistivity [94].

(b) These materials are susceptible to strain which plays a very important role in deciding the charge transport. As a result, the presence of inhomogeneous strain can cause a conductance fluctuation. It is to be noted that the strain in the grown layer (arising due to substrate quality, growth condition, lattice mismatch and the thickness) can be inhomogeneous. Therefore, the noise in these films depends on good control of the film growth, controls of strain and oxygen stoichiometry necessary to produce low noise oxide films.

(c) Devices made from artificial grain boundaries are common in these oxides. Grain boundaries are prominent sources of noise.

In this section we give a brief overview on some selected reports on low frequency resistance fluctuation phenomena in manganites in form of thin films and single crystals.

## 1.4.2 Overview on published results

We have reviewed the published papers in the following categories:

- (1) Issues of CMR and grain boundary effects,
- (2) Issues of charge ordering and other phenomena, and
- (3) Issues regarding phase separation in manganite systems.

### 1.4.2.1 Issues of CMR and grain boundary effects

Starting from 1994, CMR materials have become interesting to look into. We can observe very significant changes in resistivity even with a very low magnetic field  $\sim 0.01$  Tesla. So, electrical fluctuation phenomena in these materials revealed interesting physics of manganites.

One of the first reports on noise in manganites was made by Alers *et al.* [95] on thin films of  $\text{La}_{0.6}\text{Y}_{0.007}\text{Ca}_{0.33}\text{MnO}_x$  near metal-insulator transition. They observed the power law dependence of noise spectral density with frequency exponent  $\alpha = 1 \pm 0.2$  at all temperatures, except near the transition. The magnitude of normalized noise in ferromagnetic metallic phase was found to be many orders of magnitude larger than the typically observed in metals. This result was unconventional from any defect mediated mechanism. The authors described the observed equilibrium fluctuation of resistivity at low frequency caused by local magnetization fluctuation and the  $1/f$  noise is a result of domain fluctuation. The peak of normalized noise versus temperature was accompanied by a peak in the frequency domain

was observed in the region near transition as shown in Fig. 1.26. Authors conclude that resistance fluctuation is directly coupled to the imaginary part of the magnetic susceptibility,  $\chi''$ , through which magnetic domain fluctuations are manifested as resistance fluctuation. The resistance fluctuation is related with local magnetization as

$$\left(\frac{\delta R}{R}\right)^2 = \left(\frac{M'_s}{\rho} \frac{\delta \rho}{\delta M}\right)^2 \frac{\kappa T \chi''}{\Omega f M_s}, \quad (1.45)$$

where  $M$  is the internal local magnetization,  $M'_s$  is the small field saturation magnetization, and  $M_s$  is the large field saturation. Most of the temperature dependence of noise appears due to temperature dependence of  $\chi''$ . The effect of a magnetic field on magnetization fluctuation is to align the domains and suppress the spontaneous fluctuations of the relative alignment of neighbouring domains. Application of magnetic field causes to decrease of noise peak amplitude and such behaviour is also observed for  $\chi''$  in ferromagnetic materials at ferromagnetic transition.

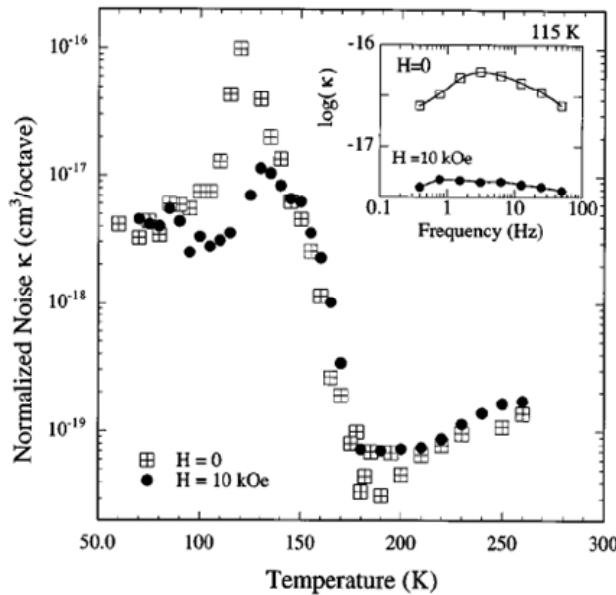


**Figure 1.26:** Temperature dependent  $1/f$  noise magnitude normalized by volume and resistivity. Inset shows the frequency dependence averaged over 1 octave at 115 K with zero field and a field of 10 kOe (adopted from Alers et al. [95]).

Rajeswari et al. [96] reported  $1/f$  noise in two hole doped manganite perovskite oxides,  $\text{La}_{0.67}\text{Ca}_{0.33}\text{MnO}_3$  (LCMO) and  $\text{Pr}_{0.67}\text{Sr}_{0.33}\text{MnO}_3$  (PSMO) oriented films, which exhibit CMR effect. They have compared their results against very high quality epitaxial films of  $\text{YBa}_2\text{Cu}_3\text{O}_7$ . They have estimated noise magnitude by calculating Hooge parameter and found 5-6 orders larger than those of the epitaxial films. The normalized noise spectral power density in the oriented films increases with decreasing temperature below the resistivity peak. The experimental data for their films has been shown in Fig. 1.27. Based on their transport measurements they have quoted possible origins: (1) the materials showed high correlation with oxygen contents, (2) the charge transport mechanism is highly governed by DE mechanism and the conduction process is related to hopping rate of the electron

between Mn<sup>3+</sup> and Mn<sup>4+</sup> ions, (3) the sensitive dependence of this hoping rate to Mn-O-Mn bond length and bond angles, (4) oxygen migration, and (d) spin dependent conductivity in FMM states. But they also found some anomalies also, like- for  $T > T_p$  (high temperature insulating state) the noise decreases with decreasing temperature, whereas, for  $T < T_p$  noise increases with decreasing temperature. The behaviour on the insulating side conforms to what is expected from the Dutta-Horn model of defect fluctuations the noise data on the metallic side is strikingly different and if interpreted in the framework of the Dutta-Horn model, implies a rise in density of states with decreasing temperature, suggestive of the presence of additional modes of fluctuations with lower characteristic energies

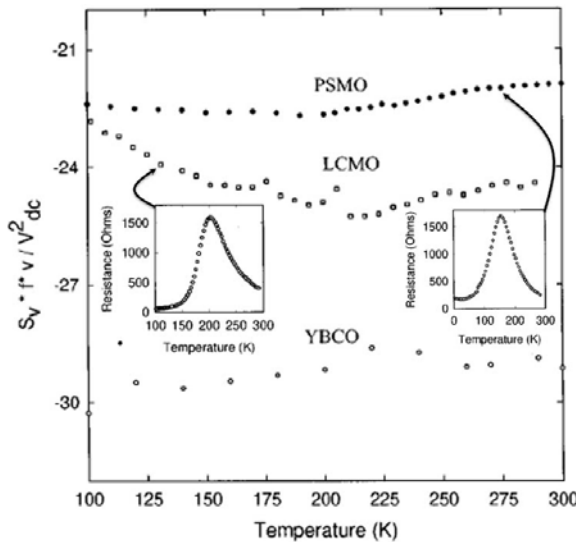


**Figure 1.27:** Comparison of the normalized noise power spectral density of epitaxial thin films of  $\text{La}_{0.67}\text{Ca}_{0.33}\text{MnO}_3$  and  $\text{Pr}_{0.67}\text{Sr}_{0.33}\text{MnO}_3$  with that of epitaxial thin films of  $\text{YBa}_2\text{Cu}_3\text{O}_7$  as a function of temperature [96]. The transport data for respective films have been shown inside the picture.

One published report by Hardner *et al.* [97] discussed the origin of resistance noise in manganites. They observed the electrical noise arising from the thermal fluctuations of magnetic domains and noise spectral density  $S(f)$  is close to  $1/f$  form. Authors argues if, for example, deviation in resistance  $\delta R$  came from fluctuations in interdomain hopping rates but  $R$  came primarily from other processes, surprisingly for  $(\delta R/R)^2$  to change by only a factor of 3 upon reducing  $H$  from 5T to zero at 115 K while  $R(H)$  changes by a factor of 80. Thus if the noise came from a weakly  $H$ -dependent component one would expect a change in fractional noise power of a factor of 6400. So, authors believed that noise is not probing the minor transport or fluctuation dynamics rather the main process responsible for the CMR in this material. The noise they observed was non-Gaussian. Individual steps in resistance had amplitude  $(\delta R/R) \approx 10^{-3}$ . If one would relate those steps to the domains in homogeneous conductor, the fluctuating domains would have to have area on the order of  $10^{-4} \text{ cm}^2$  which is quite unrealistic. These results create doubt about the current homogeneity in manganites. Later on most of the authors have supported intrinsic inhomogeneities in manganites and recognized as a general property of the material.

Reutler *et al.* [98] studied low frequency  $1/f$  noise of epitaxial thin films of manganites with temperature and applied magnetic field. Authors observed that structural disorder and strain arising from lattice mismatch between the substrate and the film can tune

the amplitude of the resistance fluctuations. They assumed that resistivity is a unique function of net magnetization. So the spectral density of the noise defined as

$$S_R(f) = S_M(f) \left( \frac{dR}{dM} \right)^2, \quad (1.46)$$

where noise spectral density due to magnetization fluctuation  $S_M(f)$  is directly related to magnetic susceptibility  $\chi''$  as

$$S_M(f) = \frac{2}{\pi} \frac{1}{f} \chi''(f) \frac{k_B T}{\Omega}. \quad (1.47)$$

They observed the normalized noise amplitude ( $a_R$  as appeared in report [98]) values obtained for strain free thin films are by several orders of magnitude smaller than data published earlier for manganites, both for thin films [95, 97, 99-103] and bulk samples. In particular, authors did not observe an increase of the noise level in the ferromagnetic regime and the  $1/f$  noise level is comparable to that of a conventional metal. The noise peak appeared near ferromagnetic transition temperature  $T_C$  at zero applied magnetic field and severely suppressed by magnetic field  $> 2$  Tesla (see left image of Fig. 1.28).

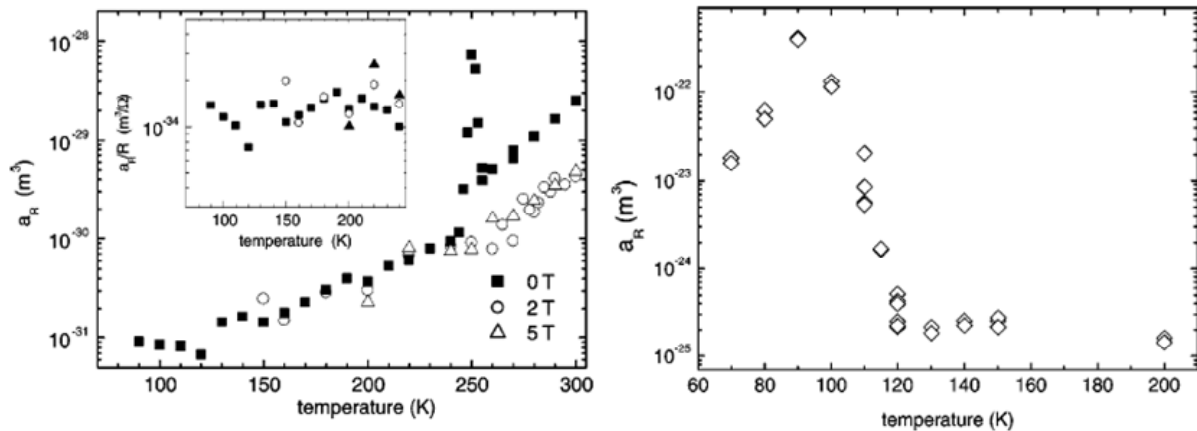


**Figure 1.28:** Left image: Temperature dependent normalized resistance fluctuation  $a_R$  with different applied magnetic fields for strain free film. Inset shows  $a_R / R$  with temperature at ferromagnetic phase, Right image: Temperature dependent  $a_R$  for a strained film (adopted from Reutler et al. [98]).

Increase of  $a_R$  arising from additional noise sources going from ferromagnetic to paramagnetic regime which is not directly related to resistance. Authors claimed that complex magnetic structure in paramagnetic region can be viewed as consisting of small ferromagnetically ordered clusters embedded into a paramagnetic environment. Additional fluctuations in disordered regions at domain boundaries or fluctuations of the domain magnetizations other than regular defect scattering are responsible for increased  $a_R$ . The suppression of noise peak at  $T_C$  by an application of magnetic field is directly related to ordered/disordered transition at magnetic phase transition. As  $T_C$  is approached large fluctuating ferromagnetic clusters freezes and helps to form ferromagnetic domains. Application of magnetic field above 2T the sample enters in homogeneous ferromagnetic metallic phase and further

increase of magnetic field causes further reduction of  $a_R$ . The strong coupling of resistance to magnetization gives rise to low frequency resistance fluctuation. The estimated Hooge parameter was reported as  $8 \times 10^{-2}$  at room temperature which is larger than the conventional metal. Authors claimed that low-strain film with less disorder can have less value of Hooge parameter than conventional metal. They performed noise experiments on strained film (1.5% lattice mismatch) and Hooge parameter obtained was  $10^6$ . This large increase of Hooge parameter as well as noise magnitude support the increased disorder plays an important role in noise. However, this result can be evidence there could be a phase separation near the metal-insulator transition.

Merithew *et al.* [104] discussed the equilibrium conductivity fluctuations of mesoscopic domains in film and bulk crystals of manganites. The average statistical properties of noise were found independent of whether it was measured below or well above coercive field  $H_C$ , and independent of field cooling versus zero field cooling. The results are expected if the fluctuation arises not between the states with different magnetization orientations but rather between the ones with different magnetization magnitudes, with the preferred orientations set by local and applied symmetry breaking field. There is fair possibility of the presence of magnetization orientation fluctuations in the system. They observed discrete two-level fluctuation process. The discrete resistance steps ( $\delta R / R$ ) were found to be  $10^4$  and the calculated domain volume was  $10^{-9}$  sample volume. Thus the homogeneous current model can be ruled out for these manganite systems. For each fluctuator Boltzmann factor (ratio of time spent in the two states) have magnetic field dependencies, strongly indicating that the stability of the mixed phase comes from a term in the free energy favouring the mixture of two microphases.

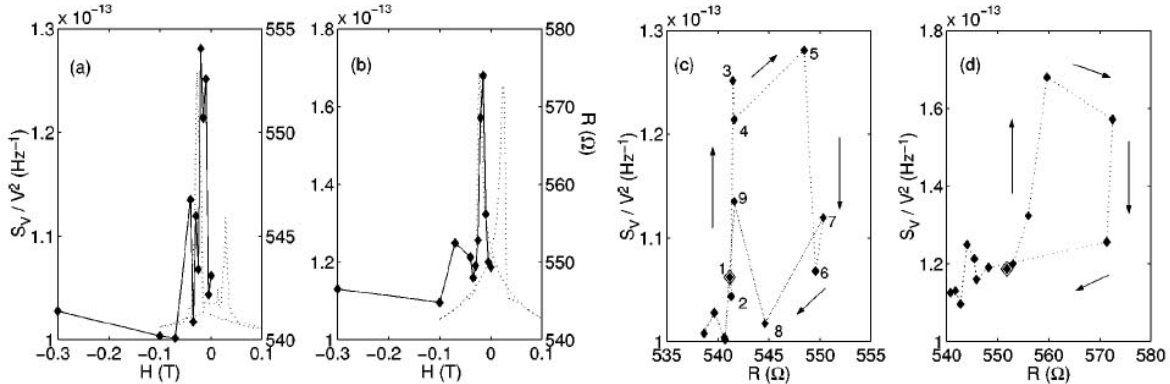


**Figure 1.29:** Magnetic-field dependence of noise level for low fields, with  $H$  parallel (a) and perpendicular (b) to the grain boundary at  $T = 10$  K. The corresponding dc resistance is shown for comparison (dotted lines). In (c) and (d) the noise levels are plotted vs the dc resistance (reproduced from reference [105]).

Mathieu *et al.* [105] studied electrical noise, which originates from grain boundaries [104]. They performed magnetoresistance as well as resistivity in  $\text{La}_{0.7}\text{Sr}_{0.3}\text{MnO}_3$  film deposited on a bicrystal substrate. The authors found that noise spectra could be characterized by  $1/f$  noise as well Lorentzian spectrum. The magnitude of the Lorentzian part of the noise wasn't proportional to the magnetic field derivative of the dc resistance and proposed that noise does not originate from random domain wall motion. The authors estimated the energy barrier and resulting domain size and concluded that domain -wall fluctuations with energy barriers determined by the pinning energy of defects, are the origin of the Lorentzian resistivity noise contribution. Magnetic field dependence of the noise level for low fields in

both orientations (perpendicular and parallel to the grain boundary) plotted against film resistance was found to be hysteresis (see figure 1.29). Thus two level fluctuators, which is responsible for the Lorentzian noise contribution is a precursor of larger and more dramatic changes in the domain configuration occurring when the resistance switches between low- and high-resistance states.

#### 1.4.2.2 Issues of Charge ordering and other phenomena

We have already discussed that depending on the composition ( $Mn^{4+}/Mn^{3+}$ ), average  $A$ -site cationic radius, temperature, and magnetic field, the ground state can in general be a FMM, charge-ordered insulator (COI), charge-disordered antiferromagnetic insulator (AFI), and even FMI. In the composition range where the  $Mn^{4+}/Mn^{3+}$  ratio is  $\sim 0.25\text{--}0.5$ , the ground state is typically FMM or COI.

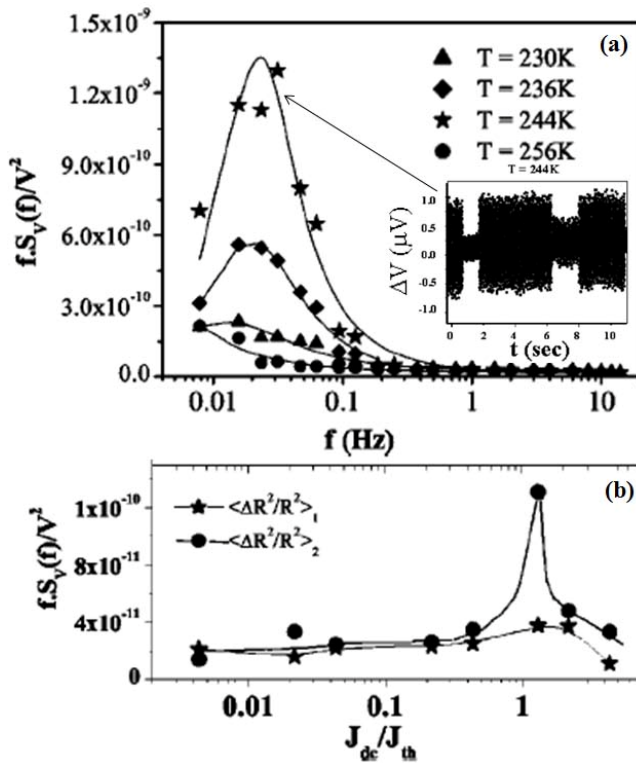


**Figure 1.30:** (a) The spectral power as a function of frequency at few representative temperatures ( $0.94 < T / T_{CO} < 1.04$ ). The appearance of a distinct Lorentzian riding on the  $1/f$  background is seen. The inset shows the appearance of RTN at  $T \sim T_{CO}$  responsible for low frequency Lorentzian fluctuations (b) The contribution of the  $1/f$  component  $\langle (\Delta R)^2 / R^2 \rangle_1$  and that of the Lorentzian  $\langle (\Delta R)^2 / R^2 \rangle_2$  as function of the dc bias  $J_{dc}$  at  $T = 226$  K. Adapted from reference [106].

Bid *et al.* [106] investigated low-frequency ( $f < 10$  Hz) noise spectroscopy of the COI system  $Pr_{0.63}Ca_{0.37}MnO_3$ , which shows a well-defined transition at  $T_{CO} \sim 245$  K. They have studied ac noise characteristics in presence of dc bias. Their investigations were not only to find whether there is a clear possibility of coexisting phases at  $T \sim T_{CO}$  but also to find out the destabilization of CO phase by inducing dc bias currents. They found that this dc bias

leads to non-linearity in conductivity due to CO destabilization. They studied a broad  $1/f$  component of noise that exists at all temperatures. But there is an additional low-frequency component that becomes very large close to  $T_{CO}$ . This low-frequency component contributes a Lorentzian of corner frequency  $f_c$  to the power spectra as shown in Fig. 1.30 (a). They have shown that the Lorentzian power spectra are associated with appearance of RTN in the time domain. Such low frequency noise components riding on the  $1/f$  spectrum also appear when a dc bias is applied above a threshold current density  $J_{th}$ . They found at  $J \approx J_{th}$ , there is onset of nonlinear conductivity in the system and as  $T \rightarrow T_{CO}$  from above (in the COI state) there is a rapid rise in the magnitude of the  $1/f$  component of the noise whose magnitude below  $T_{CO}$  remains more or less  $T$  independent at least down to  $T/T_{CO} \approx 0.8$  and shown in Fig. 1.30 (b). They mentioned that in the region close to but above the transition where the  $1/f$  noise steeply rises as  $T$  is lowered.

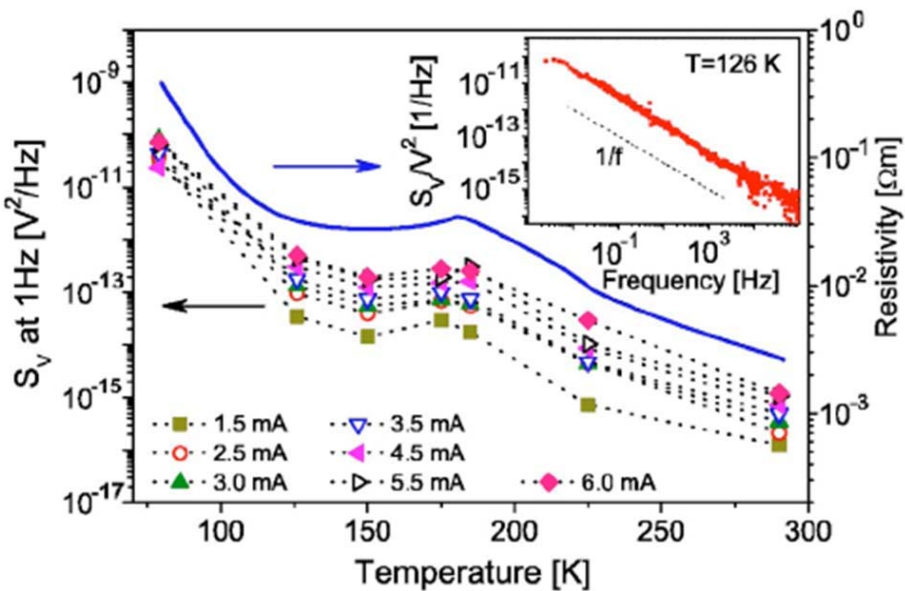


**Figure 1.31:** (a) Resistivity and  $1/f$  noise intensity at  $f = 1$  Hz as a function of temperature.  $\rho(T)$  was recorded using  $10 \mu\text{A}$  dc current bias. Inset shows a typical power spectral density of the noise in  $\text{La}_{0.82}\text{Ca}_{0.18}\text{MnO}_3$  single crystal samples; (b) Current dependence of the noise intensity at  $f = 1$  Hz. The dashed line is drawn according to  $S_V \propto I^2$  [107].

Recently, Wu *et al.* [107] investigated nonequilibrium  $1/f$  noise in  $\text{La}_{0.82}\text{Ca}_{0.18}\text{MnO}_3$  single crystals. The crystals were injected dc current bias and the noise had been investigated in such current biased systems. The authors observed that temperature dependent noise follows the resistivity changes with temperature. They observed noise scales as a square of the current as expected for equilibrium resistivity fluctuations. When the current was increased above a threshold value, the noise started to decrease. Figure 1.31 shows the temperature dependence of noise spectral power seems to follow the change in resistance with temperature, independently of the dominating conduction mechanism and magnetic state of the system. The noise spectral power  $S_V$  was found to be proportional with square of the applied current ( $I$ ) except at  $T = 77$  K. The authors found the initial increase of noise power with  $I^2$  but around 1 mA it started to decrease. Moreover, they found normalized  $S_V = S_V / V^2 = S_R / R^2 = S_r = \text{Constant}$ , where spectral density of resistance fluctuation  $S_R$

is temperature and current independent. Since  $R$  varies strongly with temperature, they suggested that at all temperatures the resistivity fluctuation equals a fixed fraction of the resistance and  $\delta R \propto R$ . This result abbreviated the surprising change in the magnetic state and dissipation mechanism of the sample with changing temperature. The current flow actually suppresses the noise at low temperatures which is more surprising. As an explanation, they proposed that  $1/f$  noise observed is an incoherent superposition of individual random two level fluctuation (Lorentzian power spectrum) processes which are thermally activated. This work reported noise feature for low doping manganite with increased current bias.

Tumer *et al.* [108] recently observed small fluctuating components in  $\text{Pr}_{0.5}\text{Ca}_{0.5}\text{MnO}_3$  system and the transition was characterized by a competition between pinned orbital domain topology that remains static and mobile domain boundaries exhibit slow, temporal fluctuations. They performed coherent soft x-ray resonant scattering measurements and analysed time as well as temperature dependent Bragg peak associated with speckle pattern near charge-ordering temperature and below. The authors recorded the time evolution of domain wall motion and change in the spackle pattern which is prominent in time scale. The dynamics is slow and they are also associated with domains that occur on large length scales, about 50 lattice spacings. They interpreted, at a given temperature; the bulk of a domain volume is static. The domain walls are pinned except for temperature very close to the transition where the domain walls are able to execute small-amplitude motion. The manganites possess a source of quenched disorder which couples to the orbital ordering parameter. Moreover, the coupling pins the domain walls, and though critical fluctuations are absent in this regime. The coupling between multiple degrees of freedom- charge, spin, and lattice has mostly been considered at the mesoscopic level. They investigated the interactions between order parameters which are complex and involve a range of length scales. The dynamic time-domain measurements give an insight not only at transition but explore new features of complex oxides.

#### 1.4.2.3 Issues of phase separation

Podzorov *et al* [109] explained noise in phase separated manganites by a model based on percolation theory. They measured  $1/f$  noise in the polycrystalline as well as single crystalline bulk samples of  $\text{La}_{5/8-x}\text{Pr}_x\text{Ca}_{3/8}\text{MnO}_3$  with  $x = 0.35$ . They observed diverging behaviour of  $1/f$  noise. In accordance with percolation theory, transition temperature  $T_C$  was determined with high accuracy. Critical components, found from scaling analysis of  $S_V$  and  $R$  on the metallic side of the CO-FM transition gave values of critical exponents in consistency with the predictions of the inverted random-void model of the continuum percolation. The magnitude of  $R$  was found to be similar for both types of samples but  $R$  for the single crystal reproducible steps as a function of  $T$  in the vicinity of  $T_C$ .

Raquet *et al.* [110] also investigated fluctuations with time in the ratio of contributions coming from the two phases. They observed the presence of fluctuators fluctuating between two discrete levels of energy states below ferromagnetic Curie temperature. They performed resistance fluctuation experiments on thin films of  $\text{La}_{0.67}\text{Ca}_{0.33}\text{MnO}_3$  grown on  $\text{LaAlO}_3$ . The authors proposed a mixed-phase percolating conduction process by which fluctuators can swap between two phases with differing conductivities on a timescale of few hundreds of milliseconds. The discrete two-level resistance fluctuation process, random telegraphic noise (RTN) was investigated by them in detail. They have observed RTN at various temperatures below the ferromagnetic Curie

temperature  $T_C$ . From 4 to 170 K, the resistance fluctuations appear due to presence of few fluctuators and hence give anomalous non-Gaussian behaviour (see left image of Fig. 1.32). In few temperatures single fluctuator dominates and gives rise to RTN. The fractional resistance  $\Delta R/R$  varies from 0.01% to greater than 0.2% and which is surprisingly high for macroscopic sample. For other temperatures where there is no RTN, noise spectral density has  $1/f$  form. They proposed that two-level fluctuation process is a thermally activated motion of the fluctuators between two accessible energy states (up and down) separated by activation energy  $E_a$ . So from Arrhenius law, the average time spent by a fluctuator in  $i$ -th state can be written as  $\tau_i = \tau_{0,i} \exp(E_a / k_B T)$  where  $\tau_{0,i}$  describes about the coupling between the thermal bath and the fluctuator. The temperature dependence of  $\tau_i$  arises purely from thermal fluctuations. They have studied the magnetic field dependence of noise and  $\tau_i$  they have defined magnetic field dependent barrier energy as shown in right image of Fig. 1.32. Thus, authors argue, that those fluctuators, even though they have a strong magnetic field dependencies, can not originate from magnetic domains. Instead, rapid variation of energy with temperature, as inferred from RTN, suggest the dynamic coexistence of two phases: a ferromagnetic metallic phase and a phase with relatively depressed magnetic and electrical properties. The RTN occurs when resistance switch back and forth between two phases. The applied magnetic field stabilizes the most favourable ferromagnetic state which has low resistance.

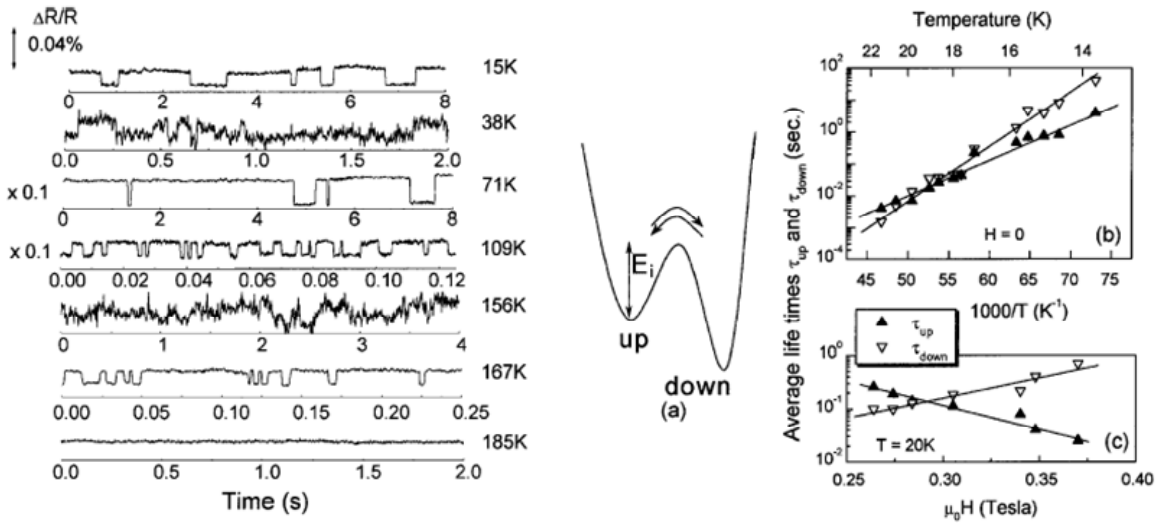


**Figure 1.32:** Left image: Resistance vs time at different temperatures. The noise alternates from a strongly non-Gaussian fluctuation-type to a random telegraphic noise (RTN) with  $\Delta R/R$  ranging from 0.01 % to 0.2%. There exists superposition of few two-level fluctuations processes with different characteristic lifetimes. At certain temperatures only a single fluctuator dominates, giving rise to RTN. Right image: (a) Schematic representation of an asymmetric double-well model used to describe the fluctuation process; (b) The measured average lifetimes for the high-resistance state ( $\tau_{up}$ ) and the low resistance state ( $\tau_{down}$ ) are plotted versus the reciprocal temperatures; (c)  $\tau_{up}$  and  $\tau_{down}$  versus magnetic field (see reference [110]).

At low temperatures, the conductivity is high and passes through ferromagnetic metallic phase. When temperature is increased, some of the ferromagnetic clusters move to depressed state with increases resistance, the resistance change results appearance of RTN. Authors proposed an existence of mixed phase percolation process to explain its complex conduction

process. In spite of, there exists a noise peat below Curie temperature as in metallic phase. Thus the conduction process is dominated by narrowest current paths. A few clusters sitting at those current paths have huge effect on conductivity in the metallic network, which results a large increase in noise level. The typical size of the switching cluster is  $(20 \text{ nm})^3$  which involve  $10^5$  Mn atoms. Finally authors emphasized that the final state was never exactly the same upon thermal cycling: the RTN could disappear altogether and, if present, displays different characteristics. The mixed phase is not related to any chemical inhomogeneity or physical disorder.

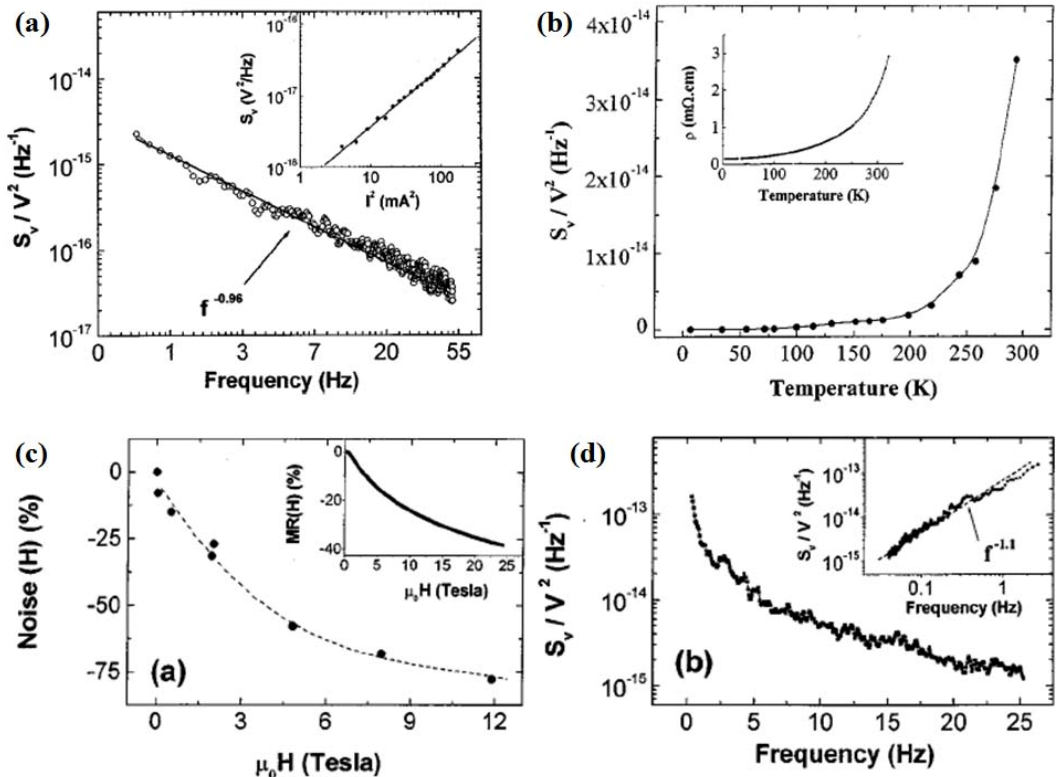


**Figure 1.33:** (a) Frequency dependence of noise spectral power at temperature  $T = 86 \text{ K}$ . In the inset, bias current of the noise spectral power density  $S_V$  for  $\text{La}_{2/3}\text{Sr}_{1/3}\text{MnO}_3$  at  $86 \text{ K}$  and  $20 \text{ Hz}$ ; (b) Temperature dependence of the normalized noise at  $20 \text{ Hz}$ . In the inset, the resistivity of the film on  $(100)$   $\text{MgO}$ ; (c) Magnetic field dependence of the normalized noise power spectral density:  $\text{Noise}(H) = [S_V/V^2(H) - S_V/V^2(0)]/[S_V/V^2(0)]$ , at room temperature and at  $20 \text{ Hz}$ . In the inset, the high magnetic field magnetoresistance of the same sample at  $300 \text{ K}$ . (d) Frequency dependence of the normalized noise power spectral density at  $12 \text{ Tesla}$  and  $300 \text{ K}$  for the same film. Adapted from reference [111].

The detailed investigation was done by Raquet *et al.* [111] on  $\text{La}_{2/3}\text{Sr}_{1/3}\text{MnO}_3$  film on  $\text{MgO}$  substrate as a function of the temperature ( $5\text{-}300 \text{ K}$ ) and magnetic field (up to  $12 \text{ Tesla}$ ). The normalized resistance noise was characterized by Dutta-Dimon-Horn model and suggested that, below ferromagnetic Curie temperature the resistance fluctuation is directly coupled to the thermally activated spin fluctuations. The authors also observed the drastic decrease of noise level when a continuous magnetic field ( $12 \text{ Tesla}$ ) was applied to the manganite sample. Figure 1.33(a) shows the normalized spectral power density at  $86 \text{ K}$  where figure 1.33(b) shows the temperature dependence of normalized noise spectral power. The spectral power clearly indicated the  $1/f$  noise and by the application of continuous magnetic field, up to  $12 \text{ Tesla}$  revealed a  $75\%$  decrease of noise level. But the authors didn't observe

any significant variation in the frequency exponent  $\alpha$  as a function of field indicated in figure 1.33(c) and 1.33(d). To explain the effects observed, the authors assumed that mean square of resistance fluctuation should be temperature dependent and the energy distribution should be multiplied by a temperature dependent function  $g(T)$ . The function expected to be temperature dependent power law. Best fitted curve was found to be proportional to  $T^{4.2}$ . Temperature dependent resistivity was related to the term  $T^{4.5}$  and which is closely related to the best fitted curve. They proposed that the fluctuations could be associated with electron-magnon interaction in the double-exchange theory. So temperature dependent resistivity can be linked up with number and strength of the fluctuators associated with the spin fluctuations in the system whose coupling to the resistivity is proportional to  $T^{4.5}$ . These arguments were supported because of suppression of noise spectral power with an application of magnetic field. The established link between noise feature and resistivity was further verified by this experiment within the framework of Dutta-Dimon-Horn model because the same scattering centres seem to be responsible for the resistivity and its fluctuations.

We have discussed that although double exchange and electron-phonon coupling effects are most common accepted interactions in manganites, but these are still insufficient to describe correctly the complex transport properties, fluctuations in resistances and obviously the features associated with phase separation. There are theoretical as well as experimental studies to rectify the intrinsic inhomogeneity due to the presence of strong tendencies towards phase separation. The submicron ferromagnetic metallic and ferromagnetic insulating regions are directly correlated with charge inhomogeneity and results conductivity fluctuations. Moreover we also discussed the dynamic behaviour of different phases of manganites. All the dynamic features keeping in mind we dedicate our dissertation on time dependent resistance fluctuation process which will explore not only the dynamic phase separation but also discuss the time dependent phenomena in different phases. In the next section we will discuss the basic theories related to resistance fluctuations (“noise”) built up the main layout of the thesis.

## **1.5 The Layout of the thesis**

Here we present our motivations regarding the work which we are going to present in this dissertation are as follows:

- To understand the underlying dynamics associated with ferromagnetic metallic state of manganites by measuring resistance fluctuations in the system using well characterized thin films of manganites.
- To understand the electrical resistance, non linear conductance process in the ferromagnetic insulating states of manganites and to study the fluctuation dynamics related to transport phenomena in this particular phase using single crystals.
- To study the resistance fluctuations in ferromagnetic insulating state with the application of external dc current. Then to study the basic characteristics of noise spectral power present in this particular state. Then to investigation the fundamental noise sources responsible for the resistance fluctuations.

We will focus ferromagnetic metallic state as well as ferromagnetic insulating states of manganites in form thin films and single crystals respectively. The film is of composition  $\text{La}_{0.67}\text{Ca}_{0.33}\text{MnO}_3$  which had been grown on oriented single crystals of  $\text{SrTiO}_3$ . We have used  $\text{La}_{0.80}\text{Ca}_{0.20}\text{MnO}_3$  single crystals to study the ferromagnetic insulating state of manganites.

The thesis contains seven chapters as follows:

- 
1. Chapter 1: In this present chapter, we presented a brief overview of the physics of manganites and the relevance of the study. This chapter includes the basic theories of resistance fluctuations which can be used as a tool to investigate dynamics of the fluctuating processes in different phases of manganites. This chapter will give an outline of the problems addressed in this dissertation.
  2. Chapter 2: In this chapter we discuss the film growth technique and give a brief overview of the methods to grow the single crystals. Then we discuss the experimental techniques to characterizations of the samples grown. The data obtained have been presented in the subsequent chapters, chapter 4 through 5.
  3. Chapter 3: We have used noise extensively as an experimental tool. In this chapter we discuss the experimental noise measurement techniques in detail. This discussion will include the low frequency noise measurement using digital signal processing to show its applicability and strength. As the low frequency noise measurements are very sensitive to external noise sources, we have dedicated a section on grounding and shielding of the system from all possible noise sources. This is to increase the sensitivity and performance of the system as well as to increase the quality of the data obtained.
  4. Chapter 4: In this chapter we have studied resistance fluctuation in thin films of composition  $\text{La}_{0.67}\text{Ca}_{0.33}\text{MnO}_3$  grown on oriented single crystalline  $\text{SrTiO}_3$  substrates. We have studied temperature dependent resistivity and low field magnetoresistance of the sample. The noise has been investigated on these films and compared with the previous data in published literatures. The film were very low noisy throughout the temperature range of investigation (77 K – 300 K, includes the paramagnetic to ferromagnetic transition regime) and we investigated how strain plays an important role in these samples. The magnetic field dependent noise has also been studied to capture the coupling between magnetization and resistance fluctuations. This important observation explores the dynamics near ferromagnetic phase transition.
  5. Chapter 5: This chapter we have studied temperature and frequency dependent noise on low doped ( $\text{La}_{0.80}\text{Ca}_{0.20}\text{MnO}_3$ ) manganite single crystals. The sample exhibits non-linear conductance in the ferromagnetic insulating regime and are very sensitive to external current bias. They follow Shklovskii-Efros hopping conduction below ferromagnetic insulating transition temperature and shows electroresistance phenomena. We have investigated very Nyquist noise with external current bias and also with varying temperature. We have measured low frequency noise by ac bias in presence of dc bias. There is a dramatic change in the nature of white noise has been observed. This chapter is dedicated to investigate the fluctuation dynamics of ferromagnetic insulating state of manganites.
  6. Chapter 6: In this chapter we have investigated a very novel system like nickel nanowire which is ferromagnetic even in the form of nanowire and remains metallic. We have already extensively investigated a ferromagnetic metallic system like hole doped perovskite ( $\text{La}_{0.67}\text{Ca}_{0.33}\text{MnO}_3$ ) and studied the magnetization fluctuations in that systems in Chapter 4. We extended and generalized our view to see the nature of the fluctuation processes in ferromagnetic metallic system and asked whether we can see the coupling of magnetization with the resistance or not. The samples were single crystalline and polycrystalline in nature. The noise amplitude depends on the crystallinity of the wires. This chapter presents an extensive work done on nickel nanowire of different diameters

varying from 15 nm to 50  $\mu\text{m}$ . Moreover, we observed thermally activated magnetization reversal process in the systems and suppression of noise spectral power with the application of low magnetic field.

7. Chapter 7: We conclude our discussion by introducing future plans and scope of further researches in this field based on the work done for this thesis.

## Bibliography:

- [1] J. B. Johnson, Phys. Rev. **32**, 97 (1928).
- [2] H. Nyquist, Phys. Rev. **32**, 110 (1928).
- [3] W. Schottky, Ann. Phys. (Leipzig) **57**, 541 (1918).
- [4] Montgomery H C Schooley W 1950 Phys. Rev. 78 646.
- [5] M. B. Weissman, Rev. Mod. Phys. **60**, 537 (1988).
- [6] A. K. Raychaudhuri, Current Opinion in Solid State and Material Sciences 6, 67 (2002).
- [7] M. B. Salamon, Rev. Mod. Phys. 73, 583 (2001)
- [8] E. Dagotto, T. Hotta, and A. Moreo, Phys. Rep. 344, 1 (2001).
- [9] E. Dagotto, Nanoscale Phase Separation and Colossal Magnetoresistance: *The Physics of Manganites and Related Compounds*, 1 ed. (Springer–Verlag, Berlin, (2002)).
- [10] M. Fäth, S. Freisem, A.A. Menovsky, Y. Tomioka, J. Aarts and J.A. Mydosh, Science **285**, 1540-2 (1999).
- [11] M. Uehara, S. Mori, C.H. Chen and S.-W. Cheong, Nature **399**, 560-3 (1999).
- [12] T. Becker, C. Streng, Y. Luo, V. Moshnyaga, B. Damaschke, N. Shannon, and K. Samwer, Phys. Rev. Lett. **89**, 237203 (2002)
- [13] Ch. Renner, G. Aeppli, B-G. Kim, Yeong-Ah Soh, and S-W. Cheong, Nature **416**, 518 (2002).
- [14] Ch. Simon, S. Mercone, C. Marritin, D. Sauref, G. André, and A. Brûlet, Phys. Rev. Lett. 89, 207202 (2002).
- [15] G. H. Jonker and J. H. van Santen, Physica **16**, 337 (1950).
- [16] K. Chahara, T. Ohno, M. Kasai and Y. Kozono, Appl. Phys. Lett. **63**, 1990 (1993).
- [17] R. von Helmolt et al., Phys. Rev. Lett. **71**, 2331 (1993).
- [18] S. Jin et al., Science **264**, 413 (1994).
- [19] S. S. P. Parkin, Z. G. Li, and D. J. Smith, Appl. Phys. Lett. **58**, 2710 (1991)
- [20] P. M. Levy, Science **256**, 972 (1992)
- [21] J. M. D. Coey, M. Viret, and S. von Moln'ar, Adv. Phys. **48**, 167 (1999).
- [22] A. Moreo, S. Yunoki, and E. Dagotto, Science **283**, 2034 (1999).
- [23] Y. Tokura, Rep. Prog. Phys. **69**, 797 (2006); Y. Tokura, editor, *Colossal Magnetoresistive Oxides* (Gordon and Breach, Monographs in Condensed Matter Science, London, 1999).
- [24] N. D. Mathur and P. B. Littlewood, Solid State Commun. **119**, 271 (2001).
- [25] A.-M. Haghiri-Gosnet and J.-P. Renard, J. Phys. D: Appl. Phys. **36**, R127 (2003).
- [26] C. Israel, M. J. Calder'on, and N. D. Mathur, Mater. Today **10**, 24 (2007).
- [27] Jeff Lynn, NIST Centre for Neutron Research, ITP 2005.
- [28] S. v. Naray-Szaba, Naturwissenschaften **31**, 466 (1943).
- [29] S. Quezel-Ambrunaz, Bull. Soc. Fr. Min. Cristallogr. **91**, 339 (1968).
- [30] J. B. A. A. Elemans, B. van Laar, K. R. van der Veen and B. O. Loopstra, J. Solid State Chem. **3**, 238 (1971).
- [31] W.E. Pickett and D.J. Singh, Phys. Rev. B **53**, 1146-60 (1996).
- [32] J. C. Chapman, Ph. D Thesis, Churchill College, University of Cambridge, UK, April 2005.
- [33] S. S. Zumdahl, *Chemistry*, Houghton Mifflin Publishers, Boston, Ma, 1997.
- [34] Y. Tokura and N. Nagaosa, Science **288**, 462 (2000).
- [35] K. Terakura, LV. Solovyev, and H. Sawada. *Colossal Magnetoresistive Oxides*. Gordon and Breach Science Publishers, New York, 2000.
- [36] J. B. Goodenough. Phys. Rev. **100**, 564 (1955); J. B. Goodenough. *Magnetism and Chemical Bonds*. Interscience Publishing, New York, 1963.

- [37] H. J. Jahn and E. Teller. *Proc. Roy. Soc.*, A161, 220 (1937).
- [38] M. Ziese and C. Srinitawarawong Phys. Rev. B **58**, 11519 (1998).
- [39] C. Zener, Phys. Rev. **82**, 403 (1951).
- [40] P.W. Anderson and H. Hasegawa, Phys. Rev. **100**, 675 (1955).
- [41] J. van den Brink, G. Khaliullin, and D. Khomskii. *Orbital Effects in manganites*. Kluwer Academic Publishers, Dordrecht, 2004.
- [42] A. J. Millis, Nature (London) **392**, 147 (1998).
- [43] K. Yoshida, Theory of Magnetism (Springer–Verlag, Berlin, 1998).
- [44] K. Dörr, J. Phys. D: Appl. Phys. **39**, R125 (2006).
- [45] T. V. Ramakrishnan, H. R. Krishnamurthy, S. R. Hassan, and G. V. Pai, Phys. Rev. Lett. **92**, 157203 (2004).
- [46] A. Bocquet, T. Mizokawa, T. Saitoh, H. Namatame, and A. Fujimori, Phys. Rev. B **46**, 3771 (1992).
- [47] T. Arima, Y. Tokura, and J. B. Torrance, Phys. Rev. B **48**, 17006 (1993).
- [48] T. Saitoh et al., Phys. Rev. B **51**, 13942 (1995).
- [49] D. D. Sharma et al., Phys. Rev. Lett. **75**, 1126 (1995).
- [50] T. G. Perring, G. Aeppli, Y. Moritomo, and Y. Tokura, Phys. Rev. Lett. **48**, 3197 (1997).
- [51] L.M. Rodríguez-Martínez and J.P. Attfield, Phys. Rev. B **63**, 024424 (2000).
- [52] H. Kawano, R. Kajimoto, M. Kubota and H. Yoshizawa, Phys Rev B **53**, R14709 (1996).
- [53] CMR, *Charge Ordering and Related properties of Manganese Oxides*, ed. C.N.R.Rao and B.Raveau, World Scientific, Singapore (1998), *Colossal Magneto-resistive Oxides*, ed. Y.Tokura, Gordon and Breach Science, Netherlands(2000)
- [54] B. B. Van Aken, O. D. Jurchescu, A. Meetsma, Y. Tomioka, Y. Tokura and T. T. M. Palstra, Phys. Rev. Lett. **90**, 066403 (2003) and references therein.
- [55] Himanshu Jain, *Investigations of hole doped rare earth manganites at low doping*, Master's thesis, Indian Institute of Science, Bangalore, 2003.
- [56] J. Foncuberta, B. Martinez, A. Seffar, S. Pinol, J. L. Garcia-Munoz, and X. Obradors, Phys. Rev. Lett., **76**, 1122 (1996); E. L. Nagaev. Phys. Lett. A, 215, 321 (1996); L. Sheng, D. Y. Xing, D. N. Sheng, and C. S. Ting. Phys. Rev. Lett., **79**, 1710 (1997).
- [57] Himanshu Jain, Ph.D thesis, Indian Institute of Science, Bangalore, India (2008).
- [58] Joy Mitra, PhD Thesis, Indian Institute of Science, Bangalore, India.
- [59] P. Schiffer, A. P. Ramirez, W.Bao, and S. -W. Cheong, Phys. Rev. Lett. **75**, 3396 (1995).
- [60] R. Mahendiran, S.K. Tiwary, A.K. Raychaudhuri, T.V. Ramakrishnan, R. Mahesh, N. Rangavittal and C.N.R. Rao, Phys. Rev. B **53**, 3348-58 (1996).
- [61] R. M. Kusters et al., Appl. Physica (Amsterdam) **155B**, 362 (1989).
- [62] G.J. Snyder, R. Hiskes, S. DiCarolis, M.R. Beasley and T.H. Geballe, Phys. Rev. B **53**, 14434 (1996).
- [63] M. Viret, L. Ranno and J.M.D. Coey, Phys. Rev. B **55**, 8067 (1997).
- [64] Hundley, M., M. Hawley, R. Heffner, Q. Jia, J. Neumeier, J. Tesmer, J. Thompson, and X. Wu, Appl. Phys. Lett. **67**, 860 (1995)
- [65] Tokura, Y., and Y. Tomioka, J. Magn. Magn. Mater. **200**, 1 (1999).
- [66] M. Jaime, P. Lin, M. B. Salamon, and P. D. Han, Phys. Rev. B **58**, R5901 (1998)
- [67] J. Mira, J. Rivas, F. Rivadulla, C. Vázquez- Vázquez, and M.A. López-Quintela, Phys. Rev. B **60**, 2998 (1999)
- [68] M. Sahana, U. K. Rössler, N. Ghosh, S. Elizabeth, H. L. Bhat, K. Dörr, D. Eckert, M. Wolf, K. –H. Müller, Phys. Rev. B **68**, 144408 (2003); M. Sahana, A. Venimadhav, M. S. Hegde, K. Nenkov, U. K. Rößler, K. Dörr, K. –H. Mülle, J. Magn. Magn. Mater. **260**, 361

- (2003); N. Moutis, I. Panagiotopoulos, M. Pissas, and D. Niarchos, Phys. Rev. B **59**, 1129 (1999)
- [69] A. Moreo, S. Yunoki, and E. Dagotto, Science **283**, 2034 (1994); A. S. Alexandrov and A. M. Bratkovsky, Phys. Rev. Lett. **82**, 141 (1999).
- [70] M. Fäth, S. Freisem, A.A. Menovsky, Y. Tomioka, J. Aarts and J.A. Mydosh, Science **285**, 1540-2 (1999).
- [71] A. J. Millis, P. B. Littlewood, and B. I. Shraiman, Phys. Rev. Lett. **74**, 5144 (1995);
- [72] G. Papavassiliou et al., Phys. Rev. Lett. **91**, 147205 (2003).
- [73] M. M. Savosta et al., Phys. Rev. B **67**, 094403 (2003).
- [74] V. Markovich et al., Phys. Rev. B 66, 094409 (2002); V. Markovich et al., Phys. Rev. B **65**, 144402 (2002).
- [75] C. S. Hong, W. S. Kim, and N. H. Hur, Phys. Rev. B **63**, 092504 (2001).
- [76] V. B. Shenoy, T. Gupta, H. R. Krishnamurthy, and T. V. Ramakrishnan, Phys. Rev. Lett. **98**, 097201 (2007).
- [77] J.-S. Zhou, J. B. Goodenough, A. Asamitsu, and Y. Tokura, Phys. Rev. Lett. **79**, 3234 (1997); G. -L. Liu, J. -S. Zhou, and J. B. Goodenough, Phys. Rev. B **70**, 224421 (2004).
- [78] B. I. Shklovskii and A. L. Efros, *Electronic Properties of Doped Semiconductors* (Springer, Berlin, 1984).
- [79] Burg J, Mayr M, Martin-Mayor V, Moreo A and Dagotto E, Phys. Rev. Lett. **87** 277202 (2001)
- [80] N.D. Mathur and P.B. Littlewood, The self-organised phases of manganites. Solid State Commun. **119**, 271 (2001).
- [81] K.H. Ahn, T. Lookman and A.R. Bishop, Nature **428**, 401 (2004).
- [82] Sh. Kogan “*Electronic noise and fluctuations in solids*”
- [83] K.E. Nagaev, Phys. Rev. B **52**, 4740 (1995)
- [84] A.H. Steinbach, J.M. Martinis and M.H. Devoret, Phys. Rev. Lett. **76**, 3806 (1996)
- [85] J. B. Johnson, Phys. Rev. **26(1)**:71-85, July 1925.
- [86] F. K. Du Pfe, Phys. Rev., **78**, 615 (1905), Phys. Rev. **78**, 5 (1950).
- [87] A. L. McWhorter, in *Semiconductor Surface Physics*, edited by R. H. Kingston (University of Pennsylvania, Philadelphia)
- [88] F. N. Hooge, Physics Letters **29A(3)**, 139-140, April 1969; F. N. Hooge, Physica, **60**, 130-144, 1976.
- [89] F. N. Hooge and L. K. J. Vandamme, Physics. Letters. **66A(4)**, 315 (1978).
- [90] F. N. Hooge, Physica **83B(1)**, 14 (1976).
- [91] P. Dutta and P. M. Horn, Rev. Modern Phys. **53**, 497 (1981)
- [92] R. P. Jindal and A. van der Ziel, Journal of Applied Physics **52(4)**, 2884 (1981).
- [93] R. F. Voss and J. Clarke, Phys. Rev. B **13**, 556 (1976)
- [94] Arindam Ghosh and A.K.Raychaudhuri, Phys. Rev B **64**, 104304 (2001); A.Ghosh, A.K. Raychaudhuri, R. Sreekala, M. Rajeswari and T. Venkatesan, J. Phys D (Appl. Phys.) (rapid commn) **30**, L 75 (1997).
- [95] G. B. Alers, A. P. Ramirez, and S. Jin, Appl. Phys. Lett. **68**, 3644 (1996).
- [96] M. Rajeswari, A. Goyal, A. K. Raychaudhuri, M. C. Robson, G. C. Xiong, C. Kwon, R. Ramesh, R. L. Greene, T. Venkatesan, and S. Lakeou, Appl. Phys. Lett. **69**, 851 (1996).
- [97] H. T. Hardner er al., J. Appl. Phys. **81**, 272 (1997)
- [98] P. Reutler, A. Bensaid, F. Herbstritt, and C. Höfener, Phys. Rev. B **62**, 11619 (2000).
- [99] M. Fäth, S. Freisem, A. A. Menovsky, Y. Tomioka, J. Aarts, and J. A. Mydosh, Science **285**, 1540 (1999).
- [100] S. K. Arora, R. Kumar, D. Kanjilal, R. Bathe, S. I. Patil, S. B. Ogale, and G. K. Mehta, Solid State Commun. **108**, 959 (1998).

- [101] S. K. Arora, R. Kumar, R. Singh, D. Kanjilal, G. K. Mehta, R. Bathe, S. I. Patil, and S. B. Ogale, *J. Appl. Phys.* **86**, 4452 (1999).
- [102] R. Raquet, J. M. D. Coey, S. Wirth, and S. von Molná'r, *Phys. Rev. B* **59**, 12 435 (1999).
- [103] M. Rajeswari, R. Shreekala, A. Goyal, S. E. Lofland, S. M. Bhagat, K. Ghosh, R. P. Sharma, R. L. Greene, R. Ramesh, T. Venkatesan, and T. Boettcher, *Appl. Phys. Lett.* **73**, 2672 [1998].
- [104] R. D. Marithew, M. B. Weissman, F. M. Hess, P. Sprsdling, E. R. Nowak, J. O' Donnell, J. N. Eckstein, Y. Tokura, and Y. Tomioka, *Phys. Rev. Lett.* **84**, 3442 (2000)
- [105] R. Mathieu, P. Svedlindh, R. Gunnarsson, and Z. G. Ivanov, *Phys. Rev. B* **63**, 132407 (2001)
- [106] A. Bid, A. Guha, A. K. Raychaudhuri, *Phys. Rev. B* **67**, 174415 (2003)
- [107] X. D. Wu, B. Dolgin, G. Jung, V. Markovich, and Y. Yuzhelvski, M. Belogolovskii, and Ya. M. Mukovskii, *Appl. Phys. Lett.* **90**, 242110 (2007).
- [108] J. J. Turner, K. J. Thomas, J. P. Hill, M. A. Pfeifer, K. Chesnel, Y. Tomioka, Y. Tokura, and S D Keven, *New Journal of Physics* **10**, 053023 (2008)
- [109] V. Podzorov, M. Uehara, M. E. Gershenson, T. Y. Koo, and S.-W. Cheong, *Phys. Rev. B* **61**, R3784 (2000).
- [110] B. Raquet, A. Anane, S. Wirth, P. Xiong, and S. von Molná'r, *Phys. Rev. Lett.* **84**, 4485 (2000)
- [111] B. Raquet, J. M. D. Coey, S. Wirth, and S. von Molná'r, *Phys. Rev. B* **59**, 12435 (1999)

# Chapter 2

## Sample Growth and Characterization Techniques

All the data presented for this dissertation was taken on hole doped rare earth transition metal oxides (manganites) as a form of highly oriented films and single crystals. In this chapter we shall discuss about the growth techniques of the samples and the instruments used for essential characterizations.

### 2.1 Introduction

Lanthanum manganites (manganites in general) can be prepared by many different synthesis techniques and in various forms, including single crystals, polycrystalline ceramics and thick or thin films. Single crystals can be grown in several ways, for instance by the floating-zone method (Urushibara *et. al.* 1995 [1]). Polycrystalline samples can be prepared by solid state mixing, involving repeated steps of mixing, grinding and heating of oxides until a single-phase manganite is obtained. Polycrystalline manganites can also be synthesized by various wet-chemical methods (Mori *et. al.*, 2000 [2]; Philip and Kutty, 2000 [3]). Thick manganite films can be produced by spraying techniques and well-defined 2D-patterns can be obtained using screen printing techniques (Balcells *et. al.* 2000 [4]). Thin films are usually grown by laser ablation (pulsed laser deposition) or sputtering using sintered polycrystalline targets (Prellier *et. al.* 2001 [5]). Depending on the substrate, thin films can be prepared in epitaxial as well as polycrystalline forms (Gupta *et. al.* 1996 [6]).

The hole doped manganites under investigation in this present work have the general formula  $\text{RE}_{(1-x)}\text{A}_x\text{MnO}_3$  and are obtained by replacing “ $x$ ” fraction of the rare earth transition metal element “RE” is La, a trivalent elements “A” is Ca, a divalent cation. This has the effect of creating  $\text{Mn}^{4+}$  ions from the  $\text{Mn}^{3+}$  ions as are present in the pristine compound  $\text{LaMnO}_3$  for  $x = 0$ . The electrical and magnetic properties of manganites are strongly dependent upon the  $\text{Mn}^{3+}/\text{Mn}^{4+}$  ratio. This ratio is also affected by oxygen non-stoichiometry or cation (La and/or A) non-stoichiometry since crystal structure of manganites admits vacancies in the La (A-site) sublattice. These factors in turn affect the crystallographic and defect structure of the compound. From a crystal growth point of view then, the adjusted formula of the compounds may be written thus:  $(\text{La}_{(1-x)}\text{A}_x)_y\text{MnO}_{3-d}$ , where “ $y$ ” quantifies the La and/or A cation non-stoichiometry, and “ $d$ ” represents the oxygen non-stoichiometry.

The Ca-doped lanthanum manganite samples characterized in the present work were films and single crystals prepared by the wet-chemical technique and by the floating zone methods respectively. For films, the divalent Ca-ion concentration was taken as 33%, i.e.,  $x = 0.33$  and the hole doped lanthanum manganites prepared as  $\text{La}_{0.67}\text{Ca}_{0.33}\text{MnO}_3$  (LCMO33). The single crystal samples prepared with Ca-ion concentration as 20% ( $x = 0.20$ ) which gives manganites as  $\text{La}_{0.80}\text{Ca}_{0.20}\text{MnO}_3$  (LCMO20). This chapter gives a description of the sample preparation and the characterization techniques. This will help to built up an idea about the data collected on the samples and presented in the subsequent chapters in this thesis.

## 2.2 Growth of the films of $\text{La}_{0.67}\text{Ca}_{0.33}\text{MnO}_3$ (LCMO33)

### 2.2.1 Overview on chemical solution deposition technique:

The chemical solution deposition (CSD) technique [7] is a method where unit species of material to be deposited is applied in a liquid/solution form at lower temperatures ( $<100^\circ\text{C}$ ) and typically atmospheric pressures on the substrate which act as a physical support where no reaction occurred. The technique, which includes the sol-gel process, is one of the most common processes used as a fabrication technique for thin films. This process can be widely used for optical, electrical, magnetic, mechanical and catalyst applications. The important advantages of the chemical solution technique are high purity, good homogeneity, lower processing temperatures, precise composition control for the preparation of multi-component compounds, versatile shaping, and preparation with simple and cheap apparatus, compared with other methods.

The chemical solution deposition technique is essentially a mass transport process. The transformation of a liquid solution to a solid crystalline film is accomplished through three steps as shown in Fig. 2.1:

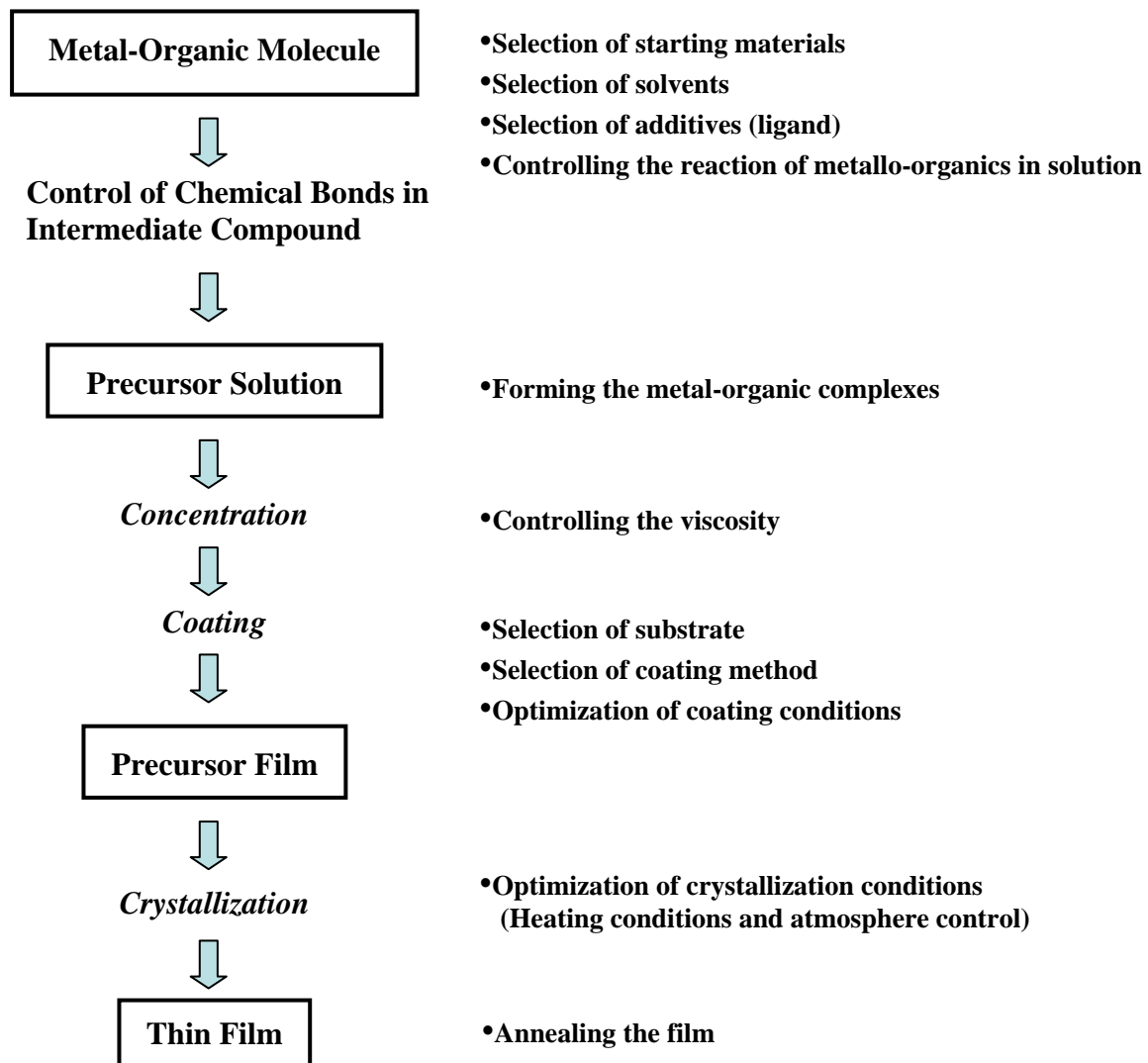


**Figure 2.1:** Flow-sheet describing the steps for chemical solution deposition technique.

In this technique, the starting raw materials are not only mixed at a molecular level in the solution, but also reacted to cause an appropriate chemical modification of the metallo-organic complexes, leading to the development of new molecular engineering.

## 2.2.2 Preparation of precursor solution

### 2.2.2.1 Materials

Commercial lanthanum acetate hydrate, calcium mono-acetate hydrate and manganese (II) acetate tetra-hydrate were purchased from Sigma-Aldrich, India [8]. Acetic acid was purchased from Merck, India [9]. The molecular structures of these materials are shown in Fig. 2.2.

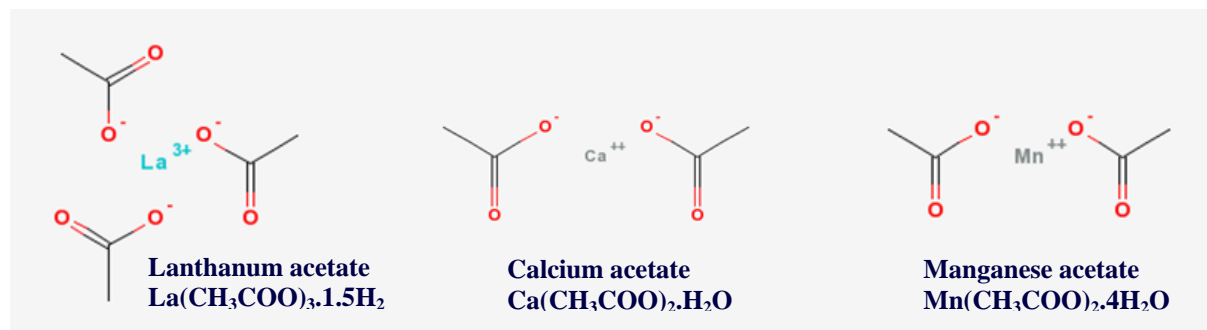
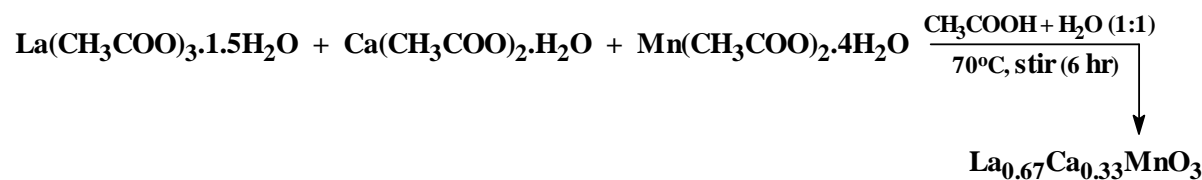


**Figure 2.2:** The molecular structures of the three compounds used for precursor solution preparation.

### 2.2.2.2 Method

The precursor solution of three component oxide was prepared from lanthanum acetate hydrate ( $\text{La}(\text{CH}_3\text{COO})_3 \cdot 1.5\text{H}_2\text{O}$ ), calcium mono-acetate hydrate ( $\text{Ca}(\text{CH}_3\text{COO})_2 \cdot \text{H}_2\text{O}$ ) and manganese (II) acetate tetra-hydrate ( $\text{Mn}(\text{CH}_3\text{COO})_2 \cdot 4\text{H}_2\text{O}$ ) by dissolving them in a solution of water and acetic acid (1:1 by volume) in the correct stoichiometric proportion. The concentration of the precursor solution was maintained at 0.4 M. The reaction was carried out at slightly elevated temperature ( $70^\circ\text{C}$ ) until the transparent solution was getting prepared.



The continuous stirring of the precursor solution was necessary for proper ionic dissociation as well as mixing of the cations. After getting the transparent solution the source of heat is withdrawn. The final precursor solution was prepared by stirring it continuously for 6 hrs at ambient temperature. The solution is preserved for film depositions. Figure 2.3 (steps from I-III) shows the precursor solution preparation schematically. Detailed of film preparation is described in reference [10].

### 2.2.3 Preparation of films

The precursor solution prepared mentioned earlier is used for the deposition of films on different substrates. We have used single crystalline Strontium Titanate ( $\text{SrTiO}_3$ ) substrates for film growth. In this section we shall discuss about the cleaning of the substrates used and the steps regarding the preparation of films.

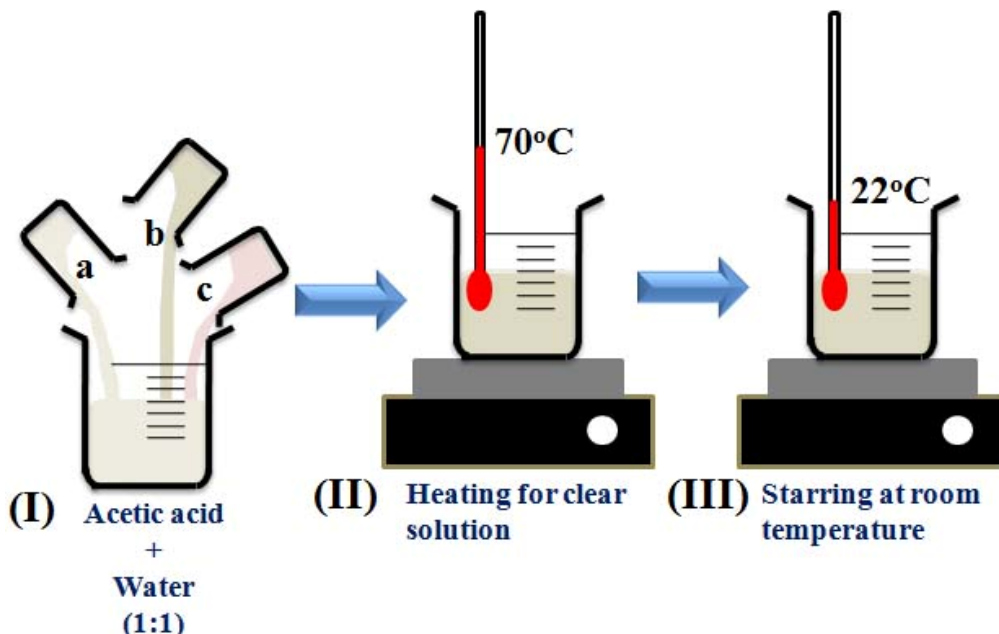


**Figure 2.3:** The schematic diagram of precursor solution preparation from three oxide components. Where, **a** =  $\text{La}(\text{CH}_3\text{COO})_3 \cdot 1.5\text{H}_2\text{O}$ , **b** =  $\text{Ca}(\text{CH}_3\text{COO})_2 \cdot \text{H}_2\text{O}$  and **c** =  $\text{Mn}(\text{CH}_3\text{COO})_2 \cdot 4\text{H}_2\text{O}$ .

#### 2.2.3.1 Cleaning of $\text{SrTiO}_3$ substrates

The most crucial step of the film preparation is cleaning of the substrate surface. The schematic diagram of the steps to be followed for cleaning is shown in Fig. 2.4. These steps of cleaning remove traces of oil, grease, any organic substances from the substrates surface. The cleaning procedure also makes the substrate surface hydrophilic otherwise the precursor solution will not be able to wet the crystal surface. The films can curl up after heat treatment due to poor cleaning of substrate surfaces. Moreover, proper cleaning reduces the impurities from the films grown which is very important for any experiments.

Films were prepared on orientated (orientation along [002] crystal plane direction) single crystalline substrates (single side polished) of Strontium Titanate  $\text{SrTiO}_3$  (STO). The dimension of these substrates is  $5\text{mm} \times 5\text{mm} \times 1\text{mm}$ . If the lattice parameters of the film and substrates are sufficiently well matched, i.e., in-plane lattice parameters of the films will lead to an in-plane lattice strain (either tensile or compressive) in the film that is likely to alter the film properties, as electron-lattice interaction in the manganites is particularly crucial. It is possible to have an epitaxial strain over  $\sim 1\%$ , e.g. LCMO33 grown on STO and a wide variation of  $T_c$  (80–280 K) is observed. Table 2.1 shows the list of lattice parameters for different substrates which can be used to grow films of LCMO33. The STO substrates have lattice parameter closer to lattice parameter of bulk LCMO33 (3.855 Å). The lattice mismatch is  $\sim 1\%$  and this lattice mismatch will lead to strained films.

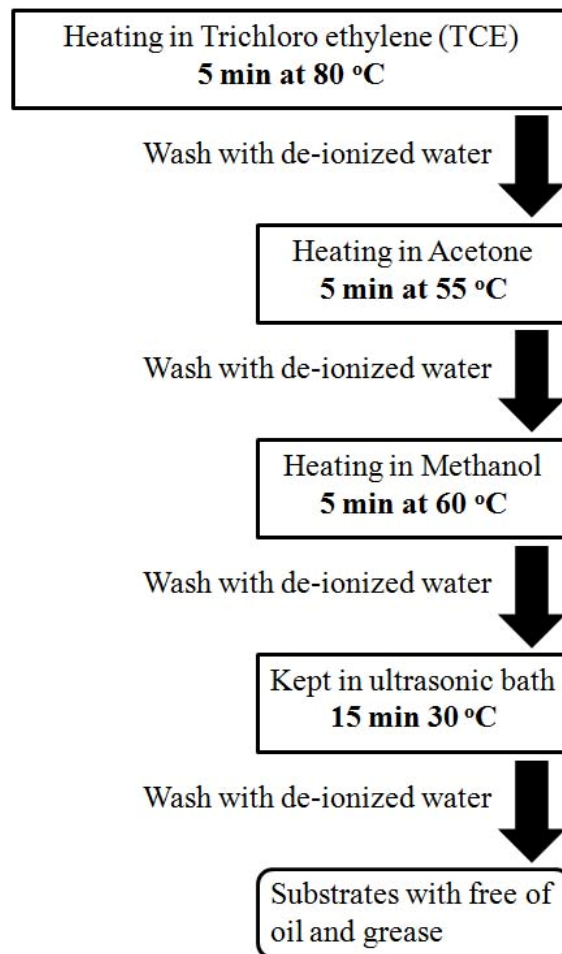


**Figure 2.4:** The schematic diagram of the cleaning steps followed to clean  $\text{SrTiO}_3$  substrates.

| Composition            | Lattice parameters at 300 K ( $\text{\AA}$ ) | Properties                  | Lattice mismatch (%) |
|------------------------|--|-----------------------------|----------------------|
| $\text{SrTiO}_3$ (STO) | 3.905  | dielectric and diamagnetic  | 1.29                 |
| $\text{LaAlO}_3$ (LAO) | 3.789  | dielectric and diamagnetic  | 1.71                 |
| $\text{NdGaO}_3$ (NGO) | 3.864  | dielectric and diamagnetic  | 2.33                 |
| $\text{MgO}$ (MGO)     | 4.21   | dielectric and paramagnetic | 9.20                 |

**Table 2.1:** Table of lattice parameters of different substrates.

### 2.2.3.2 Deposition of films

The precursor solution of lanthanum calcium manganese prepared (described in earlier subsection) with proper stoichiometric proportion was spin coated on STO with 6500 r.p.m for 30 sec each followed by pyrolysis at about  $350^\circ\text{C}$  [10]. Five consecutive coatings were done before annealing at  $900^\circ\text{C}$  for 10 min. The resulting films were oriented films of thickness  $\sim 500\text{nm}$ . The annealing time controls the size of grain boundaries in these films. The steps for the complete process have been described in Fig. 2.5.

The heat treatment was standardized according to phase evolution of manganites. The heat treatment leads to decomposition of several compounds as:

150°C: Evaporation of physically absorbed water

250-300°C: Evaporation of more strongly bonded water leads to construction of new bonds and formation of crystalline trace phases

300-600°C: Decomposition of carbonates  
Formation and dissolution of the trace phases

600-700°C: Complete decomposition of carbonates and crystallization into the perovskite phase

700-1000°C: Crystal growth, oxygen loss and increases distortion of unit cell

The evolution discussed above can be represented by Fig. 2.6. Keeping the different decomposition processes in mind, we have standardized the annealing temperatures of the film growth technique.

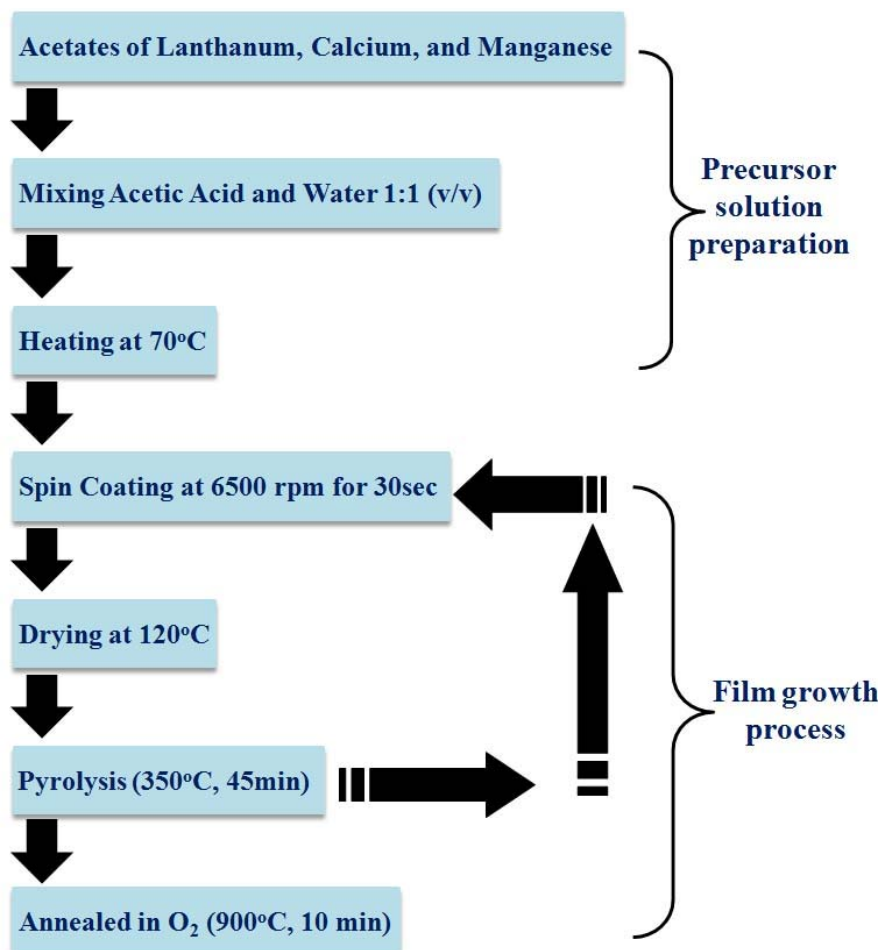


**Figure 2.5:** The schematic diagram of epitaxial film growth technique from precursor solution. The substrates have been used for growth is single crystalline oriented ( $[002]$ ) STO substrates which have ~1.3 % lattice mismatch with LCMO33.

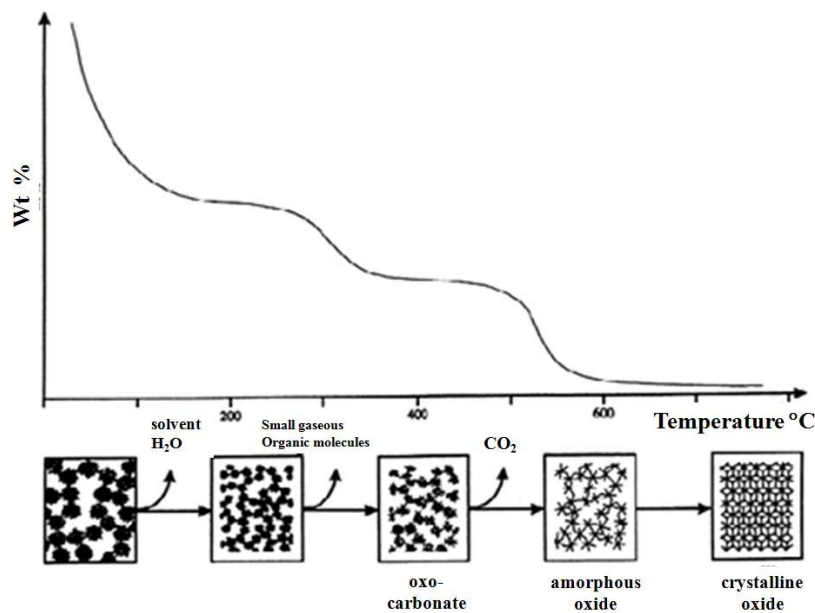


**Figure 2.6:** Typical weight versus temperature graph for a solution-to-oxide conversion, and schematic illustration of phase evolution [11].

## 2.3 Growth of single crystals by floating zone techniques

There are two well known techniques which are widely used for growing single crystals are floating zone technique and the flux growth technique. The single crystals used for the experiments were prepared by floating zone method at the Moscow State Steel and Alloy Institute, Moscow [12] by using an image furnace. The floating zone method is more favourable when it is very difficult to produce highly perfect crystals and to have high oxygen pressure over the melt where contamination of the crystallizing material must be prevented or for refractory oxides and related compounds. This technique employs a radiative heating process, i.e., it is crucible less method and avoids all possible contaminations of melt by the crucible material.

### 2.3.1 Instrumental Overview

This section briefly discusses the floating zone technique and the apparatus used for single crystal growth process. There are following requirements which allow using the floating zone method to grow manganite single crystals:

- The material to be grown should be highly defect and dislocation free perfect crystals
- The crystal should be refractory with high melting point ( $\approx 3000^\circ C$ )
- A high pressure of ambient gas (here  $O_2$ ) is required for the crystals growth and post growth annealing process.
- The gas phase over the melt during the crystal annealing should be controlled in uniform fashion.
- The annealing of growing crystals at uniform temperatures should be maintained and sufficient to relieve elastic stresses.
- The stoichiometric composition and desired doping level of metal ions should be user controlled.

- The rate of growth is required to be user controlled.
- The zone heating in radial direction should be uniform, i.e., growth front is required to be planer.

The above requirements are fulfilled by introducing image furnace in a zone melting apparatus using radiation heating. The schematic diagram of image furnace is depicted in figure 2.7(a). Its optical scheme consists of a biellipsoidal mirror assembly with a vertically positioned optical axis. A high power xenon arc lamp is positioned at the lower reflector focus and the radiation is focused at the other focus point. This configuration optimises the coefficient of utilization of light flux. The light flux concentrated on the heating object and generally uses 20% of electric source power. The other mirror is placed so that it can be moved along the optical axis. Two holders allow the sample rods to approach into the focal point where melting occurs. Out of two sample rods one is formed by pressed and sintered powder of material (feed rod) and other rod ends in a single crystal seed of the material (seed rod). The feed rod is placed in such a way that the focus of the movable mirror can be placed anywhere along the length of the feed rod. Both rods are placed in contact with each other while being slowly rotated in opposite direction. The design parameters of a typical furnace for growing crystals can be obtained from Balbashov *et al.* [13].

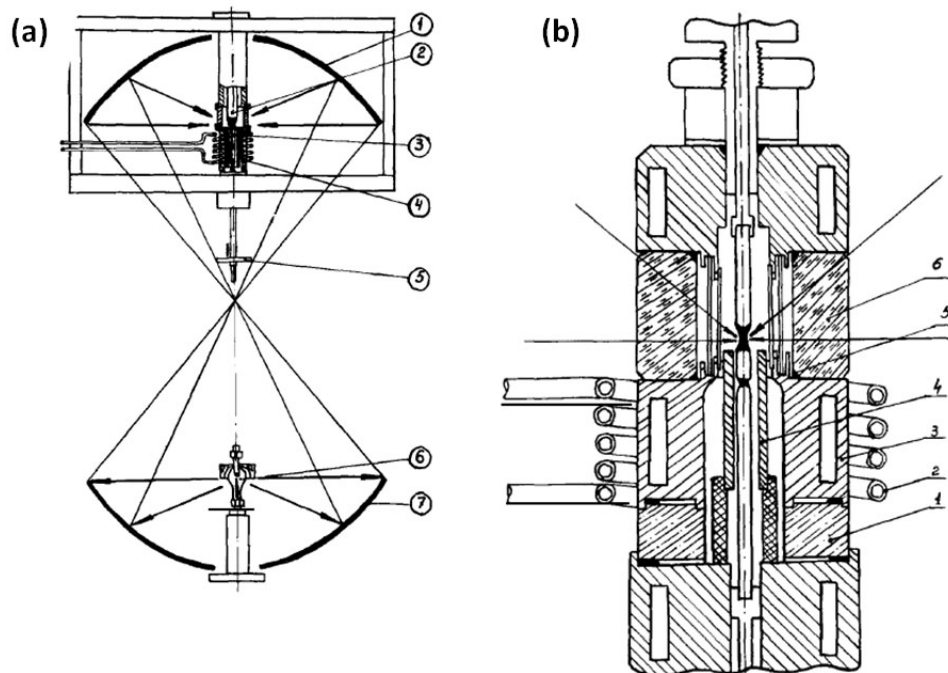


**Figure 2.7:** (a) Schematic of the floating zone melting apparatus used for the growth of  $\text{La}_{0.80}\text{Ca}_{0.20}\text{MnO}_3$ : (1,7) ellipsoidal reflectors, (2) feeding rod, (3) crystal, (4) heater, (5) light flux regulator, (6) xenon lamp. (b) Schematic of crystallization chamber: (1) Insulator, (2) RF coil, (3) eddy current concentrator, (4) annealing furnace, (5) siloxane rubber packing, (6) quartz container. From Balbashov *et al.*[13].

The design of the sample chamber is depicted in figure 2.7(b). The major and crucial element of the chamber is ring shaped power container made of optical grade fused quartz. The container has an inner diameter  $\approx 30$  mm and with a wall thickness 25 mm. During the growth process of oxide compounds it is difficult to preserve the stoichiometry of their compositions. The deviation can be caused either by loss of internal oxygen or

evaporation of other components. To establish the equilibrium partial pressures of components at gas phase, it is necessary to provide an excess pressure over the melt and it is about hundreds of atmosphere. The crystallization chamber provides a pressure  $\approx 100$  atm in the growth zone. The temperatures at the growth zone can/need be as high as  $\approx 3000^\circ\text{C}$ . Also, during the growth process, materials might escape/evaporate from the feed rod. To protect the inner wall of the container, as well as to keep it free of contamination, further replaceable quartz tubes are incorporated into the container. The quartz container also protects the mirror assembly from sample vapour. Further, two annealing furnaces are provided. The first uses a radio frequency (RF) heating scheme and achieves temperatures up to  $\approx 1600^\circ\text{C}$ . The second heater is cylindrical shaped and surrounds the cavity. This heater can achieve temperatures of up to  $2000^\circ\text{C}$ . Specific details about the design parameters of the particular heaters deployed in the image furnace used to grow the present crystals may be obtained from Balbashov *et al.* [13]. The packing of the chamber is done by siloxane rubber. The region where seed rod and feed rod meets is now slowly passed in the “hot zone”, hence the rod tips melt and fuse. Then the “hot zone” is slowly scanned along the feed rod with a predetermined speed ( $\sim$  few mm/hr). As the molten regions resolidify, the single crystalline seed acts as the nucleating site for grain growth, the feed rod grows as single crystal.

### 2.3.2 Growth of $\text{La}_{0.80}\text{Ca}_{0.20}\text{MnO}_3$ (LCMO20) single crystals

For the growth of  $\text{La}_{0.80}\text{Ca}_{0.20}\text{MnO}_3$  single crystals, the starting materials were high purity powders of  $\text{La}_2\text{O}_3$ ,  $\text{MnCO}_3$ , and  $\text{CaCO}_3$ . From the binary phase diagram (in air atmosphere) [14] shown in the Fig. 2.8, the homogeneity region of the  $\text{LaMnO}_3$  defined at 1123 K is  $0.908 < \text{La:Mn ratio} < 1.202$ .

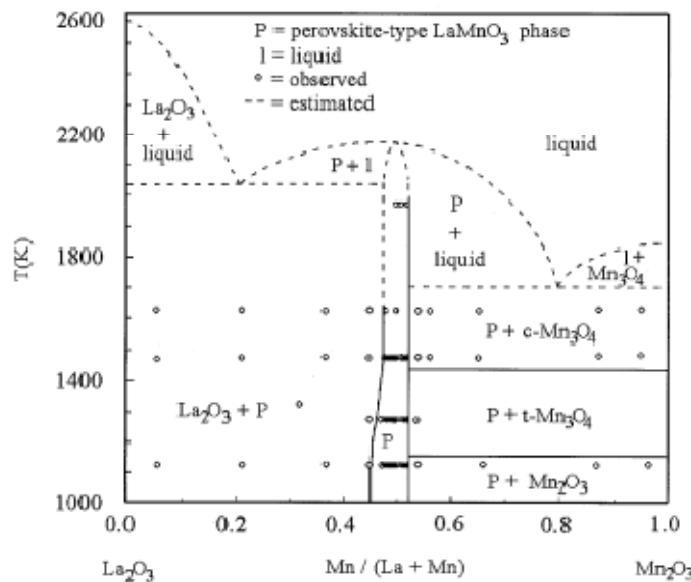


Figure 2.8: The pseudobinary  $\text{La}_2\text{O}_3\text{-Mn}_2\text{O}_3$  phase diagram in air. From Roosmalen *et al.* [14].

During the growth process, La/Mn ratio in the growing crystal depends on the composition of the zone melt established. It in turn is influenced by non-stoichiometry of the feed rod and evaporating losses of Mn from the melt. The increase of La/Mn ratio shifts the molten zone composition towards  $\text{La}_2\text{O}_3\text{-LaMnO}_3$  eutectic point (see Fig. 2.8). Because of the temperature difference is low between  $T_{\text{solidus}}$  and  $T_{\text{liquidus}}$  (as low as  $100\text{-}150^\circ\text{C}$ ) for this concentration in the diffusion layer can lead to crystallization of  $\text{La}_2\text{O}_3$  inclusion. The

distribution coefficients for Ca is defined as  $k_A = C_s / C_L$  where  $C_s$  and  $C_L$  denote the concentration of Ca in the grown-solid respectively, and in the melt-liquid zone respectively which is less than unity. The  $C_s$  distribution expressed as:

$$C_s = C_f \left[ 1 - (1 - k_A) \exp\left(\frac{-k_A z}{l}\right) \right] \quad (2.1)$$

where  $C_f$  is the concentration of the A-site element (L and/or A) in the feed rod,  $z$  is the current length, and  $l$  is the zone length. This causes the concentration of Ca to increase in the melt during the steady growth stage [15] causing the cation ratio (La+Ca)/Mn in the melt to exceed unity.

For the final growth process highly pure  $\text{La}_2\text{O}_3$ ,  $\text{MnCO}_3$ , and  $\text{CaCO}_3$  were taken with desired ratio, mixed and pressed with pressure 0.6-0.8 ton/cm<sup>2</sup> and heated in air at 1000°C for 24 h.  $\text{MnCO}_3$  was calcined in air at 1000°C for 24 h to form  $\text{Mn}_3\text{O}_4$  and  $\text{La}_2\text{O}_3$  was fired in air at 900°C for dehydration. The pressed tablets were ground and feed rods formed using a pressure 1 ton/cm<sup>2</sup> and sintered in air at 1300°C for 24 h. The growth process was carried out in Ar pressure of 3-5 bar or in air, at a crystallization rate 10-20 mm/h. A previously grown crystal was used as a seed. The feed rod and seed rod were rotated with the rotation rate 1 and 50 rpm, respectively. The phase composition of the obtained samples was studied by X-ray powder diffraction. Analyses of chemical composition were carried out using an electron probe microanalyzer (EPMA).

## 2.4 Experimental tools used for characterization

In this subsection we discuss about the experimental tools which we have used to characterize the films and single crystals. The experimental tool used for extensive noise experiments will be discussed in next chapter, Chapter 3 in details. The phase purity of polycrystalline powder and film were checked by x-ray diffraction pattern. The surface characterizations of the films were done Scanning Electron Microscopy (SEM), and Atomic Force Microscopy (AFM). The electrical, and magnetization measurements like temperature dependent resistivity, temperature and field dependent magnetization, low field magnetoresistance (MR) measurements of films and single crystals were also performed. In this section we will discuss about the basic ideas of these characterization techniques and in the proceeding chapters we shall produce data based on these measurements.

### 2.4.1 X-ray diffraction (XRD)

The starting material for epitaxial film growth process was a precursor solution which was simultaneously used to prepare the polycrystalline powder (discussed in earlier section). The polycrystalline powder was first characterized by XRD to check the phase formation of LCMO33 manganites. As the same solution was spin coated and same heat treatment was given to the substrates for film growth, we can expect a good quality of film which follows the orientation of the substrate. Monochromatic x-rays are used to determine the interplanar spacing ( $d$ ) of unknown specimens. The interaction of the x-ray with a sample creates secondary diffracted beams which are related to  $d$  following Bragg's law,

$$n\lambda = 2d\sin\theta \quad (2.2)$$

where  $n (= 1, 2, 3 \dots)$  is an integer number,  $\lambda$  is the x-ray wavelength,  $d$  the interplanar spacing and  $\theta$  is the diffraction angle. The XRD instrument used was a PANalytical X'Pert PRO [16] with CuK $\alpha$  radiation having a wavelength 1.54 Å. The operating voltage was 45 kV and the current was 40 mA. This energy is sufficient to penetrate the solids and permit to analyze the data obtained. All diffraction patterns were obtained at room temperature. As the polycrystalline samples do not have any preferential orientation and therefore all XRD peaks should present. The oriented films mainly show the peak corresponding to substrate orientation (orientation along [002] direction for STO) and a small peak appears just beside this peak.

## 2.4.2 Scanning Electron Microscopy (SEM)

The scanning electron microscope was a FEI Quanta 200 [17]. The SEM technique consists of an energetically focused beam of electrons. The highly focused beam is obtained using a series of magnetic lenses. As SEM uses electrons instead of light as used in a standard microscope, the sample has to conduct electrically relatively well. The beam hits the sample and this creates to release secondary electrons that are then counted by a detector amplified to obtain a reasonable signal. A set of scanning coils moves the beam across the specimen in order to obtain an image of area under study. The image can be gathered at various magnifications generally from 1-20000 times. We have used SEM for analyzing the film surfaces under study and we shall present SEM images in the next subsequent chapter.

## 2.4.3 Atomic Force Microscopy (AFM)

Atomic force microscopy (AFM) is a technique to obtain images and other information from a wide variety of samples, at extremely high (nanometer) resolution. AFM works by scanning a very sharp (end radius  $\sim 10$  nm) probe along the sample surface, carefully maintaining the force between the probe and surface at a set, low level by a feedback mechanism as it scans over the surface. The movement of the probe to stay at the same probe-sample distance is taken to be the sample topography.

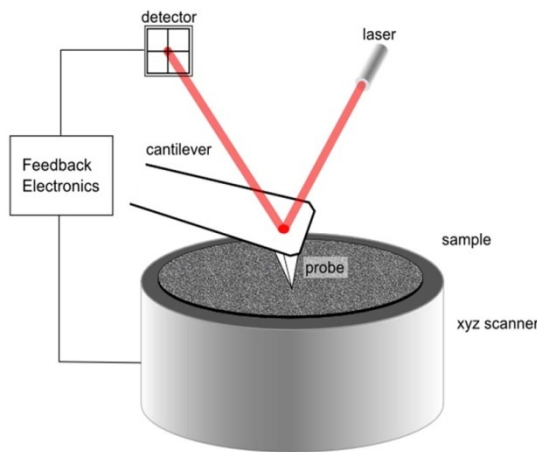


**Figure 2.9:** Schematic diagram of basic AFM operation.

Usually, the probe is formed by silicon (Si) or silicon nitride ( $\text{Si}_3\text{N}_4$ ) cantilever with a sharp integrated tip, and the vertical bending (deflection) of the cantilever due to forces acting on the tip is detected by a laser focussed on the back of the cantilever. The laser is reflected by the cantilever onto a distant photodetector (typically a split photodiode). The movement of

the laser spot on the photodetector gives a greatly exaggerated measurement of the movement of the probe. This set-up is known as an optical lever. There are a variety of modes of scanning, but in the simplest mode, the probes touches gently the sample as it moves over the surface (contact mode). The movement of the probe over the surface is controlled by a scanner. This is normally made from a piezoelectric material, which can move the probe very precisely in the x, y, and z axes. The signal from the photodetector passes through a feedback circuit, and into the z-movement part of the scanner, in order to maintain the probe-sample distance at a set value. Because the cantilever acts as a spring, this fixed cantilever deflection means a fixed probe-sample force is maintained. The amount by which the scanner has to move in the z axis to maintain the cantilever deflection is taken to be equivalent to the sample topography. The highly precise movements by the scanner, combined with the careful control of probe-sample forces allow the extremely high resolution of AFM. Depending on the details of the experiment, the resolution can be very high. z (height) resolution is extremely high and can be sub -Angstrom, whereas lateral resolution could be of the order of 1 nm. Fig. 2.9 shows the schematic diagram of basic operation principle by AFM. We have used Veeco CP II [18] for our AFM imaging in air and it had been used for study the topography of the film surface. We have measured average grain size of the LCMO33 film from these images. The average *rms* (route mean square) or peak-to-valley roughness are given for characterization of a grown film.

#### 2.4.4 Temperature dependent resistivity (*R-T*) measurement

The temperature dependent resistivity measurements were performed using standard four-probe technique. This technique consists of two leads, on the outside, used to supply the current to the specimen and two others, in the inside, to measure the voltage drop across the sample.

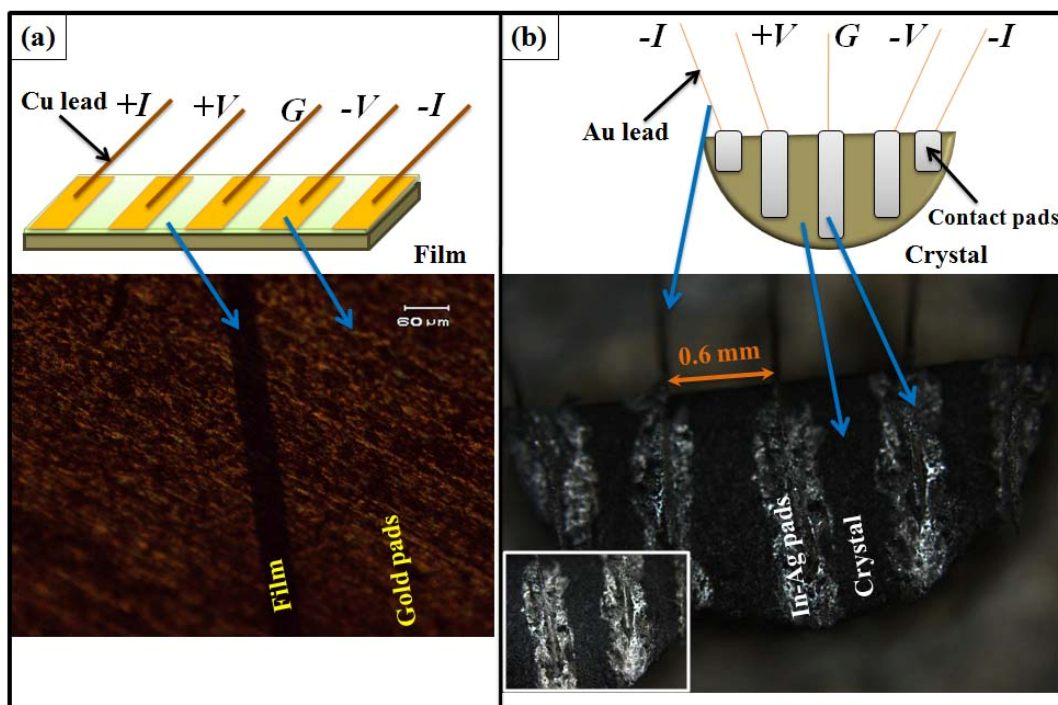


**Figure 2.10:** (a) Optical microscope image gold contact pads made by gold evaporation on film surface and thin (50 μm) Cu wires were used as leads. (b) Optical microscope image of Ag-In contact pads made on single crystal surface. Au wires were soldered on the contact pads as leads.

To make the electrical contacts on the film surfaces four linear gold contact pads were evaporated and Cu leads (diameter 50  $\mu\text{m}$ ) were soldered using silver epoxy procured from RS components [19]. The contacts over the single crystals were done by using silver-indium (Ag-In) binary alloy. In this case the leads were soldered using gold wire (diameter 50  $\mu\text{m}$ ) as the single crystals are sensitive to contact materials used. Fig. 2.10 shows the optical microscope images of the contact pads made on film surface (a) and single crystal (b) respectively. Inset of Fig. 2.10 (b) shows a closer view of Ag-In contact pads. These leads are generally low noisy electrical contacts which are extremely crucial for further noise experiments and are kept unaltered throughout the experiments. The alteration of probes can result unclean sample surface as well as can erroneous results due to noisy contacts.

The resistivity measurements were done by two methods:

1. By measuring bias current and simultaneous measurement of voltage drop across the sample with varying temperature.
2. By measuring current-voltage ( $I$ - $V$ ) characteristics at different fixed temperatures.

The resistance ( $R$ ) in ohms ( $\Omega$ ) versus temperature ( $T$ ) was measured by supplying constant current from a programmable source meter by a Keithley (Model 2400) [20] and measuring the voltage drop simultaneously recorded with a programmable digital multimeter (DMM) by Keithley (Model 2000) [20]. The current flows through the outside leads and the sample but a negligible amount of current flows in the voltmeter's leads due its large internal resistance. Therefore, this technique eliminates contact-resistance errors and it is necessary when resistance is small ( $R < 10-100\Omega$ ). Moreover, a positive negative value for each current is applied to eliminate the thermo-electric voltage or voltage offsets. This reverse current bias technique is especially advisable when measuring low voltages. The data was recorded American Standard Code for Information Interchange (ASCII) format via General Purpose Interface Bus (GPIB) interfacing cards [20] connected with a computer.

The electrical contacts were onto the sample as shown in Fig. 2.10. The measurements were performed from low-temperature (from 80 K) to room temperature by dipping the low temperature insert (with good vacuum  $10^{-3}$  mbar usually) in a liquid nitrogen dewar. Further low temperature ( $\sim 25$  K) resistivity was measured using cryo-cooled refrigerator (CCR) system. The temperature was monitored by a standard Pt-100 ( $80 \text{ K} < T < 300 \text{ K}$ ) or by a silicon diode sensor ( $25 \text{ K} < T < 300 \text{ K}$ ) using a temperature controller by Lakeshore (Model 340) [21]. A good thermal stability was maintained throughout the experiments. The schematic diagram of R-T measurement setup is shown in Fig. 2.11. The current “ $I$ ” passed through the outermost leads of the sample where the voltage drop “ $V$ ” was measured simultaneously by innermost leads. The resistance  $R = V/I$  was obtained, and from which resistivity  $\rho = AR/l$ , where “ $A$ ” is the area of cross section of current flow, and “ $l$ ” is the distance over which the current must flow is calculated. For  $I$ - $V$  characteristics, low and high current values were chosen depending on the sample properties. The low current value was chosen to be one within the regime where the  $I$ - $V$  characteristics are linear, and the high current value was chosen from within a regime where  $I$ - $V$  characteristics are strongly non-linear. This aspect will be discussed in later, in Chapter 5.

## 2.4.5 Temperature dependent electroresistance measurement

The  $I$ - $V$  characteristics in the insulating state of manganites at high current densities  $j$  are usually non-linear. The electroresistance (ER) may therefore be defined as:

$$ER\% = 100 \times \frac{\rho(j_{low}) - \rho(j_{high})}{\rho(j_{low})} \quad (2.3)$$

where,  $\rho(j_{low})$  and  $\rho(j_{high})$  refer to the value of resistivity  $\rho$  for low current density  $j_{low}$  and high current density  $j_{high}$  respectively. For measuring temperature dependent electroresistance we have used the  $R-T$  measurement setup as described in section 2.4.4 (see Fig. 2.11). The detailed characterization done by electroresistance has been discussed in Chapter 5.

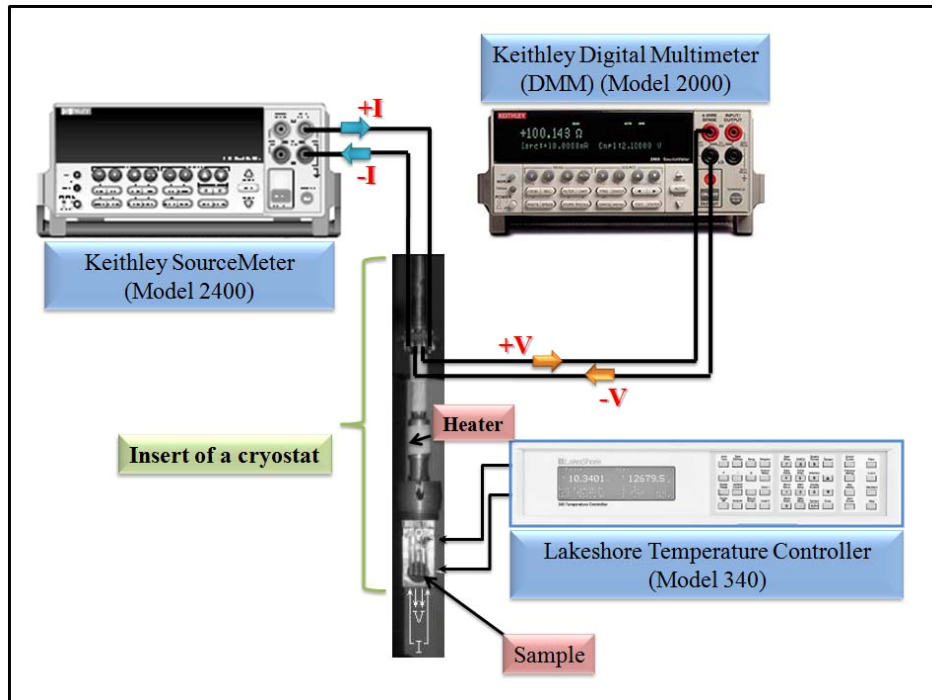


**Figure 2.11:** The temperature dependent resistivity measurement setup using low temperature cryostat (partial picture cryostat insert shown). The current source is a Source Meter by Keithley (Model 2400) and the voltage measuring instrument is a digital multimeter by Keithley (Model 2000). The temperature sensor (not shown in picture) is mounted on the sample base and temperature is monitored using a temperature controller by Lakeshore (Model 340).

#### 2.4.6 Temperature dependent low field ( $H \leq 0.12$ Tesla) magnetoresistance measurement

The magnetoresistance is the change of the resistivity on application of an external magnetic field,  $H$ . We define magnetoresistance by,

$$MR\% = \frac{\rho(H = 0) - \rho(H)}{\rho(H = 0)} \quad (2.4)$$

where,  $\rho(H = 0)$  and  $\rho(H)$  refer to the value of resistivity  $\rho$  in the absence of any magnetic field  $H$  and in the presence of a magnetic field of magnitude  $H$  respectively. The MR is an important parameter in the perovskite and therefore the development of a magnetoresistance apparatus was necessary for the characterisation of our samples. We are interested in

ferromagnetic materials, the coercive fields ( $H_c$ ) and saturation of magnetization can be observed in a very low field for these samples. In the next subsequent chapters we will show how the magnetization fluctuations contribute to the resistance fluctuations through MR. Above,  $H_c$  this contribution due to domain rotation subsides. Hence, we are not interested to study MR in high magnetic field values. We used a simple air core solenoidal magnet made of with copper wire. The calibration constant is 0.12 Tesla/amp at room temperature and measured by a hall probe.

The hardware, interface and software were put together in order to perform MR measurements at room (~300 K) and liquid nitrogen (~ 77 K) temperature. The sample was placed in a uniform longitudinal magnetic field,  $H$ , produced by a magnet having a maximum field of 0.12 Tesla with a step size of 0.04 Tesla. A current was passed through the sample and the voltage was measured. This was done under various applied magnetic fields to obtain the magnetoresistance. The sequences of measurements as well as the electronic hardware were similar to those used in the resistivity measurements. A dc current supplied by a DC power supply was passed through the magnet to create the magnetic field. The external field produced by the magnet was changed manually as no interface was available to control it. The measurement at each magnetic field was repeated a number of times to get an average and the experimental uncertainty. There was a two pole switching arrangement for reversing the magnetic field from  $+ H$  to  $- H$ .

## 2.4.7 Magnetic measurement

All the magnetization measurements were performed by using a commercial vibrating sample magnetometer (VSM) from Lakeshore (Model 7400 series) [22]. This VSM features a sensitivity of  $50 \times 10^{-6}$  emu at 10 seconds/point sampling. Model based on variable gap 4" electromagnet providing field strengths to 3 Tesla. Comprehensive Windows software featuring multi-user levels, experiment profiles for extended operation are provided by this VSM. A sliding head assembly with quick disconnect sample rod allows for easy, fast and reproducible sample exchange. An optional cryostat that operates with either liquid helium or nitrogen provides for variable temperature measurements from 8K to 425K. The schematic diagram of basic components in VSM is shown in the Fig. 2.12 (a) where Fig. 2.12 (b) illustrates the basic principle of operation. In Fig 2.12 (c) the commercial VSM setup [17] from Lakeshore is shown.

The working principle of VSM is based upon Lenz's law, according to which an e.m.f is induced in a conductor by a time-varying magnetic flux. In, VSM a sample magnetized by a homogeneous magnetic field is vibrated sinusoidally at small fixed amplitude with respect to stationary pick-up coils. The time  $t$  dependent voltage thus induced  $V_{induced}(t)$  is given as:

$$V_{induced}(t) = \frac{d\Phi}{dt} \quad (2.5)$$

$$= \left( \frac{d\Phi}{dz} \right) \left( \frac{dz}{dt} \right) \quad (2.6)$$

where,  $\Phi$  represents the magnetic flux; the axis of oscillation of the sample is conventionally chosen to be along z-axis.  $z$  represents the position of the sample along z-axis. As the sample is vibrated sinusoidally, the voltage induced in the pickup coils can be written as

$$V_{induced}(t) = cmA\omega \sin \omega t \quad (2.7)$$

where,  $c$  is the coupling constant,  $m$  is the DC magnetic moment of the sample,  $A$  is the amplitude of oscillation and  $\omega = 2\pi f$ , where  $f$  is the frequency of oscillation of the sample. The detection of magnetic moment of the sample thus accounts to measuring the coefficient of the sinusoidal voltage response  $V_{induced}(t)$  in the detection coils. For the commercial setup the actual position of the sample is well defined inside the cryostat and the oscillations are performed exactly midway between the pick up coils. There remains a facility for the rotation of the sample and it is extremely important samples with inhomogeneous distribution of magnetic moment. To detect reasonable signal above noise floor sometimes rotation is important. Generally it happens for films not for powder or single crystals. The reliability of the measurements performed using VSM dependent upon the size of the sample, the shape of the sample, and the magnitude of the magnetic moment that one is trying to measure. The temperature dependent magnetization ( $M-T$ ) and field dependent magnetization ( $M-H$ ) at different temperatures had been recorded based on this measurement technique and setup.

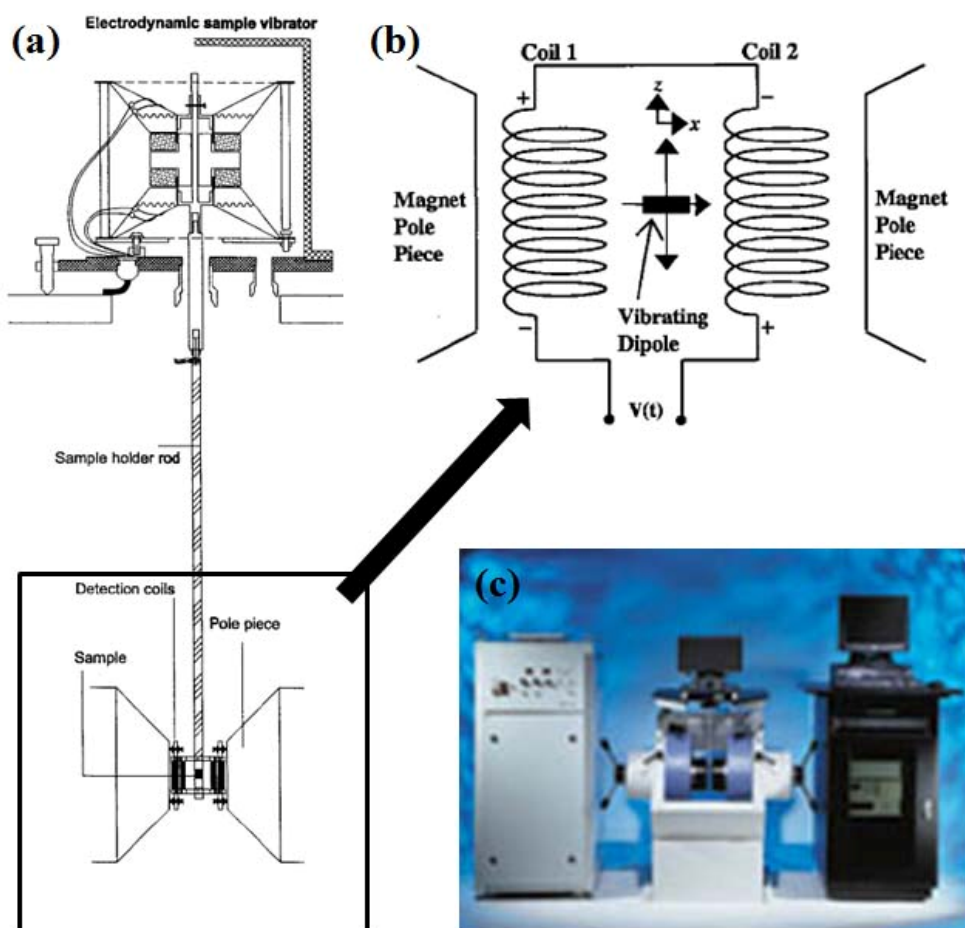


**Figure 2.12:** (a) The schematic diagram of VSM with basic components, (b) The detection coils and sample position with principle of operation is shown, (c) The commercial setup from Lakeshore (7400 series) used for magnetization measurements.

## Bibliography:

- [1] A. Urushibara, Y. Moritomo, T. Arima, A. Asamitsu, and Y. Tokura, Phys. Rev. B **51**, 14103 (1995).
- [2] M. Mori, N. M. Sammens, and G. A. Tompsett, Journal of Power Sources **86**, 395 (2000).
- [3] J. Philip, and T. R. N. Kutty, Materials Chemistry and Physics **63**, 218 (2000).
- [4] L. Balcells, A. E. Carrillo, B. Martínez, F. Sandiumenge, and J. Fontcuberta, Journal of Magnetism and Magnetic Materials **221**, 224 (2000).
- [5] W. Prellier, P. Lecoer, and B. Mercey, Journal of Physics: Condensed Matter **13**, R915 (2001).
- [6] A. Gupta, G. Q. Gong, G. Xiao, P. R. Duncombe, P. Lecoer, P. Trouilloud, Y. Y. Wang, V. P. Dravid, and J. Z. Sun, Physical Review B, **54** R15629 (1996).
- [7] J. D. MacKenzie, J. Sol. Ge. Sci. Technol. **26**, 23 (2003); C. Brinker, G. Scherer, Sol-Gel Science: “*The Physics and Chemistry of Sol-Gel Processing (New York: Academic)*” (1990).
- [8] <http://www.sigmaprolabs.com/india.html>
- [9] <http://www.merck.co.in/en/index.html>
- [10] B. Ghosh, L. K. Brar, and A. K. Raychaudhuri, J. Phys. D **37**, 1548 (2004).
- [11] G. Westin, Chem Commun. (*Stockholm University*) **4** (1994).
- [12] D. Shulyatev, S. Karabashev, A. Arsenov, and Y. Mukovskii, J. Magn. Magn. Mater. **198/199**, 511 (1999).
- [13] A. M. Balbashov and S. K. Egorov, J. Crystal Growth **52**, 498 (1981).
- [14] J. A. M. van Roosmalen, P. Van Vlaanderen, E.H.P. Cordfunke, W.L. Ijdo, D.L.W. Ijdo, J. Solid State Chem. **114**, 516 (1995).
- [15] A. M. Balbashov, S. G. Karabashev, Y. M. Mukovskiy, and S. A. Zverkov, J. Crystal Growth **167**, 365 (1996).
- [16] <http://www.PANanalytical.com>
- [17] <http://www.FEI.com>
- [18] <http://www.veeco.com>
- [19] <http://www.rsindia.com>
- [20] <http://www.keithley.com>
- [21] <http://www.lakeshore.com>
- [22] <http://www.lakeshore.com/sys/vsm/vsmm.html>

# Chapter 3

## Noise Measurement Techniques

### 3.1 Introduction to Low Frequency Noise Measurement

Measurements of noise involve both statistical analyses, which were described in Chapter 1, and experimental setup. Since we are dealing with small signals, the hardware part for noise measurements has some special requirements to be fulfilled to gain the required sensitivity. Those involve not only the sensing part to have good “noise” performance, but also the whole measuring system to be at maximum isolated from external influences as much as possible to reduce their influences on the noise to be measured. When we measure noise we need to take note of the fact that addition to the sample whose noise we would like to measure, everything else like electronics, the environment etc. can also contribute. However these extraneous sources can have different characteristics like their power spectra which one may utilize to reduce their contribution. In general a combination of hardware as well as software been used to solve this problem.

In noise measurements, the sample is usually current biased by a very low noisy source and the resistance fluctuation in the system is registered by measuring the voltage fluctuation developed across the sample  $\delta V(t) = V_0(t) - \langle V \rangle$  (where  $\langle V \rangle$  is the mean voltage). Typical voltage fluctuation measured across the sample is as small as 0.5 nV-5 nV. This is too small compared to some of the extraneous signals. The most crucial part of the noise spectroscopy is to eliminate noise coming from other sources like the measuring electronics, cable designs, electrical contacts on the sample, ground loops, improper shielding, electromagnetic interferences, impedance mismatch, presence of any sparking in electrical circuits, and temperature fluctuations of the sample. In spite of this, during data processing improper digital data acquisition acts as another source of noise. So, extreme care has been taken both for hardware and software concerned to experimental setup. We have used Digital Signal Processing (DSP) technique supported by low noisy hardware support allows us to achieve a spectral noise floor  $S_V(f)$  down to  $10^{-20} V^2/Hz$  or even less over a wide frequency range  $10^{-4}$  Hz-10 Hz. This chapter gives the opportunity to discuss about the low frequency noise measurement techniques [1] and we shall introduce some examples to show its power of applicability to noise spectroscopy.

As we mentioned earlier in Chapter 1 that the quantity which is measured the fluctuations is  $\delta V(t)$ . This can be directly connected to power spectral density  $S_V(f)$  to quantify noise as [2]:

$$S_V(f) = \lim_{T \rightarrow \infty} \frac{1}{2T} \left[ \int_{-T}^{T} \delta V(t) \exp(-2\pi ift) dt \right]^2. \quad (3.1)$$

The autocorrelation function  $C(\tau)$  is the cosine transform of power spectral density and can be expressed as:

$$C_V(\tau) = \lim_{T \rightarrow \infty} \frac{1}{2T} \int_{-T}^{T} \delta V(t + \tau) \delta V(\tau) dt. \quad (3.2)$$

The frequency range over which the spectral power is to be determined depends on the time scale of the fluctuations being investigated. If the fluctuation is occurring with a time scale of  $\tau$ , it will

show up in the power spectral density as a Lorentzian  $2\tau/(1+(2\pi f)^2)$  with a corner frequency  $f_c = 1/2\pi\tau$ . With a distribution of relaxation time  $D(\tau)$ , the power spectrum is a superposition of Lorentzian and is given by

$$S_V(f) = \int_0^{\infty} d\tau D(\tau) 2\tau / [1 + (2\pi f\tau)^2]. \quad (3.3)$$

## 3.2 The framework of noise experiments

To study the resistance fluctuation of the current biased sample and its spectral, we have used three different specified circuit arrangements depending on the need and applicability. This reduces the selected extraneous noise. Our noise measurement technique is based on four-probe [3] and five-probe ac-detection systems [4]. We have also designed another five-probe noise measurement circuit with capability for simultaneous measurements of noise of the sample while passing a current through it and of keeping track of resistance of the sample during the current stressing in the sample as well. For this an *in-situ* noise measurement setup consists of a circuit arrangement to mix a dc stressing current with ac excitation through the sample [5]. Here dc current stresses the sample while the small ac signal used as a carrier signal for detection of noise. In both cases, for four-probe or two different five-probe noise measurement circuits small ac signal was used as noise detector signal. In this section we shall discuss about the circuits used so far for noise measurements. All the noise data which will be presented for this thesis had been collected using this *home-made* setup only.

### 3.2.1 The general noise (ac) detection scheme

There is a general ac detection scheme which has been used as a basic principle of noise measurement irrespective of four-probe or five-probe setup. The sample is biased by an ac signal from dual channel lock-in amplifier (LIA) SR830 [6] at a frequency  $f_0$ . The average voltage is blanked off (reduced) by a bridge technique or digitally. The voltage developed across the sample is amplified by a low noisy preamplifier whose output is detected by the same LIA. But it is highly recommended to use a preamplifier so that the input and output impedances of the preamplifier should match to the sample impedance and LIA's input impedance respectively. Otherwise impedance mismatch (discussed later in details) will generate a huge amount of noise as well as wrong results. The basic steps regarding noise detection are as follows:

- The average voltage signal  $\langle V \rangle$  coming from the input channel of the LIA is digitally subtracted off by the LIA to give the fluctuating component  $\delta V(t)$  of the signal.
- $\delta V(t)$  is significantly amplified (generally 100 times) by the preamplifier used.
- The amplified signal  $\delta V(t)$  is demodulated by the LIA to give the noise sub bands at frequencies  $f_0 \pm \Delta f$  where  $\Delta f$  is the frequency at which noise signal of desired to be measured. This process has been depicted schematically in figure 3.1.
- The time constant  $\tau_{LIA}$  of LIA's inbuilt low-pass filter at output channel is fixed so that  $\Delta f_{max} = 1/(2\pi\tau_{LIA})$ , where  $\Delta f_{max}$  is the maximum frequency at which noise signal can be obtained.
- The signal from the preamplifier output channels are fed to the input channels of LIA and can be amplified further to increases the sensitivity of the measurements depending on the experimental requirements.

- Then the output channels of LIA are connected to the computer motherboard for data collection. The LIA output data is in analog form whereas computer collects the data in digital format. So we used a dual channel analog-to-digital (ADC) data converter (PCI-DAS6036, 32 bit and 200ksamples/sec) [7] to transfer the data from LIA to computer via a PCI-slot commercially available with the data converter. There is a C++ program which is used for data collection process.

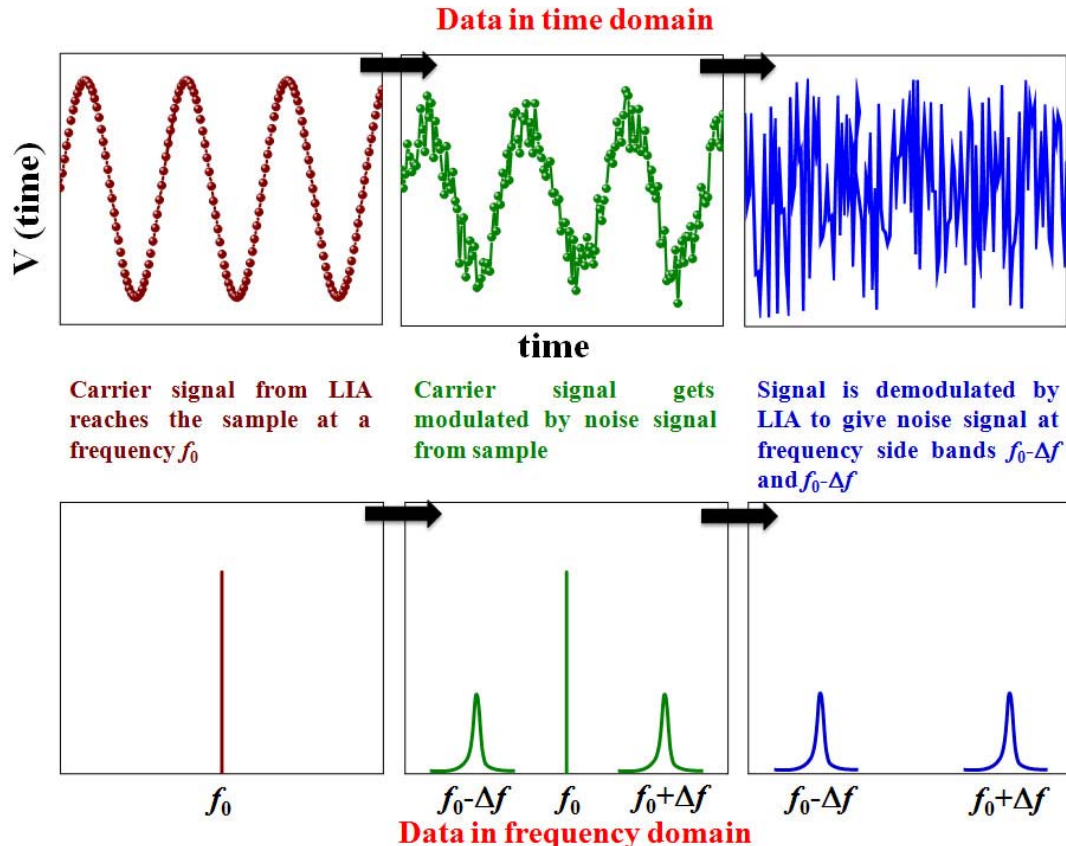


**Figure 3.1:** Schematic diagram of the basic scheme to obtain power spectra from the time series. The top panel shows the sequence of events in time domain whereas the bottom panel shows the same thing in frequency domain.

### 3.2.2 Impedance-mismatch problem and solution

The typical resistance of the sample is small ( $1\Omega \leq R_{sample} \leq 50\text{ K}\Omega$ ) compared to the input impedance of the LIA which is around  $10\text{M}\Omega$ . The voltage drop across the sample can not be fed directly to the LIA input because of large impedance mismatch between the two. This mismatch is a source of erroneous results in the noise measurements. The insertion of preamplifier with proper input and output impedance serves two purposes namely the amplification of the signal and the reduction of extra noise that could be generated from the large mismatch in impedances between sample and the detector LIA. We have used SR554 [8], a transformer preamplifier or SR560 [9], a low noise FET preamplifier for noise measurements depending on the sample impedance. Since SR554 has an input impedance of  $0.5\Omega$  and output impedance  $\geq 5\text{ K}\Omega$ , it can be inserted between the sample and detector (LIA) when sample resistance  $\approx 1\text{-}100\Omega$ . The sample resistance  $> 100\Omega$ , SR560 is used with proper selection of amplification value and frequency bandwidth of the built-in low pass filter. The preamplifier itself can be an extra noise source. To have minimum contribution

of noise from preamplifier, we have to choose carrier frequency ( $f_0$ ) of the ac signal according to the “noise figure” (NF) of the preamplifier. The NF of a preamplifier represents the dependence of the output noise of the preamplifier on the input signal’s frequency and the load at its input and it is traditionally plotted as function of frequency for different load called noise contours. The NF can be defined as

$$NF(dB) = 20 \log \frac{\text{outputnoise}}{\text{gain} \times \text{Nyquistnoise}}. \quad (3.4)$$

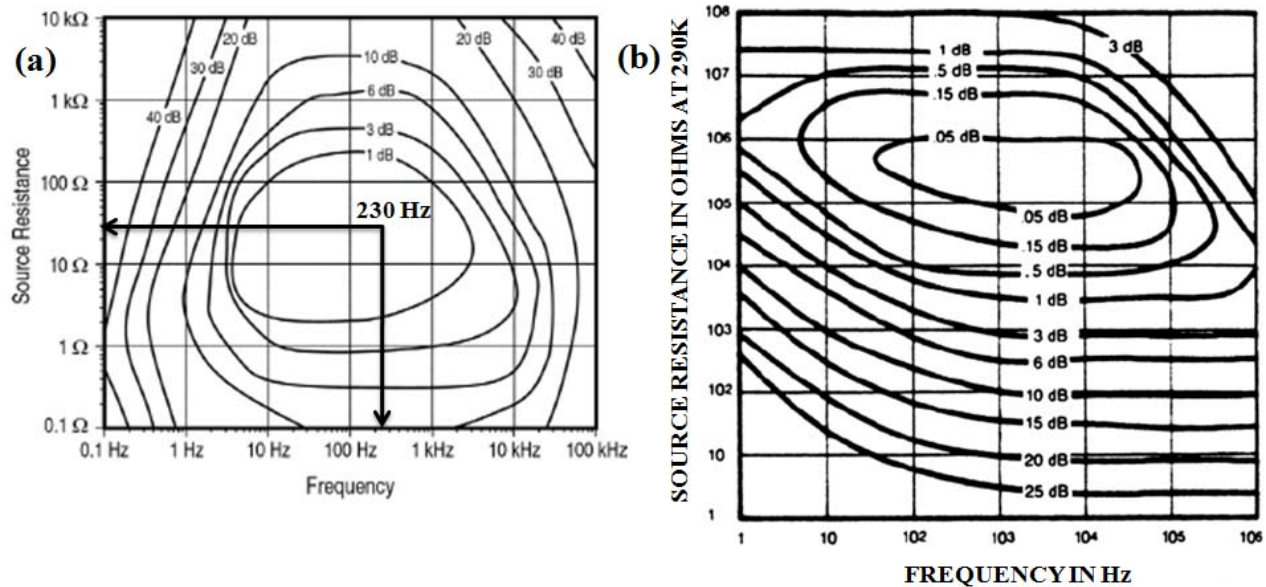


**Figure 3.2:** The NF as a function of frequency of (a) SR554 transformer preamplifier and (b) SR560 low noise FFT preamplifier.

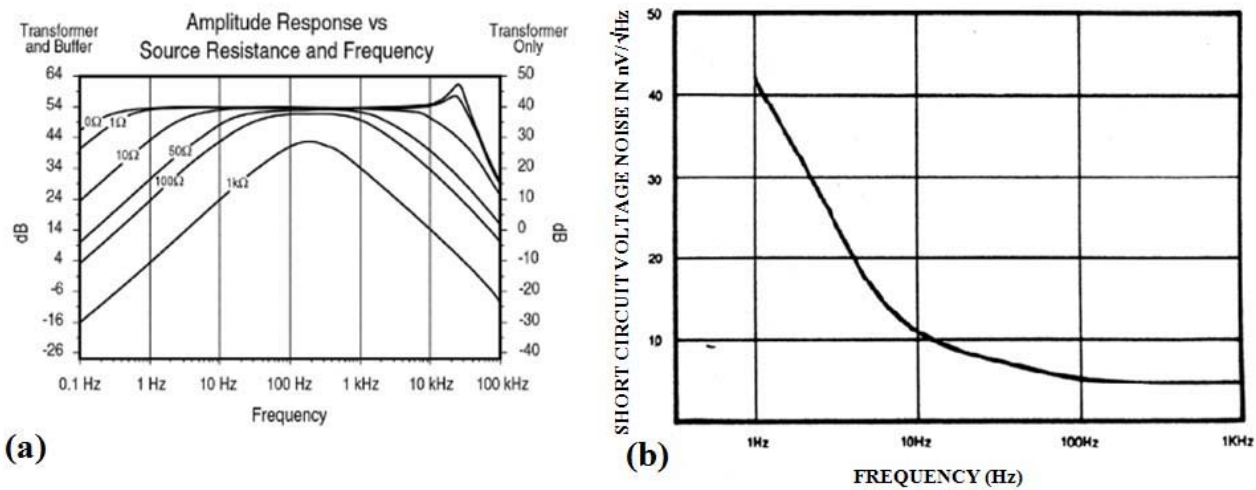


**Figure 3.3:** (a) A plot of gain versus frequency of a SR554 transformer preamplifier and (b) A plot of low noise preamplifier’s input noise voltage versus frequency.

For an ideal preamplifier all the noise appearing at the output is Nyquist noise and NF is 0 dB. Practically, in all real preamplifiers there remain considerable “ $1/f$ ” noise components which make  $\text{NF} > 0$ . The NF as a function of frequency for SR554 and SR560 is shown in Fig. 3.2(a) and

Fig. 3.2(b) respectively. It is clearly seen that while NF is minimum for  $2\text{-}200\Omega$  in case of SR554, for SR560 low noise preamplifier it is for  $5\text{ K}\Omega\text{-}10\text{ M}\Omega$  with 1dB. For this reason we have used SR554 for low resistance sample and SR560 for high resistance  $> 100\Omega$  sample. Since the gain of the preamplifier also depends on the input signal frequency and the load at its input we chose the carrier frequency  $\approx 230$  Hz, around which the gain of the preamplifier is maximum and flat (frequency independent) for a wide band (see Fig. 3.2 (a) and Fig. 3.3 (a)) and it is applicable for low resistance sample only where we can use SR554. In case of SR560, the amplifier's input voltage noise approximates that of a  $1000\Omega$  resistor about  $4\text{nV}/\sqrt{\text{Hz}}$ . In a bandwidth up to 10 Hz this will imply spectral power ( $S_V(f)$ ) of  $16\times 10^{-17}\text{V}^2$ . If the sample resistance is less than  $1000\Omega$ , the output noise will be dominated by amplifier's input voltage noise. A typical input voltage noise versus frequency is shown in the Fig. 3.3 (b) for SR560. The voltage noise increases for lower frequencies ("1/f noise"). The reason for using a carrier frequency  $f_0 = 230$  Hz is to do the detection at a frequency zone where the amplifier noise is very low as can be seen in Fig. 3.2 and Fig. 3.3.

### 3.2.3 The four-probe ac noise detection system

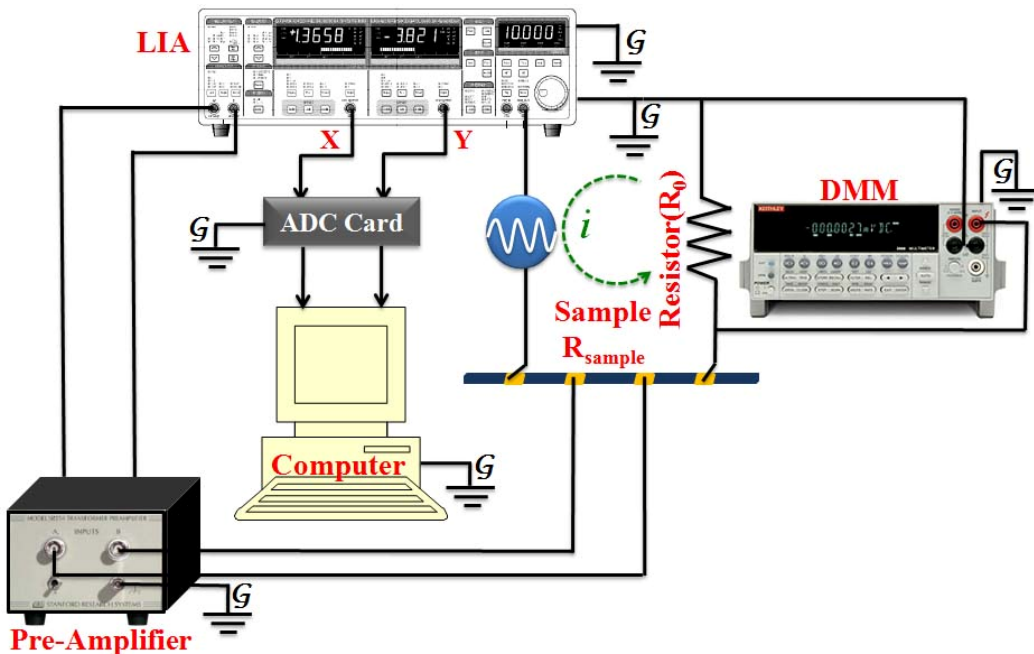


**Figure 3.4:** Schematic diagram of four-probe noise measurement technique. The ac voltage bias is fed to the sample from LIA and a standard register is connected in series with the sample so that a digital multimeter (DMM) can monitor the constant current passing through the circuit. The voltage drop generated at the innermost probes on the sample is fed to the low-noise preamplifier input. The amplified signal goes to the input channels of the LIA. The data is collected by the computer via ADC card.

The four-probe ac noise detection system is shown in Fig. 3.4. This is the simplest possible noise measurement circuit among the three mentioned earlier. This technique is used depending on the applicability, simplicity and experimental requirements keeping in mind. This technique is less sensitive than the five-probe technique, but its simple detection circuit makes the technique popular. The sensitivity depends on noise floor and the drift of voltage measured. The noise floor we generally get in this case is  $\approx 5\times 10^{-19}\text{ V}^2/\text{Hz}$  for a  $10\Omega$  resistor at 300 K. The drift of voltage is nearly  $\approx 5\text{-}20\text{ nV}$ . With careful grounding and proper shielding of instruments we achieved a noise

floor down to  $2 \times 10^{-20} \text{ V}^2/\text{Hz}$  for  $1 \Omega$  resistor at 300 K. If the sample resistance is high ( $>500\Omega$ ) enough, one can use four-probe method. This technique also follows the same detection scheme as we discussed earlier in section 3.2.1.

To measure voltage fluctuations across the sample we made the system as a constant current bias system by using a standard resistor ( $R_0$ ) in series. We used standard wire wound resistors (5W). The wire wound resistors are coiled in a volume which is very large than the sample volume under study. As noise is proportional to inverse of the volume of the resistors, the wire bound resistors will contribute very small amount of noise itself. The resistance of  $R_0$  is generally 100 times greater than the sample resistance. If the sample resistance changes with temperature in orders of magnitude, then it is difficult to maintain the constant biasing condition. So the careful measurement constraints should be kept in mind before measurements. The low noisy digital multimeter (DMM) (Keithley, Model 2000) [10] has been used to monitor the constant biasing current in the circuit. The LIA acts as a constant voltage ac source in this circuit. Instead of using ac bias, dc bias can be used but the sensitivity of measurements is greatly reduced in the second case. The chassis of all the instruments are put together to one laboratory ground point, i.e. in a star ground configuration (discussed later in details) to avoid ground loops or multiple ground points. The ground point is marked as  $\mathcal{G}$  in Fig. 3.4.

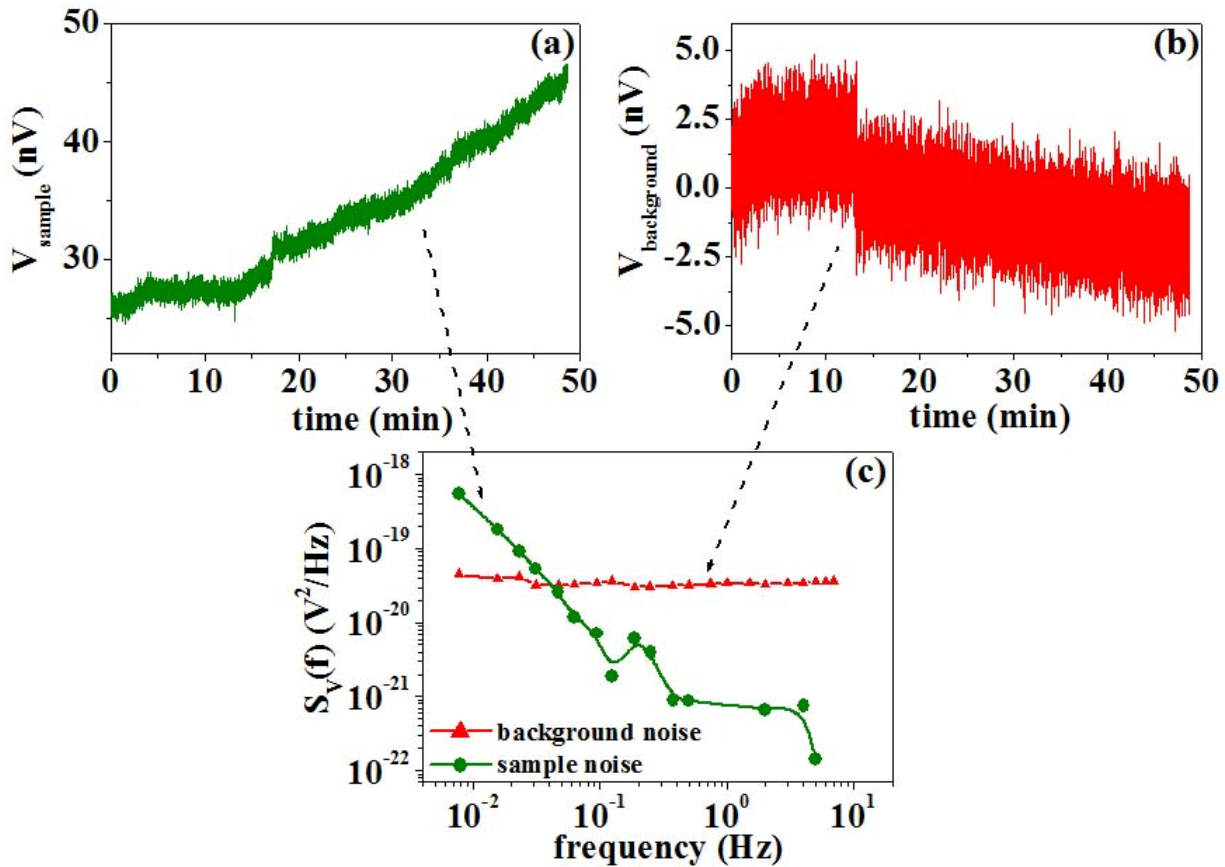


**Figure 3.5:** The raw time series data of voltage fluctuation recorded at 300 K (a) across a good quality  $1\Omega$  carbon film resistor and (b) from the background. Voltage drifts are present in both time series. (c) The corresponding power spectral density (background subtracted) along with the background noise estimated from the above time series.

In Fig. 3.5(a) and Fig. 3.5(b) we have presented the raw time series data of voltage fluctuations measured across a good quality  $1\Omega$  carbon film resistor along with its background voltage

fluctuations respectively. The typical data have been collected in four-probe ac noise detection method for  $\approx 48$  min at room temperature. The corresponding power spectral density (background subtracted) and its background noise have been estimated from the above raw time series are also shown in Fig. 3.5(c). It is very clear from the data that the noise from the sample is very low and the background is flat in the measured frequency band width. There are voltage drifts present in both time series. The voltage drifts recorded are  $\approx 25$  nV and 10 nV in sample and background time series respectively. These voltage drifts come from thermal fluctuation, poor electrical contacts on the sample, imperfect electrical connection with the instruments due to cables used for the set-up and from bad grounding. But we want to mention that in spite of all the imperfection we achieved a very low ( $\approx 4 \times 10^{-20} V^2/Hz$ ) background noise even in four-probe noise detection method.

### 3.2.4 The five-probe ac noise detection system

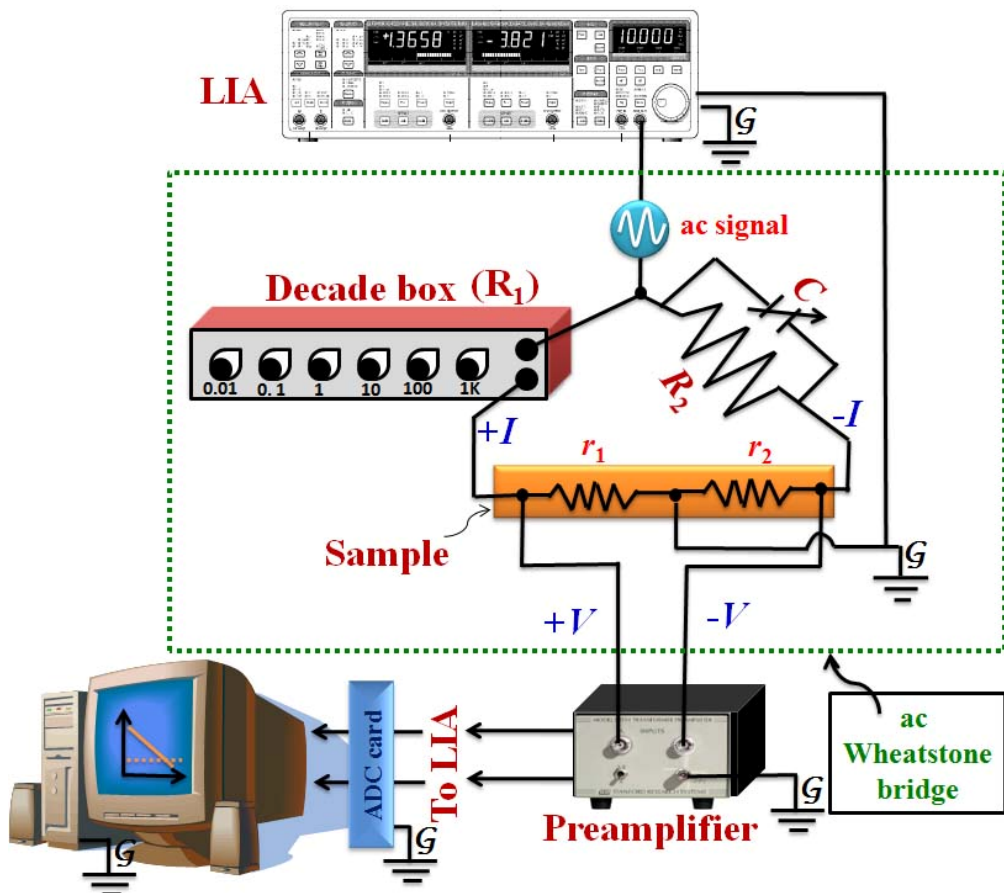


Figure 3.6: A schematic diagram of five-probe ac noise measurement setup.

We use an ac Wheatstone bridge configuration to measure resistance fluctuations as depicted schematically in Fig. 3.6. This method is most useful from sensitivity point of view than the ac/dc four-probe method discussed earlier. The technique is based on an idea suggested by Schofield [3], which has been suitably modified with digital data acquisition and processing (discussed later) techniques. The name “five-probe” came after the five electrical contact leads put symmetrically on the sample surface, where two current leads (outer leads,  $+I$  and  $-I$ ) and two voltage leads (inner leads,  $+V$  and  $-V$ ) are connected symmetrically with respect to middle grounded lead. Sample resistances are  $r_1$  and  $r_2$  with respect to ground lead serve as two lower arms of the bridge circuit.

$R_1$  is a variable resistor (low noisy decade resistance box [11]) and  $R_2$  is a standard resistor sitting at the upper arms of the bridge. We have used non-inductive wire wound resistor  $R_2$  along with a variable capacitor box  $C$  [12] across it. A carefully designed capacitor bank (variable range) with good quality dielectric capacitors [13] was also used across  $R_1$ .  $R_1$  and  $R_2$  are large current limiting resistors ( $R_1, R_2 \gg r_1$ , and  $r_2$ ), and are used to balance the Wheatstone bridge. These large resistors are kept in shielded boxes and properly grounded to reduce external noise and to avoid ground loops. For ac-bridge, it is required to balance both amplitude as well as phase, and to facilitate this we used low noisy variable capacitor or capacitor bank across the resistive upper arms of the bridge. The bridge is powered by a function generator (here internal oscillator of LIA). The voltage difference is generated from the voltage leads of the sample resistances ( $r_1$  and  $r_2$ ) are fed into a preamplifier (SR554/SR560) from which it was sent to the input of the LIA. The sample resistances  $r_1$  and  $r_2$  are attached such a way that they contribute nearly same resistance values in the lower arms. This criterion enables the bridge to be balanced by adjusting two upper arm resistances in nearly equal magnitude as well. Then the currents through each sample arm are nearly equal and when the bridge is balanced, the voltage drops are equal. The measured voltage across the two arms is the difference between the voltage biases across each arm. If the bridge is balanced perfectly, this difference only picks up the voltage fluctuations. In amplifiers, presence of common mode voltage increases the amplifier noise level. The suggested arrangement reduces the common mode voltage. It also reduces effects due to thermal fluctuations and drifts which are nearly equal in both arms. The bridge can be balanced to better than 10 nV with the help of variable resistors and variable capacitors. The resistance balance sensitivity generally achieved  $\sim 10\text{ppm}$ .

Now we briefly discuss the mathematical concept behind this measurement technique. A small excitation ac signal  $v = v_0 \sin(2\pi f_0 t)$  with carrier frequency  $f_0$  passes through the current limiting resistance in the upper arms of the bridge, so the current  $i = i_0 \sin(2\pi f_0 t + \theta)$  is limited by  $R_1$  and  $R_2$ . The phase  $\theta$  arises from the stray reactance in the circuit. The voltage measured by dual channel LIA which is capable to detect in-phase and  $90^\circ$  out-of-phase (quadrature) component of ac voltage developed across the sample. The voltage drop across the sample as a function of time can be written as

$$V(t) = V_0 + \delta V(t) \quad (3.5)$$

where  $V_0$  is the average value corresponding to average resistance  $r_0$ , and  $\delta V(t)$  is the voltage fluctuations. We can easily write  $\delta V(t)$  as

$$\delta V(t) = [\delta r_1(t) - \delta r_2(t)] \sin(2\pi f_0 t + \theta). \quad (3.6)$$

$\delta r_1(t)$  and  $\delta r_2(t)$  are the resistance fluctuations across the sample resistances  $r_1$  and  $r_2$  respectively. Hence  $\delta V(t)$  is ac coupled to the preamplifier input and amplified signal from preamplifier output is ac coupled to LIA for phase sensitive detection at a phase angle  $\theta$ . Since,  $[\delta r_1(t) - \delta r_2(t)]$  has a bandwidth of frequency components ( $\Delta f$ ), the  $\delta V(t)$  is a signal when carrier signal gets modulated by fluctuation of resistance resulting in two sidebands of frequencies ( $f_0 - \Delta f$ ) and ( $f_0 + \Delta f$ ) besides the carrier frequency  $f_0$ . Thus noise signal appear as two side bands about carrier frequency of LIA. This signal gets demodulated by LIA resulting signal with only sidebands (see also Fig. 3.1). The output of LIA is amplified and low pass filtered by its internal amplifier and low pass filters respectively. In general,  $\delta V(t)$  consists of two parts: one coming from resistance fluctuations

and other from background fluctuations, i.e.,  $\delta V(t) = \delta V_f + \delta V_{bg}$ . If the average bias is zero, the measured fluctuations contain background fluctuations only,  $\delta V(t) = \delta V_{bg}$ , since the part containing resistance fluctuations is directly proportional to the average bias across the sample. The power spectral density of the output signal of LIA is given as

$$S_V(f, \theta) \cong G_0^2 \left[ S_V^0(f_0 - f) + \frac{i_0^2}{2} S_R(f) \cos^2 \theta \right] \quad (3.7)$$

where  $G_0$  is the gain of the preamplifier and LIA,  $S_V^0(f_0 - f)$  is power spectral density of the background noise and  $\frac{i_0^2}{2} S_R(f)$  [ $= S_V(f)$ ] is the power spectral density of the sample's noise and  $f$  is the measurement frequency. The dual channel of LIA detects the input signal at a phase  $\theta$  at one channel and at a phase ( $\theta + 90^\circ$ ) at other channel. So that signal is now appearing as two outputs X and Y. The power spectral density of the X-output is

$$S_V(f, \theta)_X \cong G_0^2 \{ S_V^0(f_0 - f) + S_V(f) \cos^2 \theta \} \quad (3.8)$$

and that of Y-output

$$S_V(f, \theta)_Y \cong G_0^2 \{ S_V^0(f_0 - f) + S_V(f) \cos^2(\theta + 90^\circ) \}. \quad (3.9)$$

By adjusting  $\theta$  as 0 (adjusted with the phase-shift option in LIA), we can get X-output having a power spectral density of the total noise and a Y-output having a power spectral density of the background noise. Sample's noise (spectral power density) can be obtained by subtracting out background from the total noise. The main objective of this measurement technique is: it allows us to measure sample's noise and background noise simultaneously.

As we mentioned earlier that there is an inbuilt low-pass filter at the output channels of LIA. The time constant ( $\tau_{LIA}$ ) of this filter is optimally chosen to reject the unwanted noise coming from the power-line where the instruments are connected. The cut-off frequency of this filter is given by  $f_{LIA} = 1/(2\pi\tau_{LIA})$ . During our experiments, filter was typically set at a time-constant of 30msec or 10msec depending on the frequency of the power spectrum of our interest. The roll-off was 24dB/octave. The time constants for 30msec and 10msec we had cut-off frequencies  $\sim 5.3$  Hz and  $\sim 7.96$  Hz respectively. We can get a filter response flat for  $f < 5$  Hz and  $f < 7$  Hz in those cases. Thus a signal at the LIA output was composed of full gain signal for  $\sim 5$ Hz or 7Hz and greatly attenuated ( $\approx -90$ dB) for higher frequencies up to  $\approx 32$  Hz. Power-line noise mainly consists of the harmonics of power-line frequency 50 Hz. Hence the noise signal output in our setup is free from power-line noise. This procedure rejects the noise contribution from power-line frequency at 50Hz. With this setting, we set the maximum frequency limit approximately 7Hz of measurable noise frequency of our interest. Depending on the experimental observations we have selected our frequency ranges. The sensitivity of LIA was selected so that the demodulated signal appears in the output as  $\pm 10$ V due to amplification when it was full scale in the selected sensitivity range. Later during computation of noise the data were scaled-down by net gain from the preamplifier and LIA.

In Fig. 3.7 (a) we have presented the raw data of voltage time series measured across a  $10\Omega$  carbon film resistor in five-probe ac detection technique at 300 K. The typical data have been collected for more than 2hrs and there is very small voltage drifts can be noticed. The background

voltage fluctuation is very stable throughout the data collection time and almost free from drifts. The corresponding spectral power density  $S_V(f)$  (background subtracted) and the background noise have been estimated from the above time series data and shown in Fig. 3.7(b). The experimental background noise ( $2.3 \times 10^{-19} \text{ V}^2/\text{Hz}$ ) is very close to the calculated ( $4k_B T R_{\text{sample}}$ ) background noise. There is a slight drift in sample voltage fluctuations but still it is small for long data acquisition time. It is also clear from this data that quality of the experimental data can be improved in five-probe ac detection technique.

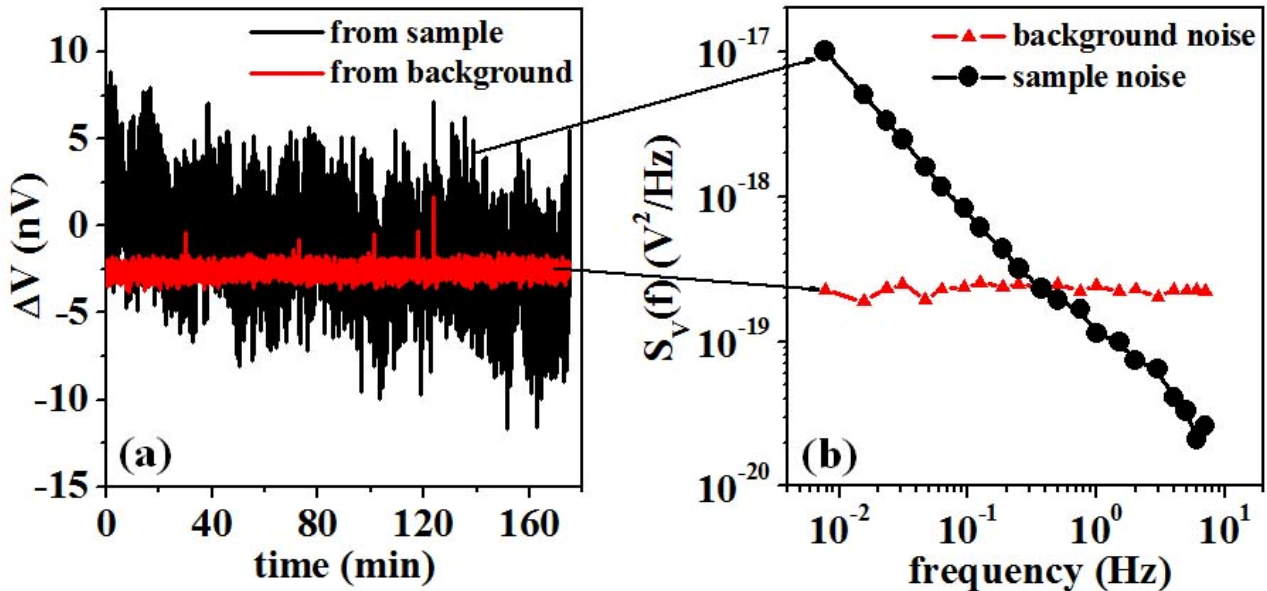


**Fig: 3.7:** (a) The raw time series data of voltage fluctuation measured across a  $10\Omega$  carbon resistor in five-probe ac noise detection method at 300 K. The sample voltage fluctuation is shown by black solid line while the background voltage fluctuation is given by red solid line. (b) The corresponding spectral power density and the background have been estimated from the time series data presented in (a).

### 3.2.5 The five-probe ac noise detection system in presence of dc bias

It is often required to measure noise in a system in the presence of a dc current, e.g. during the electromigration stressing of a sample [14] or current induced destabilization of the charged ordered manganites [15]. It also is interesting to measure noise at different dc bias values in systems showing nonlinear conduction. This is because in order to obtain the correct relative fluctuation  $S_V(f)/V^2$  the measured voltage fluctuations needs to be scaled by the measuring bias and not by the dc bias. We have developed a technique in which noise can be measured with a fixed amplitude ac signal (as described above) but one can also independently apply a dc bias which does not interfere with the noise measurements. The dc bias ( $J_{dc}$ ) was applied using a circuit shown in Fig. 3.8.

The separate control of ac ( $J_{ac}$ ) and dc ( $J_{dc}$ ) is important because it decouples the current stressing measurement from noise measurement. The observed noise  $S_V(f)$  always maintains a quadratic dependence on  $V_{ac}$ , which is the bias used to measure the noise. Thus, in this technique one can obtain nonlinear bias-dependent conductivity, and yet retain a well-defined meaning for  $S_V(f)/V^2$ . Separation of the dc stressing bias and ac noise measurement bias allows us to ensure that even at a high level of stressing current, the small ac bias ensures  $S_V(f)/V_{ac}^2$  and thus the noise

measurement process stays Ohmic. The capacitors and inductors shown in the figure decouple the ac and dc sources and prevent dc being applied to the pre-amplifier circuit. It is important to check that the capacitors and inductor do not affect the gain and the phase of the amplifier and also do not introduce additional features in the power spectra. This setup has been used to measure the noise during the current induced destabilization of the ferromagnetic insulating state in a single crystal manganite (discussed in Chapter 5). The mathematical concept behind this measurement technique is same as we discussed for five-probe ac biasing noise measurement in section 3.2.3.

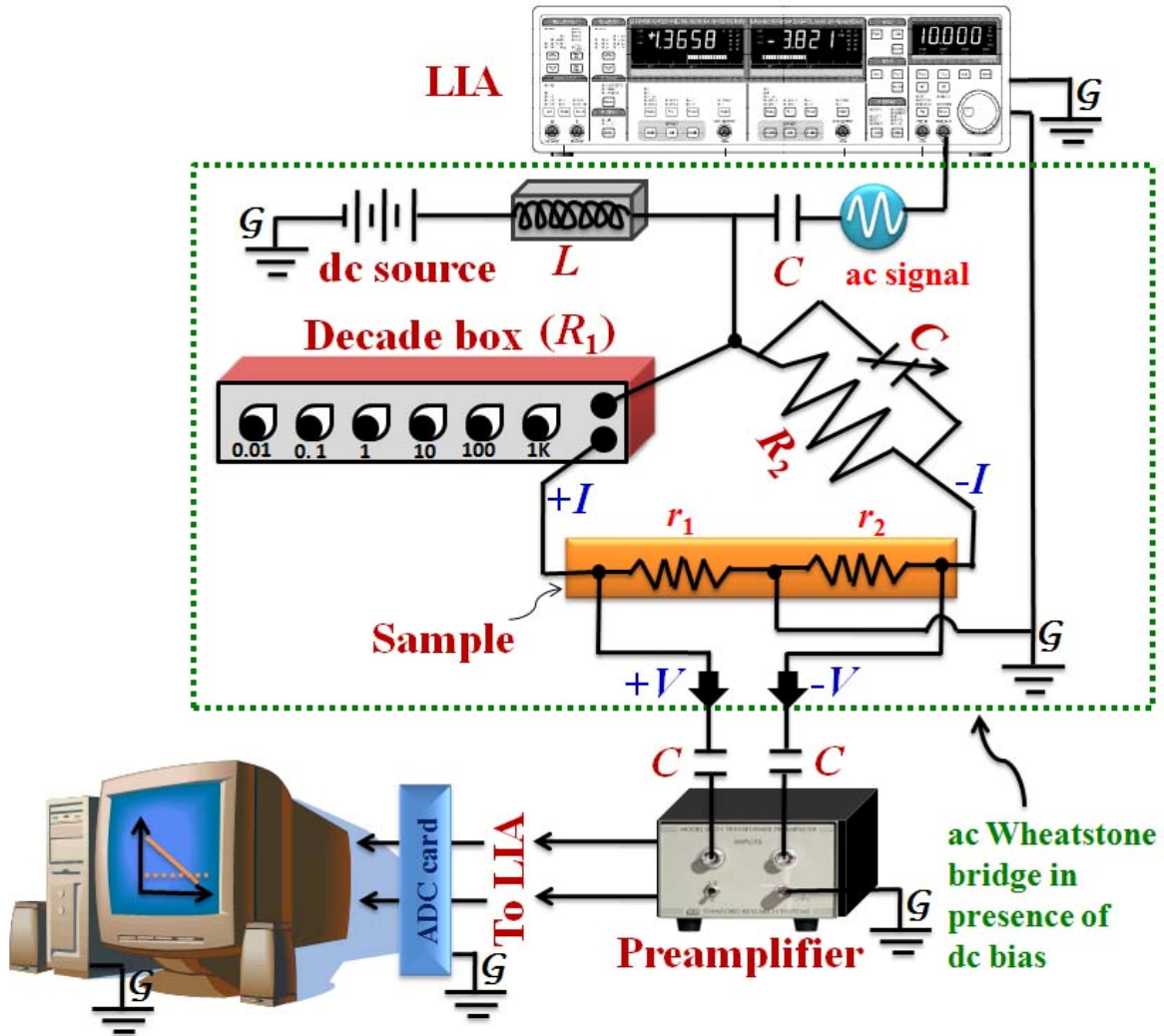


**Figure 3.8:** The schematic diagram for noise measurement setup with ac bias in presence of dc bias. The value of  $L$  is  $0.8\text{ mH}$  and  $C$  is  $10\mu\text{F}$ .

In Fig. 3.9 we have presented the power spectra data measured across a  $10\Omega$  carbon film resistor in five-probe ac biasing technique in presence of dc bias,  $L$  and  $C$ . We performed the experiments using only ac bias, with  $L$  and  $C$  without dc bias, and with  $L$ ,  $C$  and dc bias. The background noise is also shown in the same figure. It is also clear from the data that the introduction of external dc bias, electronic components like  $L$  and  $C$  do not introduce any imperfection or change in power spectrum (got from using ac bias only). The background noise remains unaltered in both noise measurements.

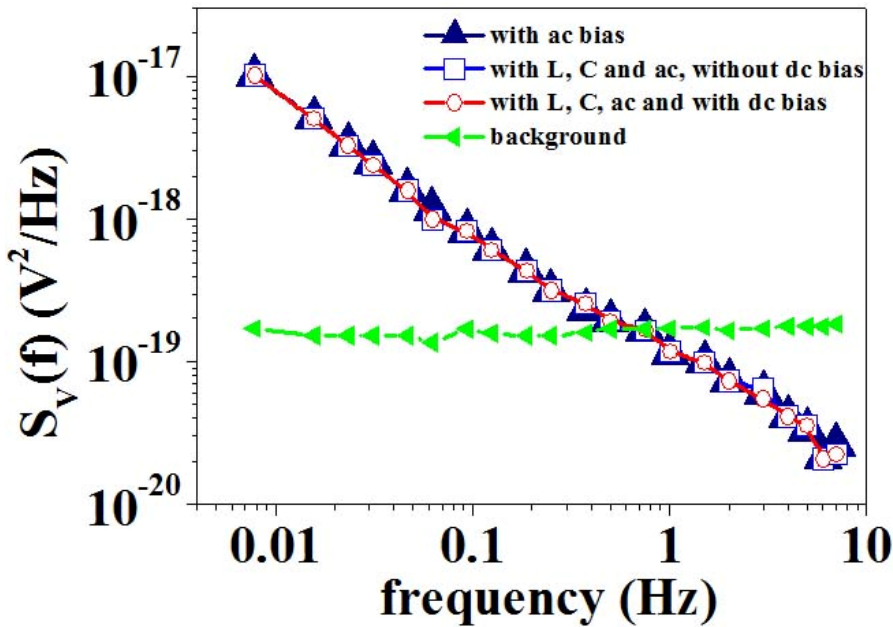


**Figure 3.9:** Comparison of noise data taken with ac bias with and without superimposed dc bias as well as with and without L and C for a  $10\Omega$  carbon film resistor.

### 3.3 Data acquisition

The entire process of noise measurements involve several steps and fall under digital signal processing (DSP) technique. There are several advantages than an analog signal processing as follows:

- No need to design large bank of analog filters with large roll-off
- Simple well-understood filter algorithms can be designed with desired roll-off and cut-off frequencies.
- Bulky electronic components can be avoided for data acquisition
- Robust with respect to aging and weather
- The efficiency is very good
- Quick to install in computer and maintenance free

The first step is data acquisition. The continuous time-domain analog signals at LIA output channels are transferred to computer via 32 bit analog-to-digital converter (ADC) card (PCI-DAS6036, 200ksamples/sec). To analyze the noise data with computer one needs to digitize the analog signal both in discrete time and amplitude and this process is done by analog-to-digital conversion by ADC card. Since the LIA analog output has a range of  $\pm 10V$ , the ADC card was set to this input range in all of the measurements. The user friendly C++ program collects required number of data points in digitized form through two output channels simultaneously. The in-phase (X-output, total noise) as well as out-of-phase (Y-output, background noise) signals are digitized at a specified rate and divided by total gain (preamplifier gain  $\times$  LIA's gain) to obtain the actual voltage values. All the data are saved in computer hard drive for further computations and analysis. Typical total gain is usually  $10^5$ - $10^8$  and a typical experiment requires  $10^6$ - $10^7$  data points at a sampling rate of 1024 data points/sec. This data collection process is called "sampling" and sampling rate is 1024 data point/sec.

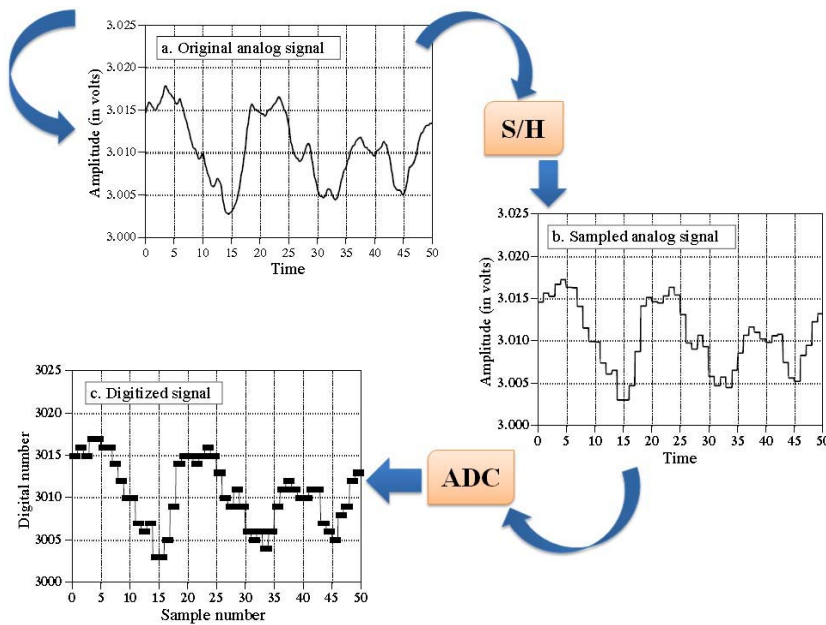


**Figure 3.10:** Waveforms illustrating the digitization process. (a) The time-domain analog voltage signal (b) S/H stage, where the only information retained is the instantaneous value of the signal when the periodic sampling takes place. (c) The ADC converts the voltage to the nearest integer number.

Figure 3.10 shows a typical example of analog-to-digital conversion process of a voltage signal in time domain. There are two sections like sample-hold (S/H) and ADC where S/H is an inbuilt component of modern ADC cards. The S/H is required to keep voltage entering the ADC card constant while the conversion is taking place. The output of S/H is allowed to change only at periodic intervals, at which time it is made identical to the instantaneous value of the input signal. Changes in the input signal that occur between these sampling times are completely ignored. The sampling converts the independent variable (time in this case) from continuous to discrete. The highest frequency used in our analysis is  $\approx 10$  Hz. Thus we are collecting data  $10^2$  times faster. Thus these issues are not much of our concern.

The large number of data points reduces the errors during measurements and voltage drifts due to thermal instability. The rate of data collection is kept high to eliminate any possibility of stray components coming into the signals through the process aliasing. Aliasing effect and its removal are going to be discussed in the next section. Other than the advantages there are several disadvantages as well, these are as follows:

- Appearance of quantization errors due to finite resolution of analog-to-digital converter and due to finite precision in representation of digitized values in computer.
- Ground loops, electromagnetic radiation, vibration from external sources, electronic noise appearing from loose cable contacts, poor performance of electronic instruments contribute reasonable amount of extra noise to the ADC card.
- Improper grounding of ADC card itself can be a noise source.
- Ill performance of computer hardware and sometimes software conflict with ADC card become problematic.

For the above reasons the digitized signals become corrupted and to recover original signal from sample one would need faster data processing that is discussed below. It is important that all other extraneous noise sources should be removed as much as possible.

### 3.3.1 The aliasing effect and its removal

Aliasing occurs when analog continuous time signal is converted in discrete time signals, i.e., during sampling. The continuous time signal changes its frequency during sampling and assumes an identity (an alias) which is not its own. Since the digital data is no longer uniquely related to a particular analog signal, an unambiguous reconstruction is impossible. There is no information regarding the original analog data and the true identity remains completely hidden. This is an effect of improper sampling.

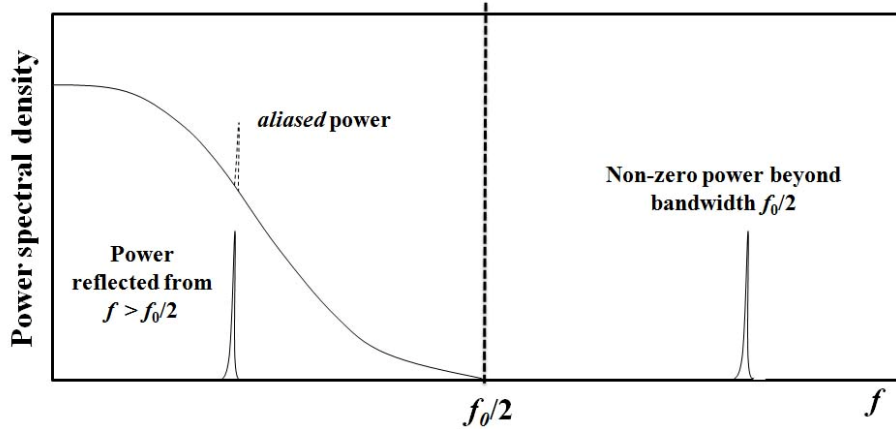


**Fig 3.11:** A schematic diagram for realizing aliasing phenomena and its contribution to the noise power spectral density.

The reason for aliasing is explained through Shannon sampling theorem or Nyquist sampling theorem. Theorem states that *a continuous signal can be sampled properly, only if it does not contain frequency components above one-half of the sampling rate*. Suppose a continuous waveform of frequency  $f_1$

$$y_1(t) = ACos(2\pi f_1 t + \delta) = ACos(\Phi_1 t + \delta) \quad (3.10)$$

is being sampled at a frequency  $F_T$ , or, interval of time  $T = 1/F_T$ . The discrete sequence of continuous signal developed at instances  $t_n = nT (= n/F_T = 2\pi n/\Phi_n)$  and can be written as

$$y[n] = ACos(2\pi f_1 t_n + \delta) = ACos(\Phi_1 n T + \delta) = ACos\left(\Phi_1 \cdot \frac{2n\pi}{\Phi_n} + \delta\right) = ACos(\omega_1 n + \delta), \quad (3.11)$$

where  $\omega_1 = 2\pi(\Phi_1 / \Phi_n) = \Phi_1 T$ . In the same way, the continuous signals of the form

$$y_{1,k}(t) = ACos[\pm(\Phi_1 t + \delta) + k\Phi_n t], \text{ for } k = 0, \pm 1, \pm 2, \dots \quad (3.12)$$

leads to the identical discrete sequence

$$y_{1,k}(nT) = ACos[(\Phi_1 + k\Phi_n)nT + \delta] = ACos\left[\frac{2\pi(\Phi_1 + k\Phi_n)n}{\Phi_n} + \delta\right] \quad (3.13)$$

$$\begin{aligned}
 &= ACos\left(\frac{2\pi\Phi_1 n}{\Phi_n} + \delta\right) \\
 &= ACos(\omega_1 n + \delta) \\
 &= y[n]
 \end{aligned}$$

Hence the spectral power at frequencies  $(\Phi_1 + k\Phi_n)$  { $k = 0, \pm 1, \pm 2, \dots$ }, where  $\Phi_n / 2\pi$  is the sampling frequency “reflected” into the frequency  $\Phi_1$ . This enhancement of spectral power due to the reflected power from outside the bandwidth can be realized as “aliasing” [16, 17, 18, 19]. The aliasing thus can enhance spectral power of signals with  $f < 10$  Hz “imprinting” large power from the 50 Hz region if care is not taken in digitizing data. The realization of aliasing effect and its contribution to the noise power spectral density is shown schematically in Fig. 3.11.

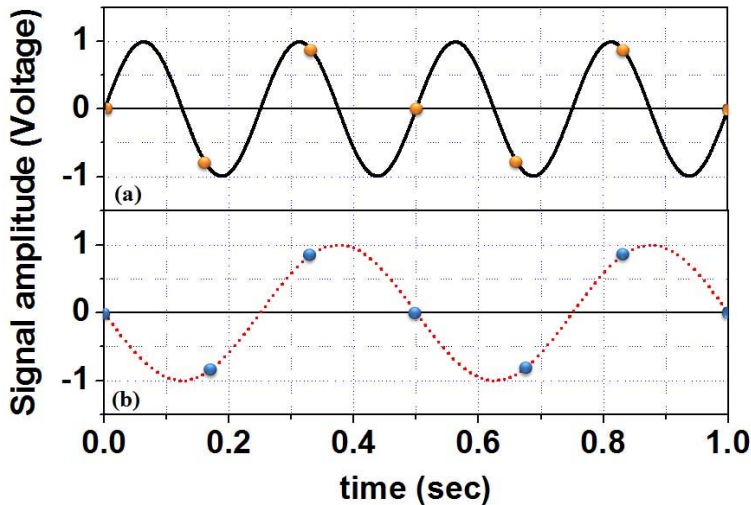


**Figure 3.12:** An example of aliasing. (a) The original sinusoidal continuous signal at frequency 4 Hz (black solid line) is digitized at a rate 6 samples/sec (orange dots). (b) The digitized signal suffered from aliasing effect and appears as a signal of frequency 2 Hz.

We can consider an example where we have a continuous sinusoidal analog signal of frequency 4 Hz with amplitude 1V in Fig. 3.12 (a) (black solid line). If the signal is sampled with a sampling rate 6 Hz (see Fig. 3.12 (a)), the digital signal will appear of frequency 2Hz (See Fig. 3.12 (b)). So if the sampling rate is less than twice of maximum desired frequency ( $f_{max}$ ), the signals with frequencies higher than  $f_{max}$  will also appear within the desired frequency band and this will lead to corruption of signal as well the wrong estimation of spectral power density. There will be an enhancement of spectral power density due to the contribution coming from aliased power. To get an aliasing free signal we have to set sampling rate higher than  $(2 \times f_{max})$ . The frequency  $f = 2f_{max}$  is called Nyquist frequency.

Using DSP technique [5, 20, 21, 22] we can solve above mentioned problems. We mentioned earlier that the signal from LIA output is up to  $\approx 32$  Hz is allowed by using a built-in low pass filter in LIA. In our experiments to avoid excessive noise coming from 50 Hz we limit  $f_{max}$  to 10 Hz, hence a sampling rate more than  $2f_{max} = 20$  Hz will be sufficient to avoid aliasing. For ease of taking fast Fourier transformation (FFT), we keep digitization rate ( $\Delta$ ) at 32 Hz ( $= 2f_{max}$ ), so that

it gives  $f_{\max} = 16$  Hz.  $\Delta$  decides to set LIA's low pass filter time constant to a value  $\tau_{LIA} = 1/(2\pi\Delta)$ . For  $\Delta = 32$  Hz,  $\tau_{LIA} = 5$  msec. The closest value for  $\tau_{LIA}$  available in SR830 model is 3msec corresponding to a frequency  $\approx 53$  Hz. The low pass frequency window of 53 Hz will allow all possible contributions from power line fluctuations at 50 Hz. We can observe peak structures in the power spectra due to this kind of contributions in voltage fluctuations. By increasing  $\tau_{LIA}$  one can reduce low pass frequency band only by a factor of 2, and improvement becomes slightly better when roll-off suppresses 50 Hz only by 24 dB, i.e., a factor of 10. This is not sufficient to filter 50 Hz power-line noise. In practice, the signal is sampled at a rate  $\Omega_s = D \times f_{\max}$ . For  $f_{\max} = 16$  Hz and  $\Omega_s = 512$  or 1024 samples/s,  $D = 16$  or 32. At these high sampling frequencies the attenuation due to the low pass filter of LIA is  $\sim -90$ dB. Thus the possibility of a signal of higher frequency aliasing itself onto a frequency lower than  $f_{\max}$  (which is our region of interest) is greatly reduced. The data is then low pass filtered with a digital filter having a roll-off as high as 80-100 dB/octave (which is virtually impossible to achieve with an analog filter because of the cost and the bulk of such a filter) and a cut-off at  $f_{\max}$ . This virtually removes all stray signals of frequency higher than  $f_{\max}$  from the digitized data. The data is then re-sampled by retaining only the  $D$ -th point to bring down the effective sample rate to the desired value of  $2f_{\max}$  and is called "downsampling". This process of digitally filtering the data and combining with subsequently reduction of the effective sampling rate from  $\Omega_s = 2 \times f_{\max}$  to  $2f_{\max}$  is called "Decimation" in the time domain. The decimated data is further used to estimate the power spectral density of noise or probability distribution function (PDF) of the voltage fluctuations. The power spectral density is calculated by using fast Fourier transformation (FFT). For PDF calculations, sample noise is separated from background noise using proper digital filer called "weiner filter" in frequency domain and then the cleaned data is transformed back to time domain (by inverse Fourier transform), histogram of voltage jumps are calculated. These steps will be discussed in the subsequent sections in this chapter.

### 3.3.2 Decimation: downsampling and digital filtering

We have already discussed about the downsampling followed by digital filtering of the signal, called "decimation". The re-sampled data is generated retaining every  $D$ -th point in time scale and  $D$  is denoted as decimation factor. For the decimation process the first step is to design low-pass digital filters. The filters fulfil two purposes: signal separation and signal restoration. Signal separation is needed when a signal has been contaminated with interference, noise, or other signals. Signal restoration is used when a signal has been distorted in some way. Any linear filter has a frequency response, an impulse response and a step response. Each of these responses contains complete information about the filter, but in different form. If one of the three responses is specified then other two are fixed and can be directly calculated. All the three responses will determine how the filter will react in different circumstances.

An ideal low-pass filter should able to pass all the frequencies up to its cutoff frequency  $f_c$  while blocking all other frequencies higher than  $f_c$ . The frequency response of an ideal low-pass filter is shown in Fig. 3.13 (a). Its frequency response can be written as

$$|H(f)| = \begin{cases} 1 & \text{for } |f| \leq f_c \\ 0 & \text{for } |f| > f_c, \end{cases} \quad (3.14)$$

and the impulse response is

$$h(n) = \int_{-f_c}^{f_c} \exp(2i\pi f n) df = 2f_c \quad \text{for } n = 0$$

$$= \frac{\sin(2\pi f_c n)}{\pi n} \quad \text{for } n \neq 0. \quad (3.15)$$

An infinite-length Fourier series could represent  $h(n)$  correctly. But in practice, this is not possible to do. Hence the function,  $h(n)$  has to be approximated by a series of finite-length with  $n$ -th coefficient of  $h(n)$  as (Now on, in our discussion “[ ]” will be used for a coefficient in discrete-time sequence while a “( )” will be used for continuous-time series)

$$h(n) = \frac{\sin\left[2\pi f_c \left(n - \frac{M-1}{2\Omega_s}\right)\right]}{\pi\left(n - \frac{M-1}{2\Omega_s}\right)} \quad (3.16)$$

where,  $M$  is the order of the filter and  $\Omega_s$  is the sampling rate. This approximation leads to appearance of large-magnitude ripples in the filter's frequency response as shown in the Fig. 3.13(c).

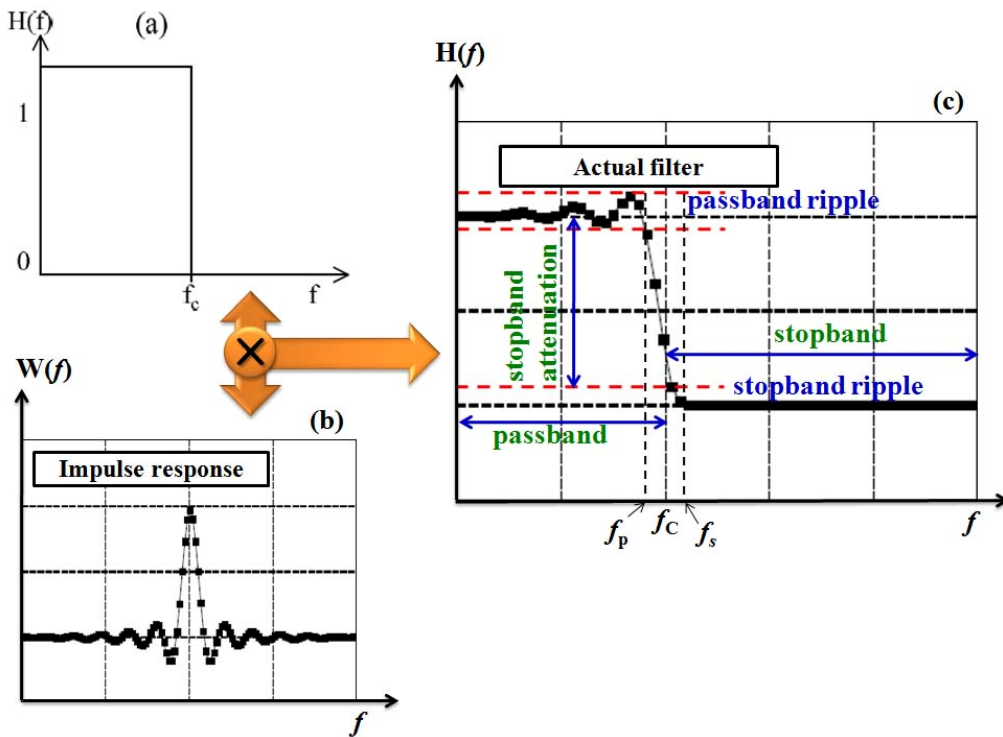


**Figure 3.13:** Frequency response of (a) an ideal low-pass filter (b) of an impulse (c) of an actual low-pass filter. The actual low-pass can be realized as convolution of the ideal filter function and impulse function.

Though the ripples can not be completely removed but their amplitude can be controlled by multiplying the impulse response  $h(n)$  by a suitable window function  $w(n)$ . The impulse response  $h'(n)$  of the resultant filter becomes

$$h'(n) = w(n)h(n). \quad (3.17)$$

Since  $w(n)$  itself is a finite length time series it also suffer from some ripples. A typical frequency response of a window function is shown in Fig. 3.13(b). Some well known window functions like Hanning, Hamming, and Kaiser window functions are shown in Fig. 3.14.

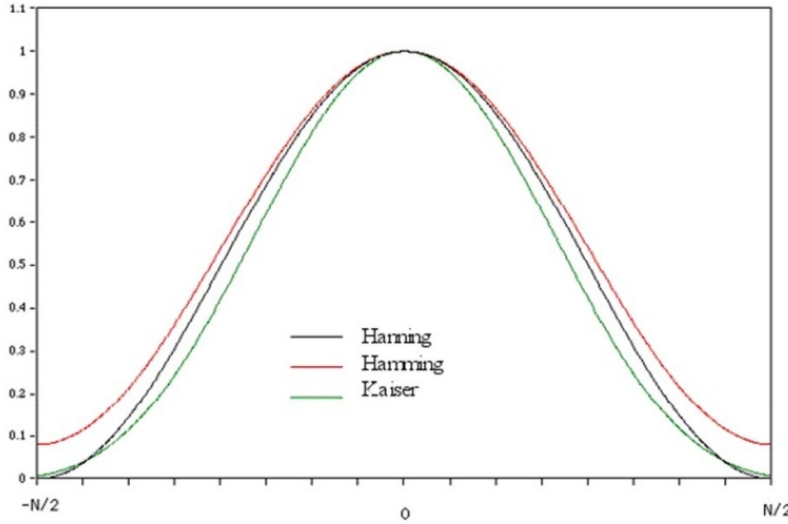


**Figure 3.14:** The well known Hanning, Hamming, and Kaiser window functions are shown.

In our case we have used Kaiser window due to its excellent control over ripples and quick decay of magnitude. Kaiser window function [18] can be written as

$$w[n] = \begin{cases} \frac{I_0\alpha(1 - [(n - \alpha)/\alpha]^2)^{1/2}}{I_0\alpha} & \text{for } 0 \leq n \leq N \\ 0 & \text{otherwise} \end{cases} \quad (3.18)$$

where,  $\alpha$  is the shaping parameter and

$$I_0(x) = 1 + \sum_{k=1}^p \left[ \frac{\left(\frac{x}{2}\right)^k}{k!} \right]^2 \quad p \text{ is a sufficiently large number.} \quad (3.19)$$

$I_0(x)$  is a zero-th order Bessel function of first kind. We used  $p = 0.30$ .

### 3.3.3 Scheme to construct digital filers

- Passband and stopband frequencies  $f_p$  and  $f_s$  are selected and they estimate the filter cutoff frequency  $f_c = (f_p + f_s)/2$ .
- Allowable passband ripple ( $A_p$ ) and stopband attenuation ( $A_r$ ) are selected.

- $$\alpha = \begin{cases} 0.1102(A_r - 8.7) & A_r > 50 \\ 0.5842(A_r - 21)^4 + 0.07886(A_r - 21) & 0 \geq A_r \geq 21 \\ 0 & \text{otherwise} \end{cases} \quad (3.20)$$

- The window length,  $D_{kw}$  with the following empirical formula

$$D_{kw} = \begin{cases} (A_r - 7.95)/14.36 & A_r > 21 \\ \text{Otherwise} & \end{cases} \quad (3.21)$$

- The order of the filter  $M$  is determined, and  $M$  should satisfy the criterion

$$M \geq \frac{\Omega_s D_{kw}}{f_s - f_p} \quad (3.22)$$

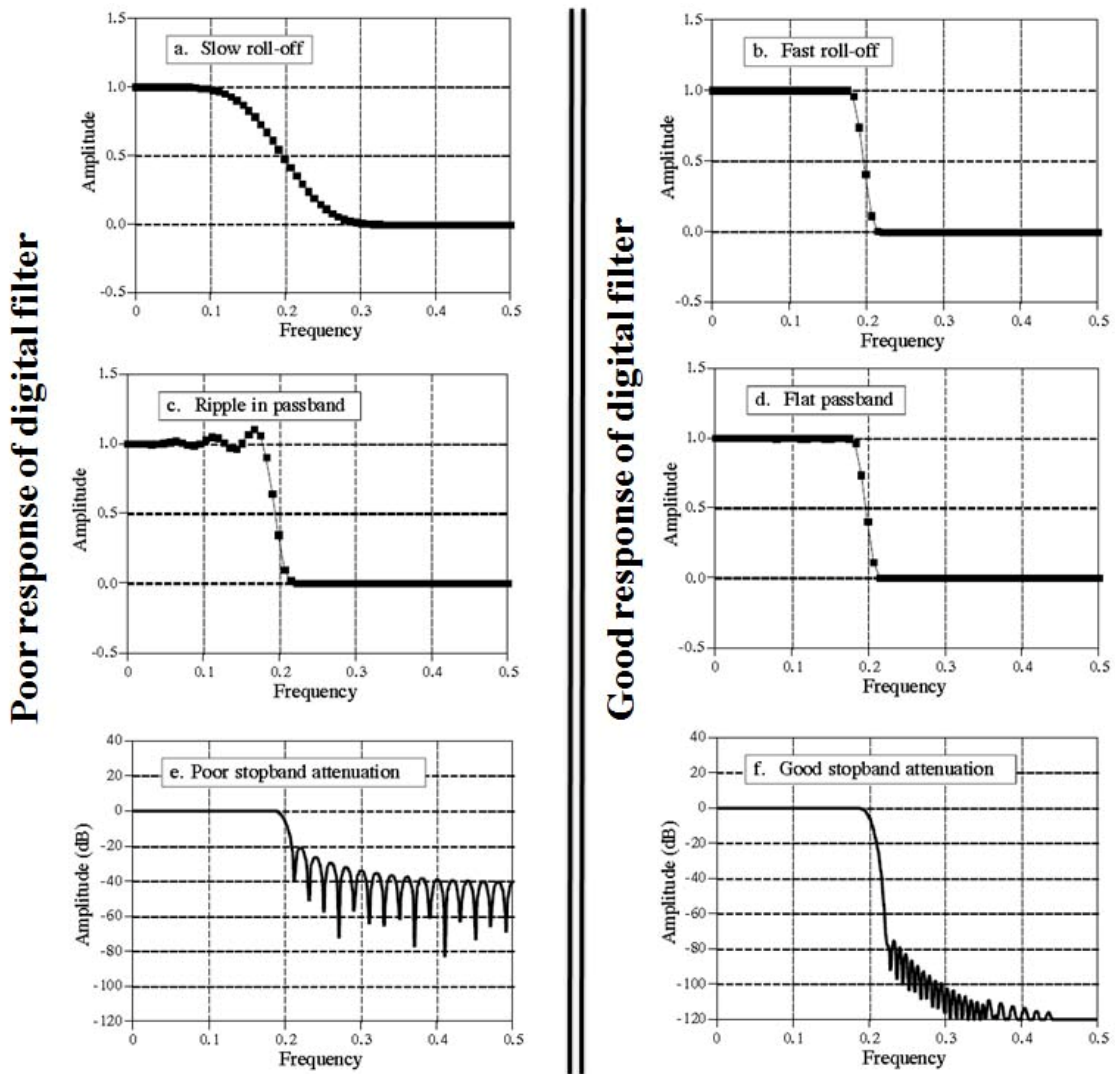


**Figure 3.15:** Parameters for evaluating frequency domain performance. The frequency responses shown are for low-pass filters. Three parameters are important: (1) roll-off sharpness, shown in (a) and (b), (2) passband ripple, shown in (c) and (d), and (3) stopband attenuation, shown in (e) and (f).

- The functions  $w[n]$ ,  $h[n]$ , and  $h'[n]$  are computed.

The decimated data can be obtained by registering  $D$ -th sample of the convolution of the signal  $x(m)$  with filter's impulse response  $h'[n]$  using the relation

$$y[n] = \sum_{m=0}^{M-1} x[m]h'[Dn-m] \quad (3.23)$$

In this case the filters are of non-recursive style and they are generally known as “finite duration impulse response” (FIR) filters [18, 20]. The comparison between the poor and good responses of digital filters is shown in Fig. 3.15. For optimization of the memory space available in the computer hard drive as well as RAM and to make the processing and data collection faster we performed decimation in three stages.

### 3.3.4 Scheme for multi stage decimation

Figure 3.16 (a) depicts the schematic diagram of multi-stage decimation process [16, 19] and Fig. 3.16 (b) is shows the actual response functions of digital filters used at different stages mentioned above. We have used the same decimation algorithm for each stage of decimation.

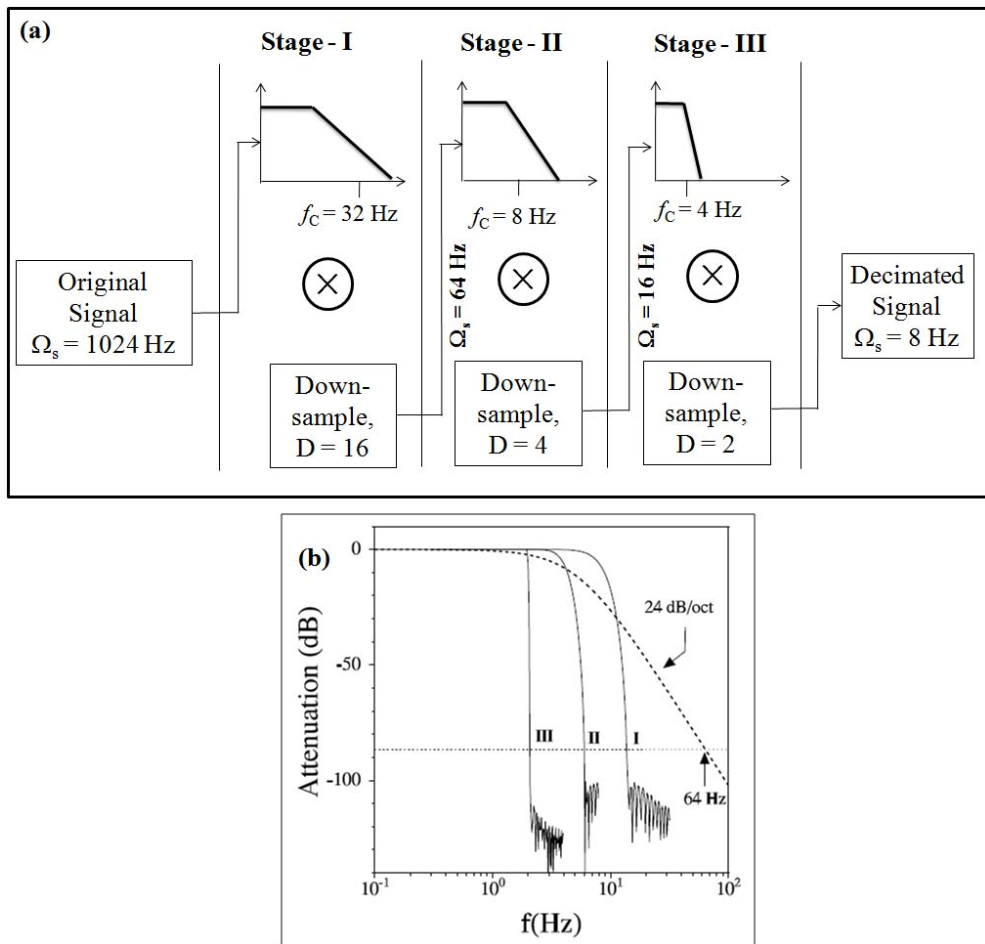


**Figure 3.16:** (a) A schematic diagram showing the multistage decimation process. (b) The response functions of the three stage digital filters used. The LIA filter response is shown for comparison as a dotted line.

The net effective decimation factor should be decided from  $f_{\max}$  value of our interest and  $D$  should be equal to  $2f_{\max}$  at least. The original sampling rate  $\Omega_s$  was 1024 samples/sec and after downsampling with decimation factor  $D = 128$ , the effective sampling rate at final stage became  $\Omega_s = 8$  samples/sec. The maximum frequency  $f_{\max}$  is 4 Hz. Decimation factors at each stage,  $D_i$ , was calculated in such a way that it is a divisor of that in the previous stage,  $D_{i-1}$  and it is just larger than  $\sqrt{D_{i-1}}$ . Thus with  $D = 128$ , the decimation factors at 1st, 2nd and last stage becomes 16, 4 and 2 respectively. For all stage  $s$  we used same  $f_p \approx 3.85$  Hz and  $f_s \approx 60, 12$ , and 4.15 Hz at first, second, and third stages respectively. The corresponding values of  $f_c$  are  $\approx 32, 8$ , and 4 Hz respectively and corresponding to roll-off values 6dB/octave, 47dB/octave, and 1283dB/octave. For all stages we allowed pass-band ripple,  $A_p = 0$ , and stop-band attenuation  $A_r = 100$  dB. Here the orders of filter in three stages are 118, 52, and 322 respectively. The higher roll-off of the digital filters we used in comparison to that of the LIA ( $= 24$ dB/octave) implies the superiority of our filters.

### 3.3.5 Detrend, a linear trend removal process

Ideally the voltage fluctuations recorded in time domain should be drift free. Sometimes due to thermal drift of average resistance in the Wheatstone bridge balancing and other arms, there is a deviation of bridge balance leading to drift. Also poor quality of cable arrangements and mostly poor thermal instability give rise to linear drift in the voltage fluctuations recorded. In this case recorded data contains frequency components with a time period which is much larger than the actual data collection period and this information has a low-frequency component which does not carry any information about the sample noise and contribute a component in power spectra.

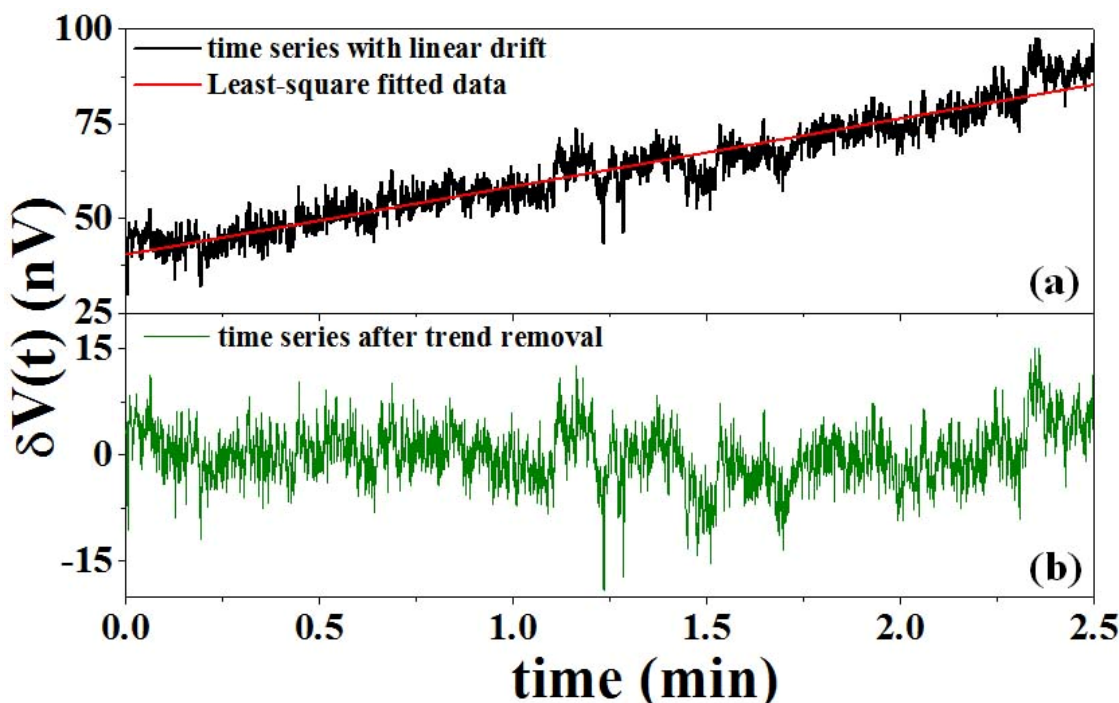


**Figure 3.17:** (a) Voltage fluctuations showing linear trend due to drift. The solid red line indicates the least-square fitted data and (b) same voltage fluctuations after trend removal. The voltage fluctuations (y-scale) are in nV.

This linear trend can be removed by a filter with “least squares fitting” [23] procedure. If the deviation does not follow linear trend then it is recommended to discard the data for further analysis. For this procedure, trend in the data,  $V_1[n]$  is first found out as

$$V_1[n] = b_0 + b_1 \left[ \frac{n}{\Omega_s} \right], \quad (3.24)$$

where  $b_0 = \frac{2(2N+1)\sum_{n=1}^N V[n] - 6\sum_{n=1}^N nV[n]}{N(N-1)}$  and

$$b_1 = \frac{\Omega_s \left\{ 2\sum_{n=1}^N nV[n] - 6(N+1)\sum_{n=1}^N V[n] \right\}}{N(N-1)(N+1)}.$$

Then by subtracting  $V_1[n]$  from original data  $V[n]$  and then we replace  $V[n]$  with trend-free data. Trend removal is a very important step to get distortion-free power spectra. The effect of trend removal is shown in Fig. 3.17.

### 3.4 Data analysis: estimation of power spectral density

The digitized and subsequently decimated data sheet gives us the filtered voltage fluctuation in time domain. We can calculate the power spectral density in frequency domain from it. The estimation of power spectral density was developed by Peter D. Welch using fast Fourier transformation and is known as “method of averaged periodogram” [24]. This method optimizes the number of computation steps along with the maximum usage of hard disk memory in the computer and obviously reduces the computation time. In this section we shall describe the essential steps regarding this method.

#### 3.4.1 Welch’s method for averaged periodogram

After decimation process the continuous voltage fluctuations have been recorded into digitized sequence of  $N$  data points with a sampling rate  $\Omega_s$ . The discrete frequencies can be estimated as  $f_k = \Omega_s k / N$  where  $k = 0, 1, 2, \dots, N/2$ . The spectral power density can be estimated as [25]

$$\begin{aligned} S[f_0] &= \frac{1}{N^2} |V[0]|^2 \\ S[f_k] &= \frac{1}{N^2} [V[k]^2 + V[N-k]^2], \quad k = 1, 2, \dots, (N/2 - 1) \\ S[f_{\max}] &= \frac{1}{N^2} |V[N/2]|^2 \end{aligned} \quad (3.25)$$

where,  $f_{\max}$  is the maximum frequency and

$$V[k] = \sum_{n=0}^{N-1} v[n] e^{2\pi i n k / N}, \quad k = 0, 1, 2, \dots, (N - 1). \quad (3.26)$$

The sequence of  $S[f_k]$  is called as “periodogram”.

There are two different roots of errors generated during this process:

- Periodograms are estimated at discrete frequencies. Thus it contains average information about the surrounding frequencies which are not desired at all. Hence the spectral density at actual frequency becomes erroneous. This effect is called as “leakage”.
- Statistical error due to finite length of the sequence in the time domain. This error generally present in any of the finite width calculation.

The first error can be removed by a useful method called “*data windowing*” and second error is resolved by a method called “*averaging of periodograms*”.

### a. Method of Data Windowing

The discrete sequence of voltage fluctuations can be written always in Fourier transform equation as

$$V[k] = \sum_{n=0}^{N-1} u[n]v[n]e^{2\pi i nk/N}, k = 0, 1, 2, \dots, (N-1) \quad (3.27)$$

$$\text{where, } u[n] = \begin{cases} 1 & 0 \leq n \leq N \\ 0 & \text{otherwise} \end{cases} \quad (3.28)$$

And power spectrum of which can be given as

$$Q[s] = \frac{1}{N^2} \left[ \frac{\sin(\pi s)}{\sin(\pi s/N)} \right]^2, \quad (3.29)$$

$Q[s]$  has finite width and sidebands and leakage information come from surrounding sidebands. A window function  $w[n]$  introduced to resolve the problem. The scheme is to weigh the actual data sequence  $v[n]$  with this window function by multiplying  $v[n]$  with  $w[n]$ . So the modified periodogram becomes

$$\begin{aligned} S[f_0] &= \frac{1}{Q_{ss}} |A[0]|^2 \\ S[f_k] &= \frac{1}{Q_{ss}} [A[k]^2 + A[N-k]^2], k = 1, 2, \dots, (N/2 - 1) \\ S[f_{\max}] &= \frac{1}{Q_{ss}} |A[N/2]|^2 \end{aligned} \quad (3.30)$$

and

$$A[k] = \sum_{n=0}^{N-1} w[n]v[n]e^{2\pi i nk/N}, k = 0, 1, 2, \dots, (N-1) \quad (3.31)$$

$$\text{where, } Q_{ss} = N \sum_{n=0}^{N-1} [w[n]]^2.$$

Any window function has a main lobe accompanied by its side lobes. Good window functions has its main lobe's magnitude much higher than its side lobe's magnitude, hence we have used Hanning window function defined as

$$w[n] = \frac{1}{2} \left[ 1 - \cos\left(\frac{2\pi n}{N}\right) \right] \quad n = 0, 1, \dots, (N-1). \quad (3.32)$$

### b. Method of Averaging Periodograms

To do the “averaging of periodogram”, the complete decimated dataset is partitioned in few segments of equal length, say of  $2L$  data points. The partitioning is done such a way that any two consecutive segments are overlapped by half segment length. That means the last  $L$  data points of the first segments are first  $L$  data points of the second segment, similarly the last  $L$  data points of the second segments are first  $L$  data points of the third segment and so on. If total number of partition is  $M$ , then there will be total  $(M+1)$  segments and  $2(M+1)L$  number of data points can be segmented that way. Now for each segment modified periodograms are estimated as described above for the discrete frequencies  $f_k = \Omega_{sk} / 2L f_k$  here  $k = 0, 1, 2, \dots, L$ . Then for each frequency,  $f_k$  power spectral density is calculated by averaging the periodograms at this frequency over all the segments. To calculate the Fourier transform 2.24, we used a fast Fourier transform (FFT) algorithm developed by Danielson and Lenczo [26] because this algorithm is very economic from the computational point of view. In this method the single Fourier transform of complete set of  $2L$  data points can be written as two Fourier transforms, one from the even-numbered positioned data and other from the even numbered positioned data as,

$$\begin{aligned} A[k] &= \sum_{n=0}^{2L-1} a[n] e^{2\pi i nk / 2L}, \quad k = 0, 1, 2, \dots, (2L-1) \text{ and } a[n] = w[n]v[n]. \\ A[k] &= \sum_{n=0}^{L-1} a[2n] e^{2\pi i (2n)k / 2L} + \sum_{n=0}^{L-1} a[2n+1] e^{2\pi i (2n+1)k / 2L} \\ &= \sum_{n=0}^{L-1} a[2n] e^{2\pi i nk / L} + e^{2\pi i nk / 2L} \sum_{n=0}^{L-1} a[2n+1] e^{2\pi i nk / L} \\ &= A_k^e + [e^{2\pi i nk / L}]^k A_k^o. \end{aligned} \quad (3.33)$$

$A_k^e$  and  $A_k^o$  are even and odd components of Fourier transform of length  $L$ . Now each component again separated to two parts each similar way and can be kept on going until finally each part becomes length of 2 data points. To achieve this we always chose  $L$  as a power of 2 (typically 512). To realize this during computation the complete data set is rearranged such that these final level data points stay next to next by a method called “bit reversal method”. From this data set the required Fourier transform can be computed with highly improved computational speed and averaged periodogram can be estimated very fast.

### 3.4.2 Recovery of “uncorrupted” time domain signal: Weiner filtering

So far we focussed on discussing about the power spectral density from the time domain series. From the time series i.e., data in time domain one would like to obtain the probability distribution function (PDF). In the case when the voltage fluctuations are orders of magnitude higher than the background level, the time domain analysis like construction of PDF is accurate if we use in-phase time series only. However, if the voltage fluctuations are such that within the measured bandwidth, it is comparable with background fluctuations, then in-phase signal is highly corrupted by the additional contributions coming from the background signals, and the effect of background should be removed before further analysis of the time domain. Hence to obtain the “uncorrupted” time

series free from background fluctuations one can use Weiner filtering. The Weiner filer sufficiently removes the background signal and we get an in-phase component containing sample information only and a quadrature component from background fluctuations. The Weiner filter translates the time domain signals into frequency domain, and retains only that fraction of the power that corresponds to the “excess” noise (i.e. from the one arm of the sample) over the background. It then re-transforms the “cleaned” spectrum into the time domain to produce an “uncorrupted” time domain signal. The power spectral density of the uncorrupted signal only contains information about “excess” noise with the backgrounds signal removed.

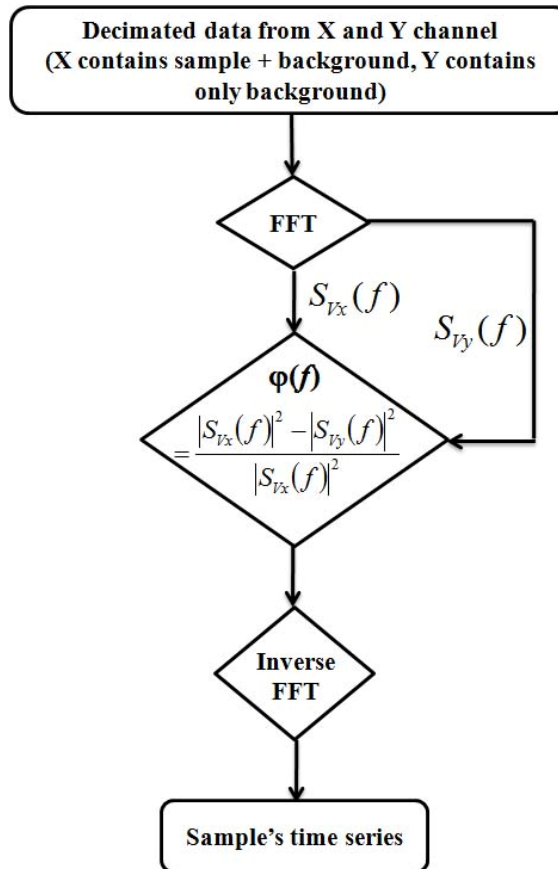


**Figure 3.18:** The flow chart of the algorithm used to execute the “Weiner filter” to eliminate the background noise from the “in-phase” signal.

As we mentioned earlier, the X-output of the LIA is noise signal containing sample noise corrupted by background noise and Y-output is only the background noise. Power spectra of both these noises namely  $S_{v_x}(f)$  and  $S_{v_y}(f)$  can be estimated as described in the last section. Now if  $S_v(f)$  is the sample’s noise excess over  $S_{v_y}(f)$ , one can design Weiner filter  $\varphi(f)$  such that when it is applied to the corrupted signal  $S_{v_x}(f)$ , one recovers a signal  $S_v^C(f)$ . This  $S_v^C(f)$  is very close approximation of the uncorrupted signal  $S_v(f)$ . The filter performance is said to be good if the least squared difference between  $S_v(f)$  and  $S_v^C(f)$  is minimum, i.e.,

$$\int_{-\infty}^{+\infty} |S_v^C(f) - S_v(f)|^2 df \quad \text{is minimum}$$

$$\text{or } \int_{-\infty}^{+\infty} |\phi(f)| [S_V(f) + S_{V_y}(f)] - S_V(f) |^2 df \quad \text{is minimum.}$$

An important assumption in this estimation is that the background and the uncorrupted signals are uncorrelated.  $S_V(f)$  becomes uncorrelated to the background one can write

$$\phi(f) = \frac{|S_V(f)|^2}{|S_V(f)|^2 + |S_{V_y}(f)|^2} . \quad (3.34)$$

Since  $|S_V(f)|^2 + |S_{V_y}(f)|^2 \approx |S_{V_x}(f)|^2$  then we can easily write  $\phi(f)$  as a function of the fluctuations which we have already estimated from the X-output and Y-output data. So

$$\phi(f) = \frac{|S_{V_x}(f)|^2 - |S_{V_y}(f)|^2}{|S_{V_x}(f)|^2}, \quad (3.35)$$

and if we operate  $\phi(f)$  on our measured X-output in frequency domain and performing inverse Fourier transformation, we can recover the original voltage fluctuations in the sample excess noise over the thermal fluctuation in time domain with which the statistical analysis is done. The algorithm to execute Weiner filtering process is depicted in Fig. 3.18.

### 3.4.3 Test of Gaussianity of noise and quantifying non-Gaussian noise

In noise measurements it is a common practice to characterize fluctuation by its power spectral density  $S_V(f)$  or equivalently by the second moment of the fluctuations. For Gaussian fluctuations this will suffice because Gaussianity implies that all higher order correlation functions  $\langle V(t)V(t+t_1)\dots V(t+t_n) \rangle$  can be expressed by decomposing them into the sum of all possible products of pair wise correlation functions [23, 27]. Thus for Gaussian noise the first moment determines higher moments. By the Central Limit Theorem, a distribution is Gaussian if and only if the individual events of the distribution are uncorrelated, i.e. the occurrence of one event does not in any way influence that of any other event. However, in many physical situations this need not be the case. In many complicated systems, the fluctuators may not be completely independent of each other, giving rise to correlations. This kind of behaviour is expected in systems near phase transitions [28, 29] or in frustrated systems like spin glass [30]. Under these circumstances, limiting the analysis of resistance fluctuations to its spectral power density only does not completely characterize the fluctuating system. When the fluctuations become non-Gaussian higher order statistics are needed to describe them. In this section we discuss two techniques used by us to quantify the non-Gaussianity of a distribution- “Probability Density Function”, “Second spectrum”

#### a. Probability Density Function (PDF) analysis

An important parameter that characterizes the nature of fluctuations in any system is the estimation of its probability density function (PDF) [20, 21]. The essential criteria for estimation of PDF are: one has to estimate the approximate frequency at which excess noise is comparable to background level, the excess noise magnitude should be at least one order higher in magnitude than the background level and the real time series of voltage fluctuations then decimated down so that the

band width is restricted below this frequency. The details of estimating PDF is shown by a flowchart as shown in Fig. 3.19.

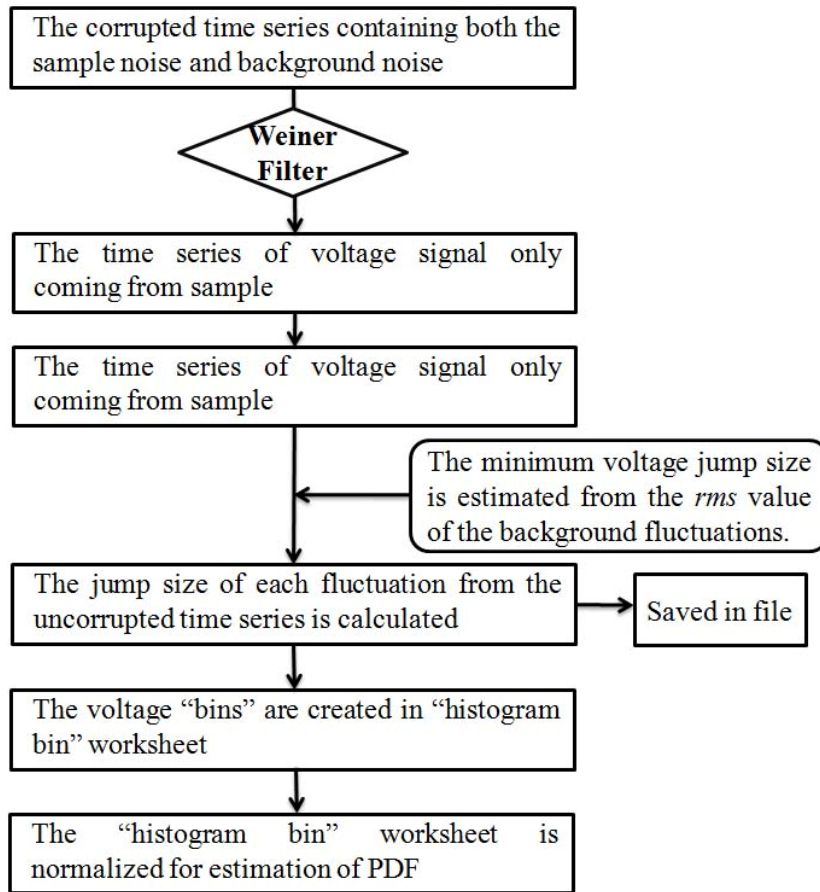


**Figure 3.19:** The flowchart showing the detailed procedure for estimation of PDF from sample time series data.

The PDF so obtained is an experimental quantity. Next step is to analyse the nature of the PDF to check whether it is Gaussian or some other distribution. In general a Gaussian probability density with zero mean can be written as

$$P(x) = \frac{1}{\sqrt{2\pi}\sigma_x} \exp\left(\frac{-x^2}{\sigma_x^2}\right) \quad (3.36)$$

where  $\sigma_x$  is the variance of the distribution. It is clear that logarithm of  $P(x)$  as a function of  $x^2$  should be a straight line and slope giving twice the variance of the distribution. In Fig. 3.20 (a) we have plotted the raw time series of voltage fluctuation of a nickel wire of diameter 50 $\mu\text{m}$  at five different temperatures. The PDF of voltage fluctuations were obtained using the above process from the above time series (see Fig. 3.20(a)). Fig. 3.20(b) shows the PDF  $P(\Delta V)$  at few representative temperatures. The data have been plotted as  $(\Delta V)^2$  versus  $\ln[P(\Delta V)]$ . We have fitted the straight line with equation  $\ln[P(\Delta V)] = K + m[(\Delta V)^2]$  (linearized form of Gaussian probability density function) where  $K$  and  $m$  are the fitting parameters. The relative variance of the voltage fluctuations  $\langle(\Delta V)^2\rangle/V^2$  calculated from the slope of the curve and is shown in the Fig. 3.20(c) (filled

triangles). The integrated power spectral density in frequency domain over a bandwidth of our interest was also calculated using DSP technique described earlier. That data (filled circles) have been plotted in the same graph for comparison. We can make out that these two techniques give identical data indicating the fluctuations are Gaussian. This also establishes that the DSP techniques do not add any artefacts to the data.

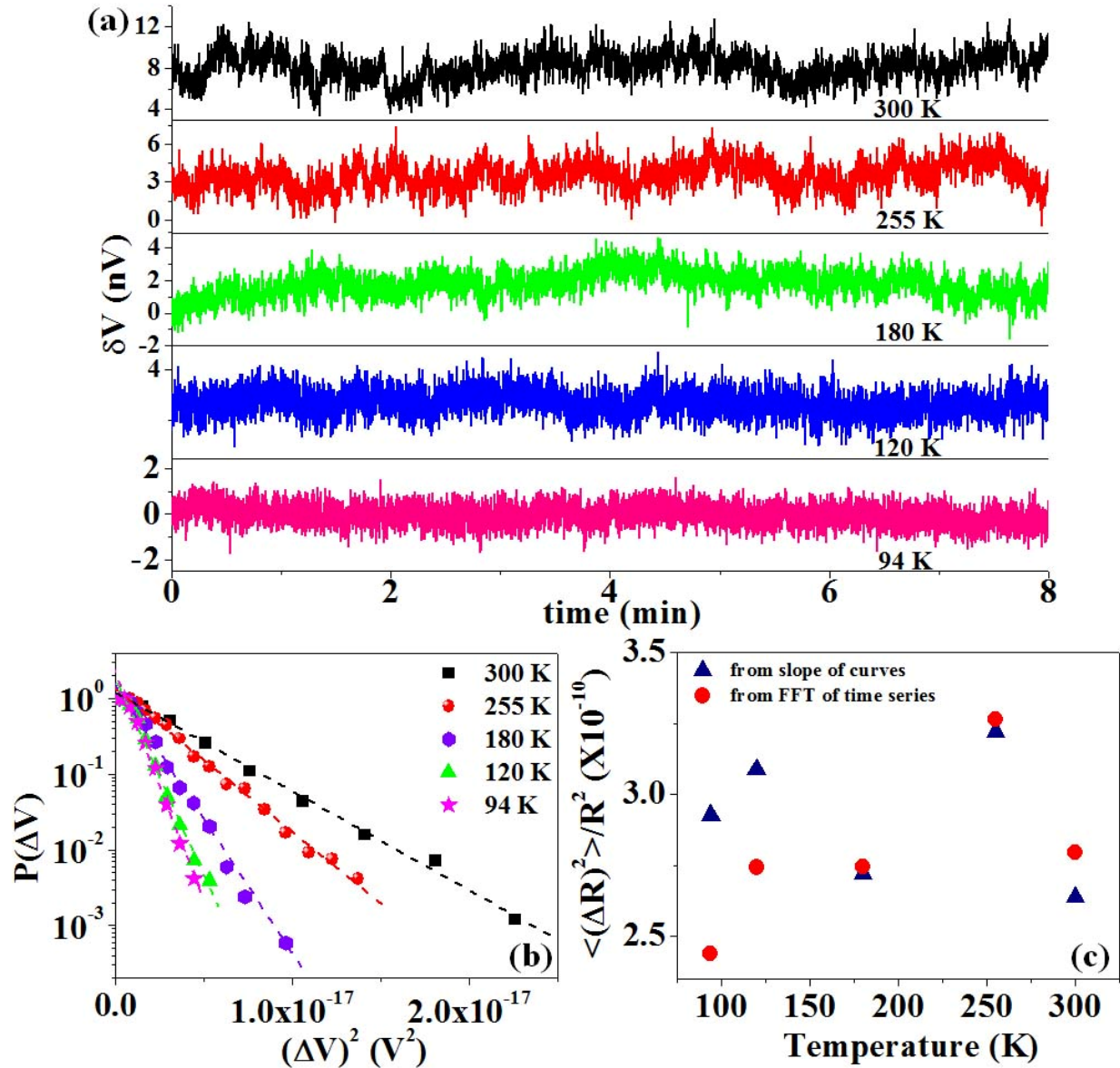


**Figure 3.20:** (a) The raw time series of voltage fluctuations recorded for a  $50 \mu\text{m}$  wire nickel wire at few representative temperatures. (b) The Probability Density function (PDF) of voltage fluctuations were measured from the above time series. Logarithm of  $P(\Delta V)$  is plotted against  $(\Delta V)^2$  and gives straight line. The inset shows the relative variance of voltage fluctuations calculated from PDF analysis (open circles) and from FFT of time series (closed circles).

### b. Second spectrum calculation and analysis

We further extend our analysis for the distribution other than Gaussian distribution. Then we have to study the nature of the noise power determined from various measurements and to compare

it with that expected from Gaussian noise [30, 31]. One of the way one can do analysis of non-Gaussian noise data is to use higher order moments and look into the variation of spectral power. This can be quantified by the second spectrum of the noise data, we explain this below. To calculate the second spectrum of noise we have to obtain repeated measurements of noise power over a frequency band to form a time series of noise power. The power spectral density of this time series gives the power spectrum of the fluctuations in noise power within a frequency band of the original spectrum and is called “Second Spectrum”. The second spectrum is fast Fourier transform of four point correlation function expressed as [32]

$$S^{(2)}(f) = \int \langle V^2(t)V^2(t+\tau) \rangle \cos(2\pi f\tau) d\tau \quad (3.37)$$

If we take infinite time approximation, the estimated power at any frequency component will not vary with time and hence the second spectrum will be identically zero. Every frequency component of the spectrum has a finite variance due to the finite bandwidth of measurement is called “noise in noise”. For uncorrelated fluctuation processes, the variance or “noise in noise” [31] is expected to have a frequency independent white spectral power.

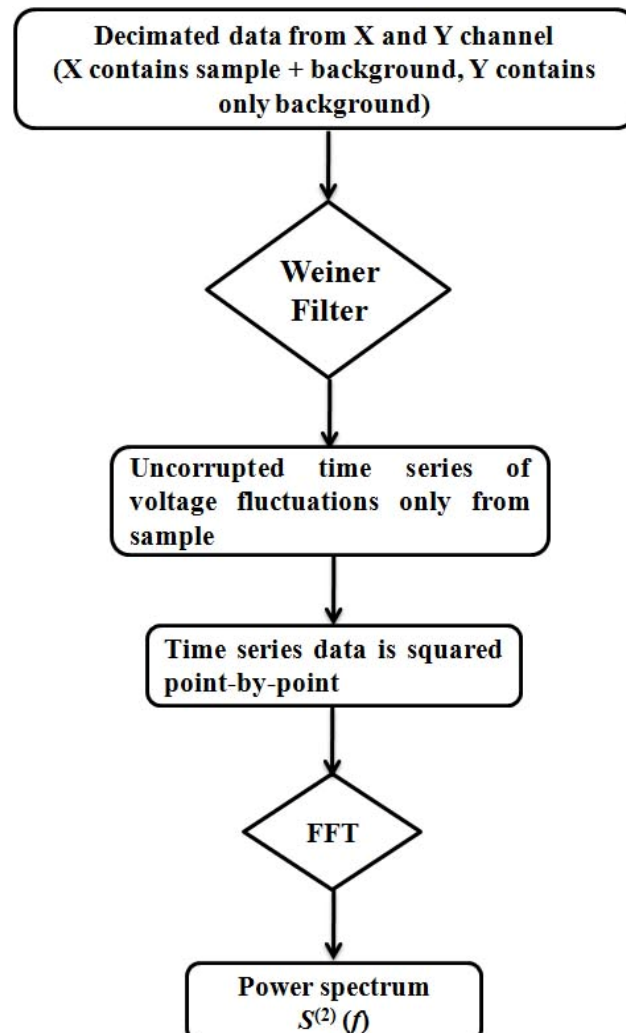


**Figure 3.21:** The flow chart showing the procedure for obtaining second spectrum from the time series data of voltage fluctuations.

The spectral power is called Gaussian background and is given by

$$\begin{aligned} \langle S_P^{(2)} \rangle_{Gaussian} &= 8T \sum_{n=b_L}^{b_H-p} \langle A_{n+p} A_{n+p}^* \rangle \langle A_n A_n^* \rangle \\ &= \frac{2}{T} \sum_{n=b_L}^{b_H-p} \langle S_{n+p}^{(1)} \rangle \langle S_n^{(1)} \rangle \end{aligned} \quad (3.38)$$

where  $b_L = Tf_L$  and  $b_H = Tf_H$ ,  $f_L$  and  $f_H$  are the lower and upper frequency of the bandpass filter,  $T$  is the total time taken for the data collection. We obtain a frequency dependence of second moment when the fluctuators are correlated in time. The scheme of derivation of second spectrum is as flows:

- The raw time series of voltage fluctuations are made uncorrupted by passing it through the Weiner filter.
- This uncorrupted signal is digitally band-passed through a small frequency window, within which the fluctuation of the spectrum is estimated.
- The time series data sequence is squared point-by-point and stored in a specified file.
- The power spectrum generated from this new time series gives the second spectrum.

Figure 3.21 shows the basic algorithm regarding the second spectrum calculations from the original time series of voltage fluctuations.

A typical data of normalized second spectrum for a  $50\mu\text{m}$  nickel wire Fig. 3.22 were calculated using the original time series data (see Fig. 3.21 (a)) is shown in Fig. 3.22. The second spectrum data also indicate Gaussian nature of the noise and the green solid line (in Fig. 3.22) indicates the Gaussian fit of the data. The second spectra data support the data which we already obtained from PDF calculation.

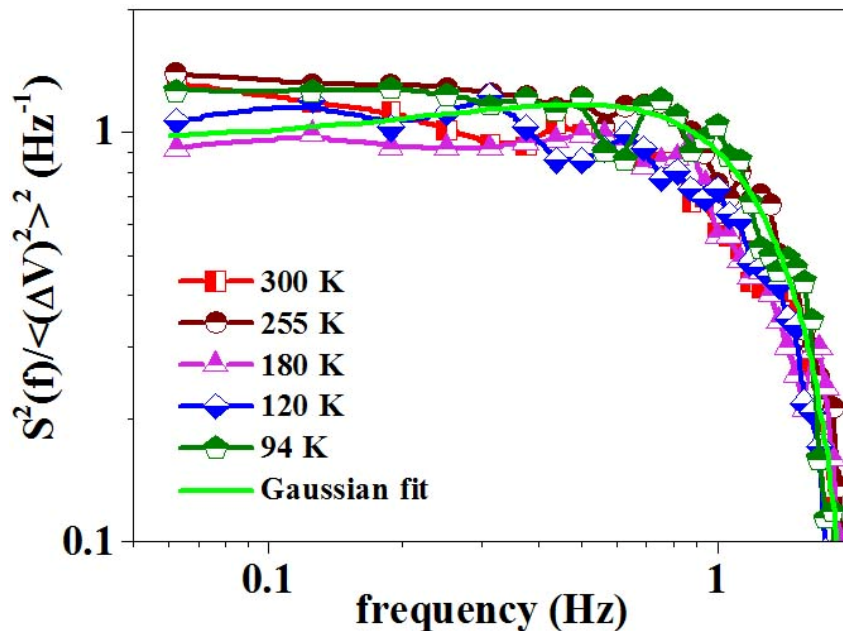


**Figure 3.22:** The plot of normalized second spectrum as a function of frequency at few representative temperatures for a  $50\mu\text{m}$  nickel wire. The solid green line indicates the Gaussian fit of the data. The normalized second spectra show the Gaussian nature of voltage fluctuations in the wire.

## 3.5 Low temperature noise measurement set-up

### 3.5.1 Design of a cryostat

Our experimental set-up is capable of resistivity against temperature measurement and simultaneous noise measurement at various temperatures. The temperature range of our measurement is from 350 K down to liquid Nitrogen temperature 77 K. We have used another cryostat which operates within temperature range from 77 K down to liquid Helium temperature 4.2 K. The complete design of the cryostat is shown in the figure 3.23.

- Cryostat body:** The cryostat is made of two non-magnetic stainless steel (SS 304) hollow cylinders. The outer cylinder has diameter 35 mm and the inner one is of diameter 15 mm. The thickness of the stainless steel sheet is 1 mm. The end of the outer cylinder is closed by 2 mm thick brass disc. An annular flange made of brass with an O-ring groove was welded at the top end. Matching to this flange there is another brass flange welded on the inner tube also, so that it can be screwed vacuum-tightly when the inner tube remains inside the outer one. We have chosen stainless steel because of its mechanical strength and low thermal conductivity through the temperature range we are interested in. In spite of this the top portion of the cryostat generally sits at room temperature whereas the bottom part is at low temperature. So a thermal gradient will arise between the top load and the sample insert. But due to low thermal conductivity of the cryostat material will not destroy the thermal stability at the sample end.

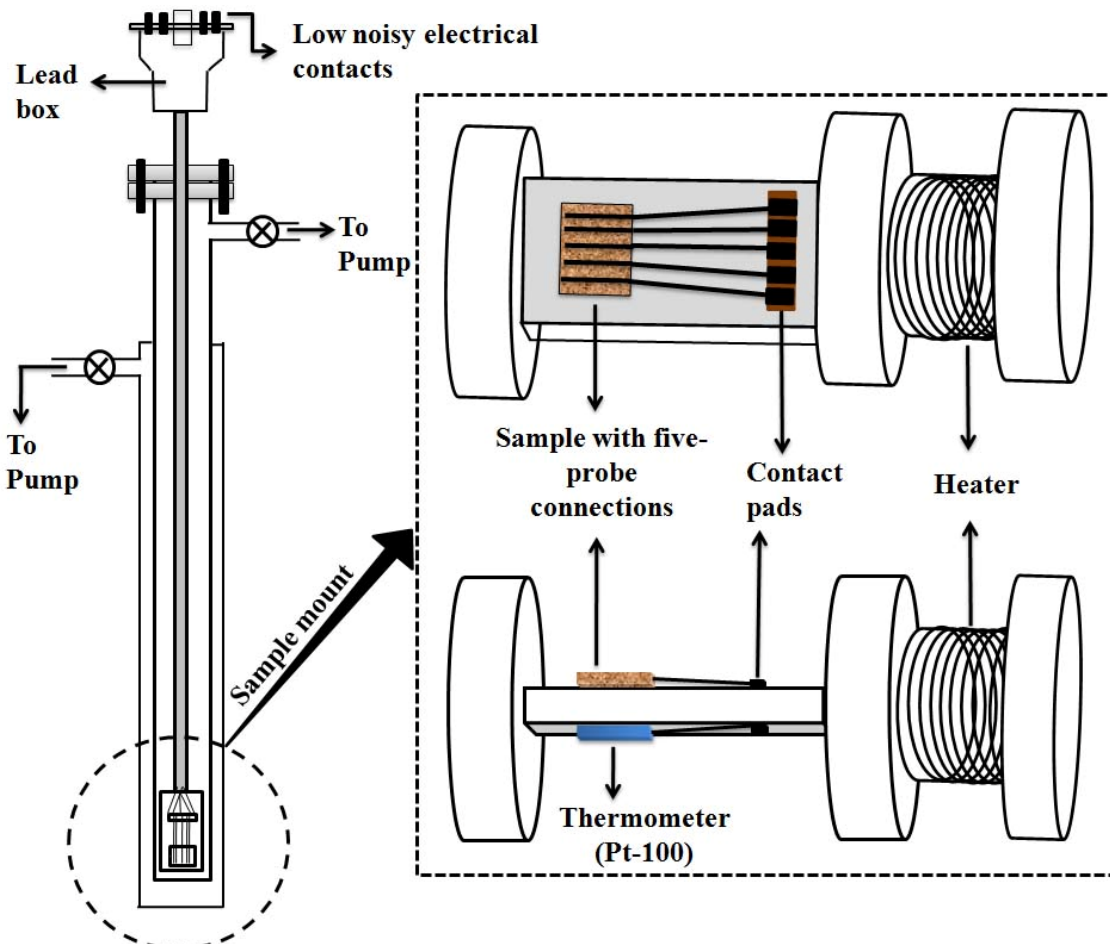
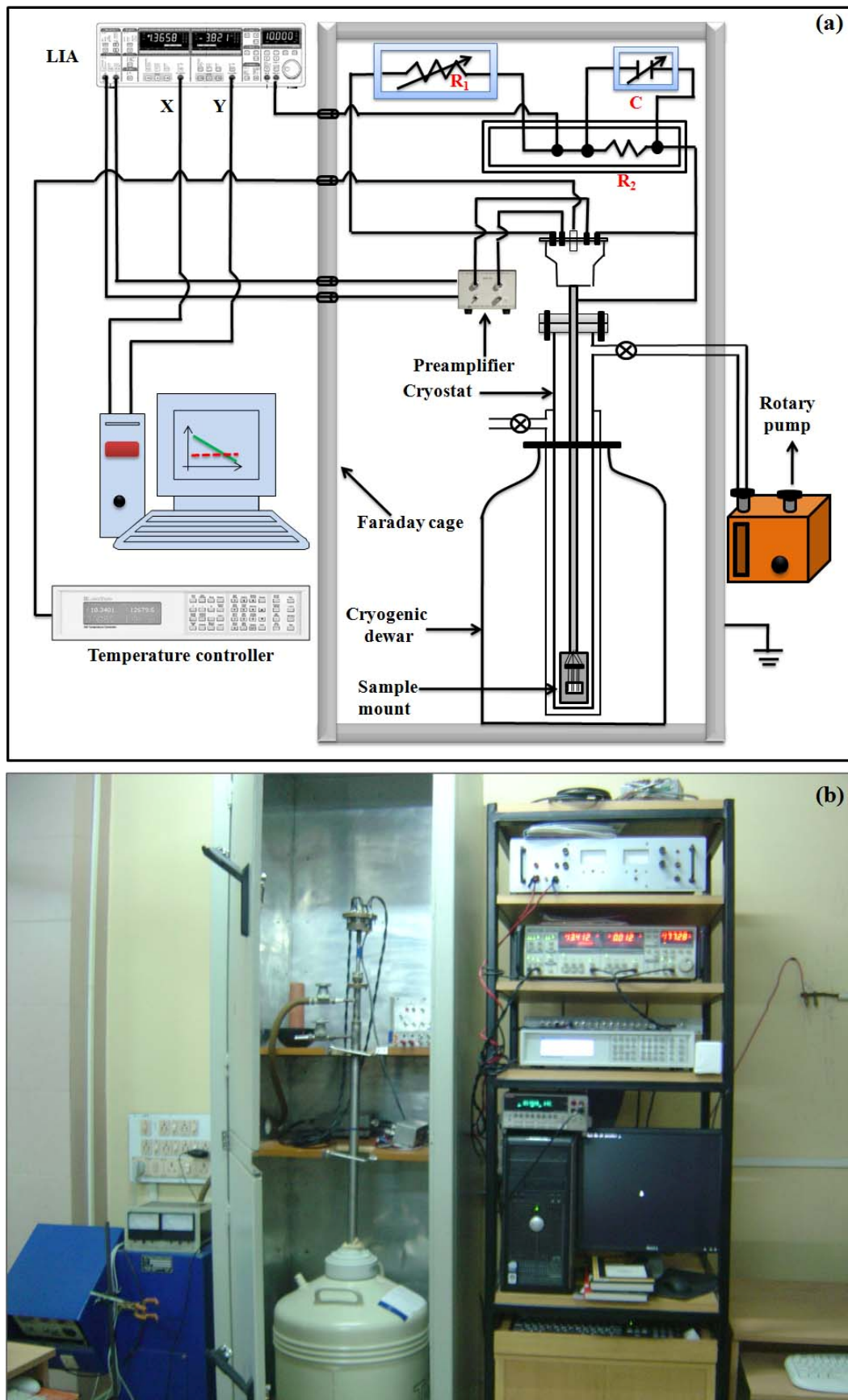


Figure 3.23: A schematic design of the cryostat used for resistivity and noise measurement setup.

- **Lead box:** There is a brass lead box welded on top of the inner tube furnished with vacuum sealed low noisy high quality BNC female connectors and one multipin (8-pins) connector [13].
- **Heater:** The lower end of the inner tube is welded firmly to a blow hole free copper bobbin wended with 4 feet manganin wire ( $12.5 \Omega/\text{feet}$ ) serves as heater in the cryostat.
- **Sample holder:** The bobbin extends as a sample holder made of thick copper plate with dimension  $8 \text{ cm} \times 3 \text{ cm} \times 0.5 \text{ cm}$ . The holder is wrapped with cigarette paper using GE-varnish. The samples are mounted on the sample holder using Apiezon N-grease [33].
- **Thermometers:** Thermometer is mounted on the sample holder by GE-varnish at opposite face of the copper plate where sample is mounted. The thermometer and its leads are carefully mounted and thermalized so that they can contribute very little thermal fluctuations at a particular temperature. The GE-varnish serves as a good thermally conducting but electrically insulating medium requires for any low temperature measurement. We have used two different thermometers for two different temperature ranges of measurements: a Pt-100 film thermometer for 77 K-350 K and a Silicon Diode thermometer (model: Lakeshore DT470) [34] for 4.2 K-77 K.
- **Vacuum:** The outer and the inner cylinders should be good vacuum sealed, otherwise the thermal fluctuations can hamper the sensitive experiments. The top load (sitting at room temperature) will be thermally connected to the sample insert (sitting at low temperatures) due to poor vacuum, which is at all not desirable. The outer cylinder is evacuated by rotary oil pump and the pressure is kept  $10^{-3} \text{ mbar}$  inside it. But the inner cylinder is kept at high vacuum of pressure  $10^{-6} \text{ mbar}$  which is sometimes required for noise experiments. Otherwise the inner cylinder can be maintained vacuum of pressure  $10^{-3} \text{ mbar}$ .
- **Electrical connections:** The electrical connections between sample leads to the BNC connectors have been done by twisted pairs of silver coated coaxial cables. The thermometer and heater connections have been done by twisted copper wires (diameter  $100 \mu\text{m}$ ) terminated to the multipin connector in the lead box. All these cables and wires go through the inner cylinder only. The electrical connections between the BNC and the measuring instruments were made through BNC cable twisted in pair and that between the multipin connector and the instruments were made through a multi core shielded cable [13].

### 3.5.2 The experimental setup

The schematic diagram of our experimental noise setup is shown in the figure 3.24(a) and the actual setup at our laboratory is shown in figure 3.24(b). The four-probe, five-probe, and ac-dc mixing set-up schematics are given in figures earlier. The low frequency and low temperature noise experiments are very sensitive and we have to take lots of precautions to acquire good and reproducible results. The setup is always kept isolated from all external noise sources like electromagnetic radiations, mechanical vibrations, power line fluctuations, any kind of electrical sparking, and improper grounding of the measuring instruments. We have dedicated power supply which is a battery based inverter for the noise measurements. The cryostat along with cryogenic dewars and the measuring electronic instruments (except LIA) are kept in Faraday cage during experiments. Faraday cage is nothing but a huge box made of layers of two metals, mild steel (2 mm thick) and aluminium (1 mm thick) which shields of electromagnetic radiations to interfere the noise experiments. The noise detection circuits (standard resistor in case of four-probe and the ac Wheatstone bridge in case of five-probe as described in section 3.2) are kept in a thick (6 mm) aluminium box. There is a  $\mu$ -metal sheet which covers the inner walls of the box.



**Figure 3.24:** (a) Schematic diagram of noise measurement setup, (b) The actual noise measurement setup at our laboratory.

During the measurement the cryostat is dipped in the liquid Nitrogen or liquid Helium dewars and the temperature at the sample end is measured and read by a digital temperature controller from Lakeshore (model: 340) using PID control. The temperature stability is always maintained  $\sim 2$  mK and we have recorded that this stabilization remains intact for more than 5 hrs. The sample is biased ac voltage by LIA (SR830) and the output voltage from the sample is amplified by preamplifier (SR554/SR560) and again fed to the LIA. The output of the LIA is recorded by ADC card (PCI-DAS6036) through computer. For resistivity measurements we have used GPIB card (IEEE-488.2) [34] for data collection. The sampling rate of ADC card is 1024 samples/sec where as GPIB card data acquisition rate is 10 points/sec, much slower than ADC card. Though GPIB card is insufficient for data acquisition for noise measurements but it suffices the requirements for resistivity measurements.

### 3.5.3 Calibration of the setup

After designing the setup, calibration is always required to check the applicability, sensitivity and reproducibility of any measurement. For calibration we simply calculated Nyquist noise ( $4k_B T R_{sample}$ ) for a standard  $1\Omega$  carbon resistor because the noise depend only those parameters which are completely known to us. The Nyquist noise also helps to find out the accurate thermal noise which is to be subtracted out to extract the actual noise information coming from the sample.

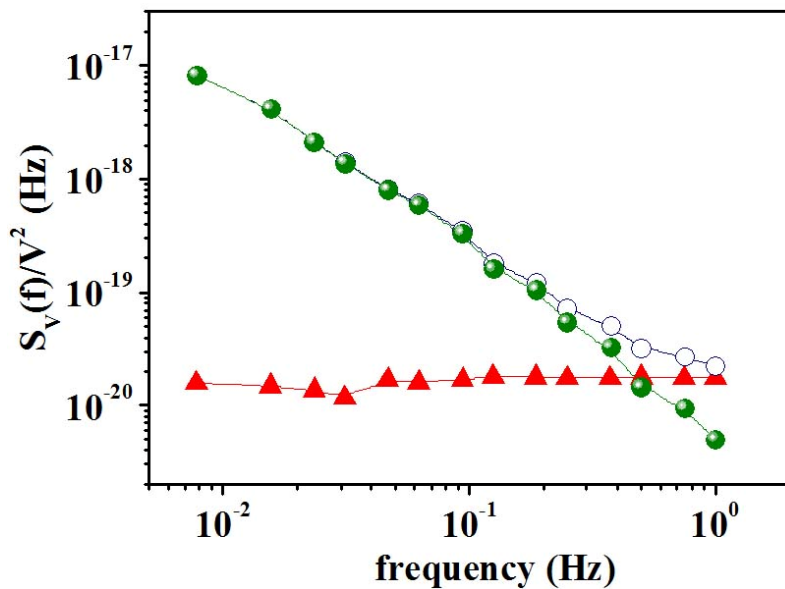


**Figure 3.25:** The noise data for a  $1\Omega$  carbon resistor, open circle and closed circles are total noise (sample noise + background noise) and sample noise (background subtracted) respectively. The triangles are showing for background ( $4k_B T R_{sample} = 1.75 \times 10^{-20} \text{ V}^2/\text{Hz}$ ) only.

If the background noise is much higher than the calculated one ( $4k_B T R_{sample}$ ) then there always exist some other noise sources like ground loops, poor thermal equilibrium, and interference of electrical noises from measuring instruments. As the Nyquist noise is “white”, i.e., frequency independent, we have to check that it should remain flat throughout the measuring frequency bandwidth. The external noise generally hampers this background noise at lower frequencies and a frequency dependent upturn is generally observed, which is not desired. Sometimes the background noise follows the trend (frequency dependence) of sample noise without being flat which is mostly caused by poor thermal equilibrium of the system under investigation. We have to make sure that these

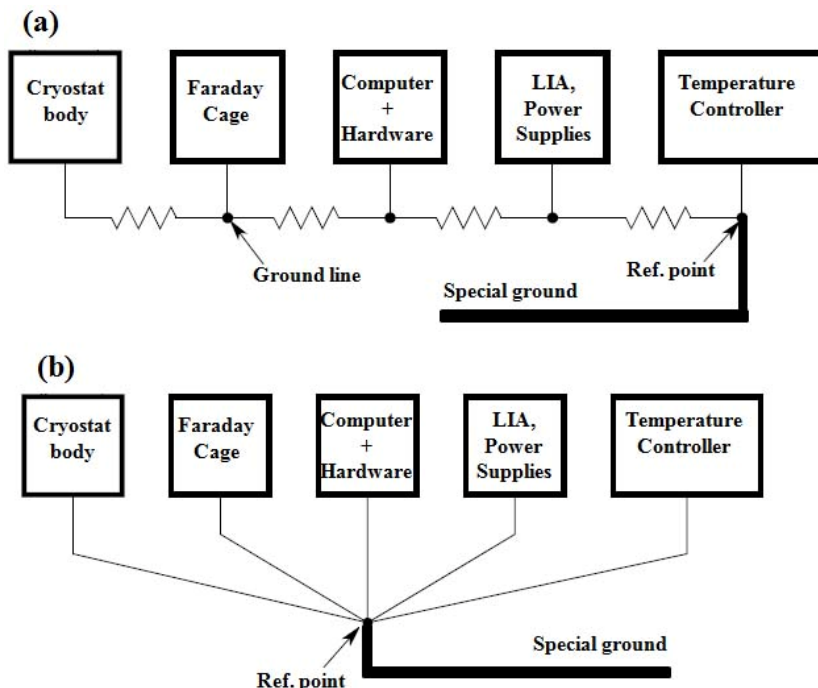
possibilities of errors should be minimized or eliminated before going to any experiment because DSP fails to correct these errors.

Figure 3.25 shows the experimental noise data for  $1\Omega$  carbon resistor (filled circle) at 300 K where background is frequency independent. The estimated Nyquist noise for this sample is  $1.656 \times 10^{-20} \text{ V}^2/\text{Hz}$  and the experimentally obtained value is  $1.75 \times 10^{-20} \text{ V}^2/\text{Hz}$ . It is recommended to make a calibration check of the system before starting a set of experiments. The good calibration depends on a basic criterion, grounding of all instruments related to the setup. We have used “star” grounding for our measurement purposes which we will discuss in the next section.

### 3.5.4 Controlling noise:

#### 3.5.4.1 Grounding:

Controlling noise in measurement systems is vital because it can become a serious problem even in the best instruments and data acquisition hardware. Most laboratories contain abundant electrical-noise sources, including ac power lines, heavy machinery, radio frequency antennas, and a variety of electronic equipment. Radio antennas generate high-frequency noise, while computers and other electronic equipment generate noise in all frequency ranges. Building a completely noise-free environment just for running tests and measurements is seldom a practical solution. Fortunately, simple devices and techniques such as using proper grounding methods, shielded and twisted wires, signal averaging methods, filters, and differential input voltage amplifiers can control the noise in most measurements. Some techniques prevent noise from entering the system, while others remove extraneous noise from the signal. Here we shall discuss how the improper grounding implants erroneous signals during sensitive noise measurements and the possible ways of removal.



**Figure 3.26:** (a) Series ground connection, (b) Parallel ground connection.

- **Grounding conflict:** The most common problem comes from “grounding conflict” when ground as a place in contact with the earth, a common return in an electrical circuit, and an arbitrary point of zero voltage potential. Grounding, or connecting some part of an electrical

circuit to ground ensures safety for personnel and it usually improves circuit operation. Unfortunately, a safe environment and a robust ground system often do not happen simultaneously. It takes planning based on systematically understanding how electricity behaves in various types of circuits. In our lab we have used special type of ground treated as reference node of for this particular instrument. The manner in which these wires connect to the actual reference point determines whether a “series” or “parallel” ground method is being used. The series and parallel ground connections are shown in Fig. 3.26(a) and Fig. 3.26(b) respectively. The series ground connection is pretty common because it’s simple and economical. However, this “cheap and dirty” connection is also the noisiest due to common ground impedance between the circuits (as indicated by the resistor symbol). When several circuits share a ground wire, currents from one circuit (flowing through the finite impedance of the common ground line) can cause variations in the ground potential of the other circuits. If the ground currents are large enough, the variations of the ground potential can cause serious disruptions in the operations of all circuits attached to the common signal ground. The parallel ground connection eliminates common ground impedance problems, but does so at the expense of using a lot of wire. Also, the impedance of each individual ground wire can be very high, and the ground lines themselves can become sources of system noise. Most of the impedance and noise problems can be minimized by choosing the correct size and type of ground conductor. We used thicker stranded grounding wire for each distribution loop. The use of large gauge wire helps reduce the ground resistance, while the use of stranded wire reduces the ground impedance. It is recommended not to use solid wire for the ground distribution loops.

We followed parallel ground connections for our set-up. We have used long solid (diameter 6 mm) copper rod which went inside the ground and serves as a ground wire. The main ac power supply comes from UPS supply of our laboratory is connected to the primary of an isolated transformer input. The output of secondary of that transformer is the main ac line voltage we used to connect all the instruments we have used for our noise measurements. Separate inverter uses the laboratory ground which is not connected to our special ground. So we tried to isolate our ac power line free from any line voltage fluctuations coming from other instruments sharing the same UPS and ground. We grounded all our measuring instruments by terminating their ground paths to a common point, i.e., our special ground point. This connection prevents the internal system from floating at an ac potential between earth ground and the input ac supply potential.

- **Ground loops:** Sometimes, a measurement error is mistakenly attributed to a ground loop problem, especially where a ground is not strictly involved. Any type of unwanted or unexpected current flowing through a ground line is referred as “ground loops”. The basic concept of the ground loop is shown in Fig. 3.27. The true problem arises as earth-ground is not really at the same potential in all locations. Earth ground potential and resistance can vary due to environmental conditions as soil composition, water content, salt contents, time of year, and corrosion of the earth ground conductor. If the two ends of a wire are earth ground at different location, the voltage difference between the “two” ground points can drive significant currents through the wire. The ground loop phenomenon relates to two types of situations; shared current flow in a circuit path, which produces unintended voltages, and inadvertent circuits that interfere with the proper operation of intended circuits. Measuring instruments that contain an earth ground as described above usually generate a ground loop. A ground loop can become a serious problem even when the ground voltage on the measured point equals the ground voltage entering the instrument through the line cord. A voltage that develops between the two grounds can be either an ac or a dc voltage of any value and frequency, and as the voltage and frequency increase, the effects of the ground loop become more troublesome.

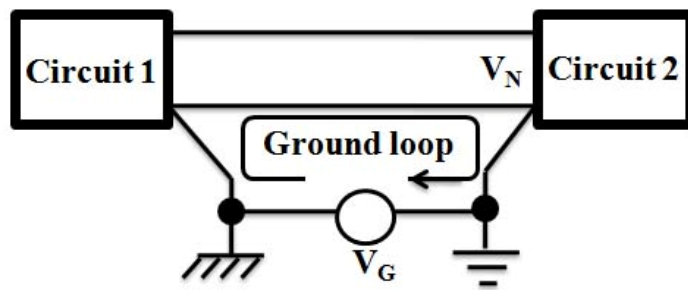


**Figure 3.27:** The schematic diagram of a ground loop affecting the noise measurements.

### 3.5.4.2 Shielded wiring:

Metallic shields placed around equipment and test leads effectively prevent noise from either entering or leaving the system. For example, loose or exposed wires become affected for radio frequency signal pickup, and can form loops that radiate noise. The best instrumentation wiring schemes consist of carefully grouped lines, twisted in pairs, occasionally covered with a second shield, and routed through a dedicated conduit or raceway. A shielded, twisted pair is quite commonly used in a channel to connect a signal from a source to an input terminal. Shields minimize capacitive coupling and twisted wires minimize inductive coupling. Proximity to other wires, especially power wires carrying high voltages and high currents can couple noise into low-level signal conductors. Capacitive coupling can exist between any two pieces of metal in close proximity, including two conductors in totally separate circuits. When the sensor or transducer is in a shielded metallic enclosure, which is also connected to earth ground, the shield may be connected at the sensor end and remain open at the input channel terminals. When the sensor is well insulated, the shield may float and connect to the analog common of the data acquisition system input terminals. Occasionally, multiple-conductor cables composed of a bundle of wires and an overall shield are acceptable for a group of high-level, dc or low-frequency signals, but would not be recommended for the general data acquisition case. Compromising a well planned wiring system with low quality wire, shared conductors or shields, and parallel, untwisted wires will produce less than optimum results. There are two common types of wires are used twisted pair cables (in shielded or unshielded form) and coaxial cables.

- **Twisted pair cables:** The twisted pair cables are generally available in two varieties, shielded and unshielded are shown in figure 3.28 (a) and 3.28 (b) respectively. The shielded variety has a grounded metal wire-braid which gives an extra protection from external interferences. Twisted pair cables are typically bundled together to form 4 or 5-pair twisted pair cables (8 or 10 wires altogether).

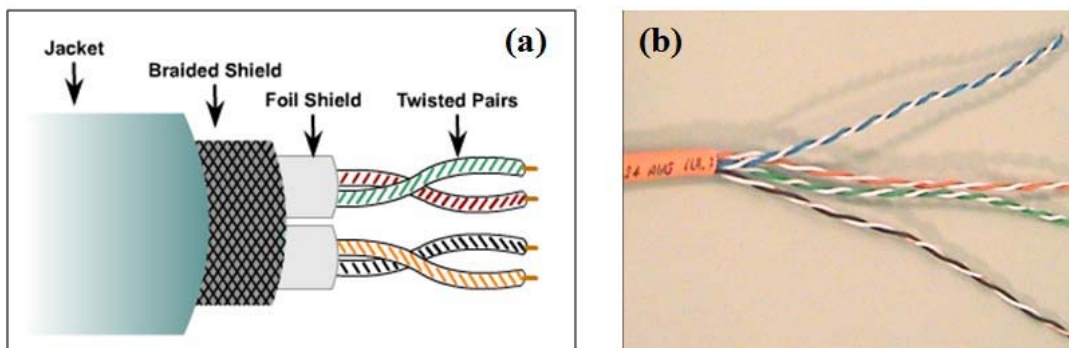


**Figure 3.28:** (a) Shielded twisted pair cable and (b) unshielded twisted pair cables.

- **Coaxial cables:** Coaxial cable consists of a silver/gold coated copper core surrounded by a grounded sheath (usually a woven braided copper mesh with silver coating). The sheath gives the copper core excellent protection from external noise and allows coaxial able to be used near machinery and other sources of electromagnetic radiation. It also reduces attenuation due to the skin effect because less energy can be radiated from the outer surface of the core. Coaxial Cable is commonly used for digital transmission. The coaxial cable we have used has a resistance of 50 Ohms/metre but cables of resistance of 75 Ohms/metre are also available. The schematic diagram of the construction of a coaxial cable is shown in figure 3.29

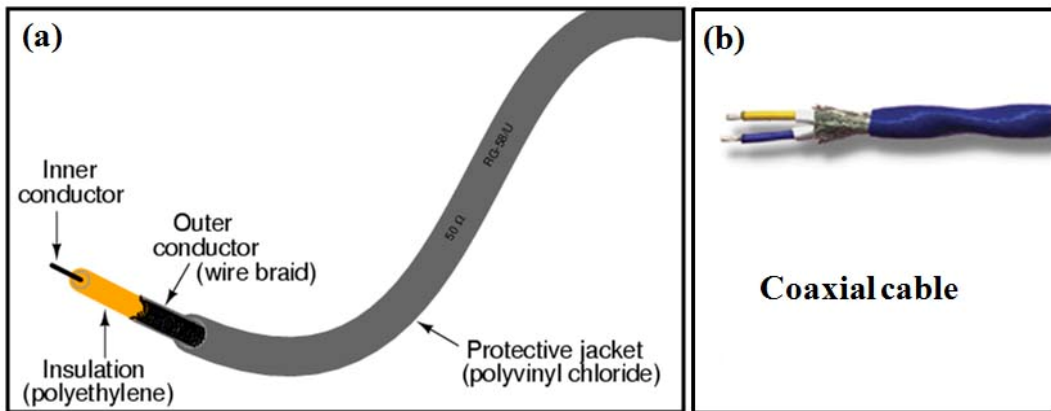


**Figure 3.29:** (a) Schematic diagram of a coaxial cable showing the components of it and (b) the actual coaxial cables available commercially.

In the following chapters we discuss the results of the resistance and resistance fluctuation measurements carried out on different sample like thin films, single crystals and nanowire using the experimental techniques described in this chapter.

## Bibliography:

- [1] Arindam Ghosh, PhD Thesis, Indian Institute of Science, Bangalore, India (2000).
- [2] Sh. Kogan, “Electronic noise and fluctuations in solids”
- [3] J. H. Scoffield, Rev. Sci. Instr. **63**, 4327 (1992)
- [4] J.H. Scofield, *Rev. Sci. Instrum.*, **58**, 985 (1987)
- [5] Arindam Ghosh, Swastik Kar, Aveek Bid and A. K. Raychaudhuri, *arXiv:Cond-Mat./0402130 v1*, 4th Feb (2004).
- [6] User Manual: SR830 Lock-in Amplifier, Stanford Research Systems, Inc. 1290-D Reamwood Ave, Sunnyvale, CA 94089, USA, <http://www.srsys.com>.
- [7] Use Manual: PCI-DAS6036, Measurement computing, 16 Commerce Boulevard, Middleboro, Massachusetts 02346 USA. <http://www.mccdaq.com>
- [8] Users Manual: SR554 Preamplifier, Stanford Research Systems, Inc. 1290-D Reamwood Ave, Sunnyvale, CA 94089, USA, <http://www.srsys.com>.
- [9] Users Manual: SR560 Preamplifier, Stanford Research Systems, Inc. 1290-D Reamwood Ave, Sunnyvale, CA 94089, USA, <http://www.srsys.com>
- [10] User Manual: Model 2000 digital multimeter, Keithley Instruments, Inc. 287775 Aurora Road, Cleveland, Ohio 44139, <http://www.keithley.com/products/dmm>
- [11] 1433-F Decade Resistor, General Radio, USA; Model N-1, Sr No. 99 Nessler Electronic and Scientific Instrument, 634-35, H. B. Colony, Ambala Cantt - 133 001. India.
- [12] Laboratory Standard Condenser, H.W. Sullivan Ltd., London, U.K.
- [13] RS Components & Controls (India) Ltd. 44, Okhla Industrial Estate Phase III, New Delhi 110020, Delhi, India.
- [14] Achyut Bora, Ph.D thesis, Indian Institute of Science, Bangalore, India.
- [15] Aveek Bid, Ayan Guha, and A. K. Raychaudhuri, Phys. Rev. B **67**, 174415 (2003)
- [16] D. J. DeFatta, J. G. Lucas and W. S. Hodgkins, *Digital Signal Processing*, (John Wiley and Sons , NY, 1988)
- [17] S.K. Mitra, *Digital Signal Processing: A Computer Based Approach*, (Tata McGraw Hill, New Delhi, 2001)
- [18] P.S.R. Diniz, E.A.B. da Silva and S.L. Netto, *Digital Signal Processing: System Analysis and Design*, (Cambridge University Press, Cambridge, UK, 2002)
- [19] A.V. Oppenheim, R.W. Schafer and J.R. Buck *Discrete-Time Signal Processing*, (Pearson Prentice Hall, 2006)
- [20] A. Ghosh “*Low frequency Conductance Fluctuation near metal-insulator transition*” Ph.D thesis (1999), Indian Institute of Science, Bangalore, India .
- [21] S. Kar “*Spectral analysis of Conductance Fluctuations in doped Silicon near the Mott-Anderson transition*” Ph.D thesis (2003), Indian Institute of Science, Bangalore, India.
- [22] A. Bid, “*Resistance Fluctuation and Instability in Metal Nanowire*”, Ph.D. Thesis (2006), Indian Institute of Science, Bangalore, India
- [23] J. S. Bendat and A. G. Piersol, *Random Data: Analysis and Measurement Procedures* (Wiley-Interscience, 1971)
- [24] P. D. Welch *Modern Spectral Analysis*, Edited by D.G. Childers (IEEE press, John Wiley and Sons, New York, 1978) page 17.
- [25] W. H. Press, S. A. Teukolsky, W. T. Vetterling and B. P. Flannery *Numerical Recipes*, (Cambridge University Press, Cambridge, UK, 1993).
- [26] H. J. Nusbaumer, *Fast Fourier Transform and Convolution Algorithms*, (Springer-Verlag, New York 1984)
- [27] M. Nelkin and A. M. S. Tremblay, J. of Stat. Phys. **25**, 253 (1981).
- [28] Sudeshna Samanta, A. K. Raychaudhuri, and Joy Mitra, Phys. Rev. B **78**, 014427 (2008)

- [29] S. Kar, A. Ghosh and A. K. Raychaudhuri , Phys. Rev. Lett. **91**, 216603 (2003).
- [30] M. B. Weissman, Rev. Mod. Phys. **65**, 829 (1993).
- [31] P. J. Restle, M. B. Weissman and R. D. Black, J. Appl. Phys. **54**, 5844 (1983).
- [32] G. T. Seidler and S. A. Solin, Phys. Rev. B **53**, 9753 (1996).
- [33] <http://www.apiezon.com/grease.htm>
- [34] <http://www.lakeshore.com/temp/sen/crt.d.html>
- [35] <http://www.keithley.com/>

# Chapter 4

## Study of very low frequency resistance fluctuations in perovskite manganite films

### 4.1 Introduction

The most canonical example of perovskite manganites are the doped manganite systems  $\text{La}_{1-x}\text{Ca}_x\text{MnO}_3$  which are medium bandwidth systems and are more susceptible to the lattice and other interactions. These mixed valence manganites are interesting because of the interplay between charge, spin, orbital, and structural degrees of freedom. This gives rise to a multitude of ordered phases and thus a very rich phase diagram as we discussed in Chapter 1. There are varieties of ordered ground states for manganites, ranging from ferromagnetic metallic state to charge and orbital ordered insulating states that can also have antiferromagnetic spin order. The presence of interactions of comparable strengths provide a delicate energy balance so that ground states sometimes may not be homogeneous, leading to mesoscopic electronic phase separation [1, 2]. The electronic phase separation that leads to this inhomogeneity couples to a number of physical properties and are ill understood. It is well established that for optimal doping concentration, i.e.,  $x \approx 0.33$ , the material undergoes a paramagnetic to ferromagnetic phase separation ( $T_c$ ) accompanied by a metal-insulator transition at the same temperature. Investigation of resistance fluctuations (noise) phenomena in the ferromagnetic metal (FMM) and paramagnetic insulating (PMI) (below the Curie temperature  $T_c$ ) states in manganite thick films of composition  $\text{La}_{0.67}\text{Ca}_{0.33}\text{MnO}_3$ . The  $\text{La}_{0.67}\text{Ca}_{0.33}\text{MnO}_3$  is abbreviated as LCMO33. LCMO33 grown on oriented single crystalline  $\text{SrTiO}_3$  substrates is the main theme of this chapter. We further study the phenomena of phase coexistence by using noise spectroscopy.

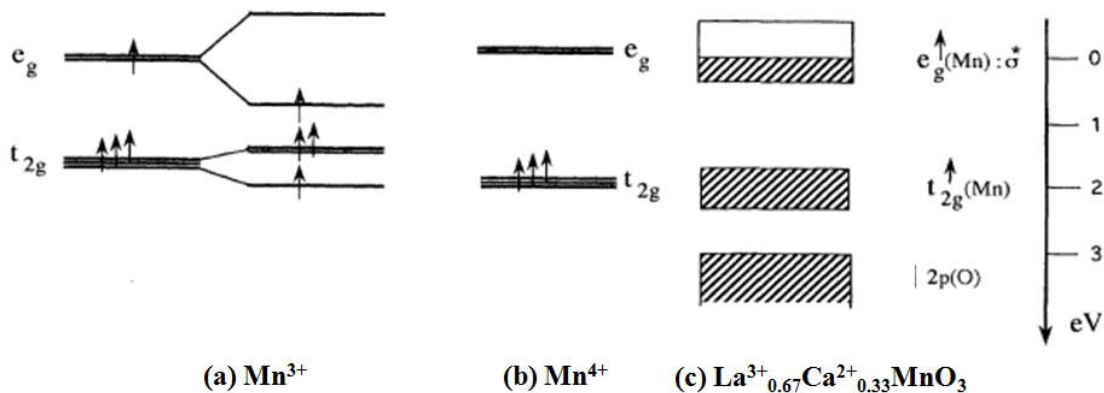


**Figure 4.1:** Electronic structure of (a)  $\text{Mn}^{3+}$  in octahedral coordination, before and after Jahn-Teller distortion; (b)  $\text{Mn}^{4+}$  in octahedral coordination; (c) energy band diagram in ferromagnetic manganites  $\text{La}_{0.67}\text{Ca}_{0.33}\text{MnO}_3$  (adapted from reference [8]).

For the specific system  $\text{La}_{1-x}\text{Ca}_x\text{MnO}_3$  for  $x = 0.22-0.4$ , there is a well defined paramagnetic to ferromagnetic transition at  $T_c$  on cooling and also a transition from a polaronic insulating state at high temperature to a ferromagnetic metallic state at low

temperature, which results in a peak in resistivity at  $T_p$ . Typically in good manganite samples,  $T_c \sim T_p$ . Besides the colossal magnetoresistance (CMR) effect near the paramagnetic (insulator) to ferromagnetic (metal) transition at  $T_c$  ( $T_p$ ), also distinguish themselves by the small coercive field and high spin polarization at the low temperature ferromagnetic region [3, 4]. Sample with optimal concentration  $x \approx 0.3$  exhibit a large peak in resistivity below  $T_c$ , which has been attributed to spin-disorder scattering of magnetic polarons [5]. Ferromagnetism occurs in the composition range  $0.1 < x < 0.5$ , where it is associated with the simultaneous presence of Mn<sup>3+</sup> and Mn<sup>4+</sup> ions as we discussed in Chapter 1 [6]. The end members ( $x = 0$ , and  $x = 1$ ) are antiferromagnetic insulators. But the intermediate compounds exhibit high conductivity and magnetization approaching the spin-only value expected for a ferromagnetic mixture of Mn<sup>3+</sup> ( $3d^4$ ) and Mn<sup>4+</sup> ( $3d^3$ ) ions. The trivalent manganese is severely Jahn-Teller distorted in octahedral sites whereas the fourth manganese  $d$  electrons, the  $e_g^\uparrow$  electrons, becomes delocalized with increasing  $x$  hopping among Mn<sup>4+</sup> ion cores. The <sup>55</sup>Mn hyperfine interaction [7] also reveals that the structure is orthorhombic with a  $(\sqrt{2}a_0, \sqrt{2}a_0, 2a_0)$  superstructure of the elementary cubic perovskite cell and O-Mn-O bonds are sufficiently linear so that the ground state is ferromagnetic. The charge carriers are delocalized and Jahn-Teller (JT) distortions are suppressed. The electronic band structure of LCMO33 is illustrated in Fig. 1; the  $e_g(\sigma^*)$  band is of energy 1 eV and the  $t_{2g} - e_g$  energy band gap is 1.5 eV wide. The  $2p(\text{O})$  level lies 3.0 eV below the Fermi energy level and the carrier density in the  $e_g(\sigma^*)$  band is  $4.5 \times 10^{27}$  electrons/m<sup>3</sup> [8].

However, for manganite films it is known that their transport properties are strongly affected by the film thickness, e.g., at the nanometer scale the films have  $T_p$  ( $T_c$ ) different from those of the thick films or bulk materials (bulk LCMO33 has  $T_p \sim 250$  K [9]) at the same doping level. Table. 1 represents some published data regarding the variation of  $T_p$  ( $T_c$ ) depending on the film thickness of LCMO33 grown on single crystalline SrTiO<sub>3</sub> substrates [9-24]. This effect may reflect the decrease of spin polarization at the interfaces and is thought to be detrimental to the performance of devices like the spinpolarized tunnel junctions [25, 26]. Although being extensively studied, the thickness effect has not been properly explained yet owing to the involvement of a variety of factors, mainly the biaxial strain induced by substrates, dimensional effects, and the oxygen deficiency as well.

The ferromagnetic metallic state observable in LCMO33 differs from the metallic state of conventional metals. Due the inadequacy of double exchange model there are several theoretical models to explain these systems. Millis *et al.* [27] argued that the physics in the paramagnetic (PM) phase is dominated by the interplay between a strong electron-phonon coupling and the large Hund coupling effect that optimizes the electronic kinetic energy by the generation of a ferromagnetic (FM) phase. A dynamical JT effect was proposed, at hole doping  $x > 0.2$  and  $T > T_c$ , without leading to long-range order but the strong electron-phonon coupling localizes the conduction band electrons as polarons. As a result the paramagnetic phase dominated by these polaronic effects which are strongly suppressed in FMM phase. The polaron effect being turned off as  $T$  is decreased through  $T_c$ , permitting the formation of a metallic state. Some experimental evidence and theoretical work [28] also predict that polaronic distortions present in the PM phase, persist in the FM phase. In this case, the high temperature competition for the FMM phase is not with the ordered mixed-valent insulator, but with something resembling a melted version of it- generally called a

“polaronic liquid”. Such polaronic effects giving rise to regions of varying conductance in the sample, which is termed “phase separation”.

| SL. No. | Reference   | Substrates (orientation)   | Film thickness $t$ (nm) | $T_p$ (K)         | Method of film growth        |
|---------|---|--|-------------------------|-------------------|------------------------------|
| 1.      | Bibes <i>et al.</i> (2002) [11]   | SrTiO <sub>3</sub> (001)   | 6                       | 110               | rf sputtering                |
| 2.      | -do-  | SrTiO <sub>3</sub> (001)   | 12                      | 130               | „                            |
| 3.      | Chou <i>et al.</i> [12]   | SrTiO <sub>3</sub> (001)   | 20                      | 146               | „                            |
| 4.      | Bibes <i>et al.</i> (2002) [11]   | SrTiO <sub>3</sub> (001)   | 27                      | 150               | „                            |
| 5.      | Pranjape <i>et al.</i> (2003) [13]<br>Reutler <i>et al.</i> (2000) [14]                                   | SrTiO <sub>3</sub> (002)<br>SrTiO <sub>3</sub> (001)                             | 40<br>110               | 198<br>110        | PLD<br>MBE                   |
| 6.      | Pranjape <i>et al.</i> (2003) [15]  | SrTiO <sub>3</sub> (002)   | 50                      | 276               | PLD                          |
| 7.      | Bibes <i>et al.</i> (2002) [11];<br>Bibes <i>et al.</i> (2001) [16]                                       | SrTiO <sub>3</sub> (001)   | 54                      | 246               | rf sputtering                |
| 8.      | Marithew <i>et al.</i> (2000) [17];<br>Palanisami <i>et al.</i> (2001) [18]                               | _____  | 70                      | 153               | MBE                          |
| 9.      | Bibes <i>et al.</i> (2001) [16]   | SrTiO <sub>3</sub> (001)   | 108                     | 260               | rf sputtering                |
| 10.     | Bibes <i>et al.</i> (2001) [16]   | SrTiO <sub>3</sub> (001)   | 180                     | 270               | rf sputtering                |
| 11.     | Pranjape <i>et al.</i> (2003) [13]<br>Mathur <i>et al.</i> (1997) [19];<br>Chou <i>et al.</i> (2006) [12] | SrTiO <sub>3</sub> (002)<br>SrTiO <sub>3</sub> (002)<br>SrTiO <sub>3</sub> (001) | 200<br>200<br>200       | 215<br>240<br>242 | PLD<br>PLD<br>rf sputtering  |
| 12.     | B. Ghosh <i>et al.</i> (2004) [20]  | SrTiO <sub>3</sub> (002)   | 500                     | 270               | Chemical Solution Deposition |

**Table 4.1:** A survey of published literature on variation of  $T_p$  with LCMO33 film thickness  $t$  grown on oriented single crystals of SrTiO<sub>3</sub> substrates.

#### 4.1.1 Microscopic fluctuations: Phase separated!

In Chapter 1, we have already discussed how charge, spin, orbital ordering, lattice preserve the delicate energy balance in manganite systems. This critical balance is very susceptible to a number of external perturbations. The overwhelming properties of manganites are stabilized by several competing interactions which make the system inhomogeneous. Fig. 4.2 reproduced from Moreo *et al.* [29] shows that in all phases, including the FMM one, and even at high temperatures, inhomogeneities have been unveiled. The particular experimental technique(s) on the basis of which was one can obtain the information corresponding to the particular  $x$  -  $T$  region is mentioned also. In literatures we find names like “droplets”, “domains”, “clusters”, “polarons”, and other, but they all refer to the same notion: the system is inhomogeneous [1].

de Gennes had suggested that FM ground state of La<sub>1-x</sub>Ca<sub>x</sub>MnO<sub>3</sub> is reached by hole doping of the parent compound LaMnO<sub>3</sub> by interpolation through a canted antiferromagnetic (AF) state [29]. The detailed theoretical studies based on one-orbital model [30] showed that instead of a canted state, an electronic “phase separated” (PS) regime interpolates between hole doped FM and undoped AF phase. Such carrier rich and deficit regions can extend up to few lattice spacings. The low doped manganites have AF regions and large FM regions can be achieved when critical doping concentration is reached. The carrier concentration mismatch effect is least in the middle of the FM region in phase diagram (see Fig. 4.2). Still

carrier concentration driven inhomogeneities were reported from different experiments like muon spin resonance [32], x-ray absorption [33], optical experiments [34] etc. In the high temperature, polaron like inhomogeneities were inferred from neutron scattering [35, 36] and x-ray absorption [37] experiments. In all cases, the characteristic length scales of the localized charges were of the order of a few lattice spacings, or 1-2 nm. Moreover, some of the experiments also predict that in PS regime, there may be a percolative kind of metal-insulating transition (MIT), where the insulating phase grows at the cost of the metallic ones as  $T_C$  is approached until it goes over to the high temperature insulating phase.

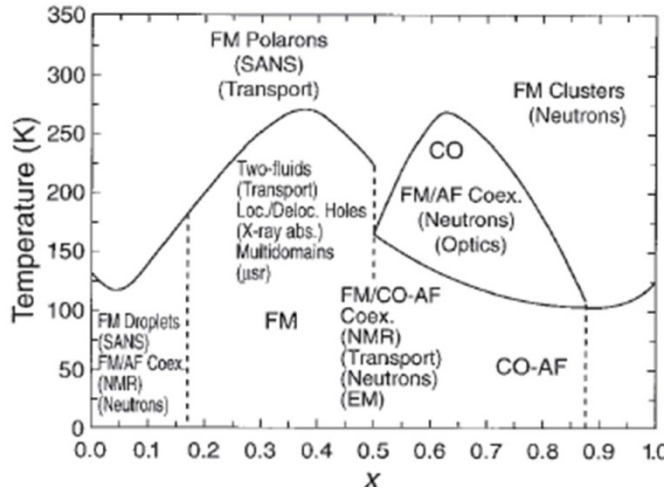


Figure 4.2: Schematic phase diagram of  $\text{La}_{1-x}\text{Ca}_x\text{MnO}_3$  from Moreo et al. [29].

From phase diagram we can observe that for  $x = 0.33$ , there exists a definite FMM to PMI transition and following the above discussion one can expect the presence of inhomogeneous region near MIT. In the PS regions, there exists two or more different phases in thermodynamic equilibrium. These thermodynamic phases generally occurs either because of disorder (where one phase is more favourable than the other) or because of an imposed conservation law. The change in external parameters e.g. mechanical strain, temperature, pressure, volume etc, two phases readjust themselves in two different proportions and this readjustment directly tunes the electrical and magnetic properties of these physical systems.

NMR studies are well known probe to study the ionization state and the local magnetic environment of  $^{55}\text{Mn}$  atoms. The coexistence of Mn(IV)/Mn(III) species can be found out by it to search the presence of metallic regions in the system [38]. Since the NMR is sensitive only to the local environment level, it fails to establish the existence of two thermodynamic phases.

Neutron data has been used to investigate short-range and long-range ordering. In LCMO33, zero-field neutron echo studies have found out the low temperature FM phase and presence of inhomogeneity in the system in a length scale of  $\leq 30\text{\AA}$ . The parallel muon studies suggest that the spin dynamics are quite different at different regimes and carrier concentration inhomogeneities reported at low temperatures from muon spin resonance [39]. Moreover, the low temperature FM phase consists of soft zone boundary of magnons and phonons and this idea is supported by inelastic neutron scattering experiments [40] also.

The existence of Jahn-Teller distortions with short range correlations and existence of local magnetic clusters were revealed by Small angle neutron scattering (SANS) studies [41]. These experiments clearly indicate that there are inhomogeneous regions over length scales comparable to unit cell dimensions. In some cases inhomogeneities may occur in longer length scales. The idea of the low temperature phase separated regime, also predicts a

percolative kind of metal-insulator transition, where the insulating phases grow at the cost of metallic ones as  $T_c$  is approached until it goes over to the high temperature insulating phase. These inhomogeneity form the subject of our interest and this chapter is dedicated to study the nature of their existence.

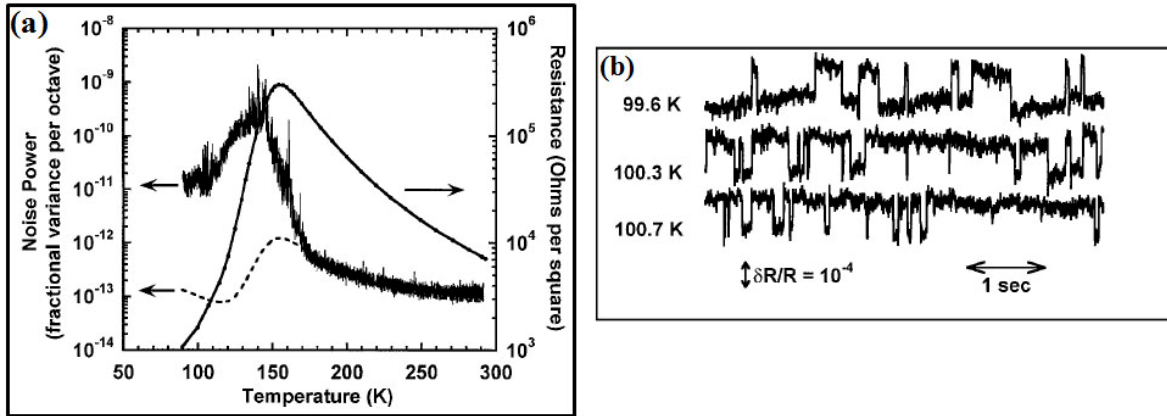


**Figure 4.3:** (a) Temperature variation of resistance and normalised noise power for  $\text{La}_{0.67}\text{Ca}_{0.33}\text{MnO}_3$ . (b) Time traces exhibiting discrete fluctuators at different temperatures. Note: The high resistance state is favoured at higher temperatures [17].

We have discussed various probes to investigate the phenomena of “phase separation” for the coexistence of mesoscopic and macroscopic/microscopic thermodynamic phases. Low frequency resistance fluctuation (noise) also indicates the two-phase coexistence; and is used as an important probe to study the phase separation in manganites. In this chapter noise has been studied extensively in the manganite systems which will give us important information about the coexistence phases in these materials. This idea will help us to build up the basis of our experiments to understand the underlying physics of manganites.

In addition to the conventional transport measurements, noise spectroscopy has been used earlier to study the dynamics of phase separation [42-45]. Figure 4.3(a) shows the variation of integrated noise data ( $S_v(f)/V^2$ ) and resistivity for  $\text{La}_{0.67}\text{Ca}_{0.33}\text{MnO}_3$  with temperature. The data is for 70 nm thick epitaxial film on STO, deposited by MBE [17]. We, however note that though the film has been grown by MBE it has an unusually broad transition and very low  $T_c$  ( $\sim 155$  K). This will imply that this film may be highly strained and has high degree of inhomogeneity. In general films of LCMO grown on STO of lower thickness show this behaviour although with  $T_c \sim 200$  K. The above results show that noise peaks up near transition temperature. This data indicated the possibility of percolation like transitions between high and low conducting phases. For such inhomogeneous transitions consist of two-level discrete resistance fluctuation process as shown in Figure 4.3(b).

There are reports [14, 46, 47] showing the sample resistance fluctuates between two resistance values, like a two-state system, giving rise to random telegraphic noise (RTN) as we discussed already in Chapter 1. The resistance fluctuation in these films is generally attributed to electronic phase separation and phase coexistence of the high resistance (paramagnetic) and low resistance (ferromagnetic) phases. Notably, the data (see figure 4.3(b)) shows that the high resistance state is more favoured at higher temperatures. It is the coexistence of these phases and the dynamical nature of the phase equilibrium that determines the time scale of the resistance fluctuations. The authors have found that for difference between two magnetic moments  $\Delta\mu$  (in two states)  $\approx 2\mu_B$  per unit cell typical size

of the fluctuators are  $10^4$ - $10^5$  unit cells. This data was supported by the results obtained by Palanisami et al. [48].

Hess *et al.* [49] reported the presence of two-state resistance switchers in single crystals of LCMO33 near mesoscopic phase separation. Most of the studies investigated noise with spectral power  $S_V(f)/V^2 \sim 1/f$  (the “ $1/f$ ” noise), a wealth of physical information came from discrete fluctuators that typically occur in small temperature windows for  $T < T_C$ .

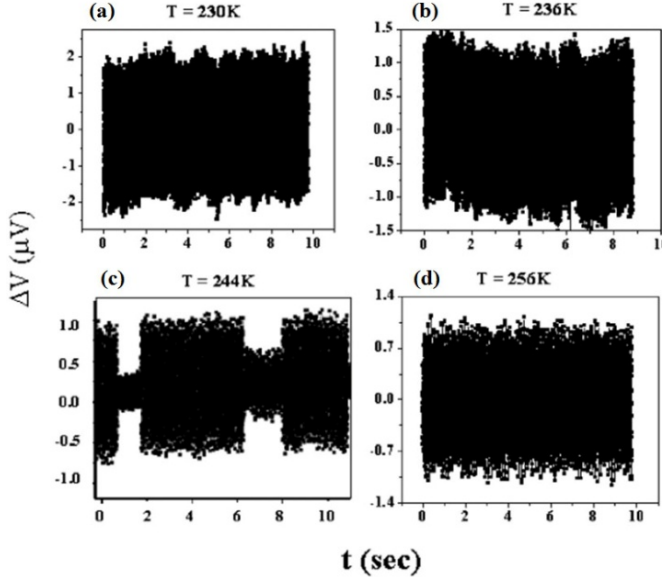


**Figure 4.4:** The time series of voltage fluctuation ( $\Delta V(t)$ ) at four representative temperatures in the range  $0.94 \leq T/T_{CO} \leq 1.04$ . (a), (b), (d) have voltage fluctuations which give rise to  $1/f$  noise in power spectral density. (c) The voltage fluctuates between “high” and “low” volatage levels and give rise to RTN [50].

We note that coexisting phases giving rise to discrete fluctuators have been seen in the case of charge ordering transition ( $T_{CO}$ ) also. Existence of low frequency discrete fluctuators showing RTN (along with broadband  $1/f$  noise) have been observed in single crystals of  $Pr_{0.7}Ca_{0.3}MnO_3$  (PCMO) reported by Bid *et al.* [50], which shows a transition from a paramagnetic insulating (PMI) state to a charge ordered insulating (COI) state. They clearly showed that at  $T \sim T_{CO}$ , there exists RTN type jumps in the time series (voltage fluctuations  $\Delta V(t)$  had been recorded with time) as shown in Figure 4.4. Only at temperature  $0.96 \geq T/T_{CO} \geq 1.04$  (see Figure 4.4 (c)), RTN dominates over  $1/f$  noise. Outside this temperature window only  $1/f$  noise (see Figure 4.4 (a), (b), and (d)) was observed and they suggested that RTN was not appearing either it doesn’t exist due to finite observation time consideration or has a very small magnitude beyond the detection limit. They also suggested that voltage fluctuation oscillates between a “high” fluctuation and “low” fluctuation level which gives rise to RTN type fluctuations. They recorded presence of a substantial component of  $1/f$  noise in the power spectra within each “high” and “low” stage voltage jumps.

These two-level fluctuation (TLF) processes were observed earlier by Anane *et al.* [51] in  $La_{2/3}Ca_{1/3}MnO_3$  system and they inferred the coexistence of FM and COI phases with different conductivities. The PCMO system shows relatively large RTN fluctuation than a La system ([51]). Actually, in the Pr system the transition is associated with two insulating phases (PMI and COI) with similar conductivities while in the La system the transition has a

percolation aspect. If we assume a phase separated sample with regions of two different conductivities and a dynamic phase separation with the clusters switching between the two conductivity states, then it is quite likely that it would be a source of electrical noise. It is likely that such switching is thermally activated and associated with these fluctuations there would be a typical time scale that describes the dynamics/energy scale of this switching [47]. Indeed if the source of the noise is due to fluctuations of these individual domains, it can give rise to RTN. However, most of the direct evidence of this phase separation via scanning probe techniques [52, 53] shows a local static tendency of phase separation (at least in the time scale of measurement) than a dynamic one, as expected from the low frequency noise measurements. The case analysis of the resistance fluctuation data, it does give us important information about electrical conduction in the sample.

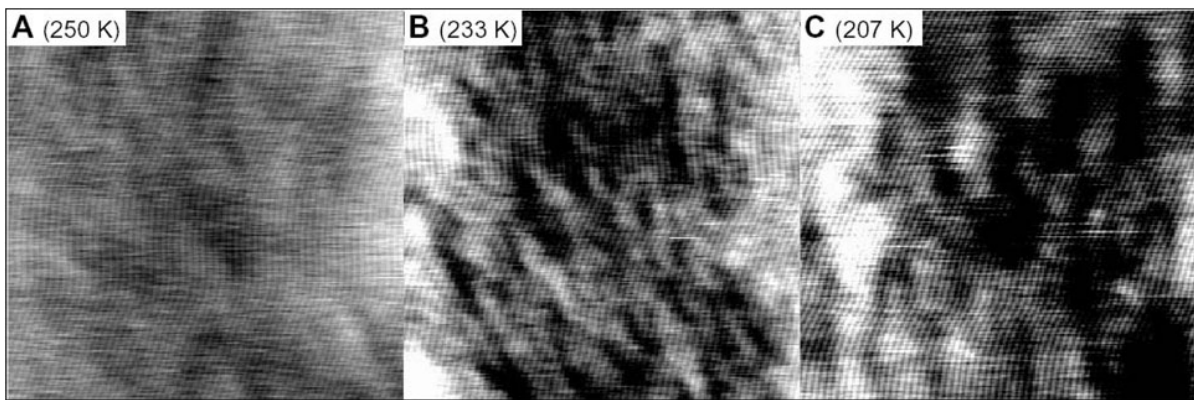


**Figure 4.5:** MFM images of  $\text{La}_{0.65}\text{Ca}_{0.35}\text{MnO}_3$  film on  $\text{SrTiO}_3$  taken at decreasing temperatures of (A) 250 K (25  $\mu\text{m}$  by 36  $\mu\text{m}$  by 52 nm), (B) 233 K (22  $\mu\text{m}$  by 32  $\mu\text{m}$  by 56 nm), and (C) 207 K (19  $\mu\text{m}$  by 27  $\mu\text{m}$  by 47 nm) [54].

Theoretically, the predicted phase separation is not only electronic but also has a magnetic character. The metallic and insulating domains are supposed to be FM and AF respectively. An ideal probe to study surface magnetic character, in the nm scale, is the magnetic force microscopy (MFM). MFM on thin films of  $\text{La}_{0.65}\text{Ca}_{0.35}\text{MnO}_3$  [54] on  $\text{SrTiO}_3$  (STO), carried out as a function of temperature showed that magnetic domains started to appear at 250 K ( $\approx T_c$ ) (Fig. 4.5). However, the domain contrast was small, which meant that there was a small domain magnetization. The domain size and contrast increased rapidly during cooling became fairly clear at 233 K and stronger at 207 K. The domain contrast says nothing about their type/direction of magnetization but does confirm that the sample in the FM phase is not fully magnetized, down till 100 K (where the domains were typically a few microns in dimension). They also observed that neighbouring domains always had opposite magnetization and as the temperature was decreased the domains increased in size and their mobility was considerably diminished. A similar study was carried out on thin film of  $\text{La}_{0.33}\text{Pr}_{0.34}\text{Ca}_{0.33}\text{MnO}_3$  grown on  $\text{NdGaO}_3$  (NGO) [55] clearly indicates the growth of FM domains below  $T_c$ , which grew in size and contrast (strength of magnetization) with the lowering temperature.

The above experiment failed to register any correlation between the MFM and the underlying topography images (except some of the scratches which probably served as domain pinning centres). Thus, the phases below  $T_c$  are also seen to be magnetically inhomogeneous. Kanki *et al.* [56] studied MFM across the  $T_c$  ( $\sim 303$  K) on  $\text{La}_{0.8}\text{Ba}_{0.2}\text{MnO}_3$  thin film on STO and calculated the magnetization from the images. Figure 1.16 shows this

data compared with magnetization measured by a SQUID and the result is shown in Fig. 4.6. The error bars also give us an idea of the spread in local magnetization  $\langle M_{local} \rangle$  in the system as a function of temperature.

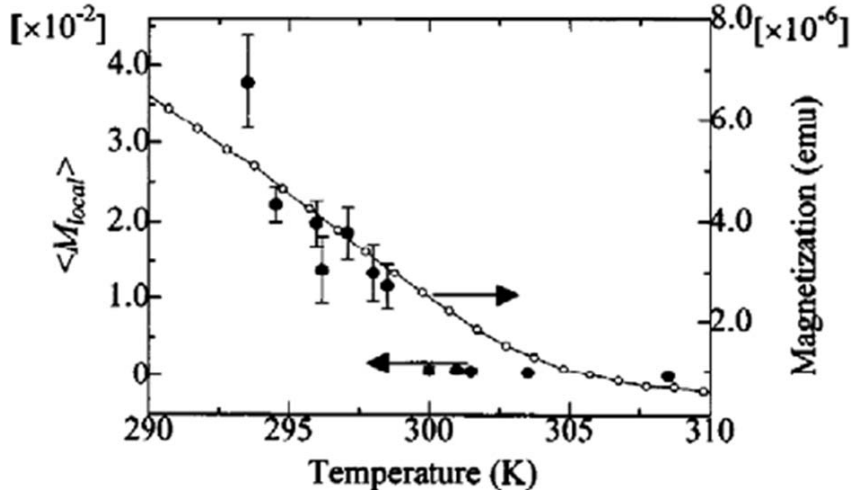


**Figure 4.6:** Temperature dependence of local magnetization calculated from MFM images and the magnetization measured by SQUID on  $La_{0.8}Ba_{0.2}MnO_3$  thin film on STO [56].

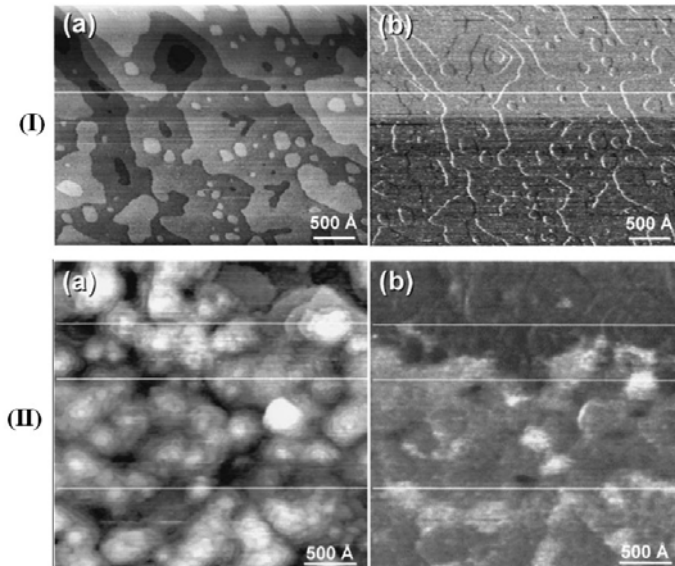


**Figure 4.7:** (I).  $La_{0.67}Sr_{0.3}MnO_3$  thin film (a) STM topography and (b) corresponding conductance map (with PtIr tip); (II)  $La_{0.67}Sr_{0.3}MnO_3$  thin film (a) STM topography and (b) corresponding conductance map (with magnetic tip). The contrast in (b) is represented by both conductance and spin-polarization contributions [57].

Akiyama *et al.* [57] carried on a unique spin polarized STM/STS studies were carried out by on epitaxial thin film of  $La_{0.7}Sr_{0.3}MnO_3$  on NGO with a  $La_{0.7}Sr_{0.3}MnO_3$ -coated PtIr and bare PtIr tips. Fig. 4.7(I) shows the simultaneously taken topography (Fig. 4.7(I) (a)) and conductance maps (Fig. 4.7(I) (b)) taken at room temperature ( $T < T_c$ ). But they failed to observe any contrast (phase separation) in the conductance maps, which correlated with the topography only at the step edges. Again Fig. 4.7(II) shows similar data taken with the manganite coated tip. The coated tip was magnetized parallel to the sample surface prior to

the experiment. In absence of any detectable phase separation in the previous experiment the contrast in this conductance map is purely due to the presence of magnetic domains with different magnetization axes and not due metallic/insulating phases. They observed broad magnetic domains ( $\sim \mu\text{m}$ ). The lower half of Fig. 4.7(II) (b) shows magnetic domains (200-500 Å) which are strongly correlated to the surface topography. This, as mentioned before, may be due to the fact that structural defects often serve as pinning centres for small magnetic domains. The above study is unique in the sense that though the spin polarized conductance maps show the existence of magnetic inhomogeneity below  $T_c$ , they do not show electronic phase separation!

Phase separation has been reported mainly in the film samples of manganites. Many people believe that phase separation is an intrinsic part of the basic physics of the manganites, and is essential to explain various observations like CMR, the large drop in  $\rho$  just below  $T_c$  and the broad transition seen from the  $\rho$  vs  $T$  data. But there is lack of conclusive evidence that it is indeed the case. It just so happens that if we assume the concept of phase separation and a percolation model, it does help us in understanding many of the observations. The observation of phase separation still remains unexplained. More importantly, it has not been established clearly that phase separation is ‘intrinsic’ to the manganites. The factors like strain, microstructures or strain inhomogeneity play an important role to nucleate phase separation and these features still need further investigations. We note that the issue of phase separation has been investigated, except one or two publications the importance of strain on noise has not been investigated. We made extensive studies by noise spectroscopy on manganite films grown on oriented single crystal substrate to segregate the response from the effects due to strain fields and phase inhomogeneity.

The experiments were carried out on 500 nm thick film of hole doped manganites of composition LCMO<sub>33</sub> grown on oriented single crystal SrTiO<sub>3</sub> substrates which have there is a well defined paramagnetic to ferromagnetic transition at  $T_c \approx 268$  K on cooling and also a transition from a polaronic insulating state at high temperature to a ferromagnetic metallic state at low temperature, which results in a peak in resistivity at  $T_p$ . Typically in good manganite samples, which are not strained have  $T_c \approx T_p$ . In the following section, we begin describing the strain accommodation in the films and the strain relaxation phenomena depending on the lattice mismatch with the substrate and the thickness of these films. Following this, we investigate the noise characteristics of these films with structural disorder and discuss about the electrical conduction mechanism. We explored noise spectroscopy focusing the region close to the ferromagnetic transition temperature where the two phases, ferromagnetic metallic and paramagnetic insulating regimes coexist. Here we also discuss magnetic field dependent resistance fluctuation phenomena near phase separated regions. Finally, we investigated strong coupling of magnetic and resistance fluctuations through the mechanism of temperature dependent magnetoresistance (MR). This is followed by the summary.

## 4.2 Structural disorder and Phase separation

The manganites are well known to be susceptible to various perturbations resulting drastic change in sample properties. For films, properties like  $\rho_0$ ,  $T_c$ , width of the transition temperature, electrical and magnetic properties and noise spectra are closely related to certain parameters: (a) film-substrate lattice mismatch induced biaxial (tensile/compressive) strain, (b) film thickness, (c) deposition technique, (d) post-deposition annealing etc. As has been pointed out by Millis *et al.* [10], due to the JT splitting term of lattice distortion (because JT

splitting of the energy levels is directly proportional to the distortion of the octahedra),  $T_p$  ( $T_c$ ) of manganite is extremely sensitive to biaxial strain.

Usually there is a critical limit of film thickness for films grown epitaxially on a lattice-mismatched substrate, and below this thickness the film is grown coherently and strained uniformly at the same time. Thus when the stored elastic energy due to strain will cross a critical value, this will make the film to relax its strain by creation of dislocations and/ grain boundaries. If the film thickness increases beyond a critical value, the lattice strain will be fully relaxed accompanying the generation of defects like dislocations in the films [58]. When the strain is relaxed partially, i.e., strain is not uniform then films are structurally inhomogeneous. Several studies [11, 59, 60] have suggested that the properties of these films are greatly dependent on manganite-insulator (film-substrate) interfaces. When the strain factors come into play for films of manganites, two physical properties are greatly modified due to strain: resistivity and the magnetization. The studies by Sun *et al.* [61] and Zeise *et al.* [62] interpreted the presence of electrical dead layers located at the interfaces which leads to the modification of resistivity (i.e.  $T_p$ ). This is accompanied by a decrease of magnetic moment and magnetically dead layers have also been detected also [63, 64]. The thickness of these dead layers is order of a few nm and highly dependent on the nature of the substrates. Millis *et al.* [65] studied theoretically the strain effect in manganite films and stated that the one must distinguish between uniform bulk strain ( $\varepsilon_{\text{Bulk}}$ ) and biaxial strain ( $\varepsilon^*$ ) effects on  $T_c$ . The author suggested that  $\varepsilon_{\text{Bulk}}$  can lead to an increase of  $T_c$  depending on the sign of the strain, while  $\varepsilon^*$  favours electron localization in  $e_g$  levels splitting by static JT distortion, causing  $T_c$  to decrease.

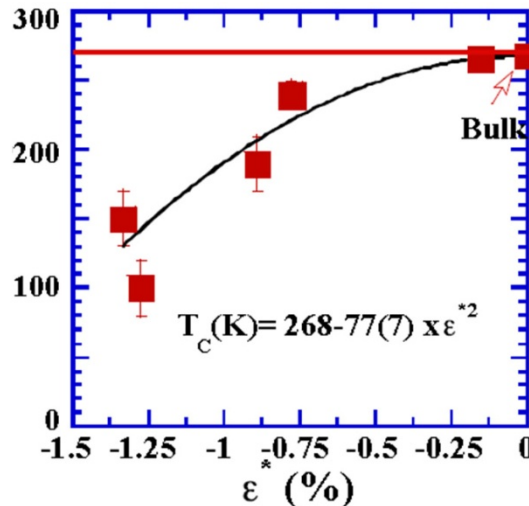


**Figure 4.8:** Experimentally observed dependence of  $T_c$  on biaxial strain in epitaxial strained  $\text{La}_{0.67}\text{Ca}_{0.33}\text{MnO}_3$  films on STO [67].

Rao *et al.* [66] followed the above model and tried to explain results for LCMO films grown on STO and found that it did not account for the decrease of  $T_c$  upon thickness reduction. We discussed before that there are evidences of existence of multiple phase separation into ferromagnetic-metallic, ferromagnetic-insulating, and non-ferromagnetic-insulating regions. The nucleation of non-metallic regions appears to be related to the modification of carrier density in the metallic phase which causes  $T_c$  to change. Hence,

doping, strain, thickness play key roles in manganite films. If  $T_c$  is sensitive to biaxial strain, the magnetic transition may also be inhomogeneous. Fig. 4.8 shows a typical example how transition temperature ( $T_c$ ) of a film varies with  $\varepsilon^*$  in the films of manganites. Hence, such subtle disorder effects are unavoidable and all these factors should be taken into account for interpretation of all current experimental data.

While strain is supposed to be most important component of the physics of manganites, very few theoretical works have been done on strain induced hallmark features for manganite films. Two parameters that permit to characterize the strain are:  $\varepsilon^*$  (biaxial strain) and  $\varepsilon_{Bulk}$  (bulk strain) defined by the equations 4.1 where  $\varepsilon_{zz}$ , and  $\varepsilon_{xx}$ ,  $\varepsilon_{yy}$  are out of plane strain and two in plane strain components respectively.  $\varepsilon^*$  and  $\varepsilon_{Bulk}$  permit to characterize the anisotropy and compaction (or expansion) in the volume of the unit cell respectively.

$$\begin{aligned}\varepsilon^* &= \frac{1}{4} (2\varepsilon_{zz} - \varepsilon_{xx} - \varepsilon_{yy}) \\ \varepsilon_{Bulk} &= \frac{1}{3} (\varepsilon_{xx} + \varepsilon_{yy} + \varepsilon_{zz})\end{aligned}\quad (4.1)$$

Bulk strain remains nearly constant with film thickness indicating that the volume of the unit cell is constant. However, the anisotropic strain is constant for film thickness below the critical film thickness for strain release, and diminishes for thicker films. According to Millis model [65] the transition temperature  $T_c$  and biaxial strain  $\varepsilon^*$  is related by a relation through two parameters,  $\beta$  and  $\Delta$  defined as:

$$T_c(\varepsilon) = T_c(\varepsilon = 0) \left[ 1 - \beta \varepsilon_{Bulk} - \frac{1}{2} \Delta \varepsilon^{*2} \right], \quad (4.2)$$

where  $\beta = (1/T_c)(dT_c/d\varepsilon_{Bulk})$  and the coupling parameter  $\Delta$  is connected to  $T_c$  and  $\varepsilon^*$  as  $\Delta = (1/T_c)(d^2T_c/d\varepsilon^{*2})$ . Millis *et al.* [65] estimated  $\beta = 10$  and  $\Delta = 1.0 \times 10^3$  for the LCMO films indicating the dependence of transport properties on  $\varepsilon^*$ . If a film is compressively strained in the in-plane direction then there must be an associated tensile strain in the direction perpendicular to the film surface and vice versa. If we assume the film is epitaxial, the out of plane strain  $\varepsilon_{zz}$  will relate with two in plane strain components  $\varepsilon_{xx}$  and  $\varepsilon_{yy}$  as

$$\varepsilon_{zz} = -\frac{\nu(\varepsilon_{xx} + \varepsilon_{yy})}{1-\nu} \quad (4.3)$$

where  $\nu$  is the Poisson's ratio. For LCMO33,  $\nu$  was found to be approximately 0.38. Note that for  $\nu < 0.5$ , the unit cell volume is reduced compared to the bulk material.

One can make a quick estimation of the strain character from the lattice parameters of bulk LCMO33 ( $a_{LCMO} = 3.855 \text{ \AA}$ ) grown on different substrates. The substrates have lattice parameters slightly greater (STO) and less (LAO) than the lattice parameter of LCMO33. Hence, the LCMO33 films grown on those substrates are expected to be under tensile or compressive stresses. The in-plane stress  $\varepsilon$  is defined as  $\varepsilon_{xx}(\%) = (a_{sub} - a_{LCMO})/a_{LCMO}$  where

$a_{sub}$  is the lattice parameter of the substrates. Considering  $\nu = 0.38$ , we can deduce the out of plane distortions  $\varepsilon_{zz} = -2\nu\varepsilon_{xx}/(1-\nu)$  where the in-plane stress  $\varepsilon_{xx} = \varepsilon_{yy}$ . In Fig. 4.9 we have shown how the tensile or compressive strain arises in film due to lattice mismatch between film and substrates.

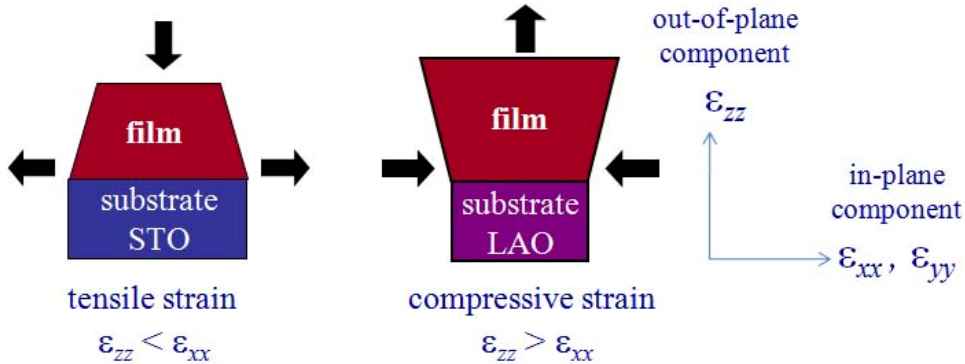


**Figure 4.9:** Schematic diagram for the mechanism of tensile or compressive strain arises in the film due to lattice mismatch between film and substrate.

| Composition              | Lattice parameters at 300 K (Å) | $\varepsilon_{xx} (\%) = (a_{sub} - a_{LCMO}) / a_{LCMO}$ | $\varepsilon_{zz} (\%) = -2\nu\varepsilon_{xx} / (1-\nu)$ |
|--------------------------|---------------------------------|---|---|
| SrTiO <sub>3</sub> (STO) | 3.905                           | 1.16  | -1.42   |
| LaAlO <sub>3</sub> (LAO) | 3.790                           | -1.68   | 2.06  |

**Table 4.2:** Lattice parameters of different substrates and amount of in-plane ( $\varepsilon_{xx}$ ) and out-of plain ( $\varepsilon_{zz}$ ) strain components for LCMO33 films grown on them STO and LAO substrates.

In Table. 2, we have listed lattice parameters of two substrates and associated in-plane and out-of-plane strain components arising in the LCMO33 films. If a film is compressively strained in the in-plane direction then there will be an associated tensile strain in the direction perpendicular to the film and vice versa. The average microscopic properties, of the films are strongly influenced by strain. In practice, the film microstructure may not be constant throughout the thickness. This is particularly true for thicker films (above ~100 nm) and films grown on substrates with a greater lattice mismatch. The thicker films may have a two layered structure of a coherently strained bottom layer and a (partially) strain-relaxed possibly defect rich upper layer, both separated by defect rich zone [68, 69]. The degree of strain will affect the crystal structure of the film and hence the physical properties. Figure 4.10 illustrates schematically how the microstructure varies with the degree of relaxation.

Investigations by Chen *et al.* [70] on the growth kinetics of films reveal that, while growing a film, a continuous wetting layer of a few monolayer thicknesses covers the substrate first, and islands are nucleated above this layer. This growth mode leads to a variation in the strain on the film, normal as well as parallel to the surface. Compressive strain leads to an island growth mode of the film and hence a non-uniform distribution of strain is generated. The top of the islands are relatively strain free while the edges of the islands are regions of very high strain (higher than the lattice mismatch strain). This type of the strain distribution limits the lateral growth of the islands, resulting in uniform island size in the entire film. This leads to a two-phase behaviour in the strained thin films with the top

of the islands displaying properties similar to the bulk compound and the edges of the islands are insulating.

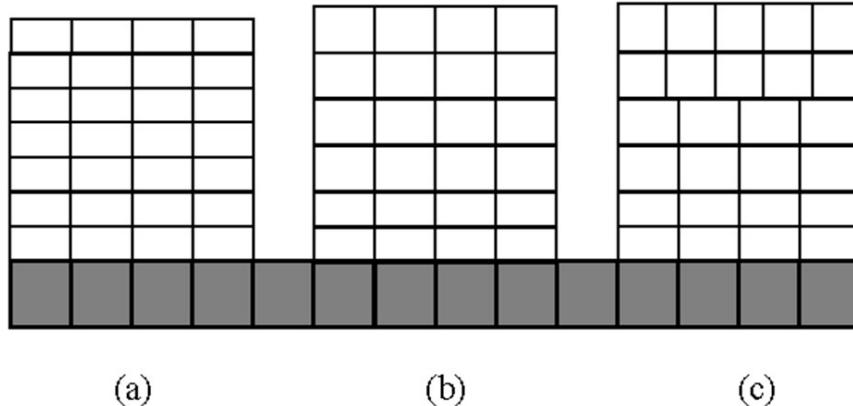


**Figure 4.10:** Schematic diagram showing the microstructure of an epitaxial film that is (a) coherently strained, (b) partially relaxed and (c) fully relaxed.

Experimentally the strain accommodation in films has been explored by several authors. Rao *et al.* [71] studied 3D strain states and crystallographic domain structures of epitaxial thin films of  $\text{La}_{0.80}\text{Ca}_{0.20}\text{MnO}_3$  of various thickness ranging from  $t = 25 \text{ nm} - 400 \text{ nm}$  on  $\text{LaAlO}_3$  (LAO) and STO. The system has bulk lattice mismatch of -2.37% (compressive strain) with LAO and +0.60% tensile strain with STO. As the thickness of the film increases, strain relaxes in the film; both in-plane and out of plane lattice parameters tend to deviate away from those of the substrates toward the bulk value. Due to larger lattice mismatch between  $\text{La}_{0.80}\text{Ca}_{0.20}\text{MnO}_3$  and LAO films grown on LAO show partial strain relaxation. The AFM topography results show that thinner films are much smoother than thicker films, due to strain relaxation in the thicker ones. The authors observed systematic variations in  $T_c$  and  $T_p$  with respect to film thickness and in turn with  $\varepsilon^*$ .

Zhang *et al.* [72] reported interesting results on magneto-transport properties of  $\text{La}_{1-x}\text{Ca}_x\text{MnO}_3$  ( $x = 0.05-0.33$ ) films grown on STO substrates where strain profile varies from tensile to compressive in nature with respect to doping concentration  $x \geq 0.20$ . They observed enhancement of FM significantly with tensile strain whereas compressive strain reduces  $T_c$ .

Paranjape *et al.* [15] reported strain induced electrical transport properties of LCMO33 films grown on  $\text{NdGaO}_3$  (NGO) and STO substrates of different substrates. They have used scanning tunnelling microscopy (STM) and potentiometry (STP) probes to study the microstructure of the films shown in Figure 4.11(a), (b) and (c). Depending on the lattice mismatch with the substrate and the thickness of the film, the LCMO33 films with thickness  $\sim 50 \text{ nm}$  can have very low strain (grown on NGO) or uniformly strained (grown on STO), and they observed a clean terrace and step-type growth pattern. Thicker films of LCMO33 (grown on oriented STO substrate) are strain relaxed and the microstructure shows platelet structure (columnar type) with misfit dislocations threading the platelet boundaries. They reported broad electrical transition characteristics on both films grown on STO. But the film grown on NGO which has best lattice match with LCMO33 has single crystal like transition with much lower resistivity values than the other films (see Figure 4.11(d)). The strain dependent suppression of transition temperature was also reported by the authors. They suggested that the height modulation seen in the microstructures leads to local fluctuations, which in turn lead to conductivity inhomogeneity that picked up in the correlated STM and

STP measurements. The presence of local strain variations in the films thus leads to inhomogeneous current flow in these materials even in the paramagnetic state.

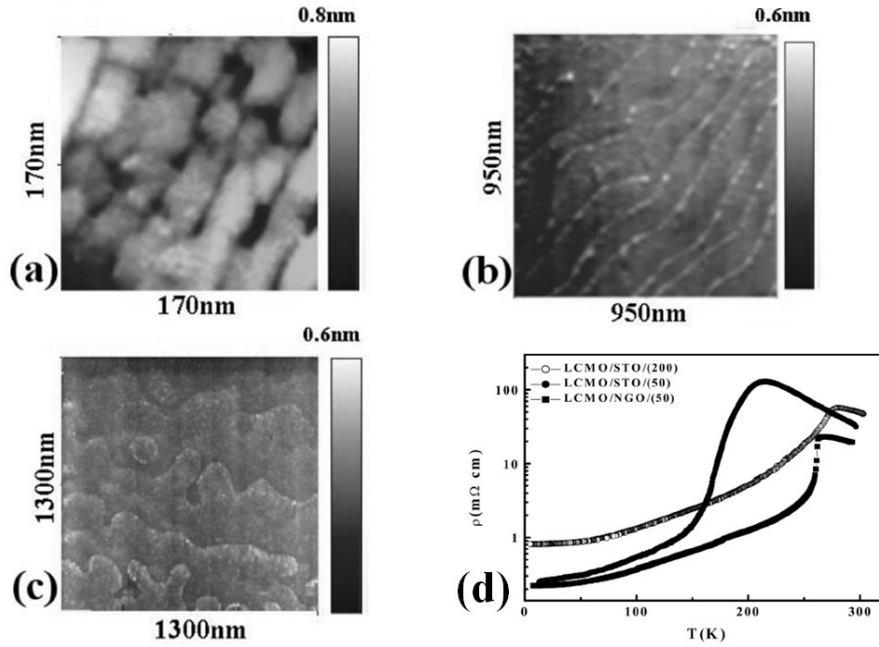


**Figure 4.11:** STM images across the platelet and step for ~ (a) LCMO/STO(200), (b) LCMO/STO(50), and (c) LCMO/NGO(50) films (arrows shown in the STP images indicate the applied current direction), (d) temperature dependence of the resistivity of LCMO/STO(200), LCMO/STO(50), and LCMO/NGO(50). Adapted from reference [15].

Biswas *et al.* [73] studied LCMO33 thin films (15 nm) deposited on NGO and LAO. The films grown on LAO are biaxially strained with compressive strain  $\sim 2\%$ . The strained film resistivity is completely insulating and it can be made metallic by the application of an external magnetic field of 8.5 Tesla which reduces  $\rho$  and a broad metal-insulator transition shows up near 200 K. The strain free NGO film differs strongly from the other one and the comparative study on the resistivity has shown in Figure 4.12(a). They suggested the presence of two phases FM metallic and charge ordered (CO) insulating phases. The field driven metal-insulator transition is associated with the coexistence of two phases with a change of metal volume fraction through a percolation threshold. The AFM images taken on the films (Figure 4.12(b)) show that the film on LAO has an island growth mode, while that on NGO has a step flow growth (step height  $\sim 4\text{\AA}$ ). These data were also supported by the transmission electron microscope (TEM) images (on LAO film) where they observed at the island boundary than at the centre. Magnetic force microscopy (MFM) images (see Figure 4.12(c)) on the same film at 80 K show that magnetic domain sizes are similar to the island sizes. The effect is absent for NGO films. They infer that low strain regions are FM metallic, while the high strain ones are CO insulating at low temperatures with the strain (structural disorder) stabilizing the insulting phase.

Bibes *et al.* [16] carried out thickness dependent studies on strained films of LCMO33 on STO using  $^{55}\text{Mn}$  nuclear magnetic resonance (NMR). They observed clear signature of coexistence of multiple phase separations like, FM metallic, FM insulating and non-FM insulating regimes. They indicated that only FM metallic and non-metallic regions are present in very thin films. But there is a critical thickness beyond which film becomes more homogeneous being primarily composed of FM metallic regions. They observed systematic

variation of magneto-transport properties depending on the phase separation. Further studies [11] by the same group on STO, LAO, and NGO revealed inhomogeneous magneto-electronic nanostructures with distinguishable regions containing localized charges. They also observed charge density fluctuations near the interfaces of the films and conclude that both the films are electrically inhomogeneous. The inhomogeneity varies with strain which is much larger in the strained film on STO than on NGO.

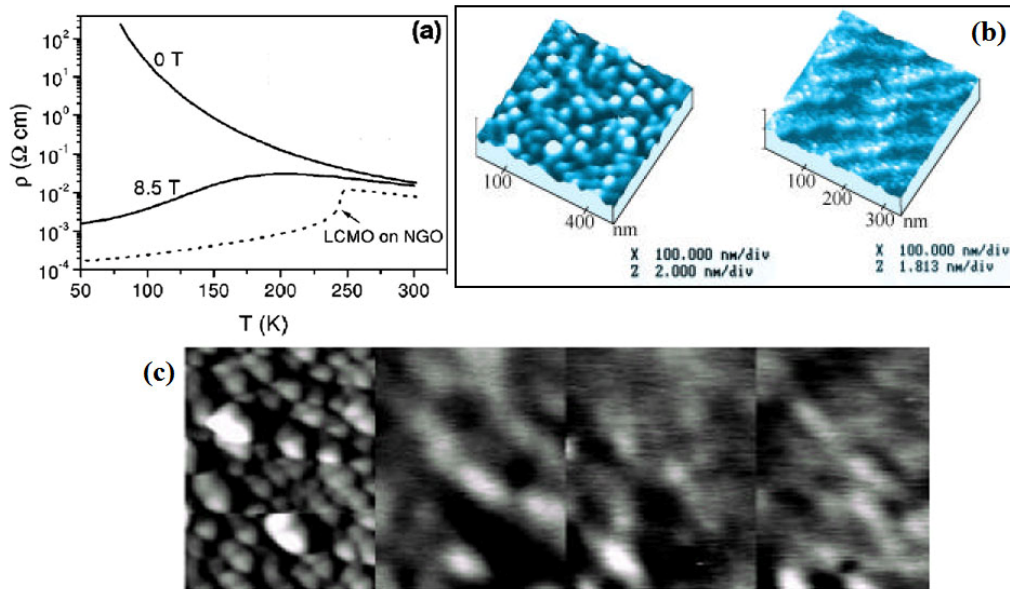


**Figure 4.12:**  $\text{La}_{0.67}\text{Ca}_{0.33}\text{MnO}_3$  thin film (a) Resistivity versus temperature for films deposited on NGO and STO; (b) AFM topography images for LAO (left image) and for NGO (right image) films; (c) MFM images of the LAO film at 80 K. The first image is a  $1.4 \times 1.4 \mu\text{m}$  topographic image showing the island growth mode. The other three are magnetic images at the same scale showing the magnetic domains. Adapted from reference [73].

Biswas *et al.* [74] observed the presence of clear phase separation near film substrate interfaces for  $\text{La}_{0.7}\text{Ca}_{0.3}\text{MnO}_3$  film on STO. They concluded that vertical growth of inhomogeneous magnetic structures in system leads to phase coexistence. But Zeise *et al.* [75] concluded that the double exchange interaction due to ordering of the atomic orbitals is responsible for phase separation. They also mentioned that the strain variation across the islands grown is far too small to induce strain related phase separation on length scale of  $\sim 100 \text{ nm}$ .

Recently Gao *et al.* [76] have performed experiments on strained as well as strain relaxed films of  $\text{La}_{0.7}\text{Ca}_{0.3}\text{MnO}_3$  on STO of thickness 50-150 nm. They observed ferromagnetic to paramagnetic transition at  $T_c \sim 260 \text{ K}$  for fully relaxed films. The partially relaxed films have inhomogeneous magnetic and structural transitions. Two thickness dependent  $T_c$  were detected for each film. All these experimental results conclude one fact that the transition temperatures are highly correlated with the film thickness mainly due to strain! The authors also mentioned that the lattice constant mismatch that induces inhomogeneities in both the strain state and magnetic transitions.

The results discussed so far are not exhaustive but give us an idea regarding the various explanations available in literatures. They all focused the presence of phase separation in the strained and strain relaxed films and creation of macroscopic and nanoscopic structures depending on the film thicknesses. There is lack of systematic investigation microstructure driven dynamics near phase transition. As stated before we

investigate how strain and strain relaxation affects noise in these systems. We have already discussed (please see in Chapter 1) some of the published results available in literature where noise has been studied thoroughly in manganites. As we stated earlier, while most of the studies investigated the noise with spectral power  $S_v(f) \sim 1/f$  (the  $1/f$  noise), a wealth of physical information came from discrete fluctuators that typically occur in small temperature windows for  $T < T_c$ . But the exact nature of their origin may not be clearly established. We have grown films which are well characterized strain relaxed and have microstructure with misfit dislocations. These films are accommodated with specific type of quenched disorder. We shall show that these films can show very low frequency  $1/f$  noise ( $0.25 \leq f \leq 1$  Hz) and in the frequency range ( $f \geq 10$  mHz) below that, discrete fluctuators start to originate. We explore the temperature range 100-300 K close to phase transition.

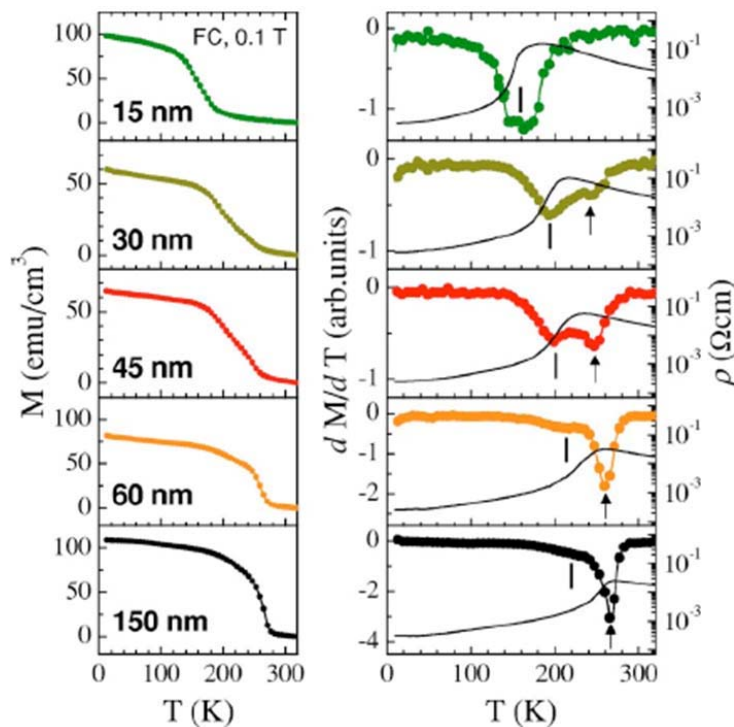


**Figure 4.13:** Field-cooling  $M$ - $T$  (left) and  $R$ - $T$  (right, lines) curves measured from the films grown on STO (001) substrates with thicknesses of 15, 30, 45, 60, and 150 nm, respectively. For each film the derivative of the  $M$ - $T$  curve (solid symbols) is shown correspondingly in the right panels. For all the films thicker than 30 nm, two magnetic transitions were observed for each  $M$ - $T$  curve. The higher transition temperature is  $T_{c1}$  and the lower is  $T_{c2}$ . Both  $T_{c1}$  and  $T_{c2}$  increase with the film thickness. Adapted from reference [76].

### 4.3 Film preparation and characterization

The oriented and strain relaxed doped perovskite manganite films studied in this dissertation were all grown by chemical solution deposition (CSD) [20, 77] technique on single crystalline STO substrate as discussed detailed in Chapter 2. Here we briefly discuss the method for completeness.

We have prepared precursor solution with proper stoichiometry from acetates of Lanthanum, Calcium and Manganese and dissolved in a solution of Acetic acid and water (with volume ratio 1:1) by heating at 70°C. The solution was spin coated with speed of 6500

r.p.m on STO substrates. Five consecutive coatings were done before annealing at 900°C for 10 min. The heat treatment was also standardized according to phase evolution of manganites and decomposition of several organic compounds. The resulting films were oriented films of thickness  $\sim 500\text{nm}$ . The annealing time controls the size of grain boundaries in these films. After growth, the crystallinity was investigated by X-ray diffraction (XRD) and the surfaces of the samples were characterized by atomic force microscopy (AFM). We have studied the transport properties of the films to investigate the phase transition from high temperature insulating to low temperature metallic phase. The films have also been characterized using magnetization measurements i.e., temperature dependent magnetization ( $M$ ) at a fixed magnetic field ( $M(T)$  vs  $T$ ) and field ( $H$ ) dependent magnetization at fixed temperatures ( $M-H$ ) using a vibrating sample magnetometer (VSM). We shall be discussing our results below which will help us to understand the basic features of the films grown.

### 4.3.1 X-ray Diffraction

The X-ray diffraction (XRD) is a non-destructive technique used to study the basic structure of the films. We have used CuK $\alpha$  radiation with  $\lambda=1.54\text{\AA}$  (PANalytical X'Pert Pro) in  $\theta$ -2 $\theta$  configuration.

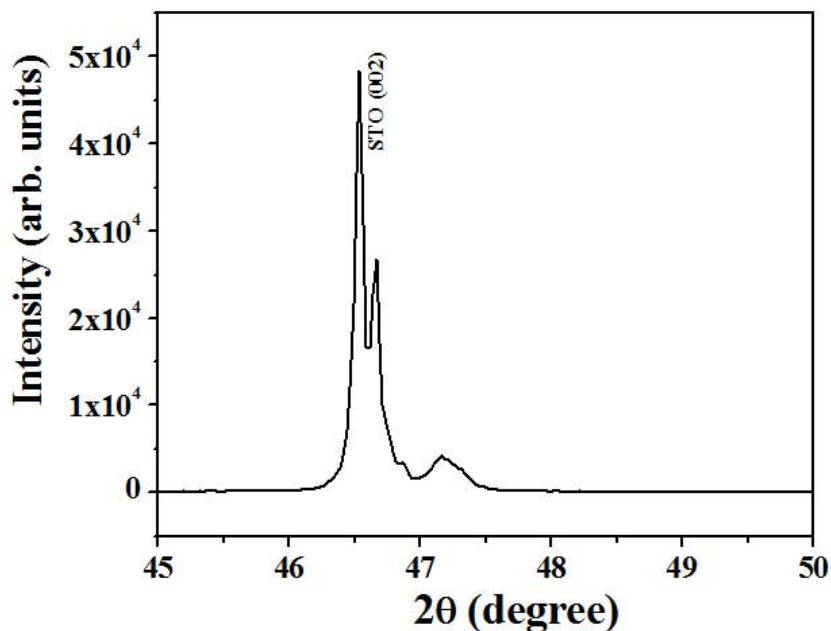


**Figure 4.14:** A typical XRD line scan data for film grown on STO (002) substrate. The film is of thickness  $\sim 500\text{ nm}$  and follows the orientation direction that of the substrate. The small sample peak appearing near STO (002) indicates the strain relaxation in film.

Figure 4.14 shows the linear scans around LCMO33 (002) from the film thickness of  $\sim 500\text{ nm}$ . The XRD data clearly indicates that films maintain the orientation direction that of the substrates. It is also observed that a small sample peak appears just beside the substrate (002) peak indicating the strain relaxation has occurred in the films due to lattice mismatch and sample thickness.

### 4.3.2 Atomic Force Microscopy

The surface morphology of the sample was investigated by contact mode atomic force microscopy (AFM). Figure 4.15 shows a topological image of the film surface. One of the major advantages of this technique is that the image obtained directly corresponds to the surface profile. The image was produced by dragging a cantilever with  $\text{Si}_3\text{N}_4$  tip across the sample. There are interatomic interactions between tip and sample surface that causes the tip to bend. A laser beam is deflected back from the cantilever and onto a piezoelectric transducer. The degree of bending of the tip can be measured by using this piezoelectric transducer together with a feedback loop. The output voltage signal is then used to produce a profile of the surface. The smoothness of the films is measured by root-mean-square (*r.m.s*) roughness and appeared  $\sim 7$  nm.

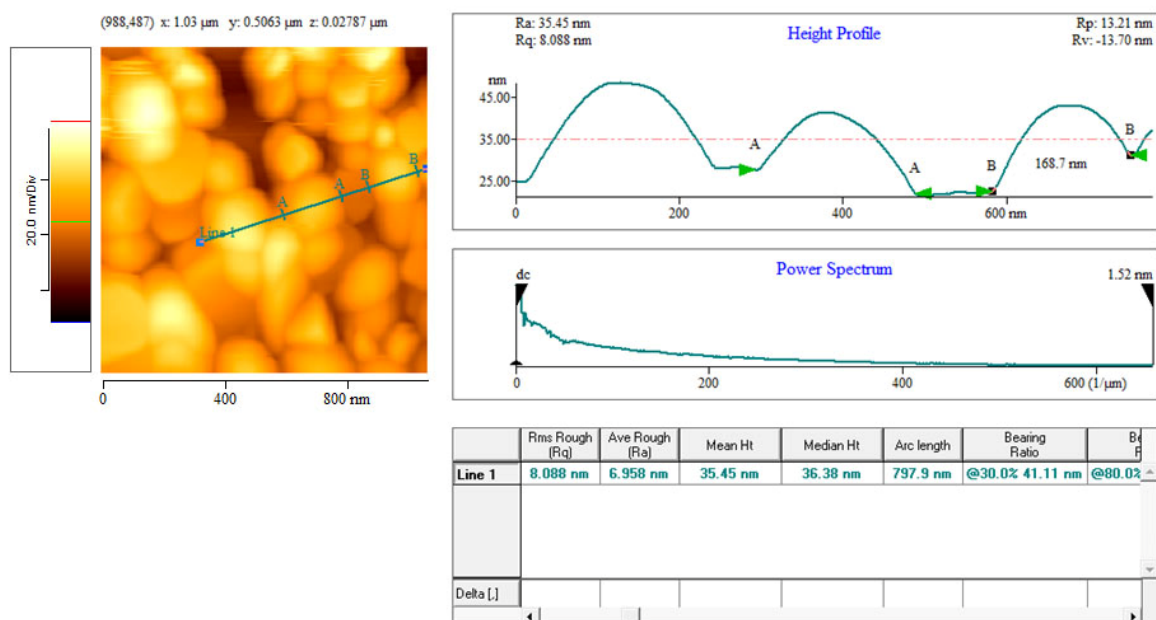


**Figure 4.15:** (a) AFM image of LCMO33 film surface grown on oriented single crystal STO. The average roughness of the film is 6.96 nm and average platelets size is  $\sim 100$ -200 nm.

The strain relaxed film show platelets. These platelets are different from grain boundaries with size  $\sim 100$ -200 nm. These platelets are forming during the strain relaxation to accommodate the strain due to lattice mismatch. The platelets boundaries consist of misfit dislocations which span from the substrate to the film surface. The surface morphology of our films is quite different from LCMO33 films grown on single crystalline substrates by pulsed laser deposition as described in reference [15]. We have performed our noise spectroscopy on strain relaxed films (thickness  $\sim 500$  nm) and compared our results with films which were with uniform strain (LCMO33/STO ( $\sim 50$  nm)) and very little strain (LCMO33/NGO (50 nm))(discussed later in detail).

### 4.3.3 Electrical transport measurements

The a.c electrical resistivity of the samples was measured as a function of temperature. Five silver contact pads were deposited using thermal evaporation of 99.99% pure Gold (procured from Kurt J. Lesker [78]). The electrical contact leads were made by 50  $\mu\text{m}$  thin Copper

wires using silver epoxy [79]. We always keep these contact pads unaltered when performing our noise measurements because this will reduce the appearance of contact noise. We have already discussed the details of temperature dependent resistivity measurement procedure in Chapter 2 (see section 2.4.4). The main aim of the electrical transport measurements was to determine the temperature of a transition (if any) from an insulating state (defined as  $d\rho/dT < 0$ ) to a metallic state (defined as  $d\rho/dT > 0$ ). This can be done by resistance values alone, but the absolute resistivity values are included for comparison with other materials. However, here we discuss about the results what we acquired from our measurements relevant to this chapter.

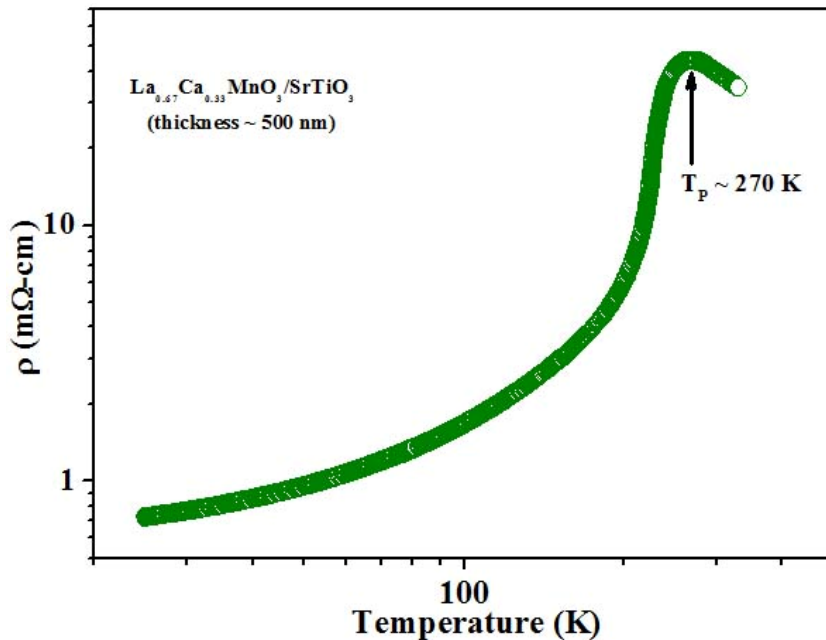


**Figure 4.16:** The temperature dependent resistivity data for a LCMO33 film grown on STO with thickness  $\sim 500 \text{ nm}$ . The resistivity shows high temperature polaronic insulating to low temperature metallic phase transition at  $T_p \approx 270 \text{ K}$ .

The resistivity ( $\rho$ ) was measured down to 25 K by a four-probe ac biasing technique. In Figure 4.16  $\rho$  shows a distinct peak corresponding to the transition from the high temperature insulating polaronic phase to the low temperature metallic phase at  $T_p \approx 270 \text{ K}$ . We have compared the residual resistivity and  $T_p$  values in our films with results obtained for two other films, namely LCMO33/STO ( $\sim 50 \text{ nm}$ ) and LCMO33/NGO ( $50 \text{ nm}$ ) [15]. The film grown on NGO, the strain being least,  $\rho_{peak} \sim 20 \text{ m}\Omega\text{-cm}$  at  $T_p \sim 268 \text{ K}$  and residual  $\rho \sim 0.2 \text{ m}\Omega\text{-cm}$ . In the uniformly strained 50 nm film grown on STO, the  $T_p$  is severely suppressed  $\sim 215 \text{ K}$  and the  $\rho_{peak}$  is considerably larger at about 130  $\text{m}\Omega\text{-cm}$ . This film, however, has a low residual  $\rho \sim 0.3 \text{ m}\Omega\text{-cm}$ . In the strain relaxed films, typical peak in  $\rho$  occurs at temperature  $T_p \sim 270 \text{ K}$ , which is similar to the unstrained films or single crystals. The film shows a peak in  $d\rho/dT$  at a temperature  $\sim 228 \text{ K}$ . The films have a typical  $\rho_{peak} \sim 45 \text{ m}\Omega\text{-cm}$  and a residual resistivity of  $\sim 0.7 \text{ m}\Omega\text{-cm}$ . The strain relaxation brings down the  $\rho_{peak}$  compared to uniformly strained films (like those grown on STO) but the presence of the platelet boundaries increase the residual resistivity. All relevant transport data have been collected in Table 4.3.

| Sample              | Thickness | $\rho_{\text{peak}}$ (mΩ-cm) | $\rho_{20 \text{ K}}$ (mΩ-cm) | $T_P$ (K) |
|---------------------|-----------|------------------------------|-------------------------------|-----------|
| LCMO33/STO (50 nm)  | 50        | 130                          | 0.3                           | 215       |
| LCMO33/NGO (50 nm)  | 50        | 20                           | 0.2                           | 268       |
| LCMO33/STO (500 nm) | 500       | 45                           | 0.7                           | 270       |

**Table 4.3:** Electrical characterizations of sample used.

#### 4.3.4 Magnetic measurements

The films were also been characterized using magnetization measurements [ $M(T)$  vs  $T$  and  $M-H$ ] using VSM. The phase diagram of LCMO33 systems was presented in Chapter 1 and shows that, the system has a well behaved ferromagnetic state below  $T_C$ . This is established on the basis of temperature and magnetic field dependent magnetization in magnetic field results which are shown in Figure 4.17 and 4.18 respectively.

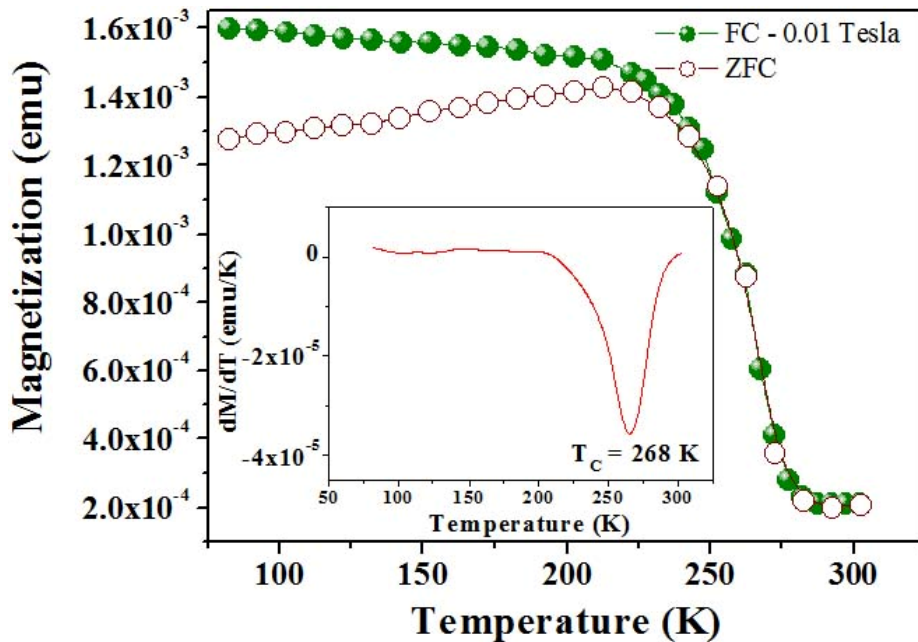


**Figure 4.17:** Temperature dependent magnetization ( $M-T$ ) has been plotted for field-cooling (FC) and zero-field-cooling (ZFC) conditions. The inset shows that films show definite paramagnetic-ferromagnetic transition at  $T_C \sim 266 \text{ K}$ .

Figure 4.17 shows temperature dependence of magnetization ( $M-T$ ) measured from the film of 500 nm thick grown on STO. From the field-cooling (FC) and zero-field-cooling (ZFC) curves, we can estimate the paramagnetic-ferromagnetic transition (Curie) temperature  $T_C = 266 \text{ K}$  (see inset of Figure 4.17). We have carried out most of the noise experiments on these films are we were interest to probe near the region of phase transition. So in Figure 4.18 (a) we have plotted magnetic field dependent magnetization at few representative temperatures around  $T_C$  for visual clarity. In Fig. 4.18(b) we have expanded the hysteresis loop around origin to show the coercive field at  $H_C \approx 0.01 \text{ Tesla}$ . The magnetization reaches technical saturation for  $H \leq 0.15 \text{ Tesla}$ . The typical films have a saturation magnetic moment in the range of  $6 \times 10^{-3} \text{ emu}$ . In the low magnetic field (0.01 Tesla), the ZFC and FC differ

below the Curie temperature  $T_C$ . This difference is the signature of spin disorder that is frozen into this ferromagnet order. This is a likely scenario because of the quenched cationic disorder  $\sigma^2 = 2.72 \times 10^{-6} \text{ nm}^2$  [80] and the competing mixed interactions that are known to be present in manganite systems. The random field created due to the randomly distributed dopant atoms (Ca) is the factor that contributes to the spin disorder and irreversibility in the system.

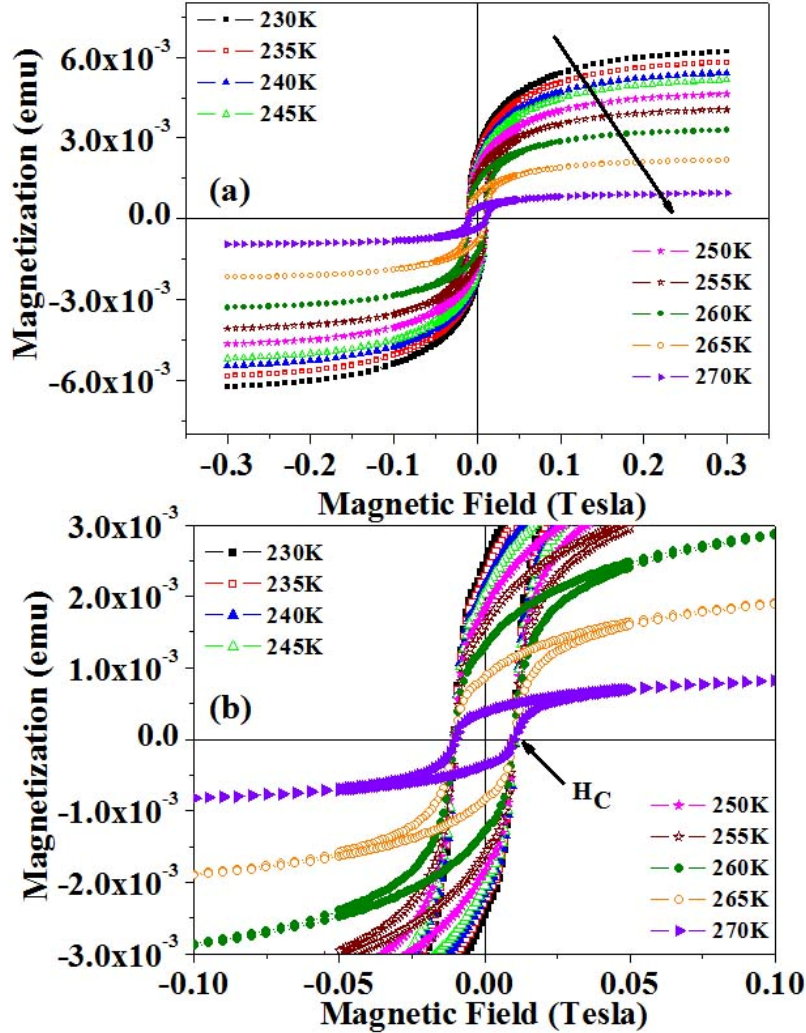


**Figure 4.18:** (a) Magnetic fields dependent magnetization ( $M$ - $H$ ) curve has been plotted at few representative temperatures around  $T_C$ . The magnetization saturates around 0.15 Tesla. The arrow is indicating the direction of temperature increase. (b) The hysteresis loop expanded around origin which shows the coercive field appears at  $H_C \approx 0.01$  Tesla.

So far we have discussed straight forward approach to characterize the samples grown. We have also established that there exists high temperature paramagnetic insulator to low temperature ferromagnetic metal transition near  $T_C \approx T_P$ . In the next section we shall use noise spectroscopy to probe the regions around this transition regime. The measured noise spectral density ( $S_V(f)$ ) consists two parts: thermal noise (Nyquist noise [80, 81]) which is independent on current and frequency, and excess noise which basically has frequency dependent component. As we discussed earlier in Chapter 3 that the origin of thermal noise is

clearly understood and its magnitude is easily estimated from resistance and temperature measurements, so our results are focused only on the excess noise. Everywhere in figures thermal noise part is subtracted otherwise we will mention in the related figure captions.

## 4.4 Resistance fluctuation in $\text{La}_{0.67}\text{Ca}_{0.33}\text{MnO}_3/\text{SrTiO}_3$ films

The analysis of noise spectroscopy in 500 nm thick films with composition  $\text{La}_{0.67}\text{Ca}_{0.33}\text{MnO}_3$  grown on STO single crystal substrates have been studied in this present section. We have scanned temperature window staring from 80 K-300 K encompassing the transition temperature  $T_c$ . We observed “ $1/f$  noise” and a contribution coming from discrete fluctuators. These discrete fluctuators show RTN in time series of voltage fluctuations. They contribute noise in very low frequency ( $< 10$  mHz) regime.

### 4.4.1 Noise measurements

Study of resistance fluctuation is a very sensitive tool to study low frequency dynamics in condensed matter systems [82-86]. The resistance fluctuation (noise) measurements were carried out using digital signal processing (DSP) based five probe ac biasing technique ([87] and section 3.3 in Chapter 3), which allows simultaneous measurement of background noise as well as bias dependent noise from the sample [87-89]. The technique has been used in the past to study resistance fluctuations in a number of systems [90-100, 50]. The sample is current biased by a low noisy source and the voltage fluctuation  $\delta v(t) = v_0(t) - \langle v \rangle$ , (where  $\langle v \rangle$  is the average voltage) is the measure of resistance fluctuation. This measurement procedure often involves detection of voltage changes of the order of 0.5 nV-5 nV.  $\delta v(t)$  is the main physical quantity which is recorded over a time period and generates a time series data. The efficiency of the noise spectroscopy lies in the elimination of contribution coming from sources other than sample. We have used both software (DSP) and hardware techniques for elimination of extraneous noises. It is challenging to detect spectral power of low noisy sample because sometimes measuring instruments noise remains high and instrument itself contribute a  $1/f$  noise. There are two specific aspects of noise measurements which I just want to mention here:

(a) first is related to hardware, involving elimination of background noise coming from the environment, poor temperature control and measuring instruments. There remain fair extraneous noise components from ground loops, impedance mismatch and electrical contacts.

(b) second aspect is related to software aspects which involves modern DSP technique [87]. The high speed data acquisition process, decimation, digital filtering, fast FFT helps to reject large amount of external noise (mostly line frequency 50 Hz and its harmonics).

The most popular way to represent the noise is through the power spectrum  $S_v(f)$  of the measured fluctuation  $\delta v(t)$ . The strength of above aspects can be realized when we successfully calibrated our apparatus down to a spectral power  $S_v(f) = 10^{-20} \text{ V}^2/\text{Hz}$  (section 3.5.3 in Chapter 3) by measuring the Nyquist noise [81]  $S_v = 4k_B T R$  for a calibrated resistor at a known temperature. The frequency range for which the spectral power is to be determined depends on the time scale of the fluctuations being investigated which in turn depends on the dynamics associated with the underlying physical process that causes the fluctuation. In general, if the dynamics is occurring at a time scale  $\tau$ , it will affect the power

spectrum around the frequency range  $f \sim (1/2\pi\tau)$ . The relaxation process that can cause the conductance to change with the characteristic time  $\tau$  makes a contribution to the power spectrum  $S_V(f)$  of the voltage fluctuation which is given by a Lorentzian  $2\tau/(1+(2\pi f)^2)$  [see section 1.3.2 in Chapter 1]. Our experimental observations involve very low frequency range ( $> 0.3$  mHz). So a complete set of time series data at each temperature consists of  $5 \times 10^6$  data points or more and from which the spectral power density  $S_V(f)$  was determined numerically by using fast Fourier transform (FFT). For long time data-acquisition process, which is needed here, we have to subtract a monotonous long time drift by a least-square fit to the data (we have already discussed linear trend removal process in section 3.3.5 in Chapter 3). We have ensured that such a subtraction does not distort the power spectrum. The low frequency limit of the spectral power has been limited by the drift process, and the temperature control was sufficiently good to ensure stability of such low frequency i.e., long time series data. We found that the typical temperature drift for a set of time series data is  $\sim 2$  mK (time taken is  $\sim 2$  hr). The lowest frequency limit ( $f_{\min}$ ) has been imposed by the temperature stability.

As we have already discussed the circuit diagram of five-probe ac biasing noise measurement in Chapter 3 (section 3.2.4), here we do not go into detail. In this technique, the sample is biased by an a.c bias from lock-in-amplifier and the signal is demodulated by lock-in amplifier itself. This shifts the detection frequency to a region where the preamplifier (transformer preamplifier or low noise preamplifier) has very low  $1/f$  component. Typical carrier frequencies are around 228 Hz. Generally the carrier frequency is much larger than the bandwidth of the power spectrum measured. The choice of the carrier frequency is to operate on region of low noise figure of the preamplifier and the lock-in amplifier. The output of the preamplifier is fed to a lock-in amplifier. In this case the bandwidth of the output low-pass filter of the lock-in amplifier will decide the upper-band limit of the spectrum. The output low-pass filter of the lock-in amplifier has been set at 3 msec with a rolloff of 24dB/octave. For a 3 msec time constant the output filter of the lock-in amplifier with 24 dB/octave is flat to  $f < 10$  Hz. This determines the upper limit of our spectral range. The output of the lock-in amplifier is sampled by a 32 bit analog to digital card and stored in the computer. We used samples of dimension  $5\text{mm} \times 5\text{mm} \times 500$  nm. Five silver contact pads were evaporated on the sample and the contacts to the sample were subsequently made by soldering  $40\text{ }\mu\text{m}$  copper wires using silver epoxy. It may be noted that making low noise and low resistance contacts is always a problem in noise experiments. We always recorded background noise, when the experiment is carried out in a well shielded enclosure, we should have a spectral power close to  $S_V = 4k_B T R$ . We find that when the contact resistance is low the background noise is close to  $4k_B T R$ . To quantify noise the relative variance of the resistance fluctuation  $\langle(\Delta R)^2 / R^2\rangle$  within the detection bandwidth ( $f_{\min} \rightarrow f_{\max}$ ) was obtained by integrating the power spectrum and it is given by the following equation

$$\left\langle \frac{(\Delta R)^2}{R^2} \right\rangle = \frac{1}{V^2} \int_{f_{\min}}^{f_{\max}} S_V(f) df. \quad (4.4)$$

The normalized resistance fluctuation  $\langle(\Delta R)^2 / R^2\rangle$  for the sample of resistance  $R$  quantifies the resistance fluctuations in it. When we compared our data with different films [LCMO33 films grown on STO (50 nm) and on NGO (50 nm)], we used the quantity  $\beta$  defined as

$$\beta = \Omega \left\langle \frac{(\Delta R)^2}{R^2} \right\rangle, \quad (4.5)$$

where  $\Omega$  is the volume of the region of the film on which the noise measurement has been made. This normalization is needed because the volume used for measurements is different for different films. If the noise arises from the bulk then  $\langle (\Delta R)^2 / R^2 \rangle$  is proportional to  $1/\Omega$ . This is rationale for the multiplication in equation 4.5.

#### 4.4.2 Noise in strain relaxed films at room temperature

In this section we discuss the results of our study of resistance fluctuations as a function of frequency in our strain relaxed films of thickness 500 nm at room temperature. We abbreviate it as LCMO33/STO (500 nm) in the following subsections.

As we mentioned earlier the noise measured using five-probe ac biasing technique. During the noise measurements we ensured that the spectral power  $S_V(f) \propto V^2$  where  $V$  is the bias voltage (typically few hundreds of  $\mu$ V). We have plotted this  $S_V(f)$  at  $f = 1$  Hz as a function of  $V$  in Fig. 4.19. The solid line gives the least square fit to the data. This is also clear that the spectral power follows  $V^2$  dependence.

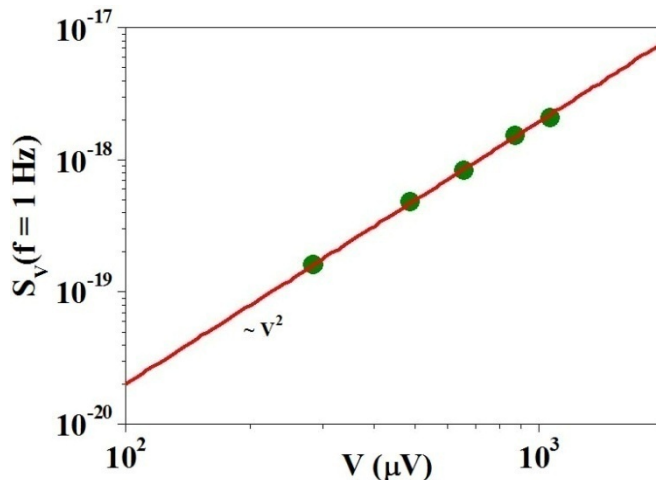


**Figure 4.19:** Plot showing the  $V^2$  dependence of the measured noise for LCMO33/STO (500 nm) film at 300 K. The straight line is a least square fit to the data.

In Fig. 4.20 we present a typical example of raw voltage time series data for the film at 300 K. The upper panel of Fig. 4.20 shows voltage fluctuations ( $\Delta V_{sample}$ ) measured coming from the sample while, the lower panel shows the background voltage fluctuations ( $\Delta V_{bg}$ ). The magnitude background voltage fluctuation is one order less than the measured voltage fluctuations coming from the sample. There is sharp difference between the two time series which has to be noted. This difference is reflected when we extract the frequency dependence of power spectral density from these two time series. The sample voltage time series contains large number of small peaks, whereas background voltage time series does'nt.

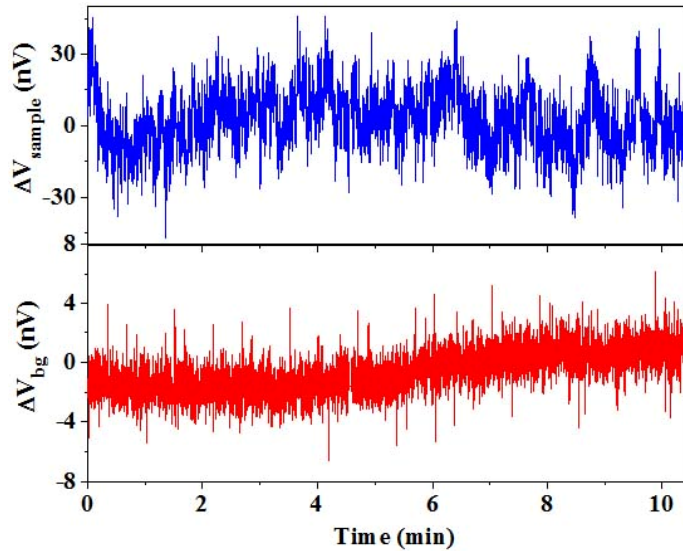


**Figure 4.20:** The raw voltage time-series measured across the film sample (upper panel) and from background (lower panel) at 300 K. The sharp difference between the two time series should be noted.

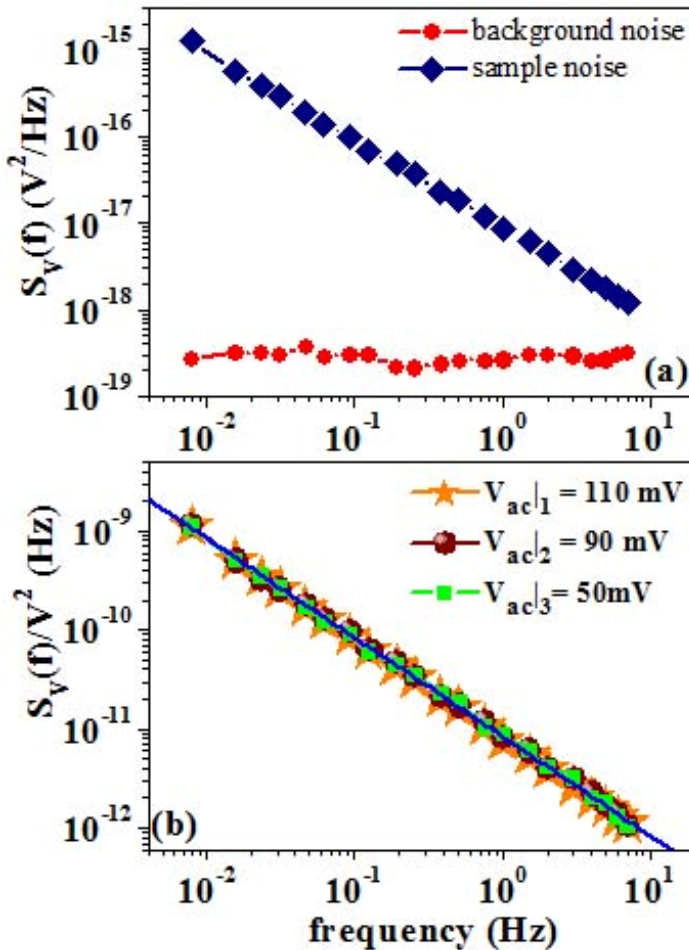


**Figure 4.21:** (a) The plot showing the power spectra  $S_v(f)$  along with the background estimated from the two time series represented in Fig. 4.20 (upper panel and lower panel respectively). (b) The power spectral density  $S_v(f)/V^2$  for three different ac bias voltages at 300 K. The solid line shows for which  $\alpha = 1$ .

In Fig. 4.21(a) we have plotted the spectral power  $S_V(f)$  of the noise measured across the sample as well as the background. The background is “white” in frequency scale. These power spectra have been estimated from the above time-series presented in Fig. 4.20. Fig. 4.21(b) shows three different power spectral densities measured across the film for three different ac bias voltages at 300K. These spectra show the reproducibility of our noise data with changing bias voltages. We can see there is a clean  $1/f^\alpha$  noise at room temperature with  $\alpha \sim 1.0$ . The solid line in the graph shows plot with  $\alpha = 1.0$ .

It is interesting to see how noise is behaving as a function of temperature and whether it retains its  $1/f^\alpha$  behaviour or not. In the next section we have explored the noise mechanism at low temperatures.

#### 4.4.3 Temperature dependent low-frequency noise in strain relaxed films

We have selected two distinct temperature regions: one is FMM region i.e.,  $T < T_c$  and other is PI region i.e.,  $T \geq T_c$ . Later we see that the nature of the spectra have actually separated these two temperature regions for further investigations. Here we have chosen frequency range  $0.3 \text{ mHz} < f < 10 \text{ mHz}$  for our investigations.

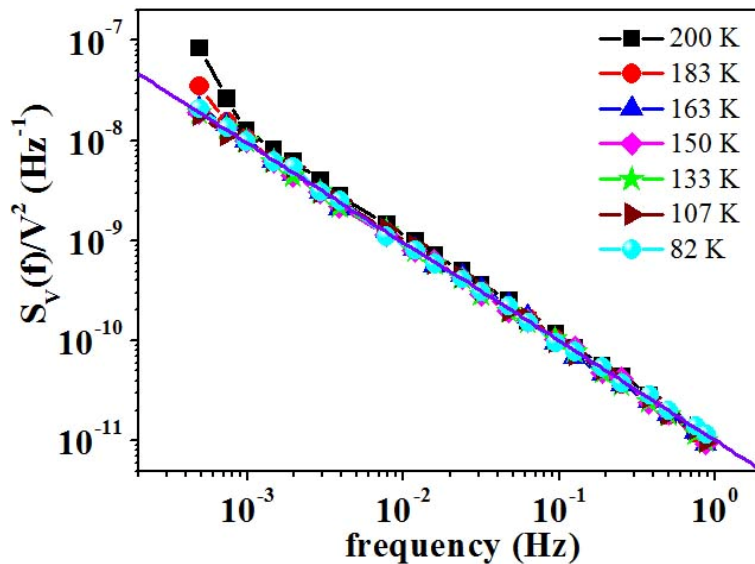


**Figure 4.22:** The plot showing the power spectral density  $S_V(f)/V^2$  as a function of frequency for few representative temperatures below  $T_c$ . The noise at low temperatures i.e., sufficiently below  $T_c$  shows  $1/f^\alpha$  noise. The solid line shows for which  $\alpha = 1$ . The spectra started deviating from  $1/f$  nature at low frequencies approaching towards  $T_c$ .

In Figure 4.22 first we plot the typical nature of power spectral density of the resistance noise appearing from the strain relaxed film below  $T_c$ . We have selected few representative temperatures in this respect. We can see that for temperatures well below  $T_c$  the noise spectra are following  $1/f^\alpha$  behaviour. The solid line in the graph gives the line for  $\alpha = 1.0$ . We can clearly observe that approaching towards  $T_c$ , the power spectra started to

deviate at low frequencies. To show the deviation clearly at low frequencies we have plotted  $f.S_V(f)/V^2$  for the same temperatures as shown in Fig. 4.23. The change is observed for higher temperatures. We discuss this temperature dependence in detail in the next part. Such a change in spectra is rather interesting and would indicate the presence of additional noise mechanisms in these samples which are not present at low temperatures. This issue is dealt with in further detail in the next part where we discuss the temperature dependence of noise in these samples above  $T_C$ .

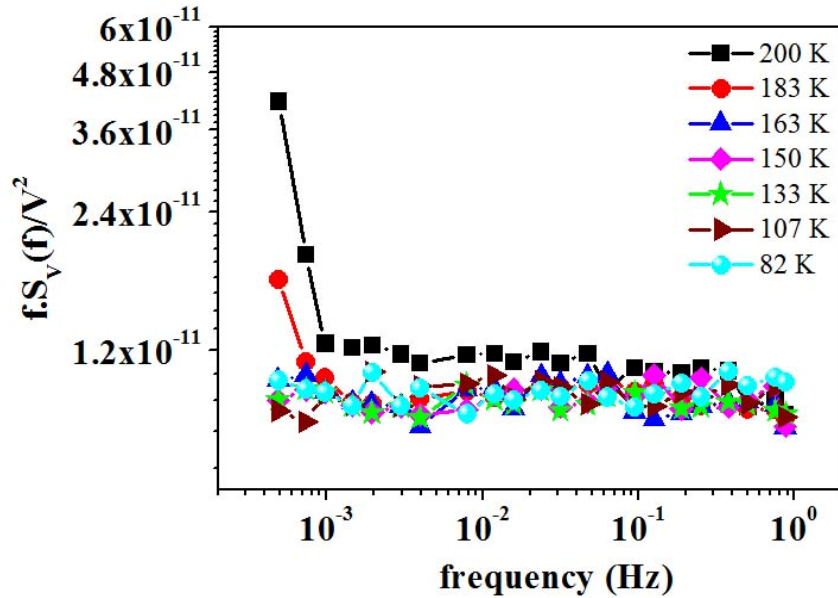


**Figure 4.23:** The plot showing the power spectral density  $f.S_V(f)/V^2$  as a function of frequency for the same temperatures mentioned in Fig. 4.22. The spectra started deviating from  $1/f$  nature at low frequencies approaching for higher temperatures.

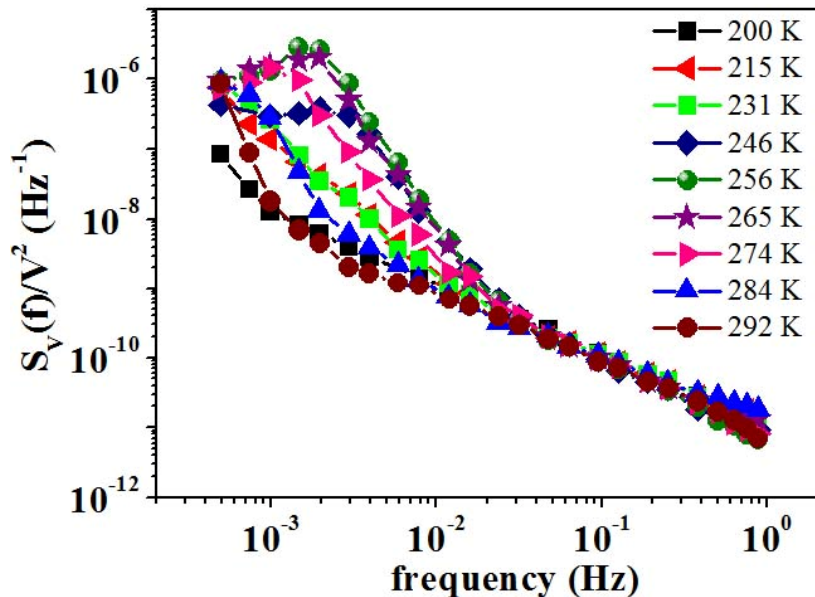


**Figure 4.24:** The spectral power  $S_V(f)/V^2$  measured at few representative temperatures as a function of  $f$  covering the transition temperature  $T_C$ . The significant change in nature of the power spectra near transition is noted.

In Fig. 4.24 we have plotted  $S_V(f)/V^2$  for few representative temperatures encompassing  $T_C$ . We can observe the significant changes in nature of these power spectra around FMM-PI transition. For  $f > 10$  mHz, we can see all the power spectra collapse together and follow  $1/f$  noise. Again, for  $f < 10$  mHz, the spectra separate out from each other and show up low frequency Lorentzian noise component clearly. To accentuate the low frequency deviation from  $1/f$  dependence we plotted  $f.S_V(f)/V^2$  in Fig. 4.25. It is also clear from this figure that there is an enhanced low frequency component of noise in the frequency range  $0.3$  mHz  $< f < 10$  mHz in a narrow temperature range around transition. For  $f \geq 10$  mHz, the spectral power exhibits a clean  $1/f$  dependence below and above  $T_C$ .

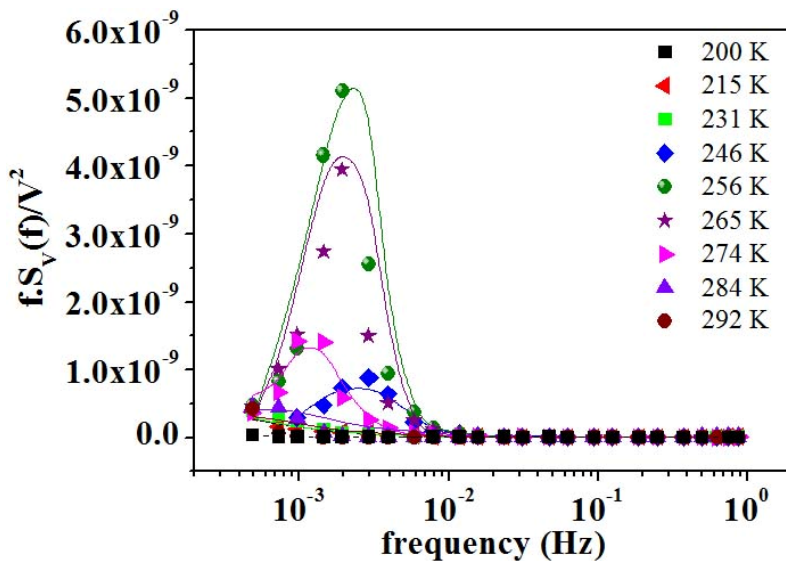


**Figure 4.25:** The spectral power  $f.S_V(f)/V^2$  measured at few representative temperatures as a function of  $f$  covering the transition temperature  $T_C$ .

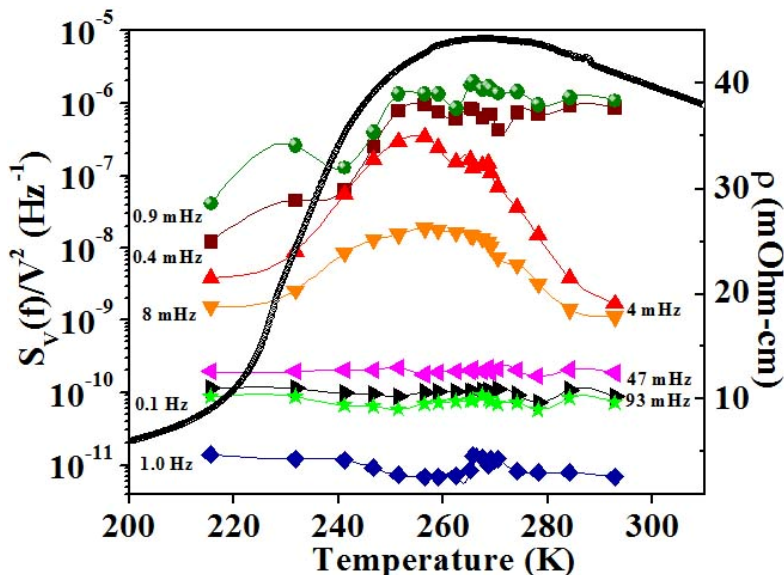


**Figure 4.26:** The scaled spectral power  $S_V(f)/V^2$  measured at few representative frequencies as a function of  $T$  along the sample resistivity  $\rho(T)$ .

In Figure 4.26 we show that the spectral power  $S_V(f)/V^2$  for 500 nm film measured at few representative frequencies as a function of  $T$  along with the sample resistivity  $\rho(T)$ . This is the consequence of previous graph to show that at low frequencies ( $f \leq 10$  mHz), spectral power has a nontrivial temperature dependence around the transition temperature while at high frequencies ( $f \geq 10$  mHz), there is no dependence on temperature. We want to mention that spectral power at low frequencies passes through a distinct maxima at transition region while the higher-frequency spectral power does not have any such distinct features close to transition. This observation also implies that close to  $T_C$ ,  $S_V(f)$  severely deviates from its  $1/f$  frequency dependence at transition regime. A similar kind of result was reported by Bid *et al.* [50] in charge ordered manganite sample near charge ordering transition temperature  $T_{CO}$ . But the frequency range of their investigations was  $1$  mHz  $< f < 10$  Hz which is 10 times higher than the frequency range our investigations.

#### 4.4.4 Temperature dependent time-series of voltage fluctuations and analysis of noise spectral power density

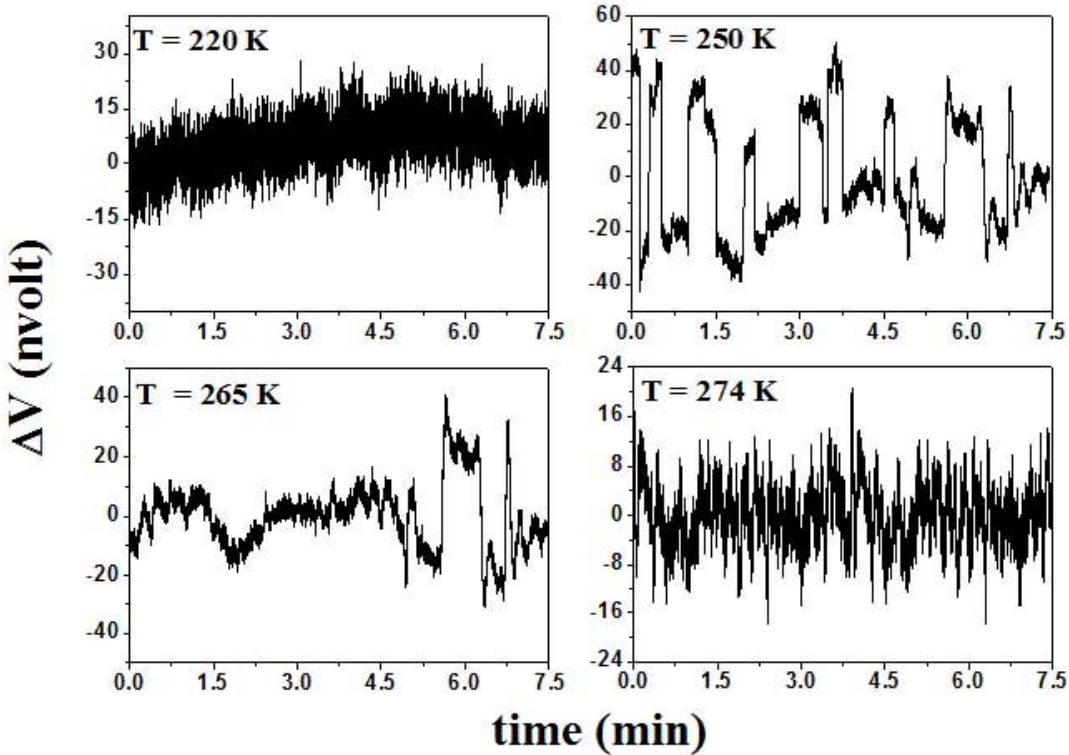


**Figure 4.27:** The voltage time series data at few representative temperatures showing RTN in time series.

The nature of the spectral power appearing in Fig. 4.24 and Fig. 4.25 can be realized by investigating the voltage time series ( $\Delta V(t)$  with time  $t$ ) data at temperatures where we have measured noise. The voltage time series data is presented in Fig. 4.27 at few temperatures. We observed the presence of RTN in voltage time series at few temperatures just below  $T_C$ . For an example, we show that at 250 K and 265 K RTN noise is more prominent and the nature of the voltage time series significantly differs from the time series

at 220 K and 274 K (i.e., which are far from  $T_c$ ). The RTN type time series appears due to presence of discrete fluctuators which has been established earlier. We also infer that RTN-type time series shows that the fluctuators causing the resistance fluctuations are of two-level type. However, it appears that there may be two or more superimposed two-level fluctuators with different levels. We have already discussed in Chapter 1 that the presence of RTN will give us a Lorentzian type spectral power in frequency domain. Similarly we recorded Lorentzian nature of spectral power (see Figure 4.25) for the temperatures where RTN picks up. Mathematically, the spectral power density of this fluctuation can be written in Lorentzian form as:

$$S(f) \propto \frac{2\tau}{1 + (2\pi f\tau)^2}, \quad (4.6)$$

which has  $1/f^2$  frequency dependence. We have fitted the spectral power at each temperature  $T$  in the complete frequency region by the following relation (Eq. 4.7) which consists of a  $1/f$  term and a Lorentzin term with temperature-dependent parameter  $f_c(T)$ , called corner frequency,

$$\frac{S_v(f)}{V^2} = \frac{A(T)}{f} + \frac{B(T)f_c(T)}{f^2 + f_c^2(T)}. \quad (4.7)$$

The fitted data is shown by the solid line in Figure 4.25 and we can clearly separate out two spectral components ( $1/f$  part and Lorentzian part) in well separated frequency domain. The temperature-dependent constants  $A(T)$  and  $B(T)$  are obtained from the fitted data and they give relative weights of the two contributions.

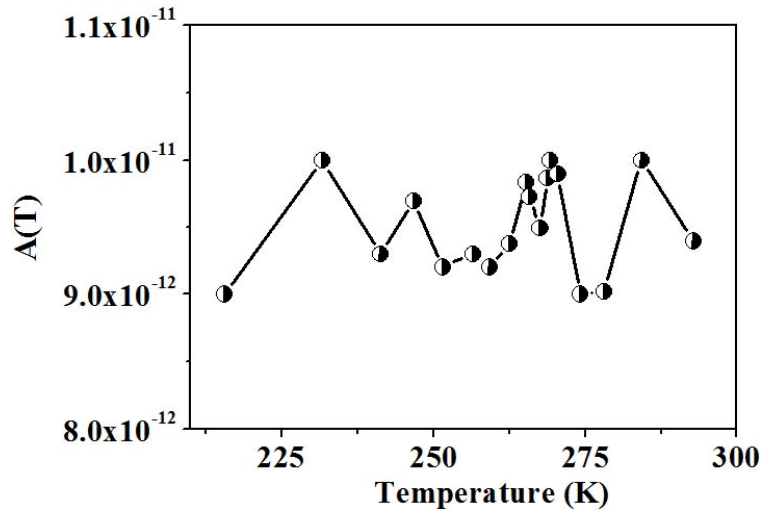


**Figure 4.28:** The plot of temperature dependent weightage of  $1/f$  noise  $A(T)$ .

Plot of  $A(T)$  as a function of temperature is shown in Fig. 4.28.  $A(T)$ , the weight of the  $1/f$  term has very little temperature dependence. Plots of  $f_c(T)$  and  $B(T)$  as functions of  $T$  are shown in Figure 4.29. Both  $f_c(T)$  and  $B(T)$  show nontrivial temperature dependence, in

particular, around the transition region ( $T/T_c \approx 0.9-1.0$ ) where they become substantially large. Both of them reach a maximum at  $T/T_c \approx 0.95$ . The observed corner frequencies  $f_c(T)$  are low and  $< 5$  mHz.

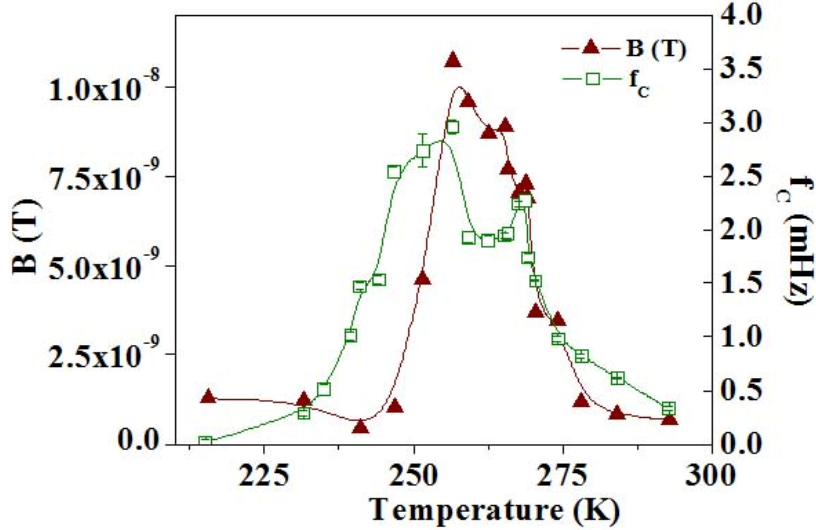


**Figure 4.29:** The temperature dependence of  $B(T)$  and Lorentzian corner frequency  $f_c(T)$ .

Note that in earlier studies, the reported spectral range was for  $f > 100$  mHz. As a result these fluctuations could not be observed. The discrete fluctuators in this temperature range were seen earlier studies in epitaxial films grown on NGO [14]. We point out that this kind of fluctuation in strain relaxed films with quenched disorder has not been reported in any of the past studies. The average time scale for the two-level-fluctuators (TLF)  $\tau_c$  is related to the corner frequency  $f_c$  seen in the power spectrum by the relation  $\tau_c^{-1} = 2\pi f_c$ . The data show that, near the ferromagnetic transition, the TLF fluctuators become measurable in the time scale of the measurements ( $f_c$  becomes more than 0.25 mHz) and also there number density increases.

In order to compare the relative resistive fluctuation  $\langle (\Delta R)^2 / R^2 \rangle$  by integrating  $S_V(f)/V^2$  within the experimental bandwidth  $f_{\min} \approx 0.1$  mHz and  $f_{\max} \approx 1$  Hz and using Eq. 4.7 we can write

$$\begin{aligned} \left\langle \frac{(\Delta R)^2}{R^2} \right\rangle &= \int_{f_{\min}}^{f_{\max}} \frac{A}{f} df + \int_{f_{\min}}^{f_{\max}} \frac{B f_c}{f^2 + f_c^2} df \\ &= \left\langle \frac{(\Delta R)^2}{R^2} \right\rangle_1 + \left\langle \frac{(\Delta R)^2}{R^2} \right\rangle_2 . \end{aligned} \quad (4.8)$$

The temperature dependence of the total fluctuation  $\langle (\Delta R)^2 / R^2 \rangle$  and the contribution of  $1/f$  component  $\langle (\Delta R)^2 / R^2 \rangle_1$  and that of the Lorentzian  $\langle (\Delta R)^2 / R^2 \rangle_2$  are shown in Figure 4.30. It is clear that Lorentzian component contribution to the total noise is much higher in

comparison with the component coming from  $1/f$  noise. The nontrivial temperature dependence of  $f_c$  has been plotted simultaneously and it follows qualitatively nearly same temperature dependence as  $\langle(\Delta R)^2 / R^2\rangle$ .

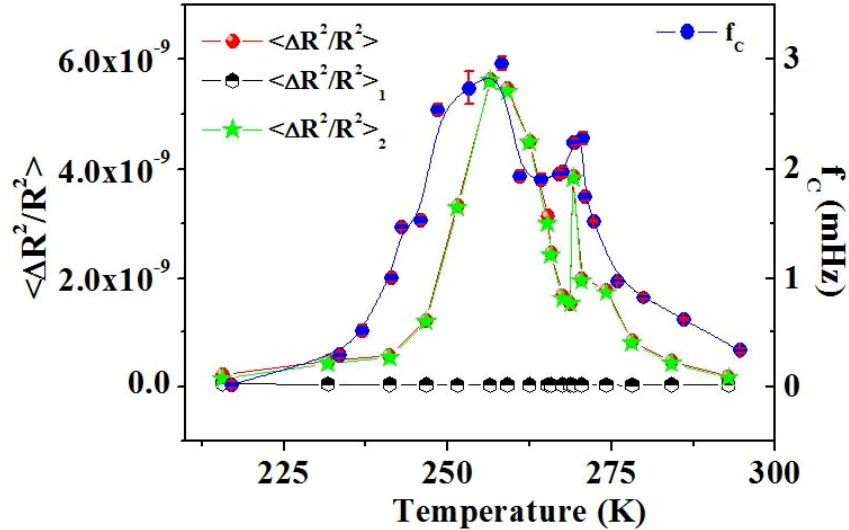


**Figure 4.30:** The variation of relative resistive fluctuation  $\langle(\Delta R)^2 / R^2\rangle$  with temperature along with Lorentzian corner frequency  $f_c$  has been plotted.

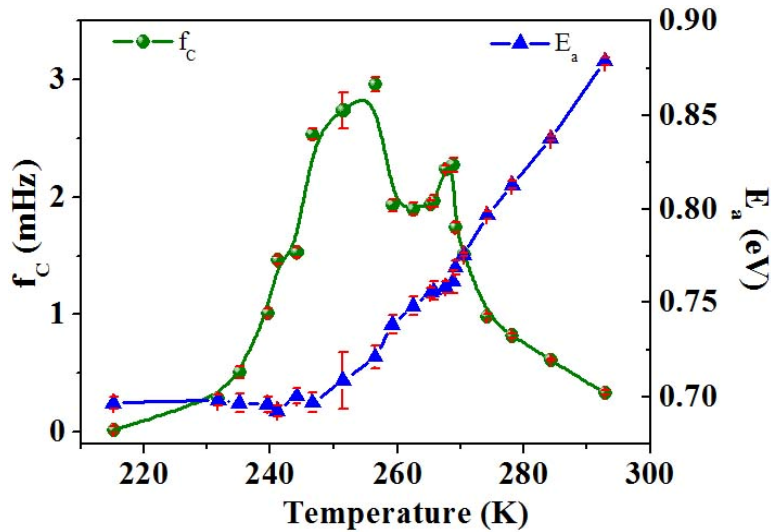


**Figure 4.31:**  $f_c$  is related to thermally activated process with activation energy  $E_a$  and are plotted simultaneously with temperature.

We have already discussed that  $f_c$  is related to TLF process can be expected to arise from thermal activation through a barrier energy  $E_a$ . In this case we can write

$$f_c = f_0 \exp\left(-\frac{E_a(T)}{k_B T}\right). \quad (4.9)$$

In Figure 4.31 we have plotted  $f_c$  and  $E_a$  together with temperature. This may arise from temperature dependence of attempt frequency  $f_0$  but it is less possible.

Temperature dependence of  $E_a$  is very small for  $T < 250$  K and reaches its maximum value at the vicinity of  $T_c$  (just below  $T_c$ ) and gives a small peak at  $T_c$ . This result is directly related to the TLF process and spectral power near transition is dominated by single-frequency Lorentzian two-level-type fluctuators. These TLF type fluctuators are associated with phase separation near  $T_c$ . We have calculated the attempt frequency  $f_0 = 4.5 \times 10^{14}$  Hz. The activation energy of the discrete fluctuators reported so far in  $\text{La}_{1-x}\text{Ca}_x\text{MnO}_3$  system ( $x \sim 0.3\text{-}0.33$ ) have much lower activation energy  $E_a < 0.1$  eV.

From our experimental results we have gathered information about the discrete fluctuators with very high activation energy related to the very small relaxation time so they contribute to the very low frequency range in the noise power spectra. The challenge of observing such a low frequency noise from discrete fluctuators is to reduce the  $1/f$  noise that can become substantial in this frequency region.

Now we show in the next section that a very low  $1/f$  noise can be achieved in oriented films of LCMO33, which have quenched disorder created by strain relaxation. Interestingly, the  $1/f$  noise in these films can even be less than that seen in low strain LCMO33 films grown on NGO. Such a low  $1/f$  noise in the strain relaxed films facilitates observation of very low frequency discrete fluctuators.

#### 4.4.5 Comparison of noise in strain relaxed films with films of low and negligible strain

The power spectra of a film with low strain (see Table 4.3) (thickness of 50 nm) grown on NGO and those of uniformly strained films grown on STO show only  $1/f$  dependence. These films (50 nm) on STO and NGO were grown using PLD. However, the spectral power in the uniformly strained film grown on STO is much larger (by nearly two orders of magnitude), as can be seen in Fig. 4.32 where the quantity has been plotted as function of temperature for the films. The noise peaks close to  $T_c$  in the film grown on STO. However, (in the film grown on NGO) does not show any peak and shows a small decrease as it is cooled through  $T_p$ . In the film grown on STO, the  $1/f$  noise is too large for observation of any discrete fluctuators. However, the existence of the discrete fluctuators (close to  $T_p$ ) cannot be ruled out. A clean separation of the noise power between a  $1/f$  dependence and the Lorentzian-type contribution from discrete fluctuators was not possible. The data presented here match very well with those reported before on STO and NGO films [14]. For the films with quenched disorder, the observed noise is very different. In particular, in the film with thickness of 500 nm, one can cleanly separate out the  $1/f$  part and the contribution from the discrete fluctuators. As can be seen from Fig. 4.32, this film has  $\beta$  which is less than that seen even in the LCMO33 (50 nm) grown on NGO. The total noise has a  $1/f$  noise component that is essentially temperature independent. At  $T = 300$  K (where the noise has substantial  $1/f$  contribution), the Hooge parameter [102] has a value of  $\sim 500$ . This film, close to the transition region, also shows very low frequency noise.

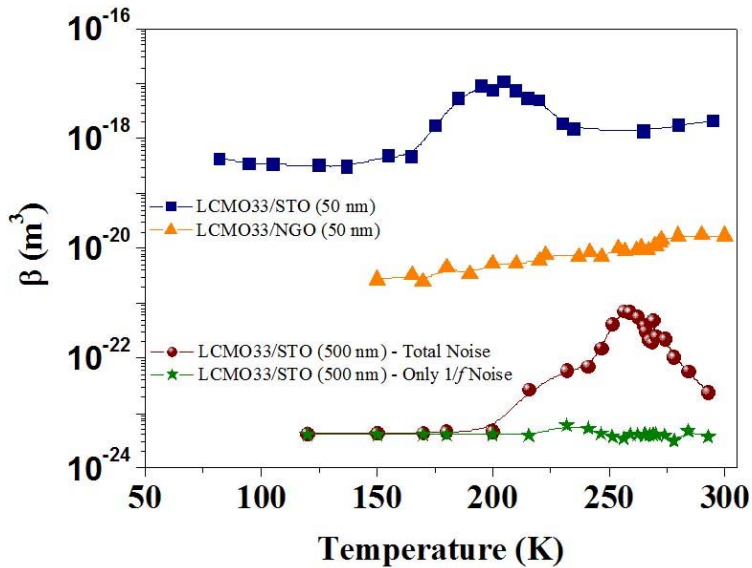


**Figure 4.32:** Temperature variation of  $\beta$  for LCMO33/STO (50 nm), LCMO33/NGO (50 nm) [9], and LCMO33/STO (500 nm) film [101].

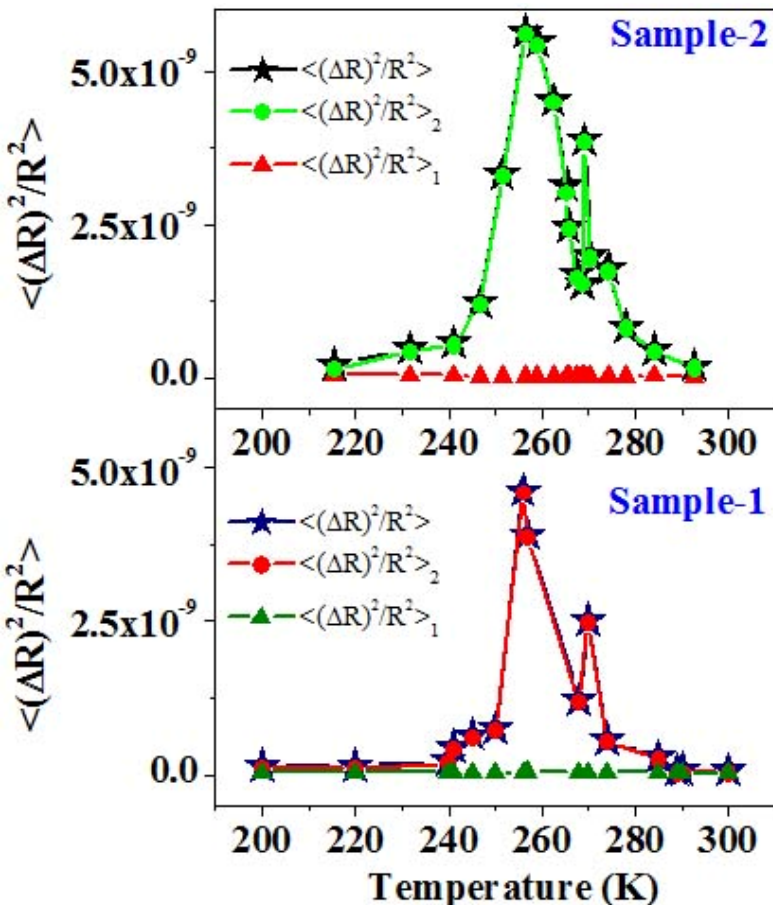


**Figure 4.33:** The variation of relative resistive fluctuation  $\langle (\Delta R)^2 / R^2 \rangle$  with temperature measured in two different samples i.e., for Sample-2 (upper panel) and Sample-1 (lower panel). This data check the reproducibility of the noise of different samples under study.

The type of noise behaviour we discussed so far was repeatedly seen in these type of films. In Fig. 4.33 we present noise data for two samples (Sample-2 and Sample-1) to check the reproducibility of our noise magnitude. These films have been grown independently by maintaining the same growth mechanism and conditions. From this data we can easily infer that these types of noise properties are inherent character of such strain relaxed films and due to quenched disorder which is created by strain relaxation. Thus not only strain but also microstructure can change the nature of resistance fluctuation in these films, not only quantitatively (by orders of magnitude) but also qualitatively.

#### 4.4.6 Discussion on the results obtained for strain relaxed films

Our observation shows that the strain (as well as the microstructure) plays an important role in determining the magnitude of noise power as well as the spectral nature of the resistance fluctuation in manganite films. In particular, in films with quenched disorder, there is a significant drop in the noise and it is even lower than that of the film grown on the NGO, which has very little strain. This is a particularly important observation that quenched disorder can lead to suppression of noise. One way that we may justify this observation is if the fluctuators that contribute to the noise in the films with quenched disorder have very large energy for thermal activation. In that case only a small number of fluctuators will be observable in the frequency window of the resistance noise measurements and it is the slow kinetics that makes most of the fluctuators unobservable in the observation window. Large energy for thermal activation ( $E_a$ ) can arise if the fluctuation process involves long-range strain accommodation that would be needed to have coexisting phases. Although there is no direct experimental evidence, there are suggestions that coexisting phases can have martensite-type long-range strain accommodation [103] In case of the LCMO with  $x \approx 0.3$ - $0.35$ , the coexisting phases close to  $T_c$  are the ferromagnetic metallic (FMM) phase and the polaronic paramagnetic insulating state. There is a difference in the JT distortion around the  $Mn^{3+}$  ions in the two phases, and when phases are coexisting in dynamic equilibrium, there will be small strain accommodation. The physical size of such strain accommodation will be limited by the misfit dislocations. In that case the strain accommodation occurs over regions with diameter of approximately 50-100 nm and thickness limited by the film thickness 500 nm. With a bulk modulus of  $\Xi = 190$  GPa, as reported for LCMO33, the strain accommodation will lead to  $E_a \approx 0.25$ - $1.0$  eV even for a small strain of only  $\varepsilon \approx 2 \times 10^{-5}$ .

The corner frequency  $f_c$  is small and has a strong dependence on temperature close to  $T_c$ . At lower temperatures, for  $T < 250$  K when  $f_c$  increases in heating, one can associate a thermally activated process for relaxation of the two-level fluctuators. Using the limited range of data available ( $T < 250$  K) and the Arrhenius relation  $f_c = f_0 \exp(-E_a / k_B T)$ , we evaluated the attempt frequency,  $f_0 = 4.5 \times 10^{14}$  Hz, and the activation energy,  $E_a \sim 0.7$  e.V. The high value of the activation energy justifies the very low value of  $f_c$  seen in these materials. This observation of high  $E_a$  supports the suggestion made in the previous paragraph. We note that fluctuators with such high  $E_a$  have been seen near the charge ordering transition before [50]. We also note that there is a decrease in  $f_c$  for  $T > 250$  K. We do not have any clear explanation for this behaviour. This can occur due to a hardening of  $E_a$  and/or a decrease in the attempt frequency. It may also be that the RTN that contributes to the spectral power in this region may have a complex temperature-dependent behaviour. As pointed out before, the RTN observed may actually be a superposition of two RTN processes

with their corner frequencies having different temperature dependences. The nontrivial temperature dependence of  $f_c$  may be a reflection of this.

#### 4.5 Dependence of resistance fluctuation (noise) on magnetic field in $\text{La}_{0.67}\text{Ca}_{0.33}\text{MnO}_3/\text{SrTiO}_3$ strain relaxed films

The magnitude of the Lorentzian-type noise that arises from the discrete fluctuators can be tuned even by a small field. Hence the resistance fluctuation has a distinct dependence on the applied magnetic field ( $H$ ), particularly at low fields.

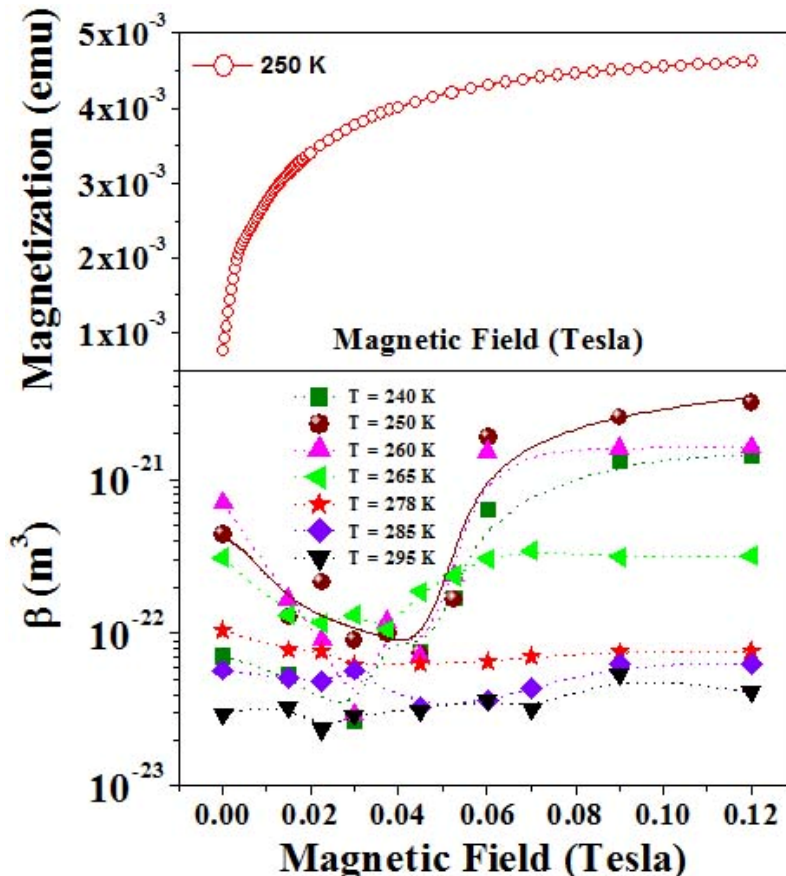


**Figure 4.34:**  $\beta$  as function of magnetic field  $H$  at few representative temperatures. The upper panel shows the saturation of the magnetization at 250 K.

In Figure 4.34, we plot relative resistance fluctuations  $\beta$  with  $H$  at few representative temperatures. In the top part of the same graph, we show a part of the  $M$ - $H$  curve at  $T = 250$  K where the noise power shows a peak. The  $M$ - $H$  curve establishes the scale of the magnetic field. The field dependence becomes very weak as  $T \rightarrow T_c$ . Power spectrum (not shown to avoid repetition) shows that most of the spectral weight comes from the region with  $f \leq 10$  mHz. The noise is suppressed initially for low magnetic field (0.05 Tesla), which is similar to (but somewhat lower than) the value  $H_c$  of the film. Beyond that it starts rising for higher fields and shows saturation. The saturation magnetic field is lower than the technical saturation seen in  $M$ - $H$  curve. It is important to note that such a small field has substantial effect on the noise power. One important observation merits attention although the magnitude

of the resistance fluctuation has strong dependence on the magnetic field: the value of the corner frequency  $f_c$  has negligible dependence on the magnetic field. This is in contrast to past studies [17].

In our case, the absence of an effect on  $f_c$  is expected because the applied field is small and the scale of  $M \cdot H$  is far too small compared to the activation energy  $E_a$ . As an origin for the dependence of the resistance noise on the magnetic field, we note that the local resistance can change if they are coupled to the magnetization  $M$ . The only quantity that changes substantially at temperatures close to  $T_p$  and that can also be changed by such a low field is the magnetization  $M$ . The resistance fluctuation at very low frequency that appears can be related to the fluctuation in local magnetization. Such a fluctuation will couple to the resistance fluctuation via magnetoresistance ( $MR = dR/dH$ ) and the derivative of the magnetization  $dM/dH$ . The low-field MR at different  $T$  is shown in Figure 4.35. The  $dR/dH$  has been obtained by actual measurements in low field ( $H \leq 0.1$  Tesla). The  $R$  decreases linearly in  $H$  and  $dR/dH$  peaks near  $T_C$ , as shown in the inset of Figure 4.34.

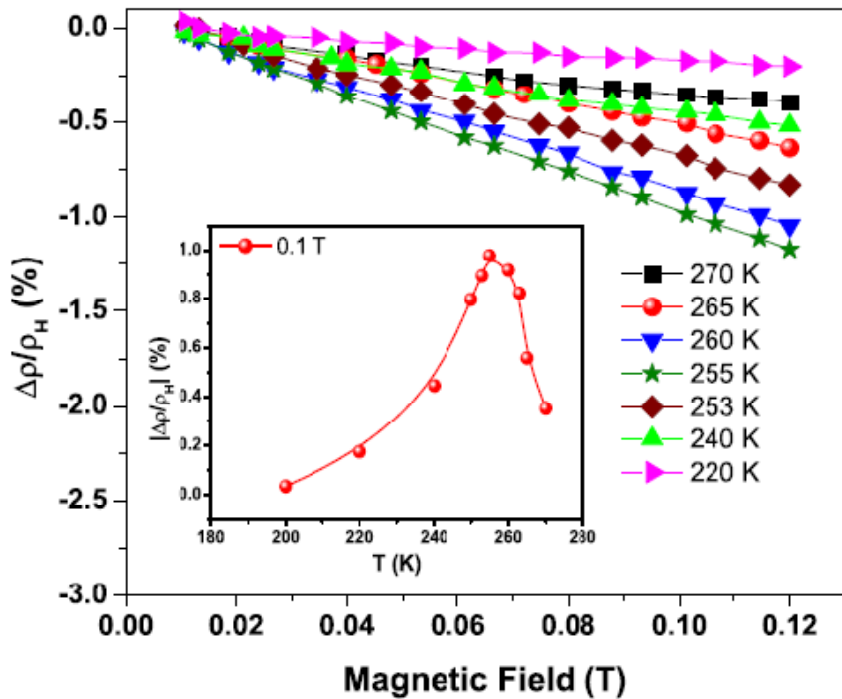


**Figure 4.35:**  $MR$  as a function of magnetic field for few representative temperatures.  $MR$  as a function of temperature (measured with field  $0.1$  T) is shown as an inset.

The magnetization fluctuation  $\langle (\Delta M)^2 \rangle$  will give rise to the resistance fluctuation:

$$\left\langle \frac{(\Delta R)^2}{R^2} \right\rangle = \xi \left( \frac{1}{R} \frac{dR}{dM} \right)^2 \langle (\Delta M)^2 \rangle, \quad (4.10)$$

where  $\xi$  is the constant that takes care of the fact that the current flow is inhomogeneous and, if the fluctuators sit on a path of high current concentration, even a small magnetization fluctuation leads to much larger resistance fluctuations. Such an effect has been also seen in

past studies on discrete fluctuators [48]. Since  $dR/dM = (dR/dH)/(dM/dH)$  one would expect

$$\left\langle \frac{(\Delta R)^2}{R^2} \right\rangle^{0.5} \propto \frac{dR}{dH}. \quad (4.11)$$

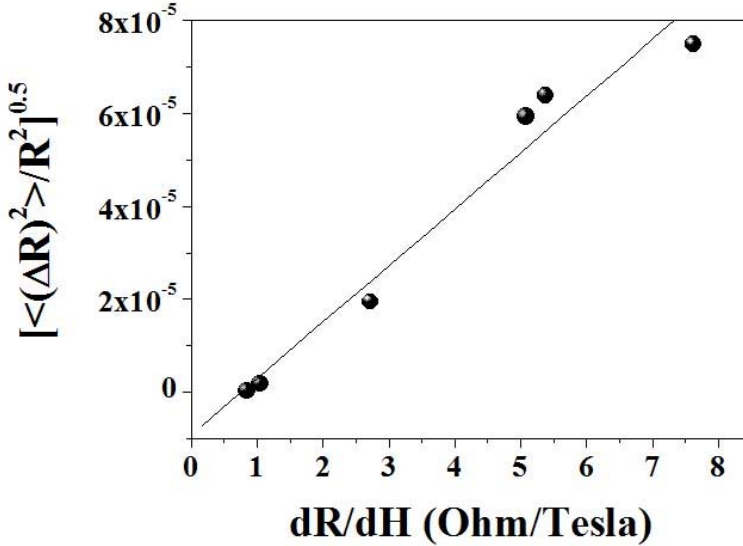


Figure 4.36:  $\left\langle \frac{(\Delta R)^2}{R^2} \right\rangle$  as a function of  $dR/dH$  at temperatures  $T < T_c$ .

Such a linear relation exists, as can be seen in Figure 4.36. Very close to and above  $T_c$ , the linearity breaks down because the magnetization itself collapses. The fluctuation in magnetization ( $\Delta M$ ) can occur due to two reasons:

- Close to  $T_c$ , a contribution due to domain rotation can arise. The contribution of the domain rotation to  $\left\langle \frac{(\Delta R)^2}{R^2} \right\rangle$  is expected to decrease as  $H$  increases and eventually at  $H \geq H_c$ , this contribution should subside. Thus a variation  $\left\langle \frac{(\Delta R)^2}{R^2} \right\rangle \propto 1/H^\alpha$  is expected.
- Another contribution to  $(\Delta M)$  can arise from the coexisting phases. The two coexisting phases that give rise to the noise have different magnetization. One of the phases with lower resistance will be the ferromagnetic phase with higher magnetization, and the other higher resistance phase will be paramagnetic or even antiferromagnetic and will have low moment. The contribution to  $(\Delta M)$  due to difference in the magnetization of the two coexisting phases is thus expected to become larger as  $M$  becomes larger on application of the field. A simple expectation will be  $\left\langle \frac{(\Delta R)^2}{R^2} \right\rangle \propto 1/M^n$ , where  $n \approx 2$ . In the range of

our data ( $H$  below technical saturation),  $M \propto H^\eta$ , where the observed  $\eta \approx 0.25\text{-}0.27$ . Thus one would expect  $\left\langle \frac{(\Delta R)^2}{R^2} \right\rangle \propto H^\gamma$ , where  $\gamma = n\eta$ .

We fitted the experimental field dependence of the resistance fluctuation to the empirical relation

$$\left\langle \frac{(\Delta R)^2}{R^2} \right\rangle^{0.5} = \frac{P}{H^\alpha} + Q(H - H_c)^\gamma \quad (4.12)$$

and find that such a relation indeed fits the data, as shown by the solid line in Figure 4.34. The observed  $\gamma \approx 0.4$  compares well with expected estimate of  $\gamma \approx 0.5$ . The above discussion strongly suggests that the observed resistance fluctuation arises from the magnetization fluctuation and the coupling occurs by magnetoresistance.

## 4.6 Investigation of correlation between temporal and special fluctuations

Till now we have discussed about the temporal fluctuations which can be probed directly by noise spectroscopy. The special fluctuations can also be recorded by local probes like STM [9, 104] and STM topography images of the films taken at room temperature which are shown in Fig. 4.37. One can investigate direct correlation between these two different kinds of fluctuation processes. The variation of local fluctuation in  $g$ , as measured by STM, shows that these films have substantial degree of special phase separation. The establishment of such a correlation between these fluctuations, although tempting, has its problems, which is related to the time scales of the image acquisition in the local probe methods and thermal drift in the subsequent scans.

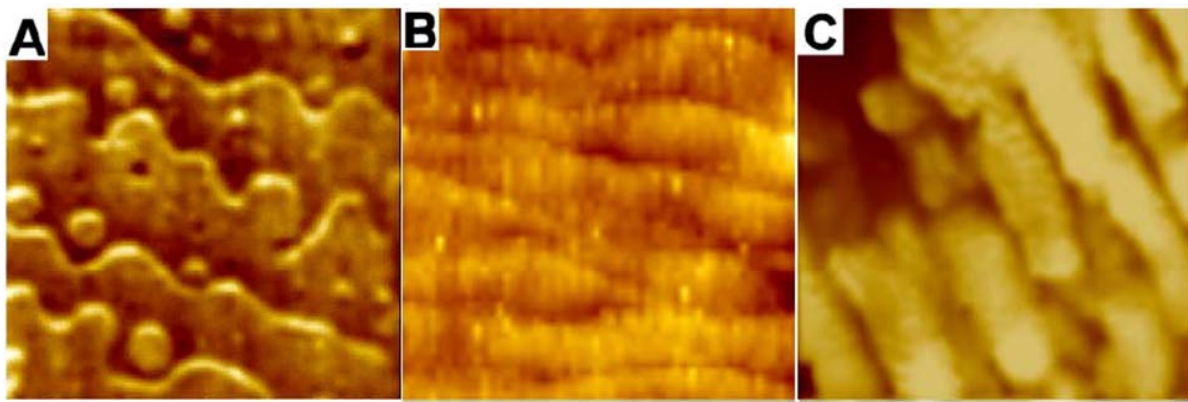


**Figure 4.37:** STM topography of LCMO33 films. (A) LCMO/NGO ( $1.2\mu\text{m} \times 1.2\mu\text{m} \times 0.5\text{nm}$ ), (B) LCMO/STO(50) ( $0.95\mu\text{m} \times 0.95\mu\text{m} \times 0.6\text{nm}$ ) and (C) LCMO/STO(200) ( $0.15\mu\text{m} \times 0.15\mu\text{m} \times 0.8\text{nm}$ ). Adapted from reference [9].

The coexisting phases are electronically distinct and thus are expected to have different density of state at the Fermi level  $[N(E_F)]$ . Thus  $[N(E_F)]$  is expected to show

spatial fluctuations as one scans the local tunneling conductance  $g$  ( $g \propto [N(E_F)]$ ) of the phase-separated regions by the STM. From the measured local map of  $g$ , we can compute the root-mean-square (RMS) relative fluctuation in the local tunneling conductance  $\langle(\Delta g)^2\rangle^{0.5} / g$ . The special fluctuation in these films generally peaks up around  $T \sim T_p \sim 1-0.95$  and is found to be largest in the uniformly strained 50 nm film grown on STO as shown in Fig. 4.38.

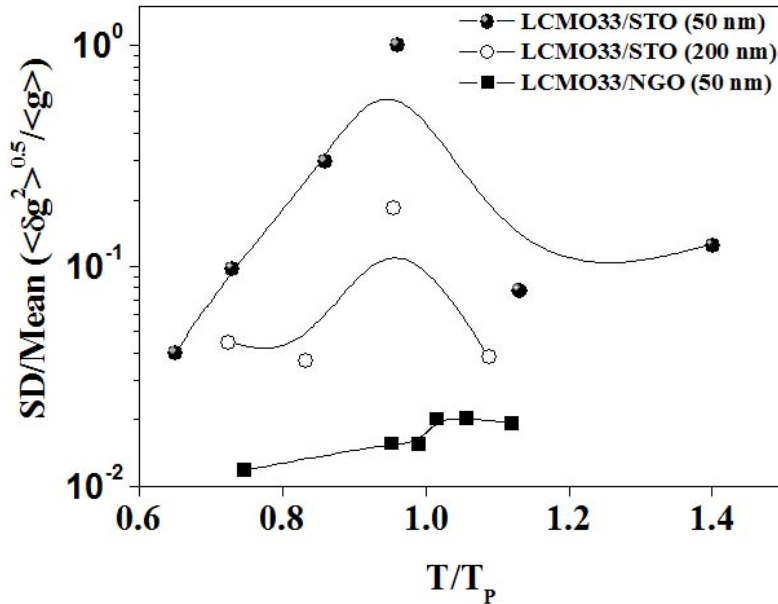


**Figure 4.38:**  $\langle(\Delta g)^2\rangle^{0.5} / g$  calculated from line scans across local conductance mapping of LCMO33/STO (50 nm), LCMO33/STO (200 nm), LCMO33/NGO (50 nm) films as a function of temperature [9].

We suggest that the large conductance noise in LCMO33/STO (50 nm) is related to phase separation and large inhomogeneity in the system. A dynamic fluctuation between regions of different conductivity can give rise to large conductance fluctuations. The conductivity mapping is the direct evidence of conduction inhomogeneity. A comparison of the noise (see Figure 4.32) in LCMO33/NGO (50 nm) and LCMO33/STO (50 nm) indicates that the lattice mismatch strain in LCMO/STO (50 nm) is primarily responsible for the increased noise level both in the paramagnetic and ferromagnetic regime. As we stated earlier that even in the FMM phase, an appreciable enhancement in the noise, over 2 orders of magnitude, is observed as compared to strain free film and the strain relaxed films are even less noisy than a strain free film. So we can infer that there exist a direct correlation between phase separation and strain accommodation which fix the noise levels by controlling the conductance inhomogeneity in the samples.

We want to mention that the map of  $g$  from which the special fluctuation has been computed was taken over a time scale of  $\sim 1$  sec. It can be regarded as a “snapshot.” This is faster than the time scale over which the RTN occurs. In fact if we keep the STM tip at a point on the sample, we can clearly observe the RTN-type fluctuation in the time series of the tunneling current. This is in addition to the usual  $1/f$  noise of the STM amplifier. If the data are taken over by a longer time scale, some of these features get averaged out, showing the dynamic nature of the spatial image. However, over longer time scales, there is a thermal drift that blurs out some of the contrast in the images of spatial fluctuation. Due to these effects,

the time scale associated with the spatial fluctuations cannot be uniquely specified. Where conductance map in STM probes the static inhomogeneity in the surface, conductance fluctuations probe the dynamics of the fluctuating electrical conductance. Noise spectroscopy directly maps the dynamic nature of conductance fluctuation in temporal fluctuation spectra.

## 4.7 Conclusions

In conclusion we can summarize the results presented in this chapter as follows:

1. We have performed investigation of very low frequency ( $0.3 \text{ mHz} < f < 1 \text{ Hz}$ ) resistance fluctuations in  $\text{La}_{0.67}\text{Ca}_{0.33}\text{MnO}_3$  films near ferromagnetic to paramagnetic phase transition  $T_c$ . These films are strain relaxed with quenched disorder.
2. These films are very noisy than films with low strain and with uniform strained films. We observed well behaved RTN at very low frequencies which are appearing due to the strain relaxation and phase coexistence. RTN are two-level-fluctuation (TLF) type and gives rise to Lorenzian contribution to the spectral power other than  $1/f$  noise. Where the RTN driven relative resistance fluctuations have nontrivial temperature dependence, the  $1/f$  noise is temperature independent. The TLFs fluctuators have large activation energy  $\sim 0.7 \text{ eV}$ .
3. There exists a distinct dependence of these fluctuations on applied magnetic field. We observed the saturation of total fluctuations in presence of magnetic field also. This can be understood by taking into account the strong coupling of magnetic and resistance fluctuations through the mechanism of magnetoresistance. The magnetic fluctuation is found to have a contribution from both domain rotations as well as from coexisting phases. It is observed that the strain and microstructure play an important role in determining the noise power as well as the spectral nature of the resistance fluctuation in manganite films.
4. We have investigated a close correlation between temporal fluctuation and special fluctuations in these films. We used noise to probe temporal fluctuations of resistance and STM conduction map probes special fluctuations in conduction. Around  $T_c$  temporal fluctuations driven by conduction fluctuations gives the idea of phase coexistence in this region.

## Bibliography:

- [1] E. Dagotto, T. Hotta, and A. Moreo, Phys. Rep. **344**, 1 (2001); Nanoscale Phase Separation and Colossal Magnetoresistance, edited by E. Dagotto (Springer-Verlag, Berlin, 2002).
- [2] Electronic Noise and Fluctuations in Solids, edited by S. Kogan (Cambridge University Press, Cambridge, England, 1996).
- [3] J.-H. Park, E. Vescovo, H.-J. Kim, C. Kwon, R. Ramesh, and T. Venkatesan, Phys. Rev. Lett. **81**, 1953 (1998).
- [4] J. M. D. Coey, M. Viret, and S. von Molnár, Adv. Phys. **48**, 167 (1999).
- [5] R. von Helmholz, J. Wecker, B. Holzapfel, L. Schultz, and K. Samwer, Phys. Rev. Lett. **71**, 2331 (1993); S. von Molnár and T. Kasuya, Phys. Rev. Lett. **21**, 1757 (1968).
- [6] J. B. Goodenough, *Magnetism and the Chemical Bond* (Interscience, New York, 1963).
- [7] G. Masumoto, J. Phys. Soc. Jpn. **29**, 615 (1970).
- [8] J. M. D. Coey, M. Viret, and L. Ranno, Phys. Rev. Lett. **75**, 3910 (1995).
- [9] J. Mitra, Ph. D Thesis, Indian Institute of Science, Bangalore India.
- [10] A. J. Millis, T. Darling, and A. Migliori, J. Appl. Phys. **83**, 1588 (1998).
- [11] M. Bibes, S. Valencia, Ll. Balcells, B. Martinez, J. Fontcuberta, M. Wojcik, S. Nadolski, and E. Jedryka, Phys. Rev. B **66**, 134416 (2002).
- [12] H. Chou, M. -H. Tsai, F. P. Yuan, S. K. Hsu, and C. B. Wu, J. Y. Lin, C. I. Tsai, Y. -H. Tang, Appl. Phys. Lett. **89**, 082511(2006).
- [13] Mandar Paranjape, J. Mitra, and A. K. Raychaudhuri, N. K. Todd, N. D. Mathur, and M. G. Blamire, Phys. Rev. B **68**, 144409 (2003).
- [14] P. Reutler, A. Bensaid, F. Herbstritt, C. Hofener, A. Marx, and R. Ross, Phys. Rev. B. **62**, 11619 (2000)
- [15] Mandar Paranjape, and A. K. Raychaudhuri, N. D. Mathur, and M. G. Blamire, Phys. Rev. B **67**, 214415 (2003).
- [16] M. Bibes, L. Balcells, S. Valencia, J. Fontcuberta, M. Wojcik, E. Jedryka, and S. Nadolski, Phys. Rev. Lett. **87**, 67210 (2001).
- [17] R. D. Merithew, M. B. Weissman, F. M. Hess, P. Spradling, E. R. Nowak, J. O'Donnell, J. N. Eckstein, Y. Tokura, and Y. Tomioka, Phys. Rev. Lett. **84**, 3442 (2000).
- [18] A. Palanisami, R. D. Merithew, M. B. Weissman, and J. N. Eckstein, Phys. Rev. B **64**, 132406 (2001).
- [19] N. D. Mathur, G. Burnell, S. P. Isaac, T. J. Jackson, B. -S. Teo, J. L. MacManus-Driscoll, L. F. Cohen, J. E. Evetts, and M. G. Blamire, Nature **387**, 266 (1997).
- [20] Barnali Ghosh, Loveleen K. Brar, Himanshu Jain, and A. K. Raychaudhuri, J. Phys. D **37**, 1548 (2004).
- [21] A. de Andres, J. Rubio, G. Castro, S. Taboada, J. L. Martinez, and J. M. Colino, Appl. Phys. Lett. **83**, 713 (2003).
- [22] M. Ziese, H. C. Semmelhack, K. H. Han, S. P. Sena, and H. J. Blythe, J. Appl. Phys. **91**, 9930 (2002).
- [23] M. Angeloni, G. Balestrino, N. G. Boggio, P. G. Medaglia, P. Orgiani, and A. Tebano, J. Appl. Phys. **96**, 6387 (2004).
- [24] G. Gao, S. Jin, and W. Wu, Appl. Phys. Lett. **90**, 012509 (2007).
- [25] H. Yamada, Y. Ogawa, Y. Ishii, H. Sato, M. Kawasaki, H. Akoh, and Y. Tokura, Science **305**, 646 (2004).
- [26] J. Z. Sun, W. J. Gallagher, P. R. Duncombe, L. Krusin-Elbaum, R. A. Altman, A. Gupta, Y. Lu, G. Q. Gong, and G. Xiao, Appl. Phys. Lett. **69**, 3266 (1996).

- [27] A. J. Millis, B. I. Shraiman, R. Mueller, Phys. Rev. Lett. **77**, 175 (1996); Phys. Rev. B **54**, 5389 (1996); A. J. Millis, Nature **392**, 147 (1998); A. J. Millis, B. I. Shraiman, R. Mueller, Phys. Rev. B **54**, 5405 (1996).
- [28] M. Jaime, P. Lin, S. H. Chun, M. B. Salamon, P. Dorsey and M. Rubinstein, Phys. Rev. B **60**, 1028(1999).
- [29] A. Moreo, S. Yunoki, and E. Dagotto, Science **283**, 2034 (1999).
- [30] P. G. de Gennes, Phys. Rev. **118**, 141 (1960).
- [31] E. Dagotto *et al.* Phys. Rev. **58** B, 6414 (1998).
- [32] R. H. Heffner et al., Phys. Rev. Lett. **77**, 1869 (1996).
- [33] C. H. Booth *et al.*, Phys. Rev. B **57**, 10440 (1998).
- [34] S. Yoon et al., Phys. Rev. B **58**, 2795 (1998); H. L. Liu et al., Phys. Rev. B, **58**, R10115 (1998).
- [35] J. W. Lynn et al., Phys. Rev. Lett. **76**, 4046 (1996).
- [36] J. M. De Teresa et al., Nature **386**, 256 (1997).
- [37] A. Lanzara et al., Phys. Rev. Lett. **81**, 878 (1998).
- [38] G. Papavassiliou, M. Fardis, M. Belesi, T. G. Maris, G. Kallias, M. Pissas, D. Niarchos, C Dimitropoulos, and J. Dolinsek, Phys. Rev. Lett. **84**, 761 B000.
- [39] R. H. Heffner, J. E. Sonier, D. E. MacLaughlin, G. J. Nieuwenhuys, G. Ehlers, F. Mezei, S. -W. Cheong, J. S. Gardner, H. Röder, Phys. Rev. Lett. **85**, 3285 (2000); R. H. Heffner et al., Phys. Rev. Lett. **77**, 1869 (1996).
- [40] P. Dai, H. Y. Hwang, J. Zhang, J. A. Fernandez, -Beca, S. -W. Cheong, C. Kloc, Y. Tomioka, Y. Tokura, Phys. Rev. B **61**, 9553 (2000).
- [41] H. Röder, J. Zang, A. R. Bishop, Phys. Rev. Lett. **76**, 1356 (1996).
- [42] Aveek Bid, Ayan Guha, and A. K. Raychaudhuri, Phys. Rev. B **67**, 174415 (2003).
- [43] A. Anane, B. Raquet, S. von Molnar, L. Pinsard-Godard, and A. Revcolevschi, J. Appl. Phys. **87**, 5025 (2000).
- [44] Ayan Guha, Arindam Ghosh, and A. K. Raychaudhuri, Appl. Phys. Lett. **75**, 3381 (1999).
- [45] C. Barone, C. Adamo, A. Galdi, P. Orgiani, A. Yu. Petrov, O. Quaranta, L. Maritato, and S. Pagano, Phys. Rev. B **75**, 174431 (2007).
- [46] H. T. Hardner, M. B. Weissman, M. Jaime, R. E. Treece, P. C. Dorsey, J. S. Horwitz and D. B. Chrisey, J. Appl. Phys. **81**, 272 (1997).
- [47] B. Raquet, A. Anane, S. Wirth, P. Xiong, and S. von Molnar, Phys. Rev. Lett. **84**, 4485 (2000).
- [48] Akilan Palanisami, M. B. Weissman, and N. D. Mathur, Phys. Rev. B **71**, 014423 (2005).
- [49] F. M. Hess, R. D. Marithew, M. B. Weissman, Y. Tokura, and Y. Tomioka, Phys. Rev. B **63**, 180408(R) (2001)
- [50] Aveek Bid, Ayan Guha, and A. K. Raychaudhuri, Phys. Rev. B. **67**, 174415 (2003).
- [51] A. Anane, B. Raquet, S. von Molnar, L. Pinsard-Godard, and A. Revcolevschi, J. Appl. Phys. **87**, 5025 (2000).
- [52] M. Fath, S. Friesem, A. A. Menovsky, Y. Tomioka, J. Aarts and J. A. Mydosh, Science **285**, 1540 (1999).
- [53] T. Becker, C. Streng, Y. Luo, V. Moshnyaga, B. Damaschke, N. Shannon and K. Samwer, Phys. Rev. Lett. **89**, 237203 (2002).
- [54] Qingyou Lu, Chun-Che Chen, Alex de Lozanne, Science **276**, 2006 (1997).
- [55] Liuwan Zhang, Casey Israel, Amlan Biswas, R. L. Greene, Alex de Lozanne, **298**, 805 (2002).
- [56] Teruo Kanki, Run-Wei Li, Yasuhisa Naitoh, Hidekazu Tanaka, Takuya Matsumoto and Tomoji Kawaia, Appl. Phys. Lett. **83**, 1184 (2003)

- [57] R. Akiyama, H. Tanaka, T. Matsumoto, and T. Kawaia, *Appl. Phys. Lett.* **79**, 4378 (2001).
- [58] S. H. Oh and C. G. Park, *J. Appl. Phys.* **95**, 4691 (2004).
- [59] Z.W. Dong, R. Ramesh, T. Venkatesan, M. Johnson, Z.Y. Chen, S.P. Pai, V. Talyansky, R.P. Sharma, R. Shreekala, C.J. Lobb, and R.L. Greene, *Appl. Phys. Lett.* **71**, 1718 (1997).
- [60] J.-H. Park, E. Vescovo, H.J. Kim, C. Kwon, R. Ramesh, and T. Venkatesan, *Phys. Rev. Lett.* **81**, 1953 (1998).
- [61] J.Z. Sun, D.W. Abraham, R.A. Rao, and C. Eom, *Appl. Phys. Lett.* **74**, 3017 (1999).
- [62] M. Ziese, *Phys. Rev. B* **60**, R738 (1999).
- [63] R.B. Praus, G.M. Gross, F.S. Razavi, and H.-U. Habermeier, *J. Magn. Magn. Mater.* **211**, 41 (2000).
- [64] R.P. Borges, W. Guichard, J.G. Lunney, J.M.D. Coey, and F. Ott, *J. Appl. Phys.* **89**, 3868 (2001).
- [65] A.J. Millis, T. Darling, and A. Migliori, *J. Appl. Phys.* **83**, 1588 (1998).
- [66] R.A. Rao, D. Lavric, T.K. Nath, C.B. Eom, L. Wu, and F. Tsui, *Appl. Phys. Lett.* **73**, 3294 (1998).
- [67] J. C. Chapman, Ph. D Thesis, Churchill College, Cambridge, UK, April 2005.
- [68] O. I. Lebedev, G. V. Tendeloo, S. Amelinckx, B. Leibold, H. –U. Habermeier, *Phys. Rev. B* **58**, 8065 (1998).
- [69] B. Wiedenhorst, C. Höfener, Y. Lu, J. Klein, L. Alff, R. Gross, B. H. Freitag, W. Mader, *Appl. Phys. Lett.* **74**, 3636 (1999).
- [70] Y. Chen and J. Washburn, *Phys. Rev. B* **63**, 184424 (2001).
- [71] *CMR, Charge Ordering and Related properties of Manganese Oxides*, ed. C. N. R. Rao and B.Raveau, World Scientific, Singapore (1998); *Colossal Magneto-resistive Oxides*, ed. Y.Tokura, Gordon and Breach Science, Netherlands (2000).
- [72] J. Zhang and E. W. Plummer, *Surf. Science*, **393**, 64 (1997).
- [73] Amlan Biswas, M. Rajeswari, R. C. Srivastava, Y. H. Li, T. Venkatesan, R. L. Greene and A. J. Millis, *Phys. Rev. B* **61**, 9665 (2000); Amlan Biswas, M. Rajeswari, R. C. Srivastava, T. Venkatesan, R. L. Greene, Q. Lu, A. L. de Lozanne and A. J. Millis, *Phys. Rev. B* **63**, 184424 (2001)
- [74] Amlan Biswas, Suja Elizabeth, A. K. Raychaudhuri, and H. L. Bhat, *Phys. Rev. B* **59**, 5368 (1998).
- [75] M. Ziese, H. C. Semmelhack, and K. H. Han, *Phys. Rev. B* **68**, 134444 (2003).
- [76] Guanyinn Gao, Shaowei Jin, and Wenbin Wu, *Appl. Phys. Lett.* **90**, 012509 (2007).
- [77] Sohini Kar, Jayanta Sarkar, Barnali Ghosh, and A. K. Raychaudhuri, *Phys. Rev. B* **74**, 085412 (2006).
- [78] <http://www.lesker.com>
- [79] <http://in.rs-online.com>
- [80] R. D. Shannon, *Acta Crystallogr., Sect. A: Cryst. Phys., Diffraction, Theor. Gen. Crystallogr.* **32**, 751 (1976).
- [80] J.B. Johnson, *Phys. Rev.* **32**, 97 (1928).
- [81] H. Nyquist, *Phys. Rev.*, **32**, 110 (1928).
- [821] A. Van Der Ziel , *Adv. in electronics and electron physics* **24**, 225 (1979).
- [83] P.Dutta and P.M. Horn, *Rev. Mod. Phys.* **53**, 497 (1981).
- [84] M. B. Weissman, *Rev. Mod. Phys.* **60**, 537 (1988).
- [85] M. B. Weissman, *Rev. Mod. Phys.* **65**, 829 (1993).
- [86] B.K Jones, *Adv. in electronics and electron Physics* **87**, 201 (1994).
- [87] Arindam Ghosh, Swastik Kar, Aveek Bid and A. K. Raychaudhuri, *arXiv:Cond-Mat./0402130 v1*, 4th Feb (2004).

- [88] J. H. Scofield, Rev. Sci. Instrum. **58**, 985 (1987).
- [89] A. K. Raychaudhuri, Curr. Opin. Solid State Mater. Sci. **6**, 67 (2002).
- [90] A. Ghosh and A.K.Raychaudhuri,R Sreekala , M Rajeswari and T Venkatesan, J. Phys D: Appl. Phys **30L**,75 (1997)
- [91] A.Ghosh and A.K.Raychaudhuri, J.Phys.:Condens. Matter **11**, L457 (1999).
- [92] A.Ghosh and A.K.Raychaudhuri, Phys. Rev B **58(R)**, 14665 (1998).
- [93] A.Ghosh and A.K.Raychaudhuri, Phys. Rev. Letts. **84**,4681 (2000).
- [94] A. Ghosh and A.K. Raychaudhuri, Proc. of the 16th International conference on Noise in Physical Systems and 1/f Fluctuations (World Scientific) 2001, page 107.
- [95] A.Ghosh and A.K.Raychaudhuri, .Phys. Rev B, **64**,104304 (2001)
- [96] S.Kar and A.K. Raychaudhui, J. Phys. D: Appl. Phys. **34**, 3197 (2001).
- [97] A.K. Raychaudhuri et al., Pramana - Journal of Physics **58**, 343 (2002).
- [98] A.Ghosh and A.K.Raychaudhuri,Phys. Rev. B **65**, 033310 (2002) .
- [99] S.Kar and A.K. Raychaudhuri, Appl. Phys. Lett. **81**, 5165 (2002).
- [100] S.Kar, A.Ghosh and A.K.Raychaudhuri , Phys. Rev. Letts. **91**, 216603(2003)
- [101] Sudeshna Samanta, A. K. Raychaudhuri, and Joy Mitra, Phys. Rev. B **78**, 014427 (2008)
- [102] F. N. Hooge, Phys. Lett. **29A**, 139 (1969); F. N. Hooge, Physica B & C **83**, 14 (1976).
- [103] N. D. Mathur and P. B. Littlewood, Solid State Commun. **119**, 271 (2001).
- [104] J. Mitra, A. K. Raychaudhuri, Ya. M. Mukovskii and D. Shulyatev, Phys. Rev. B, **68**, 134428 (2003).

# Chapter 5

## Probing ferromagnetic insulating state of manganites by resistance fluctuations

### 5.1 Introduction

We have already discussed about the ferromagnetic insulating (FMI) phase of manganites  $\text{La}_{1-x}\text{Ca}_x\text{MnO}_3$  from phase diagrams in Chapter 1. In this chapter we shall try to understand the physical mechanism dominated by transport properties of FMI state of  $\text{La}_{0.80}\text{Ca}_{0.20}\text{MnO}_3$  (LCMO20) by noise spectroscopy. The FMI state as we will see below is a unique state that it is ferromagnetic and yet an insulator and it has all the indications that the electrons are localized due to strong Coulomb interaction (long range) as in an electron glass. It also appears to have strong magnetic inhomogeneity. The central theme of this chapter is to explore these issues using low frequency noise spectroscopy which allows us to explore the charge dynamics in it. One may use the following simple arguments to show why the noise spectroscopy (at low frequency) can explore the charge dynamics. The electrical conductivity is  $\sigma_C \approx ne\mu$  where  $\sigma_C$  is the conductivity,  $n$  is the carrier density and  $\mu$  is the mobility. In a typical metal, the fluctuation in noise arises from fluctuations in the mobility  $\mu$  which being determined by scattering of electrons from defects or phonons or similar collective excitations mainly give information on the kinetics of scattering centres. In contrast, in an insulator, the main fluctuation would arise from a fluctuation in the carrier due to carrier trapping and de-trapping processes. Such fluctuations have been explored in the past in doped semiconductors like the McWhorter model (discussed in Chapter 1). In a glassy system a part of the charge fluctuations occur in a time scale which can be slow. Low frequency noise spectroscopy will be able to explore such long time charge fluctuations. We will see that the noise spectroscopy can be used to study slow dynamics in FMI state of manganites as it is cooled down to an electron glass.

The work reported in this chapter is carried out in three parts. In the first part we show that the FMI state follows an Efros- Shklovskii (ES) type hopping and has a non-zero density of states at the Fermi level. This is in the line of the work done by Jain *et al.* [1]. Next we measure the excess noise or the resistance noise that has a powers spectrum nearly with  $1/f$  spectra. This data have been analyzed using concepts of second spectrum to show to what extent the noise is correlated. This noise is close to what one may call as a probe of equilibrium charge fluctuations. In this part we will establish unambiguously that in the FMI state of manganites the charge fluctuations freeze kinetically controlled by an activation gap that quantitatively matches with the Coulomb gap determined from the conductivity data. In the next part we have probed the charge dynamics by probing the Nyquist noise to probe whether there is an electron heating. This is a new approach to the physics of manganites and we show that there is a strong evidence of breakdown of ergodicity as the electronic system becomes glassy. Recently, hot-electrons have been suggested as a model for non-linear conduction in these systems [2]. Our experiment to use noise spectroscopy is a significant new step to explore the issue of electron heating and the resulting non-ergodicity.

In the following we give a brief review of the state of the art of the knowledge understanding of this field. FMI state typically occurs at low hole doping levels when the ground state of the system has become ferromagnetic, but not yet metallic. In  $\text{La}_{1-x}\text{Ca}_x\text{MnO}_3$

the electronically active orbitals are the Mn  $d_{x^2-y^2}$  and  $d_{3z^2-r^2}$ . The mean number of  $d$  electrons per Mn site is  $(4-x)$ . The Hund's rule coupling is believed to be stronger than  $d-d$  hopping and spin-orbit coupling so the spins of all of the  $d$  electrons of a given site must be parallel [3]. Three of the  $d$  electrons go into tightly bound core-like  $d_{xy}$ ,  $d_{xz}$ , and  $d_{yz}$  orbitals forming a core spin of magnitude  $3/2$ , to which the outer shell electron (which may hop from site to site) is aligned by Hund's rule coupling. It has always been modelled with phenomena of “double exchange” (DE) where relevant physics is the tendency of carrier hopping to line up neighbouring spins [4]. The detection of ferromagnetic insulating state (FMI) phase in manganites indicates that DE is inadequate for full description of the basic properties (magnetic and electrical transport) in these systems. The understanding via the Anderson localization effect considers the motion of itinerant  $e_g$  electrons in a disordered background of  $t_{2g}$  spins leads to the localization of the electronic states close to the Fermi energy  $E_F$  [5]. However, calculations by Li *et al.* [5] have shown that, even for the maximum possible disorder of  $t_{2g}$  spins, the fraction of electronic states localized via the Anderson localization effect are  $\leq 1\%$ . Recent experimental studies on angle resolved photoemission spectroscopy (ARPES) results support the unlikelihood of the above conjecture [6]. Detailed calculations by Millis *et al.* [7] proposed that in addition to DE there exists a strong electron-phonon coupling arising from Jahn-Teller (JT) splitting of the outer Mn  $d$  levels plays a crucial role. Their theory successfully describes some of the features like size of the magnetoresistance, metal-insulator transition and phase coexistence close to Curie temperature  $T_c$ .

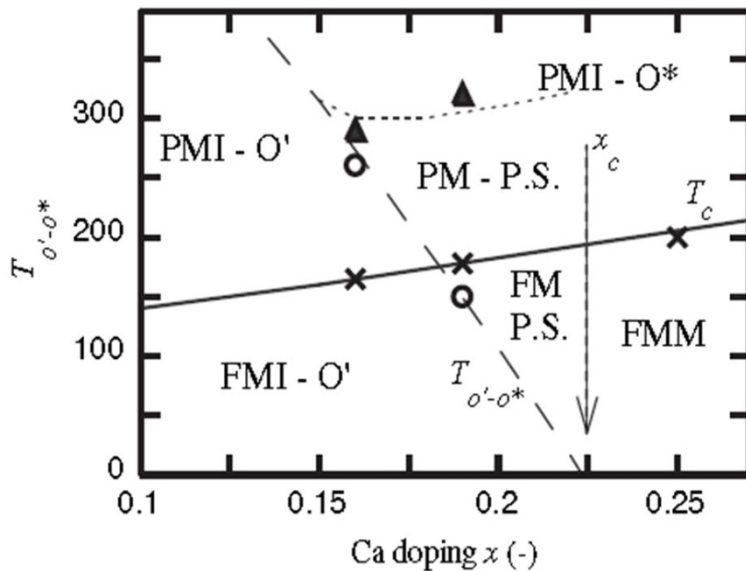


**Fig. 5.1:** Phase diagram of  $La_{1-x}Ca_xMnO_3$  near the FMI-FMM transition, modified from Uehara *et al.* [8]. The critical concentration  $x_c$ , indicates the metal-insulator transition at  $T = 0$ . The phase separated region is indicated by P.S..

Uehara *et al.* [8] sketched phase diagram partially (later modified by Van Aken *et al.* [9]) in Fig. 5.1, shows the doping induced FMI to ferromagnetic metal (FMM) transition at a critical concentration  $x_c \sim 0.21$ . The origin of the coexistence of ferromagnetism with insulating behaviour is not clear, but might stem from a delicate balance of charge localisation by orbital ordering (OO), due to the JT effect, and ferromagnetic interactions

between  $\text{Mn}^{3+}$ - $\text{Mn}^{4+}$ . Neither the exact concentration dependence of this transition nor the interaction of this orbital order transition with the magnetic ordering and the temperature- or doping-induced metal-insulator transition are known. The O'-O\* (orbital order to not orbital order) transition is typically associated a re-entrant insulating behaviour [9]. There are some theoretical [10, 11, 12] and experimental results [13, 14] where OO has been accepted as an important factor controlling the  $e_g$ -hole mobility. In a typical sample like  $\text{La}_{(1-x)}\text{Sr}_x\text{MnO}_3$  with doping concentration  $0.1 \leq x \leq 0.15$ , FMM to FMI transition is associated with charge ordering, OO, and strong reduction of the JT lattice distortion in low temperature phases [13, 14]. A similar kind of transition was proposed for  $\text{La}_{(1-x)}\text{Ca}_x\text{MnO}_3$  (LCMO) systems for  $0.125 \leq x \leq 0.2$  [15, 16]. There are few results which show that the onset of FMI state is associated with diffuse structural transition, characterized by strong reduction of the orthorhombicity [15], and rotation of the easy axis of magnetization [17]. These characteristics set the nature of the orbital ordering phenomena on cooling.

The electronic configuration of  $\text{Mn}^{3+}$  in  $RM\text{nO}_3$  ( $R$  = rare earth atoms) is  $t_{2g}^3 e_g^1$ , in an octahedral coordination. There exists double orbital degeneracy and a strong JT effect. On the other hand, the  $e_g$  orbitals are empty in  $\text{Mn}^{4+}$ . When  $RM\text{nO}_3$  is doped with holes, namely, puts  $\text{Mn}^{4+}$  ions in the background of the  $\text{Mn}^{3+}$  ions, the  $e_g$  orbitals of all the  $\text{Mn}^{3+}$  site surrounding the  $\text{Mn}^{4+}$  site tend to be directed towards it as displayed in Fig. 5.2. Such an orbital orientation occurs for two reasons. One is simply steric: oxygen ions sitting in between the Mn ions move towards the  $\text{Mn}^{4+}$  site and, consequently, the  $\text{MnO}_6$  octahedra of the neighbouring  $\text{Mn}^{3+}$  sites are elongated along the axis pointing to the  $\text{Mn}^{4+}$  site. Another factor is that the orbital occupation helps to optimize the covalency between the  $\text{Mn}^{3+}$  and  $\text{Mn}^{4+}$  sites: the  $e_g$  orbitals directed towards  $\text{Mn}^{4+}$  site allow for maximal Mn-O-Mn hopping. An important consequence of such an orbital ordering is that, the exchange interaction between the  $\text{Mn}^{3+}$  and  $\text{Mn}^{4+}$  in this cluster is ferromagnetic. Thus one can treat this object simultaneously as a lattice (both breathing-type and Jahn-Teller-type) polaron, a ferromagnetic polaron, and an orbital polaron. Considering this conjecture Mijokawa *et al.* [18] theoretically calculated that these orbital polarons may crystallize into an orbitally ordered FMI state in lightly hole low doped manganites.

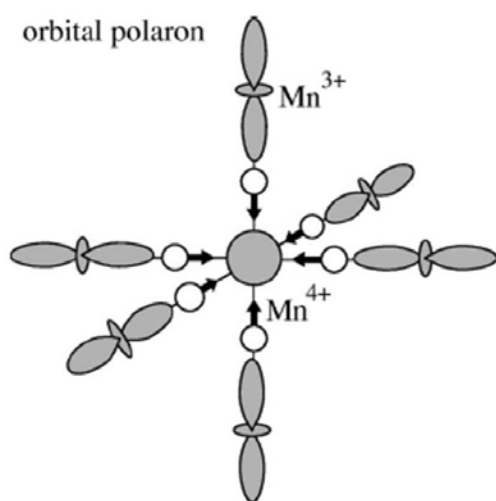


**Figure 5.2:** Schematic drawings of the orbital polaron around  $\text{Mn}^{4+}$ -ion. The shaded orbitals and circles indicate the  $\text{Mn}^{3+}$  and  $\text{Mn}^{4+}$  sites, respectively. The open circles show the oxygen ions sitting between the  $\text{Mn}^{3+}$  and  $\text{Mn}^{4+}$  sites. The arrows indicate the shifts of the oxygen ions. Adapted from reference [18].

Dai *et al.* [19] reported the results on glassy freezing in doping region  $0.17 \leq x \leq 0.20$ . They used neutron scattering experiments on single crystals to demonstrate the presence of lattice polarons and their short-range correlation effects. They observed diffused neutron scattering arising from lattice distortions associated with polarons because these lattice distortions (polarons) occur for manganese sites containing  $e_g$  electrons ( $Mn^{3+}$ ) [20-22]. They also considered the effect of polaron-polaron correlations for short range charge ordering [20-22]. They have shown that for doping  $x = 0.20$ , LCMO has an insulating ground state, i.e., resistivity first decreases below  $T_c$  but, upon further cooling, shows a sharp upturn with low temperature insulating behaviour shown in Figure 5.3(a). In Figure 5.3(b) the intensity of neutron diffuse scattering has been plotted with temperature at the peak positions of charge ordering modulation wave vectors and away from them. They observed clear presence of diffuse scattering around  $(0,1,0)$ ,  $(0,2,0)$ , and  $(-1,2,0)$  Bragg peaks shown in Figure 5.3(c). The diffuse scattering increases below  $T_c$  for ferromagnetic insulating  $La_{0.8}Ca_{0.2}MnO_3$ . Moreover, they proposed that butterfly-shaped diffuse scattering at about  $(0,2,0)$  has a origin of lattice distortions. The temperature dependence of diffuse scattering (Figure 5.3(b)) is a measure of polaron-polaron correlation and single polaron scattering to investigate the nature of transport properties. While the scattering at the ordering peak positions gives information about the population of the correlated polarons (●), the intensity of away from them measures the total number of uncorrelated polarons in the system (○).

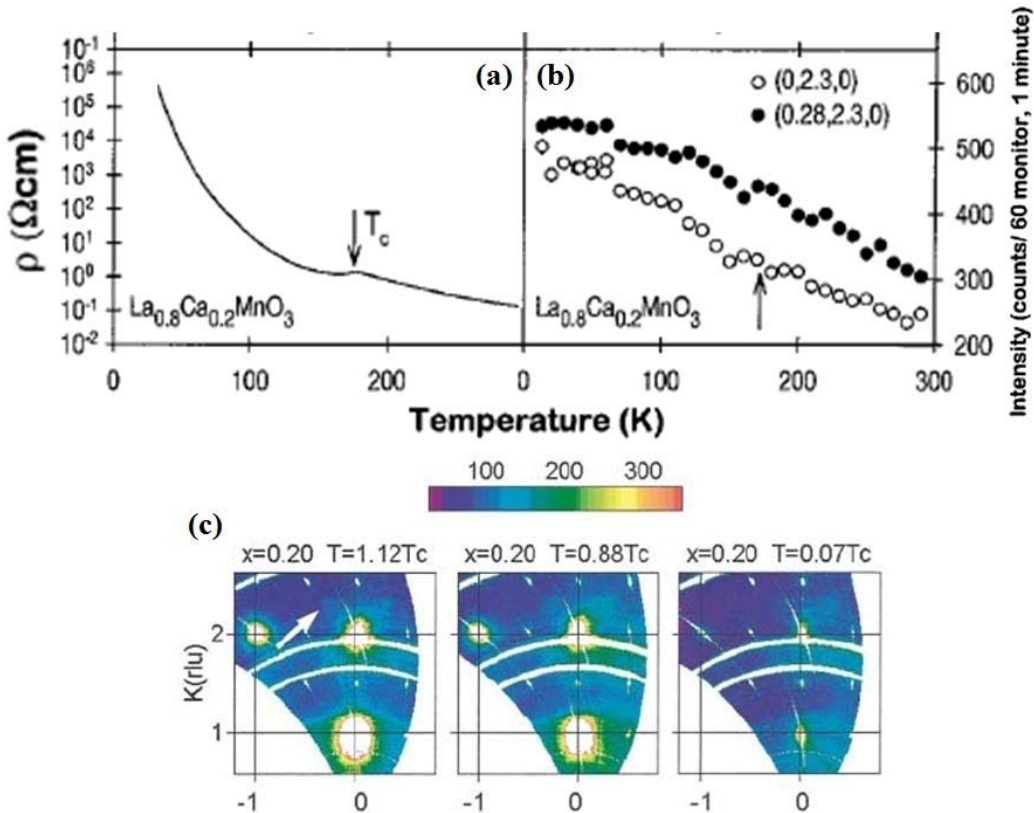


**Figure 5.3:** (a) Temperature dependence of the resistivity for (a) LCMO20. (b) The intensity of neutron diffuse scattering at the peak positions of charge ordering modulation wave vectors (●) and away from them (○) for LCMO20. (c) The observed neutron diffraction patterns of LCMO20 at various temperatures in the  $[H,K,0]$  reciprocal plane obtained by the WAND diffractometer. The arrows indicate structural diffuse scattering, and the horizontal color bars represent the intensities in counts per 5 min. Adapted from Dai *et al.* [19].

They observed that the population of correlated polarons decreases with reducing temperature in LCMO20. The resistivity rise below  $T_C$  is controlled mostly by uncorrelated polarons. So they inferred that lattice polarons and their short range interactions are directly imaging the transport properties of LCMO20 sample. Their experimental results suggest that LCMO20 does not require the development of long-range charge or orbital order. These results contrast with the previous results with the expectation of the DE model, where long-range ferromagnetic order should facilitate metallic behaviour. Their short-range polaron correlations in insulating LCMO20 indicate that long-range charge [23] orbital [24], or canted anti-ferromagnetic ordering [25] are not prerequisites for localizing the conduction band electrons. They established that the population of correlated and uncorrelated polarons, and competition between the charge correlations and the ferromagnetic DE mechanism determine the low temperature transport and conduction properties in these materials.

Papavassiliou *et al.* [16, 26] investigated low doping ferromagnetic insulating state by  $^{55}\text{Mn}$  NMR spectroscopy and showed that less conductive phase exhibits a faster nuclear spin resonance. From  $^{55}\text{Mn}$  NMR line shape of LCMO for doping level  $0.17 \leq x \leq 0.20$ , they suggested that a mixed ferromagnetic state exists which is comprised of ferromagnetic insulating and ferromagnetic metallic regions. Though the above two phases are different in OO, at an increasing temperature they cross over a  $T_{OO}$  line and establish an orbitally disordered ferromagnetic metallic state. This transition at the  $T_{OO}$  was also interpreted as a re-entrant transition to spin glass phase [27] or a transition from a polaron liquid to a polaron crystal [28].

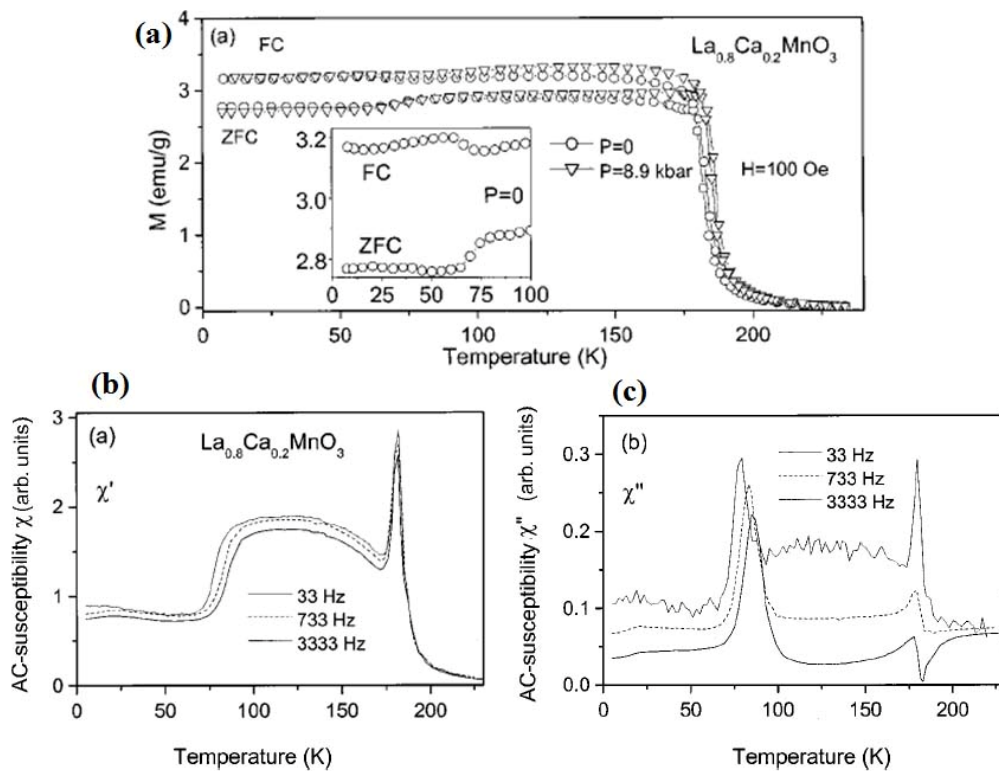


**Figure 5.4:** (a) Field cooled and zero field cooled magnetization ( $M_{FC}, M_{ZFC}$ ) of  $\text{La}_{0.8}\text{Ca}_{0.2}\text{MnO}_3$  single crystal measured at applied magnetic field of  $H = 100$  Oe, for  $P = 0$  and  $P = 8.9$  kbar. Inset: the same curves for  $P = 0$  in extended scale. (b) Temperature dependence of ac susceptibility of  $\text{La}_{0.8}\text{Ca}_{0.2}\text{MnO}_3$  single crystal measured at different frequencies: real component  $\chi'$  and (c) imaginary component  $\chi''$  [32].

Hong *et al.* [29] investigated single crystals of LCMO20 and observed onset of FMI state below  $T_C$ . They proposed that the system lies in the vicinity of the critical doping region at which metal-insulator transition takes place. So they inferred that charge/orbital fluctuation would be reinforced in this particular system. They observed divergence between field cooled and zero field cooled magnetization versus temperature dependence curves below  $T_C$ . They inferred that this observed phenomena can be attributed to the magnetic frustration arising from competition between ferromagnetic and antiferromagnetic interactions. They mentioned that charge/orbital fluctuations are enhanced in LCMO20 samples. They mentioned the presence of short-range charge ordering as a likely mechanism in these systems and long-range ferromagnetic ordering is hindered in these systems. They verified their conjecture with the results of specific-heat coefficient relating to the Debye temperature [30] and the orbital fluctuation [31] in the doped manganites.

Markovich *et al.* [32] performed measurements of magnetization and ac susceptibility on single crystals of LCMO20. They observed distinct frequency dependent cluster spin-glass or superparamagnetic-like behaviour in ac susceptibility. Both real and imaginary components of ac susceptibility  $\chi'$  and  $\chi''$  exhibit a sharp change around  $T \sim 80$  K, corresponding to the change in slope of magnetization, see Figure 5.4 (a). Both the observed drop in  $\chi'$  and peak of  $\chi''$  (see Figure 5.4(b) and (c)) was found to be frequency dependent and therefore could not ascribe a homogeneous FM ground state. They proposed that FMM clusters, dispersed in a FMI phase may exhibit a characteristic superparamagnetic frequency, described by Arrhenius relation in frequency,  $f = f_0 \exp(-\Delta E / k_B T)$  where  $f_0$  is the frequency of attempts for a cluster to change its spin direction.  $\Delta E = KV$  where  $K$  is the magnetic anisotropy and  $V$  is the volume of the cluster. They obtained  $\Delta E = 0.47$  eV using  $K \sim 10^5$  erg/cm<sup>3</sup> and obtained the size of the FMM cluster at appropriate temperature is  $\sim 10$  nm. They concluded that in LCMO20 samples, there is mixed phase ferromagnetic metallic-ferromagnetic insulating ground states below  $T_C$ . The similar study was done by Savosta *et al.* [33] where they reported temperature dependence of relaxation rate in FMM and FMI clusters. The authors suggested that the above two type of regions are intertwined on a microscopic scale. Finally their experimental results indicate that the FMI state can be viewed as a cluster glass, which is supported by temperature and frequency dependence of ac susceptibility. Similar result was reported previously for La<sub>0.86</sub>Sr<sub>0.14</sub>MnO<sub>3</sub> having a doping level below critical doming concentration  $x_C \sim 0.16$  [34].

| Composition | $n(x)$<br>(cm <sup>-3</sup> ) | $\rho_{300\text{ K}}$<br>( $\Omega\text{cm}$ ) | $\rho_{55\text{ K}}$<br>( $\Omega\text{cm}$ ) | $\sigma^2$<br>(nm <sup>2</sup> ) | $\langle r_A \rangle$<br>(nm) | $T_C$<br>(K) | $T_{\text{FMI}}$<br>(K) |
|-------------|-------------------------------|--|---|----------------------------------|-------------------------------|--------------|-------------------------|
| LCMO18      | $3.1 \times 10^{21}$          | 32   | 164000  | $1.91 \times 10^{-6}$            | $1.21 \times 10^{-1}$         | 165          | 107                     |
| NPMO30      | $5.1 \times 10^{21}$          | 4  | 1150  | $7.34 \times 10^{-5}$            | $1.21 \times 10^{-1}$         | 150          | 130                     |

**Table 5.1:** The list showing some of the important physical parameters in LCMO20 and NPMO30 single crystal samples. The data have been adapted from Jain *et al.* [1].

Ramakrishnan *et al.* [35] proposed the theory of interactions between JT-polaron and a hole when are nearest neighbours give rise to virtual DE mechanism. They also infer that other interactions like ferromagnetic or antiferromagnetic superexchange interaction between t<sub>2g</sub> spins along with virtual DE mechanism are responsible for survival of FMI state. It has been proposed that due to minimal carrier concentration and presence of very dissimilar sizes of A-site cations can also give rise to cationic disorder in a low hole doping system. The cation-site disorder is quantified as the second moment (variance) of the A-site cation radius

distribution,  $\sigma^2 = \sum_i y_i r_A^2 - \langle r_A \rangle^2$ , where  $y_i$  is the fractional substitution level of the  $i^{\text{th}}$  A-site species with ionic radius  $\langle r_{Ai} \rangle$ , and  $\langle r_A \rangle = \sum_i y_i r_A$  represents the average A-site cation radius. It has been investigated that increasing cation-cite disorder leads to the metal-insulator transition and stabilizes the insulating state [36-39]. The experimental observation regarding the cationic disorder has been reported by Jain *et al.* [1] in low hole doped  $\text{La}_{0.82}\text{Ca}_{0.18}\text{MnO}_3$  (LCMO18) and  $\text{Nd}_{0.70}\text{Pb}_{0.30}\text{MnO}_3$  (NPMO30) systems and the relevant data are shown in the Table 5.1 [1]. They reported  $\sigma^2$  (NPMO30) >  $\sigma^2$  (LCMO18) gives rise to  $T_C$  (NPMO30) <  $T_C$  (LCMO18) but  $T_{FMI}$  (NPMO30) >  $T_{FMI}$  (LCMO18). Thus the cationic size disorder strengthens the FMI state while weakening the FM order.

Shenoy *et al.* [40] by using simulation have shown that Coulomb interactions and dopant ion disorder can lead to electronic inhomogeneities. They linked ferromagnetism, insulating conductance, and Coulomb interactions by introducing a new model Hamiltonian. The investigation is based on the general frame work of the model proposed by Ramakrishnan *et al.* [35]. Generally, manganites are considered as “orbital liquid” due to lack of long-range orbital order for  $x$  in the range  $0.1 \leq x \leq 0.4$ . The model proposed the phase diagram shown below.

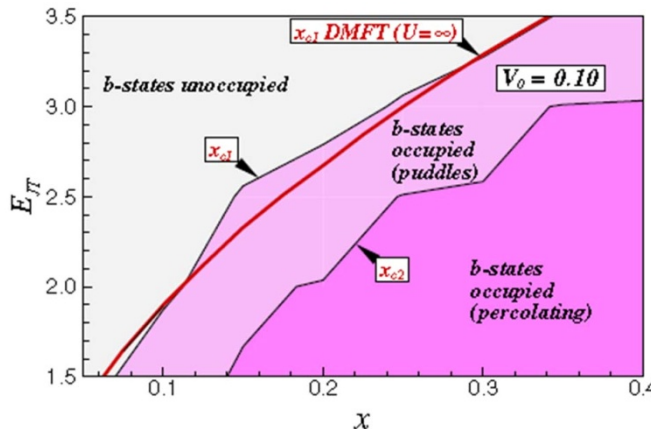


**Figure 5.5:** Critical doping levels  $x_{c1}$  and  $x_{c2}$ .  $x_{c1}$  separates the lightest region, where no  $b$  states are occupied, from the intermediate shade region, which has  $b$  states occupied in puddles. The darkest shaded region, with  $x > x_{c1}$ , has some occupied  $b$  states that percolate through the  $10^3$  box. Results shown are averages over 100 realizations of the dopant ions. Adapted from reference [40].

The investigation showed that the electronic configuration is strongly dependent on  $E_{JT}$  and the doping concentration  $x$ . At a fixed value of  $E_{JT}$  they have considered two critical doping concentrations namely,  $x_{c1}$  and  $x_{c2}$  as shown in Figure 5.5. They discussed three cases as:

For  $x < x_{c1}$  : there are no occupied  $b$  electron states in the systems, and the holes form insulating states. Further increase of doping level leads to the metallic behavior in the system. Again the polarons opens up a soft gap at the chemical potential, as in the classical Coulomb glass [41, 42-45]. They mentioned that the electrical transport will follow the relation  $\sigma_C \approx e^{-A/\sqrt{T}}$ . (5.1)

For  $x_{c1} < x < x_{c2}$ : There should be two contributions- one from Coulomb glass due to  $l$  polarons and second a variable range type hopping of the electrons in the  $b$  puddles.

For  $x > x_{c2}$ : They found a highly resistive metal.

They concluded that the long-range Coulomb interaction is a “singular perturbation” that prevents the macroscopic phase separation where the sizes and distribution of clumps (on a hole cluster, which has two or more sites, each accessible to the other by electron hoppes) are determined by the distribution of dopant ions. Their quantitative analysis discussed the presence of long-range Coulomb interactions frustrating the phase separation induced by local correlation. Finally, they emphasized that the inhomogeneities can lead to the nanoscale insulating regions even in FMM states.

The above discussion shows that the issue of Coulomb interaction in the low doped regions are important and its role has not been settled. The investigations will be presented in the thesis is thus important for it addresses some of these issues directly through experiments.

The results we have discussed so far indicate nonequilibrium phenomena, and likely onset of quasiperiodicity (“freezing”) on cooling. A spin-glass transition in low doped LCMO systems has also been suggested in published literature [46]. There exist competitions between critical slowing down and spin freezing that makes characterization of the spin and orbital dynamics in the system a nontrivial task. These results are all from the view point of absence of proper long range order in the spin system. In this chapter our main focus as stated before is to explore the charge fluctuations in the ferromagnetic insulating state in which long range Coulomb interactions can play an important role. The current theoretical developments do point towards possibility of charge freezing either in the band electrons or development of a Coulomb glass due to the polarons. Use of noise spectroscopy allows us to investigate these issues.

### 5.1.1 Theoretical models regarding insulating temperature dependence of resistivity

The insulating nature of temperature dependence of resistivity has been investigated by various theoretical models. Among them the Arrhenius model [47, 48], the Mott variable range hopping model [49-50], the Efros -Shklovskii variable range hopping (ES-VRH) model [42, 52], the polaron hopping model [53] are mostly distinguished models to discuss.

#### 5.1.1.1 Arrhenius model

Thermally activated conductivity can manifest itself in two distinct ways. If one assumes a model of thermally activated hopping between nearest neighbour impurity centres spaced an average distance of  $2R_1$  apart, where  $R_1$  is the radius of an average spherical impurity volume, then the overlap of the impurity 1s ground state wave functions is proportional to  $\exp(-2\alpha R_1)$ , where  $\alpha$  is the coefficient of exponential decay of the hydrogenic 1s wave functions, i.e.,  $(\alpha - 1)$  is the spatial extent of the wave function localized at a single site, one obtains an Arrhenius temperature  $T$  dependence of resistivity  $\rho$ :

$$\rho = \rho_{0A} \exp\left(\frac{E_a}{k_B T}\right) \quad (5.2)$$

where,  $\alpha$  is the average temperature independent activation energy account the random local field generated at the site due to the other impurities. This kind of insulating electrical conduction process is generally observed in the high temperature paramagnetic state in manganites.

### 5.1.1.2 Mott variable range hopping model

This model consider that the hopping occur only between nearest neighbour sites. Any electron hopping between any two sites are determined by the potential energy difference and the distance between these two sites. Mott showed that as the temperature is lowered the conductivity changes from its usual activated form (see Equation 5.2). This has been termed as “variable range hopping” as the carrier tends to optimize between the distance of the hop and the barrier energy of the hop. The 3D Mott conduction process can be written as:

$$\rho \propto \exp\left(\frac{T_0}{T}\right)^{1/4} \quad (5.3)$$

where  $T_0 = \lambda\alpha^3 / k_B N(E_F)$  and  $\lambda$  is a dimensionless constant whose value depends on specific microscopic model considered. Generally  $\lambda \sim 16$  [49] or 18 [54],  $\alpha^{-1}$  is the localization length within the Mott variable hopping range model, and  $N(E_F)$  is the density of states at the Fermi level.

### 5.1.1.3 Efros-Shklovskii variable range hopping model

Though Mott’s formula successfully analyse a large number of experimental results but it ignores the Coulomb interactions between the carriers. Coulomb interactions change the temperature dependence of conduction mechanism qualitatively from Mott’s formula described earlier. In a lightly doped system at low temperatures electrons are localized and the conductivity is due to hopping between the two sites. There are two well known regimes of hopping transport. At relatively high temperatures electrons use almost all the sites for hopping. This regime is called nearest-neighbour hopping. In this case energy scatter due to random potentials of charge carriers plays only a secondary role, leading to fixed activation energy of conductivity. At low enough temperatures activation required for the use of charge carriers becomes very costly and charge carriers are only within a narrow band of energies around the Fermi level participate in the conductivity. With decreasing temperature the width of this band shrinks and hops become longer. This explains the name “variable range hopping”. Due to Coulomb interaction of localized electrons there appears a Coulomb gap near Fermi energy level. The density of states  $N(E)$  under this model can be written by self consistent equation as:

$$N(E) = N_0 (E - E_F)^2 \quad (5.4)$$

where,  $N_0 \approx \kappa^3 / e^6$  and  $\kappa$  is the dielectric constant of the sample. The increase in localization manifest as an increase in the exponent of temperature in equation 5.3 to 1/2:

$$\rho \propto \rho'_0 \exp\left(\frac{T_0}{T}\right)^{1/2} \quad (5.5)$$

with,  $T_0 = C / \xi k_B N_0^{1/3}$  where,  $\xi$  is the localization length of the electrons and  $C \approx 2.8$ . The proportionality factor  $\rho' = \rho'_0 T^{1/2}$ .

#### 5.1.1.4 Polaronic hopping model

In manganites, for high temperatures and  $T > T_C$ , the conductivity is ruled by localization of charge carriers on small polarons. The localization is a consequence of large electron-phonon interactions. In the high temperature regime, magnetic interactions become negligibly small and electron-lattice interaction becomes dominant. In this model the resistivity can be written in the form as:

$$\rho = \left( \frac{\hbar a}{e^2} \right) \left( \frac{T}{T_p} \right)^n \left[ \frac{1}{c(1-c)} \right] \exp \left[ \frac{\varepsilon_0 + W - \lambda^3 - 2n}{k_B T} \right] \quad (5.6)$$

or,  $\rho = \rho_p T^n \exp \left( \frac{E_p}{k_B T} \right)$

where “ $a$ ” is the hopping distance,  $c$  is the polaron concentration,  $2W$  is the polaron formation energy,  $k_B T_p$  is a characteristic polaron energy scale which gives the polaron tunnelling rate,  $\lambda$  is the transfer integral and  $\varepsilon_0$  is the energy required to produce intrinsic carriers. Depending on the magnitude of the optical phonon frequencies there are two physical limits for these hopping processes: For  $k_B T_p \gg \hbar \omega_{ph}$  (where,  $\omega_{ph}$  is the characteristic phonon frequency involved in the polaron formation) the hopping is termed adiabatic meaning that the relevant optical mode lattice vibration of frequency  $\omega_{ph}$  is long lived compared to the relevant polaron tunneling event. In this adiabatic limit, the exponent  $n = 1$  in equation 5.6. In the other case, for non-adiabatic transport, the electron tunneling event is not necessarily fast compared to the relevant optical mode lattice vibration, the exponent  $n = 3/2$  and  $T_p$ ,  $\lambda$  and  $2W$  are related as  $k_B T_p = (\pi \lambda^4 / 4W)^{1/3}$ .

In the following section we present the resistivity data to show how the conduction process is dominated by ES-VRH mechanism. Then we try to focus on the fact that why noise is important to study the insulating phase of manganites where Coulomb interactions come into play.

#### 5.1.2 Electrical conduction process in FMI phase: Efros-Shklovskii variable range hopping

In this section we look into the temperature dependent resistivity for single crystals of LCMO20. As shown in the figure 5.6, the sample undergoes insulator-metal (I-M) transition in the temperature range 25-300 K within which resistivity is investigated. As one lowers the temperature from 300 K (where sample is in paramagnetic insulating state), the first I-M

transition is encountered nearly concomitant with its Curie transition at  $T_p \cong 186$  K. The second I-M (or rather metal-insulator) transition is encountered when the sample transition to its ferromagnetic insulating phase at temperature  $T_{FMI} \cong 120$  K. It is also clearly seen that for  $T < T_{FMI} < T_c$  the sample LCMO20 is ferromagnetic as well as insulating.

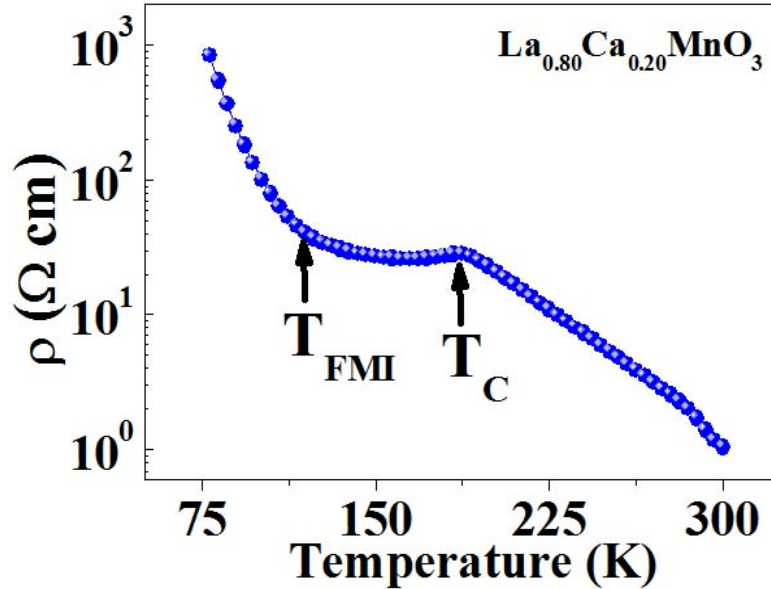


**Figure 5.6:** The temperature dependence of resistivity  $\rho$  of LCMO20. The paramagnetic to ferromagnetic Curie temperature is  $T_c \cong 186$  K. The ferromagnetic insulating transition occurs at  $T_{FMI} \cong 120$  K.

From equations 5.2 one sees that Arrhenius dependence is revealed if a plot of  $\ln(\rho)$  vs  $1/T$  is a straight line and this model fails to fit the experimental resistivity data obtained as shown in Fig. 5.7(a). From equation 5.3, one sees that a Mott variable range hopping behaviour may be present if a plot of  $\ln(\rho)$  vs  $1/T^n$ , where “ $n$ ” is an appropriate exponent, is also a straight line. We have fitted the experimental data with the Mott variable range hopping model as shown in Fig. 5.7(b) and the deviation of experimental data from model it also very clear. An ES-VRH mechanism as given by equation 5.5 is revealed if a plot of  $T^{-1/2} \ln(\rho)$  vs  $T^{-1/2}$  is a straight line. In Fig. 5.7(c) we show the temperature dependent resistivity of LCMO20 in the FMI state below  $T_{FMI} \cong 120$  K. The data are plotted as  $T^{-1/2} \ln(\rho)$  vs  $T^{-1/2}$ , and give a definite indication of the ES-VRH nature of the electrical conductance in the FMI state of these materials. In Fig. 5.7(d) we have plotted the Polaronic hopping model which satisfies equation 5.6. The solid line in each plot shows the least square best fit curve. From the all fitted curves shown in Fig. 5.7, we can immediately conclude that below  $T_{FMI}$ , the electrical conduction process follows ES-VRH model (see Fig. 5.7(c)). Hence, we can easily estimate the values of  $\rho_0$  and  $T_0$  by fitting the temperature dependent resistivity data in the FMI state to equation 5.5. These values allow us to calculate another important parameter namely hopping length of the charge carriers. The expression of the Coulomb gap can be written as:  $\Delta_{CG} = e^3 N(E_F)^{1/2} \kappa^{3/2}$  [52], where  $e$  is the electronic charge,  $N(E_F)$  is the density of states near Fermi energy level,  $\kappa$  is the dielectric constant of the

system. The dielectric constant for LCMO20 is  $\kappa \sim 20$  [55]. For the calculation of  $\Delta_{CG}$  we assumed that ES-VRH conduction process emerges at a temperature  $T_{SE}$  when the activation energy for nearest neighbour hoping becomes equal to the ES-VRH Coulomb gap energy [42]. This assumption will allow us to calculate  $\Delta_{CG}$  in terms of  $T_0$  and  $T_{SE}$  as,  $\Delta_{CG} = k_B(T_0 T_{SE})^{1/2}$  [56]. We have taken  $T_{SE} \cong T_{FMI}$  and listed the value of  $\Delta_{CG} \cong 152$  meV in Table 5.2.

| Composition  | $\rho_0$<br>( $\Omega\text{cmK}^{-1/2}$ ) | $T_0$<br>(K)       | $\Delta_{CG}$<br>(meV) | $\xi$<br>(nm) |
|--|---|--------------------|------------------------|---------------|
| La <sub>0.80</sub> Ca <sub>0.20</sub> MnO <sub>3</sub> | $1.09 \times 10^{-6}$                     | $2.59 \times 10^4$ | 152                    | 0.25          |

**Table 5.2:** The list of parameters estimated from temperature dependent resistivity data shown in Fig. 5.6((a) and (d)).

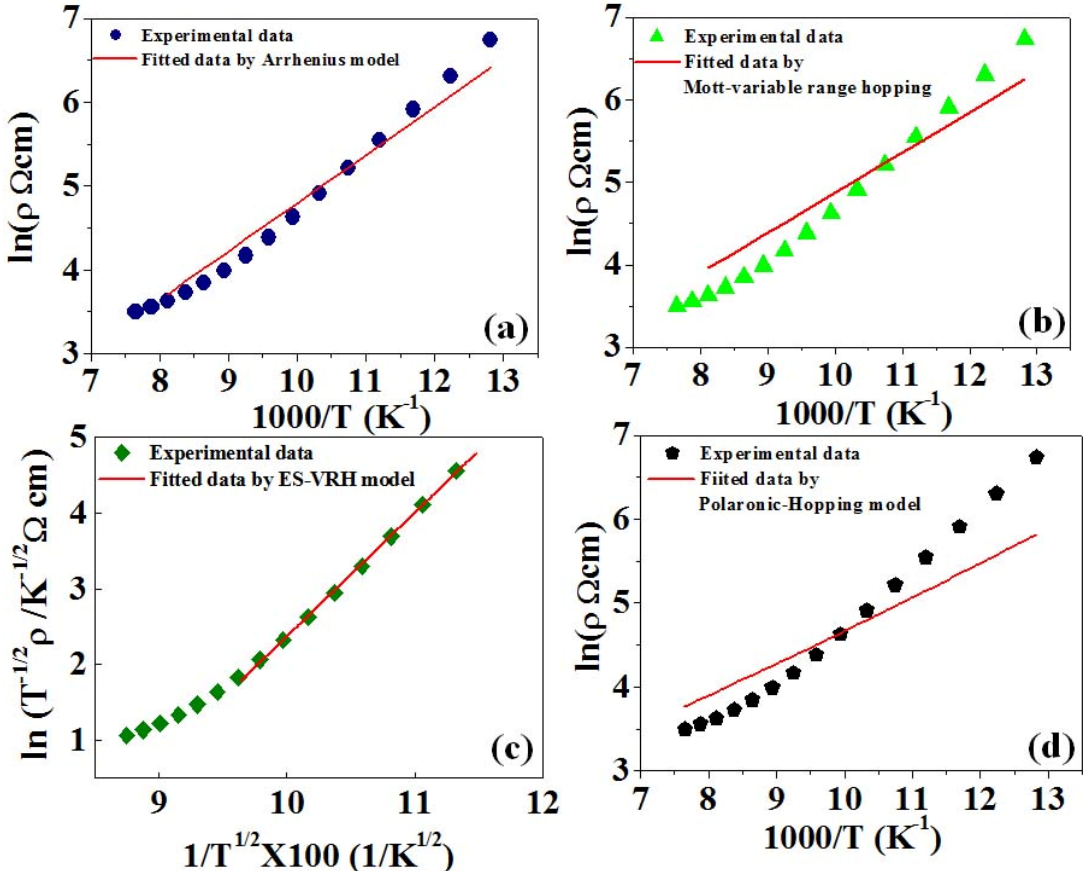


**Figure 5.7:** The experimental  $\ln(\rho)$  vs.  $1000/T$  data has been plotted and compared with different theoretical models like: (a) Arrhenius model, (b) Mott variable range hopping model, (c) ES-VRH model in the FMI state of LCMO20. (d) Polaronic hopping model (with  $n=1$ ). The data ((a), (b), (c) and (d)) are shown for temperatures below  $T_{FMI}$ . The solid line is the least square best fit curves.

The value of localization length can be expressed as:  $\xi = Ce^2 / \kappa k_B T_0$ , where  $C \cong 2.8$  [52]. The value of  $N(E_F) = 1.6 \times 10^{24} \text{ eV}^{-1}\text{mol}^{-1}$ . This value of  $\xi$  can be used to calculate the hopping length  $l_h$  using the expression  $l_h \cong (\xi/4)(T_0/T)^{1/2}$ . The temperature dependent

hopping length  $l_h$  is plotted in Figure 5.8. The value of perovskite unit cell is  $a_0 \approx 0.547$  nm. Here we want to mention that  $T < 120$  K, i.e., below  $T_{FMI}$ , the hopping length  $l_h$  is increasing considerably from perovskite unit parameter  $a_0$ . From the known molar volume of the sample  $\sim 36 \times 10^{-6} \text{ m}^3$ , the number density can be estimated by following the relation  $n(x) = 1.7 \times 10^{28} x$  carriers/m<sup>3</sup> [57]. So the carrier density for our sample is  $n_{LCMO20} \approx 3.4 \times 10^{27}$  carriers/m<sup>3</sup>. We can estimate the distance  $\langle r \rangle$  between two hopping sites where the Coulomb interaction is taking place. Using the relation  $\langle r \rangle / 2 = [3/(4\pi n_{LCMO20})]^{1/3}$ , the estimated value of  $\langle r \rangle \approx 0.8$  nm. From Fig. 5.8 we can infer that at the lowest possible temperature below  $T_{FMI}$ , the value of  $\langle r \rangle$  is nearly equal to the value of  $l_h$  at-least in order of magnitude. We can also suggest that electrons are localized in the FMI state. The above analysis is a review of the analysis done by Jain *et al.* [1].

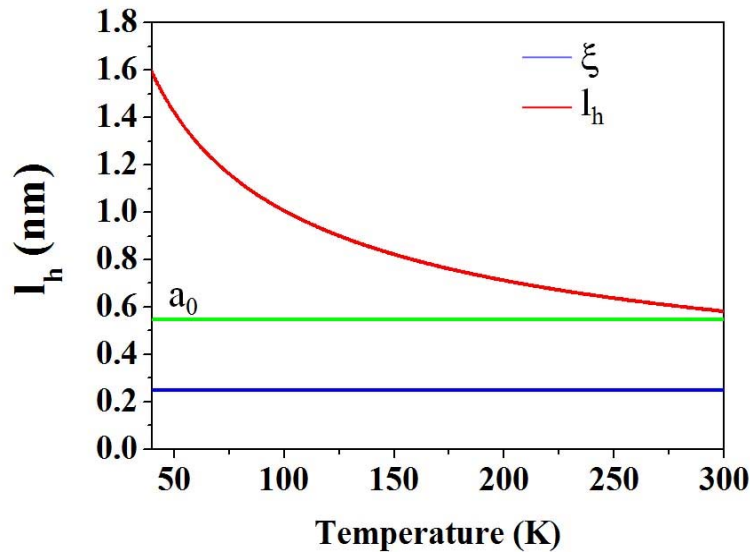


**Figure 5.8:** Temperature dependence of ES-VRH hopping length  $l_h$  in FMI phase of LCMO20 has been plotted along with the correlation length  $\xi$  and unit cell parameter  $a_0$ .

In the last section we have seen that in the low doped perovskite manganites LCMO20 at low temperature, electron transport is dominated by variable range hopping of localized electrons. We have also seen the Coulomb interaction between the localized electrons give an important contribution to the energy of an electron. In this disordered system with highly localized electronic states will strongly influence the special distribution of electrons by long-ranged Coulomb repulsion between them. This leads to a depletion of the single particle density of states (DOS) near the chemical potential known as Coulomb gap. It is also expected to cause deviation at low temperatures from Mott's  $T^{-1/4}$  law [49] for electrical conduction and opening up a soft Coulomb gap energy  $\Delta_{CG}$  near Fermi level considering ES-VRH. Both experimental and theoretical studies have demonstrated the presence of a “soft Coulomb gap” and the phenomena is believed to be related with glassy behaviour of electrons. The classic work of Efros *et al.* [42] has clarified some basic aspects of this behaviour. Despite a number of studies the underlying physics of hopping systems, Coulomb glasses, and glassy properties are still unclear. In the following sections we discuss

about the basic properties of glassiness in electronic systems and discuss about the dynamics which will further motivate us to study noise spectroscopy in such systems.

### 5.1.3 Glassiness in electronic systems: Electron glass

First Pollak [58] and Ambegaokar [59] pointed out that actually electron-electron Coulomb repulsion should reduce the density of states near Fermi energy in a disordered system where electronic states are localized near Fermi surface. Interacting electrons localized by disorder often form an “electronic glass” state. The term “glass” is due to the many features it shares with other glasses, indicating the slow dynamics and aging. The sluggish relaxation phenomena are basic observable properties in these glasses. The relevant study was extensively done by Efros and Shklovskii [60] where they assumed that the quantum localization length is much smaller than the distance between the centres and overlapping of the wavefunction is negligible. The energy of the system can be written as:

$$H = \sum_i \varepsilon_i n_i + \frac{1}{2} \sum_{i \neq j} e_{ij} n_i n_j \quad (5.7)$$

where,  $\varepsilon_i$  is the energy of the electronic state “ $i$ ” not taking into account the contribution of electron-electron interaction,  $e_{ij} = e^2 / \kappa r_{ij}$  is the energy of electron-electron interaction,  $r_{ij} = |r_i - r_j|$  is the distance between the states “ $i$ ” and “ $j$ ”,  $\kappa$  is the dielectric constant and  $n_i$  is the occupation number ( $n_i = 0, 1$ ). However, it should be noted that  $r_{ij}$  is the distance between the two sites which is much larger than the spacing of the atoms of the host lattice, so the electronic states in the doping band can indeed be taken as localized. The authors introduced the energies of one-particle excitation as:

$$E_i = \varepsilon_i + \sum_j e_{ij} n_j . \quad (5.8)$$

At temperature  $T = 0$ ,  $n_i = 1$  for  $E_i < E_F$  and  $n_i = 0$  for  $E_i > E_F$ , where  $E_F$  is the Fermi level. Energy cost of removing an electron at site  $i$  is  $-E_i$ . Similarly energy cost of adding an electron at site “ $j$ ” (site “ $i$ ” being empty) is  $-E_j$ . The schematic diagram of the hopping mechanism is shown in Figure 5.8. The change in the system energy due to an electron hopping from site “ $i$ ” to “ $j$ ” is then

$$\Delta H_{i \rightarrow j} = E_j - E_i - e_{ij} > 0. \quad (5.9)$$

The last term in equation 5.8 gives Coulomb-interaction due to created electron-hole pair and its presence causes the Coulomb gap. The schematic diagram of this interaction mechanism is shown in Fig. 5.9. So in the ground state any two energies  $E_i$  and  $E_j$  separated by the Fermi level should satisfy the inequality (equation 5.9). Detailed mathematical calculations concludes the presence of a energy gap  $\Delta_{CG}$  (Coulomb gap) which also satisfies the relation  $N(\Delta_{CG}) = N_0$ . The Coulomb gap is “soft” gap because it vanishes at  $E = E_F$  and can be

distinguished from Hubbard gap, as it is due to short range forces. This ground state shows behaviour of a glass.

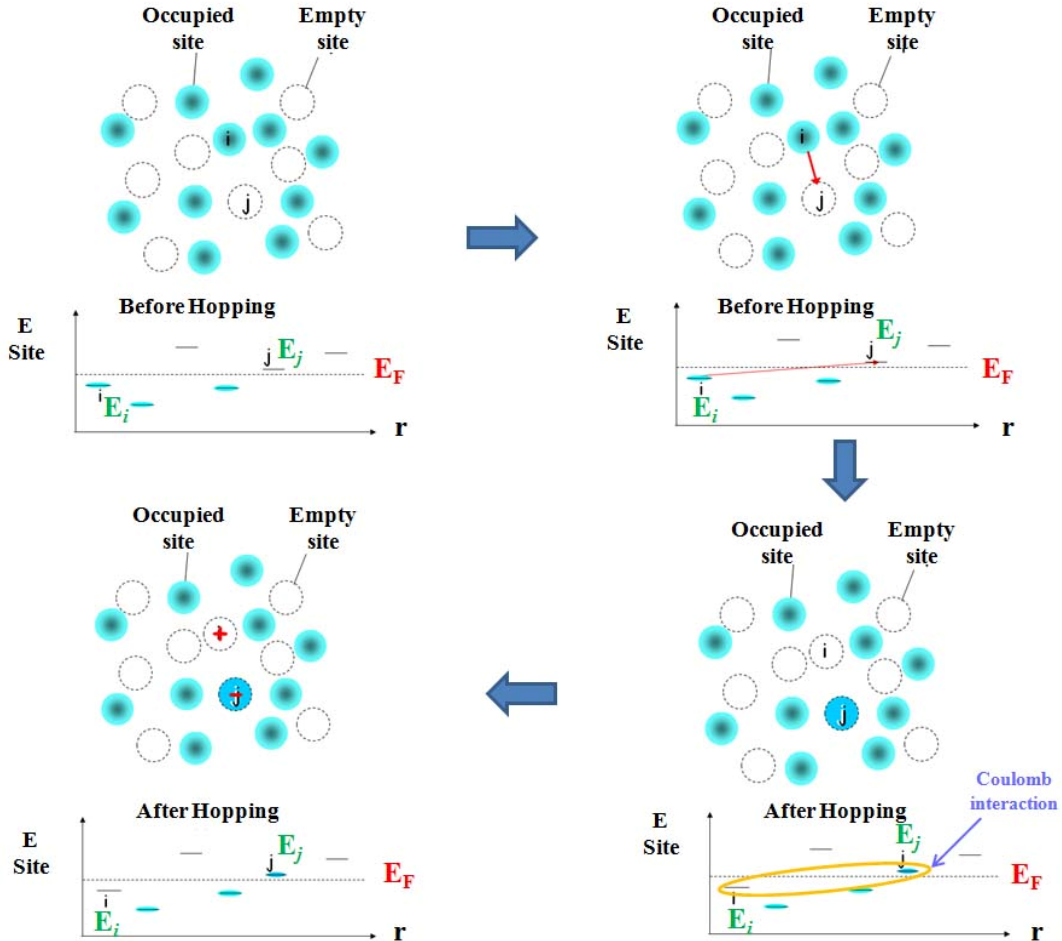


**Figure 5.9:** The schematic diagram for Efros-Shklovskii variable range hopping mechanism. The hopping cost of energy appears to be  $\Delta H = E_j - E_i - e^2 / \kappa r_{ij}$ .

Davis *et al.* [61] carried out extensive numerical simulations to explore the properties of electron glass. The authors have rewritten the equation 5.7 in an Ising form by setting  $n_i = \Psi_i = 1/2$  and the Hamiltonian for the half filled band can be written as

$$H = \sum_i \varepsilon_i \psi_i + \frac{1}{2} \sum_{i \neq j} e_{ij} \psi_i \psi_j . \quad (5.10)$$

The site energies are considered to be distributed about zero energy. In this case, the Hamiltonian is in random field, but with the long-range antiferromagnetic interactions. This is analogous to Ising spin glass model but authors have introduced it for simplistic realization. The detailed estimation of order parameter gives a non-zero value at low temperature revealing a glass transition in the systems. They considered two- and three-dimensional models of highly localized electrons interacting by unscreened Coulomb potential. They found that at low temperature, single particle excitations might not be bare, but rather might be electron polarons. If an electron (or hole) is added to a site, the system

can relax in order to lower the total energy of the transition, if nearby electrons move away thereby creating a polarization cloud.

The Coulomb gap for polarons is clearly much narrower than that for bare excitations. These polarons may be important for the electrical conductivity at low temperature, but the details of this remain controversial. A polaron is essentially localized around the starting site. The electronic ground state and the low lying excited states of the system with an added electron will have less energy than this polaron, and many of them are selected site occupied. Hence, to achieve such states it is necessary to rearrange a large number of electrons. These states may not therefore be accessible from the starting site at low temperatures. This picture of inaccessible phase space is typical of a “glass”. They inferred that glassy state arises from the competition between Coulomb energies and the random site-energies. The authors solved the Hamiltonian (see equation 5.10) by mean-field approach to solve the electronic properties of the systems of localized Coulomb-interacting electrons. Their simulation also results appearance of a large number of metastable states in the energy space. After “heating up” the system and subsequently slowly cooling down, lower metastable states are reached. They have shown that akin to spin glasses, their calculations results good agreement to experimental specific heat, susceptibility and order parameter which strongly supports the existence of an electron glass.

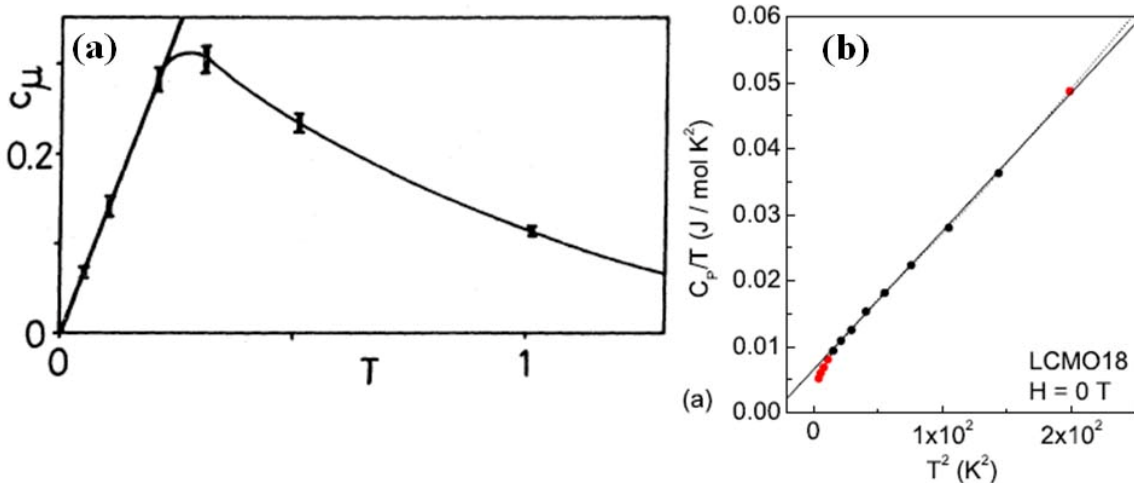


**Figure 5.10:** (a) Specific heat  $c_\mu$  has been plotted against  $T$  and linear variation of it is noted [61]. (b) Molar specific heat  $C_p$  versus temperature  $T$  for  $\text{La}_{0.82}\text{Ca}_{0.18}\text{MnO}_3$  (LCMO18) has been plotted to reveal the linear contribution in the specific heat. The solid line is the curve for least square fit to the equation  $C_p = \gamma T + \beta T^3$ , where  $\gamma$  and  $\beta$  are the coefficients of the electronic and lattice contributions to the specific heat [1].

Efros *et al.* [60] pointed out that the Coulomb gap exists only in the spectrum of energies  $E_t$  which corresponds to the withdrawal of one electron or its addition to the system. There are other small-energy excitations in the system appearing due to electron-hole pairs with separation between the electron and hole. The energy of such an excitation is given by  $\omega_j = E_j - E_t - e^2 / \kappa r_j$ . It was shown that the density of states  $N(E)$  is small near the Fermi level. The density of states of such electron-hole pairs is finite when  $\omega \rightarrow 0$  and is order of  $N_0$ . Therefore the temperature dependence of the heat capacity is linear. The specific heat ( $C_p$ ) was calculated from the derivative of the total energy with respect to temperature and from the variance of the fluctuations of energy, with insignificant differences. The numerical calculations by Davis *et al.* [61] also found the linear temperature dependence of specific heat

as shown in Fig. 5.10(a). They have plotted specific heat  $c_\mu = \gamma T$  and found  $\gamma = 1.36$  which indicates large DOS  $\sim 0.83$  per site per unit energy. They inferred that large contribution to  $c_\mu$  is coming from complicated excitations whose energies lie near Coulomb gap. We have discussed already that the electron glass has been considered in both theory and simulation, with an emphasis on the many-body effects that should contribute to the long-time relaxation. This theoretical result discussed so far has been supported by experimental observations of specific heat experiments. Jain *et al.* [1] reported the presence of a finite electronic contribution  $\gamma T$  to the specific heat for low doping  $\text{La}_{0.82}\text{Ca}_{0.18}\text{MnO}_3$  single crystal samples below  $T_{FMI}$  and is shown in Figure 5.10(b). The linear term specifies the finite DOS ( $N(E_F)$ ) near Fermi energy  $E_F$  and is consistent with ES-VRH conduction mechanism we discussed already. On the other hand most electron-hole pairs with small excitation energies are very compact and isolated from each other and they cannot contribute to the DC conductivity.

A disordered many-electron system (“electron glass”) with long range Coulomb interaction is turned into a “Coulomb glass” and this long-range nature of the Coulomb interaction can give rise to complex rearrangements of electrons across a spectrum of free energies and times. A Coulomb glass shares the same properties as an electron glass does and its ground state can only be reached by the displacement of several electrons. Usually a complex pattern of relaxation paths has to be taken into account, comprising not only one-electron hopping but also many electron displacements over a long distances. Hence, several relaxation time scales are important for the overall relaxation process which is typical for a glassy behaviour. These systems are interesting to study because of their transport properties at low temperatures are strongly influenced by the movements of the particles which are strongly correlated due to interactions. These correlations become especially important for interactions with longer-range. This long-range Coulomb interaction is also important in case of our low-doped LCMO20 single crystals under study where electrons can hop over fairly long distance and follow variable range hopping process (ES-VRH) at low temperatures. Although Coulomb glasses have been studied extensively, the number of analytical well established results is rather limited [60, 62-65]. The first theoretical simulation model on Coulomb glass was performed by Kurosawa *et al.* [66]. The theoretical understanding of Coulomb glass was further studied by several researchers [35, 40, 61, 67]. Since then, a number of numerical works has been steadily growing and recently a work has been reported by Kirkengen *et al.* [68] on dynamics of Coulomb glass. There are several experiments have been performed which emphasize nature of “glassiness” in different systems [69-71]. Despite the number of numerical studies the underlying physics of hopping systems, Coulomb glasses, and glassy properties are still unclear. In the following sections we discuss about the basic properties of glassiness in such electronic systems and discuss about the dynamics which will further motivate us to study noise spectroscopy in such systems.

An important and characteristic feature of the Coulomb glass is the many valley structure of its configuration space, not only concerning single-particle hops, but also with respect to some classes of more complex excitations. Baranovskii *et al.* [63, 65] found, by computer simulation of a simple model of the electron glass, several energy minima, i.e., metastable, or pseudoground, states, very close to the lowest-energy minimum that can be considered as the ground state. The same structure of the low-energy states was found also for a more realistic model of the Coulomb glass [62]. It was also found in Ref. 63, 65 and 62 that the differences between the energies of the ground state and these metastable states are very small, usually less than or of the order of the characteristic energy of the Coulomb interaction at the mean distance between neighbouring donor impurities,  $E_C = e^2 n_D^{1/3} \kappa$ , where  $n_D$  is the concentration of the major shallow impurity, and  $\kappa$  is the dielectric

permittivity of the host crystal. The ground state and these low-lying pseudoground states are called below “valleys.” The low lying energy states are separated by a high enough activation or tunnel barriers and the transitions among those valleys take long enough relaxation times. Davis *et al.* [61] performed computer simulations with their theoretical model which also confirmed the presence of cluster of low-lying energy states. The relaxation times of these low-lying excited states in Coulomb glass have been studied by Mochena *et al.* [72]. The authors found extremely slow relaxation processes and associated them with relaxation from metastable states of the Coulomb glass. The schematic diagram of the relaxation process in the low-lying configuration space, Coulomb interactions and the hopping mechanism are shown in the Figure 5.11. As a result of presence of valleys and barriers, slow approach to the equilibrium process is hindered in these systems at low temperatures. The system is trapped for a relatively long time in one of the local minima before it manages to cross a barrier and move to another metastable state.

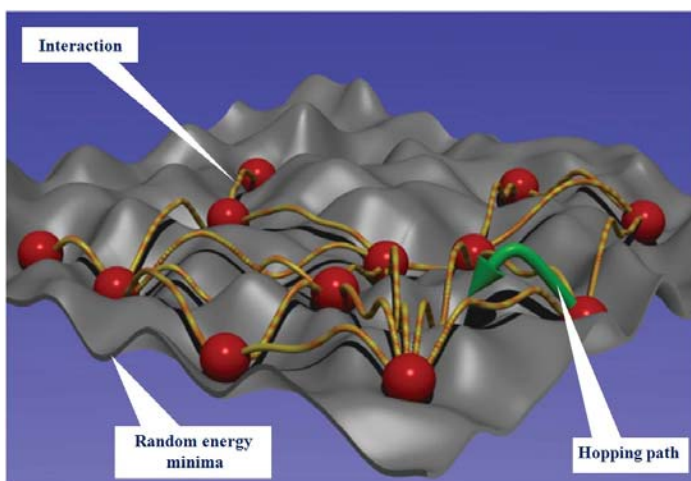


**Figure 5.11:** Glassy behaviour in disordered Coulomb systems. The electrons (red) in a random landscape interact with other (yellow-orange lines). The properties at low temperature are governed by collective hopping of these electrons (green arrow). Adapted from reference [73].

We can infer from the above discussion that transport is accomplished by correlated electron hopping e.g., sequential hops as well as simultaneous or collective hopping. But the approach is more difficult theoretically and is harder to verify experimentally. So our motivation is to understand the dynamics experimentally in Coulomb glass systems seems to appear in FMI state of manganites at low doping concentration level. The measurements could help us to determine if correlated electron motion involved in transport in Coulomb glasses. However noise comes from the fluctuations from microscopic entities and it can act as a probe of what happening physically at the microscopic scale.

#### 5.1.4 Review of published reports on 1/f noise in Coulomb glass systems

Coulomb glass is a special example of electron glass where electrons are localized and interact with each other via long range Coulomb potential. We have already studied that these systems appear to be glassy and electron hopping can occur on very long time scales. The transitions between low-lying energy valleys of the glassy systems are a real source of hopping conduction noise. Each inter-valley transition, in general a reconstruction of a large number of electrons, which can occur by one electron hops, but by a great number of such hops. Moreover, only the transitions which have long enough relaxation times contribute to

the growth of the spectral density of noise at *low frequencies*. The LCMO20 system is very interesting below its FMI transition where it follows SE-VRH conduction process and electrons are appeared to be localized in this regime. There are very few experimental results are available in Coulomb glass noise. Here we discuss about the available results in literatures. In general, the studies regarding Electron glass, Coulomb gap and other such many-electron effects have been studied mostly in doped Si. Study of these effects in doped Si needs low temperatures and often temperature below 1 K. This is because the scale of Coulomb gap is very small in doped semiconductors ( $\sim$ 1-5 meV) since the carrier density is small. In case of oxides with large carrier density the scale of the Coulomb gap is large ( $\sim$ 100meV) and as a result one observes these effects at a fairly high temperatures( $\sim$ 100 K) in contrast to the case of oxides where these effects are visible at low temperatures ( $\sim$ 1K).

Doped materials are strongly correlated systems and well known examples of electron glasses. Most of the experiments deal with variable range hopping and focus on temperature dependence of  $1/f$  noise [74-76]. Voss [77] reported the experimental studies on doped Silicon and shown that low frequency  $1/f$  noise is produced solely by hopping conduction. Massey [78] found that in Silicon  $1/f$  noise amplitude decreases when temperature goes down, while McCammon [79] observed exponential increase of  $1/f$  noise with the decreasing temperature. Again Kar *et al.* [80] investigated noise in doped Silicon also and reported that the noise is independent of temperature at lower temperatures (2-20 K) and decrease with temperature at higher temperatures. Hence, the results seem to be quite controversial.

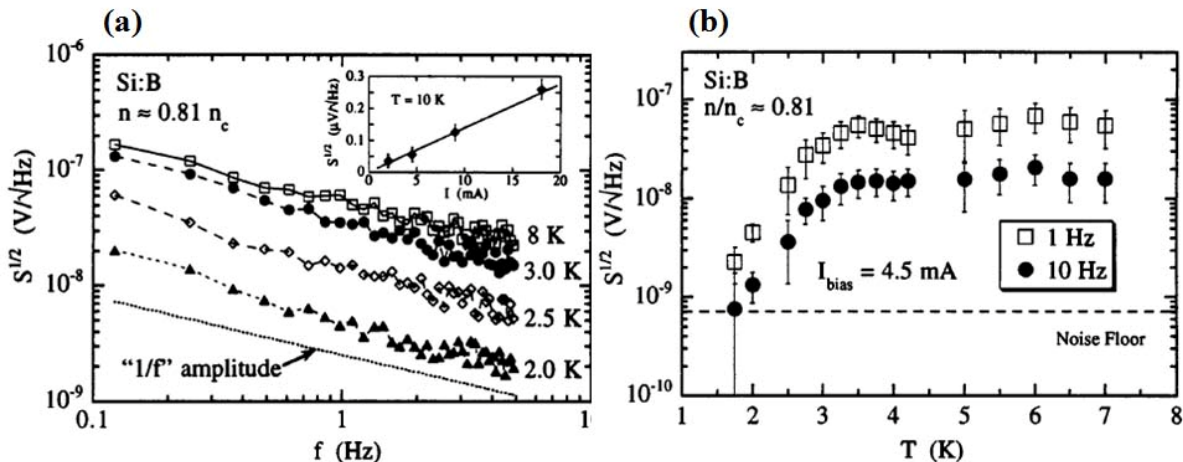


**Figure 5.12:** (a) Noise amplitude ( $S^{1/2}$ ) spectra of an 81% Si:B sample at several different temperatures. The bias current is 4.5 mA. The noise power shows  $1/f$  noise. Inset shows noise amplitude at 2 Hz as a function of the dc bias current. (b) Noise amplitude ( $S^{1/2}$ ) at 1 Hz and 10 Hz as a function of temperature at same bias current. Adapted from reference [78].

Massey *et al.* [78] used low frequency noise probe to study the interacting charge dynamics in variable range hopping in Boron doped Silicon. They have quantified noise spectral power  $S(f)$  with dc current bias injected in the system. Measurements of dynamics without injecting excess charge can elucidate the roles of single and many particle excitations on transport. They studied low frequency ( $0.1 \text{ Hz} < f < 12 \text{ Hz}$ ) electronic noise spectra and found  $S(f) = \beta I^2 f^\alpha$ , where  $\beta$  describes overall noise magnitude,  $I$  is the dc current bias, and  $\alpha$  is the spectral exponent as illustrated in Figure 5.12(a). They also observed decrease in spectral power for a particular frequency over a temperature interval as shown in Figure

5.12(b). The spectral power exponent was found to be slightly greater than unity for all possible temperatures. Finally they found an energy scale in the temperature and frequency range over which the noise features are appreciable is  $E^* = -k_B T \ln(2\pi f \tau_0) \approx 60\text{-}100 \text{ K}$ . This energy was found to be ten times larger than the Coulomb energies determined from response to single-particle charge perturbations [81, 82]. They infer the existence of thermally activated rearrangement of many electrons among random sites. This idea is supported by theoretical investigations by Kogan [83] where  $1/f$  noise in interacting variable range hopping systems can appear from fluctuations among low energy, many electron configurations. His simulations show that the charge arrangements have a large number of nearly degenerate total energy minima all lying within a Coulomb gap energy, of order 1 K, of each other. These energy valleys are separated by a broad distribution of energy barriers which can greatly exceed the gap energy, leading to thermally activated configurational fluctuations between energy minima when the temperature is of the order of the Coulomb gap.

We have already mentioned that low frequency  $1/f$  noise was investigated in many materials with wide variety of transport mechanism (See Chapter 1 and Chapter 3). But we found no detailed experimental observations (except one discussed later in detail) regarding the hopping conduction in low doped perovskite single crystals. The single crystals are excellent for studies as there are free from random common defects like grain boundaries. These single crystal samples increase the efficiency and quality of the experimental data also. To discuss the noise with hopping transport we want to mention the two well-known regimes of the hopping transport. At relatively high temperatures where electrons use almost all sites for hopping and called nearest neighbourhood hopping (NNH). This hopping mechanism leads to fixed activation energy for conductivity. At low temperatures the activation required for the use of the carriers becomes very costly and a very narrow band of energies around the Fermi level participate in the conductivity. With decrease of temperature the width of the band shrinks and hops become longer and called variable range hopping (VRH) (eg. ES-VRH conductivity). The original theory of  $1/f$  noise in the hopping transport by Shklovskii *et al.* [84] and Kogan *et al.* [85] deals only with NNH and at sufficiently high temperature where NNH conductivity is temperature independent. According to their theory there are several electron traps in the system, trap electrons from the transport path i.e., from conducting media and releases it back, both having characteristic time scales. They also mentioned that these time scales are much larger than the time scales of VRH hopping conductivity. This capture and release mechanism of charge carriers lead to modulation of the number density of the conducting carriers at low frequency  $\omega$  and the spectral density of current noise  $I_\omega^2$  with a behaviour of  $1/\omega$  or  $1/f$ . This idea is based to the similar explanation given by Mc.Worter number fluctuation number fluctuation ( $\Delta n$ ) theory [86] which states that  $1/f$  noise is generated by fluctuations in the number of carriers due to charge trapping in surface states. The theory explained origin of  $1/f$  noise in semiconductor-oxide interface and found that the fluctuation of the carrier density will cause the resistance to fluctuate giving rise to noise. But in case of hopping transport these traps are located throughout the conducting media.

Shklovskii [87] carried out theoretical calculations to generalize the idea of Refs. 84 and 85 to the VRH conductivity and found the characteristics of current noise  $I_\omega^2$  which approximately follows Hooge law with frequency exponent  $\alpha$  in VRH case. They also found that this noise decreases with temperature in these systems. According to the authors the relative fluctuations of the concentration of charge carriers lead to the fluctuations of conductivity, i.e.,

$$\frac{I_\omega^2}{I^2} \propto \frac{n_\omega^2}{N^2(\delta)} \quad (5.11)$$

where  $I_\omega^2$  is the spectral density of current fluctuations,  $I$  is the average current through the sample,  $n_\omega$  is the spectral density of the fluctuations of the concentration of conducting electrons and  $N(\delta)$  is the concentration of donor impurities in the  $\delta$  band around Fermi level. They estimated  $I_\omega^2 / I^2$  and found the Hooge law as:

$$\frac{I_\omega^2}{I^2} = \frac{\Gamma(\omega, T)}{\omega N_D V}, \quad (5.12)$$

where,  $N_D V$  is the total number of donors and  $\Gamma$  is the Hooge coefficient. Discussing the above relation we want to mention that when the majority carriers are free electron in any system then fluctuations of the carrier concentration of free electrons directly lead to  $I_\omega^2 / I^2 = n_\omega^2 / n^2$  at a fixed electric field where  $n$  is the concentration of free electrons. For NNH such proportionality between fluctuations of  $I$  and  $n$  is obvious for strongly compensated samples, where electrons play the role of carriers, or for a weakly compensated semiconductor, where the role of carriers is played by a small concentration of holes (empty donors). However, even in this case there could be such an intermediate compensation ratio  $N_A / N_D$ , where the coefficient in linear proportionality between fluctuations of  $I$  and  $n$  vanishes. Here  $N_A$  is the concentration of acceptors. In VRH conductivity connection between fluctuations of  $I$  and  $n$  is not so obvious and the relation is non-trivial. Moreover, without Coulomb interactions fluctuations of the concentration of charge carriers are uniform. Coulomb interactions make these fluctuations localized because of screening of trapped electrons. Hence, fluctuations of the concentration of conducting electrons do not propagate to the bulk of the conducting media. As a result conducting electrons gets perturbed locally and affect the total current of the sample. They mentioned that in case of Coulomb glass which is formed by a frozen distribution of interacting electrons on random donors have energy valleys with different conductivities. These can lead to  $1/f$  noise and eventually it is difficult to evaluate and estimate the noise in such systems. However, we believe that the basic relation spectral power  $\sim n_\omega^2$ , will be of general validity and the measured spectral power will thus give us information on the spectral power of the charge fluctuation in the system.

This investigation as well as the investigation of Jain *et al.* [1] established unambiguously that variable range hopping mechanism describes charge transport in FMI state of low-doped manganites. However, noise spectroscopy in perovskite manganites at FMI regions is not well studied at all, as mentioned before. We found only a single report that has been published recently in  $\text{La}_{0.82}\text{Ca}_{0.18}\text{MnO}_3$  single crystal sample. Wu *et al.* [88] investigated nonequilibrium  $1/f$  noise in  $\text{La}_{0.82}\text{Ca}_{0.18}\text{MnO}_3$  single crystals and their results are shown in Fig. 5.13. They followed the same experimental scheme as described by Massey *et al.* [78] and Shklovskii [87]. The crystals were injected varying dc current bias and the noise had been investigated in such current biased systems. The authors observed that temperature dependent noise follows the resistivity changes with temperature (please see Fig. 5.13(a)). They observed noise scales as a square of the current ( $I^2$ ) as expected for

equilibrium resistivity fluctuations (please see Fig. 5.13(b)). When the current was increased above a threshold value, the noise started to decrease. This result showed the onset of nonequilibrium fluctuations in the system. The work of Wu *et al.* [88] however, has several ambiguities which are pointed out below.

- From experimental point of view, the authors have used simple four-probe dc biasing technique to measure noise in the single crystal samples which is less sensitive than ac biasing technique which we followed in our studies. In particular, the subtraction of the background is non-trivial.
- They have injected dc bias current  $I$  and was used again to estimate the relative spectral power of noise. But, these systems show non-linear conductance throughout the temperature regimes (77-300 K) of their interest and the resistivity is strictly bias current dependent. Hence, it is not desirable to use the same current to excite the sample as well as to study the fluctuation phenomena in it.
- They did not discuss about whether there is any noise contribution coming from phase coexistence or not. The external bias can force the change the topology of phase separation. No data has been presented considering these facts.
- Finally, we have talked about the glassy nature of the low doped perovskite which follow ES-VRH conduction mechanism. It has been found earlier [1] the  $\text{La}_{0.82}\text{Ca}_{0.18}\text{MnO}_3$  single crystals samples fall in this category. The authors did not discuss what happened to the fluctuators at low temperature where very few of them are accessible for electronic transport, in particular whether there is a glass-like freezing.

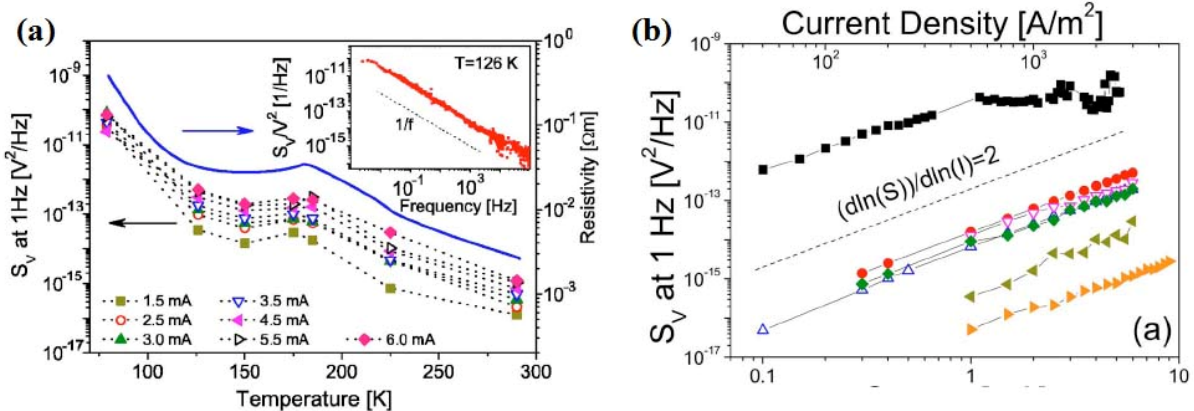


**Figure 5.13:** (a) Resistivity and  $1/f$  noise intensity at  $f = 1 \text{ Hz}$  as a function of temperature.  $\rho(T)$  was recorded using  $10 \mu\text{A}$  dc current bias. Inset shows a typical power spectral density of the noise; (b) Current dependence of the noise intensity at  $f = 1 \text{ Hz}$ . The dashed line is drawn according to  $S_V \propto I^2$ . Adapted from reference [88].

In our investigations we addressed to the lacuna in the earlier studies and also directly addressed the issues like possibility of glass-like freezing in the electronic system. Our approach to use the noise spectroscopy for study of the FMI phase, as we have pointed out before, is to use it as a tool to investigate the following issues:

- (a) To use the excess noise (that is not white) as a probe of charge dynamics and to study how in the insulating state ( $T < T_{FMI}$ ) the spatial correlation develops that leads to non-Gaussian fluctuations.
- (b) To study the white noise as a function of electron heating which have been suggested as the origin of strong non-linear conduction and Colossal Electroresistance in these materials. For this work we have used a technique of measuring the noise by ac in presence of dc. This is required in strongly non-linear systems and has been successfully employed before in study of charge ordering using noise spectroscopy where also one observes a strong non-linear conduction [89]. It is shown that in non-linear systems, the current that produces the non-linearity need be separated out from the current that measures the noise.

In the next section we describe the experimental methodology where we studied the non-linear transport in our system first and then we describe the study of the noise spectroscopy in the LCMO20 single crystals samples by five-probe ac measuring technique in presence of dc bias. We shall present the temperature dependent noise data in the temperature range 40-300 K covering two transition temperatures namely  $T_C$  and  $T_{FMI}$  for a fixed dc bias. Following it we shall present noise spectroscopy in the same by varying dc current from  $1\mu\text{A}$ - $1\text{mA}$ . Below 40K the resistance is too large to make a meaningful measurement.

## 5.2 Experimental methodology

All the noise studies have been performed on  $\text{La}_{0.80}\text{Ca}_{20}\text{MnO}_3$  (LCMO20) single crystals grown by floating zone technique. The details of growth mechanism have been presented earlier in Chapter 2. The main features of measurement techniques are presented here. Five gold contact pads were evaporated onto the crystals and Cu leads (diameter  $40 \mu\text{m}$ ) were soldered onto the pad using an Ag-In alloy paste. Four probes among the five were used for temperature dependent resistivity measurements and current-voltage ( $I$ - $V$ ) characteristics. The probes are kept always unaltered for noise measurements. All the measurements should be done on a single batch of contact probes otherwise huge contact noise can hinder the experimental results seriously. The ac four probe temperature dependent resistivity measurement setup had been used for temperature dependent  $I$ - $V$  characteristics which we have already discussed in Chapter 2.

We have used five-probe ac noise measurement setup in presence of dc biasing current. While the ac biasing current is going to measure noise, the dc current will induce charge carriers and stress the sample. The working principle of electrical circuit has been already mentioned in Chapter 2. Here we have studied frequency dependence excess noise spectra at a particular dc current with the lowest possible current available, i.e.,  $1\mu\text{A}$ . In the next paragraph we discuss the reason behind the selection of a particular biasing current value. Again temperature dependence of excess noise will help us to study the dynamics near phase separated regions. We shall also discuss what happens to the white noise (“Nyquist noise”) with the application of varying dc bias current.

## 5.3 Non-linear conduction and Colossal Electroresistance

Continuing the study of ferromagnetic insulating (FMI) phase one important aspect of this phase is the presence of “colossal” electroresistance (ER) in LCMO20 sample. The ER, arising from a strong non-linear dependence of resistivity  $\rho$  on current density  $j$ , attains a

value  $\approx 100\%$  in FMI state. The severity of the non-linear behaviour of resistivity at high current densities is progressively enhanced with decreasing temperature. Jain *et al.* [90] has reported that concomitant with this built of ER, there is a sharp drop of MR. The author has shown that the MR collapses to  $< 20\%$  even in a magnetic field 14 Tesla in  $\text{La}_{0.78}\text{Ca}_{0.18}\text{MnO}_3$  (LCMO18) shown in Fig. 5.14. They inferred that the phenomenon supports decoupling mechanism of ER and MR in FMI state.

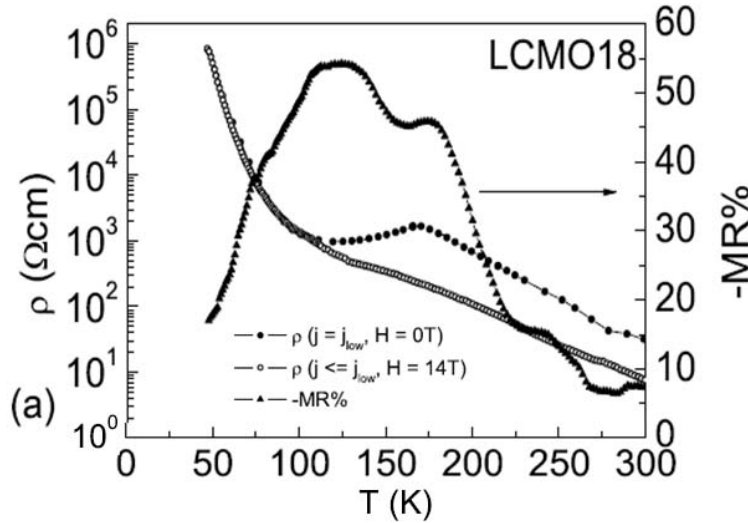


**Figure 5.14:** Temperature dependence of resistivity  $\rho$  in the absence of a magnetic field, and in the presence of the magnetic field 14 Tesla. The collapse of the MR is established when sample is entering in the FMI state. The values of current densities are  $j_{low} = 9.5 \times 10^{-4} \text{ A/cm}^2$  and  $j_{high} = 9.5 \times 10^{-1} \text{ A/cm}^2$ . Adapted from reference [1].

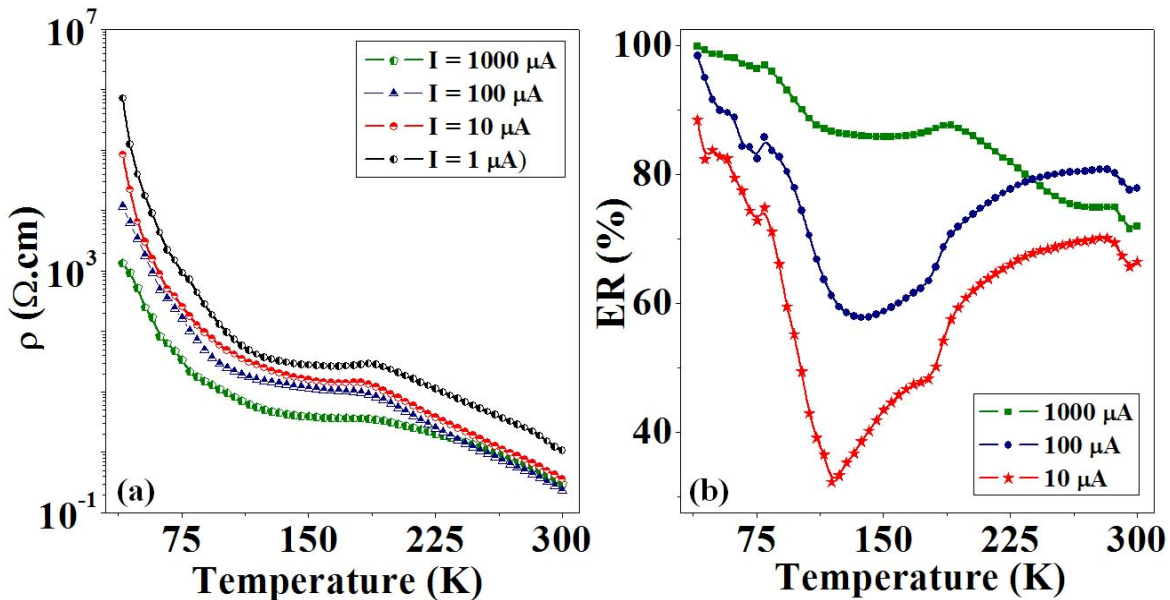


**Figure 5.15:** (a) Temperature dependence of resistivity  $\rho$  for four representative current bias ranging from  $1 \mu\text{A}$ - $1000 \mu\text{A}$ . The suppression of resistivity with increasing current bias is noted. (b) Temperature dependence of electroresistance at three current densities  $j_{high}$  ( $1000 \mu\text{A}$ ,  $100 \mu\text{A}$ , and  $10 \mu\text{A}$ ) has been plotted. The value of  $j_{low} = 1 \mu\text{A}$  has been taken for estimation of electroresistance. The electroresistance value reached to  $\sim 100\%$  in FMI phase.

Fig. 5.15(a) shows the temperature dependence of resistivity of LCMO20 sample for four representative bias currents. The values of lowest and highest current densities are  $j_{low} = 1 \times 10^{-4} \text{ A/cm}^2$  (for  $I = 1 \mu\text{A}$ ) and  $j_{high} = 1 \times 10^{-1} \text{ A/cm}^2$  ( $I = 1 \text{ mA}$ ). We have chosen the value of  $j_{low}$  such that  $\rho(j_{low})$  is independent of measuring current density for all temperatures of measurements. To confirm the scenario we studied temperature dependence of  $I$ - $V$  curve for the sample and we have seen that temperature dependence of  $\rho(j_{low})$  can be considered to be the pristine linear response of the sample. The resistivity exhibits a peak near  $T_C \cong 186 \text{ K}$  and below which the sample enters in FMM phase. This FMM phase however, appears to be highly resistive and percolative in character. The behaviour in this phase, of the  $\rho$ - $T$  curve, suggests that the FMM phase may be coexisting with an insulating phase. The resistivity exhibits a small drop till  $T_{FMI} \cong 120 \text{ K}$ . Further reduction of the temperature results in the build-up of the FMI state below  $T_{FMI} \cong 120 \text{ K}$  where  $d\rho/dT$  becomes negative, i.e., the resistivity takes an upturn. It may be recalled that, in the last chapter it was shown that in the FMI state, the temperature dependence of the resistivity follows ES-VRH behaviour.

The comparison of two resistivity data confirms that there is a strong suppression of  $\rho$  with increased current density below  $T_{FMI}$ . Since the sample is highly resistive and  $d\rho/dj < 0$  in this underlying state the contributions of Joule heating to the observed depression of resistivity at high current density need to be ascertained. But Jain [1] had shown that in LCMO18 sample at lowest possible temperature,  $T = 55 \text{ K}$  (i.e., at highest possible resistance) the contribution of Joule heating is not more than a percent ( $\sim 2\text{-}3\%$ ) of the observed effects. The ER arises from strong non-linear dependence of resistivity  $\rho$  on the current density  $j$ . This phenomenon limits the current value of our “excess” noise measurements. We wanted to avoid additional current stressing of the sample by external bias. As the resistivity is strongly dependent on current density  $j$  we have to be extremely careful about the selection of the bias current. The depression in current induced resistivity in Fig. 5.14(a) can be quantified in terms of electroresistance defined as

$$ER\%(T) = 100 \times \frac{\rho(j_{low}) - \rho(j_{high})}{\rho(j_{low})}(T). \quad (5.13)$$

The observed ER is positive indicating the decrease of resistivity with increasing current density for all temperatures of measurements as shown in Fig. 5.15(b). The ER continues to rise with decreasing temperature and reaches nearly 100% at the lowest possible temperature observed. Though we are focusing mainly the FMI phase, there is a substantial component of ER for  $T > T_C$ . For  $T = 300 \text{ K}$ , resistivity is nearly  $1.0 \Omega\text{cm}$  with high value of ER nearly 70%. But the physics of ER in two insulating phases namely, FMI phase for  $T < T_{FMI} < T_C$  and PI phase for  $T > T_C$  are completely different.

There are few points that we also note. The nature as well as the value of the ER is a strong function of the measuring current. This is expected since the transport is non-linear. The data at a current as small as  $10 \mu\text{A}$ , which has low power dissipation, the ER is still high. It is more than 60% at room temperature, which is the polaronic conduction region. It dips considerably in the FMM region below  $T_c$  and as the FMI state is approached it increases again and at  $40\text{K}$  for a current as small as  $10 \mu\text{A}$  the ER approaches 90%. The trend is qualitatively similar at  $100 \mu\text{A}$ , although the ER is larger than 60% in most regions and it approaches 100% at lowest temperatures. With a measuring current of  $1000 \mu\text{A}$ , the nature of

the ER is somewhat different that the dip in the FMM region is almost absent. We see below that with such a measuring current we may be in a very different non-equilibrium regime as seen by the noise spectroscopy as well as the non-linear  $I$ - $V$  curve.

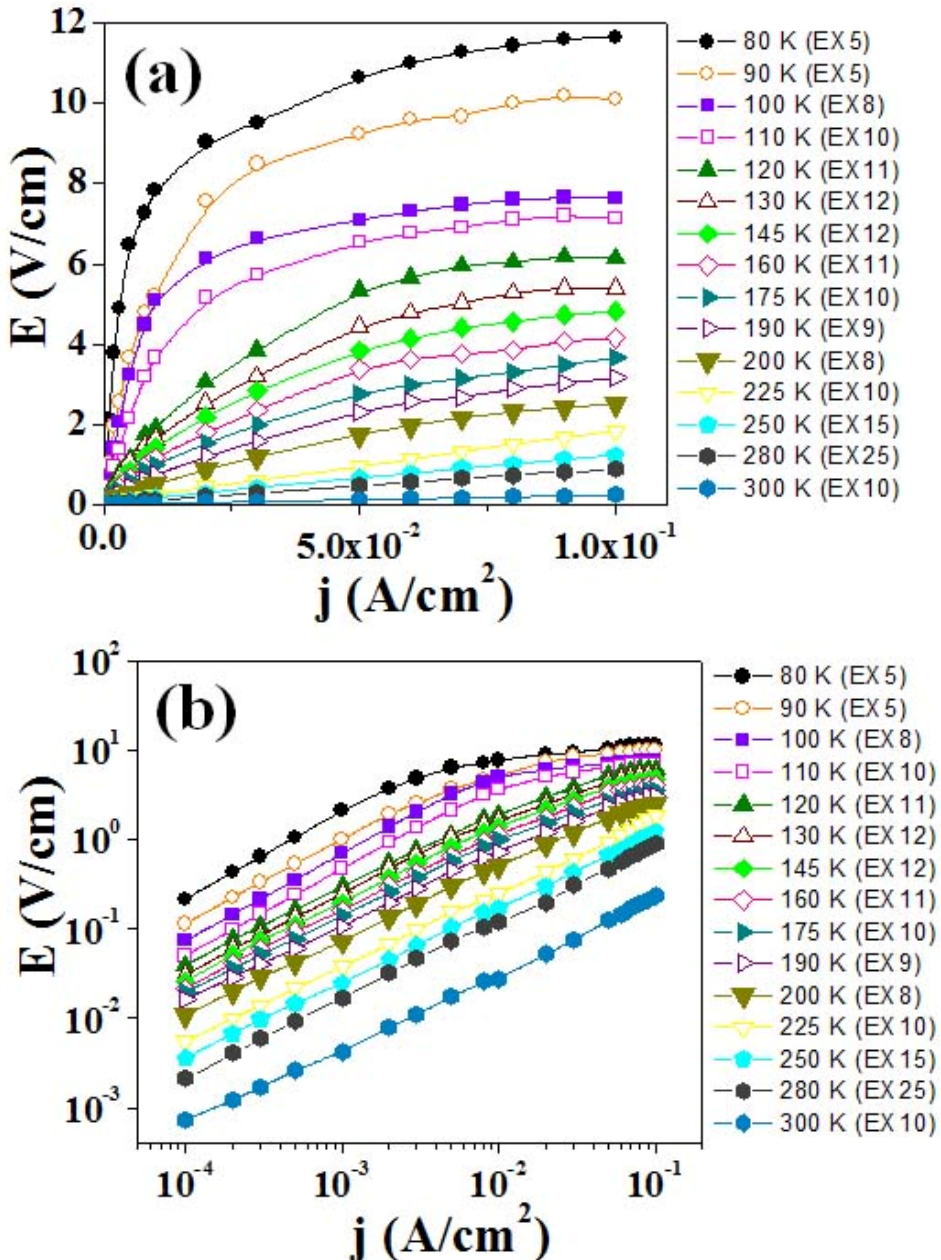


**Figure 5.16:** (a) Current density versus electric field ( $j - E$ ) characteristics at few representative temperatures covering two transition temperatures  $T_{FMI}$  and  $T_C$ . (b) The same  $j - E$  characteristics have been plotted in log-log scale to show the power law dependence between  $j$  and  $E$ .

We have studied the temperature dependent  $I$ - $V$  characteristics. As we mentioned earlier that it will help us to choose the specific value of current bias for noise spectroscopy. We have varied current from  $1\mu\text{A}$ - $1\text{mA}$  and the variation differs by three orders of magnitude. The data is rendered independent of particular sample dimensions by plotting it in specific units as current density ( $j$ ) versus electric field ( $E$ ), i.e.,  $j - E$  characteristics and shown in Fig. 5.16(a). The temperature  $T$  mentioned over here is the temperature of

phonons  $T_{ph}$  and different from the electron temperature  $T_e$  (will be discussed later in detail). The non-linear nature of the conduction in the FMI state below  $T_{FMI} \approx 120$  K is clearly evident, and the data reveal a continuous decrease in  $\rho (= E / j)$  as  $j$  increases. The non-linearity becomes progressively more severe with decreasing temperature. Further in Fig. 5.16(b), we plot the same  $j - E$  characteristics on a log-log plot. From these plots, it is evident that the  $j$ - $E$  plots are non-hysteretic and that there is a power law relationship between  $j$  and  $E$ .

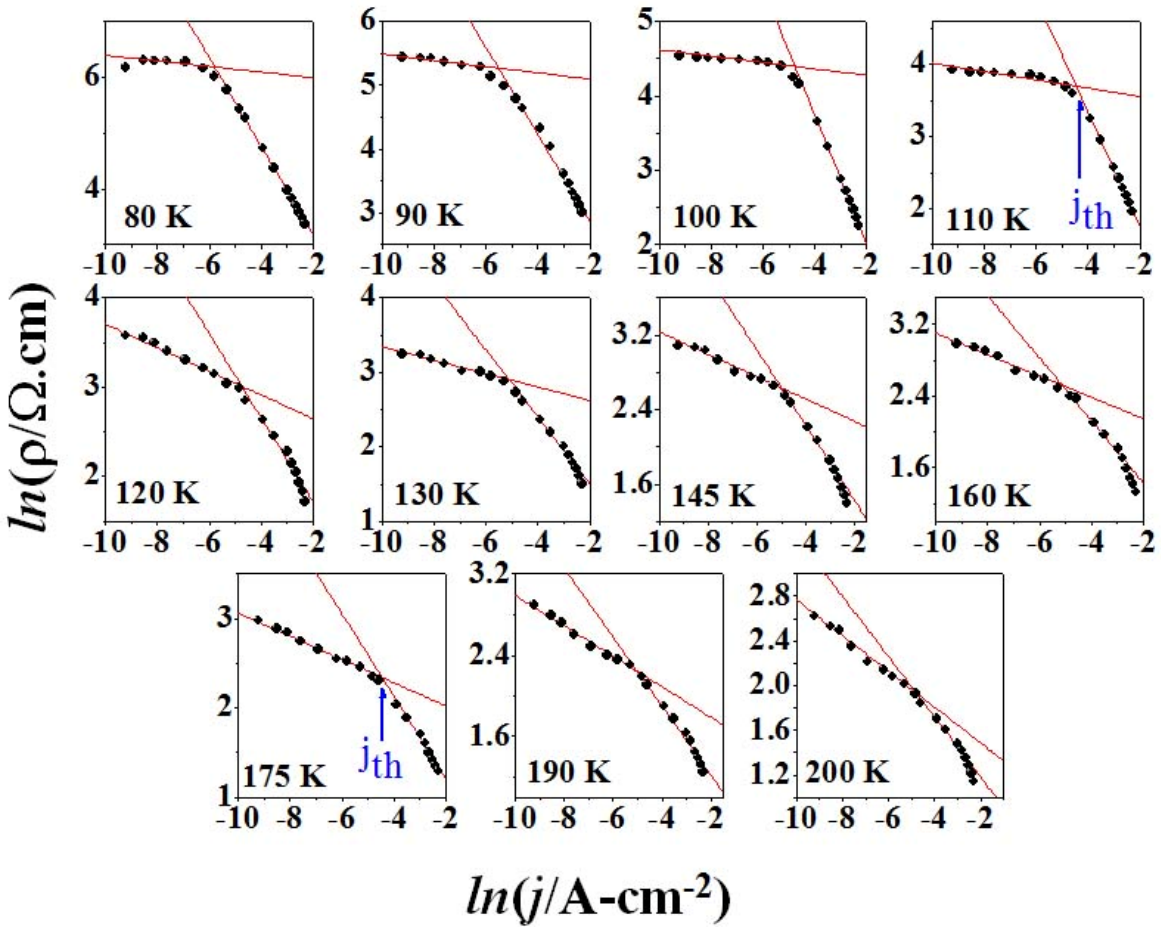


**Figure 5.17:** Representative log-log plots showing two regimes of power law variation of representative  $\rho$  as a function of current density  $j$  for different temperatures. The threshold current density  $j_{th}$  separates out two power law regimes,  $j < j_{th}$  and  $j > j_{th}$ . The solid lines are best fit curves with equation 5.14 (see text).

For further clarification we plot the resistivity  $\rho = E / j$  as a function of current density  $j$  individually in *log-log* scale for few representative temperatures as shown in Fig. 5.17. Plotted individually in this way, it is clearly seen that there exists a threshold current density  $j_{th}$  for each temperature separating two  $\rho - j$  regimes. We have fitted the data with the equation

$$\rho = \alpha_n j^{m_n} \quad (5.14)$$

at a particular temperature where  $\alpha$  is a fitting parameter,  $n=1$ , and  $2$  for  $j < j_{th}$  and  $j > j_{th}$  respectively. We can see that there is a current which we denote as  $j_{th}$  so that for  $j < j_{th}$ ,  $\rho$  is weakly dependent on  $j$  and  $\rho \propto j^{m_1}$  where  $m_1$  is close to zero, as it should be for a ohmic ands linear transport.. But for  $j > j_{th}$ , the non-linearity sets in and  $\rho$  decreases severely with increasing  $j$ . In this situation  $\rho \propto j^{m_2}$  the exponent  $m_2$  deviates from zero strongly and the coefficient  $\alpha_2$  quantifies the extent of the non-linearity in the system.

Our analysis below has been performed keeping in mind the above observation of the temperature dependent threshold current density that separates two power law regimes of  $j$  dependence of resistivity. The analysis captures the temperature dependence of the non-linear conductivity for two power law regimes, viz.,  $j > j_{th}$ , and  $j < j_{th}$ , i.e., Fig. 5.17 captures the development of the non-linear conductance (NLC), i.e., the strong current dependence of the resistivity, in the low temperature FMI phase. The  $j_{th}$  is marked in Fig 5.17. The existence as well as its definition at this stage is rather empirical and there is a clear theoretical ground form which we can claim its existence.

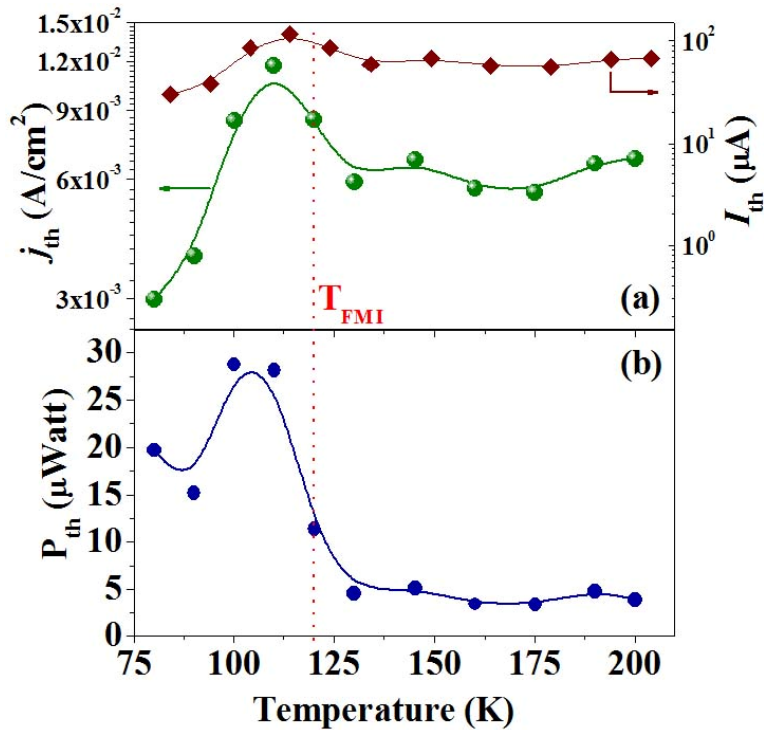


**Figure 5.18:** (a) The temperature dependence of threshold current density  $j_{th}$  showing a distinct feature below  $T_{FMI}$ . The lowest possible  $j_{th} = 3 \times 10^{-4} A/cm^2$  ( $I_{th} = 30 \mu A$ ) at 80 K. (b) The temperature dependence of threshold power  $P_{th}$  showing the maximum power dissipation is  $\sim 28 \mu Watt$ .

In Fig. 5.18 the temperature dependence of the relevant parameters including  $P_{th}$  ( $= I_{th} R_{th}$ , where  $R_{th}$  is the value of the sample at  $I_{th}$ ). It is evident from Fig. 5.18(a) that  $j_{th}$  does not have significant variation for  $T > T_{FMI}$ . However, it increases below  $T_{FMI}$  and at even lower temperature there is a down turn. In Fig. 5.18(b) we have plotted  $P_{th}$  against  $T$  and we can observe a sharp rise of it below  $T_{FMI}$  though it is nearly temperature independent

above  $T_{FMI}$ . The above discussion though empirical brings out the salient features of the electrical conduction in the FMI state and shows that the conduction in thios state has distinctive features that make it different from the conduction in then regime  $T > T_{FMI}$ . We will again take up these issues when we seek an understanding in terms of an electron heating model.

The above discussion also helps to choose the suitable value of the bias current for equilibrium noise measurements so that non-linear effects due to high bias current can be avoided. We will see below that the bias we used for equilibrium noise is taken much smaller than the lowest possible value of  $I_{th}$ .  $P_{th}$  in these materials is not more that  $30\mu\text{W}$ . We have chosen bias current even less, i.e.,  $1\mu\text{A}$  (power dissipation  $\sim 20 \text{ nW}$  at  $80 \text{ K}$ ) for our “excess” noise measurements to avoid any contribution coming from non-linear conduction process in the FMI phase.

## 5.4 Temperature dependent noise spectroscopy without dc bias: Investigation of the “excess” noise.

In this section we report the temperature and frequency dependence of “excess” noise of the LCMO20 single crystal samples. This noise is the equilibrium noise in the sense that the measuring current does not take the system to a non -equilibrium state unlike what happens in presence of a strong d.c bias that leads to electron heating.

The temperature range we are interest for our measurement is  $40\text{-}300 \text{ K}$  and frequency range is  $60 \text{ mHz}\text{-}10 \text{ Hz}$ . The measured  $T_C \approx 186 \text{ K}$  and FMI state is realized below  $T_{FMI} \approx 120 \text{ K}$ . We have already studied the temperature dependent resistivity phenomena in the LCMO20 sample to separate out different conductivity regimes. To concentrate in noise spectroscopy we have to discuss about the power spectrum as a function of frequency for different temperatures. For this purpose we have used ac bias current  $1\mu\text{A}$  without ant dc bias. The excess noise investigated here is thus an equilibrium noise which will not be affected by such issues as electron heating etc and the noise is expected to give us information on the charge fluctuations and the slow dynamics associated with the charge fluctuations.

### 5.4.1 Magnitude of “excess” noise

Fig. 5.19 shows a representative data of power spectrum  $S_V(f)$  of the excess noise (with background noise subtracted) a temperature  $80 \text{ K}$ . The back ground noise (without any measuring power) is also shown. The magnitude of the background noise if it the experiment is properly and without any extraneous noise power contributing to the background should be given by the Nyquist noise ( $4k_B T R$ ) of a resistor  $R$  at a temperature  $T$ . The Nyquist noise which has been plotted simultaneously in the same graph and it is much less (six orders of magnitude) from the sample noise. These are typical representative data that we will discuss in more details later on. The power spectrum shows that the noise spectral power has predominantly  $1/f$  character. We show in the next section that there are details in the power spectrum like small contributions form narrow band discrete frequency Lorentzians.

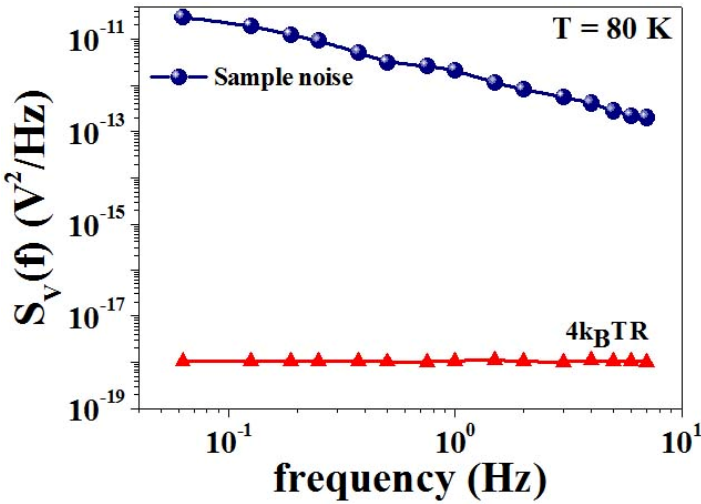


**Figure 5.19:** The noise power spectrum as a function of frequency at  $T = 80\text{ K}$  below  $T_{FMI}$ . The background noise is also plotted to show that the white noise in this case is given by the Nyquist value. The observed data show that the spectral power is predominantly  $1/f$  noise.

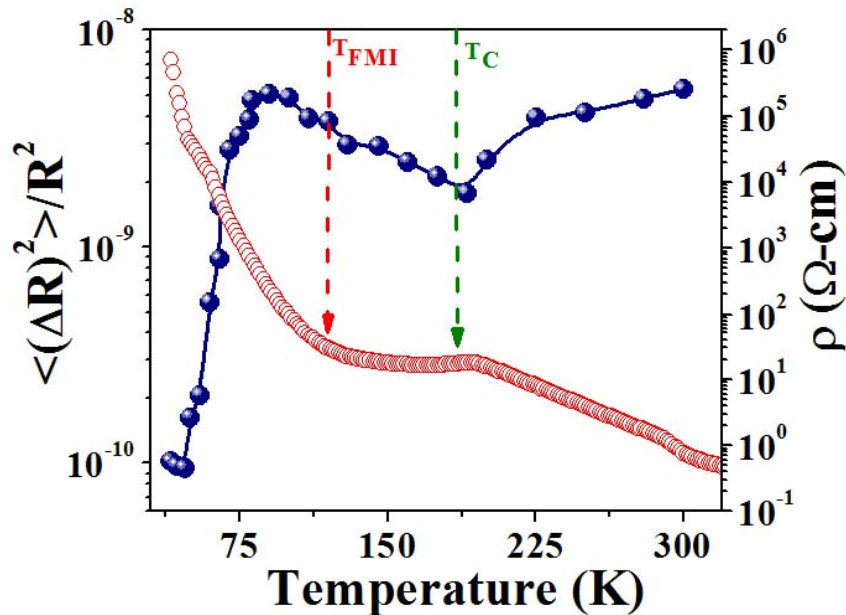


**Figure 5.20:** The relative resistance fluctuations  $\langle(\Delta R)^2\rangle/R^2$  as a function of temperature has been plotted where two transition temperatures have been marked also. The resistivity plotted in the right ordinate simultaneously to distinguish different conductivity regimes.

The measured noise can be quantified by the relative resistance fluctuations (mean squared fluctuations)  $\langle(\Delta R)^2\rangle/R^2$ . The  $\langle(\Delta R)^2\rangle/R^2$  has been calculated by integrating the power spectrum over the frequency range for all temperatures. In Fig. 5.20,  $\langle(\Delta R)^2\rangle/R^2$  has been plotted as a function of temperature along with the resistivity  $\rho$  in the right ordinate. It is clear from the graph that there exists a nontrivial dependence of  $\langle(\Delta R)^2\rangle/R^2$  with temperature. We have marked two transition temperatures in the same graph to distinguish

nature of total noise characteristics in different conductivity regimes. Following the resistivity plot we can separate out three temperature regions, namely  $T > T_C$ ,  $T_{FMI} < T < T_C$ , and  $T < T_{FMI}$ . While there are shallow temperature dependences in the other temperature regimes, the most visible change, however occurs in the range of temperature below  $T_{FMI}$ . The very sharp fall in the  $\langle (\Delta R)^2 \rangle / R^2$ , seen below 80K is an important observation. Such a large drop can happen due to kinetic freezing of the charge fluctuation. The charge fluctuation is associated with the existence of the Coulomb gap  $\Delta_{CG}$ , hence the rate of fluctuation, if it is thermally activated would imply crossing an activation barrier  $E_a$ . The size of the activation barrier thus can be measured from the kinetic freezing. To check that a kinetic freezing indeed occurs we have studied the frequency dependence of the spectral power  $S_V(f)/V^2$ .

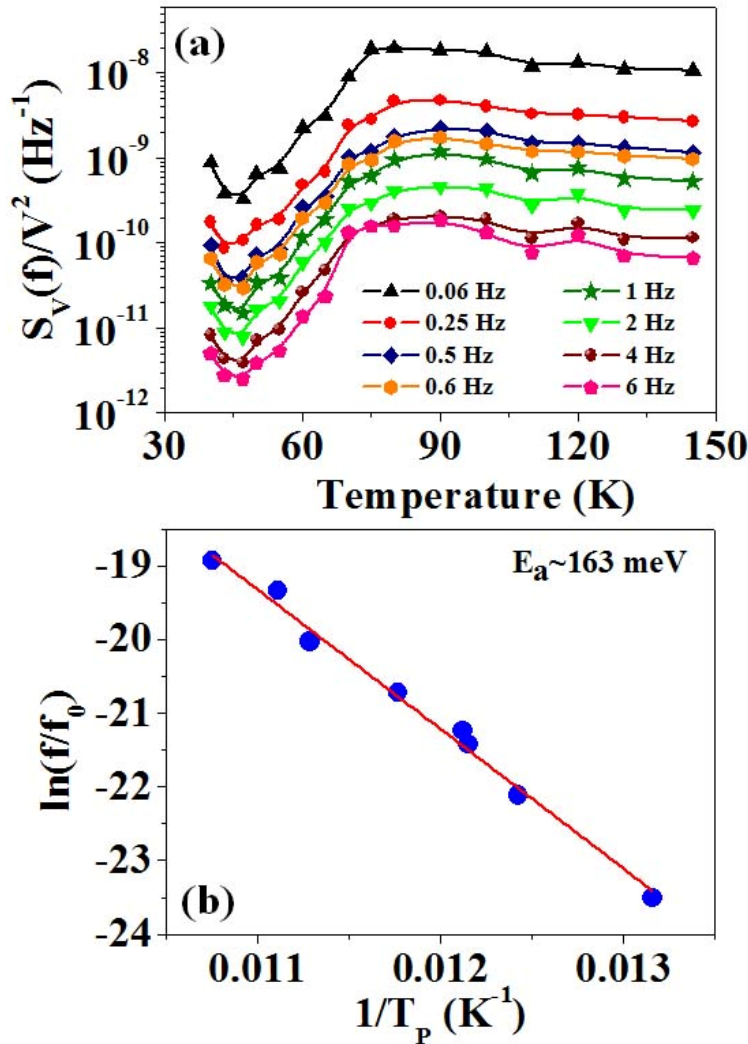


**Figure 5.21:** (a) The variation of  $S_V(f)/V^2$  as a function of temperature at eight representative frequencies. There are distinct peaks appearing at low temperatures. The peaks shift towards high temperature at higher frequencies. There are also broad peaks appearing in PI region but the nature of peak shift is not clearly observable. (b) The graph showing the plot of  $\ln(f/f_0)$  versus  $1/T$  for the above three frequencies (filled circles). The experimental data have been fitted with Arrhenius model and solid line shows the best fit curve which is linear. The activation energy calculated is  $\sim 163$  meV with  $f_0 = 10^9$  sec<sup>-1</sup>.

We have plotted  $S_V(f)/V^2$  for eight frequencies as a function of  $T$  in Fig. 5.21(a). The spectral power has much weaker temperature dependence above  $T_{FMI}$ . However, for  $T < T_{FMI}$  in the lowest temperature region the spectral power is strongly temperature dependent and it shows a large and sharp down turn. The down turn is spectral power is shown as distinct peaks in temperature. The data shown are for different values of  $f$ . We call the temperature at which the peak occurs  $T_p(f)$  for a given  $f$ . The peak temperature  $T_p$  has strong temperature dependence. We can clearly see that the peaks get shifted towards low temperature at low frequencies. We would explore whether  $T_p$  is like a kinetic freezing temperature. The dependence of  $T_p$  on frequency can be of the type that we expect in case of kinetic freezing.

To investigate whether the freezing process is due to the thermal activation mechanism we checked whether  $T_p(f)$  followed an Arrhenius model of activated kinetics as

$$f = f_0 \exp(-E_a/k_B T_p). \quad (5.15)$$

We plotted  $\ln(f/f_0)$  as a function of inverse temperature ( $1/T_p$ ) (filled circles) as shown in Fig. 5.21(b). The solid line is the linear best fit curve and the activation energy estimated from it is  $E_a \cong 163$  meV. This value is very close to the Coulomb gap energy  $\Delta_{CG} \cong 152$  meV which we found from resistivity data previously. It is thus interesting that the two independent measurements lead to very similar energy scales. The close proximity of  $E_a$  and  $\Delta_{CG}$  clearly shows that the charge fluctuation in the electronic system is activated across the Coulomb gap. The rapid fall of the noise below  $T_p$  thus can be taken a signature of kinetic freezing of the charge fluctuations as the electronic system with long range Coulomb interaction enters an insulating state in the FMI state. We however, note that at the lowest temperature there is a small upturn in the power spectrum (below 45K). At this point we are not sure whether it is an experimental artefact since due to very high sample resistance the current stability cannot be ensured by the series resistor. This can lead to extra noise.

Yu *et al.* [91] investigated noise in electron glass systems by simulation studies. They found that spectral density  $S_\omega \sim \omega^{-\alpha}$  and  $\alpha$  vary from 1.07-1.16 in electron glass systems by charge fluctuations due to hopping between isolated sites. They have shown that noise amplitude decreases due to Coulomb gap at low temperatures. This result exactly matches with our result as shown in Fig. 5.20. At high temperature they also found saturation of noise amplitude. They inferred that the decrease in the noise amplitude is due to the presence of activated hopping processes which decreases with decrease of temperature. We also found the same kind of activated processes in the regions  $T < T_{FMI}$  as the authors have suggested. Hence, we can conclude that our results have a good theoretical agreement where the systems are considered as electron glass.

### 5.4.2 Analysis of resistance fluctuation time series

Power spectral density is the most commonly used method of characterizing fluctuations, however, it is often not enough as it contains only the information about two-point correlations in the system. An important aspect of the fluctuation in systems that are correlated is that the fluctuation may deviate from Gaussian behaviour. Gaussian behaviour arises when the fluctuators are independent. In systems under consideration, the glassy behaviour develops due to long range Coulomb interaction. One would thus expect

development of correlated fluctuations in a glassy system. In the manganites the insulating states are intrinsically correlated. As a result one would expect correlated fluctuations to occur over a wide temperature range.

A study of non-Gaussian noise involves the study of a rather different set of statistical variables- the most commonly used and most informative methods are Probability density Function (PDF) and Second Spectrum (generally called “Noise of noise”). The detailed description regarding the estimation of these quantities has been described in Chapter 3. While the PDF can show large deviations from Gaussian spectrum, the more sensitive tool is the second spectrum. An example of development of large non-Gaussian fluctuations in doped Si undergoing insulator-metal transition has been reported before. Kar *et al.* [70] have investigated systems like doped Si near metal-insulator transition (MIT) and reported appearance of large non-Gaussian components in PDF ( $P(\Delta V)$ ) as shown in Fig. 5.22(a). They found that the non-Gaussian tails follow log-normal dependence of voltage fluctuation ( $\Delta V$ ). They also estimated the second spectrum near MIT to check the non-Gaussian fluctuations clearly in the frequency scale and the second spectra have been shown in Fig. 5.22(b). This data clearly show that in the regime of strong electron correlation, one would expect appearance of non-Gaussian fluctuation. In the part below we apply the above concepts in the manganites.

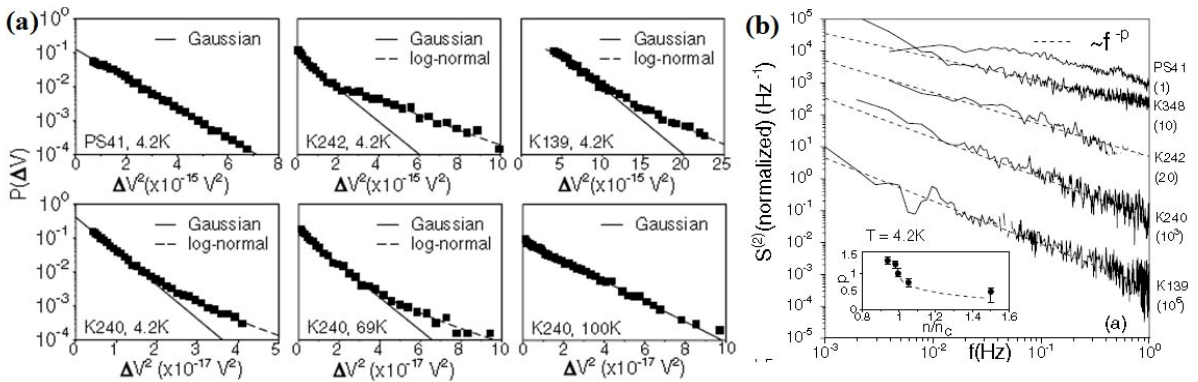


**Figure 5.22:** (a) Upper three panels show the PDF at 4.2 K for the metallic sample PS41, and insulating samples K242 and K139, which develop a non-Gaussian tail. The lower panels show how this tail grows for another insulating sample K240 with decreasing  $T$ . (b) Normalized second spectrum  $S^{(2)}(f)$  at 4.2 K. The spectra have been shifted down vertically by factors shown in brackets. The inset shows the sharp growth of frequency dependence at the critical concentration  $n = n_c$  at 4.2 K.

In Fig. 5.23(a) we have plotted PDF of voltage fluctuations of the LCMO20 sample at different temperatures below  $T_{\text{FMI}}$ . The PDF of voltage fluctuations for other temperatures are shown in Fig. 5.23(b). For Gaussian fluctuation, the probability of the voltage fluctuation follows the relation (as given in Chapter 1):

$$P(\Delta V) = \frac{1}{\sqrt{2\pi w^2}} e^{-\frac{(\Delta V)^2}{2w^2}}, \quad (5.16)$$

Thus a plot of  $\ln[P(\Delta V)]$  against  $(\Delta V)^2$  should give a straight line if the fluctuation is Gaussian and deviation from a straight line will be manifestation of non-Gaussianity in PDF.

The inverse slope of the straight line will give the width of the distribution  $w$ . The process of obtaining the PDF from the time series (after Wiener Filtering the data) has been discussed in Chapter 3. The Bin size used is 0.5 nV. This implies that voltage jumps above 2 nV can be trusted as data and below that it is a part of the background.

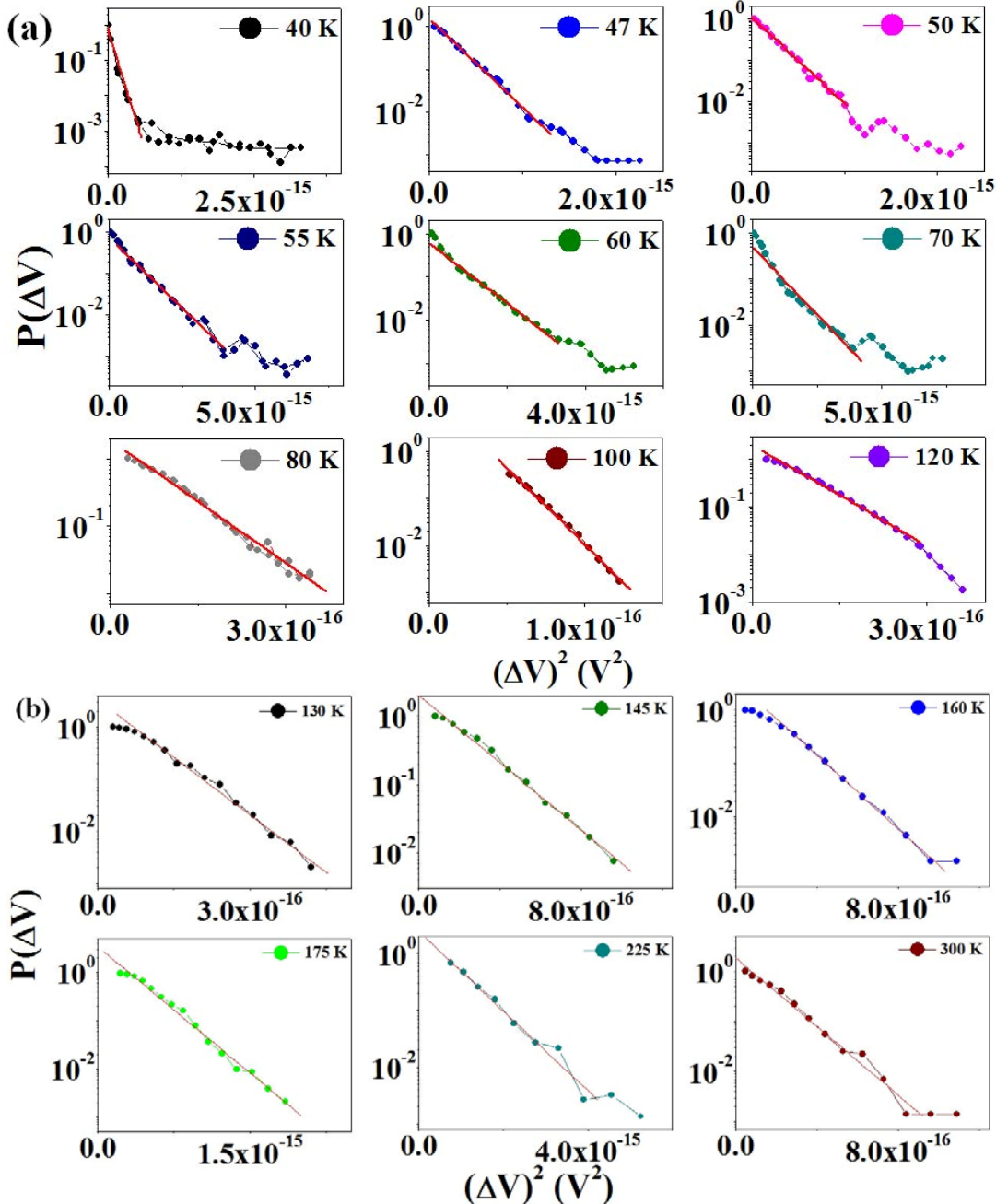


**Figure 5.23:** The calculated Probability Density Functions (PDF) as a function of voltage fluctuations ( $(\Delta V)^2$ ) have been plotted for few representative temperatures (a) below and (b) above  $T_{FMI}$ .

It can be seen that for  $T < T_{FMI}$ , the PDF is predominantly Gaussian as the plot of  $\ln[P(\Delta V)]$  against  $(\Delta V)^2$  is a straight line as is expected for a Gaussian. Even if there is a small non-Gaussian component, it is not visible. However, in the insulating phase we can

observe sharp deviation from Gaussian nature. For the low temperatures below 70K, we can observe long tails in PDF as a signature of onset of non-Gaussian components in voltage fluctuations. These tails disappeared for  $T_{FMI} < T < T_c$ . Typically at lowest temperature, the *rms* fluctuation is so small that the PDF becomes Gaussian again. It is likely that above  $T_c$ , in the insulating phase, the non-Gaussian tails may appear again. However the extent of the deviation from the Gaussian PDF may not be too large that it shows up in the PDF data.

### 5.4.3 Analysis of second moment-the correlated nature of the fluctuation:

The PDF analysis showed existence of deviation non-Gaussianity in the low temperature PDF. The non-Gaussian nature of the fluctuation can be studied quantitatively using the concept of second moment. The concept of second moment has been expressed in Chapter 3. In Fig. 5.24 we plot second moment  $S^{(2)}(f)$  of voltage fluctuations as a function of frequency at few representative temperatures of our study in LCMO single crystal sample. In order to estimate the non-Gaussian component (NGC) in the fluctuations of resistance, we have evaluated the second spectrum  $S^{(2)}(f)$  which is the Fourier transform of the four-point correlation function, within each window of  $T$  as:

$$S^{(2)}(f) = \int_0^{\infty} \langle \Delta R^2(t) \Delta R^2(t + \tau) \rangle_t \cos(2\pi f \tau) d\tau \quad (5.17)$$

In effect,  $S^{(2)}(f)$  measures a “spectral wandering” or fluctuations of the power spectrum itself within a chosen frequency band ( $f_L, f_H$ ), so that NGC is reflected as a non-white contribution to the frequency dependence of  $S^{(2)}(f)$ . Because of the finite detection bandwidth ( $f_H - f_L$ ), where  $f_L = 1$  Hz and  $f_H = 3$  Hz for our experiments, a white Gaussian background limits the sensitivity of  $S^{(2)}(f)$  to non-Gaussian effects which are hence expected to dominate only at low frequencies [92]. The integrated power in some band  $f_L < f < f_H$  will have a large variance and will itself have a power spectrum reflecting the frequency modulation of fluctuators by their neighbours.

Fig. 5.24(a) and Fig. 5.24(b) illustrate the normalized second spectrum of resistance fluctuations estimated using the relation:

$$s_N^{(2)}(f) = \frac{S^{(2)}(f)}{\left[ \int_{f_L}^{f_H} S_V(f) df \right]^2} \quad (5.18)$$

at few temperatures of our measurement. The expected Gaussian background is calculated from the measured  $S_V(f)$  within the same frequency band, and shown as the thick dark line. While the spectrum at 300 K shows no evidence of a non-Gaussian component down to  $\sim 60$  mHz and agrees completely with the estimated background,  $S_N^{(2)}(f)$  at the other temperatures show a steep rise at low  $f$  ( $\leq 300$  mHz). The solid green line in Fig. 5.24(a) and (b) shows the calculated Gaussian background as well.

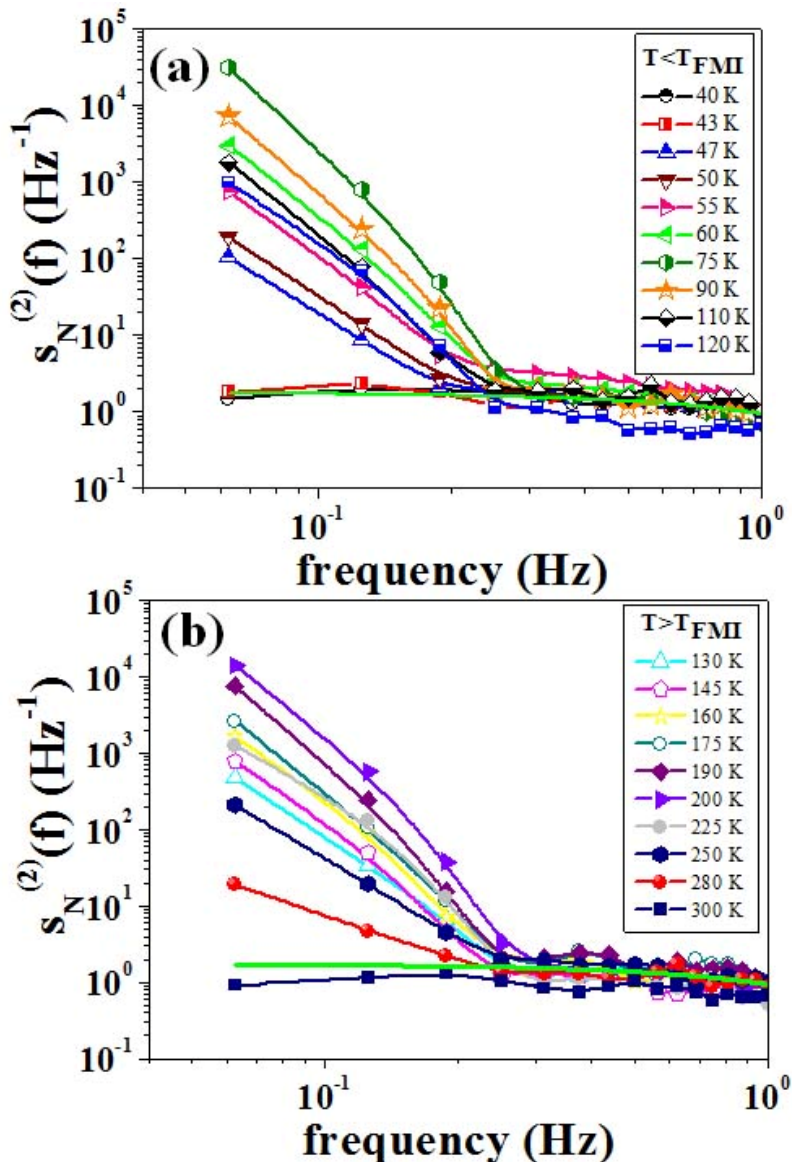


**Figure 5.24:** Plot of normalised second spectra  $S_N^{(2)}(f)$  as a function of frequency at frequency representative temperatures (a)  $T < T_{FMI}$ , and (b)  $T > T_{FMI}$ . The solid line shows the calculated Gaussian background in the same graph.

In Fig. 5.25 we have plotted  $S_N^{(2)}(f)$  as a function of  $T$  at lowest possible frequency  $f \approx 60$  mHz because we found the highest value of normalized second moment at this particular frequency for all temperatures. We observed a sharp drop in  $S_N^{(2)}(f)$  at a temperature exactly where we observed a sharp drop in total noise power (see Fig. 5.20). We can see this typical normalized second spectrum is showing nearly same temperature dependency what we have observed in Fig. 5.21 (where we have plotted  $S_V(f)$  as function of  $T$ ). The second spectrum deviation from unity is due to non-Gaussianity. It is clear that low frequency the built-up of temporal correlation that leads to long charge fluctuation relaxation time leads to non-Gaussian fluctuations. We take this as signature of entry into the glassy phase. However, at lower temperatures as the fluctuations freeze out kinetically the long term correlations also freezes out and the fluctuation again becomes Gaussian.

As we mentioned earlier that these types of PDF and second spectrum have been observed earlier by Kar *et al.* [70] in the insulating side of doped Si:P(B) predominantly below 10K. It is interesting that in a very different electronic system (the manganites) we see rather similar behaviour. The marked qualitative difference is that these type of behaviour in the oxides at much higher  $T$ . This is due to the much larger value of energy scales like  $\Delta_{CG}$ . The deviation of the second spectrum from white “Gaussian” kind indicates the correlated dynamics. We observed a shift of spectral weight towards low frequencies. It can be inferred that the onset of very slow correlated dynamics is strongly coupled to the transport process.

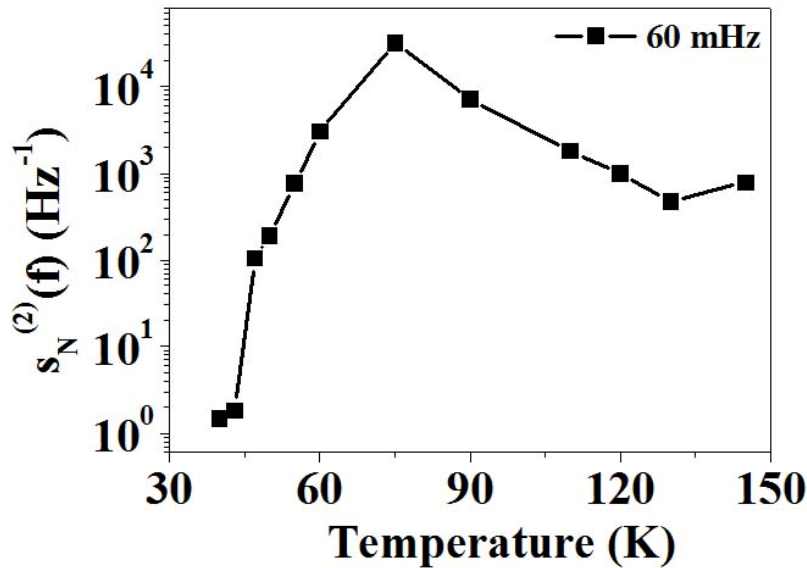


Figure 5.25: Plot of normalised second spectra  $S_N^{(2)}(f)$  as a function of temperature below  $T_{FMI}$  at frequency  $f \approx 60$  mHz.

#### 5.4.4 Power spectral density of resistance fluctuations

In this subsection we discuss the detailed power spectral content of the noise power, in particular its deviation from the  $1/f$  only dependence. We have studied the frequency dependent spectral power density for few representative temperatures, which encompass two transition regimes (around  $T_C$  and  $T_{FMI}$ ) are shown in Fig. 5.26(I.(a)) and (II.(b)). The data have been plotted as  $f.S_V(f)/V^2$  as a function of frequency in Fig. 5.26(I.(a) and (II(b)). We can see the spectral power is not purely  $1/f$  type. There are discrete frequency components that “ride” on the  $1/f$  broad back ground. These discrete frequency components seem to have contributions above 100 mHz.

We have fitted the spectral power at each temperature  $T$  by the following relation which consists of a  $1/f$  term and a Lorentzian term with a temperature dependent corner frequency  $f_C(T)$  [93],

$$\frac{S_V(f)}{V^2} = \frac{A(T)}{f^\alpha} + \frac{B(T)f_C(T)}{f^2 + f_C(T)^2}. \quad (5.19)$$

The temperature dependent  $A(T)$  and  $B(T)$  represent the weightage of two terms, i.e.,  $1/f$  and Lorentzian term respectively. We have fitted our experimental noise data using the equation 5.19 and the solid lines show the respective fitting curves at each temperature. We can clearly see the excellent arrangement with the above equation (equation 5.19). The fitted curves clearly show peaks with  $f_C$  at low frequencies.

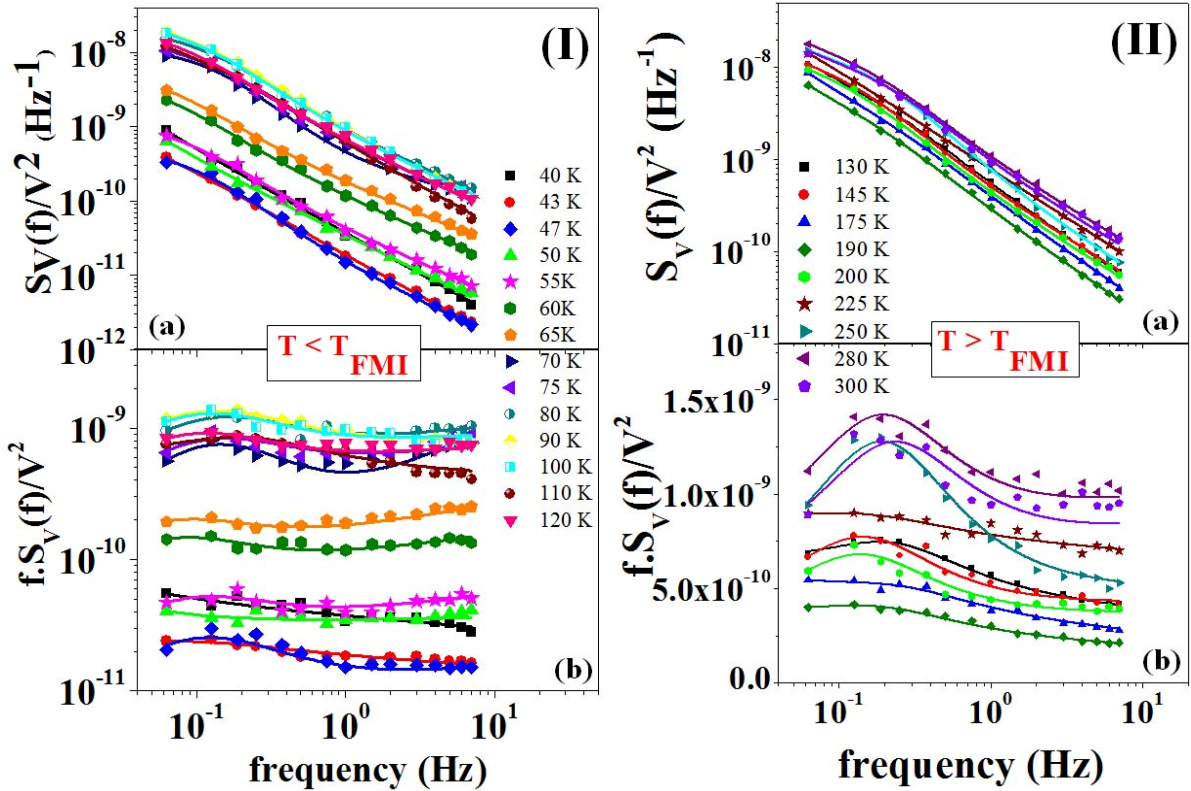


**Fig. 5.26:** The noise power spectra as a function of frequency at few representative temperatures in LCMO20 single crystal have been plotted in (I) and (II)  $T_{FMI}$  respectively. Two temperature regions have been separated considering the FMI region. In (I.(a)) and (II.(b)) we have plotted the raw power spectral density  $S_V(f)/V^2$  for  $T < T_{FMI}$  and  $T > T_{FMI}$  respectively. Corresponding  $f.S_V(f)/V^2$  as a function of frequency in two temperature regions have been plotted in (I.(b)) and (II.(b)). The solid lines show the fitting using equation 5.19.

In order to compare the relative resistive fluctuation  $\langle(\Delta R)^2\rangle/R^2$  by integrating  $S_V(f)/V^2$  within the experimental bandwidth  $f_{\min} \approx 60$  mHz and  $f_{\max} \approx 7$  Hz and using equation 5.20 we can write

$$\begin{aligned} \langle(\Delta R)^2\rangle/R^2 &= \int_{f_{\min}}^{f_{\max}} \frac{A}{f} df + \int_{f_{\min}}^{f_{\max}} \frac{Bf_C}{f^2 + f_C^2} df \\ &= \left[ \langle(\Delta R)^2\rangle/R^2 \right]_1 + \left[ \langle(\Delta R)^2\rangle/R^2 \right]_2 \end{aligned} \quad (5.20)$$

The temperature dependence of the total fluctuation  $\langle (\Delta R)^2 \rangle / R^2$  and the contribution of  $1/f$  component [ $\langle (\Delta R)^2 \rangle / R^2 ]_1$  and that of the Lorentzian [ $\langle (\Delta R)^2 \rangle / R^2 ]_2$  are shown in Fig. 5.27. It is clear that Lorentzian component contribution to the total noise is slightly higher in comparison with the component coming from  $1/f$  noise.

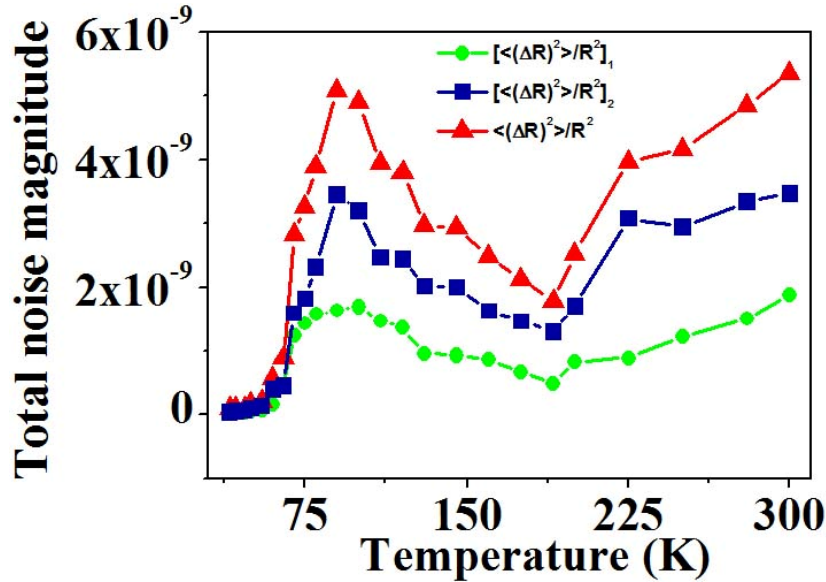


**Figure 5.27:** The temperature dependence of the total fluctuation  $\langle (\Delta R)^2 \rangle / R^2$  and the contribution of  $1/f$  component [ $\langle (\Delta R)^2 \rangle / R^2 ]_1$  and that of the Lorentzian [ $\langle (\Delta R)^2 \rangle / R^2 ]_2$ .

We have plotted the temperature dependent fitting parameters  $A(T)$ ,  $B(T)$ , relative weightages of Lorentzian component over  $1/f$  component  $B(T)/A(T)$ ,  $f_c$  and  $\alpha$  with error bars in Fig. 5.28(a), (b), (c), (d), and (e) respectively. The error bars are fitting errors. Here we shall discuss the results we plotted in Fig. 5.28 in three temperature regions separately. Our observations are as follows:

- (a)  $T < T_{FMI}$ : At lowest possible temperatures ( $< 60$  K), we found the weightage of  $A(T)$ ,  $B(T)$  are low compared to other  $T$  in this temperature range. But the magnitude of both noise increase sharply and reaches maximum value around 100 K and then started to decrease. The relative variation of  $B(T)$  over  $A(T)$  is relatively high below  $T_{FMI}$ . The corner frequencies  $f_c$ 's are lying above 75 mHz except at 40 K. In this region  $\alpha$  varies significantly from 0.85-1.2 having nontrivial temperature dependencies.
- (b)  $T_{FMI} < T < T_C$ : This region is metallic region sandwiched between two insulating regimes. There is a very little temperature dependencies were observed for  $A(T)$  and  $B(T)$ . They are nearly temperature independent. The values of  $f_c$  are lying high frequency regimes  $> 120$  mHz. It is also noted that the weightage of two kind of

fluctuations having nearly equal contributions to the spectral power. In this region  $\alpha$  varies within 1.0-1.1 showing well behaved  $1/f$  noise components in this region.

- (c)  $T \geq T_c$ : This regime is paramagnetic insulating region and at  $T_c$ ,  $\alpha$  reaches its maximum value 1.2. Otherwise,  $\alpha \approx 1.0$  for all other temperatures. It should be also noted that around two transition temperatures values of  $f_c$  are relatively high. Instead of this,  $f_c$  is quite independent of temperature for  $T > T_c$ . We observed nearly temperature independent nature of two weightage factors in this region.

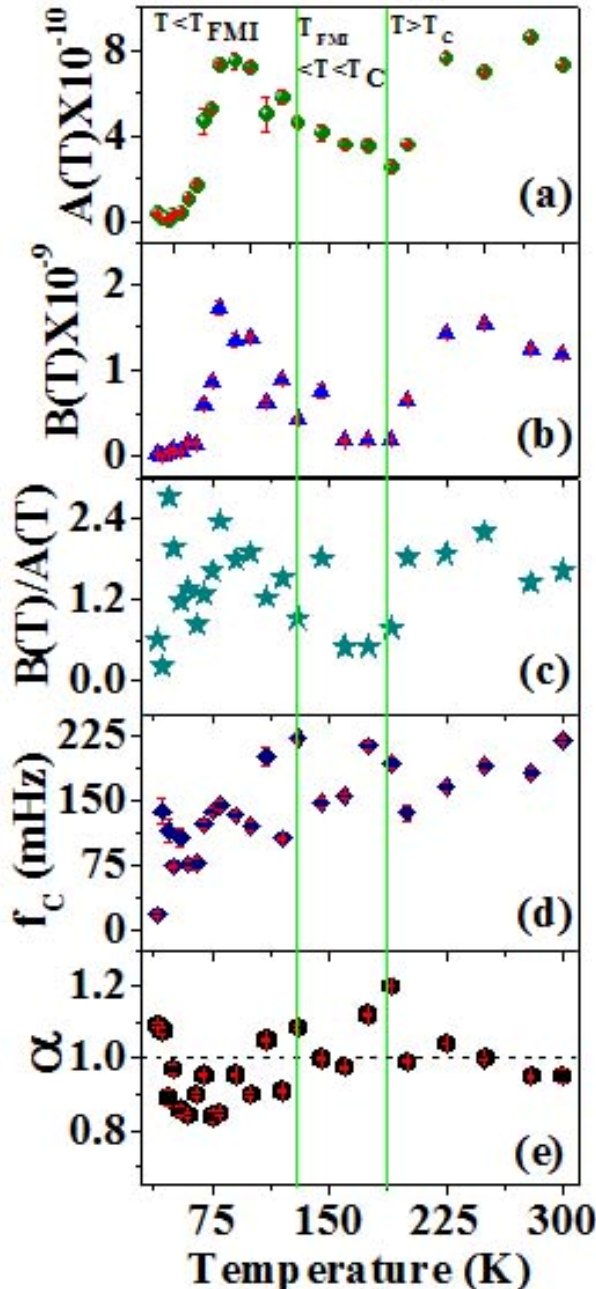


**Fig. 5.28:** The variation of fitting parameters (a)  $A(T)$ , (b)  $B(T)$ , (c)  $B(T)/A(T)$ , (d)  $f_c$  and (e)  $\alpha$  as a function of temperature encompassing three different temperature regimes:  $T < T_{FMI}$ ,  $T_{FMI} < T < T_c$ , and  $T \geq T_c$ . The error bars are also shown in respective graphs which are fitting errors.

These observed phenomena are very new and as per our knowledge this is the first report on noise spectroscopy investigated for LCMO20 in a wide temperature range at low frequency scale. The Lorentzian-type contribution to the power spectrum with a corner frequency  $f_c$  arises from the discrete fluctuators, which show random telegraphic noise (RTN) in the time series. The RTN-type time series generally shows that the fluctuators causing the resistance fluctuations are of two-level type. However, there may be a number of superimposed two-level fluctuators processes can be possible. Hence, discrete two-level process may not be clearly observable in the time series. We also found the time series of voltage fluctuation as a superimposition of large number of discrete fluctuators instead of discrete and distinct two-level processes. The average time scale for the two-level-fluctuators is related to the corner frequency  $f_c$  seen in the power spectrum by the relation  $\tau_c = 1/2\pi f_c$ . In our case,  $\tau_c$  is order of few seconds.

## 5.5 Investigation of hot-electron effect using non-linear resistance and “white” noise spectroscopy

It has been shown before that due to strong non-linear electrical conduction the electrical resistivity in the low doped manganites that show FMI state depends on the measuring current. The strong non-linear effects lead to reversible colossal Electroresistance. This colossal resistance effect that occurs in the FMI state below  $T_{FMI}$  is reversible and is distinct from resistive switching in oxides that show hysteresis and leads to memory effects even at room temperatures [94] which generally owe their origin to ionics. Existence of an insulating state that shows ES hopping with a finite Coulomb gap and a finite linear term in heat capacity raises a unique opportunity of hot electron-effects which may lead to strong non-linear conduction. It has been shown recently [2] that strong nonlinear electron transport in the ferromagnetic insulating state of manganites, can occur due to a hot electron effect. It was shown using a model that the temperature of the electron and lattice baths can decouple at high input power levels, leading to heating of the electron bath. Parameters of the hot electron effect model were independently determined via time dependence experiments and are in good agreement with the experimental values.

Effect of hot electron in disordered films (at low temperatures) has also been investigated very recently both experimentally and theoretically by Altshuler *et al.* [95]. In this part of the thesis we have investigated hot-electron effects in the FMI state using noise spectroscopy along with investigation of conventional non-linear conduction. The basic idea that we used here is that to have a measure of the electron temperature (which is expected to be larger than the lattice or phonon bath temperature,  $T_{ph}$ ) when the two baths decoupled by using the non-linear conductance or resistance data and have an estimate of the same temperature using the white noise when it equals the Nyquist noise  $S_{Nyquist} = 4k_B T_e R_{sample}$ , where  $R_{sample}$  is the sample resistance and  $T_e$  is the electron temperature. The use of the Nyquist noise to measure the electron temperature assumes that the electron bath forms a proper temperature bath in equilibrium. If there is large deviation of the observed broad band white noise from the simple estimate of  $4k_B T_e R_{sample}$  it may be concluded that the electron system is not in thermal equilibrium and it is not an ergodic system. The two measures of the electron temperature ( $T_e$ ) are going to be similar when the electron system can establish thermal equilibrium within itself but these two temperatures will differ when the electron system becomes non-ergodic (glassy state) and the Fluctuation-Dissipation theorem (FDT)

breaks down. It is noted that this is the first such work where these issues have been addressed to using this physical approach.

The investigation will be presented in two parts. In the first part we present the non-linear conductance/resistance data as measured by us and evaluate the electron temperature using the hot-electron model discussed by Jain *et al.* [1, 2]. In the next part we make the investigation of the white noise.

### 5.5.1 Hot electron effects and two separate temperature scales for electron and phonon baths

As has been made evident, the electrical conductance in the FMI state is unique in that it is activated below  $T_{FMI}$ , and yet the FMI state is not a conventional band or Mott-Hubbard insulating state that has a hard gap in the electronic density of states near the Fermi level  $E_F$ . As was shown in last section 5.1, low temperature heat capacity measurements of LCMO20 reveals the presence of a finite electronic contribution  $\gamma T$  to the heat capacity. This is consistent with the observation of ES-VRH range hopping conductance in the FMI state wherein exists a soft gap (Coulomb gap)  $\Delta_{CG}$  in the electronic density of states at the Fermi level  $N(E_F)$ . Thus, as was discussed earlier, the temperature dependence of the resistivity  $\rho$  follows ES-VRH conductance. Subsequently, we had seen (see the data in section 5.1.2) very strong non-linear conductance (NLC) effects in the FMI state and the consequent phenomena of ER and MR. Now, for systems in which the electrical conductance takes place via variable range hopping, such as is the case for LCMO20, the cause underlying the NLC can be the electric field that is present within the sample, or it can be caused due to another effect, such as an electron heating effect. For such systems, the electric field induced non-linear, i.e., non-Ohmic, effects manifest for values of electric field  $E$ , such that the following condition is satisfied:  $E \geq k_B T / e l_h$  [96, 97]. The maximum value of electric field  $E_{\max}$  developed during the present current bias measurement is much lower than the ratio  $k_B T / e l_h$ . It is therefore clear that the NLC as observed in the present samples is likely not electric field driven.

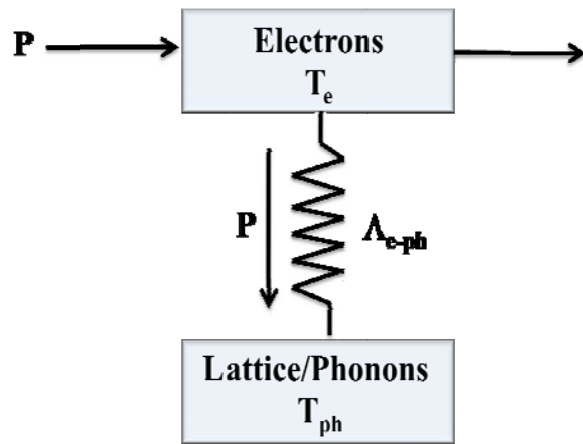


**Figure 5.29:** The schematic diagram of hot-electron model where  $T_e$  and  $T_{ph}$  are the electron and lattice/phonon temperatures respectively.  $\Lambda_{e-ph}$  represents the thermal conductance which couples the electron bath to the phonon bath. Adapted from reference [2].

When a source of electrical power, such as for instance a current or a voltage source is connected to a sample in which the electron-phonon thermal coupling is finite, then the applied electrical power is dissipated in the electron bath which, because the coupling between the electron and phonon baths is weak, can consequently be driven out of thermal equilibrium with the sample phonon bath. Under these conditions, the temperature of the electrons can increase above the temperature of the phonons, and the electrons are consequently referred to as “hot” electrons. In an insulating regime of temperature dependent resistance, this can then manifest as a NLC. In connection of this effect we want to mention that the temperature  $T$  which we record is known as bath temperature or phonon temperature  $T_{ph}$ . The data is taken at indicated fixed temperatures  $T_{ph}$ . The temperature has been qualified with the subscript “ph” in anticipation of a later discussion in this chapter, where we will argue that there exist two distinct temperature scales within a sample, one of the electrons  $T_e$ , and another of the phonons  $T_{ph}$ , and that the “temperature” referred to until now, represents the temperature of the phonons. We first discuss about the relevance of “hot” electron modelling and the origin of two separate temperature scales in the observed system.

We have modelled NLC effect observed in manganites by hot electron effects where exist two separate temperatures for electron and phonon/lattice baths. This effect has been demonstrated in metals [98-101], in semiconductors [102-105]. In metals, at room temperatures the hot electron effects are extremely small due to strong electron-phonon coupling at high temperatures but below 1 K one may see hot electron effects. Very recently Jain *et al.* [2] investigated the FMI state of manganites  $\text{La}_{0.82}\text{Ca}_{0.18}\text{MnO}_3$  systems and demonstrated the presence of two separate temperature scales in it. They inferred that in the FMI state, which they show is an insulator with a Coulomb gap, the temperature of the electron and lattice baths can decouple at high input power levels, leading to heating of the electron bath. We shall discuss our experimental data using the approach of Jain *et al.* [1, 2] and will make it more quantitative and will investigate new aspects like noise spectroscopy.

The simple hot-electron model [1, 2] has been chosen is shown in Fig. 5.29. Bias power is assumed to be dissipated in the electron system and distributed among the electrons involved in conduction to establish a temperature scale independent of the lattice phonon system. Thee authors proposed that the NLC effects in manganites arise due to heating of the electrons because of the presence of a thermal conductance  $\Lambda_{e-ph}$ , that is finite, between the electron bath and the phonon bath. In this situation the electron bath temperature  $T_e$  will get decoupled from that of the phonon bath  $T_{ph}$  when the input power  $P$  is large. Joule dissipation due to the flow of current will result in heating of only the electron bath. Consequently the temperature of the electron bath will rise above the temperature of the phonon bath, i.e., a temperature differential gets generated between the two baths. They have also shown that even at the lowest measured temperature, where the Joule dissipation is highest, the rise in the phonon temperature  $T_{ph}$  is not substantial [ $< 5 \text{ K}$ ] [90]. In the present model, the heat exchange happen through  $\Lambda_{e-ph}$  and can be expressed empirically as

$$\Lambda_{e-ph} = \Lambda_0 T^\alpha \quad (5.21)$$

where  $\Lambda_0$  and  $\alpha \geq 1$  are parameters. The sample sits very close to the bath and the model ignores the finite thermal resistance between the phonon bath and base. The base temperature has been taken equals to the base temperature. From the definition of thermal conductance one can write

$$\frac{dP}{dT} = \Lambda_0 T^\alpha \quad (5.22)$$

and for  $P$ , equation 5.22 is integrated between phonon temperature  $T_{ph}$  and electron temperature  $T_e$  as:

$$P = \int_{T_{ph}}^{T_e} \Lambda_0 T^\alpha dT \quad (5.23)$$

The working relation between  $T_e$ ,  $T_{ph}$ , and  $P$  can be expressed as:

$$T_e = \left( T_{ph}^{\alpha+1} + \frac{\alpha+1}{\Lambda_0} P \right)^{1/(\alpha+1)} \quad (5.24)$$

Using the equation 5.24 and equation 5.5 for resistivity we get the following equation of  $\rho$  as a function  $T_{ph}$  and  $P$  as

$$\rho = \rho_0 \sqrt{\left( T_{ph}^{\alpha+1} + \frac{1+\alpha}{\Lambda_0} P \right)^{1/(\alpha+1)}} \exp\left( \sqrt{T_0 \left( T_{ph}^{1+\alpha} + \frac{1+\alpha}{\Lambda_0} P \right)^{-1/(1+\alpha)}} \right). \quad (5.25)$$

The above model was applied by Jain and Raychaudhuri and they showed that  $\Lambda_{e-ph} = \Lambda_0 T^\alpha$  is a valid way to discuss the electron-phonon coupling and the parameters estimated from the model match with direct determination where a current has been pulsed into the system (i.e., energy has been pulsed) and the resulting relaxation of the electron temperature to an equilibrium value has been monitored.

### 5.5.2 Hot electron temperature estimated from the non-linear resistivity data

The model discussed above has been applied to the NLC data taken by us and the relevant parameters are evaluated. In the low power limit, the  $T_{ph}$  and  $T_e$  are necessarily very close to each other. One may thus obtain the parameters  $T_0$  and  $\rho_0$  by performing a temperature dependent resistance measurement at very low power levels. This data from such a measurement was presented earlier in section 5.1, where the values of  $T_0$  and  $\rho_0$  were obtained. Having thus fixed  $T_0$  and  $\rho_0$ , the hot electron model represented by equation 5.25 has only two free parameters now, namely  $\Lambda_0$  and  $\alpha$ . The NLC data shown in figures Fig. 5.16 to Fig. 5.18 in section 5.3 are now fitted to equation 5.25 using  $\Lambda_0$  and  $\alpha$  as two parameters to be evaluated from the fits to the experimental data.

Representative fits to this hot electron model for LCMO20 indicated  $T_{ph}$  are shown in 5.30 (red solid curve). We have fitted the NLC data for temperatures below  $T_{FMI}$ , this because the model fails to fit the NLC data above  $T_{FMI}$  (we used resistivity equation 5.25 which is applicable below  $T_{FMI}$  only). The value of  $\Lambda_0 = 1 \times 10^{-7} \text{ W/K}^2$  where  $\alpha = 1$ . We observed that even for the lowest possible temperatures we got reasonable fit to the data fitted curves. However, there is a power level above  $10^{-3}$  Watt where there are deviations. It is noted that at this power level and higher the whole sample heats up and  $T_{ph}$  becomes undefined. Thus we kept all fits below this level.

Given the simplicity of the model, we feel the model fits the data well. The simple model however, neglects few points. We have not considered the electronic inhomogeneity in the FMI state. Moreover, we assumed uniform power dissipation within the sample which is not true in case of manganites and strictly saying in the composition like LCMO20. The systems with metal-insulator phase transitions can have inhomogeneous conductivity which can lead to non-uniform power dissipation in the system. This non-uniformity can give an inhomogeneous distribution of  $T_e$ . The inhomogeneous electronic state is also envisaged in the model of Shenoy *et al.* [40].

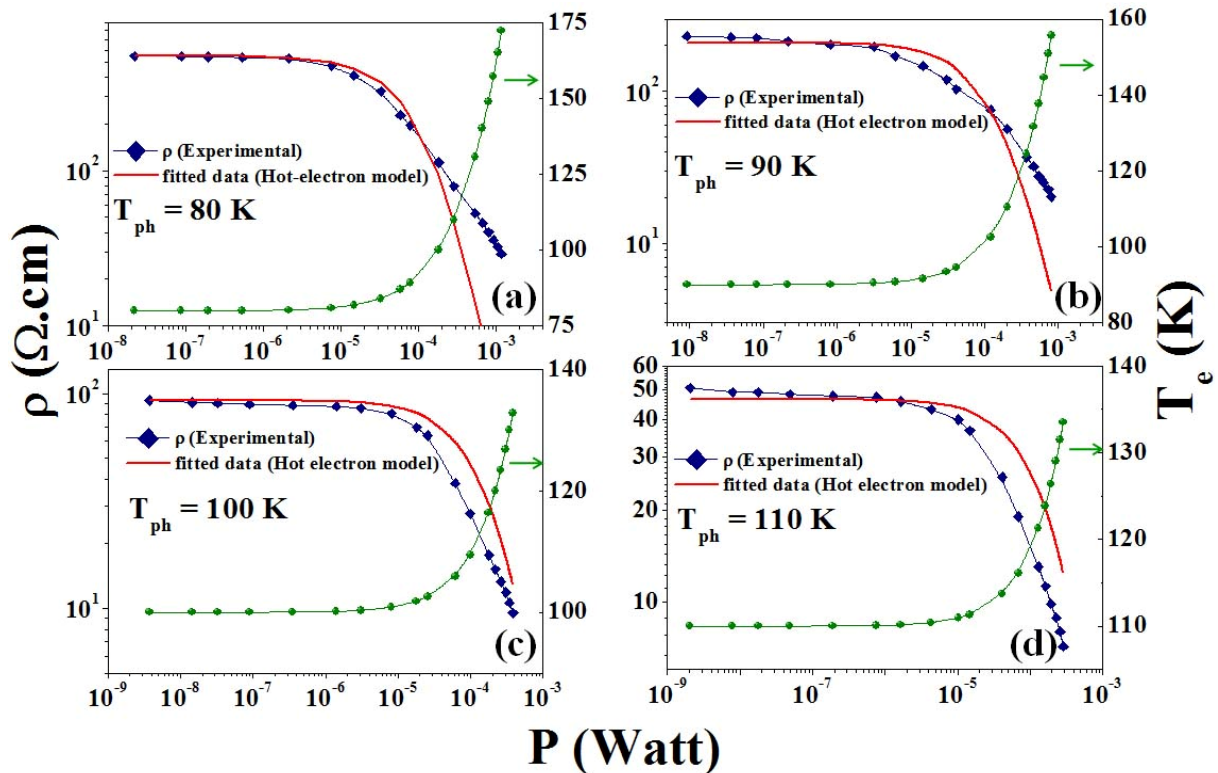


**Figure 5.30:** Left ordinate: experimentally observed variation of resistivity  $\rho$  as a function of power  $P$  for LCMO20, at indicated fixed phonon temperature  $T_{ph}$ . The respective fits to the hot electron model (see equation 5.25) are shown in red. Right ordinate: power dependence of electron temperature  $T_e$ , calculated as per equation 5.24, is shown in green. The fixed phonon temperatures at which the data was obtained are (a)  $T_{ph} = 80 \text{ K}$ , (b)  $T_{ph} = 90 \text{ K}$ , (c)  $T_{ph} = 100 \text{ K}$ , and (d)  $T_{ph} = 110 \text{ K}$ .

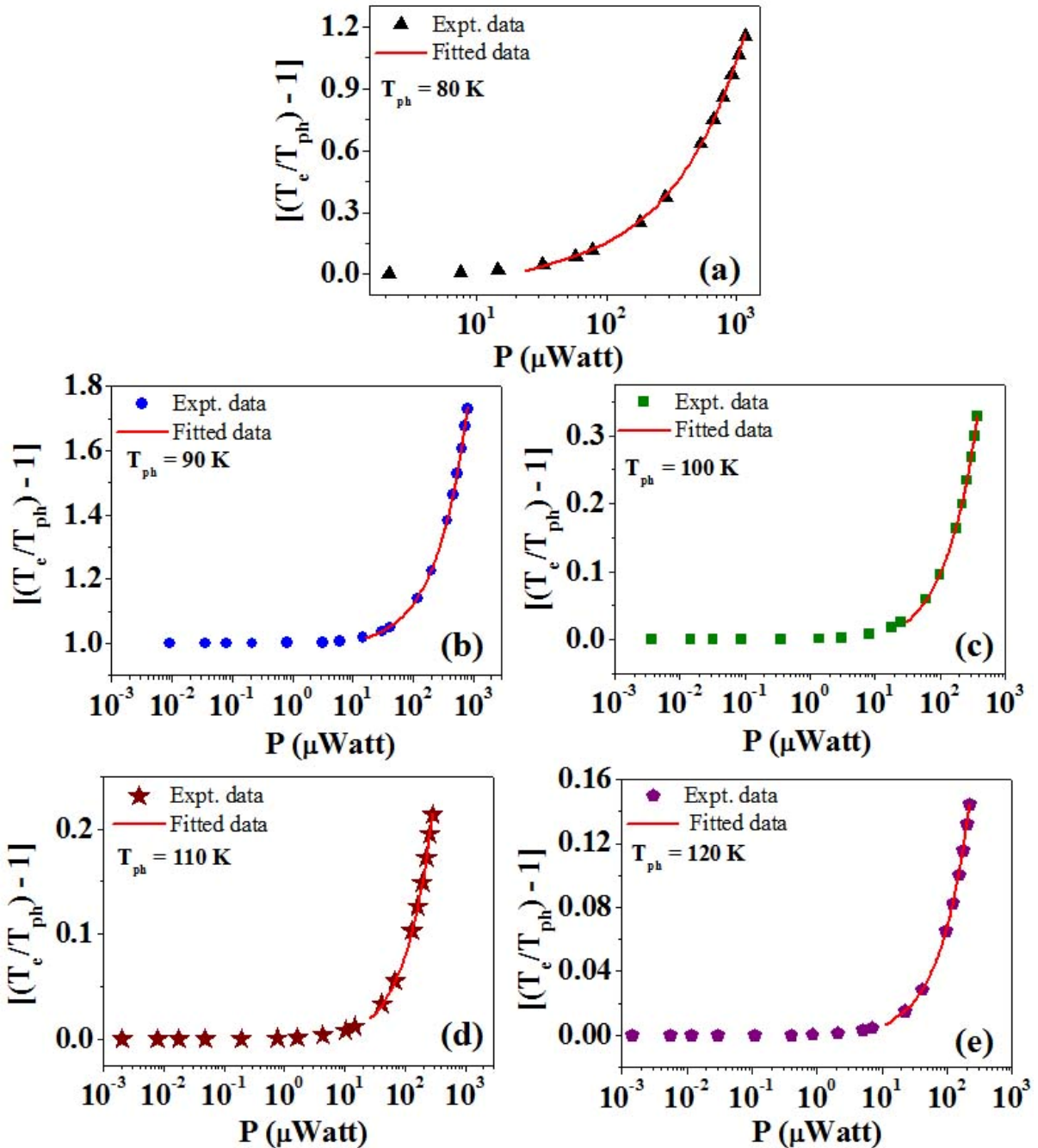


**Figure 5.31:** The ratio of  $(T_e / T_{ph} - 1)$  as a function of power  $P$  have been plotted as a function of input power for fixed phonon temperatures  $T_{ph}$ , i.e., (a) 80 K, (b) 90 K, (c) 100 K, and (d) 110 K. The data shows deviation of the electron temperature  $T_e$  from the lattice temperature  $T_{ph}$  that occurs beyond a threshold power  $P_c$ .

In Fig. 5.31 we plot the power dependence of the ratio  $T_e / T_{ph}$  as a function of the input power  $P$  for all  $T_{ph}$  (80-120 K). It can be seen that the ratio  $T_e / T_{ph} \approx 1$ , for low power and then at higher power it deviates. We find that there is indeed there is a threshold power

$P_c$  beyond which  $T_e$  becomes larger than  $T_{ph}$ . The threshold power  $P_c$  has been identified by fitting the quantity  $(T_e / T_{ph} - 1)$  to the empirical relation:

$$(T_e / T_{ph}) - 1 = (P - P_c)^{n_c}. \quad (5.26)$$

The fit to the above relation is also shown in Fig. 5.31 as lines. There is a variation of  $P_c$  and  $n_c$  with temperature. In Fig 5.32 we plot  $(T_e / T_{ph})$  as function of  $(P / P_c)$  to bring out that the empirical relation is followed at all  $T$  below  $T_{FMI}$ .

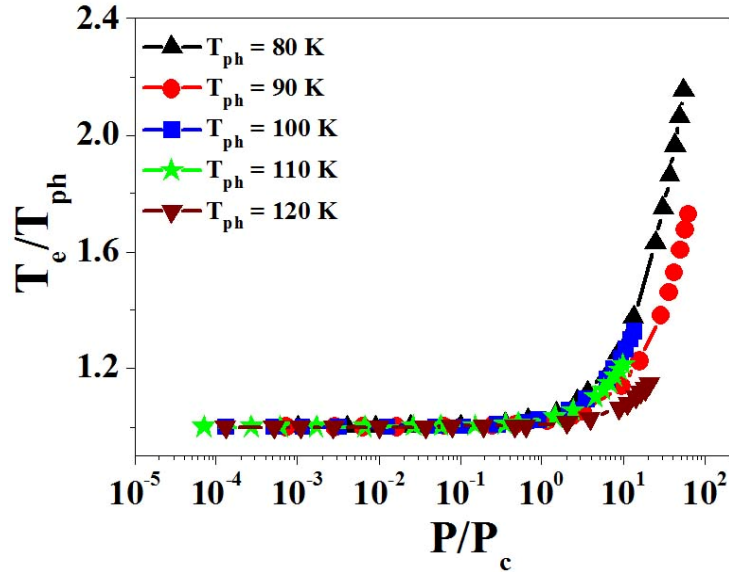


**Figure 5.32:** The plot of  $T_e / T_{ph}$  as a function of  $(P / P_c)$ . Each curve is for a fixed phonon temperature mentioned in the graph and all temperatures are considered below  $T_{FMI}$ .

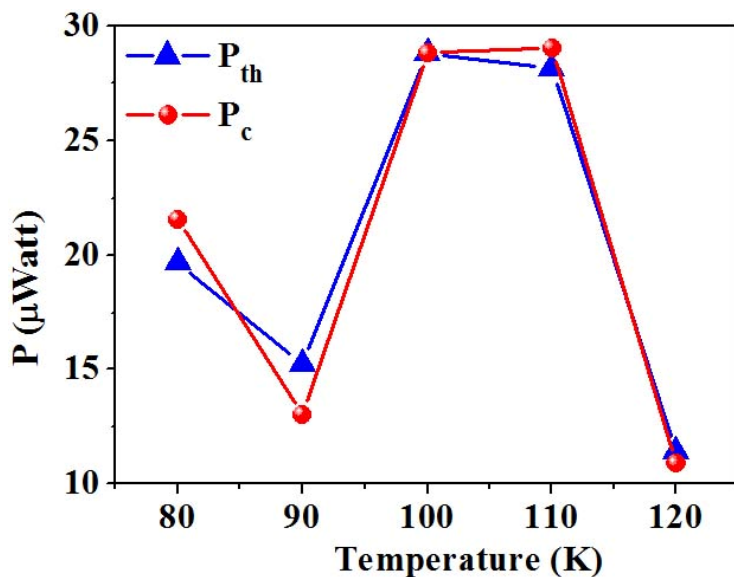


**Figure 5.33:** The plot showing the comparison between the threshold power ( $P_{th}$ ) for NLC and  $P_c$  (see text).

In Fig. 5.33 we show a comparison of  $P_h$ , the threshold power for severe non-linear conduction as discussed in section 5.1.2 and that of  $P_c$ , the power threshold for electron heating. It can be seen that in the temperature range below  $T_{FMI}$ , the on-set of substantial NLC coincides with electron heating. This is a reassertion of the hot-electron model in a much more quantitative way. We note that even above  $T_{FMI}$  and even above  $T_c$  in the polaronic insulator regime, there is non-linear conduction. However, the scope of the thesis is to restrict the investigation to the regime below  $T_{FMI}$  where is substantially larger.

### 5.5.3 The broad band white noise and its comparison to the electron temperature.

In this section we explore the crucial idea whether we can use the white noise to estimate the crucial electron temperature independently and compare it with that obtained from the NLC data in section 5.3. We recapitulate first some of the important aspects of the white noise, in particular the Nyquist Noise that are relevant to our discussions.

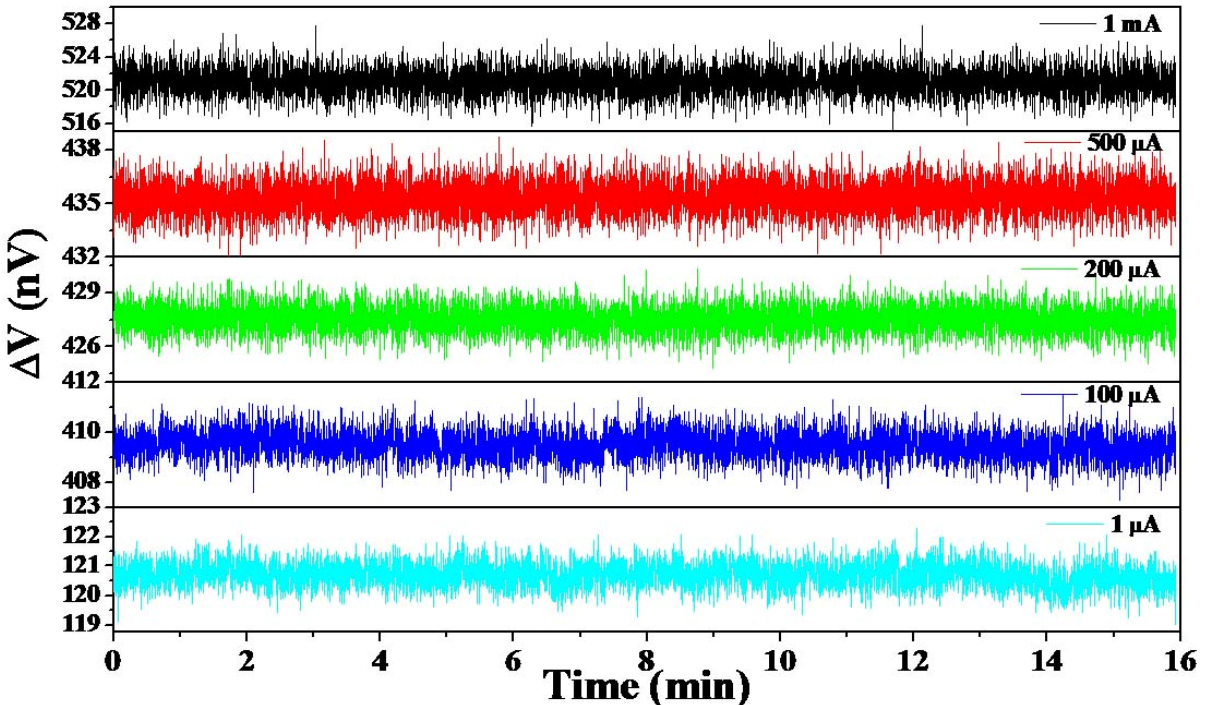


**Figure 5.34:** Typical WBN voltage fluctuation time series data at 80 K for few representative dc current biases.

Our noise spectroscopy set-up (as described in details in Chapter 3) allows us to measure the total noise (sample “excess noise” + background white noise (BWN)) and only the BWN simultaneously. The measured WBN is also a measure of sensitivity of the system to extraneous noise sources. One can always calibrate the set-up by measuring the BWN only using a standard resistor as all the parameters ( $R_{sample}, T$ ) are known. In this case the BWN should equal the Nyquist noise for a resistor  $R_{sample}$  at  $T$ . We have calibrated our system by measuring the BWN and comparing that with the expected Nyquist noise at a particular temperature and for a known resistance described in Chapter 3. The typical value of Nyquist

noise we achieved is  $2 \times 10^{-20}$  V<sup>2</sup>/Hz for a  $1\Omega$  resistor at 80 K and the voltage series demonstrates the efficiency of our measurement system (we reproduce Fig 3.25 here as Fig. 5.34 for quick reference.) In this section we investigate the temperature and dc current bias dependence of the BWN in the LCMO20 sample. Before discussing the results we want to discuss few relevant things for completeness of our measurements.

Nyquist-Johnson theory for voltage fluctuations (equilibrium fluctuations) follows from the fundamental Fluctuation-dissipation theorem [106]. The theorem has been further generalized by Callen and Welton [107] for generalized dissipation (e.g that arises from the radiation) so that one can have a general impedance as a dissipation element. This is in addition to the Joule heating type dissipation that occurs in a resistor. More recent developments using many body techniques show how the theorem can provide a measure of hot electron temperatures on semiconductor devices [108, 109]. The use of the Nyquist noise formula,  $S_{Nyquist} = 4k_B T_e R_{sample}$  and thus gives us a measure of the electron temperature  $T_e$ . It follows that the relation depends on the validity of the FDT, which assumes that electron system is an equilibrium bath. The temperature enters the Nyquist relation through the use of equipartition theorem. However, it may happen that the noise can have a white noise spectrum yet the temperature  $T_e$  obtained from the noise power may not represent an equilibrium temperature. We show that at high power input below the  $T_{FMI}$ , such a situation can arise. We will show that such a situation may be interpreted that the electron system being a glass, the electron bath is no longer an equilibrium system.

The experimental methodology for obtaining the BWN in presence of d.c bias is described below. The temperature is fixed at a particular bath temperature ( $T_{ph}$ ), the background noise which is a white noise has been measured. This can be easily separated from the excess noise that has  $1/f$  character. We have used ac five-probe noise measurement technique where we can collect the sample voltage fluctuations (*xpower*) and background voltage fluctuations (*ypower*) simultaneously. The *xpower* time series contains information about noise coming from sample as well from background. We can separate out sample noise completely by using Weiner filter (please see section 3.4.3.b). The *ypower* is completely uncorrelated with *xpower*, so we can measure background noise without any interference of *xpower*. The BWN in equilibrium situation (which indeed occurs in absence of d.c bias) is the Nyquist noise. Experimentally we varied the input dc power and measured the BWN. If we extract the power spectra from each of the time series we get a frequency independent power spectrum i.e., white spectrum. This is the BWN. At this point we test the system with a standard linear resistor that the BWN is not a function of the applied dc bias. This establishes that what we observe is not an artefact of the experimental system.

The data shows that BWN does not get enhanced due to the dc bias. The raw voltage time-series across the standard resistor for three bias currents have been shown in Fig. 5.35. We have estimated the power spectra from the above mentioned time series. Both results show that the spectral power is independent of the bias when measured on a standard linear resistor. The ratio  $\zeta \equiv \frac{BWN}{4k_B T_{ph} R_{sample}}$  in case of a resistor of resistance  $R_{sample}$  in thermal equilibrium with a thermal bath at temperature  $T_e / T_{ph}$  is close to 1. We find that in case of the standard linear resistor is indeed the case as shown in Fig. 5.36. Thus the measurement on the standard resistor thus establish what is expected of a standard resistor in thermal equilibrium and it establishes a bench mark for the ratio  $\zeta$ .

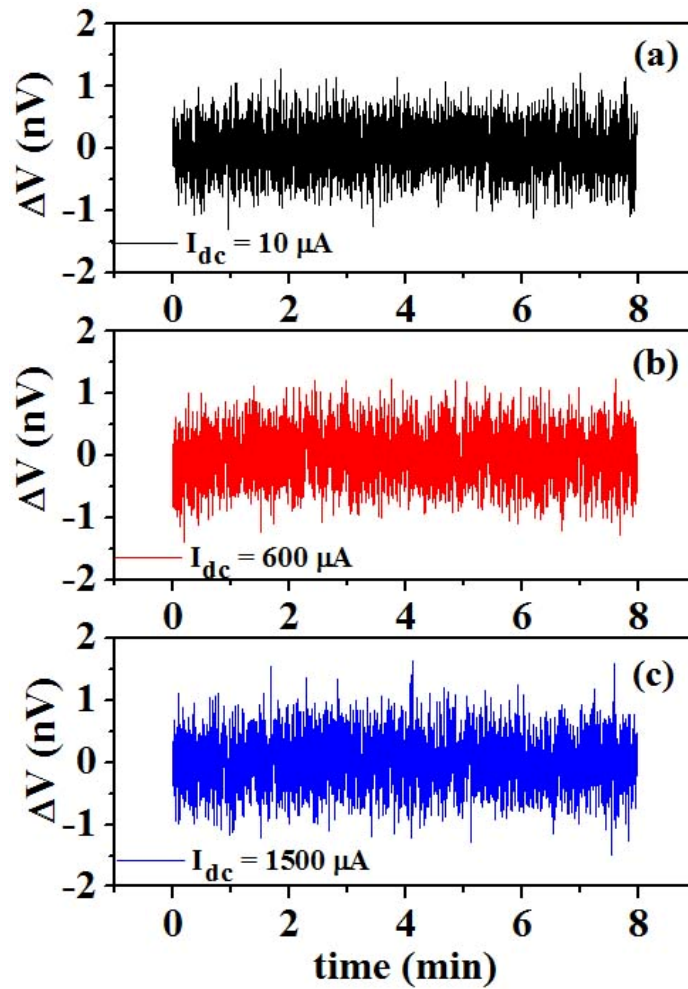


**Figure 5.35:** The raw time series of voltage fluctuations taken at three different dc current biases for a fixed resistor. The voltage fluctuation is  $\sim 2 \text{ nV}$ .

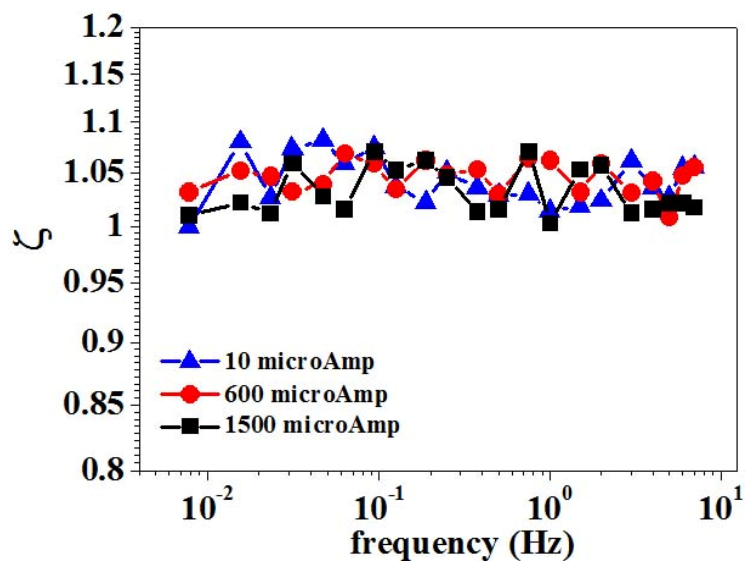


**Figure 5.36:** The frequency dependence of  $\zeta$  for a standard resistor for three representative dc bias currents. The data shows the power independent character of  $\zeta$  for the standard resistor. The value of  $\zeta = 1$  for all the current biases as we expected.

In contrast to the standard resistor we observed an increase of BWN in the insulating regimes of LCMO20 sample with the increase of biasing current, i.e., with the increase of power  $P$  (see Fig. 5.34). It is noted that our method of measuring the noise with a.c bias allows us to separate out the BWN from the  $1/f$  type “excess” noise. On application of a stressing current, the observed white nature of this noise remains unaltered but there is an enhancement of its magnitude. It can become quite high compared with its base value, when BWN is equal to the Nyquist noise where the  $T_e = T_{ph}$ . The enhancement of BWN noise we demonstrate the as observed voltage time-series data with increased current biases at 80 K (a temperature below  $T_{FMI}$ ) in Fig. 5.37. The time series itself shows that there is enhancement of the BWN when the power input is enhanced by enhancing the dc input.

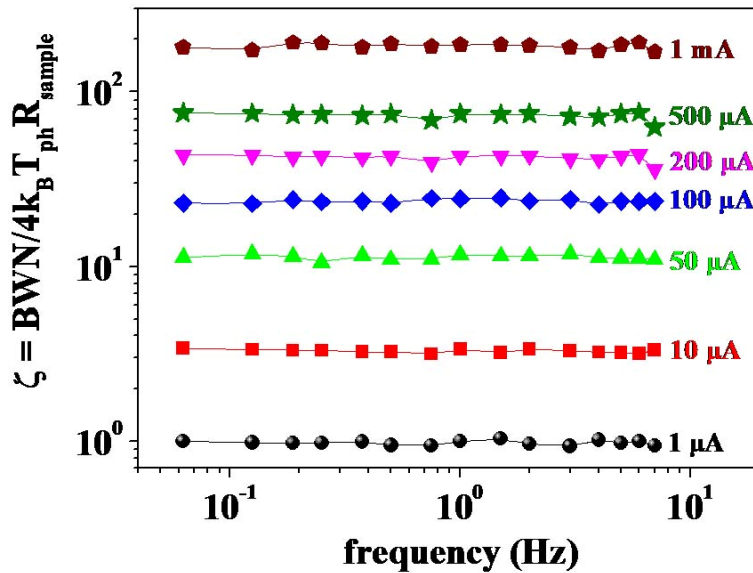


**Figure 5.37:** The plot of spectral decomposition of  $\zeta$  at  $T_{ph} = 80$  K at few representative dc current biases mentioned in the graph. The spectra have been extracted from the raw time series shown in Fig. 5.34. Note that current bias changes by order of magnitude from  $1\mu A$  to  $1mA$ .

If we extract the power spectra from each of the time series (as shown in Fig. 5.34) we get a frequency independent power spectrum BWN for given bias as shown in Fig. 5.37. We have plotted left ordinate as normalised fashion i.e.,  $BWN / 4k_B T_{ph} R_{sample}$  to provide a basis because both  $R_{sample}$  and  $T_e$  change significantly with current bias current due to non-linear conduction.. The normalizing factor  $S = 4k_B T_{ph} R_{sample}$  gives us a measure of the expected spectral power of the Nyquist noise when the electron and phonon systems are in equilibrium with each other and  $T_e = T_{ph}$ . The deviation of the ratio  $\zeta \equiv BWN / 4k_B T_{ph} R_{sample}$  would show how much the electron temperature  $T_e$  has deviated from the phonon temperature  $T_{ph}$  if the magnitude of the WBN can be taken as a measure of  $T_e$ . In equilibrium when the two systems are not decoupled, this should be ideally 1 which we observed (see Fig 5.35 and 5.36). We want to mention that at low bias ( $1\mu A$ ) the ratio  $\zeta$  is indeed unity as it should be. However, an applied bias raises the ratio and it can even be more than 100 with current bias of  $1\text{ mA}$  at 80 K. The frequency and current dependence of

normalized BWN at few representative temperatures (below  $T_{FMI}$ ) are shown in Fig. 5.38. The temperatures marked are the phonon temperatures  $T_{ph}$ .

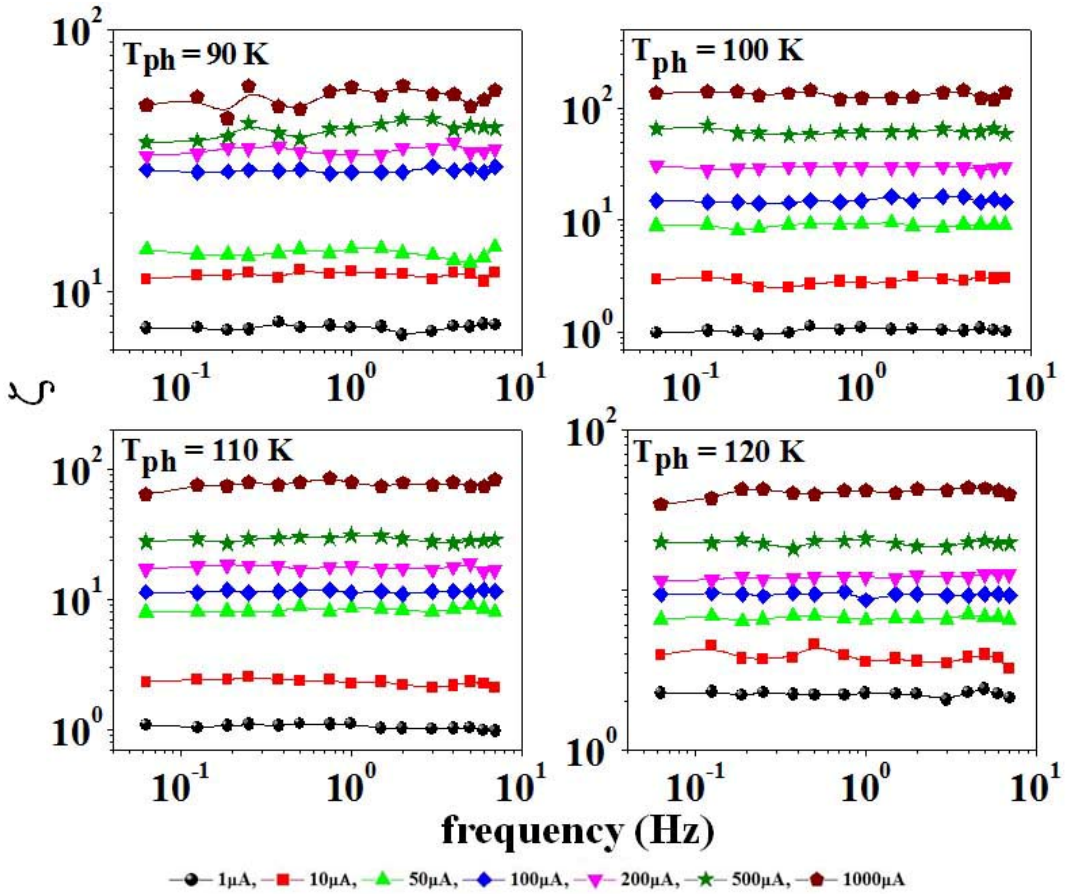


**Figure 5.38:** Plot of normalized white noise as a function of frequency at few representative temperatures below  $T_{FMI}$ . The temperatures marked in the respective graphs are phonon temperatures where the noise has been calculated. The dc current biases are also mentioned in the graph.

In Fig. 5.39 we plot the ratio  $\zeta \equiv \frac{BWN}{4k_B T_{ph} R_{sample}}$  as measured at different temperatures as function of the d.c power  $P$ . The power has been scaled by the  $P_c$  at a given temperature to bring the graphs to the same scale. This graph can be compared to figure XX where we plotted the ratio  $(T_e / T_{ph})$  as a function of  $(P / P_c)$ . The dependence of the ratio  $\zeta$  as function of  $(P / P_c)$  at all temperatures below  $T_{FMI}$  seem to fall on the same scaled graph. The enhancement as a function of  $(P / P_c)$  is also non-trivial and it appears to occur in stages. It can be seen that at low power, typically  $P \leq 10^{-3} P_c$ , the ratio  $\zeta$  like the ratio  $(T_e / T_{ph})$  is close to 1. This is the regime where one does not see any deviation from what is expected of a system in thermal equilibrium. However, at a somewhat larger power,  $\zeta$  begins to differ from 1 but for  $(P / P_c) \leq 10^{-1}$  the deviation is not large and  $\zeta \approx 2$ . However at larger power as the power  $P \rightarrow P_c$  and beyond there is substantial deviation of  $\zeta$  from unity and for  $(P / P_c) \approx 10^2$  it approaches a rather large value of 100.

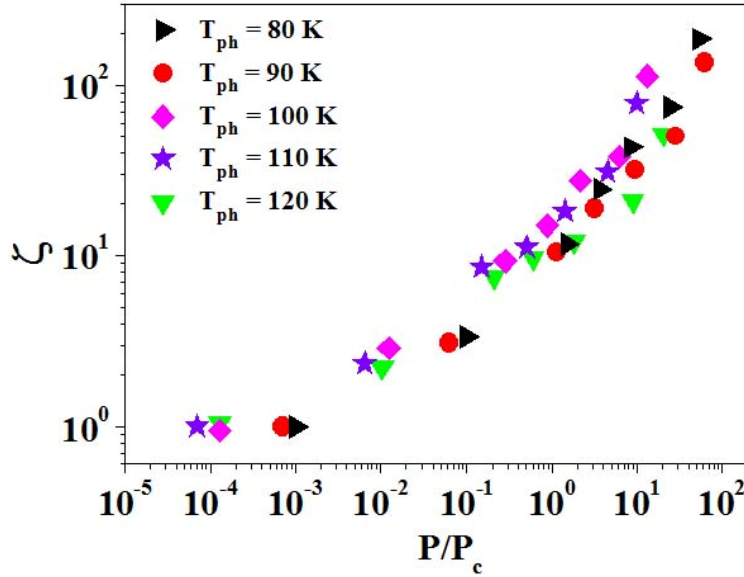


**Figure 5.39:** The variation of  $\zeta$  as a function of  $(P / P_c)$  for all  $T_{ph}$  below  $T_{FMI}$ .

It can be seen that substantial deviation of the ratio  $\zeta$  from unity occurs where the  $(T_e / T_{ph})$  starts to differ from 1 and we see large NLC. In this context we note that though large NLC sets in for  $P > P_c$  even for a lower power the transport is not truly linear. It has a mild non-linearity (see figures). It is worth noting that in then range of the low power when  $\zeta$  differs from unity and is  $\sim 2$ , the charge transport already is non-linear although much less prominent than that occurs for  $P > P_c$ .

The large deviation of the ratio  $\zeta$  from unity and also from the ratio  $(T_e / T_{ph})$ , points very clearly to the fact that the electronic system becomes a non-equilibrium system with application of rather low input power in the FMI state. We clearly see signature of break down of the Fluctuation-Dissipation Theorem (FDT) that would ensure that the ratio  $\zeta \approx 1$ , which indeed is the case at very low power. The break down of FDT at a reasonably small power can be interpreted as the case where the input of small power puts the electrons in a state of energy from which it does not have a simple path to relax to more equilibrium condition. This one would expect in a system that is kinetically frozen. This of violation of FDT in non-equilibrium systems like a glassy system has been a topic of considerable theoretical research in the field of non-equilibrium thermodynamics. In particular, it has been established that in systems, such as a glassy system the effective temperature can be considerably different from the equilibrium temperature and the effective temperature can slowly evolve over long time. In the particular electronic system studied by us, which undoubtedly gets into a situation which is far from equilibrium, the FDT will thus not be obeyed. Our observation thus would clearly point to the fact that the insulating state in this case is indeed a glassy phase.

There are certain other issues that need be pointed out. The ratio  $(T_e / T_{ph})$ , which we obtain from the non-linear conduction data using a simple hot electron model is well behaved that the ratio is not unphysically large unless the ratio  $\zeta$  which even for a low power is much larger. Ideally, if the electronic system (the electronic system as a thermal bath) would have maintained internal equilibrium then even under electron heating one would expect  $\zeta \sim (T_e / T_{ph})$ . The fact that even for a large  $\zeta$  we can find a reasonable value of  $T_e$  from the

NLC data is interesting. It appears that the electrons that are taking part from the conduction process (e.g, those with energy close to the chemical potential) are in equilibrium among themselves that an effective  $T_e$  can be defined even in presence of electron heating. The BWN on the other hand gets its contribution from all electrons. Thus it may happen that the large BWN is originating from that part of the electronic spectrum that is not close to the chemical potential. Thus the process of relaxation separates the fast electrons close to the chemical potential from those away from it which have long relaxation time.

It will be interesting to carry out these investigations in the polaronic insulating regime above  $T_c$ , our preliminary investigation using the tool of noise spectroscopy shows that such issues as described above may also be relevant in that state in a general way.

## 5.6 Conclusions

To summarize, we have a detailed investigation of the Ferromagnetic insulating state of manganites using noise spectroscopy. This is the first extensive investigation of the FMI state of manganites using the tool of noise spectroscopy which as we have seen addresses a number of new questions.

- (a) The FMI state is caused by electron localization due to long range Coulomb interaction, i.e., that the charge transport is of the Efros-Shklovskii-variable range hopping (ES-VRH) type, we had obtained the value of the Coulomb-gap  $\Delta_{CG}$ . The coulomb gap in the FMI state is large  $\sim 152$  meV. The  $\Delta_{CG}$  sets the temperature scale for the manifestation of the hot electron effects to  $\sim 10^1\text{-}10^2$  K.
- (b) In addition to noise spectroscopy we have investigated the resistivity and non-linear conduction in the ferromagnetic insulating (FMI) state. We have used a model of hot electron model to explain the NLC observed and quantified the electron temperature as the electron bath is heated.
- (c) Using the noise spectroscopy we have investigated the slow and glassy dynamics of FMI state and in particular from the temperature dependent power spectral identified a freezing temperature. We have also identified that the freezing process is kinetically governed with the time scale determined by an activation energy that is similar to the Coulomb gap which we determined from the transport data. Some of the other important noteworthy points are:

## Bibliography:

- [1] Himanshu Jain, Ph.D Thesis, Indian Institute of Science, Bangalore, India (2008).
- [2] Himanshu Jain, and A. K. Raychaudhuri, Appl. Phys. Lett. **93**, 182110 (2008).
- [3] C. Herring, in *Magnetism*, edited by J. Rado and H. Suhl (Academic, New York, 1965), Vol. 2.
- [4] C. Zener, Phys. Rev. **82**, 403 (1951).
- [5] Q. Li, J. Zang, A. R. Bishop, and C. M. Soukoulis, Phys. Rev. B **56**, 4541 (1997).
- [6] Z. Sun et al., Nature (London) **3**, 248 (2007).
- [7] A. J. Millis, P. B. Littlewood, and B. I. Shraiman, Phys. Rev. Lett. **74**, 5144 (1995); A. J. Millis, R. Mueller, and B. I. Shraiman, Phys. Rev. B **54**, 5405 (1996).
- [8] M. Uehara, B. Kim, and S.-W. Cheong (2000), personal communication.
- [9] B. B. Van Aken, A. Meetsma, Y. Tomioka, Y. Tokura, and Thomas T. M. Palstra, arXiv:cond-mat/0204103v1 [cond-mat.mtrl-sci] 4 Apr 2002.
- [10] Y. Tokura and N. Nagaosa, Science **288**, 462 (2000).
- [11] E. Dagotto et al., Phys. Rep. **344**, 1 (2001).
- [12] T. Mizokawa et al., Phys. Rev. B **61**, R3776 (2000).
- [13] Y. Endoh et al., Phys. Rev. Lett. **82**, 4328 (1999).
- [14] Y. Yamada et al., Phys. Rev. Lett. **77**, 904 (1996).
- [15] G. Biotteau et al., Phys. Rev. B **64**, 104421 (2001).
- [16] G. Papavassiliou, M. Fardis, M. Belesi, T. G. Maris, G. Kallias, M. Pissas, D. Niarchos, C. Dimitropoulos, and J. Dolinsek, Phys. Rev. Lett. **84**, 761 (2000).
- [17] V. Markovich et al., Phys. Rev. B **66**, 094409 (2002).
- [18] T. Mizokawa, D. I. Khomskii, and G. A. Sawatzky, Phys. Rev. B **63**, 024403 (2000).
- [19] P. Dai et al., Phys. Rev. Lett. **85**, 2553 (2000).
- [20] A. J. Millis *et al.*, Phys. Rev. Lett. **77**, 175 (1996)
- [21] H. Röder *et al.*, *ibid.* **76**, 1356 (1996)
- [22] A. S. Alexandrov and A. M. Bratkovsky, *ibid.* **82**, 141 (1999).
- [23] Y. Yamada *et al.*, Phys. Rev. Lett. **77**, 904 (1996).
- [24] Y. Endoh *et al.*, Phys. Rev. Lett. **82**, 4328 (1999).
- [25] H. Kawano *et al.*, Phys. Rev. B **53**, R14 709 (1996).
- [26] G. Papavassiliou, M. Belesi, M. Fardis, M. Pissas, J. Dolinsek, C. Dimitropoulos, J. P. Ansermet, ArXiv:cond-mat/0210422v2 [cond-mat.str-el] 21 Oct 2002
- [27] R. Laiho, E. Lahderanta, J. Salminen, K. G. Lisunov, and V. S. Zakhvalinskii, Phys. Rev. B **63**, 094405 (2001).
- [28] G. Allodi, M. C. Guidi, R. De Renzi, A. Ganeiro, and L. Pinsard, Phys. Rev. Lett. **87**, 127206 (2001).
- [29] Chang Seop Hong, Wan Seop Kim, and Nam Hwi Hur Phys. Rev. B **63**, 092504 (2001).
- [30] T. Okuda, Y. Tomioka, A. Asmitsu, and Y. Tokura, Phys. Rev. B **61**, 8009 (2000).
- [31] Y. Tokura and N. Nagaosa, Science **288**, 462 (2000).
- [32] V. Markovich, I. Fita, R. Puzniak, M. I. Tsindlekht, A. Wisniewski, and G. Gorodetsky, Phys. Rev. B **66**, 094409 (2002)
- [33] M. M. Savosta, V. I. Kamenev, and V. A. Borodin, arXiv:cond-mat/0208033v1 [cond-mat.str-el] 2 Aug 2002.
- [34] J. S. Zhou and J. B. Goodenough, Phys. Rev. B **62**, 3834 (2000).
- [35] T. V. Ramakrishnan, H. R. Krishnamurthy, S. R. Hassan, and G. V. Pai, Phys. Rev. Lett. **92**, 157203 (2004).
- [36] K. F. Wang et al., Appl. Phys. Lett. **89**, 222505 (2006).
- [37] K. F. Wang et al., Phys. Rev. B **73**, 134411 (2006).

- [38] A. Maignan, C. Martin, G. V. Tendeloo, M. Hervieu, and B. Raveau, Phys. Rev. B **60**, 15214 (1999).
- [39] J. A. Souza and R. F. Jardim, Phys. Rev. B **71**, 054404 (2005).
- [40] V. B. Shenoy, T. Gupta, H. R. Krishnamurthy, and T. V. Ramakrishnan, Phys. Rev. Lett. **98**, 097201 (2007).
- [41] G.V. Pai *et al.*, Europhys. Lett. **64**, 696 (2003); T.V. Ramakrishnan *et al.*, Phys. Rev. Lett. **92**, 157203 (2004); J. K. Freericks and V. Zlatić, Rev. Mod. Phys. **75**, 1333 (2003); J. K. Freericks *et al.*, Phys. Rev. Lett. **88**, 106401(2002).
- [42] A. L. Efros and B. I. Shklovskii, J. Phys. C **8**, L49 (1975).
- [43] S. D. Baranovskii *et al.*, J. Phys. C **12**, 1023 (1979).
- [44] J. H. Davies *et al.*, Phys. Rev. B **29**, 4260 (1984).
- [45] T. Vojta and M. Schreiber, Philos. Mag. B **81**, 1117 (2001).
- [46] J. A. Mydosh, Spin Glasses: An Experimental Introduction, 1 ed. (Taylor & Francis, London, 1993).
- [47] G. J. Snyder, R. Hiskes, S. DiCarolis, M. R. Beasley, and T. H. Geballe, Phys. Rev. B **53**, 14434 (1996).
- [48] M. Zeise and C. Srinitiwarawong, Phys. Rev. B **58**, 11519 (1998).
- [49] N. F. Mott, Conduction in Non-Crystalline Materials, 2 ed. (Clarendon Press, Oxford, 1993).
- [50] V. Ambegaokar, B. I. Halperin, and J. S. Langer, Phys. Rev. B **4**, 2612 (1971).
- [51] J. M. D. Coey, Philos. Trans. R. Soc. London **356**, 1519 (1998).
- [52] B. I. Shklovskii and A. L. Efros, *Electronic Properties of Doped Semiconductors* (Springer-Verlag, Berlin, 1984).
- [53] G. N. Banerjee, Electronic Conduction in Metallic Perovskite Oxides, PhD thesis, Indian Institute of Science, Bangalore, 1998.
- [54] M. Viret, L. Ranno, and J. M. D. Coey, Phys. Rev. B **85**, 8067 (1997).
- [55] J. L. Cohn, M. Peterca, and J. J. Neuimeier, arXiv: cond-mat/0410657v1 [cond-mat.str-e1] 26 Oct 2004.
- [56] X. J. Chen, C. L. Zhang, J. S. Gardner, J. L. Sarrao, and C. C. Almasan, Phys. Rev. B **68**, 064405 (2003).
- [57] J. J. Hamilton, E. L. Keatley, H. L. Ju, A. K. Raychaudhuri, V. N. Smolyaninova, and R. L. Greene, Phys. Rev. B **21**, 14926 (1996).
- [58] M. Pollak, Discuss. Faraday Soc. **50**, 13 (1970).
- [59] Vinay Ambegaokar, B. I. Halperin, and J. S. Langer, Phys. Rev. B **8**, 2612 (1971).
- [60] A. L. Efros, N. Van Lien, and B. I. Shklovskii, J. Phys. C **12**, 1869 (1979)
- [61] J. H. Davis, P. A. Lee, and T. M. Rice, Phys. Rev. B **8**, 4260 (1984).
- [62] A. L. Efros, J. Phys. C **9**, 2021 (1976)
- [63] S. D. Baranovskii, A. L. Efros, B. L. Gelmont, and B. I. Shklovskii, J. Phys. C **12**, 1023 (1979).
- [64] B. I. Shklovskii, and A. L. Efros, Fiz. Tech. Poluprovodn **14**, 825 (1980) [Sov. Phys.-Semicond. **14**, 487 (1980)]
- [65] S. D. Baranovskii, B. I. Shklovskii, and A. L. Efros, Sov. Phys. -JETP **51**, 199 (1980)
- [66] T. Kurosawa and H. Sugimoto, Prog. Theor. Phys. **57**, 217 (1975).
- [67] Vikas Malik and Deepak Kumar, J. Phys. Ondens. Matter **15**, 5451 (2003)
- [68] M. Kirkengen and J. Bergli, Phys. Rev. B **79**, 075205 (2009)
- [69] Z. Ovadyahu, Phys. Rev. B **73**, 214208 (2006).
- [70] S. Kar, A. K. Raychaudhuri, A. Ghosh, H. v. Löhneysen, and G. Weiss, Phys. Rev. Lett. **91**, 216603 (2003).
- [71] J. Jaroszyński, D. Popović, and T. M. Klapwijk, Phys. Rev. Lett. **89**, 276401 (2002)

- [72] M. Mochena and M. Pollak, Phys. Rev. Lett. **67**, 109 (1991); M. Mochena and M. Pollak, J. Non-Cryst. Solids **131–133**, 1260 (1991); M. Mochena, M. Pollak, J. Ruiz, and M. Ortuño, Physica A **201**, 178 (1993).
- [73] Glatz *et al.* Phys. Rev. Lett. **98**, 196401 (2007)
- [74] O. Cohen and Z. Ovadyahu, Phys. Rev. B **50**, 10 442 (1994).
- [75] S-I. Han, R. Almy, E. Apodaca, W. Bergmann, S. Deiker, A. Lesser, D. McCammon, K. Rawlins, R. L. Kelley, S. H. Moseley, F. S. Porter, C. K. Stahle, and A. E. Szymkowiak, in *EUV, X-ray, and Gamma-Ray Instrumentation for Astronomy IX*, edited by O. H. Seigmund and M. A. Gummin; Proc. SPIE **3445**, 660 (1998);
- [76] V.Ya. Pokrovskii, A.K. Savchenko, W.R. Tribe, and E.H. Linfield, Phys. Rev. B **64**, 201318 (2001).
- [77] R. F. Voss, J. Phys. C **11**, L923 (1978)
- [78] J. G. Massey and M. Lee, Phys. Rev. Lett. **79**, 3986 (1997);
- [79] D. McCammon, M. Galeazzi, D. Liu, W.T. Sanders, P. Tan, K.R. Boyce, R. Brekosky, J.D. Gygax, R. Kelley, D.B. Mott, F.S. Porter, C.K. Stahle, C.M. Stahle, and A.E. Szymkowiak, Phys. Status Solidi B **230**, 197 (2002).
- [80] Swastik Kar, A. K. Raychaudhuri, and Arindam Ghosh, Phys. Rev. Lett. **21**, 216603 (2003)
- [81] D. Monroe *et al.*, Phys. Rev. Lett. **59**, 1148 (1987);
- [82] J. G. Massey and M. Lee, Phys. Rev. Lett. **75**, 4266 (1995); Phys. Rev. Lett. **77**, 3399 (1996).
- [83] Sh. Kogan, Phys. Rev. B **57**, 9736 (1998).
- [84] B.I. Shklovskii, Solid State Commun. **33**, 273 (1980).
- [85] Sh. M. Kogan and B.I. Shklovskii, Fiz. Tekhn. Poluprovodn **15**, 1049 (1981) [Sov. Phys. Semicond. **15**, 605 (1981)].
- [86] A. L. McWhorter, in *Semiconductor surface Physics*, edited by R. H. Kingston (University of Philadelphia Press, Philadelphia, PA, 1957), pp. 207–228.
- [87] B. I. Shklovskii, Phys. Rev. B **67**, 045201 (2003).
- [88] X. D. Wu, B. Dolgin, G. Jung, V. Markovich, Y. Yuzhelevski, and Ya. M. Mukovskii, Appl. Phys. Lett. **90**, 242110 (2007)
- [89] Aveek Bid, Ayan Guha, and A. K. Raychaudhuri, Phys Rev. B **67**, 174415 (2003)
- [90] Himanshu Jain, A. K. Raychaudhuri, Nilotpal Ghosh, and H. L. Bhatt, Appl. Phys. Lett. **89**, 152116 (2006).
- [91] K. Shtengel and C. C. Yu, Phys. Rev. B **67**, 165106 (2003); C. C. Yu, phys. stat. sol. (c) **1**, No. 1, 25-28 (2004).
- [92] P. J. Restle *et al.* Phys. Rev. B **31**, 2254 (1985); G. T. Seider and S. A. Solin, Phys. Rev. B **53**, 9753 (1996).
- [93] Sudeshna Samanta, A. K. Raychaudhuri, and Joy Mitra, Phys. Rev. B **78**, 014427 (2008).
- [94] R. Waser M. Aono, Nat. Mat. **6**, 833 (2007).
- [95] B. L. Altshuler, V. E. Kravstov, I. V. Lerner, I. L. Aleiner, Phys. Rev. Lett. **102**, 176803 (2009).
- [96] H. Fritzsch, editor “*Transport, Correlations and Structural Defects*” (World Scientific, Singapore, 1990).
- [97] S. Marianer, and B. I. Shklovskii, Phys. Rev. B **46**, 13100 (1992).
- [98] K. V. Maslov and V. A. Shklovskii, Sov. Phys. JETP **51**, 617 (1980).
- [99] V. A. Shklovskii, J. Low Temp. Phys. **41**, 375 (1980).
- [100] F. C. Wellstood, C. Urbina, and J. Clarke, Phys. Rev. B **49**, 5942 (1994).
- [101] K. Johnson, M. N. Wybourne, and N. Perrin, Phys. Rev. B **50**, 2035 (1994).
- [102] M. Galeazzi et al., Phys. Rev. B **76**, 155207 (2007).

- [103] M. E. Gershenson, Y. B. Khavin, B. Reuter, P. Schafmeister, and A. D. Wieck, Phys. Rev. Lett. **85**, 1718 (2000).
- [104] I. Zutic, J. Fabian, and S. D. Sharma, Rev. Mod. Phys. **76**, 323 (2004).
- [105] S. M. Sze, Physics of Semiconductors (Wiley–Interscience, New York, 1981).
- [106] H. Nyquist, Phys. Rev. **32**, 110 (1928).
- [107] H. B. Callen, and T. A. Welton, Phys. Rev. **83**, 34 (1951).
- [108] M. Max, Phys. Rev. **109**, 1921 (1958).
- [109] F. Green, Phys. Rev. B **54**, 4394 (1996).

# Chapter 6

## Study of low frequency resistance fluctuations in magnetic nanowires

### 6.1 Introduction

In the previous two chapters our focus has been on studying two types of manganites, on an oriented film of ferromagnetic metallic manganite  $\text{La}_{0.67}\text{Ca}_{0.33}\text{MnO}_3$  (LCMO,  $x = 0.33$ ) and single crystal ferromagnetic insulator  $\text{La}_{0.80}\text{Ca}_{0.20}\text{MnO}_3$  (LCMO,  $x = 0.20$ ). The scope of investigation in the first sample was to look for the contribution to 1/f noise by magnetic excitation, while in the second sample the scope was to look into charge fluctuations in the ferromagnetic insulating state. In general, the “excess” noise that gives rise to the celebrated 1/f noise arise in films and polycrystalline samples predominantly from structural defects and noise from other origins like magnetic and charge fluctuations get buried under the noise from structural origin. In case of the oriented film of  $\text{La}_{0.67}\text{Ca}_{0.33}\text{MnO}_3$  the quenched disorder with high activation energy led to extremely small noise from structural origin so that noise from magnetization fluctuations can be studied. In case of the FMI sample, the single crystalline nature of the sample led to low noise from structural origin and we did observe the noise from charge fluctuation. (Note: In this sample also in the range  $T_{\text{FMI}} < T < T_C$  there may a small contribution from ferromagnetic spins as in the LCMO,  $x = 0.33$  sample. However, in this sample charge fluctuation predominates). It is thus clear that high quality samples are needed to observe the types of noise that have been investigated in this thesis. In this chapter though not directly connected to the manganites we have investigated another magnetic system namely Ni nanowire to study the excess noise due to magnetic origin. The motivations for studying Ni nanowires as part of the thesis problem are two-fold:

- (a) The challenge of growing yet another material whose excess noise due to structural origin can be suppressed so that magnetic noise can be studied.
- (b) To investigate the resistance fluctuation in a material where the resistance fluctuation though magnetic is more subtle that it arises from the domain wall resistance with fluctuations controlled by magnetic reversal.

High quality single crystalline nanowires of Ni have been grown in our laboratory by Mr. Venkata Kamalakar inside porous alumina templates using the method of electrodeposition [1]. The high structural quality and single crystalline nature of the wires, tempted us to investigate whether the materials indeed has low enough noise due to structural origin so that magnetic noise can be investigated.

The resistance fluctuation in ferromagnetic materials can couple to the magnetization fluctuation through the mechanism of magnetoresistance where it is substantial in manganites. The relation of the resistance fluctuation to the magnetization fluctuation is linked by the relation:

$$\frac{\langle (\Delta R)^2 \rangle}{R^2} = \xi \left( \frac{1}{R} \frac{dR}{dM} \right)^2 \langle (\Delta M)^2 \rangle, \quad (6.1)$$

which has been discussed in Chapter 4 adequately. In this case the magnetization fluctuation is within a ferromagnetic domain because in the film we have multiple domains and this masks any contribution from domain walls. In case of Ni nanowire, where we do experiments with very small diameter sample ( $\sim 35\text{nm}$ ), the main contribution to the MR likely arises from domain walls. Thus there is a subtle but important difference between the resistance fluctuations in these two magnetic systems.

With the development of advance studies on sub-micron magnetic structures, electronic noise measurement has become a unique and promising tool to probe the physics of spin fluctuation in a nanometric scale. Resistance fluctuations, at low frequencies allow us to identify the slow dynamics regarding the magnetic instabilities in ferromagnetic nanowires. We note that though there are reports of  $1/f$  noise in nanowires and devices of this dimension, there is no report of magnetic noise due to spin fluctuations.

The chapter starts with some basics on domains and domain walls in ferromagnetic nanowires before the issue of magnetization reversal and fluctuations are taken up.

## 6.1.1 Domains and domain wall resistance in ferromagnetic systems

### 6.1.1.1 Formation of domain walls

A magnetic system like Ni is a very good ferromagnetic (FM) material even in form of nanowires. Recent studies done in our laboratory has shown that even in wires with diameter down to 20 nm there is a finite  $T_C$  of 520K [2]. In nanowires of Ni the domain formations as well as domain walls width are determined by parameters like the exchange energy, characterized by the parameter  $A_{ex}$ , the anisotropy energy characterized by the constant  $K$  (that consists of the shape as well as the single-crystalline anisotropy). Another important parameter that is important in this context is the saturation magnetization  $M_s$  which determines the coercive field  $H_c$  along with other parameters.

In physical systems such as nanowires domain walls have been found to exhibit a number of interesting electron transport properties. In particular, the presence of domain walls can enhance the electrical resistance and, reciprocally, the application of a large current can cause a domain wall to be displaced.

An important length scale for such a magnetic system is the thickness of the domain walls (DW)  $d_{dw}$  [3, 4] the size of the domain wall is determined by the relation,

$$d_{dw} \approx \left( \frac{A_{ex}}{K} \right)^{1/2}.$$

In a ferromagnetic nanowire, the relative size of the  $d_{dw}$  with respect to the diameter  $d$  decides the magnetic nature of the wire. For a magnetic wire with diameter is  $d \leq \sqrt{2}d_{dw}$ , and length  $L \gg d_{dw}$  can be called one-dimensional. Moreover, in a ferromagnetic nanowire there are two different anisotropic energies namely, shape anisotropy and magnetocrystalline anisotropy which determine the easy axis for magnetization [5-7]. For nickel nanowire, the shape anisotropy energy is at least one order more than the magnetocrystalline anisotropy; the easy axis of magnetization is along the axis of the wire. For Ni the domain wall width is  $d_{dw} \approx 35\text{-}40\text{nm}$ . Thus Ni nanowires with diameter  $d \leq 50\text{ nm}$  can be considered as one-dimensional magnetic system with spins aligned along the axis of the nanowire. The domain walls in such systems will be  $180^\circ$  domain walls.

In such nanowires, substantial contribution to the transport property can arise from the DW resistance. The origin of the DW resistance is attributed to the mixing of up-spin and down-spin electrons due to the mistracking of the electron's spin on passing through the DW [8]. The narrower DW width results in a larger angle between the magnetization directions of successive atomic layers thereby lowering the electron transmission and hence enhancing the resistance.

### 6.1.1.2 Magnetic behaviour in Ni nanowire samples

Magnetic behaviour of one-dimensional magnetic wires like that of Ni has been extensively investigated. We refer to the reviews Ref. 9-15 for this. Generally in such nanowires, if they are properly crystalline, the shape of the  $M$ - $H$  curve depends on the orientation of the field vis-à-vis the easy axis. For Ni nanowires with diameter 50 nm or below where the easy axis is along the wire axis, for field applied parallel to the wire axis, the hysteresis loop is close to a rectangle as shown in Fig. 6.1. The shape anisotropy of a wire leads to the existence of two stable orientations of the magnetic moment, namely pointing parallel or antiparallel to the wire axis. These orientations correspond to a symmetric double well potential with two energy minima separated by a barrier energy  $U$ . As the magnetic field along the wire axis increases, the double wall becomes asymmetric and  $U$  decreases. At a particular switching field the barrier vanishes and even at zero temperature the magnetization will switch irreversibly [3, 4]. Of importance to our investigation of the resistance fluctuation studied here is the fact that the magnetization reversal is thermally activated across the barrier and the dynamics of such fluctuation will be determined by the dynamics of barrier crossing. The coupling to the resistance fluctuation to the thermally activated magnetization reversal occurs through the DW resistance. The experiment done below captures this physics.

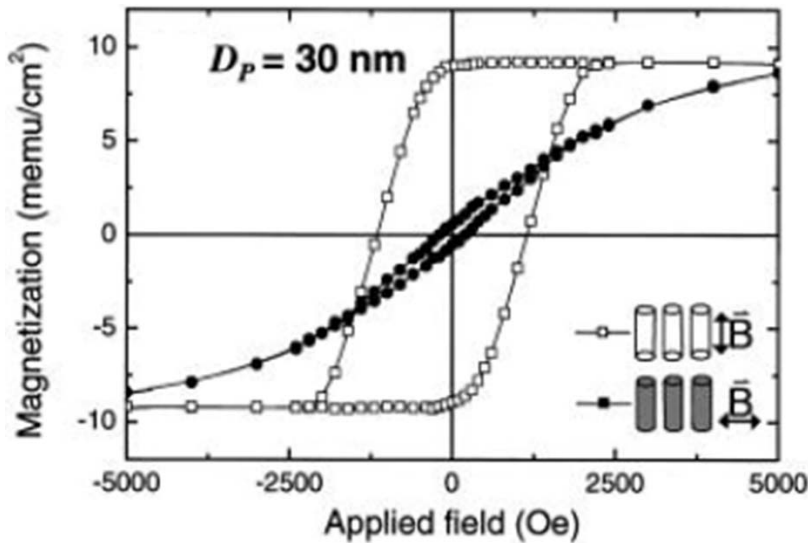


**Figure 6.1:** The magnetization ( $M$ ) versus ( $H$ ) loops studied on Ni nanowires of diameter  $D_p = 40$  nm [12]. The applied magnetic field is along parallel (//) and perpendicular (⊥) direction to the wire axes.

### 6.1.2.2 Synthesis of nanowires in templates and the experimental arrangements

We used electrodeposition method to grow nanowires in nanoporous templates. For details of the growth we refer to the thesis of Mr. Venkata Kamalakar [2] who has grown these wires.

The wires were characterized by X-Ray diffraction and microscopy tools like SEM and TEM. Representative XRD and TEM data along with the selected area diffraction pattern on single crystalline Ni nanowire of diameter 35 nm on which we have studied the magnetic noise are shown in Fig. 6.2 (a), (b), and (c) respectively. The nanowires used in the experiment have length in the range of 50  $\mu\text{m}$ .

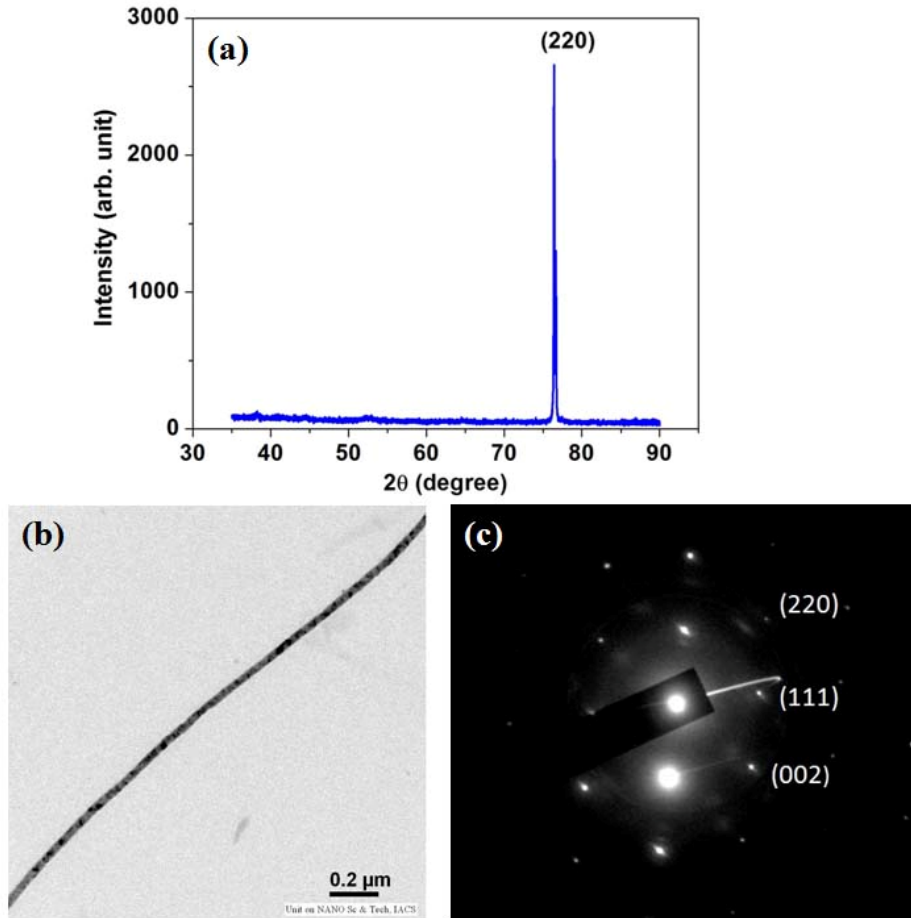


**Figure 6.2:** (a) X-ray diffraction data for and (b) TEM image and (c) selected area diffraction pattern of 35 nm Ni nanowires (Reprinted with permission [2]).

In this section we shall discuss about the experimental setup for our noise measurements done on arrays of nickel nanowires. The nanowire samples appear to be metallic [1, 2] through out our experimental temperature regime 77-300 K.

We have used ac four-probe noise measurement scheme as described in Chapter 3 in detail. The schematic diagram for noise measurement is shown in Fig. 6.3(a). The silver film coated in one side of the template is used for one current ( $I_+$ ) and one voltage probe ( $V_+$ ). We allowed overgrowth of the nickel nanowires in another side and used silver epoxy to make other two low noisy electrical contacts, i.e.,  $I_-$  and  $V_-$ . The sample is fed with suitable ac voltage ( $V_0$ ) from lock-in-amplifier (LIA). We used a large resistance  $R$  (typically  $1\text{k}\Omega$  or  $10\text{k}\Omega$ ) in series with the sample and voltage source (LIA) to make the sample as constant current biased system. The typical current we allow to flow through the sample is few microamp. The voltage drop across two voltage probes ( $V_+$  and  $V_-$ ) is fed to the input of a low noise transformer preamplifier and the gain of the amplifier is set to 100. The preamplifier output voltage is then again goes back to the two inputs (X-channel and Y-

channel) of LIA. The simultaneous measurements of X and Y channel voltages give us voltage fluctuations from sample and background respectively. Using digital signal processing (DSP) technique (see Chapter 3) we can measure the resistance fluctuation hence the power spectral density for the nanowires.

During electrodeposition some of the nanowires do not grow from end to end and these will not contribute in any of the electrical measurements. Sometimes there is no uniform distribution of pores in the templates. Hence we can not estimate the exact number of nanowires in contact. But we can definitely draw an equivalent circuit as shown in Fig. 6.3(b) where each of the nanowire is with resistance  $R_s$ . We assumed that there are N identical numbers of nanowires in parallel to each other contributing to sample resistance. The normalized resistance fluctuation  $\langle (\Delta R)^2 \rangle / R^2$  for a nanowire of resistance  $R$  is obtained by integrating the power spectral density  $S_V(f)/V^2$  over the detection bandwidth ( $f_{\min} \rightarrow f_{\max}$ ) of measurement and is given by

$$\frac{\langle (\Delta R)^2 \rangle}{R^2} = \left( \frac{1}{V^2} \right) \int_{f_{\min}}^{f_{\max}} S_V(f) df. \quad (6.2)$$

Where we have taken  $f_{\min} \sim 60$  mHz and  $f_{\max} \sim 5$  Hz.

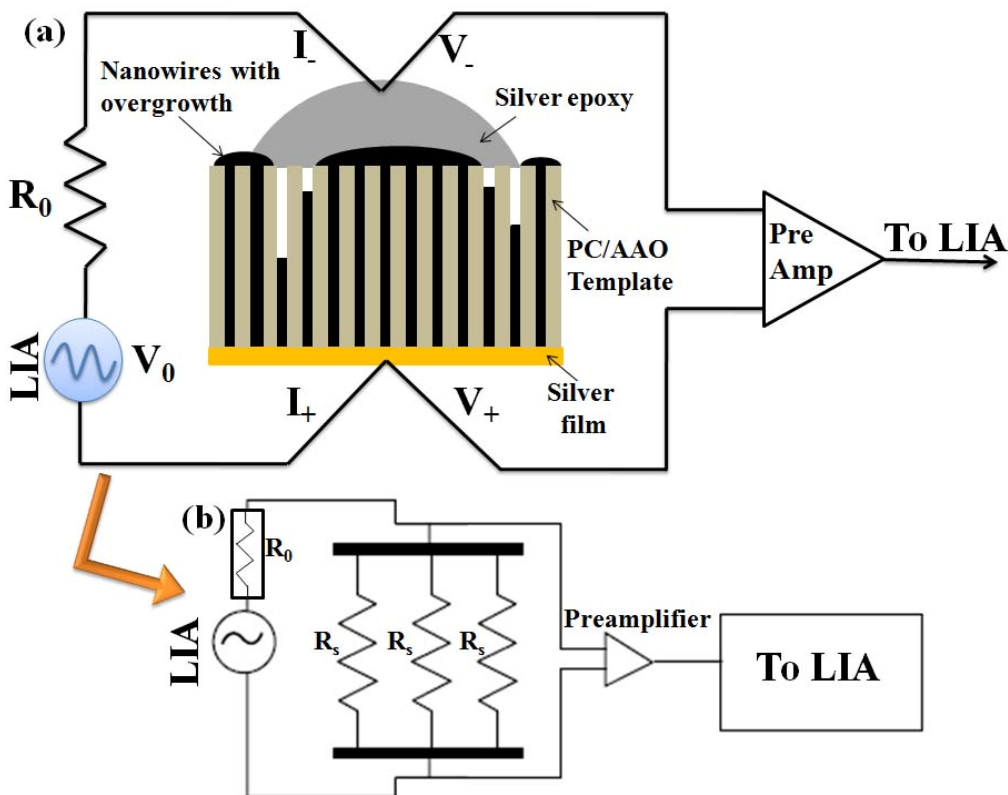


**Figure 6.3:** (a) Schematic diagram for electrical measurements  $R_0$  is a large resistance compared to sample resistance  $R$  and the sample is fed ac bias voltage  $V_0$  through lock-in amplifier (LIA). The voltage across the nanowires is fed into low noise preamplifier and measured by two inputs of LIA. (b) The schematic of the equivalent circuit shown in (a) where  $R_s$  is the resistance of each nanowire.

The above equation, while giving correctly the relative resistance fluctuation of a single wire, is also applicable when there is more than one wire in parallel. If  $R$  is the total sample resistance then  $1/R = N/R_s$ . Thus  $\langle (\Delta R)^2 \rangle / R^2 \rangle_N = \langle (\Delta R_s)^2 \rangle / R_s^2$  and resistance fluctuations is independent of nanowires in parallel. Each of the nanowire acts as an independent noise source. Though the resistance fluctuation  $\langle (\Delta R)^2 \rangle$  depends on the numbers of noise sources but relative fluctuation is independent of the number of nanowires in the templates under study. This also implies that nanowires are well separated from each other. This effect has been checked earlier by Bid *et al.* [16] for Ag nanowires. In the next section we shall discuss about the results of our study in nickel nanowires as a function of wire diameter at room temperature.

## 6.2 Diameter dependent noise in nanowires at room temperature

We have discussed in the earlier section (see section 6.2) and Chapter 3 that the noise was measured using a four-probe ac technique. During the noise measurements we ensured that the current through the sample is low enough, otherwise it will unnecessary warm up the sample and will introduce additional noise. The spectral power  $S_V(f)$  is  $\propto V^2$ , where  $V$  is the sample bias voltage (typically few tens of  $\mu\text{V}$ ). The  $V^2$  dependence of  $S_V(f)$  for two samples, 15 nm nanowire and 50  $\mu\text{m}$  bulk wire are plotted in Fig. 6.4 (a) and Fig. 6.4 (b) respectively.

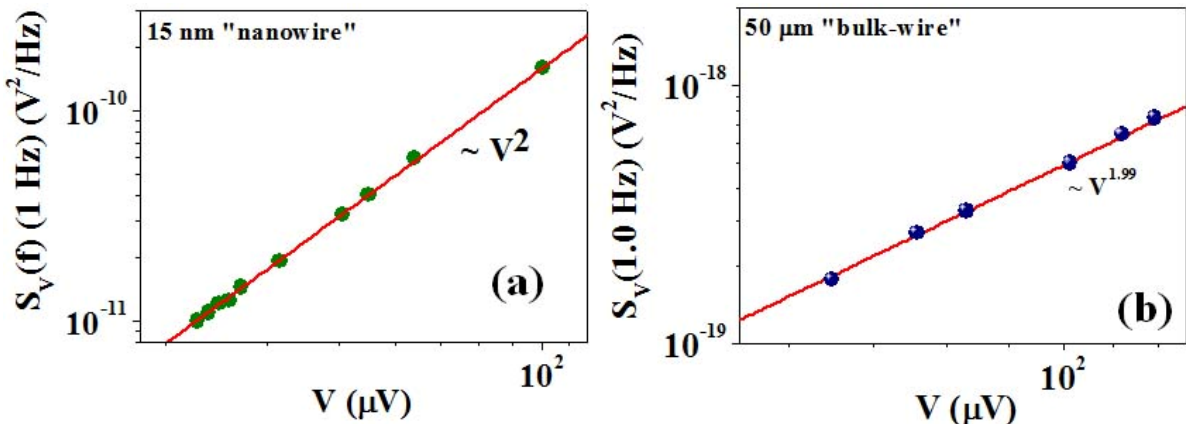


**Figure 6.4:** The spectral power  $S_V(f)$  at 1 Hz has been plotted with bias voltage  $V$  for (a) 35 nm and (b) 50  $\mu\text{m}$  wire. There exists  $V^2$  dependence for both cases.

In Fig. 6.5(a) we show that the typical low frequency power spectral density of the voltage noise arising from resistance fluctuations in the current biased nickel nanowires diameter ranging from 15 nm to 50  $\mu\text{m}$ . The power spectra show  $1/f^\alpha$  nature and are independent of the nature of the templates. To know the diameter dependence of  $\alpha$  we have plotted  $fS_V(f)/V^2$  as a function of frequency in Fig. 6.5(b). It is clear that for wires with diameter  $d \geq 35$  nm shows noise with clear  $1/f$  dependence. For the other two wires 15 nm and 20 nm, spectral power deviates significantly at low frequencies. The deviation is more severe for 20 nm wire. So we can conclude that there is an enhancement of low frequency noise component for low dimensional wires. The noise seen in the nanowires can arise from structural as well as magnetic origin. The purpose of the present investigation is to have

nanowires with low enough noise due to structural origin so that magnetic noise can be studied.

From the data presented we find that the magnitude of the noise is the least in case of  $d = 35$  nm diameter nickel wires. This is a single crystalline wire. All the other wires are polycrystalline in nature and they show higher noise. So, good crystallinity reduces the noise even in the nanowires. We shall be discussing this issue later in this chapter in detail.

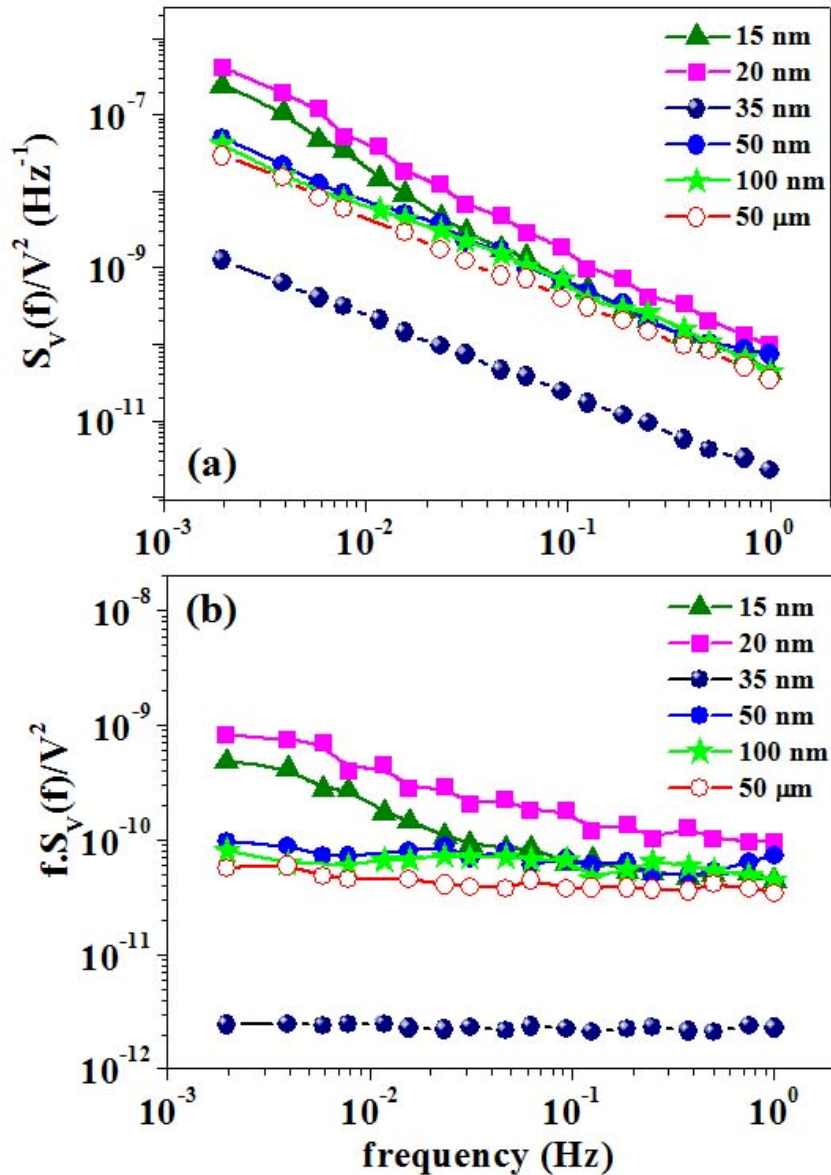


**Figure 6.5:** (a) Low frequency power spectrum  $S_V(f)$  of the voltage noise arising from the resistance fluctuations in current biased Ni nanowires of diameters ranging from 15 nm to 200 nm. (b)  $f.S_V(f)/V^2$  has been plotted to accentuate the deviation of the spectral power at low frequency regime.

In Fig. 6.6(a) we have plotted diameter dependence of frequency exponent  $\alpha$  for nanowires. The value of  $\alpha$  was calculated by plotting  $\ln(S_V(f))$  vs.  $\ln f$  and the errors bars are the fitting errors. For nanowires with  $d \geq 35$  nm,  $\alpha \approx 1$  but its value increase for lower diameter wires. The value obtained for larger diameter is very similar which we generally

obtain for good metal films. This type of noise is expected to arise from thermally activated defect kinetics [17] as discussed in Chapter 1 (see McWhorter and Dutta-Horn model). The increase of  $\alpha$  indicates the extra component of noise arising in smaller diameter wires which is significantly absent in large dimensional wires. This type of result was also reported earlier by Bid *et. al.* for 15 nm Ag and Cu wires [16]. We want to mention that single crystalline wires ( $d = 35$  nm) have  $\alpha$  value is very close to unity and lower than the values of  $\alpha$  obtained for other large dimensional wires. We have plotted  $\langle (\Delta R)^2 \rangle / R^2$  as a function of  $d$  at 300 K in Fig. 6.6(b). We can see the noise magnitude is significantly high at lower diameter wires, i.e. for 15 nm 20 nm. Compared to other wires, 35 nm is much less noisy than other wires. We have collected noise data for different samples and the error bars are calculated from the statistical deviation of the data. Below we investigate in details the data on the 35 nm wires where we can study the magnetic noise. The noise in the other polycrystalline nanowires arises mainly from structural defects. The investigation of such defects is beyond the scope of the thesis.

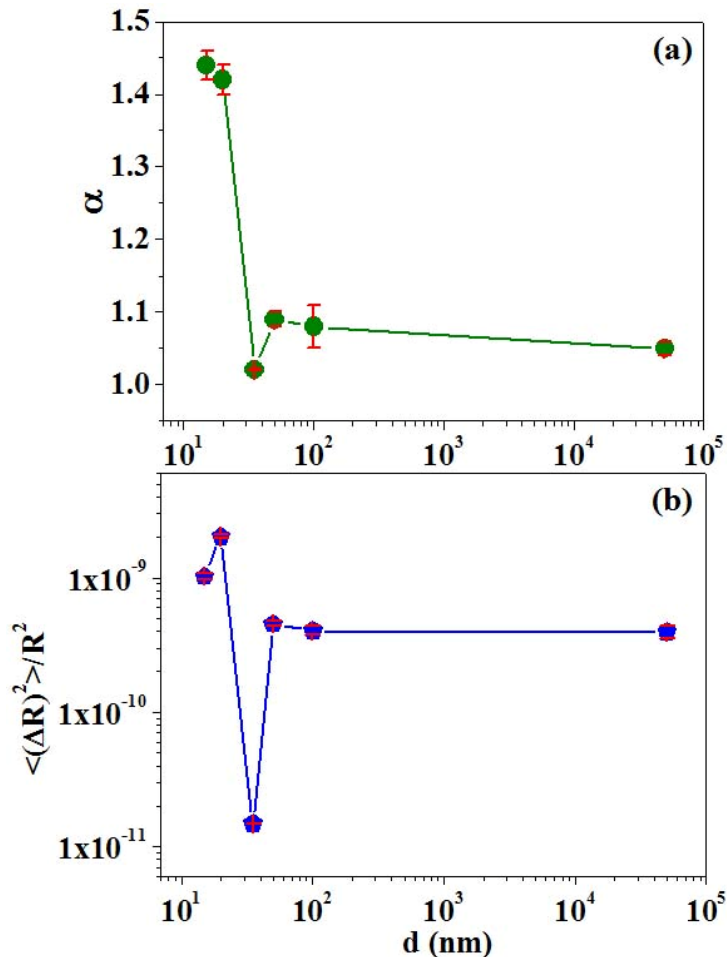


**Figure 6.6:** Diameter dependence of frequency exponent (a)  $\alpha$  and (b) normalised relative resistance fluctuation  $\langle (\Delta R)^2 \rangle / R^2$  at 300 K. The error bars are also plotted simultaneously in the graphs.

### 6.3 Origin of excess noise in nanowires

As mentioned earlier, the magnetization reversal an important property of the low dimensional magnetic wire which strictly depends on the diameter of the wire. In particular,

in nanowires which have length much larger than the diameter, the nucleation of domain walls and its propagation between opposing magnetic domains (magnetization reversal) has been a topic of recent investigations [3, 4, 18-20]. The uniform rotation is energetically favourable when  $d \leq \sqrt{2}d_{dw}$ . We mentioned already that for Ni,  $d_{DW}$  is  $\approx 35$  nm. We can expect a reversal mechanism of this type for the wires with diameter  $< 50$  nm. This has been tested by detailed investigation in Ni nanowires [21, 22].

The important thesis of this chapter is that the reversal mechanism can be an important source of low frequency noise in magnetic systems, because this is thermally activated through an activation barrier. Such a barrier has been seen in experiments like magnetic hysteresis. In general, there are two principal mechanisms by which resistance fluctuation can couple to magnetic fluctuations:

- First mechanism is through domain walls which can directly couple to resistance fluctuation because they offer an electrical resistance. The magnetization reversal would mean creation and motion of domain walls leading to resistance fluctuations.
- Second mechanism is the intra domain mechanism by which resistance can couple to magnetic fluctuation by the mechanism of magnetoresistance. This is what we have seen in manganites and this is governed by the equation 6.1.

In Ni nanowires, we will see that the first mechanism is operational. In Ni nanowire, as mentioned before the shape anisotropy determines the orientation of the magnetic moment. The moment will be aligned along the wire axis with parallel or anti-parallel orientation. The parallel and antiparallel magnetization states of a nanowire are generated by a symmetric double well potential separated by an energy barrier  $\varepsilon_b$ . In principle, the magnetization can switch both from parallel to antiparallel and vice versa. The magnetization reversal would thus need overcoming barrier energy  $\varepsilon_b$ . This is schematically shown in Fig. 6.7.

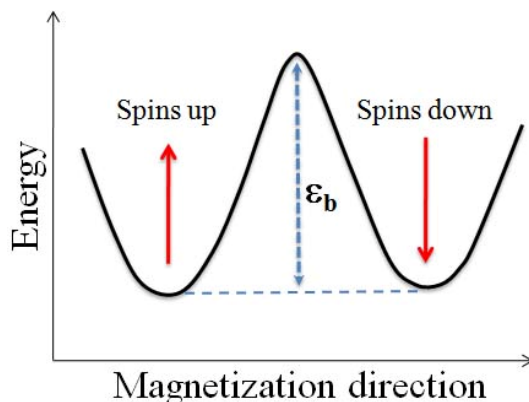


**Figure 6.7:** Schematic representation of the energy barrier for the magnetization in double well potential model.

In these wires the magnetization reversal processes have been well studied in the nanosecond and microsecond range which is the time scale of the magnetization reversal either in a field and or by a current [23]. However, in addition, there is a finite though small probability of thermally activated magnetization reversal and resulting domain nucleation and propagation. The kinetics of domain wall motion involves nucleation, pinning/de pinning and transit through the sample and thus has an element of stochastic process. It is thus expected that the domain wall kinetics may show low frequency fluctuations. This fluctuation can give

rise to resistance fluctuation due to finite domain wall resistance and thus the study of low frequency noise can be an important tool to probe domain wall dynamics and low frequency magnetization fluctuation phenomena in nanowires. The origin of the magnetic part of the resistance noise is traced to the fluctuations in domain wall and it has a direct correlation to the magnetoresistance (MR) that arises from the domain wall resistance. The low field MR which due to finite resistance of the domain walls can couple to low frequency domain wall dynamics and can show noise that is correlated to the MR.

The thermally activated magnetization can be described as follows. In thermal equilibrium these two orientations will be in dynamic equilibrium with reversal rate  $\tau^{-1}$  determined by an Arrhenius rate equation  $\tau^{-1} = \tau_0^{-1} \exp(-\varepsilon_b/k_B T)$ , where  $\varepsilon_b$  is an attempt frequency  $\tau_0^{-1} \approx 10^9\text{-}10^{10} \text{ sec}^{-1}$  [21]. It has been estimated that  $\varepsilon_b$  (as determined by shape anisotropy energy) is inversely proportional to  $d^2$  and for 20 nm wires  $\varepsilon_b \sim 3 \times 10^4 \text{ K}$  [21, 24]. We can thus estimate the characteristic rate  $\tau^{-1}$  for our system. As can be seen this is of the scale as that one observes from the power spectrum of the resistance fluctuation. Thus thermally estimated magnetization reversal can give rise resistance fluctuations. The activation energy barrier  $\varepsilon_b$  will depend on various imperfections. This will give a distribution of  $\varepsilon_b$  and thus the power spectra originating from such a process will be broad as has been observed. The process of magnetization reversal in this case involves motion of domain walls. Since the magnetization just flips between two orientations without change in magnitude, the magnetoresistance mediated coupling mechanism will not be an effective mechanism in this case. Instead, the domain wall resistance can provide effective coupling mechanism. Since the low frequency dynamics is essentially the dynamics of domain walls, this will give rise to an effective coupling mechanism resulting in resistance fluctuation. The low frequency noise in magnetic nanowires can also have structural origin (non-magnetic) other than magnetic sources as we stated earlier. In general in most cases, this is the noise that dominates. However, for the 35 nm wire this noise is low, a separation is possible. We used an external applied magnetic field to separate out these two noise components from each other. To investigate the noise sources in nanowires we have chosen single crystalline 35 nm nickel nanowires. There are few reasons behind this choice: crystalline quality of the 35 nm nanowire is very good, hence the stability of measurements and reproducibility of the data is very good, and there is no hysteresis in the resistivity measurements as well as noise data in heating or cooling cycles and is sensitive even to a small external magnetic field. In the next section we study the temperature dependence noise phenomena in presence of low applied magnetic field  $\approx 0.12$  Tesla. The  $\mu_0 H_C$  for these wires is = 0.09 Tesla, thus the investigation has been done for  $B/B_C \sim 1.3$ .

## 6.4 Noise spectroscopy in nanowires ( $d \approx 35$ nm) in presence of external magnetic field

In this section we shall study the noise phenomena in 35 nm nickel nanowires with the application of low magnetic fields ( $\leq 0.12$  Tesla). In all our measurements we allowed the magnetic field along the axis of the wires.

### 6.4.1 Magnitude of the noise as a function of magnetic field and temperature

We have studied the magnetic field dependence of low frequency ( $1 \text{ mHz} < f < 10 \text{ Hz}$ ) noise magnitude  $\langle (\Delta R)^2 \rangle / R^2$  as a function of magnetic field at few representative temperatures as shown in Fig. 6.8. We observed the suppression of normalised resistance fluctuations for all temperatures. For all temperatures the noise starts to decrease first for magnetic fields  $\leq 0.04$  Tesla, and becomes saturated for higher field strengths. Two different regimes are clearly observed from the above data. One part is highly magnetic field dependent ( $B \leq 0.04$  Tesla) and other part is magnetic field independent ( $B > 0.04$  Tesla). The phenomenon of reduction of noise with an application of external magnetic field is definitely an indication of the presence of magnetic contribution to noise.

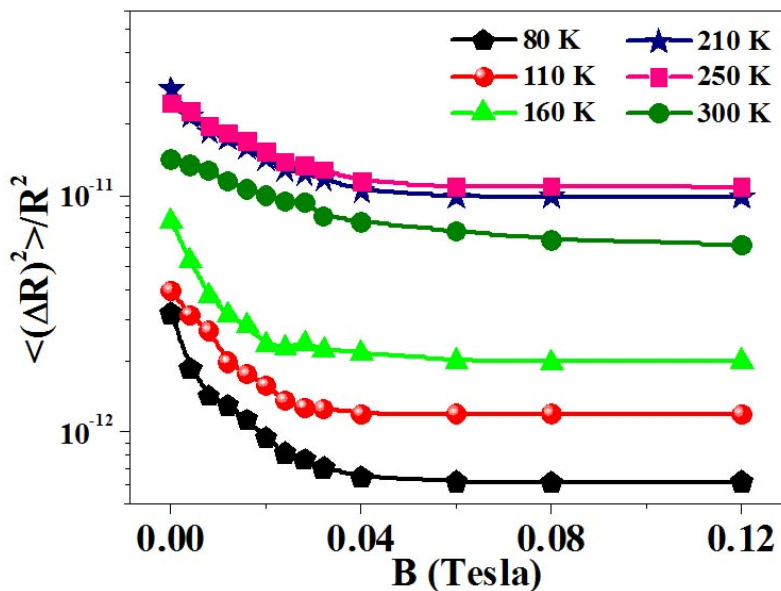


**Figure 6.8:** The variation of  $\langle (\Delta R)^2 \rangle / R^2$  as a function of magnetic field at few representative temperatures for nanowires of diameter 35 nm. The noise gets saturated for fields  $B > 0.04$  Tesla for all temperatures.

The scale of the magnetic field can be seen from the magnetization versus magnetic field ( $M$ - $B$ ) of the wires as shown in Fig. 6.9. The magnetic measurements were done using Variable Sample Magnetometer (VSM) retaining the nanowires in the templates. The magnetic field is applied along the axis of the wires. The coercive field of 35 nm wires is  $B_c \approx 0.09$  Tesla at 300 K. The  $M$ - $B$  curve shows saturation magnetization at  $B < 0.25$  Tesla and its value is  $5 \times 10^{-3}$  e.m.u. The retention ratio is  $m_r = \mathfrak{M}_R / M_s \approx 0.90$  where  $\mathfrak{M}_R$  is the remanent magnetization at zero field value and  $M_s$  is the saturation magnetization. This indicates that the alignment of all the wires is not perfectly parallel to the magnetic field. We have chosen the maximum magnetic field value 0.12 Tesla just greater than  $B_c$ . The value of  $B_c$  does not depend much on the length though it does depend on diameter of the wires. In the temperature range of our interest  $B_c$  has a shallow temperature dependence and in wire of diameter of this value from the room temperature value on cooling (almost linearly with  $T$ ) to 80K.

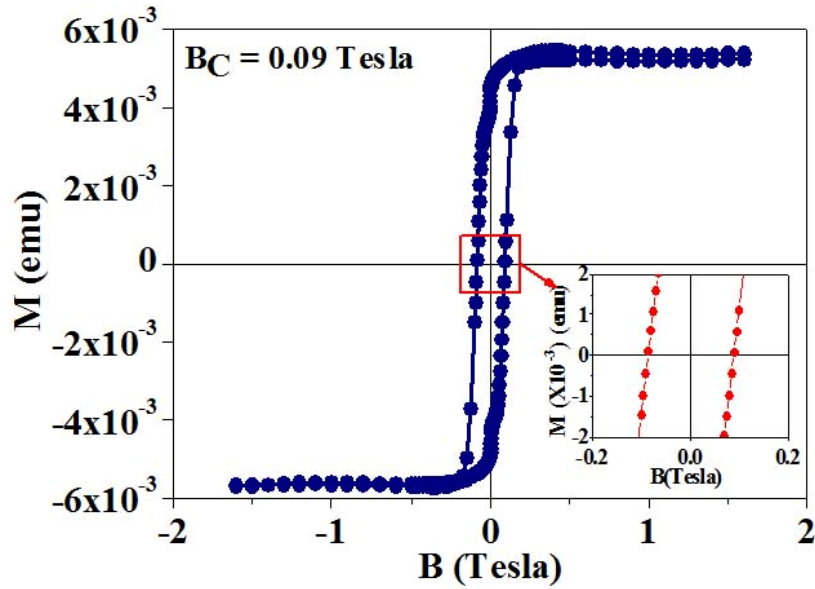


**Figure 6.9:** The variation of magnetization ( $M$ ) as a function of magnetic field ( $B$ ) at 300 K for 35 nm nickel wires. The coercive magnetic field is  $B_C \approx 0.09$  Tesla. The data is reprinted with permission [2].

The dynamics of the localized nucleation phenomena is controlled by the dynamics of the domain walls so created. In zero field value the probability of reversal by thermal energy alone is low, given the height of the activation barriers, however, it is still finite and give rise to slow spin dynamics. Hence, the fluctuation phenomenon which we observed is closely related to domain wall dynamics. As we mentioned earlier that domain wall fluctuation dynamics is correlated with MR in the nanowires. We will discuss this again in next subsection. For applied magnetic field  $B > B_C$ , when the material is fully magnetized there is no domain wall and all of them collapse. In this range the source of noise is primarily of structural origin.

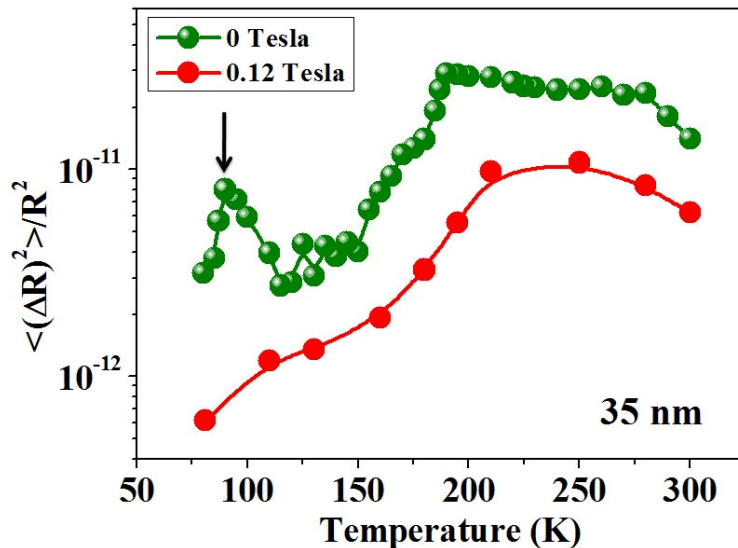


**Figure 6.10:** The variation of normalized resistance fluctuations  $\langle (\Delta R)^2 \rangle / R^2$  as a function of temperature in presence and absence of magnetic field. The data has been collected for arrays of 35 nm nickel wires.

To look into the magnetic field independent part, we have used a magnetic field of  $B = 0.12$  Tesla to suppress the magnetic contribution. This field is larger than  $B_c$  and as the data shows, changes in  $\langle (\Delta R)^2 \rangle / R^2$  as a function of field saturates for  $B \sim 0.5 B_c$ . We have plotted  $\langle (\Delta R)^2 \rangle / R^2$  as a function of temperature in Fig. 6.10. We have plotted the zero field noise data along with it for comparison the field dependent reduction in noise magnitude. But the peak near 100 K at zero magnetic field (marked by arrow) is absent in magnetic field dependent noise data. For each temperature at  $B = 0.12$  Tesla, we have marked  $\langle (\Delta R)^2 \rangle / R^2$  values as  $(\langle (\Delta R)^2 \rangle / R^2)_{nm}$ . We subtracted out the  $(\langle (\Delta R)^2 \rangle / R^2)_{nm}$  part from total  $\langle (\Delta R)^2 \rangle / R^2$  to extract the magnetic noise part  $(\langle (\Delta R)^2 \rangle / R^2)_m$  at each temperature.  $(\langle (\Delta R)^2 \rangle / R^2)_{nm}$  and  $(\langle (\Delta R)^2 \rangle / R^2)_m$  stands for “non-magnetic” and “magnetic” fluctuation parts of total  $\langle (\Delta R)^2 \rangle / R^2$  respectively.

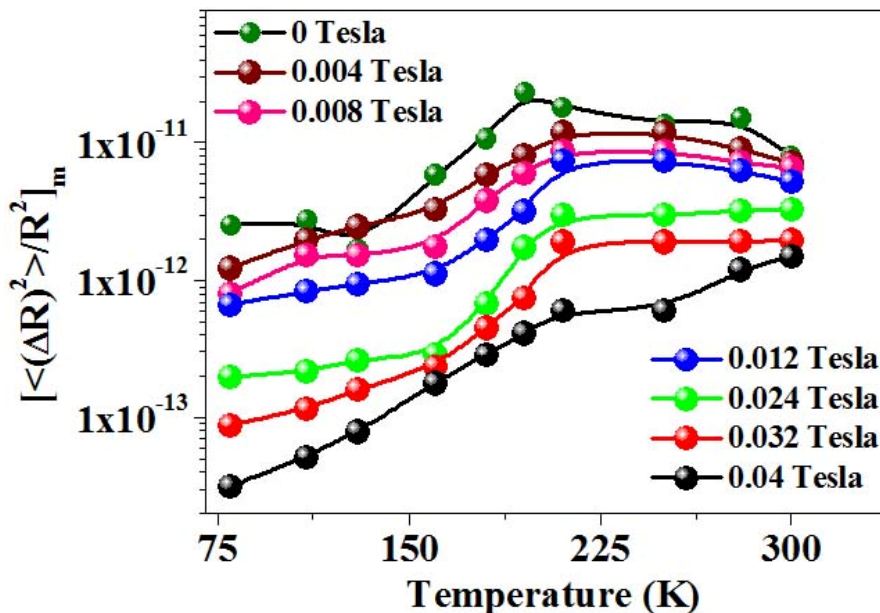


**Figure 6.11:** (a) The variation of magnetic noise component  $[\langle (\Delta R)^2 \rangle / R^2]_m$  at few representative magnetic field  $\leq 0.04$  Tesla. The non magnetic noise component of total noise has been estimated the values of  $\langle (\Delta R)^2 \rangle / R^2$  at highest magnetic field ( $B = 0.12$  Tesla) and has been subtracted out to get the magnetic part.

In Fig. 6.11 we have plotted magnetic noise part  $[\langle (\Delta R)^2 \rangle / R^2]_m$  as a function of temperature at few representative magnetic fields. The magnetic field values have been chosen below a certain field (here 0.04 Tesla) above which the total noise gets saturated. This field is approximately  $\sim 0.4\text{--}0.5 B_c$ . When the magnetic field is low, the major contribution to  $\langle (\Delta R)^2 \rangle / R^2$  is coming from magnetic sources. This magnetic noise is suppressed by higher magnetic field. The reduction of the fluctuations in magnetic field is almost temperature independent (nearly one order of magnitude) but starts to decrease above 225K. It is to be noted that though magnetic field can be used to separate out the two contributions, there appear to be some “cross-talk” between the two mediated by defects. It is noted that in most nanowires of FCC metals like Cu and Ag, there is a temperature dependent part of the structural noise (with activated character) occurring in the temperature range above 100K

[25, 26]. Similar things happen in Ni nanowires also. We elaborate on this issue for the sake of completeness in the next part.

We observed that in the temperature range  $140 < T < 200$  K, the noise is enhanced (see Fig. 6.10). This is present in the data with field as well as without field. This temperature dependence has an activated nature. We have fitted the magnetic data with Arrhenius activated model to calculate the activation energy in the above temperature range. The estimated activation energy  $E_{mag}$  is 93 meV which is more or less same with the value of activation energy found for the data with field ( $E_{max} \sim 97$  meV). The experimental data (with  $B = 0$  and  $B = 0.12$  Tesla) and the corresponding fit to the Arrhenius model are shown in Fig. 6.12.

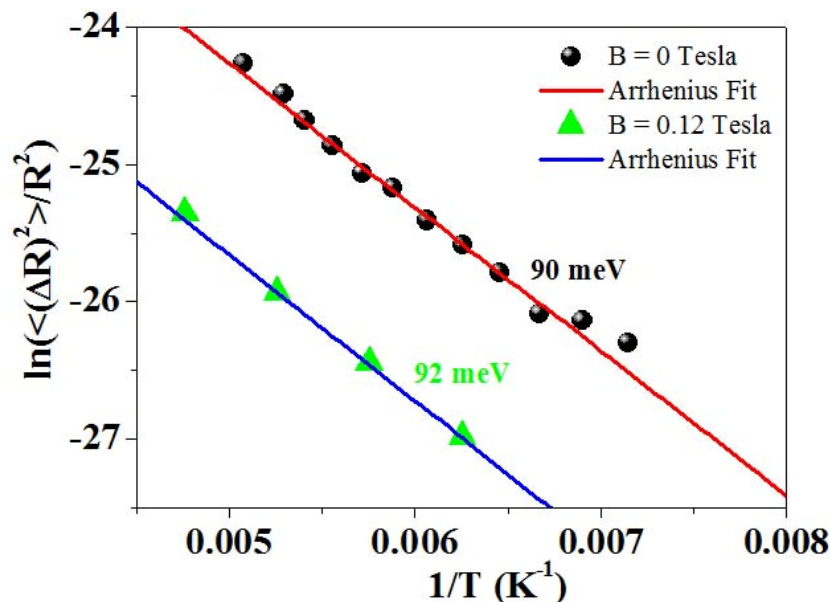


**Figure 6.12:** Plot showing  $\ln[\langle (\Delta R)^2 \rangle / R^2]$  as a function of inverse temperature for  $B = 0$  and  $B = 0.12$  Tesla. The corresponding fits to the experimental data with Arrhenius model are also shown. The estimated activation energy is  $\sim 90$  meV obtained from fitted data.

We thus find that the noise without magnetic field also has a component that has thermally activated kinetics for mobile defects and it does not alter even with the application of external magnetic field. In this case the dynamics of domain walls that control the magnetic part of the noise is also controlled by structural defects. We seek an independent proof of this from direct magnetic experiment.

#### 6.4.2 Power spectral density of noise as a function of applied magnetic field and temperature

In this section we shall study the frequency as well as temperatures dependence of power spectra in presence of external applied magnetic field up to 0.12 Tesla.

In Fig. 6.13 we have plotted the frequency and magnetic field dependence of the power spectral density at few representative temperatures. For all temperatures we can see the decrease of magnitude of spectral power with the increase of magnetic field. The suppression is maximum at  $B = 0.12$  Tesla for all temperatures. These power spectra have been integrated over the frequency range to estimate the total resistance fluctuation of the system (see equation 6.2). It is also clear from the data that the power spectra of noise do not change

much for  $B > 0.04$  Tesla. This effect has been reflected in experimental data explained in section 6.4.1 also. Moreover, for magnetic field  $B > B_C$ , no additional noise response of magnetic field is observed in the system. We already mentioned that at  $B = 0$ , the noise is coming from both nonmagnetic and magnetic sources. When magnetic field increases the domains collapse gradually and contributions coming solely from magnetic sources decrease. Finally, for  $B > B_C$ , all the domains collapse and effect of magnetic field is no more observed. Hence, the spectral power at  $B = 0.12$  Tesla represents the fluctuation coming due to nonmagnetic as well as structural noise sources. The type of power spectral density shows  $S_V(f)/V^2 \propto 1/f^\alpha$  noise for all temperatures and magnetic fields.

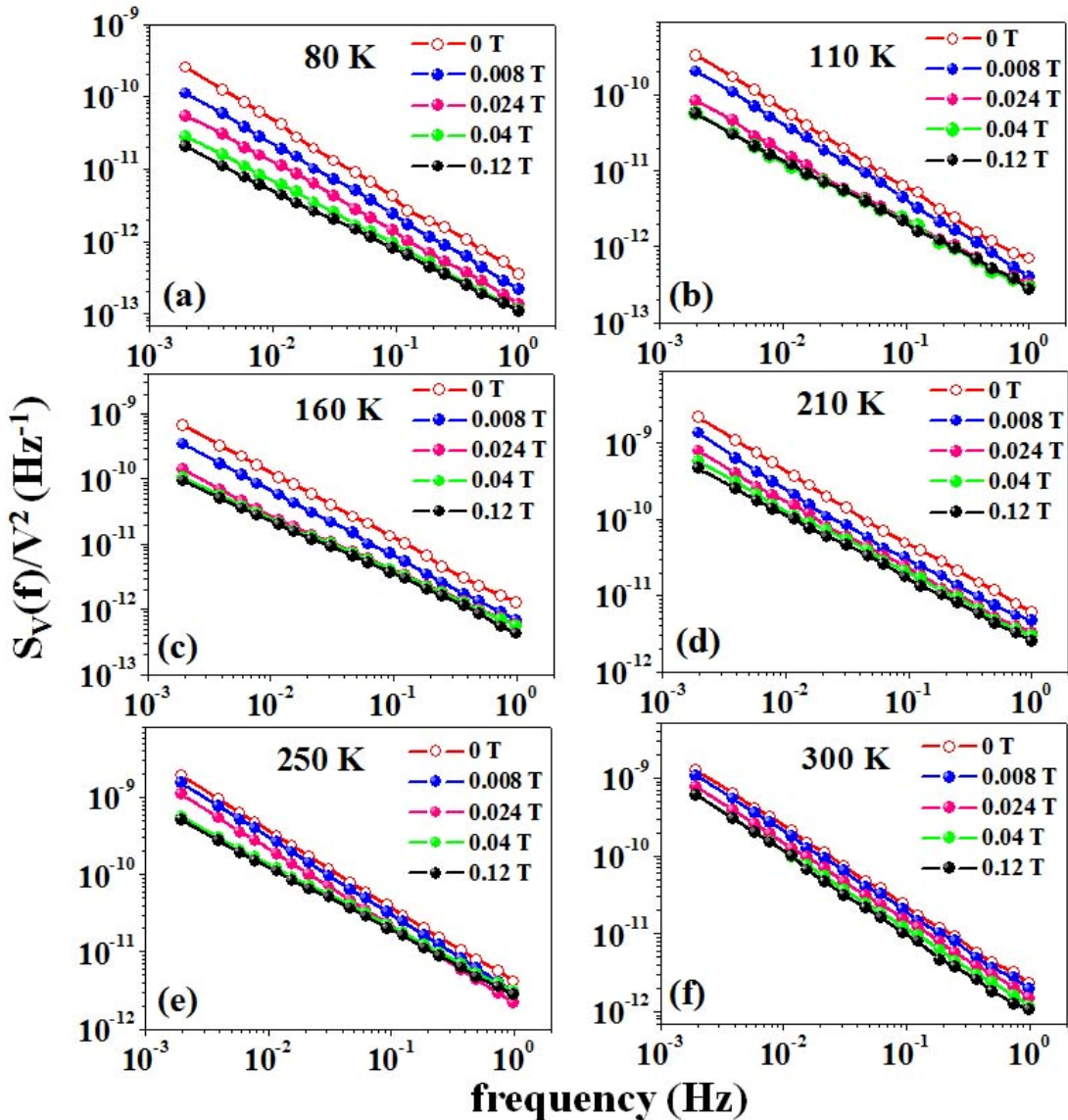


**Figure 6.13:** The variation of power spectral density of resistance fluctuation as a function of frequency at few representative magnetic fields at temperatures (a) 80 K, (b) 110 K, (c) 160 K, (d) 210 K, (e) 250 K and (f) 300 K. We can see the decrease of magnitude in power spectral density with the application of magnetic field at all temperatures.

In Fig. 6.14 we have plotted frequency exponent  $\alpha$  as a function of magnetic field for few representative temperatures at which the power spectra have been demonstrated in Fig.

6.13. The value of  $\alpha$  varies from 0.84-1.12 and decreases with increase of  $B$ . The value of  $\alpha$  is minimum at  $B = 0.12$  Tesla and is  $\approx 0.84$  for temperatures other than 300 K. Only at 300K,  $\alpha$  does not change much from 1. Thus the resistance fluctuation shows  $1/f$  noise in presence of magnetic field also. However, there is a small variation in the spectral component  $\alpha$ , which shows that it is lowered in presence of a field. It would imply that the lower frequencies fluctuations are predominantly suppressed in a magnetic field.

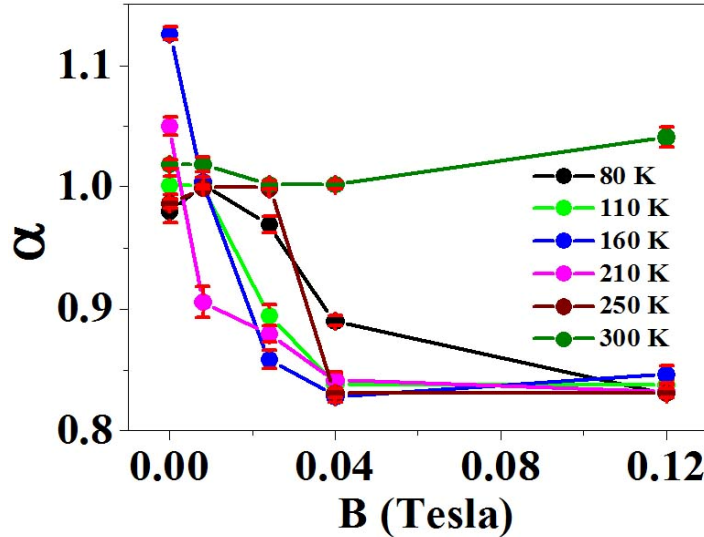


**Figure 6.14:** The magnetic filed dependence of frequency exponent  $\alpha$  at few representative temperatures where the power spectral density has been plotted in Fig. 6.13. The values of  $\alpha$  vary from 0.84-1.12. At 300 K,  $\alpha$  values do not change much with the increase of  $B$ .

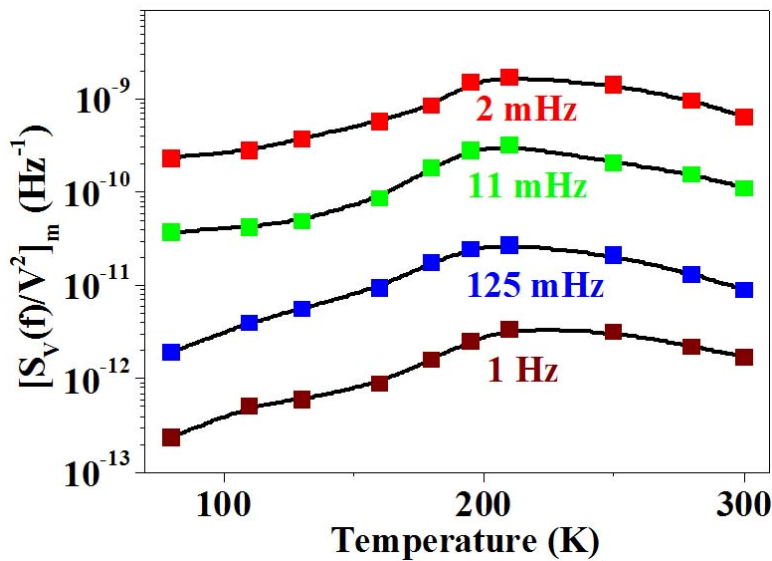


**Figure 6.15:** The magnetic part of the power spectral density  $[S_V(f)/V^2]_m$  as a function of temperature at few representative frequencies.

In Fig. 6.15 we have plotted the variation of magnetic part of the power spectral density  $[S_V(f)/V^2]_m$  at few representative frequencies. We have written the total power spectral density as a sum of two contributions:  $S_V(f)/V^2 = [S_V(f)/V^2]_m + [S_V(f)/V^2]_{nm}$

where  $m$ , and  $nm$  stand for magnetic and nonmagnetic terms respectively. We have considered temperature dependent  $[S_V(f)/V^2]_{nm}$  values from values of  $S_V(f)/V^2$  at  $B = 0.12$  Tesla. Then  $[S_V(f)/V^2]_m$  has been estimated by subtracting it from  $S_V(f)/V^2$  values at  $B = 0$  Tesla. The temperature dependence of  $[S_V(f)/V^2]_m$  shows an activated nature in the frequency scale. Thus we have plotted  $\ln(f/f_0)$  as a function of inverse temperature followed by Arrhenius activated kinetics in Fig. 6.16. The temperatures are taken where  $[S_V(f)/V^2]_m$  peaks at four respective frequencies. The linear fit is also shown in the same graph and the experimental error bars have been estimated from the chi-square fitting. The activation energy  $E_a \approx 0.68$  eV is high enough and is seven times higher than the activation energy at  $B = 0.12$  Tesla (0.097 eV).

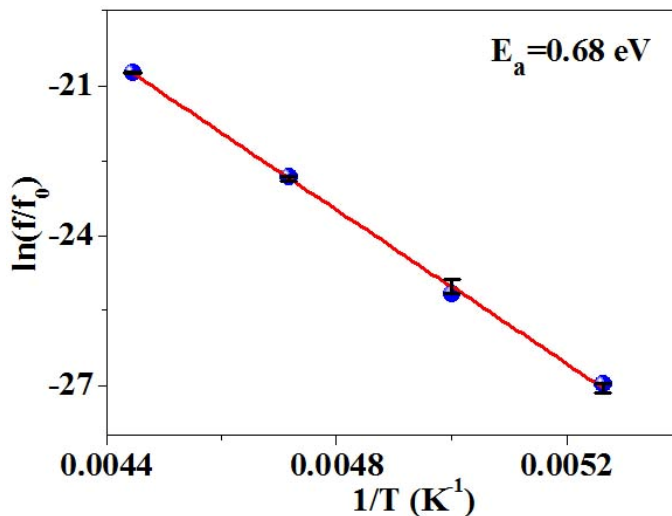


**Figure 6.16:** The variation of  $\ln(f/f_0)$  as function of inverse temperature to estimate the activation energy in presence of magnetic field.

#### 6.4.3 Magnetic fluctuations at 80 K

In Fig. 6.17 we have plotted magnetic field dependence of relative resistance fluctuation along with resistance of nanowire arrays and MR at 80 K.

In Fig. 6.17(a) we have shown  $\langle (\Delta R)^2 \rangle / R^2$  as a function of magnetic field  $B$  at 80 K. The resistance change in magnetic field is shown in Fig. 6.17(b). The reduction of the resistance  $R$  in magnetic field is small though distinct and it saturates for  $B > B_c$  as shown in Fig. 6.17(b). Beyond 0.04 Tesla, the field dependence is shallow. The magnetic field axis is scaled by  $B_c$ . The corresponding change in MR of the nanowire taken at 80K is also plotted simultaneously in Fig. 6.17(c). We connect the resistance change at low field predominantly arising from domain walls which in such ferromagnetic wires can have a positive resistance of around  $\approx 1\text{-}2\%$  [27]. When the wire is fully magnetized there is no domain wall in the wire (uniformly magnetized) and the resistance mainly arises from nonmagnetic sources. In zero fields (which we start as a demagnetized virgin state) there are domains present in the system. Thus the negative MR seen in the samples occur predominantly due to positive resistance of the domain walls. It can be seen that when the resistance change nearly saturates, the fluctuation also reaches a field independent value. The

main change in resistance as well as the noise occurs for  $B / B_c \leq 0.5$ . The above correlation of the MR and the magnetic field dependence of the resistance fluctuations are seen over the whole range of temperature. Thus, the likely magnetic source of resistance fluctuation in a narrow ferromagnetic nanowires ( $d < \sqrt{2}d_w$ ) can be linked to the domain wall resistance and their dynamics that accompanied the thermally activated magnetization reversal mechanism.

We now relate to the relation  $\frac{\langle (\Delta R)^2 \rangle}{R^2} = \xi \left( \frac{1}{R} \frac{dR}{dM} \right)^2 \langle (\Delta M)^2 \rangle$ . When  $B \rightarrow B_c$ , the magnetization

fluctuations  $\langle (\Delta M)^2 \rangle \rightarrow 0$ . It is thus understandable that  $\frac{\langle (\Delta R)^2 \rangle}{R^2} \rightarrow 0$ , as  $B \rightarrow B_c$ . Important,

however, is the observation that the MR as represented by  $\left( \frac{dR}{dM} \right)$  saturates at a field  $B \sim 0.5$

$B_c$ , which is much smaller than the field for technical saturation. The saturation of magnetization as with  $B > B_c$ , in this case is noteworthy, because in an ideal case of a ferromagnetic wire, one would expect a rectangular  $M-H$  loop where saturation occurs at  $B_c$ . It appears that the collapse of the domain walls (that reduces  $R$ ) occurs predominantly at fields below  $B_c$ . The MR and the resulting fluctuation are saturated at fields  $< B_c$ .

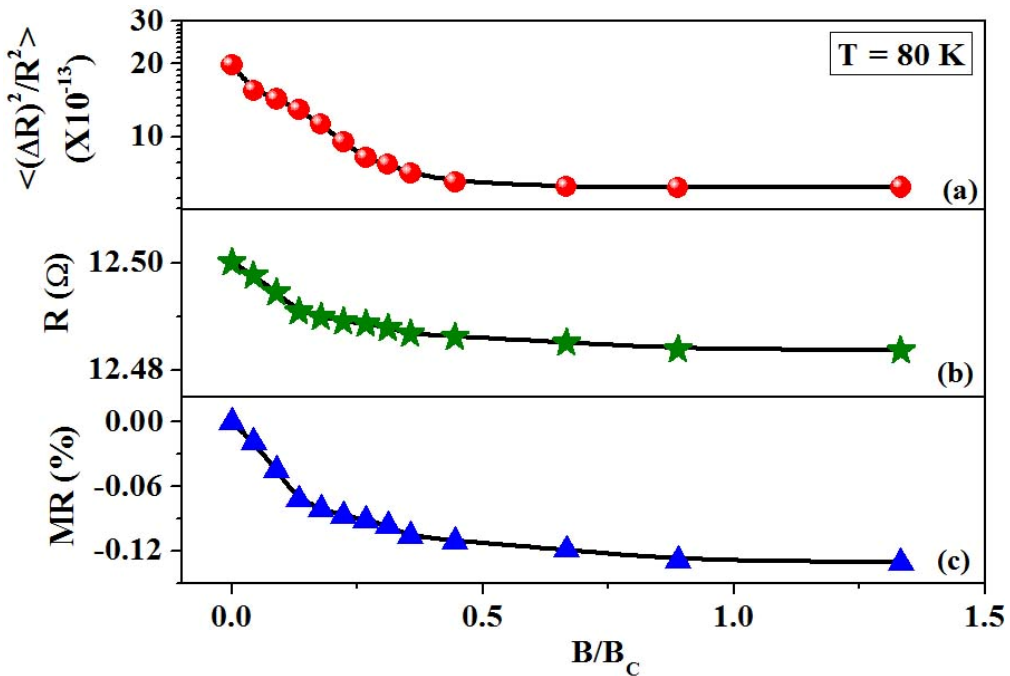


**Figure 6.17:** The variation of (a) relative resistance fluctuation  $\langle (\Delta R)^2 \rangle / R^2$ , (b) resistance of nanowire arrays  $R$  and (c) Magnetoresistance (MR) as a function of magnetic field  $B$  at 80 K.

The observed magnitude of  $[\langle (\Delta R)^2 \rangle / R^2]_m$  is  $10^{-12}$ . If all the domain walls that contribute to the resistance would have contributed to the noise in the time scale of the measurements, the fluctuation  $[\langle (\Delta R)^2 \rangle / R^2]_m$  would be  $\approx 10^{-4}$ . This is much larger than what we observe. This is because what we observe within our detection band width ( $f_{\min} = 10^{-3}$ Hz to  $f_{\max} = 1$  Hz) are those fluctuations that occur within the time scale  $1/2\pi f_{\max}$  sec  $< t$

$< 1/2\pi f_{\min}$  sec. Fluctuations outside this time window will not be recorded by us. Thus the experiment captures a small fraction of the total fluctuators. This is expected as stated above that the magnetization reversal and associated domain dynamics due to the stochastic nature can occur over a substantial time scale. The  $1/f$  nature of the power spectrum occurs from this long distribution of time scale. In the arrays that we are making measurements there are nearly 100 nanowires in parallel, each of which acts as an independent source. This leads to a distribution of the relaxation time and the  $1/f$  nature of the power spectrum.

## **6.5 Conclusions**

To summarize the results discussed so far:

1. We have observed low frequency resistance fluctuations for ferromagnetic nanowires with diameter ranging from 15 nm to 50  $\mu\text{m}$  in the temperature range 77-300 K and the spectral power density for 15 nm and 20 nm wires show substantial noise components at low frequency. The spectral power density for wires with diameter  $\geq 35$  nm shows perfect  $1/f$  noise throughout the whole experimental temperature range.
2. The presence of structural component responsible for noise in nanowire. All the nanowires except 35 nm are polycrystalline in nature. The noise in polycrystalline samples may come from diffusion of charge carriers through grain boundary and defects and give high noise magnitude than single crystalline wires.
3. We continued our investigations of resistance fluctuation in 35 nm single crystalline wire in presence of magnetic field. We found there are two main components namely, magnetic and nonmagnetic component in noise. The magnetic component can be suppressed with the application of external magnetic field while the nonmagnetic component remains intact. This nonmagnetic part of noise magnitude has a structural origin. The magnetic part is associated with domain wall resistance fluctuation through magnetoresistance and magnetization reversal mechanism.
4. Here we have carried out a systematic investigation in ferromagnetic metal nanowires with large variety of diameters and studied how the magnetic fluctuation couples to the resistance fluctuation in magnetic samples.

## Bibliography:

- [1] M. V. Kamalakar, A. K. Raychaudhuri, Phys. Rev. B **97**, 205417 (2009).
- [2] M. Venkata Kamalakar, Ph.D Thesis, S. N. Bose National Centre for Basic Sciences, Kolkata, India, 2009.
- [3] E.H. Frei, S. Shtrikman, D. Treves, Phys. Rev. **106**, 446 (1957).
- [4] A. Aharoni, S. Shtrikman, Phys. Rev. **109**, 1522 (1958).
- [5] R. Ferre' and K. Ounadjela, J. M. George, and L. Piraux and S. Dubois, Phys. Rev. B **56** 14066 (1997).
- [6] D. H. Qin, C. W. Wang, Q. Y. Sun, and H. L. Li, Appl. Phys. A **74**, 761 (2002).
- [7] A. J. Yin, J. Li, W. Jian, A. J. Bennett, and J. M. Xu, Appl. Phys. Lett. **79** 1039 (2001).
- [8] G. G. Cabrera and L. M. Falicov, Phys. Status Solidi B **61**, 539 (1974).
- [9] G.T.A. Huysmans, J.C. Lodder, J. Wakui, J. Appl. Phys. **64**, 2016 (1988).
- [10] P. M. Paulus, F. Luis, M. Kröll, G. Schmid, L. J. de Jongh, J. Mag. Mag. Mat. **224**, 180 (2001).
- [11] F. Tian, J. Zhu, and D. Wei, J. Phys. Chem. C **111**, 12669 (2007).
- [12] K. Neilsch, R. B. Wehrspohn, J. Barthel, J. Kirschner, U. Gösele U, S. F. Fischer, and H. Kronmüller, Appl. Phys. Lett. **79**, 1360 (2001).
- [13] D. J. Sellmyer, M. Zheng, and R. Skomski, J. Phys: Cond. Matter **13**, R433 (2001).
- [14] F. Tian, J. Zhu, and D. Wei, J. Phys. Chem. C **111**, 6994 (2007).
- [15] R. Ferré, K. Ounadjela, J. M. George, L. Piraux, and S. Dubois, Phys. Rev. B **56**, 14066 (1997).
- [16] Aveek Bid, Ph.D thesis, Indian Institute of Science, Bangalore, India (2006).
- [17] P. Dutta and P. M. Horn, Rev. Mod. Phys. **53**, 497 (1981).
- [18] H.-B. Braun, Phys. Rev. Lett. **71**, 3557 (1993).
- [19] J.E. Knowles, J. Magn. Magn. Mater. **61**, 121 (1986).
- [20] A. Aharoni, IEEE Trans. Magn. **22**, 478 (1986).
- [21] P. M. Paulus, F. Luis, M. Kröll, G. Schmid, L. J. de Jongh, J. Mag. Mag. Mat. **224**, 180 (2001).
- [22] Li Cheng-Zhang and J. C. Lodder, J. Magn. Magn. Mater. **88**, 236 (1990).
- [23] D. Atkinson, Dan A. Allwood, G. Xiong, M. D. Cooke, C. C. Faulkner, R. P. Cowburn, Nat. Phys. **2**, 85 (2003).
- [24] H. Yu, J. Li, R. A. Loomis, L. W. Wang, and W. E. Buhro, Nat. Mater. **2**, 517 (2003)
- [25] Aveek Bid, Achyut Bora, and A. K. Raychaudhuri, Phys. Rev. B **72**, 113415 (2005).
- [26] Aveek Bid, Achyut Bora, and A. K. Raychaudhuri, Nanotechnology **17**, 252 (2006).
- [27] R. Danneau, P. Warin, J. P. Attané, I. Petej, C. Beigné, C. Fermon, O. Klein, A. Marty, F. Ott, Y. Samson, and M. Viret, Phys. Rev. Lett. **88**, 157201 (2002).

# Chapter 7

## Concluding remarks and scope for future work

### 7.1 Conclusions

The focus of this dissertation was to study the noise spectroscopy in hole doped rare-earth perovskite manganites. We have extensively studied low frequency resistance fluctuations in two different perovskite systems in form of single crystals ( $\text{La}_{0.80}\text{Ca}_{0.20}\text{MnO}_3$ , LCMO20) and oriented films ( $\text{La}_{0.67}\text{Ca}_{0.33}\text{MnO}_3$  on  $\text{SrTiO}_3$ ) with different doping concentration of Ca. We have also studied a magnetic nanowire (nickel) system to study the “excess” noise due to magnetic origin. The systematic investigations in systems of three different verities enable us to understand the transport properties as well as the fundamental fluctuation dynamics related of these systems. In the final chapter we summarize some important observations of this dissertation, the deduction we draw from them and their significance with respect to other experimental and theoretical work. We also give an outline for future work, taking the present set of investigations to a better conclusion.

(1) The films of  $\text{La}_{0.67}\text{Ca}_{0.33}\text{MnO}_3$  (LCMO33) were grown on oriented single crystalline  $\text{SrTiO}_3$  substrate. The system showed a metal-insulator ( $T_p$ ) as well as paramagnetic-ferromagnetic ( $T_c$ ) transition. We extensively studied very low frequency fluctuation dynamics in this system and found the presence Lorentzian fluctuations riding over  $1/f$  noise. Generally, noise in polycrystalline samples comes predominantly from structural defects. Due to presence of strain relaxation along with quenched disorder the noise arose due to structural origin was very low. We were able to study noise coming from magnetic sources with the application of external magnetic field. We concluded that observed noise is appearing due to a coupling mechanism between resistance fluctuations with magnetization fluctuations through magnetoresistance.

(2) We extensively studied the ferromagnetic insulating state (FMI) of manganites in form of single crystals of composition  $\text{La}_{0.80}\text{Ca}_{0.20}\text{MnO}_3$  encompassing the electrical transport property in FMI state which follows Efros-Shklovskii variable range hopping. In such a lightly doped system at low temperatures electrons are localized and activation required for the use of charge carriers becomes very costly. The charge carriers are only within a narrow band of energies around the Fermi level participate in the conductivity and the conductivity is due to hopping between the two sites. With decreasing temperature the width of this band shrinks and hops become longer.

- ✓ In the disordered systems with highly localized electronic states will strongly influence the special distribution of electrons by long-ranged Coulomb repulsion between them. This leads to a depletion of the single particle density of states near the chemical potential known as Coulomb gap ( $\sim 152$  meV) near Fermi energy.
- ✓ We experimentally verified the non-linear conduction phenomena in FMI state.

- ✓ In context of non-linear conduction effect we have explained our results with “hot electron model”. There exists a weak thermal conductance coupling between electron-phonon systems in FMI state. This weak coupling defines two different temperature scales, one for electron and other for phonon bath. We found that the electronic system actually gets decoupled from its phonon bath with the increasing electrical power. As a result the electron bath is getting heated and driven out of equilibrium of its phonon bath. We estimated the rise of electronic temperature ( $T_e$ ) above its phonon temperature ( $T_{ph}$ ) by hot-electron model.
- ✓ We observed colossal electroresistance as a manifestation of non-linear conductance in these systems and found it reaches nearly 100% in FMI state.

(3) We experimentally established that LCMO20 sample becomes an electron glass system in FMI phase and due to long range Coulomb interactions between the charge carriers. System appears to be a Coulomb glass. By ac noise spectroscopy we investigated the charge fluctuation dynamics in such glassy systems.

(4) By the extensive investigations on noise spectroscopy we found rapid fall of the noise below  $T_{FMI}$  which we taken as a signature of kinetic freezing of the charge fluctuations. Our experimental results are supported by the theoretical results as well. The investigation regarding the kinetic freezing using resistance fluctuation process is not been reported earlier. This is the first time we have investigated such effects in FMI phase of manganites.

(5) We found that the charge fluctuation is activated across the Coulomb gap. The activation energy according to Arrhenius model gives  $E_a \sim 163$  meV which is same with Coulomb gap energy. Two independent set of experiments found the same energy values which is very consistent.

(6) We also studied “white” noise spectroscopy using ac biasing technique in presence of dc bias in LCMO20. We observed the increases of this white noise with increase of the dc bias. We experimentally demonstrated that with the injection of dc bias in the system, there is a marked increase of  $T_e$  over  $T_{ph}$ . We found a critical power above which  $T_e$  becomes  $> T_{ph}$  and the systems falls out of equilibrium and becomes nonergodic. Hence in this case, by entering into the FMI state, the Fluctuation Dissipation Theorem (FDT) breaks down.

(7) We studied fluctuation spectroscopy in single crystalline nickel nanowires with diameter 35 nm. In such magnetic systems one possibility of low frequency noise is because of magnetic fluctuations originating from domain wall dynamics. As domain walls contribute a finite resistance to the sample, the fluctuations in domain walls couple to the resistance fluctuations through magnetoresistance (MR). The low frequency noise in nanowire systems can have structural origin. As the sample is very good single crystalline in nature, the structural noise is relatively low and we can separate out the noise components coming from magnetic and non-magnetic origins. We studied noise due to the magnetization fluctuations in such systems in presence of low external magnetic field  $\approx 0.12$  Tesla.

## **7.2 Scope for further investigations**

The noise spectroscopy is a sensitive and non-destructive tool to investigate the fundamental kinetic processes of any system. So there are lots of new problems which can be looked into by noise spectroscopy. We want to mention some of those possibilities as an extension of our work presented in this dissertation as:

- ❖ We investigated noise in thick oriented films of LCMO33 where strain is relaxed within the film. But there is lack of systematic investigation in thin / ultra-thin films where strain plays an important role by tuning the transport and magnetic properties of the system. By using different substrates and varying thickness one can investigate noise phenomena in them. We suggest that the presence of noise other than  $1/f$  noise can be more informative one which can be investigated. The transition regions need more attention.
- ❖ The hysteresis and reversible polarity-dependent resistive switching effect can be studied in thin films varying dc bias stress, voltage stress or by pulsed voltage amplitude and duration. In such systems one can study noise phenomena by varying above parameters.
- ❖ Nanowires of complex oxides can be fabricated as Field Effect Transistors (FET) structures. Low frequency noise can be investigated by varying drain current. We expect that in such systems we can observe RTN attributed to correlated carrier number and mobility fluctuations. This will be a very interesting problem can be further looked into.
- ❖ We studied MR and magnetization fluctuation phenomena in arrays of magnetic nanowire systems at very low field. But noise spectroscopy on a single magnetic nanowire is completely unexplored problem. One can study the noise spectroscopy with the application of high external magnetic field. It will give a better understanding for the origin of magnetic noise coming from domain wall resistance.
- ❖ The study of temperature dependent current induced resistive switching by injecting dc current pulses in LCMO20 samples need to be investigated.
- ❖ The photoconductivity and low temperature scanning tunnelling microscopy can be helpful to find out the possible presence of electronic and magnetic inhomogeneity in the sample.
- ❖ We have studied “white” noise spectroscopy in FMI state of manganites. One has to search for a suitable theoretical model which can do an estimation of the electronic temperature from white noise spectroscopy.
- ❖ The noise spectroscopy should be done in epitaxial thin films of the same composition LCMO20. The non-linear conductance and related phenomena which we studied in single crystals can be investigated as a function of strain effect. One can also demonstrate the validation of hot-electron effect in strain induced films.